Spectroscopy of Polymers

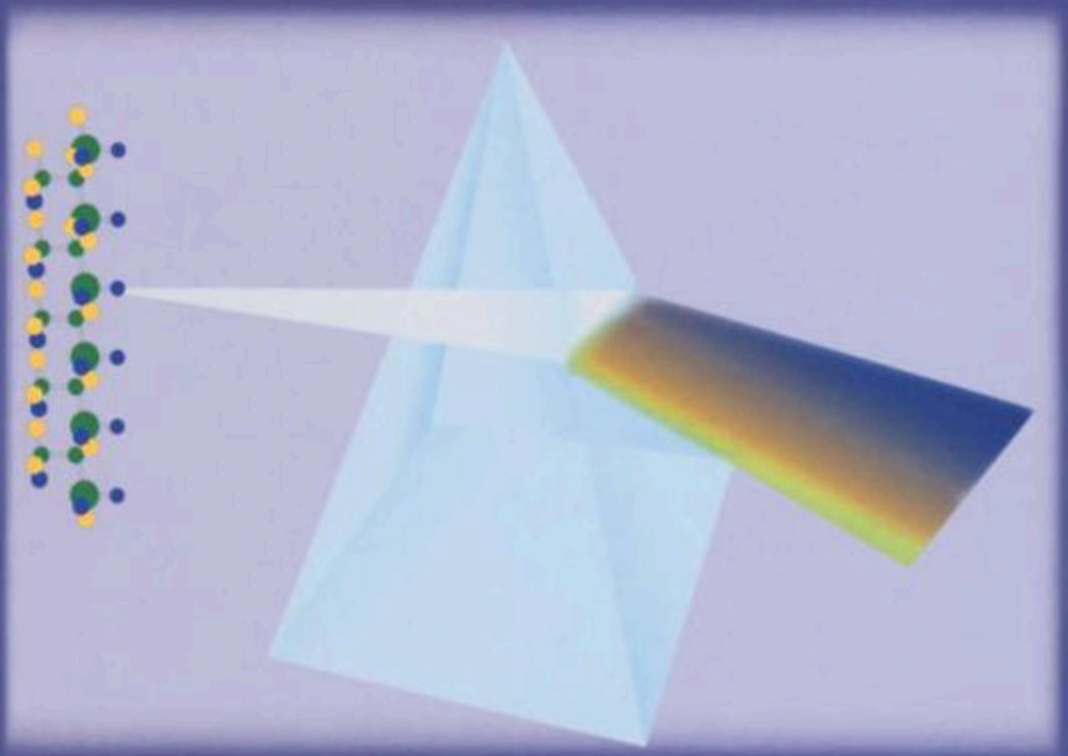

Jack L. Koenig

Second Edition

ELSEVIER SCIENCE Inc.
655 Avenue of the Americas
New York, NY 10010, USA

First edition 1999
Library of Congress Cataloging in Publication Data
A catalog record from the Library of Congress has been applied for.

ISBN: 0-444-10031-8

♾ The paper used in this publication meets the requirements of ANSI/NISO Z39.48-1992 (Permanence of Paper).

Printed in The Netherlands

Contents

Preface to the second edition

How time flies! How rapidly things change! It is hard to believe that the first edition of *Spectroscopy of Polymers* is not only out of date but also out of print. Therefore, I took the opportunity to rewrite major sections of the book in an effort to bring in the large number of recent advances in the spectroscopy of polymers. The challenges of characterizing the molecular structure of synthetic polymers continue to grow as the polymer chemists for a broad range of new materials applications are synthesizing exciting new structures.

The first chapter on the theory of polymer characterization is essentially unchanged with only minor editions and tightening of some of the text. The second chapter has been substantially modified to include both Raman and Infrared in the description of the molecular basis of vibrational spectroscopy. This makes for a more consistent approach and will better guide the student to the more subtle differences in the applications of the two complementary methods of vibrational spectroscopy. The chapter on infrared instrumentation and sampling techniques has been modified to include innovations in instrumentation such as step-scan and focal array detector imaging interferometers. The sections in this chapter on data processing and quantitative analysis have been updated to reflect the major impact in this field of fast computers with large memories. The chapter on applications of infrared has been updated by including some of the new developments in the continuing astronomical growth in the applications of infrared to polymers. It is possible to include only a small number of the numerous new examples that are available and those selected were based on the utility as pedagogical examples for the student.

Raman spectroscopy has become a most important tool for characterization of polymers as low frequency lasers have improved so Raman spectroscopy excited in the infrared frequency range can be used to minimize the effect of fluorescence. Advances in Raman instrumentation have been dramatic and the polymer spectroscopists must now seriously consider the use of Raman as complementary to infrared. In many cases Raman spectroscopy will be the preferred method as the many new applications in this revised chapter illustrate.

Advances in solution NMR arise from the greater availability of high field instruments and the fast computers with large memories. The higher applied magnetic field results in greater dispersion so the resolution is higher and the information content is extended as longer stereo and comonomer sequences are observed. The improved computers allow the complex computational problems associated with two-dimensional techniques to be overcome so the multidimensional NMR techniques are available to the ordinary user. The spectral editing chapter of the first edition has been incorporated in this chapter. The applications of solution NMR chapter has been expanded to reflect the advances made using the higher applied magnetic field. A large number of new chemical structures are resolved including endgroups, branches, crosslinks and stereosequences.

The utility of solid state NMR continues to grow. Many new applications, particularly those based on motional differences of the phases, are developing, as experiments are easier to do with better spinners and decoupling methods.

The final chapter is an entirely new one describing mass spectrometry and its increasing importance in polymer characterization. Vaporization and ionization techniques are being developed that make macromolecules fly with little fragmentation. Therefore, the advantages of short measurement and analysis times make mass spectrometry an important tool in polymer characterization. I wish to thank Robert Latimer of B.F. Goodrich for introducing me to the potential of the technique and for kindly making a number of valuable suggestions on the manuscript.

I want to thank my professional colleagues and those many students from around the world that have made comments on the first edition of the *Spectroscopy of Polymers*. I have made an effort to incorporate many of the constructive suggestions in the second edition.

I want to thank Barbara Leach and June Ilhan for their efforts in turning rough text and figures into a readable manuscript and pursing all of the innumerable details associated with production of a second edition.

Again, I want to thank my wife, Jeanus, for her giving up time that we would ordinarily share together for me to work on the book. Her constant support is appreciated.

Finally, it is unusual to have a second edition of a book published by a different publisher. The first edition was published by ACS publications. However, ACS decided not to publish monographs any longer and kindly released the copyright of the first edition to me. Elsevier has agreed to publish the second edition. Jonathan Glover was instrumental in making the selection of Elsevier as the publisher and I thank him for his efforts.

Chapter 1

Theory of polymer characterization

The primary motivation for determining the molecular structure of a polymer chain is to relate the structures to the performance properties of the polymer in end use. If the polymer chains are completely characterized and the structural basis of its properties are known, the polymerization reaction can be optimized and controlled to produce the optimum properties from the particular chemical system.

Elements of polymer structure

The following basic terms are used for defining a polymer structure.

- The *composition* (or *constitution*) of a molecule defines the nature of the atoms and the type of bonding irrespective of the spatial arrangement.
- The *configuration* of chemical groups characterizes the chemical state of a polymer. Different configurations constitute different chemical entities and cannot be interconverted into one another without rupture of chemical bonds.
- The *conformation* of chemical groups characterizes the geometrical state of a polymer. Different conformations of a polymer can be produced by rotation about single bonds without rupture of chemical bonds. Changes in conformation arise from physical considerations such as temperature, pressure, or stress and strain.

Polymer chains are made up of sequences of chemical repeating units that may be arranged regularly or irregularly on the backbone.

- The chemical *microstructure* is defined as the internal arrangement of the different chemical structures or sequences on the polymer chain.

Polymers can exhibit phase transitions and show a number of fundamental spatial distributed macroconformations that define the crystalline and amorphous phases.

- The polymer *morphology* defines the intermolecular packing of the polymer molecules as crystals or spherulites in the bulk.
- Polymer chains can exhibit different chain topologies where topology describes the molecular packing of the chains. Chain alignments, orientation and entanglements are topologic features.

The mechanical properties such as modulus, tenacity, and yield are properties which depend on the dynamics of the polymer chain.

- The *molecular motion* depends on the intramolecular and intermolecular constraints imposed on the structure of the chain and the non-bonded neighbors in the vicinity.

From a structural point of view polymers are chainlike molecules.

X–A–A–A–A–A–A–A–A–A–A–A–A–A–A–A–A–Y

The structural elements of an *ideal* polymer molecule with a single structural repeating unit can be represented by the molecular formula, $X(A)_nY$, where A represents the repeating unit of the polymer molecule and n is the number of repeating units of A, X and Y are the end-group units which are chemically different from A. The number of connected repeating units, n, can range from 2 to greater than 100,000. The chemical nature of the repeating unit A determines the chemical properties of the polymer. The chemical structure of the repeating unit can be very simple (e.g., CH_2 for polyethylene) or very complicated.

The end-group units X and Y can be substantially different in chemical structure from A or very similar depending on the nature of the polymerization process.

Structural variations within the chain can be represented by the letters B, C, etc., to indicate the differences in the chemical, configurational, or conformational structure.

The polymerization reaction converts the initial bifunctional monomers into a chain of chemically connected repeating units. The process of polymerization can be written in the following form:

$$nM \rightarrow (-A-A-A-A-\cdots\cdots-A)_n \tag{1.1}$$

where M is the monomer. We have neglected for the moment the fact that the end groups X and Y are different structures from A.

However, this representation of the ideal polymerization reaction is incomplete, as the polymerization reaction is statistical in nature and does not generate a single molecule of a specified length n. Rather millions of polymerization reactions are occurring simultaneously, generating millions of molecules of various lengths ranging from 1 to a very large number (e.g., 100,000) depending on how many reactions have occurred between the individual molecules during the polymerization. So more precisely, the polymerization reaction must be written

$$\sum_{n=2}^{n=\infty} nM \rightarrow \sum_{n=2}^{n=\infty} (-A-A-A-A-\cdots\cdots-A)_n \tag{1.2}$$

Thus, in contrast to chemistry of simple molecules, which produce a single molecular

species, the polymerization batch contains a mixture of chain molecules ranging in length from very short to very long. For this simple ideal polymer system, the only structural variables are the lengths n of the chains and the number of molecules of these various lengths $N(n)$. In other words, to determine the structure of the polymer we need to know the number fractions of molecules having different specific lengths.

Approach to polymer structure determination using probability considerations

Let us start with the simplest structural example: the degree of polymerization (DP). With the polymerization model just described, and assuming an equal likelihood for the selection of any polymer molecule from the mixture, it is possible to calculate the *probability distribution function for the chain length n*. The probability distribution function for n is the probability of finding a molecule with a given chain length n in a polymer sample. For experimental purposes, the probability function is the fraction of all polymer molecules that possess the stated chain length, n.

> *You can visualize the probability approach as one of reaching into the reaction mixture and pulling out a single polymer molecule. You must then calculate the probability that the molecule selected has a specified length.*

Let P be the probability that a propagation polymerization reaction has occurred and Q be the probability of termination; that is, the molecule has not undergone propagation and is terminated from further polymerization. This is a simple description of an ideal simple chain/addition polymerization (a chain reaction in which the growth of a polymer chain proceeds exclusively by reactions between monomers and reactive sites on the polymer chain with regeneration of the reactive sites at the end of each growth step). This is illustrated in the following diagram:

Polymerization	Event	Probability
Propagation	$\sim A_n^* + A \rightarrow A_{n+1}^*$	P
Termination	$\sim A_n^* \rightarrow A_n$	Q

The instantaneous probability of propagation, P, in this case, is given by

$$P = \frac{\text{Number of propagation events}}{\text{Total number of events}} = \frac{\text{Rate of propagation}}{\text{Rate of propagation} + \text{Rate of termination}}$$

For termination

$$Q = \frac{\text{Number of termination events}}{\text{Total number of events}} = \frac{\text{Rate of termination}}{\text{Rate of propagation} + \text{Rate of termination}}$$

We will make the Flory assumption that the probabilities of propagation and termination are independent of chain length. We will also neglect the contribution of the initiation reaction, in other words, we will assume a high molecular weight chain and the contribution of the initiation can be neglected.

There are only two events occurring, propagation and termination, so for completeness (something must happen) it is necessary that

$$P + Q = 1$$

so

$$Q = 1 - P$$

Let $P(n)$ be the probability that a molecule of length n has been formed. At any given instant of the polymerization process, the probability that a chain will propagate and terminate to give a length n is the product of the probability of the individual propagation steps and the probability of termination at that chain length. If the propagation polymerization probabilities are independent (i.e., occur randomly and do not depend on chain length), the probability of forming a molecule of length n = 2 is the probability P that one propagation reaction coupling two monomer units has occurred times the probability Q $(= 1 - P)$ that termination or no further reaction has occurred. Hence,

$$\begin{array}{lcccc} & P & (1-P) & \text{Product} & \\ P(2) = P(1-P) & \text{A}^* \rightarrow \text{A–A}^* & \rightarrow \text{A–A} & \text{A}_2 & (1.3) \end{array}$$

A chain molecule of $n = 3$ is formed by two propagations and a termination; the probability of the first propagation, P, times the probability of the second propagation, P, forming the trimer times the probability of termination, $(1 - P)$, or that no reaction has occurred. Hence,

$$\begin{array}{lccccc} & P & P & (1-P) & \text{Product} & \\ P(3) = P^2(1-P) & \text{A}^* \rightarrow \text{A–A}^* & \rightarrow \text{A–A–A}^* & \rightarrow \text{AAA} & \text{A}_3 & (1.4) \end{array}$$

A chain molecule of $n = 4$ is formed by three propagations, P3, and a termination. So

$$\begin{array}{lccccccc} & P & P & P & (1-P) & & \text{Product} & \\ P(4) = P^3(1-P) & \text{A}^* \rightarrow \text{A–A}^* & \rightarrow \text{A–A–A}^* & \rightarrow \text{AAA}^* & \rightarrow \text{AAAA} & & \text{A}_4 & \\ & & & & & & & (1.5) \end{array}$$

A general trend is emerging. The number of propagations is always one less than the length of the chain and one termination step is always required, so the general formulation for any chain length n can be written

$$\begin{array}{lcccccccc} & P & P & P & P & P^{n-1} & (1-P) & \text{Product} & \\ P(n) = P^{n-1}(1-P) & \text{A}^* \rightarrow & \rightarrow & \rightarrow & \rightarrow & \cdots\cdots \text{A}_n^* & \rightarrow \text{A}_n & \text{A}_n & (1.6) \end{array}$$

Equation (1.6) is the probability distribution function for the structural parameter of interest, which in this case, is the chain length n of the polymer. From the probability distribution function for n, any desired information or property arising from the chain-length distribution of the system can be obtained by appropriate mathematical calculations. In this case, we can calculate the molecular weight averages and distributions. Inversely, and equally important from our perspective, experimental determinations of the molecular weights and molecular-weight distributions allow a determination of the probability of propagation, P, which is the characteristic quantity controlling the ideal polymerization process we are using as a model in this case. More complicated polymerization models lead to different probability distribution functions as we will see.

These chain-length probabilities must sum to 1 (i.e., the complete condition, meaning that something must happen):

$$\sum_{n=1}^{\infty} P(n) = 1 \tag{1.7}$$

because n must have some value between 1 and infinity. This relationship indicates that the individual $P(n)$ are simply the number fraction of individual molecules in the mixture:

$$P(n) = \frac{N_n}{N} \tag{1.8}$$

where N_n is the number of molecules of length n, and N is the total number of polymer molecules in the polymerization batch.

Structure calculations using the probability distribution function

A simple example: degree of polymerization [1]

The structural variable in this case is the length of the polymer chain or the degree of polymerization, DP, defined as the number of similar structural units linked together to form the polymer molecule. This number is converted to molecular weight by multiplying by the molecular weight of a single structural or repeating unit. Measurement of the molecular weight of the polymer system by any physical means yields numbers representing the weighted averages of the DPs of all the molecules present.

A colligative property measures the number of molecules in solution. A colligative property measurement, for example, osmotic pressure, freezing-point depression,

boiling-point elevation, or vapor pressure lowering, of a polymer solution yields a 'number-average' DP or molecular weight (simply by multiplying by the molecular weight of a single repeating unit). The effective DP measured is the sum of the DPs of all the molecules divided by the number of molecules present.

$$\overline{\mathrm{DP}}_n = \frac{1N_1 + 2N_2 + 3N_3 + 4N_4 + \cdots}{N_1 + N_2 + N_3 + N_4 + \cdots} \tag{1.9}$$

$$\overline{\mathrm{DP}} = \frac{\sum nN_n}{\sum N_n} \tag{1.10}$$

where N_n is the number of molecules present whose DP is n. The $N_n = N$ is the total number of molecules in the system. The number of molecules having a specific length N_n corresponds to the probability of finding molecules of this length multiplied by the total number of molecules

$$N_n = NP(n) = NP^{n-1}(1 - P) \tag{1.11}$$

Substituting Eq. (1.11) in Eq. (1.10) yields

$$\overline{\mathrm{DP}} = \frac{\sum nNP(n)}{N} \tag{1.12}$$

Substituting for $P(n)$

$$\overline{\mathrm{DP}} = \sum nP^{n-1}(1 - P) = \frac{1}{(1 - P)} \tag{1.13}$$

Equation (1.13) demonstrates that a measurement of the average degree of polymerization, $\overline{\mathrm{DP}}$, allows a determination of the probability of propagation for this model of chain polymerization. The $\overline{\mathrm{DP}}$ can also be written

$$\overline{\mathrm{DP}} = \frac{N_0}{N} = \frac{1}{(1 - P)} \tag{1.14}$$

where N_0 is the number of monomer units at the start of the polymerization, so

$$N = N_0(1 - P) \tag{1.15}$$

Therefore, the *number distribution function* can be written

$$N_n = N_0(1 - P)^2 P^{n-1} \tag{1.16}$$

The number distribution function is plotted in Fig. 1.1.

With knowledge of P, the derived probability distribution function can be used to calculate the other parameters of the polymerization, including the various types of average molecular weights such as the weight and z average and the moments of the molecular-weight distribution. For this simple ideal polymerization model, a determination of P is all that is required for a complete structural evaluation because the only structural variable is the length of the chains.

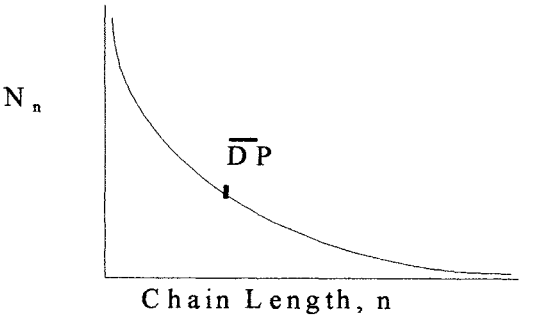

Fig. 1.1 The number distribution function as a function of chain length.

Number-average molecular weights

For a monodisperse system, the *molecular weight* is given by

$$M_n = \frac{W}{N} \tag{1.17}$$

where W is the weight of the sample in grams and N is the number of molecules. For a polydispersed system,

$$W = \sum N_n M_n \tag{1.18}$$

and

$$N = \sum N_n \tag{1.19}$$

so the *number-average molecular weight* is given by

$$\overline{M}_n = \frac{\sum_{n=0}^{\infty} N_n M_n}{\sum_{n=0}^{\infty} N_n} \tag{1.20}$$

The number-average molecular weight is an average based on the number of molecules, N_n, of a particular size, M_n, taken over the total number of molecules. This definition of the number-average molecular weight in grams contains Avogadro's number of molecules and on this basis is entirely consistent with the definition of molecular weight for a monodisperse molecular species.

Now, for a single repeating unit, it is obvious that

$$M_n = nM_0 \tag{1.21}$$

where M_0 is the molecular weight of the repeating unit. The number distribution function can be used in these equations to calculate $\overline{M}_n$ in terms of the probability of

condensation, P,

$$\overline{M}_n = \frac{M_0}{1 - P} \tag{1.22}$$

Note that the number-average molecular weight is the molecular weight of the repeating unit divided by the probability of termination, $(1 - P)$. So a determination of $\overline{M}_n$ yields an evaluation of P, the probability of propagation for this simple model.

Weight-average molecular weight measurements

Averaging on the basis of weight fractions, w_n, of molecules of a given mass, M_n, gives a description of the weight-average molecular weight. For example, with light-scattering measurements of polymer solutions, the effect is proportional to the molecular weight of the molecules in solution, so a weight-average molecular weight is measured. The weight-average molecular weight is given by

$$\overline{M}_w = \frac{\sum_{n=0}^{\infty} w_n N_n}{\sum_{n=0}^{\infty} w_n} = \frac{\sum_{n=0}^{\infty} N_n M_n^2}{\sum_{n=0}^{\infty} N_n M_n} \tag{1.23}$$

In Fig. 1.2 is shown the wt% of molecules of n length versus molecular weight. $\overline{M}_w$ is shown as the maximum on the curve.

It is apparent then that

$$\sum_{n=0}^{\infty} w_n = W \qquad w_n = nM_0N_0 \tag{1.24}$$

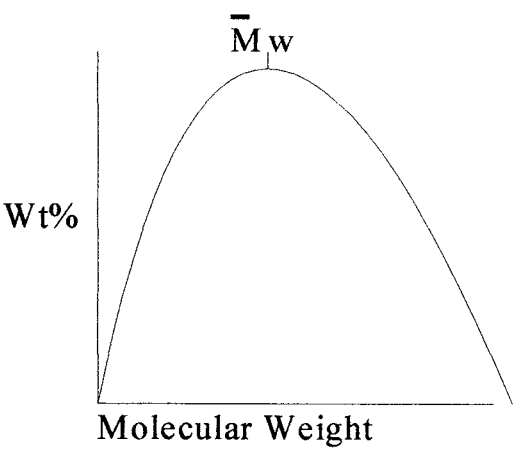

Fig. 1.2. The weight-fraction molecular weight distribution as a function of molecular weight.

$$W = M_0 N_0 \tag{1.25}$$

Substitution and evaluation reveals

$$\overline{M}_w = \frac{M_0(1 - P)}{1 - p} \tag{1.26}$$

With this equation, from a measurement of the weight-average molecular weight, the probability of propagation, P, can be determined.

Distributions of molecular weight

The distributions of molecular weight that can be measured with gel permeation chromatography and sedimentation can also be calculated for the simple model given, and in fact correspond to the molecular distribution functions previously described. Moment analysis is commonly used to characterize the distributions, where in our case the first moment is the number-average molecular weight, $\overline{M}_n$; the second moment is the weight-average molecular weight, $\overline{M}_w$; and the third moment is the $\overline{M}_z$, the z-average molecular weight. The ratio of the weight-average to number-average molecular weights is termed the *dispersity*.

It can be recalled from Eq. (1.6) that $P(n) = (1 - P)P^{n-1}$; then one can write

$$\frac{\mathrm{d}[P(n)]}{\mathrm{d}n} = \ln P \tag{1.27}$$

This indicates that a plot of ln chain length distribution [ln $P(n)$] vs. n should give a straight line with slope ln P [12].

Chemical heterogeneity in the polymer chain

Consider a copolymer chain with only two different structural elements, A and B; the number of different chain species possible is 2n, where n is the polymerization index or the number of units in the chain, whichever is greater. The value of n is generally a large number, >10,000. Consequently, the number of different possible chemical structures is enormous. There is no point in trying to completely define the spatial coordinates of the atoms with such a large number of possible structures. To make matters even worse, most real synthetic polymers have more than two different structural elements in the same chain, so the possible number of structures is even larger.

Some of the possible structural variables found in synthetic polymers are as follows:

- *chain length:* molar mass of polymer chain reflecting variations in number of repeating units in the chain;
- *chemical defects:* impurities in feed, monomer isomerization, and side reactions;
- *enchainment defects:* positional, stereospecific, branches, and cyclic isomers;
- *chain conformations:* stiff ordered chains and flexible amorphous chains;
- *morphological effects:* crystal phases, interfacial regions, and entanglements.

This list of structural possibilities is long, and some polymers exhibit a number of these structural variables simultaneously. Hence the total number of possible structures for a single chain is very large, indeed.

The problem is further complicated by the fact that synthetic polymers exhibit chemical heterogeneity along the chain. Chemical heterogeneity reflects the distribution of the structural entities in the chain. The nature of the chemical heterogeneity influences the ultimate properties of the polymer as it produces heterogeneity in the molecular mobility of the chains.

Let us consider the case of a copolymer of two monomer units A and B. A simple copolymerization model is represented by the following reactions and their corresponding rates in terms of kinetic rate constants and concentrations of reacting species:

Terminal group	Added group	Rate	Final group
$\sim A^*$	[A]	$k_{AA}[A^*][A]$	AA^*
$\sim B^*$	[A]	$k_{BA}[B^*][A]$	BA^*
$\sim A^*$	[B]	$k_{AB}[A^*][B]$	AB^*
$\sim B^*$	[B]	$k_{BB}[B^*][B]$	BB^*

where A^* and B^* are the propagating terminal species. The amount and type of chemical heterogeneity of the copolymer chain is determined by the relative chemical reactivity of the monomers A and B with the propagating terminal groups $\sim A^*$ and B^* (more about this later in the chapter).

The systematic types of distributions of structural elements that can occur are as follows:

Type	Nature of polymerization process
Random	No chemical correlation
Skewed toward alternation	A−B chemical correlation
Skewed toward blockiness	A−A or B−B chemical correlation
Block $(A)_N-(B)_M$	A−A followed by B−B chemical correlation by change of monomers
Alternating $[(A)_1-(B)_1]_n$	Exclusive A−B chemical correlation
Irregular	Fluctuations in process variables

These structural distributions are determined by the nature of the polymerization process; that is, the random distributions arise from a copolymerization which shows no differences in chemical reactivity between the chemical monomers A and B and the growing chain ends A^* and B^*. The skewed toward alternation sequence distributions are nonrandom systematic structures determined by differences in chemical reactivity between the chemical monomers A and B and the growing chain ends A^* and B^*. The block structure is produced by chemical design (monomer feed)

of the polymerization process in which monomer A polymerizes to depletion and monomer B is added. The alternating ordered distribution can only be obtained when monomer A does not react with A* and B with B*. The irregular distribution reflects the nonstationarity of the polymerization process arising from fluctuations in the polymerization process variables such as temperature, pressure, flow, monomer feed, etc.

The chemical sequence heterogeneity influences the characterization of the polymer in two ways:

(1) The chain structure is highly variable because the polymerization process is a statistical process determined by probability considerations. Thus, polymer samples are always multicomponent complex structural mixtures as well as made up of different chain lengths.

(2) Detailed molecular pictures of the structure are not possible because our experimental measurements are going to provide only some weighted average structure which depends on the nature of the response of the measurement technique.

Characterization of polymer microstructure [3]

Structural model of the polymer chain

For a microstructural model of the polymer chain, we use a model made up of connected repeating units of similar or different structures. Letters A and B designate the different structural types of the repeating units.

The microstructure of the chains are structurally presented as sequences of similar or different units, that is A, AA, AAA, B, BB, BBB, AB, AAB, BBB, etc. Additional structural components can be indicated by the use of additional letters, C, D, E, and so forth. The application of this model to copolymers A and B and terpolymers A, B, and C is obvious. Positional, conformation, and configurational isomerism as well as branching and crosslinking are considered as copolymer analogs although they are not generated by copolymerization.

In polymer characterization, the goal is to generate the structural sequence distribution function of the polymer chain in order to calculate the structurally significant information, which represents the chain and can be used to correlate with the performance properties of the system.

Our aims are:

- *to relate these average sequence structures to the performance properties of the polymer under consideration, and*
- *to seek the polymerization mechanism and parameters that generate the sequence structure in order to optimize and control the polymer structure.*

For simplicity, we begin with the experimental measurements that are possible on the microstructure of a polymer chain made up of only two structures, A and B. The following is a portion of such a chain:

Sample copolymer chain

−A−B−B−A−B−B−B−A−B−A−
1 2 3 4 5 6 7 8 9 10

which is a chain of 10 repeating units made of A and B. We assume that this portion of the chain is representative of the complete chain.

In mathematical terms, this assumption is called the stationary condition, that is, the distribution of the two structural elements of the chain does not change as the polymerization proceeds. We could have selected any length of segment that we desired, but the counting process becomes tedious if the segment is too long, and we cannot demonstrate the various points if the chain is too short.

Again for simplicity, we also assume that the molecular weights are sufficiently large so that the end groups need not be taken into consideration.

Measurement of polymer structure using composition

If spectroscopically we have infinite structural resolution or the ability to detect the differences between the two structural elements A and B, we can measure the individual number of A and B structural elements in the polymer. That is, we can count the relative number of A and B elements taken one at a time, which we will term mono-ads or 1-ads and write $N_1(\mathrm{A})$ as the number of mono-ads of A. Using the perfect resolution of the human eye, in this case for the model copolymer segment shown previously, the number of the two types of mono-ads are

$$N_1(A) = 4 \qquad N_1(B) = 6 \tag{1.28}$$

Spectroscopically, the number of mono-ads cannot actually be counted, but the fraction of units in the chain can be measured. This result can be expressed in terms of the experimental number fraction for mono-ads $\langle \mathrm{A} \rangle$ and $\langle \mathrm{B} \rangle$ by dividing by the total number of segments ($N = 10$). So

$$\langle \mathrm{A} \rangle = \frac{N_\mathrm{A}}{N} \qquad \langle \mathrm{B} \rangle = \frac{N_\mathrm{B}}{N} \tag{1.29}$$

and for our model copolymer system

$$\langle \mathrm{A} \rangle = \frac{N_\mathrm{A}}{N} = \frac{4}{10} = 0.4 \qquad \langle \mathrm{B} \rangle = \frac{N_\mathrm{B}}{N} = \frac{6}{10} = 0.6 \tag{1.30}$$

This result, ⟨A⟩ or ⟨B⟩, is the fractional composition in terms of A and B units of the polymer when we assume that the 10-segment portion of the polymer is representative of the total chain. Also,

$$\langle A\rangle + \langle B\rangle = 1 \tag{1.31}$$

as is required because for our model copolymer only A and B repeating units are allowed (end groups are ignored as the molecular weight is assumed to be large).

Measurement of polymer structure using dyad units

Chain A−B−B−A−B−B−B−A−B−A−|−A−next sequence

Dyads AB−BB−BA−AB−BB−BB−BA−AB−BA−AA−

On a slightly more sophisticated level, we can analyze this 10-unit segment by counting sequences two at a time, that is, counting the number of dyads (2-ads) in the chain. The final AA dyad arises because the adjacent segment that is identical to this segment starts with A. There are four possible types of dyads, AA, BB, AB, and BA, and for this chain

$N_2(\mathrm{AA}) = 1$
$N_2(\mathrm{BB}) = 3$
$N_2(\mathrm{AB}) = 3$
$N_2(\mathrm{BA}) = 3$

Can we truly experimentally distinguish between the heterodyads AB and BA? In this particular case they are differentiated with our eyes by the direction of the counting (left to right), but what if the chain segment were reversed? The AB dyads would become BA dyads and vice versa. Which direction of the chain is the proper one? Clearly, both directions are equally likely, and we will never know from examination of the final polymer chain in which direction it grew during the polymerization. Therefore, AB and BA are equally likely outcomes and so [4]

$$N_2(\mathrm{AB}) = N_2(\mathrm{BA}) \tag{1.32}$$

The equality saves the day for spectroscopic measurements, because no known method of spectroscopic measurement can distinguish between AB and BA, and so from a spectroscopic point of view they are indistinguishable.

Consequently any practical experimental measurement of the AB dyad units measures the sum $N_2(\mathrm{AB}) + N_2(\mathrm{BA})$, which we will designate as:

$$N(\overline{\mathrm{AB}}) = N_2(\mathrm{AB}) + N_2(\mathrm{BA}) \tag{1.33}$$

The experimental number fraction of each dyad ⟨AA⟩, ⟨BB⟩ and $\langle\overline{AB}\rangle$ can be determined by using N_2 (total) = 10.

$$\langle AA\rangle = \frac{N_2(AA)}{N} \tag{1.34}$$

$$\langle BB\rangle = \frac{N_2(BB)}{N} \tag{1.35}$$

$$\langle\overline{AB}\rangle = \frac{N_2(AB)}{N} + \frac{N_2(BA)}{N} \tag{1.36}$$

For our 10-segment polymer chain

$$\langle AA\rangle = \frac{N_2(AA)}{N} = 0.1 \tag{1.37}$$

$$\langle BB\rangle = \frac{N_2(BB)}{N} = 0.3 \tag{1.38}$$

$$\langle\overline{AB}\rangle = \frac{N_2(AB)}{N} + \frac{N_2(BA)}{N} = 0.6 \tag{1.39}$$

The experimental completeness condition is

$$\langle AA\rangle + \langle AB\rangle + \langle BA\rangle + \langle BB\rangle = 1 \tag{1.40}$$

is satisfied. Or, in terms that can be measured spectroscopically

$$\langle AA\rangle + \langle\overline{AB}\rangle + \langle BB\rangle = 1 \tag{1.41}$$

Measurement of polymer structure using triad segments

We can now proceed to dissect the polymer structure in terms of higher n-mers in spite of the fact that we might introduce a certain amount of boredom with the process. Let us determine the structure of the polymer chain in terms of triads or 3-ads, that is, counting the units as threes. For triads, there are a total of eight possible structures.

Chain A–B–B–A–B–B–B–A–B–A–|–A–B–next sequence

Triads –ABB–BBA–BAB–ABB–BBB–BBA–BAB–ABA–BAA–AAB–

Once again, the final two triads are recognized by the adjoining segment that corresponds to the first two units in the beginning of this segment. Well, how many do

we have?

$$\begin{aligned} N_3(\text{AAA}) &= 0 \\ N_3(\text{AAB}) &= 1 \\ N_3(\text{ABA}) &= 1 \\ N_3(\text{BAA}) &= 1 \\ N_3(\text{ABB}) &= 2 \\ N_3(\text{BBA}) &= 2 \\ N_3(\text{BAB}) &= 2 \\ N_3(\text{BBB}) &= 1 \\ \text{with } N_3(\text{total}) &= 10. \end{aligned}$$

The two 'reversibility relations' for the triads are

$$N_3(\text{AAB}) = N_3(\text{BAA}) \quad \text{and} \quad N_3(\text{BAA}) = N_3(\text{BAA}) \tag{1.42}$$

and the completeness condition is satisfied representing the sum of all of the triads. We can now calculate the number fraction of each triad

$$\begin{aligned} \langle \text{AAA} \rangle &= 0.0 \\ \langle \overline{\text{AAB}} \rangle &= 0.2 \\ \langle \text{ABA} \rangle &= 0.1 \\ \langle \overline{\text{BBA}} \rangle &= 0.4 \\ \langle \text{BAB} \rangle &= 0.2 \\ \langle \text{BBB} \rangle &= 0.1 \end{aligned} \tag{1.43}$$

Measurement of polymer structure using higher n*-ad segments*

We could continue with tetrads, pentads, etc., up to the 10-ads for the case at hand, but you have now gotten the idea of the process (and at this stage you are completely bored). We could derive the necessary relations observing that the total number of different combinations for the higher n-ads goes up as $2n$ where n is the n-ad length. Therefore, the number of combinations increases very rapidly, and the task gets tedious although not difficult. Heptamers have been observed in high-resolution NMR spectroscopy, so it may be necessary to plow through the derivation process (or look it up in the literature).

The ability to count the fraction of the different n-ads is a function of the sensitivity of the spectroscopic method involved. In some cases, the spectroscopic method allows the observation of only isolated units, in others dyads, and in some triads, etc. We will discuss the nature of the spectroscopic n-ad sensitivity and how it can be determined for the polymer system being studied at the appropriate time.

Relationships between the various orders (lengths) of sequences

As might be expected, all of the n-ad sequences are related to all the others in some fashion through the structural distribution function. But at the moment, we haven't

the slightest idea what this structural distribution function is. Rather there are some required relationships between the different levels of n-ads, and these relationships are easily derived.

Take the simplest case first: the relationship between the 1-ads (isolated units) and the 2-ads (dyads). We know that the dyads are formed from the 1-ads by the addition of another unit and that there are only two possible ways of making the addition — before and after the unit. Since we will be using the a priori probabilities (the number fraction probabilities) for more general purposes later, let us use them for this discussion remembering for the moment that there is a simple relationship between them: i.e. $P_1(\mathrm{A}) = \langle \mathrm{A} \rangle$, $P_2(\mathrm{AA}) = \langle \mathrm{AA} \rangle$, etc.

So we start with an A unit:

$$P_1(\mathrm{A}) = \underset{\text{Units added after the A unit}}{\overset{\downarrow}{P_2(\mathrm{AA})} + \overset{\downarrow}{P_2(\mathrm{AB})}} \tag{1.44}$$

$$P_1(\mathrm{A}) = \underset{\text{Units added before the A unit}}{\overset{\downarrow}{P_2(\mathrm{AA})} + \overset{\downarrow}{P_2(\mathrm{BA})}} \tag{1.45}$$

so it is required that

$$P_2(\mathrm{AB}) = P_2(\mathrm{BA}) \tag{1.46}$$

We have derived the reversibility relationship (Eq. (1.32)) to which we had previously alluded.

Experimentally, we have

$$P_1(A) = P_2(\mathrm{AA}) + \tfrac{1}{2} P_2(\overline{\mathrm{AB}}) \tag{1.47}$$

In a similar fashion,

$$P_1(\mathrm{B}) = P_2(\mathrm{BB}) + \tfrac{1}{2} P_2(\overline{\mathrm{AB}}) \tag{1.48}$$

The relationships between the various n-ads are shown in Table 1.1 [3].

These relationships between the various orders of the n-ads are useful because they represent a quantitative requirement to be met by the experimental measurements and a test of the structural assignments made by the spectroscopists (who are not always infallible).

Calculation of polymer structural parameters from sequence measurements

The measured sequence information on the n-ads can now be used to calculate structural information about the nature of the polymer, which will be useful in comparing one polymer system to another. Calculations of various average quantities

Table 1.1
Necessary relations between relative concentrations of comonomer sequences of different lengths

Sequence	A-priori probability for individual units	Total number-fraction probability
Dyad–monad	$P(\mathrm{AA}) + \frac{1}{2}P(\overline{\mathrm{AB}})$	$P(\mathrm{A})$
	$P(\mathrm{BB}) + \frac{1}{2}P(\overline{\mathrm{AB}})$	$P(\mathrm{B})$
Triad–dyad	$P(\mathrm{AAA}) + \frac{1}{2}P(\overline{\mathrm{AAB}})$	$P(\mathrm{AA})$
	$P(\mathrm{BAB}) + \frac{1}{2}P(\overline{\mathrm{AAB}}) + P(ABA) + \frac{1}{2}P(\overline{\mathrm{ABB}})$	$P(\mathrm{AB})$
	$P(\mathrm{BBB}) + \frac{1}{2}P(\overline{\mathrm{AAB}})$	$P(\mathrm{BB})$
Tetrad–triad	$P(\mathrm{AAAA}) + \frac{1}{2}P(\overline{\mathrm{AAAB}})$	$P(\mathrm{AAA})$
	$P(\mathrm{BAAB}) + \frac{1}{2}P(\overline{\mathrm{AAAB}}) + \frac{1}{2}P(\overline{\mathrm{AABA}}) + \frac{1}{2}P(\overline{\mathrm{AABB}})$	$P(\mathrm{AAB})$
	$\frac{1}{2}P(\overline{\mathrm{ABAB}}) + \frac{1}{2}P(\overline{\mathrm{BABB}})$	$P(\mathrm{BAB})$
	$\frac{1}{2}P(\overline{\mathrm{ABAB}}) + \frac{1}{2}P(\overline{\mathrm{AABA}})$	$P(\mathrm{ABA})$
	$P(\mathrm{ABBA}) + \frac{1}{2}P(\overline{\mathrm{ABBB}}) + \frac{1}{2}P(\overline{\mathrm{AABB}}) + \frac{1}{2}P(\overline{\mathrm{BABB}})$	$P(\mathrm{ABB})$
	$P(\mathrm{BBBB}) + \frac{1}{2}P(\overline{\mathrm{ABBB}})$	$P(\mathrm{BBB})$

as those derived for the degree of polymerization will be useful in understanding the type of polymer we are studying in terms of the distribution of its microstructure.

Structural composition

The structural composition of the polymer can be defined as the ratio of the fractions of the various types of chemical structures. When the number fraction of single units A or B is measured, the composition can be calculated from the ratio of these measurements:

$$\text{Structural compositions} = \frac{\langle A\rangle}{\langle B\rangle} \tag{1.49}$$

For our demo copolymer example,

$$\frac{\langle \mathrm{A}\rangle}{\langle \mathrm{B}\rangle} = \frac{0.4}{0.6} = 0.67 \tag{1.50}$$

Sequence order parameter

If both mono-ads and dyads are measured, a statistical parameter can be calculated that yields information about whether the distribution of the structures is random, and whether it tends towards an alternating or block distribution. This order parameter, χ,

is defined as

$$\chi = \frac{\frac{1}{2}P_2(\overline{AB})}{P_1(A)P_1(B)} = \frac{\frac{1}{2}\langle\overline{AB}\rangle}{\langle A\rangle\langle B\rangle} \tag{1.51}$$

If

$$\tfrac{1}{2}P_2(\overline{AB}) = P_1(A)P_1(B) \tag{1.52}$$

the probabilities are independent, and the structural result is termed *random*. When

$$\tfrac{1}{2}P_2(\overline{AB}) \neq P_1(A)P_1(B)$$

the probabilities of the polymerization reactions are not independent and the subsequent structure is determined by *chemical correlation*. That is, when A is more reactive to B* than B, we have an AB chemical correlation (a preference in the copolymer chain structure for AB sequences). The resulting copolymer sequence structure is skewed and not random.

Value	Sequence structure	Chemical correlation
$\chi = 1$	random distribution of A and B	none
$\chi > 1$	skewed toward alternating tendency	A−B
$\chi < 1$	skewed toward block tendency	AA or BB
$\chi = 2$	completely alternating A and B	exclusive AB addition
$\chi = 0$	complete blocks of A and B	exclusive AA or BB addition

The measurement of χ is useful in differentiating the sequence structure for polymers, which have essentially the same composition but yield different physical or mechanical properties due to the role of specific sequences in determining specific properties.

For our model copolymer, χ has a value of 1.25 which indicates that it is a nonrandom copolymer having an AB chemical correlation.

Number-average sequence lengths

The number of $N_A(n)$ is given

$$N_A(n) = \frac{P_{n+2}(BA_nB)}{\sum P_{n+2}(BA_nB)} \tag{1.53}$$

Also,

$$P_2(AB) = \sum P_{n+2}(BA_nB) \tag{1.54}$$

and

$$P_2(BA) = \sum P_{n+2}(AB_nA) \tag{1.55}$$

so

$$N_A(n) = \frac{P_{n+2}(BA_nB)}{P_2(BA)} \tag{1.56}$$

The number-average sequence length, $\bar{l}_A$, has the definition

$$\bar{l}_A = \frac{\sum nN_A(n)}{\sum N_A(n)} = \sum nN_A(n) \tag{1.57}$$

Substitution yields

$$\bar{l}_A = \frac{\sum nP_{n+2}(BA_nB)}{P_2(BA)} \tag{1.58}$$

and because

$$\sum nP_{n+2}(BA_nB) = P_1(A) \tag{1.59}$$

the number-average sequence length is obtained in terms of simple measurable sequences

$$\bar{l}_A = \frac{\langle A\rangle}{\frac{1}{2}\langle\overline{AB}\rangle} \tag{1.60}$$

and likewise

$$\bar{l}_B = \frac{\langle B\rangle}{\frac{1}{2}\langle\overline{AB}\rangle} \tag{1.61}$$

With the required n-ad relationships, this result can be expressed in terms of the measured dyads only:

$$\bar{l}_A = \frac{[\langle AA\rangle + \frac{1}{2}\langle\overline{AB}\rangle]}{\frac{1}{2}\langle\overline{AB}\rangle} \tag{1.62}$$

and likewise

$$\bar{l}_B = \frac{[\langle BB\rangle + \frac{1}{2}\langle\overline{AB}\rangle]}{\frac{1}{2}\langle\overline{AB}\rangle} \tag{1.63}$$

For our model copolymer, we have

$$\bar{l}_B = 2.0 \quad \bar{l}_A = 1.3$$

These results indicates that the B sequences on average are longer than the A sequences.

If triads are being measured, the number-average sequence length can be calculated by using

$$\bar{l}_A = \frac{[\langle BAB\rangle + \langle\overline{AAB}\rangle + \langle AAA\rangle]}{\frac{1}{2}\langle\overline{AAB}\rangle + \langle BAB\rangle} \tag{1.64}$$

$$\bar{l}_B = \frac{[\langle ABA\rangle + \langle \overline{BBA}\rangle + \langle BBB\rangle]}{\frac{1}{2}\langle \overline{BBA}\rangle + \langle ABA} \tag{1.65}$$

As a test of our measurements on the model copolymer, you might like to calculate the number average sequence lengths using the triad information and compare with the dyad results!

Of course, if tetrads or higher n-ads are measured, corresponding relationships can be derived for calculating the number-average sequence lengths.

Relating the polymer structure to the polymerization mechanism

What factors in the polymerization reaction are responsible for the sequence structure of the polymer? When the sequence distribution of the polymer chain is completely characterized, and when proper control has been exercised, it should be possible to relate the structure to the basic polymerization process. In the ideal circumstance, discovering the relationships between the chemistry and the structure is quite easy. However, in the real case, it is quite difficult due to process fluctuations and experimental error in the measurements. In every case, it is possible to gain some insight into the nature of the polymerization process. Here, we will demonstrate the ideal case and later point the direction for the cases observed in the real world.

Microstructure of terminal copolymerization model

For a simple copolymerization model, the terminal copolymerization model, the rate of addition of comonomer depends on the nature of the terminal group and the reactivity of the respective monomers. The following reactions and their corresponding rates in terms of kinetic rate constants and concentrations of reacting species represent this model:

Terminal group	Added group	Rate	Final
$-A^*$	[A]	$k_{AA}[A^*][A]$	AA^*
$-B^*$	[A]	$k_{BA}[B^*][A]$	BA^*
$\sim A^*$	[B]	$k_{AB}[A^*][B]$	AB^*
$\sim B^*$	[B]	$k_{BB}[B^*][B]$	BB^*

where A^* and B^* are the propagating terminal species. The rate constants, k_{AA}, k_{BA}, k_{AB}, and k_{BB}, are specific to the chemical nature of A and B as well as to the type of copolymerization, i.e. free radical, anionic, cationic or catalyzed.To understand the nature of the copolymer microstructure resulting from this polymerization, we need to know the probability that an A unit is next to another A, or perhaps next to a

B. That is, what is the probability that an A unit has added an A* or a B*? These kinds of probabilities are termed *conditional probabilities* and will be designated by the notation $P(B/A^*)$ which represents the conditional probability that a B unit has been added to an A* unit.These conditional probabilities start with the assumption that one has an A* unit and then asks the question what is the probability that a B unit is added, or alternatively that an A unit is added. Like all probabilities, these conditional probabilities are determined by the relative rates of addition of the A or B units to the terminal A* unit. The terminal conditional probabilities can be written as the ratio of the rate of formation of the desired product (AA* or AB*) to the rates of the reaction of the starting unit (A*):

$$P\left(A/A^*\right) = \frac{k_{AA}[A][A^*]}{k_{AA}[A][A^*] + k_{AB}[B][A^*]} \tag{1.66a}$$

Now we can put this equation into a more useful form:

$$P\left(A/A^*\right) = \frac{k_{AA}[A]/k_{AB}[B]}{(k_{AA}[A]/k_{AB}[B]) + 1} = \frac{r_A x}{1 + r_A x} \tag{1.66b}$$

and

$$P\left(B/A^*\right) = \frac{1}{1 + r_A x} \tag{1.67}$$

where r_A is the reactivity ratio for [A*]:

$$r_A = \frac{k_{AA}}{k_{AB}} \tag{1.68}$$

and x is the monomer feed ratio

$$x = \frac{[A]}{[B]} \tag{1.69}$$

Likewise, a treatment of the reactions of B* yields

$$P\left(B/B^*\right) = \frac{r_B/x}{1 + (r_B/x)} \qquad P\left(A/B^*\right) = \frac{1}{1 + (r_B/x)} \tag{1.70}$$

where r_B is the reactivity ratio for [B*]

$$r_B = \frac{k_{BB}}{k_{BA}} \tag{1.71}$$

There are only two independent terminal conditional probabilities, that is, there is the completeness condition indicating that only an A or a B be added to an A*:

$$P\left(A/A^*\right) + P\left(B/A^*\right) = 1 \tag{1.72}$$

and

$$P\left(B/B^*\right) + P\left(A/B^*\right) = 1 \tag{1.73}$$

We will use $P(A/B^*)$ and $P(B/A^*)$ in further calculations.

We need to relate these conditional probabilities to the measured n-ads. For example, Bayers' theorem yields the relative probability of the dyad sequence as

$$P_2(\mathrm{BA}) = P_1(\mathrm{B})P\left(A/B^*\right) \tag{1.74}$$

concluding that the dyad fraction is given by the probability of finding a B, which is the a priori $P_2(\mathrm{B})$ probability, times the conditional probability of adding an A given a B unit, which is $P(\mathrm{A/B^*})$. With this in mind, there are a number of routes we could take, but let us begin by using the reversibility relationship (Eq. (1.48)):

$$P_2(\mathrm{AB}) = P_2(\mathrm{BA}) \tag{1.75}$$

Writing this equation in terms of the terminal conditional probabilities,

$$P_1(\mathrm{A})P\left(\mathrm{B/A^*}\right) = P_1(\mathrm{B})P\left(\mathrm{A/B^*}\right) \tag{1.76}$$

and rearranging, we obtain our first useful result (that is, the composition in terms of the conditional probabilities)

$$\frac{P_1(\mathrm{A})}{P_1(\mathrm{B})} = \frac{P(\mathrm{A/B^*})}{P(\mathrm{B/A^*})} \tag{1.77}$$

This equation gives the relationship between the a priori probabilities, $P(\mathrm{A})$ and $P(\mathrm{B})$ and the conditional probabilities, $P(\mathrm{A/B^*})$ and $P(\mathrm{B/A^*})$. Substitution from Eqs. (1.67) and (1.70) yields:

$$\frac{\langle \mathrm{A} \rangle}{\langle \mathrm{B} \rangle} = \frac{P_1(\mathrm{A})}{P_1(\mathrm{B})} = \frac{1 + r_\mathrm{A} x}{1 + (r_\mathrm{B}/x)} \tag{1.78}$$

This result is known as the Mayo–Lewis equation expressing the polymer composition in terms of the fundamental polymerization parameters. For the terminal model, there is a nonlinear relationship between the polymer composition ratio and x, the monomer feed ratio.

For a moment consider this Eq. (1.78). If $r_\mathrm{A} = r_\mathrm{B} = r$, the relationship between the ratio of the polymer composition and the monomer feed ratio is linear with a slope of r. A copolymer model which obeys this $r_\mathrm{A} = r_\mathrm{B} = r$ relationship is termed 'ideal'. The ideal model is a reduction in the absolute rate constants such that $k_{\mathrm{AA}} = k_{\mathrm{AB}} = k_\mathrm{A}$ (correspondingly $k_{\mathrm{BB}} = k_{\mathrm{BA}} = k_\mathrm{B}$) and $r = k_\mathrm{A}/k_\mathrm{B}$. In this case, there is no 'terminal' effect, the reactivity does not depend on the end group only the monomer. When $k_\mathrm{A} = k_\mathrm{B}$, than $r = 1$, there is a further simplification. In this case, there is a direct relationship between $P(\mathrm{A})/P(\mathrm{B})$ and x.

Substituting in the following can derive the dyad concentrations

$$P_2(\mathrm{AB}) = P_2(\mathrm{BA}) = P_1(\mathrm{A})P(\mathrm{B/A^*}) = \frac{P(\mathrm{A/B^*})P(\mathrm{B/A^*})}{P(\mathrm{B/A^*}) + P(\mathrm{A/B^*})} \tag{1.79}$$

$$P_2(\mathrm{BB}) = 1 - 2P_2(\mathrm{AB}) - P_2(\mathrm{AA}) \tag{1.80}$$

$$P_2(\mathrm{AA}) = P_1(\mathrm{A})P(\mathrm{A}/\mathrm{A}^*) = \frac{P(\mathrm{A}/\mathrm{B}^*)[1 - P(\mathrm{B}/\mathrm{A}^*)]}{P(\mathrm{B}/\mathrm{A}^*) + P(\mathrm{A}/\mathrm{B}^*)} \tag{1.81}$$

The triad fraction normalized for the composition of A, (F_{XXX}), also be written

$$F_{\mathrm{AAA}} = \frac{P_3(\mathrm{AAA})}{P_1(\mathrm{A})} = [1 - P(\mathrm{B}/\mathrm{A}^*)] \tag{1.82}$$

$$F_{\mathrm{BAB}} = [P(\mathrm{B}/\mathrm{A}^*)]^2 \tag{1.83}$$

$$F_{\mathrm{BAA}} = F_{\mathrm{AAB}} = P(\mathrm{B}/\mathrm{A}^*)[1 - P(\mathrm{B}/\mathrm{A}^*)] \tag{1.84}$$

In fact, all of the experimental parameters can be calculated in terms of the two conditional probabilities $P(\mathrm{B}/\mathrm{A}^*)$ and $P(\mathrm{A}/\mathrm{B}^*)$, or the correspondingly r_{A}, r_{B}, and x, which are the basic parameters of the terminal model copolymerization mechanism.

The order parameter is given by

$$\chi = P(\mathrm{A}/\mathrm{B}^*) + P(\mathrm{B}/\mathrm{A}^*) \tag{1.85}$$

and the $r_{\mathrm{A}}r_{\mathrm{B}}$ product determines whether the copolymer is alternating, random, or block. When $r_{\mathrm{A}}r_{\mathrm{B}} < 1$, then $\chi > 1$ and the polymer has an alternating tendency. If $r_{\mathrm{A}}r_{\mathrm{B}} = 1$, the polymer is random. If $r_{\mathrm{A}}r_{\mathrm{B}} > 1$, then $\chi < 1$ and the polymer has a block character.

The number-average sequence in terms of the terminal conditional probabilities becomes

$$\bar{l}_{\mathrm{A}} = \frac{1}{P(\mathrm{B}/\mathrm{A}^*)} = 1 + r_{\mathrm{A}}x \tag{1.86}$$

$$\bar{l}_{\mathrm{B}} = \frac{1}{P(\mathrm{A}/\mathrm{B}^*)} = 1 + \frac{r_{\mathrm{B}}}{x} \tag{1.87}$$

As shown previously, $\bar{l}_{\mathrm{A}}$ or $\bar{l}_{\mathrm{B}}$ can be determined from the measurement of the various n-ads (Eqs. (1.60) and (1.61) for dyads and Eqs. (1.64) and (1.65) for triads). Consequently, the terminal model can be tested by the relationships in Eqs. (1.86) and (1.87); that is, plotting $\bar{l}_{\mathrm{A}}$ versus x. If a linear relationship is found, then r_{A} is the slope. Similarly, plotting $\bar{l}_{\mathrm{B}}$ versus $1/x$ yields r_{B} as the slope.

Likewise, the number fraction of A (or B) sequences allows the calculation of the amount of As (or Bs) of varying sequence length in the copolymer chain can be calculated for the terminal model from

$$N_{\mathrm{A}}(n) = \left(\frac{[r_{\mathrm{A}}/x]^{n-1}}{1 + r_{\mathrm{A}}x}\right)\left(1 - \frac{r_{\mathrm{A}}x}{1 + r_{\mathrm{A}}x}\right) \tag{1.88}$$

$$N_{\mathrm{B}}(n) = \left(\frac{[r_{\mathrm{B}}/x]^{n-1}}{1 + (r_{\mathrm{B}}/x)}\right)\left(1 - \frac{(r_{\mathrm{B}}/x)}{1 + (r_{\mathrm{B}}/x)}\right) \tag{1.89}$$

By jove, I think we've done it! We have related the observed structure to the type of polymerization mechanism and devised a method to determine the fundamental parameters, at least for the terminal model. Admittedly, a number of assumptions have been made including isothermal conditions, reactivities independent of chain length, and instantaneous conditions (no conversion) but it has demonstrated the approach we are taking. However, before we become enraptured with our success, let us examine a polymerization model, which is slightly more complicated, that is, the penultimate polymerization model.

Microstructure of the penultimate polymerization model

When the nature of the penultimate (next to last) unit has a significant effect on the absolute rate constants for addition of the monomers in the copolymerization, eight addition reactions are required. The penultimate conditional probabilities can be derived in terms of the eight absolute rate constants, k_{XXX}, and the monomer feed ratio, x. The penultimate conditional probabilities can be written in terms of the relative number of chemical reactions occurring for each penultimate unit. The reactions and their corresponding rates are as follows:

Penultimate group	Added group	Rate	Final
~AA*	[A]	k_{AAA}[AA*][A]	~AAA*
~AA*	[B]	k_{AAB}[AA*][B]	~AAB*
~BA*	[A]	k_{BAA}[BA*][A]	~BAA*
~BA*	[B]	k_{BAB}[BA*][B]	~BAB*
~AB*	[A]	k_{ABA}[AB*][A]	~ABA*
~AB*	[B]	k_{ABB}[AB*][B]	~ABB*
~BB*	[A]	k_{BBA}[BB*][A]	~BBA*
~BB*	[B]	k_{BBB}[BB*][B]	~BBB*

The conditional probabilities are calculated in the same fashion as previously, that is, by determining the relative rates of addition to the penultimate group. In other words, we must calculate the conditional probability of A adding to AA* rather than A*, as was used for the terminal model. The $P(A/AA^*)$ can be written in terms of the relative rate of addition of A to AA* relative to the total rate of addition to AA* which is the sum of the relative rates of adding both A and B to AA*. Thusly,

$$P(A/AA^*) = \frac{k_{AAA}[A][AA^*]}{k_{AAA}[A][AA^*] + k_{AAB}[B][AA^*]} \tag{1.90a}$$

$$P(\mathrm{A/AA^*}) = \frac{(k_{\mathrm{AAA}}[\mathrm{A}]/k_{\mathrm{AAB}}[\mathrm{B}])}{(k_{\mathrm{AAA}}[\mathrm{A}]/k_{\mathrm{AAB}}[\mathrm{B}]) + 1} = \frac{r_{\mathrm{A}}x}{1 + r_{\mathrm{A}}x} \tag{1.90b}$$

Four independent conditional probabilities can be written, with four monomer reactivity ratios, in a manner similar to the terminal model:

$$P(\mathrm{B/AA^*}) = \frac{1}{1 + r_{\mathrm{A}}x} \qquad P(\mathrm{A/AA^*}) = 1 - P(\mathrm{B/AA^*}) \tag{1.91}$$

$$P(\mathrm{A/BA^*}) = \frac{r'_{\mathrm{A}}x}{1 + r'_{\mathrm{A}}x} \qquad P(\mathrm{B/BA^*}) = 1 - P(\mathrm{A/BA^*}) \tag{1.92}$$

$$P(\mathrm{B/AB^*}) = \frac{r'_{\mathrm{B}}/x}{1 + (r'_{\mathrm{B}}/x)} \qquad P(\mathrm{A/AB^*}) = 1 - P(\mathrm{B/AB^*}) \tag{1.93}$$

$$P(\mathrm{A/BB^*}) = \frac{1}{1 + (r_{\mathrm{B}}/x)} \qquad P(\mathrm{B/BB^*}) = 1 - P(\mathrm{A/BB^*}) \tag{1.94}$$

where

$$r_{\mathrm{A}} = \frac{k_{\mathrm{AAA}}}{k_{\mathrm{AAB}}} \qquad r'_{\mathrm{A}} = \frac{k_{\mathrm{BAA}}}{k_{\mathrm{BAB}}} \tag{1.95}$$

$$r_{\mathrm{B}} = \frac{k_{\mathrm{BBB}}}{k_{\mathrm{BBA}}} \qquad r'_{\mathrm{B}} = \frac{k_{\mathrm{ABB}}}{k_{\mathrm{ABA}}} \tag{1.96}$$

The composition of the copolymer in terms of the conditional penultimate probabilities is found by substitution:

$$\frac{P_{\mathrm{l}}(\mathrm{A})}{P_{\mathrm{l}}(\mathrm{B})} = \frac{P(\mathrm{A/B})}{P(\mathrm{B/A})} = \frac{1 + \dfrac{P(\mathrm{A/BA^*})}{P(\mathrm{B/AB^*})}}{1 + \dfrac{P(\mathrm{B/AB^*})}{P(\mathrm{A/BB^*})}} \tag{1.97}$$

You might find it useful to test your understanding to derive the above relationship (Eq. (1.97)) between the terminal model and the penultimate model!

These results can be expressed in terms of the reactivity coefficients and monomer feed:

$$\frac{P_{\mathrm{l}}(\mathrm{A})}{P_{\mathrm{l}}(\mathrm{B})} = \frac{1 + r'_{\mathrm{A}}\dfrac{(1 + r_{\mathrm{A}}x)}{(1 + r'_{\mathrm{A}}x)}}{1 + \dfrac{\dfrac{r'_{\mathrm{B}}}{x}(1 + \dfrac{r_{\mathrm{B}}}{x})}{(1 + \dfrac{r'_{\mathrm{B}}}{x})}} \tag{1.98}$$

Table 1.2
Relations between experimental parameters, conditional probabilities, and reactivity ratios for the penultimate model of copolymerization

Experimental	General	Conditional probabilities	Reactivity ratios and monomer feed
$P_2(\mathrm{AB})$	$2P_2(\mathrm{BA})$	$\dfrac{2}{P(\mathrm{A/BA})/P(\mathrm{B/AA})} + 2 + \dfrac{P(\mathrm{B/AB})}{P(\mathrm{A/BB})}$	$\dfrac{2}{\dfrac{r'_{\mathrm{A}}\chi(1+r_{A}\chi)}{1+r'_{\mathrm{A}}\chi} + 2 + \dfrac{(r'_{\mathrm{B}}/\chi)(r_{\mathrm{B}}+\chi)}{r'_{\mathrm{B}}+\chi}}$
χ	$\dfrac{P_2(\mathrm{BA})}{P_1(\mathrm{B})P_1(\mathrm{A})}$	$\dfrac{P(\mathrm{A/BA})/P(\mathrm{B/AA}) + 2 + P(\mathrm{B/AB})/P(\mathrm{A/BB})}{P(\mathrm{A/BA})/P(\mathrm{B/AA}) + 1 + P(\mathrm{A/BA})/P(\mathrm{B/AA})P(\mathrm{B/AB})P(\mathrm{A/BB})/P(\mathrm{B/AB})P(\mathrm{A/BB})}$	$\dfrac{r'_{\mathrm{A}}\chi\left(\dfrac{1+r_{\mathrm{A}}\chi}{1+r'_{\mathrm{A}}\chi}\right) + 2 + \dfrac{r'_{\mathrm{B}}}{\chi}\left(\dfrac{r_{\mathrm{B}}+\chi}{r'_{\mathrm{B}}+\chi}\right)}{r'_{\mathrm{A}}\left(\dfrac{1+r_{\mathrm{A}}\chi}{1+r'_{\mathrm{A}}\chi}\right) + 1 + r'_{\mathrm{A}}r'_{\mathrm{B}}\left(\dfrac{1+r_{\mathrm{A}}\chi}{1+r'_{\mathrm{A}}\chi}\right)\left(\dfrac{r_{\mathrm{B}}+\chi}{r'_{\mathrm{B}}+\chi}\right) + \dfrac{r'_{\mathrm{B}}}{\chi}\left(\dfrac{r_{\mathrm{B}}+\chi}{r'_{\mathrm{B}}+\chi}\right)}$
$\bar{l}_{\mathrm{A}}$	$\dfrac{P_1(\mathrm{A})}{P_2(\mathrm{AB})}$	$1 + \dfrac{P(\mathrm{A/BA})}{P(\mathrm{B/AA})}$	$1 + \left[r'_{\mathrm{A}}\chi\left(\dfrac{1+r_{\mathrm{A}}\chi}{1+r'_{\mathrm{A}}\chi}\right)\right]\chi$
$\bar{l}_{\mathrm{B}}$	$\dfrac{P_1(\mathrm{B})}{P_2(\mathrm{BA})}$	$1 + \dfrac{P(\mathrm{B/AB})}{P(\mathrm{A/BB})}$	$1 + \dfrac{r'_{\mathrm{B}}\left(\dfrac{r_{\mathrm{B}}+\chi}{r'_{\mathrm{B}}+\chi}\right)}{\chi}$
$1/\alpha_{\mathrm{A}}$	$\dfrac{P_1(\mathrm{A})}{P_2(\mathrm{BA})}$	$1 + \dfrac{P(\mathrm{B/AA})}{P(\mathrm{A/BA})}$	$1 + \dfrac{1}{\left[r'_{\mathrm{A}}\left(\dfrac{1+r_{\mathrm{A}}\chi}{1+r'_{\mathrm{A}}\chi}\right)\right]\chi}$
$1/\alpha_{\mathrm{B}}$	$\dfrac{P_1(\mathrm{B})}{P_2(\mathrm{BB})}$	$1 + \dfrac{P(\mathrm{A/BB})}{P(\mathrm{B/AB})}$	$1 + \dfrac{\chi}{r'_{\mathrm{B}}\left(\dfrac{r_{\mathrm{B}}+\chi}{r'_{\mathrm{B}}+\chi}\right)}$

All of the other parameters can be calculated for the penultimate model and are shown in Table 1.2.

The relationships are not particularly difficult, but they are cumbersome, partly because four different parameters are involved, as opposed to two parameters for the terminal model.Similar to the reduction from the terminal to the ideal model, when the following requirement is met

$$k_{AAA} = k_{BAA} = k_{AA}, \qquad k_{ABA} = k_{BBA} = k_{BA},$$
$$k_{BBB} = k_{ABB} = k_{BB}, \qquad k_{BAB} = k_{AAB} = k_{AB},$$

the penultimate model reduces to the terminal model. Chemically, this reflects the fact that the reactivity of the penultimate unit is not contributing to the polymerization and only the terminal unit plays a role. Therefore, the model is terminal.

Higher order models of copolymerization and other complications

Of course, the actual polymerization mechanism can be more complicated in a number of ways. Any intramolecular action or intermolecular interaction will change the results. The effects of longer terminal units influencing the polymerization are possible. In some cases, one or both of the monomers may associate with the active growing end or the solvent. It is also possible for one of the monomers to show a tendency for depolymerization to occur simultaneously with polymerization. The individual radicals can react with two different energy states, for example, when the monomer isomerizes, it will have different reactivities for the different isomers. Mathematical methods have been devised to work with these types of complications [5,6]. The major modification is the necessity to use matrix calculations, if for no other reason than to make the bookkeeping tractable.The probabilistic method described in the preceding sections does not account for time-dependent or conversion processes, but these processes can be introduced through integration procedures [2].

Differentiation between model mechanisms of copolymerization

Most investigations of the mechanism of copolymerization involve an analysis of the composition of the initial copolymers formed, but it is often difficult to distinguish between the various models for copolymerization on the basis of their fit to the composition data alone. This is a consequence of the rather small differences in polymer composition which often approach the experimental error of the composition measurement. The distribution of monomer sequences in the copolymer contains more information about the polymerization system than does the copolymer composition.

The general approach is to prepare copolymers over a range of comonomer compositions and measure the sequence distributions obtained [2]. The sequence distributions are mathematically fitted recognizing the nonlinear nature of the problem

to the various calculated structural parameters, and a 'best-fit' model is determined. Care must be taken to account for the effect of conversion on the polymer sequence distribution in performing the calculations. Objective tests have been described to assess the accuracy of the copolymerization models, including the statistical F test [7]. This test is based on the ratio F of the residual sums of the squares of the models A and B to be differentiated, where B is a special case of the model A. The equation involved is

$$F = \frac{\dfrac{[SS_B - SS_A]}{[p_A - p_B]}}{S\dfrac{S_A}{[n - p_A]}} \tag{1.99}$$

where SS is the sum of the squares, p_A and p_B are the numbers of parameters for each model, and n is the number of experimental observations. The ratio F is compared with critical values of $F(\ )$ that are available in tables [8]. This test is highly recommended.

The problem with determining the mechanism of the polymerization is due primarily to the difficulty in making sufficiently accurate analytical measurements of

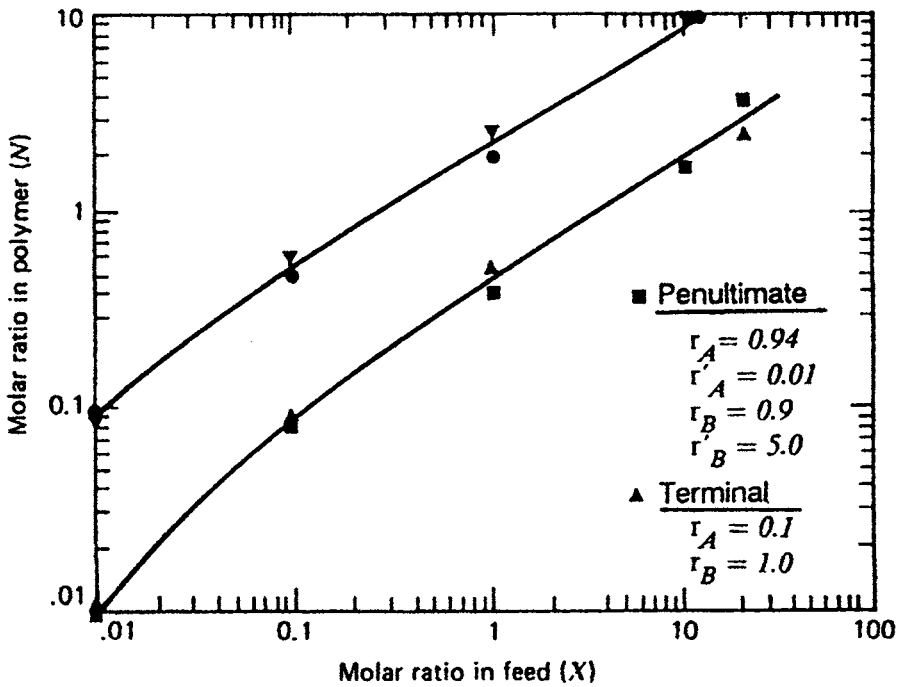

Fig. 1.3. Comparison of the molar ratio in the polymer as a function of the molar ratio in the feed for the terminal and penultimate models with two sets of reactivity ratios. The reactivity ratios for the terminal model were $r_A = 0.1$ and $r_B = 1.0$. For the penultimate model, the reactivity ratios were $r_A = 0.94$, $r_A = 0.01$, $r_B = 0.9$, and $r_B = 5.0$. (Reproduced with permission from Ref. [9]. © 1964 John Wiley and Sons, Inc.)

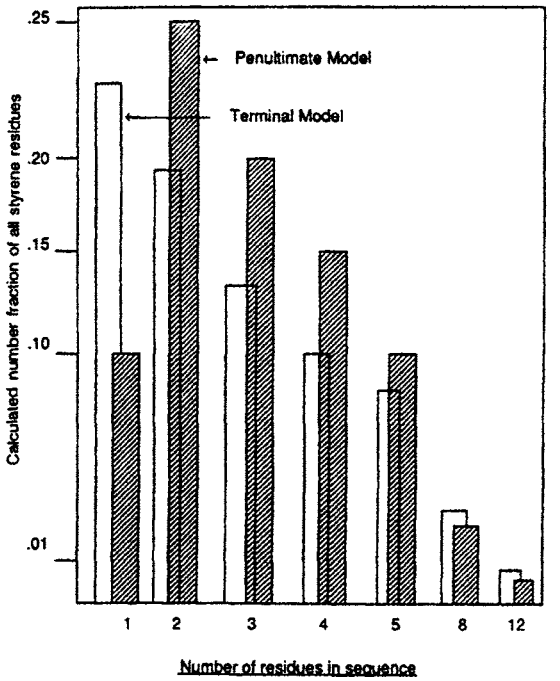

Fig. 1.4. Number distribution of monomer sequences calculated from terminal and penultimate models. The reactivity ratios for both models were the same as in Fig. 1.3. (Reproduced with permission from Ref. [9]. © 1964 John Wiley and Sons, Inc.)

the composition and sequence structure. There are only relatively small differences in composition expected theoretically between the two models, as is shown in Fig. 1.3 [9].

This figure shows the molar ratio in the polymer versus the molar ratio in the feed, x, calculated for reactivity ratios in the intermediate range for the terminal and penultimate models. This figure clearly shows the small differences (2%) in composition between the two mechanisms of polymerization. This result might seem unimportant. Let us examine the sequence distribution using the same reactivity ratios for the two models. The number distribution of sequences is shown in Fig. 1.4, and the weight-average distribution is shown in Fig. 1.5 [9].

Now the concentration differences are quite substantial, particularly for the shorter sequence lengths. Furthermore, these differences in the concentration of the sequences influence the physical and mechanical properties of a polymer. Therefore, when the sequence distribution is altered, differences in the performance properties of the polymer will be observed.

From another point of view, the results depicted in Figs. 1.4 and 1.5 point to the possibility of measuring these short sequences for determining the nature of the polymerization model. Although the compositional differences are small, the

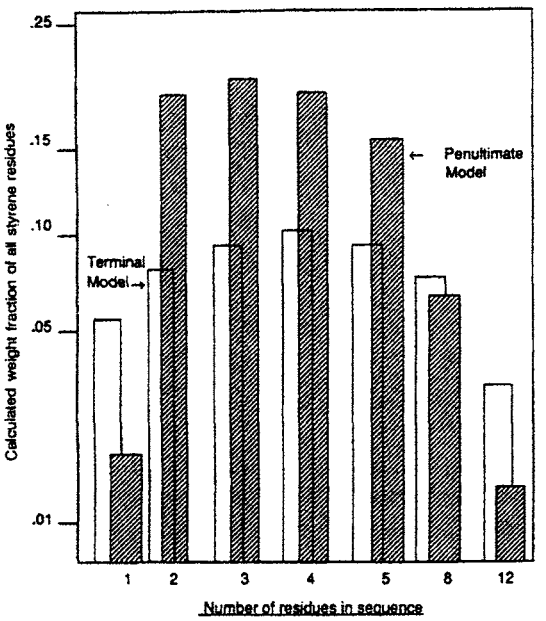

Fig. 1.5. Weight distribution of monomer sequences calculated from terminal and penultimate models. The reactivity ratios for both models were the same as in Fig. 1.3. (Reproduced with permission from Ref. [9]. © 1964 John Wiley and Sons, Inc.)

number and kind of comonomer sequences are substantially different. It is also clear that the short sequences dominate the microstructure and therefore are amenable to measurement using sequence-sensitive analytical techniques.

In Table 1.3, the sequences are given that must be satisfied by the model. For example, with the ideal model, only the composition need be measured, as it is a linear function of the monomer feed ratio. From the composition measurements, the reactivity ratio for the ideal model can be determined. In order to test the ideal model it is desirable to calculate the dyad fractions using the experimentally determined reactivity ratio and compare the experimental with the theoretical predictions of the ideal model. Verification of the model can further be achieved by comparing the experimental triad measurements with the predictions of the ideal model. In a similar manner, for the terminal model, the fraction of dyads with the composition

Table 1.3
Monomeric sequences for copolymer model evaluation

Model	Sequence for parameter measurement	Sequence needed for testing	Verification sequence
Ideal	⟨A⟩	⟨AA⟩	⟨AAA⟩
Terminal	⟨AA⟩	⟨AAA⟩	⟨AAAA⟩
Penultimate	⟨AAA⟩	⟨AAAA⟩	⟨AAAAA⟩

can be used to determine the two reactivity ratios for the terminal model. Using these experimentally determined reactivity ratios, the triad fractions can be computed and compared with the experimentally determined triad measurements. Verification of the terminal model can be made comparing the measurements for the tetrads. Corresponding measurements can be made for the penultimate model but longer sequences are required: i.e. triads, tetrads and pentads.

Determination of polymerization mechanism for model copolymer

Let us return to our model copolymer whose structure is

Sample copolymer chain

−A−B−B−A−B−B−B−A−B−A−
1 2 3 4 5 6 7 8 9 10

If the copolymerization were 'terminal', the terminal conditional probabilities are calculated from the dyad fractions:

$$P(\mathrm{A/A}) = \frac{\langle \mathrm{AA} \rangle}{\langle \mathrm{A} \rangle} = 0.25 \quad P(\mathrm{B/B}) = \frac{\langle \mathrm{BB} \rangle}{\langle \mathrm{A} \rangle} = 0.5$$

$$P(\mathrm{B/A}) = \frac{\frac{1}{2}\langle \mathrm{AB} \rangle}{\langle \mathrm{A} \rangle} = 0.75 \quad P(\mathrm{A/B}) = \frac{\frac{1}{2}\langle \mathrm{AB} \rangle}{\langle \mathrm{B} \rangle} = 0.5$$

We are forced to conclude that the copolymerization model of our copolymer is not ideal!

To test the terminal model, we can use the terminal conditional probabilities obtained from the dyads to calculate the fractions of triads. A comparison of the predicted and experimental measurements will determine whether the terminal model is correct or whether the penultimate model should be tested.

Test data for determination of copolymerization mechanism of model copolymer

Triads	Experimental	Predicted for terminal	Difference
AAA	0.0	0.025	−0.25
AAB	0.2	0.150	+0.050
ABA	0.1	0.150	−0.050
ABB	0.4	0.300	+0.100
BAB	0.2	0.225	−0.025
BBB	0.1	0.150	+0.050

The average difference is 0.050 that indicates agreement between the experimental and predicted triad fractions and establishes that the model copolymer is made by a terminal mechanism rather than a penultimate mechanism. We cannot determine the parameters of the polymerization models, i.e. r_A and r_B, since we only have one polymer system to examine rather than a number of polymers prepared by systematically varying x.

Determination of the polymerization parameters

Once the mechanism of the copolymerization process is determined, the next step is to determine the polymerization parameters, or more precisely, the reactivity ratios of the comonomer system. Generally, the ratios are determined from a plot of the data obtained from samples with different feed ratios. In most cases, the equations are reorganized to yield linear relationships whose slopes and intercept values reflect the reactivity ratios. These linearized relations, although apparently useful, can yield misleading results because of the different weighting of the data and the corresponding experimental error [10]. Nonlinear methods have also been used, and some of their difficulties and advantages have been discussed [11].Whatever the method you use, remember that the calculated reactivity ratios are not universal constants. That is, their values depend on the environment of the polymerization, including the temperature, pressure, ionic strength, and so forth. However, if your numbers are substantially different from those recognized values in the literature for polymerizations similar to your own, I think you might reexamine your data.

Summary

This chapter has demonstrated, in the simplest possible terms, the approach that is necessary to go from spectroscopic measurements (in this case, the spectrometer was the human eye) of the microstructure of the polymer chain to an evaluation of the nature of the copolymerization addition mechanism and finally the determination of the fundamental parameters of the polymerization process. After all, that is what we really want to know! Although it would be interesting to know the position and geometric relationship between every atom in a polymer chain, what would we do with the information? Spectroscopically, we can measure only the average structure of the polymer chains in the sample. Therefore, our only choice is to try to relate these structural parameters to the performance properties of the polymer and to the polymerization route that gave the polymer structure. Believe it or not, this step is possible using the spectroscopic techniques to be described in the later chapters of this book.

The shape of things to come

Spectroscopic techniques for the study of polymers must yield high-resolution, narrow linewidth spectra that provide selectivity and structural information. Because polymer systems are always complex mixtures of structure and molecules, the spectroscopic probe must permit selective monitoring of more than one structural type at a time. It must possess sufficient sensitivity to detect and monitor very low levels of structure in the polymer, as small structural changes produce much larger effects on the physical and mechanical properties. The spectroscopic probe must be very specific in its informational content, as we will need to determine not only the structure of the single repeating units but also how they are connected together and to what extent the units are ordered. The technique should be nondestructive and noninvasive, because the polymer samples will need to be evaluated by other methods besides spectroscopic characterization. The probe should be capable of studying the polymer in its useful form, be it fiber, film, composite, coating, or adhesive.The majority of the spectroscopic techniques do not meet the specifications of the spectroscopic probe for polymers. However, four spectroscopic techniques have evolved for polymer analysis that do fit these criteria: Fourier transform infrared (FTIR), Raman, high-resolution NMR spectroscopy of the solid state and mass spectroscopy. These techniques used individually or in combination can provide detailed structural information on polymers for research, analysis, and quality control. High-resolution NMR spectroscopy of solutions does not meet the specification of being capable of studying the polymer in its final engineering form, but the contributions that NMR spectroscopy has made to our understanding of the structure of polymers are so great that it must be considered in any textbook on spectroscopy of polymers.

References

[1] Lowry, G.G. (Ed.), Markov Chains and Monte Carlo Calculations in Polymer Science. Dekker, New York, NY, 1969.
[2] Koenig, J.L., Chemical Microstructure of Polymer Chains. Wiley, New York, NY, 1982. Reprinted in 1990 by Kreiger, Melbourne, FL.
[3] Randall, J.C., Polymer Sequence Determination. Academic Press, New York, NY, 1977.
[4] Flory, P.J., Principles of Polymer Chemistry. Cornell University, Ithaca, NY, 1953, Chapter 3.
[5] Price, F.P., in: G.G. Lowry (Ed.), Markov Chains and Monte Carlo Calculations in Polymer Science. Dekker, New York, NY, 1969.
[6] Lopez-Serrano, F., Castro, J.M., Macosko, C.W., Tirrell, M., Polymer 24 (1980) 263.
[7] McFarlane, R.C., Reilly, P.M., O'Driscoll, K.F., J. Polym. Sci. Polym. Lett. Ed. 18 (1980) 81.
[8] Wilson, E.B., An Introduction to Scientific Research. McGraw-Hill, New York, NY, 1952, p. 204.
[9] Burger, E., Kuntz, I., J. Polym. Sci. 2A (1964) 1687.
[10] Kennedy, J.P., Kelen, T., Tudos, F., J. Polym. Sci., Polym. Chem. Ed. 13 (1975) 2277.
[11] Joshi, R.M., J. Macromol. Sci., Chem. A7 (1973) 1231.
[12] Moad, G., Moad, C.L., Macromolecules 29 (1996) 7727.

Chapter 2

Vibrational spectroscopy of polymers

Introduction to vibrational spectroscopy

Infrared (IR) spectroscopy is one of the most often used spectroscopic tools for the study of polymers. There are a number of reasons for the success of IR. The IR method is rapid and sensitive with sampling techniques that are easy to use. Also, the instrumentation is inexpensive, the operation of the equipment is simple, and service and maintenance of the equipment are not expensive. Finally, interpreting the spectra is not particularly difficult and can be learned easily, although better results may be obtained by an infrared professional.

The primary limitations of IR spectroscopy are in quantitative measurements. Although IR measurements are precise about the relative ranking of the amount of specific structures in a set of samples, making accurate absolute quantitative infrared measurements is a demanding process.

Raman spectroscopy is complementary to IR and due to differences in the nature of the selection rules yields vibrational information not obtainable from IR. In many cases, Raman spectroscopy is particularly useful when ease of sampling and remote sampling is important. Raman also is advantageous in aqueous solution due to low Raman scattering of water. On the other hand, Raman has been utilized more as a research tool than an analytical tool for polymers. The basic reason for this practical limitation is the ubiquitous fluorescence which occurs with polymers. However, in recent years, tremendous progress has been made and Raman is becoming a more common tool for polymer analysis.

In this chapter, we will briefly review the basis of vibrational spectroscopy (IR and Raman) and the type of results to be expected from polymer samples. Much of the theory of Raman spectroscopy is the same as IR so we will deal with them at the same time. More specific comparisons of the two forms of vibrational spectroscopy are in Chapter 5.

Elementary theory of vibrational spectroscopy

Vibrational spectra including infrared and Raman result from the interactions of the vibrational motions of a molecule with electromagnetic radiation. These vibrational interactions can be described by a simple harmonic oscillator model.

After separating the electronic contributions, each molecule has an internal vibrational energy, U, which can be expressed in terms of the coordinates and interbond forces between the atoms constituting the molecule. A nonlinear molecule consisting of N atoms has $3N - 6$ degrees of freedom. Thus a set of $3N - 6$ generalized coordinates, G_i, can be found that completely describes the internal motions of this nonlinear molecule. The internal energy of the molecule can be written as:

$$U = U(G_1, \ldots, G_i) \tag{2.1}$$

where $i = 3N - 6$.

It can be shown that the internal energy can be written:

$$U = U_0 + \tfrac{1}{2} \sum Q_i{}^2 \Lambda_{ii} + \ldots \tag{2.2}$$

where Q_i are a set of normal coordinates and Λ_{ii} is a diagonal matrix. Thus, we have a system of weakly coupled harmonic oscillators. The first term U_0 is the internal potential energy of the molecule in the equilibrium state. The second term represents the contribution to the potential energy from the fundamental collective vibrational bands, while the cubic and higher terms are responsible for combination, difference, and overtone bands.

The decomposition of coupled harmonic oscillators into a collection of independent oscillators is known as a normal mode expansion and the independent oscillators are called *normal modes*. Normal modes are defined as modes of vibration where the respective atomic motions of the atoms are in 'harmony'; that is, they all reach their maximum and minimum displacements at the same time. These normal modes can be expressed in terms of bond stretches and angle deformation (termed internal coordinates) and can be calculated by using a procedure called normal coordinate analysis.

Infrared spectroscopy

A normal vibrational mode in a molecule may give rise to resonant infrared absorption (or emission) of electromagnetic radiation only when the transition is induced by the interaction of the electric vector $\mathbf{E}$ of the incident beam with the electric dipole moment, μ_i, of the molecule. That is, the dynamic dipole moment of the ith normal mode, $\partial\mu_i/\partial q_i$ or μ_i is nonzero. The intensity of the transition is proportional to the square of the transition dipole moment, i.e., the matrix element of the electric dipole moment operator between the two quantized vibrational levels involved.

Raman spectroscopy

Raman scattering is envisaged as the process of reradiation of scattered light by dipoles induced (P) in the molecules by the incident light and modulated by the vibrations of the molecules. In normal Raman scattering by molecules in isotropic media, the dipoles are simply those which result from the action of the electric field component **E** of the incident light on the molecules,

$$\mathbf{P} = \alpha \mathbf{E} \tag{2.3}$$

where α is the molecular (dipole) polarizability.

The Raman effect occurs when a sample is irradiated by monochromatic light, causing a small fraction of the scattered radiation to exhibit shifted frequencies that correspond to the sample's vibrational transitions. Lines shifted to energies lower than the source are produced by ground-state molecules, while the slightly weaker lines at higher frequency are due to molecules in excited vibrational states. These lines, the result of the inelastic scattering of light by the sample, are called Stokes and anti-Stokes lines, respectively. Elastic collisions result in Rayleigh scattering and appear as the much more intense, unshifted component of the scattered light.

In normal Raman scattering, a molecule is excited to a virtual state, which corresponds to a quantum level relating to the electron cloud distortion created by the electric field of the incident light. A virtual state does not correspond to a real eigenstate (vibrational or electronic energy level) of the molecule, but rather is a sum over all eigenstates of the molecule. The energy level diagram is shown in Fig. 2.1.

The molecule will scatter light at the incident frequency. However, the molecule vibrates with its own unique frequencies. If these molecular motions produce changes in the polarizability,, the molecule will further interact with the light by superimposing its vibrational frequencies on the scattered light at either higher or lower frequencies.

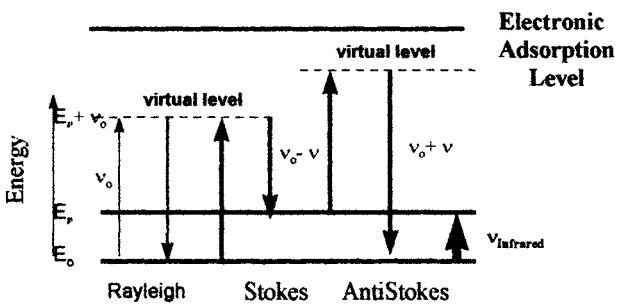

Fig. 2.1. The vibrational energy level diagram showing a single transition from the ground state to the excited state with the infrared transition. The Rayleigh transition is shown as a transition from the ground state to the virtual level and return without an exchange of a photon. The Stokes line is shown as a transition from the ground state to the virtual state and return with a loss of a vibrational photon. The anti-Stokes transition is from the excited vibrational state to the virtual level and return to the ground state with an increase in energy by acquiring a vibrational photon.

Vibrational spectroscopy as an identification tool

Molecules consist of atoms held together by valence forces. These atoms vibrate by thermal energy, giving every molecule a set of resonance vibrations analogous to the resonance modes of mechanical structures. Accordingly, when impinging radiation passes through the material it is absorbed only at frequencies corresponding to molecular modes of vibration, and a plot of transmitted radiation intensity versus frequency shows absorption bands (absorption spectrum). IR and Raman spectroscopy measure the vibrational energy levels of molecules. The characteristic band parameters measured in IR spectroscopy are frequency (energy in wavenumbers, cm^{-1}), intensity (polar character), band shape (environment of bonds), and the polarization of the various modes, that is, transition-moment directions in the molecular framework. Because the vibrational energy levels are distinctive for each molecule (and its isomers), the vibrational spectrum has often been called the *fingerprint* of a molecule. In the sense that the IR and Raman spectra register the most specific information concerning the molecule, this description is useful [1–3].

> *The IR absorption spectrum of a compound is probably its most unique physical property. Except for optical isomers, no two compounds having different structures have the same IR spectrum. In some cases, such as with polymers differing only slightly in molecular weight, the differences may be virtually indistinguishable but, nevertheless, they are there. In most instances the IR spectrum is a unique molecular fingerprint that is easily distinguished from the absorption patterns of other molecules.* — A. Lee Smith [4]

Vibrational spectroscopy should be used whenever chemical specificity and selectivity are needed. As an identification tool, IR has no close spectroscopic competitor. Commercial laboratories have thousands of spectra filed on computers, and 'seek and identify' programs have been written to aid in the identification process [5,6]. All of the identification procedures are based on the assumption that the compound is pure, but routine samples are seldom pure. Therefore, it is advisable to ascertain the purity of the sample before spectral analysis is undertaken. For polymer samples, additives such as fillers, antioxidants, lubricants, and mold release agents can generate spectral interferences [7]. However, except for fillers and plasticizers, the process and stabilizer additives generally amount to 1% by weight of total polymer and contribute very little to the total spectrum.

Due to the recent developments in Raman spectroscopy there are a limited number of spectral catalogues available for use in identification purposes but one for polymers has been developed [8]

Basis of vibrational spectroscopy as a structural tool

Our primary interest is in determining the structure of polymers so we need to understand the molecular basis of vibrational spectroscopy as a structural tool.

Structural dependence of vibrational frequencies

A vibrational spectrum either IR or Raman is ordinarily recorded in wavenumbers, (cm^{-1}), which is the number of waves per centimeter. The relationship between ν and the wavelength, λ (μm), is

$$\nu\ (cm^{-1}) = \frac{(10^4)}{\lambda}\ (\mu m) \tag{2.4}$$

which can also be written

$$\nu\ (cm^{-1}) = 3 \times 10^{10}\ Hz \tag{2.5}$$

The wavenumber scale is directly proportional to the energy and vibrational frequency of the molecule.

In wavenumbers

$$\Delta E_{vib} = hc_s\nu\ (cm^{-1}) \tag{2.6}$$

where ΔE_{vib} is the vibrational energy level separation, h is Planck's constant (6.62×10^{-27} erg s), and c_s is the speed of light (3×10^{10} cm/s).

The fundamental IR region arbitrarily extends from 4000 cm^{-1} to approximately 300 cm^{-1}. The far-IR region extends from 300 to 10 cm^{-1}, and the observed bands are due to molecular torsional motions as well as lattice and intermolecular modes but the low IR source energy makes this region generally inaccessible except with special instrumentation. The near infrared (NIR) extends from 14,000 to 4,000 cm^{-1} (0.7–2.5 μm) and the observed bands consist of overtones and combinations of fundamental mid-IR bands. The near infrared is becoming an important infrared method particularly in quality control. These definitions of the different regions, which were originally based on instrumental requirements of dispersion and detectors, are less important now with Fourier transform IR (FTIR) spectroscopy, but the terms are still in common usage.

In Raman spectroscopy, a single instrument can scan from 4000 cm^{-1} down to $\sim$10 cm^{-1} and so it is not necessary to describe the different frequency regions.

The vibrational energy levels can be calculated from first principles by using a technique called normal coordinate analysis [8], and as a result some of the factors influencing spectra have been discovered.

The vibrational frequencies of a molecule depend on:

- Nature of the motion.
- Mass of the atoms.

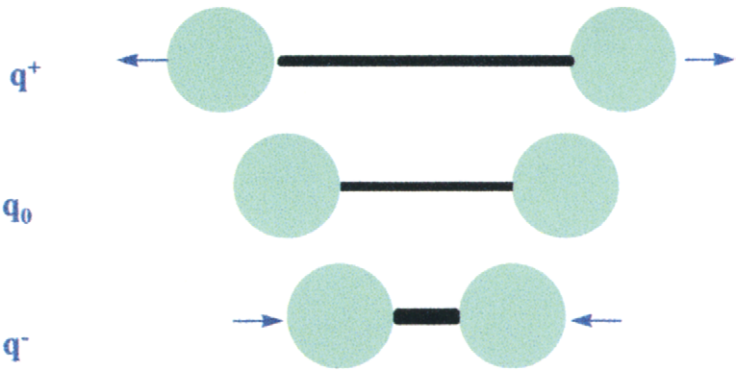

Fig. 2.2. Bond stretching motion; q^+ is the extension, q_0 is the equilibrium, and q^- is the compression of the bond.

- Detailed geometric arrangements.
- Nature of the chemical bonding.
- Chemical and physical environment.

> *There is no obvious relationship between the observed IR and Raman frequencies and the chemical reactivity of a molecule. The bond stiffness is the important parameter, and this parameter has little to do with the chemical reactivity of the bond. However, every year someone discovers a new correlation between vibrational frequencies and reactivity. Don't let it fool you!*

In Fig. 2.2 the bond-stretching motion of a chemical bond is shown.

The model of a chemical bond in IR spectroscopy is one of point masses connected by a harmonic spring, as shown in Fig. 2.3 [8].

The vibrational frequency of the stretching mode of a diatomic molecule A–B can be easily calculated by using Eq. (2.7).

$$\upsilon\ (\mathrm{cm}^{-1}) = \left[k_f \frac{[M_A + M_B]}{M_A M_B} \right]^{1/2} \tag{2.7}$$

where k_f is the force constant, or stiffness of the bond, and M_A and M_B are the masses of the two atoms. The force constant can be expressed in the form

$$k_f \propto N_b \left[\frac{X_A X_B}{d^2} \right]^{3/4} \tag{2.8}$$

where N_b is the bond order; d is the bond length; and X_A and X_B are the electronegativities of atoms A and B, respectively. An increase in the stiffness, k_f, of the bond increases the frequency. One obvious way to increase bond stiffness is to increase the bond order from sp^3 to sp^2 to sp hybridization. When this occurs, the frequency of the stretching vibration will inevitably increase. The vibrational frequency of the C=O

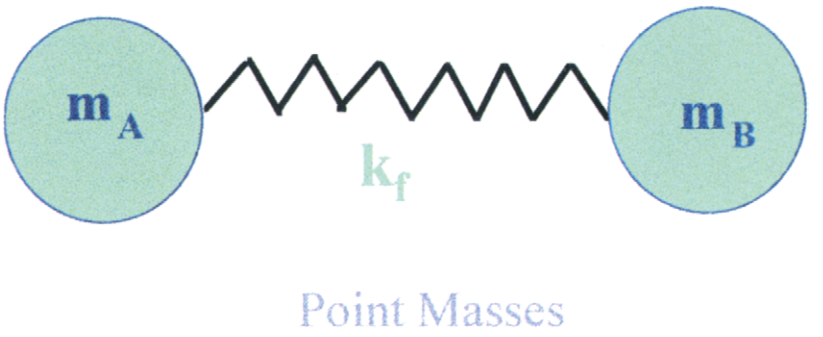

Fig. 2.3. Mechanical model of the chemical bond made up of point masses and a harmonic spring of stiffness k_f.

group is approximately 1700 cm^{-1} while for a C−O group the frequency is 1100 cm^{-1}. With an increase in mass the frequencies also go down. For example, the stretching force constant is nearly the same for the C−H and C−Cl bonds but due to the increased mass the C−H vibration is found at 2900 cm^{-1} while the C−Cl is at 600 cm^{-1}.

If all molecules were diatomic, the vibrational spectra would not be very interesting, because there would be only a single observable mode. When the atoms are different, the mode is observed in the infrared and when they are the same, the observable mode occurs in the Raman spectra.

A molecule made up of N atoms can be visualized as a set of N masses connected by springs (chemical bonds). The vibrations can be resolved into $3N-6$ normal modes (the six modes have zero energy corresponding to translation and rotation in the x, y and z directions. Normal modes are defined as modes of vibration where the respective atomic motions of the atoms are in 'harmony'; that is, they all reach their maximum or minimum displacement at the same time. These normal modes can be expressed in terms of bond stretches and angle deformations (termed the internal coordinates) and can be calculated by using a procedure called normal coordinate analysis [8]. The normal coordinate analysis method is a computer intensive process requiring the construction of the spatial coordinates of all of the atoms and the estimation of the force field between the atoms. It is not an easy technique to learn or use!

I am compelled to relate a story about one of the more famous IR spectroscopists — the late Professor Bellamy, who wrote several books on characteristic group frequencies. He said that when he looked at a new molecule and its complex IR spectrum, he would often have the urge to perform a normal coordinate analysis to help him with the spectral interpretation. He also said that when this happened he would lie down until the feeling passed! With modern computers, the normal coordinate analysis problem is much simpler but still is nontrivial to the inexperienced and untrained, so we will take the approach of Bellamy whenever we feel the need for using normal coordinate analysis for band structural assignments.

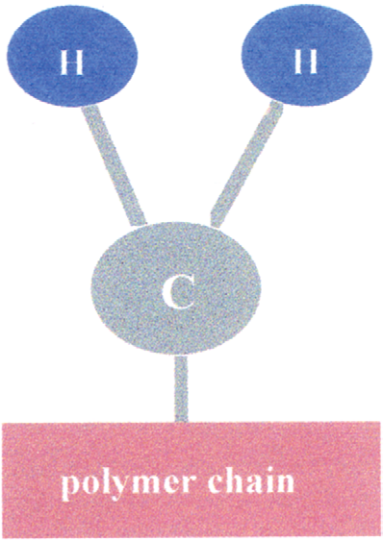

Fig. 2.4. Methylene unit attached to a polymer chain.

Consider molecules that are only slightly more complicated than a diatomic molecule, for example a methylene group. In fact, consider a special type of methylene group: one that is attached rigidly to a polymer chain. It has three atoms: a carbon and two hydrogens. Because it is attached to a polymer chain, this special methylene unit cannot translate freely (this will simulate the situation in a polyethylene chain). This methylene structure is shown in Fig. 2.4.

> *As you have probably guessed, I want to examine the vibrational motions of the methylene units of a polyethylene chain, but for now we will ignore the adjoining carbons.*

Because normal coordinate analysis will not be used here to solve the problem (Painter et al. have written a very useful book on this subject [10]) the vibrational analysis must begin with intuitive thinking. First, the C−H bonds stretch or compress like springs in relation to each other when vibrating.

> *We can simulate the motion by using our bodies and letting the hands be the hydrogen atoms and the body be the carbon. Don't laugh until you have tried it!*

Because the carbon is attached firmly to the polymer chain, the atoms cannot fly off into space but must reach their maximum extension and return to their minimum point in harmony, and continue this oscillation or vibrational motion. This motion is called vibrational C−H stretching. But, there are two identical C−H bonds, and each

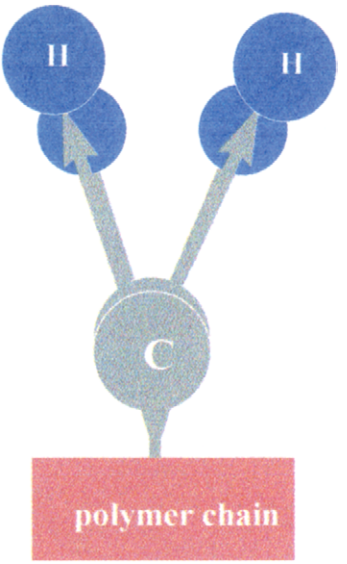

Fig. 2.5. The symmetric methylene stretching mode which occurs at 2850 cm^{-1}.

undergoes the aforementioned vibrational motion in phase with the other while they are connected to the same carbon atom. Because there are two identical C−H bonds, the oscillators can couple and two different types of stretching vibrations result. The vibrations are observed at higher and lower energies than those of the isolated C−H mode. Because the energies are different, there is some restriction on their individual motions, and the result is two normal modes. In one case, the maximum displacements of the C−H groups occur at the same time (like moving our hands out together at the same time), and the motions are in-phase, as shown in Fig. 2.5.

This vibrational mode is the *symmetric* C−H stretching mode, $\nu_s(CH_2)$, which occurs at 2850 cm^{-1}.

The second C−H stretching mode occurs when the two C−H bonds reach their maximum displacement completely out of phase; that is, one is extended by stretching, and the other is compressed. One of the C−H bonds is compressed to its minimum, and the other is extended to its maximum. One hand moves away from the body, while at the same time the other hand is pulled toward the chest. This mode is the asymmetric C−H stretching mode, $\nu_a(CH_2)$, shown in Fig. 2.6 which occurs at 2925 ± 25 cm^{-1}.

The allowed motions are restricted by the fact that the vibrational motion cannot displace the center of mass of the molecule. Considering this restriction, the displacement of the carbon atom attached to the two moving hydrogen atoms must compensate for the mass displacement of the hydrogens. Therefore, the displacement of the carbon is quite different in the in-phase and out-of-phase stretching modes described, even though the hydrogens are moving in an identical fashion, except that

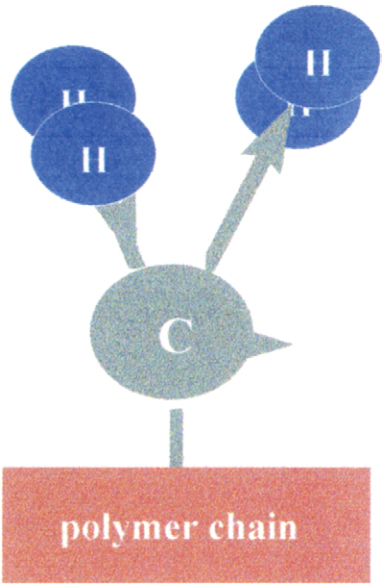

Fig. 2.6. The asymmetric methylene stretching mode which occurs at 2925 cm^{-1}.

they have different phases relative to each other (Figs. 2.5 and 2.6). Because the carbon is moving in a different manner to compensate for the hydrogen motion, the resulting vibrational energies of these two C−H stretching modes are different, and the two stretching modes are not degenerate; that is, they absorb at different IR frequencies. This intuitive result is confirmed by experiment. The symmetric stretching mode of the methylenes in polyethylene occurs at 2853 cm^{-1}, and the asymmetric mode appears at 2926 cm^{-1}.

There are also angle bending motions where the hydrogens move towards each other resulting in the deformation of the HCH angle between them. Now consider the motion of the hydrogens toward each other — a bending of the H−C−H angle of the methylene group. From a molecular point of view, this involves the bending or deformation of the angle between the two C−H bonds. This motion may be visualized by extending both your arms and moving the hands toward each other in a clapping motion — but the hands cannot touch because of natural restrictions of atomic size and packing. Spectroscopists call this vibrational motion the methylene bending motion because the angle between the two hydrogens is being bent. This is the symmetric methylene bending mode, $\delta_s(CH_2)$ occurring at 1470 ± 25 cm^{-1}. This motion involves the symmetric movement of the hydrogens away each other (Fig. 2.7).

If you use your hands at the end of your extended arms to represent the hydrogens for this motion, you will notice that it is necessary for you (the carbon atom) to wag or rotate your body to accomplish the motion. Hence, the spectroscopists call this mode the methylene wagging mode, $\nu_w(CH_2)$, which has frequencies ranging from 1308–1170 depending on the environment of the methylene unit and it has a different

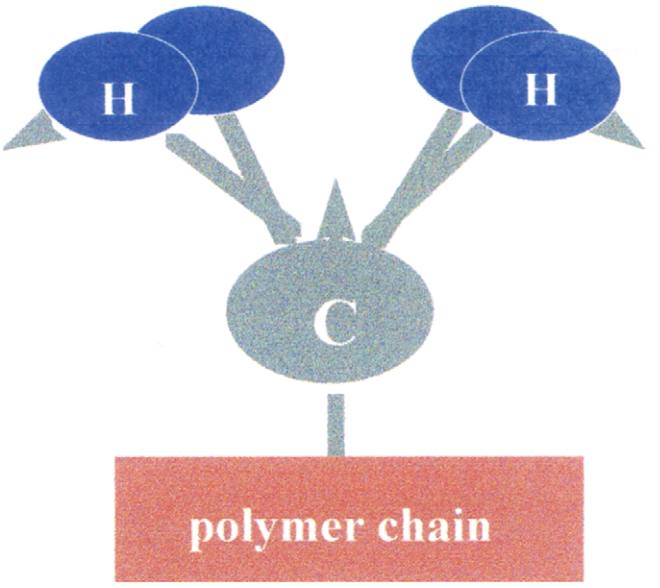

Fig. 2.7. The methylene bending motion found at 1470 cm^{-1}.

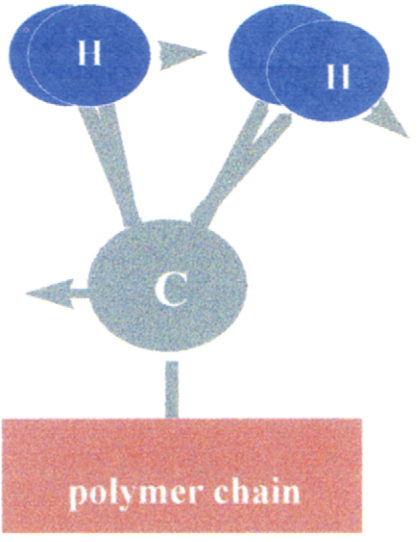

Fig. 2.8. The methylene wagging mode located from 1308–1179 cm^{-1}.

vibrational frequency than the bending mode previously described (Fig. 2.8). These two modes are the symmetric and asymmetric bending or deformation modes.

The additional methylene vibrational modes are the wagging and rocking modes which are deformations in the z direction, i.e. perpendicular to the methylene groups. These motions are shown in Fig. 2.9.

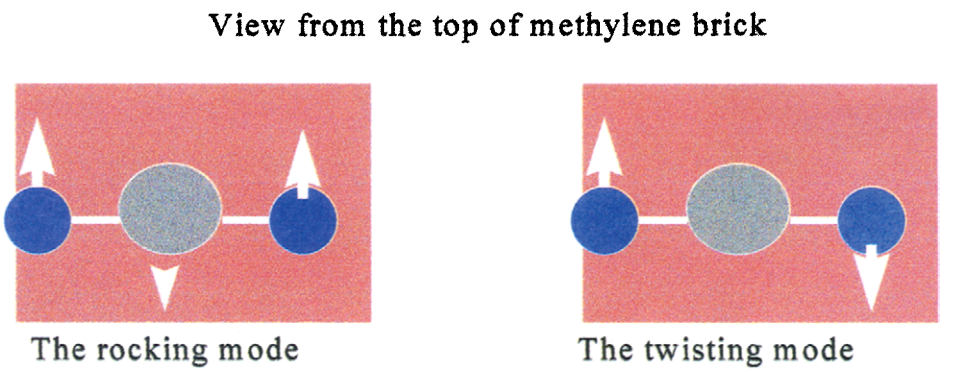

Fig. 2.9. The methylene rocking and twisting modes.

These modes are shown from a top view of the methylene in Fig. 2.9. The twisting mode $\delta_{twist}(CH_2)$, range near 1200 cm^{-1} depending on the environment. The rocking mode $\delta_{rock}(CH_2)$ shows an interesting progression of frequencies with the number of methylenes in a sequence as shown in Table 2.1.

This progression of frequency with the length of the methylene sequence arises from 'vibrational coupling'. For the study of polymers, the nature of the coupling, not only between two C−H groups on the same carbon, but also between methylene groups on the same carbon chain, must be understood [10], see the section on 'Coupled infrared vibrations as a polymer structure probe' (page 65). We will discuss this matter more thoroughly shortly.

The point here is that the same chemical group can have a number of vibrational modes with different energies arising from the different internal modes. Thus, to

Table 2.1
The frequencies of the methylene rocking mode as a function of methylene sequence

Methylene sequence n	Methylene rocking cm^{-1}
X X C−CH_2−C−	1	815
X X C−CH_2−CH_2−C−	2	752
X X C−CH_2−CH_2−CH_2−C−	3	733
X X C−CH_2−CH_2−CH_2−CH_2−C−	4	722
X X C−CH_2−CH_2−CH_2−CH_2−CH_2−C−	5	722
X X C−$(CH_2)_n$−C−	n	722

identify a given chemical group in a polymer, the different IR modes can be used to confirm the existence of the group without having to rely on a single observed mode [3]. To identify the polymer itself the collection of functional groups and their associated frequencies will be sufficient to uniquely define the spectrum of the polymer.

Infrared selection rules

The first requirement for IR absorption is that a frequency in the impinging source of IR radiation must correspond to the frequency of the vibration as expressed in Eq. (2.3). Frequency matching is a necessary condition for absorption but not the only one. An additional requirement is some mode of interaction between the impinging IR radiation and the molecule (there must be something to catch the radiation). Even if the IR radiation has the same frequency as the normal vibration of the molecule, it will be absorbed only under certain conditions. The rules determining optical absorption are known as *selection rules*.

For simplicity, let us take a classical rather than a quantum mechanical approach to selection rules. An oscillating dipole can emit or absorb radiation. Consequently, the periodic variation of the dipole moment of a vibrating molecule results in the absorption or emission of the same frequency as that of the oscillation of the dipole moment (Fig. 2.10). The absorption occurs because the electric field of the light interacts directly with the molecule's dipole and with the vibration the magnitude of the dipole moment is changed. When the dipole moment of the molecule is greater in the higher vibrational states adsorption occurs.

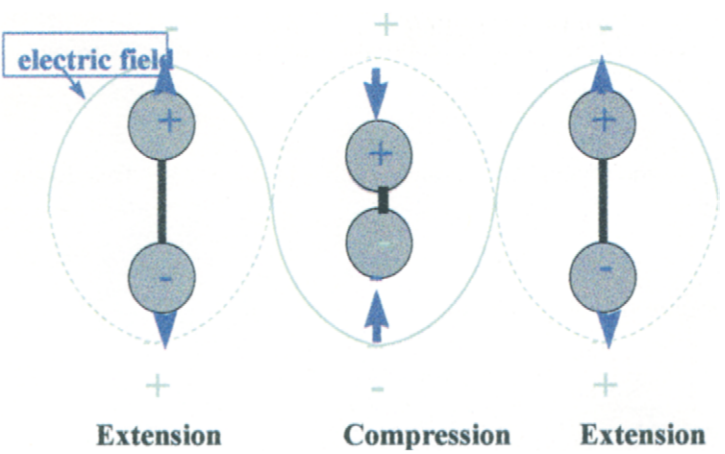

Fig. 2.10. The periodic variation of the dipole moment of a chemical bond resulting from the interaction with light of the same frequency as the bond stretching mode of the bond.

Raman selection rules

The Raman effect is a second order interaction of the electric field of the light and the molecule's dipole moment. It is actually the effect of the photon's electric field on the interaction between the field and the dipole. IR spectroscopy involves a change in polarization, but Raman spectroscopy occurs because of a change in the molecule's polarization. Raman scattering is a process of light scattered by dipoles P induced in the molecules by the incident light and modulated by the vibrations of the molecules. In normal Raman scattering by molecules in isotropic media, the dipoles are simply those which result from the action of the electric field component **E** of the incident light on the molecules,

$$\mathbf{P} = \alpha \mathbf{E} \tag{2.9}$$

where α is the molecular (dipole) polarizability.

Because the electric field oscillates as it passes through the molecule, the induced dipole moment in the molecule also oscillates. This oscillating dipole moment radiates light at the frequency of oscillation in all directions except along the line of action of the dipole. The electric field is an oscillating function that depends upon the frequency of the light, ν_0, according to

$$E = E_o \cos 2\pi \nu_0 t \tag{2.10}$$

where E_o is the impinging electric field, and t is time.

Substitution gives

$$P = \alpha E_o \cos 2\pi \nu_0 t \tag{2.11}$$

The polarizability, α, depends on the motion of the nuclei in the molecule. The motion of the nuclei of a diatomic molecule can be expressed in terms of the normal coordinate of the vibration, q, and the dependence of α on q (the change in internuclear separation with vibration) can be approximated by a series expansion

$$\alpha = \alpha_o + \left(\frac{\delta \alpha}{\delta q}\right) q + \cdots \tag{2.12}$$

The normal mode is a time-dependent vibration with a frequency ν_1. This dependence can be expressed as

$$q = q^\circ \cos 2\pi \nu_1 t \tag{2.13}$$

where q°_1 is the equilibrium position. Substitution gives

$$P = (E_o \cos 2\pi \nu_0 t) \left[\alpha_o + \left(\frac{\delta \alpha}{\delta q}\right) q\right] (q^\circ_1 \cos 2\pi \nu_1 t) \tag{2.14}$$

From basic trigonometry

$$\cos(\theta) + \cos(\phi) = \frac{\cos(\theta + \phi) + \cos(\theta - \phi)}{2} \tag{2.15}$$

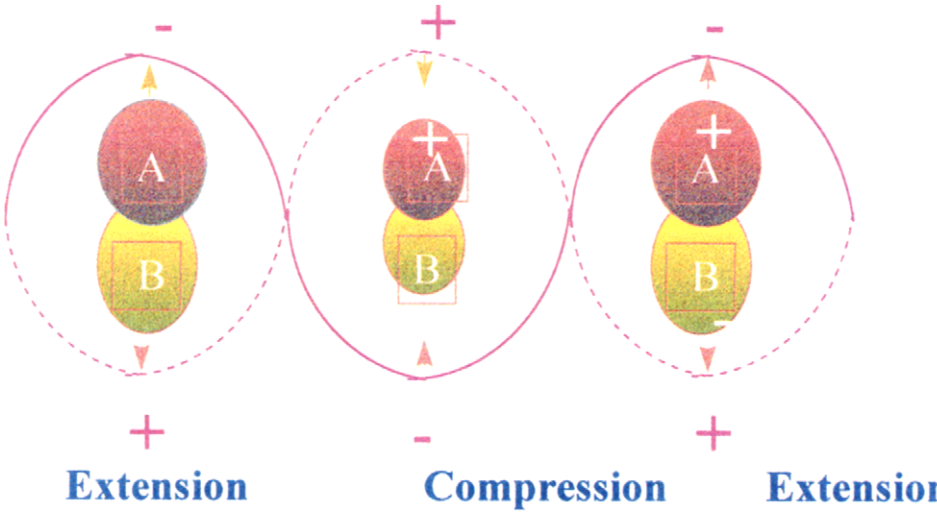

Fig. 2.11. The change in the molecular polarizability of a chemical bond A−B as induced by the electric field of the incident light beam.

Substitution gives

$$P = (\alpha_o E_o \cos 2\pi \nu_0 t) + \tfrac{1}{2} E_o q \frac{\delta\alpha}{\delta q}[\cos 2\pi(\nu_0 + \nu_1)t + \cos 2\pi(\nu_0 - \nu_1)t] \quad (2.16)$$

This complex equation demonstrates that three lines are predicted in the light scattered by a diatomic molecule. The α_o term represents the light that is not shifted in frequency (Rayleigh scattering). If the normal mode produces a change in the molecular polarization $\{(\delta\alpha/\delta q)$ does not equal $0\}$, Raman lines are shifted higher and lower in frequency than ν_0 by, the frequency of vibration of the molecule. If $(\delta\alpha/\delta q)$ equals 0, the second term is 0, and no Raman lines are observed. This change in polarization with the vibrational motion of the nuclei, $\delta\alpha/\delta q$, is the basis for the selection rule governing the Raman activity of a vibrational mode. This is illustrated in Fig. 2.11. For simple molecules, it is easy to determine whether or not the polarizability changes during the vibration. For a chemical bond, the electron clouds are ellipsoid with circular cross sections. The electrons are more polarizable along the chemical bond than in the direction perpendicular to it [40].

Stretching vibrations of polar bonds (atoms with different electronegativities) modulate the dipole moment and show strong infrared intensities. Vibrations of non-polar (atoms of the same or similar electronegativity) show infrared bands of weak intensity, but they do modulate the molecular polarizability and therefore sow strong Raman bands.

The intensity of the absorption or emission is proportional to the square of the change in the dipole moment. So the IR intensity, I_k, of the kth mode is

$$I_k = C\left[\frac{\partial\mu}{\partial Q_k}\right]^2 \quad (2.17)$$

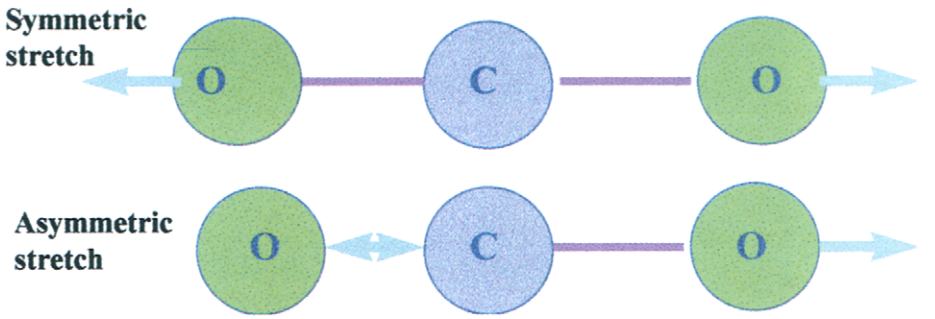

Fig. 2.12. The two in-plane stretching vibrations of carbondioxide. The symmetric stretch is IR inactive, but Raman active (A). The asymmetric mode is IR active (A) and Raman inactive (IA).

where C is a proportionality constant, μ is the dipole moment, and Q_k is the displacement of the kth normal coordinate of the motion. If there is no dipole moment, then no IR absorption can occur. In other words, it is possible for molecular vibrations having the proper IR frequency to occur, but be totally invisible to the IR beam. This is the nature of the selection rules.

The intensities are determined by the magnitude of the change in the dipole moment with the displacement generated by the normal mode. If the dipole moment is large, (i.e., a highly polar group of atoms with different electronegativities), then the change in the dipole moment with bond stretching will be large and the IR absorption intensity will be high. If the dipole moment is small, (i.e., atoms of similar electronegativity), the IR absorption intensity will be small. For example, consider the two in-plane stretching vibrations of CO_2 (Fig. 2.12).

The molecular dipole moment of the symmetric unperturbed molecule is zero when the dipole displacements of both bonds are added. In the totally symmetric vibration (Fig. 2.12), the two oxygen atoms move in phase successively from and toward the carbon atom. The change in dipole moment of one C−O bond is balanced by the change in the opposite C−O bond. The symmetry of the molecule is maintained in this vibration, and there is no total change in dipole moment. For this mode of vibration, there is no IR absorption but strong Raman scattering). The change in the polarization is shown in Fig. 2.13.

However, in the asymmetric stretching vibration (Fig. 2.12), the symmetry of the molecule is perturbed, there is a change in the net dipole moment, and IR absorption occurs. However, the molecular polarizability cancels in this vibration ($d\alpha/dq = 0$), and there is no Raman scattering for this mode.

For the CO_2 molecule, the vibrational selection rules can be obtained by mere inspection of the vibrations occurring. For more complicated molecules, the selection rules can be determined from symmetry considerations [8], because symmetry is helpful in determining the type of motion that is allowed. In fact, the normal modes fall into different symmetry species. For symmetrical molecules, the normal modes and the symmetry modes are nearly the same. The symmetry analysis is quite simple

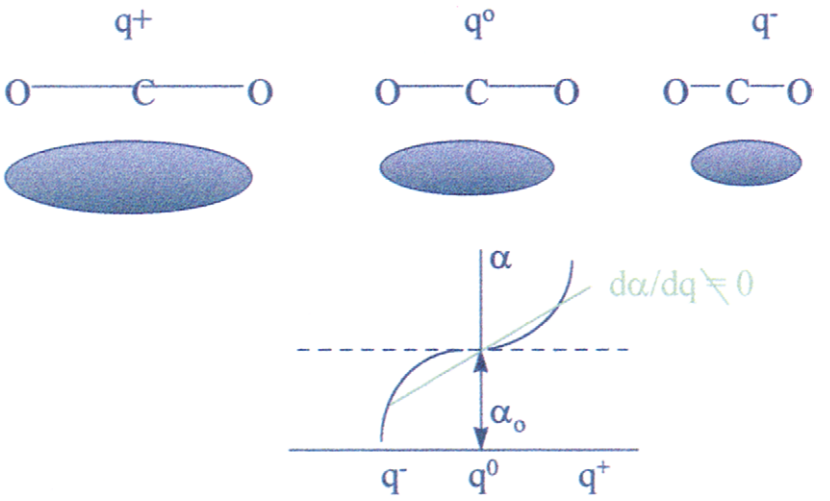

Fig. 2.13. The change in polarizability for CO_2 for the symmetric stretching mode which shows that symmetric mode is Raman active as $d\alpha/dq$ greater than zero.

but highly tedious and generally uninteresting. For simple types of low-molecular-weight molecules, tables are available with the results for the various geometries [11]. However, if you wish to learn the process, a number of excellent books are available [11,12]. For polymers, the symmetry relations for most simple vinyl systems also are available [10].

A simple rule is that polar bonds yield strong IR absorption and weak Raman effect, and nonpolar bonds are weak or absent in IR but strong in the Raman. If this rule is applied to polymer molecules, it can be determined that for hydrocarbon polymers with carbon backbones, the IR absorption of the backbone will be weak, and this result has been observed under experimental conditions. However, substituted groups like C−H, C−F, and C=O will have polar bonds because of differences in electronegativity, and the IR absorption will be strong. Again this speculation has been observed under experimental conditions.

To further complicate the interpretation of the observed vibrational spectra, unwanted bands appear in the spectra. These bands are called overtone and combination bands, and they result from the effect of anharmonic terms in the potential energy. Overtone bands appear at approximately $2\nu_i$, where i is one of the fundamental modes. Combination bands appear at approximately $\nu_i + \nu_j$ where i and j are fundamental modes. Some methods of symmetry analysis can help determine which overtones might be allowed, but these methods will not be investigated here [11]. Before making structure assignments to the observed bands, it is usually a good idea to consider the possibility that the band under consideration may be an overtone. To determine if this is the case, multiply the frequencies of some of the stronger lower frequency bands by 2 and see if a match is found. The overtone and combination bands are always weaker than the corresponding fundamental bands.

Infrared intensities

The IR intensity usually refers to the integrated absorbance

$$A_f = \left[\frac{1}{cb}\right] \int \ln\left(\frac{I_o}{I}\right) d\nu \tag{2.18}$$

If c is the concentration in moles per liter (millimoles per cubic centimeter), b is the path length in centimeters, and $d\nu$ is in reciprocal centimeters, A_s is given in centimeters per millimole (sometimes called darks). In these units, the value of A_s is approximately 1000 cm/mmol for a very intense absorption and approximately 0.1 cm/mmol for a very weak absorption.

When IR radiation is absorbed by a molecule, the intensity of the absorption depends on the movement of the electronic charges during the molecular vibrations. Therefore, the IR intensities should provide information about the electronic charge distributions in molecules and about how the electrons redistribute themselves during molecular vibrations.

The electric dipole moment of a molecule is given by

$$\mu_o = \sum_{i=1}^{n} e_i X_i \tag{2.19}$$

where e_i is the charge of the ith particle and X_i is the position of the ith particle given in the space-fixed coordinate system. The electric dipole moment, μ, for a molecule undergoing vibration can be expanded into a power series in the normal coordinates, Q_s,

$$\mu = \mu_o + \sum \left[\frac{\partial \mu}{\partial Q_s}\right]_o Q_s + \cdots \tag{2.20}$$

where the subscript 'o' denotes the value of the equilibrium position, and μ_o is the static molecular dipole moment. In practice, only the first two terms are necessary, so μ may be evaluated by knowing the values of μ_o and the parameters $\partial\mu/\partial Q_s$.

The IR intensity A_s is related to the molecular parameters as follows [13]:

$$A_s = \left[\frac{8\pi^2 N_A}{3hc_s}\right] \nu_s \left[\frac{\partial \mu}{\partial Q_s}\right]^2 \tag{2.21}$$

where N_A is Avogadro's number, h is Planck's constant, c_s is the speed of light, and ν_s is the frequency of the band center (cm^{-1}). This relationship can be expressed inversely as

$$\left|\frac{\partial \mu}{\partial Q_s}\right| = 0.03200(A_s)^{1/2} \tag{2.22}$$

Hence, each IR intensity can be related to the dipole moment derivative with re-

spect to the Q_s normal coordinate. The sign of the derivative of the bond moment is always ambiguous, because it is a squared function of the IR intensities. The determination of the sign must come from evidence outside the intensity measurement itself.

Each valence bond is characterized by a bond dipole moment, μ_n, and the derivative of this bond moment with respect to bond length, $\delta\mu_n/\delta r_n$. For the C−H bond, μ_o(CH) is positive in the sense −C−H+, and $\delta\mu_n/\delta r_n$(CH) is negative, indicating that μ(CH) decreases when the bond stretches.

The IR intensities can be calculated for some molecules, but the calculations are difficult and involve a number of assumptions about the signs and orientations of the dipole moments [13].

For quantitative analysis, the IR intensities for each vibrational mode are given by Beer's law,

$$A = abc \tag{2.23}$$

where A is the absorbance, a is the absorptivity, b is the path length, and c is the concentration of the characteristic group of the vibration. It is necessary to determine a before a quantitative analysis can be made. This determination can be done by calibration using an independent chemical or physical technique or by proper deconvolution of the spectra of mixtures containing the desired component. We will discuss the quantitative aspects of IR spectroscopy later (see Chapter 3).

As a tool for the discrimination of structural elements, the IR intensities are significantly more sensitive to small changes in structure or bond environment than are the IR frequencies. Intensities would be expected to be a most valuable structural tool in IR spectroscopy. The problem with using IR intensities to determine structural elements in solids and polymers is the difficulty in obtaining accurate measurements and in transferring such measurements from one IR instrument to another. With the advent of FTIR and the analog-to-digital converter, the linearity of the absorbances is much greater than with the optical comb used in dispersion instruments.

> *My belief is that we are approaching the time in IR spectroscopy where measurements of IR intensities should be made with the objective of using the results for the refinement of structure and as an additional tool to complement the IR frequency correlations. Work must be done in this area, but the rewards will be high!*

However, a reasonable IR spectrum for a polymer may be constructed empirically by using the measured intensity values, A_j, of the characteristic vibrational modes of similar systems. The integrated intensities measured by transmission spectroscopy [14] are indicative only of the possibility of combining characteristic group frequencies with characteristic group intensities for further specificity in identification of polymer structural components.

Raman intensities

To discuss the Raman intensities, first, one must expand the simple equation

$$\mathbf{P} = \alpha \mathbf{E} \tag{2.24}$$

since both **P** and **E** are vectors consisting of three components in the x, y, and z directions.

$$\begin{aligned} P_x &= \alpha_{xx}E_x + \alpha_{xy}E_y + \alpha_{xz}E_z \\ P_y &= \alpha_{yx}E_x + \alpha_{yy}E_y + \alpha_{yz}E_z \\ P_z &= \alpha_{zx}E_x + \alpha_{zy}E_y + \alpha_{zz}E_z \end{aligned} \tag{2.25}$$

In matrix form, this is written:

$$\begin{aligned} P_x &= \alpha_{xx} \quad \alpha_{xy} \quad \alpha_{xz} \quad E_x \\ P_y &= \alpha_{yx} \quad \alpha_{yy} \quad \alpha_{yz} \quad E_y \\ P_z &= \alpha_{zx} \quad \alpha_{zy} \quad \alpha_{zz} \quad E_z \end{aligned} \tag{2.26}$$

The matrix α is called the *polarizability tensor*. This polarizability tensor is symmetric: $\alpha_{xy} = \alpha_{yx}$, $\alpha_{xz} = \alpha_{zx}$, $\alpha_{yz} = \alpha_{zy}$. If any of the components of the polarizability tensor are changed during a molecular vibration, the mode is Raman active.

In Raman spectroscopy, one observes a fascinating phenomenon whereby a randomly ordered molecule can give rise to a highly polarized scattered Raman signal! The experimental setup for making 90° Raman scattering measurements is shown in Fig. 2.14.

Suppose a highly symmetric molecule is irradiated by plane polarized light (E_z). Then, the induced dipole also oscillates in the same yz plane. If the vibrational

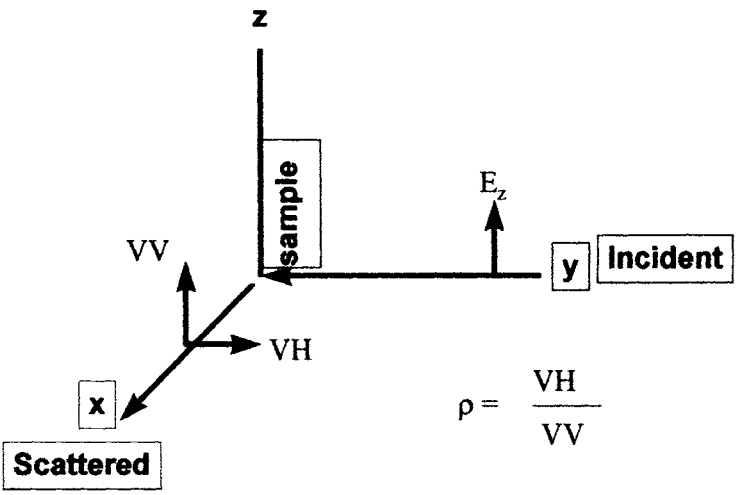

Fig. 2.14. The geometry for the measurement of the polarization ratio.

motion is totally symmetric, the polarizability ellipsoid remains a sphere and the molecule is polarized equally in all directions. Under these circumstances, $VH = 0$ since the oscillating dipole emitting the radiation occurs in the xz plane. Thus $\rho_P = 0$. Such a vibration is called *polarized.* If the molecule is performing a non-totally symmetric vibration, the polarizability ellipsoid changes its shape from a sphere to an ellipsoid during the vibration. Then, the induced dipole is highest along one of the minor axes of ellipsoid. Since these axes are randomly oriented in liquids and solutions, the induced dipole moments would also be randomly oriented. In this case, the ρ is nonzero, and the vibration is called *depolarized.*

An alternate notation expressed in terms of the laboratory coordinate system is $A(BC)D$, where A is the direction of of travel of the incident beam; B and C are the polarization of the incident and scattered light, respectively; and D is the direction in which the Raman scattered light is observed.

The Raman scattered light emanating from even a random sample is polarized to a greater or lesser extent. For randomly oriented systems, the polarization properties are determined by the two tensor invariants of the polarization tensor, that is, the trace and anisotropy tensors. The depolarization ratio is always {less or equal} 3/4. For a specific scattering geometry, this polarization is dependent upon the symmetry of the molecular vibration giving rise to the line. As shown in Fig. 2.15, the line of CCl_4 at 457 cm^{-1} is completely polarized.

The partial polarization of the other two modes indicates that the motions of the CCl_4 are antisymmetric. The unique polarization properties of this new 'radiation' led C.V. Raman to believe that he was observing a new phenomenon rather than normal emission such as fluorescence.

For solids, the problem of polarization is more complicated, but the results are

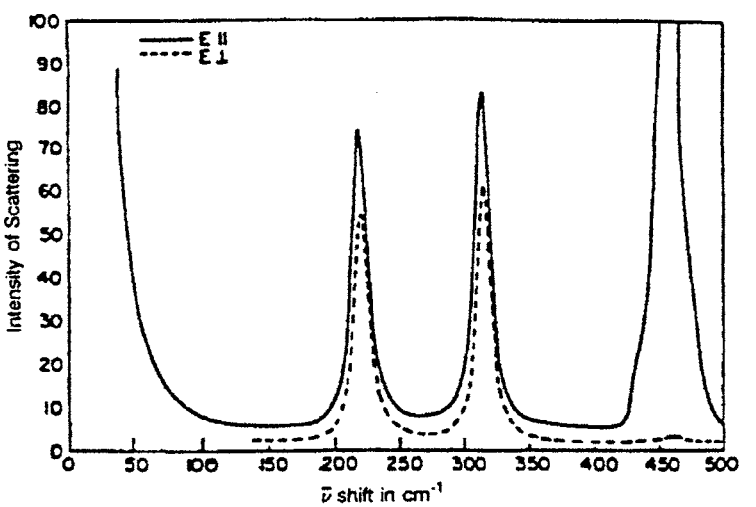

Fig. 2.15. The Raman spectra of carbon tetrachloride.

more rewarding. In solids, the molecular species are oriented with respect to each other. Therefore, the molecular polarizability ellipsoids are also oriented along definite directions in the crystal. Because the electric vector of the incident laser beam is polarized, the directionality in the crystal can be used to obtain Raman data from each element of the polarizability ellipsoid. When the laser polarization and collection are along the z axis, a spectrum from the a_{zz} component of the tensor is obtained. Rotating the analyzer by 90° allows collection of the x-polarized light while still exciting along the z axis, and in this manner α_{zx} is obtained.

However, some polymeric samples contain crystallites or voids comparable in size to the visible wavelengths of the laser. These crystallites or voids scramble the incident laser polarization and thereby prevent any useful measurement of depolarization ratios. Some error in Raman polarization measurements arises because the incident light and Raman scattered light are multiply reflected at the surface of the sample and are also refracted upon entering or leaving the sample. The light-polarization directions are therefore poorly defined. Immersing the sample in a liquid that has a refractive index close to that of the polymer helps to minimize this problem [4].

To study the orientation of the sample, the aforementioned experiments must be related to the molecular polarizabilities. By using upper-case letters for the laboratory coordinate system and lower-case letters for the molecule-fixed coordinate system, the derived polarizability tensor can be found. For excitation polarized along F, the scattered radiation, which is polarized along F', will have an intensity that is proportional to $[(\alpha_k)FF']^2$ (F and F' may be either vertical or horizontal). The appropriate relationships have been determined [5,6]. In an isotropic system, there are orientationally invariant terms, δ and γ, that are defined as

$$\delta = \tfrac{1}{3}\sum \alpha_{ii} \tag{2.27}$$

and

$$\gamma^2 = \tfrac{1}{3}\sum_{i<J}[(\alpha - \alpha_j)^2 - 6\alpha_{ij}^2] \tag{2.28}$$

The contributions of the various geometries of three-dimensionally isotropic systems to the Raman spectrum are shown in Table 2.2.

Table 2.2
Contribution to spectrum for three-dimensionally isotropic systems

Experiment	Geometry	Symmetric	Anisotropic
VV	X(YY)Z	δ^2	$4\gamma^2/45$
VH	X(YZ)Z	0	$\gamma 2/15$
HV	X(ZY)Z	0	$\gamma^2/15$
HH	X(ZX)Z	0	$\gamma^2/15$

(Source: reproduced from Ref. [6]. © 1984 American Chemical Society.)

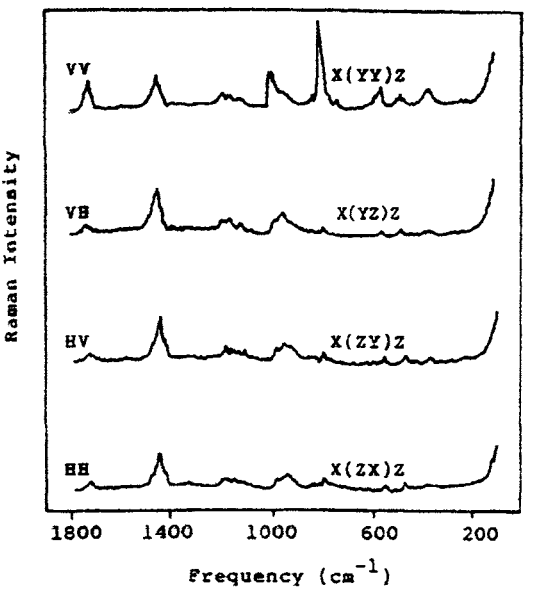

Fig. 2.16. Polarized waveguide Raman spectra of an unoriented thin film of isotactic PMMA. The TE spectra (VV and VH) are at the top, and the TM spectra (HV and HH) are at the bottom. (Reproduced from Ref. [6]. © 1984 American Chemical Society.)

These results show that the intensities of the VH, HV, and HH experiments should be identical. These results have been confirmed, as shown in Fig. 2.16, which shows the polarized Raman spectra of a thin film of an unoriented isotactic poly(methyl methacrylate) (PMMA) sample.

Theoretically, the depolarization ratio can have values ranging from 0 to 3/4, depending on the nature and symmetry of the vibrations. Nonsymmetric vibrations give depolarization ratios of 3/4. Symmetric vibrations have depolarization ratios ranging from 0 to 3/4, depending on the polarizability changes and symmetry of the bonds in the molecule. Accurate values of the depolarization ratio are valuable for determining the assignments of Raman lines, and, in conjunction with dichroic measurements from IR spectroscopy, the two measurements represent a powerful tool for the structural determination of polymers. Because the laser beam is inherently polarized and highly directional, polarization measurements can be made easily.

The total Raman intensity (photons sr^{-1} s^{-1}) from a sample illuminated by a collimated laser beam of power I_o (photons s^{-1}) is given by

$$I = I_o \sigma N r \tag{2.29}$$

where σ is the Raman cross section (cm^2 sr^{-1} molecule^{-1}), N is the number density of scatterers (molecules cm^{-3}), and r is the excitation path length (cm) of the laser beam in the sample observed by the spectrometer. In this expression, it

is assumed that both the excitation and collection path lengths are constant. The transmittance decreases exponentially with collection path length x. So the intensity variation produced as a function of the lateral movement of the laser beam will be

$$I_x = I_o \sigma N r e^{-\gamma x} \tag{2.30}$$

where γ is the sample coefficient of absorption (cm^{-1}) at the Raman frequency of interest.

The intensity of the Raman spectrum $I(\nu)$ is determined by scattering activity, $S(\nu)$, and a Boltzmann factor, $B(\nu)$, shown below

$$I(\nu) = \frac{S(\nu)}{B(\nu)} \tag{2.31}$$

where

$$B(\nu) = \nu[1 - \exp\left(\frac{-h\nu}{kT}\right) \tag{2.32}$$

Infrared dichroism in solids

For each vibrational mode of a molecule, there is a transition-moment vector, $\mathbf{M}_q$. Because the transition moment is a vector quantity, it has both magnitude and direction. Each of the IR vibrational modes has a transition-moment vector at some angle, α_ν, to the major axis of the molecule [15].

The intensity of the IR absorption band depends on the angle that the electric vector of the incident radiation makes with the transition moment. For gases, liquids, and solutions, the movement of the molecules is sufficient to yield a random orientation of these transition-moment vectors. For solids, on the other hand, there is often a preferred orientation of the molecules.

When IR radiation is plane-polarized such that when the electric vector, **E**, is parallel to the transition-moment vector, **M**, strong absorption occurs and when **E** is perpendicular to **M**, no absorption occurs. For highly oriented solids, there can be an orientation selection rule. If the matching frequency of the incident light is known, and if the proper change in the dipole moment for IR absorption occurs, it is possible to observe no absorption with linearly polarized light if the sample is perfectly oriented.

The absorption of each mode (I) is proportional to the square of the dot product of the electric (**E**) and transition-moment (**M**) vectors

$$I = C(\mathbf{E} \cdot \mathbf{M})^2 = (\mathbf{EM}\cos\theta)^2 \tag{2.33}$$

where C is a proportionality constant and **E** and **M** are the magnitudes of the electric field of the incident beam and the transition moment, respectively. The angle, θ, is the angle between the two vectors. This relationship is shown in Fig. 2.17.

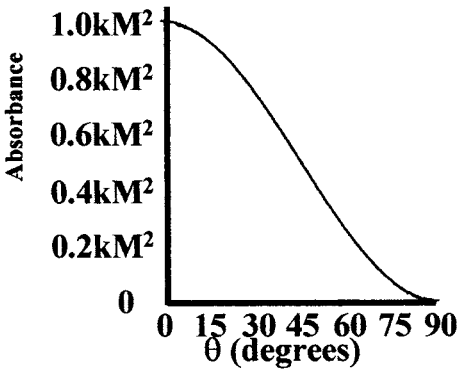

Fig. 2.17. The relationship between the intensity (in units of M^2) as a function of the angle θ.

For an oriented solid sample, in order for the light to be absorbed, a component of the oscillating electric field vector of the incident light must be oriented in a plane parallel to the electric dipole transition moment. Light polarized perpendicular to the dipole transition moment will not be absorbed (Fig. 2.17).

When the absorbing groups are oriented as in solids, they exhibit IR absorptions that depend not only on how many groups are present in the sample but also on how the groups are oriented with respect to the beam.

By using linearly polarized IR radiation, the orientation of the functional groups in a polymer system can be measured.

Measurement of IR linear dichroism requires light polarized both parallel and perpendicular to a fixed reference direction of the sample. For parallel polarized light, the absorbance is termed A , and the absorbance with perpendicular polarized light is termed $A_\perp$. The dichroic ratio, R, is defined as

$$R = \frac{A}{A_\perp} \tag{2.34}$$

For random orientation, $R = 1$. The measured absorption bands are generally classified as parallel (π-bands), or as perpendicular (σ-bands) depending on whether R is greater or less than 1. This classification of the dichroic behavior is helpful in assigning the various modes to the symmetry types of the normal modes in solids [17,18]. The character table of the symmetry group lists the symmetry species of translational motions along the x, y and z axis as well as the symmetry species of the six components of polarizability. The IR-active vibrations have their transition moments preferentially parallel to the corresponding x, y and z axis depending on the symmetry type. If z is the fixed reference direction, the IR bands can be classified parallel or perpendicular based on whether R is greater or less than 1. As will be indicated later, this information is useful for structural analysis of polymers as well as in determining the relative orientation of polymer chains in an oriented system.

For unidirectional molecular orientations, such as for uniaxially drawn polymers, these dichroic parameters can be related to the Herman orientation function, F. This quantity is equivalent to the second moment of the orientation distribution function for the molecular axis and is given by [19]

$$f = \frac{3\langle \cos^2 \theta \rangle - 1}{2} \tag{2.35}$$

The orientation angle θ is the angle between the draw direction and the local molecular chain axis.

The Herman function is equal to 1 when the chain axis is parallel to the film orientation, 0 when the system is randomly oriented, and 1/2 when the chain axis is perpendicular to the film orientation direction. This function can be calculated from measurements of the dichroic ratio by using [20]

$$f = \frac{(R-1)(R_0+2)}{(R+2)(R_0-1)} \tag{2.36}$$

where R_0 is the dichroic ratio for perfect uniaxial order. The value of the constant R_0 is unknown and can be different for every IR band studied [20].

For perfect uniaxial order, it is assumed that the polymer chains are all oriented parallel to the draw direction, and the transition moments associated with the vibrations lie on a cone with a semiangle ψ to the chain axis direction [21]. The dichroic ratio is then expressed by

$$R_0 = 2\cot^2 \psi \tag{2.37}$$

As ψ varies from 0 to π, R_0 varies from 0 to infinity. No dichroism ($R_0 = 1$) will be observed for $\psi = 54°44'$ (the *magic angle*).

In practice, the orientation of the polymer chains is imperfect and is often described in terms of f_p, the fraction of polymer that is perfectly oriented, while the remaining fraction $(1 - f_p)$ is randomly distributed. The dichroic ratio is

$$R = \frac{[f_p \cos^2 \psi + \frac{1}{3}(1 - f_p)]}{[\frac{1}{2} f_p \sin^2 \psi + \frac{1}{3}(1 - f_p)]} \tag{2.38}$$

To solve this problem an independent, quantitative experimental method for determining the unknown constant, f_p, is needed.

An alternate method of defining the imperfect orientation is to suppose all the molecular chains are displaced from parallelism with the draw direction by the same angle θ [15]. The expression for R then becomes

$$R = \frac{[2\cot^2 \psi \cos^2 \theta + \sin^2 \theta]}{\left[\cot^2 \psi \sin^2 \theta + \frac{1}{2}(1 + \cos^2 \theta)\right]} \tag{2.39}$$

If the direction of the transition moment with respect to the chain axis is known,

the average orientation of the chain segments can be determined from the measured dichroic ratio.

Fortunately, the Herman orientation function, F, can be determined by a number of independent techniques, including X-ray diffraction, birefringence, sonic modulus, and refractive index measurements. These methods, coupled with IR dichroic measurements of absorption, can be used to calculate quantitative values for the transition-moment angles by using Eq. (2.15). A plot of F measured by X-ray diffraction versus $(R-1)/(R+2)$ will be linear with a zero intercept. A least-squares evaluation of the data from this line will yield the slope, $(R_0+2)/(R_0-1)$. When ψ_n is 0° (parallel to the molecular chain axis) the slope equals 1.0 and when ψ_n equals 90°, the slope equals −2.0. A quantitative value of the transition-moment angle can then be calculated. Transition-moment angle measurements have been published for isotactic polypropylene and some of the results are as follows [22]:

Frequency	ψ_ν	Frequency	ψ_ν
928	90°	1220	90°
973	18°	1256	0°
998	18°	1307	0°
1045	0°	1363	90°
1103	90°	1378	70°
1168	0°		

(Source: reproduced with permission from Ref. [22]. © 1981 Hüthig and Wepf Verlag, Basel)

If it is assumed that the transition moments are parallel to the chemical bonds, the results can be used to determine the structural angles of the molecule or polymer.

Once the transition-moment angles have been identified for a particular chemical group of the polymer, it is possible to measure the orientation of the polymer molecules in a sample by measuring the IR dichroism at the appropriate absorption frequencies. By using the data for polypropylene just presented, the Herman orientation function for samples of polypropylene that are oriented can be calculated from the dichroic measurements. The results are shown in Table 2.3 [23].

The advantage of using IR spectroscopy for measuring orientation in polymers is that it can detect the orientation of the geometric isomers in the disordered or amorphous regions, as well as the orientation of the preferred isomer found in the ordered or crystalline phase, because they generally appear as separate IR bands. The other experimental techniques such as X-ray diffraction (crystalline phase only) and refractive index (crystalline and amorphous phases) cannot easily separate the contributions of the separate phases. This attribute of IR dichroism is particularly important in multiphase systems [24] and blends [25].

The classical dichroic ratio is a two-dimensional measurement, but the actual sample is usually oriented in three dimensions. To completely characterize the orientation,

Table 2.3
Dichroic ratios, orientation function, and average angles of orientation for drawn polypropylene films

Draw ratio[a]	R	F	$\theta°$
1	1.015	−0.010	55.1
1.5	0.745	0.186	
4	0.536	0.366	40.6
7.	0.056	0.918	13.5
8	0.51	0.926	12.9
9	0.036	0.947	10.8

The frequency was 1220 cm^{-1}, and the bond (ψ) angle was 90°.
[a] The number shown is the ratio of the length of the drawn film to the initial length of the film.
(Source: adapted from Ref. [23]. © 1987 John Wiley and Sons, New York)

three-dimensional IR measurements are required [26–29]. The macroscopic coordinate directions of a uniaxially drawn film are defined by y in the stretching direction, x in the transverse direction, and z in the direction that is normal to the film.

The orientation in three dimensions is completely characterized if the A_z component of the absorption is determined together with the A_x and A_y components. The classical dichroic ratio in this reference system is

$$R_{xy} = \frac{A_y}{A_x} \tag{2.40}$$

If either R_{zy} or R_{zx} is known in addition to R_{yx}, the remaining ratio can be found as a function of the other two: $R_{zy} = R_{zx}/R_{yx}$.

The important parameter to be determined is the structure factor A_0 [26]

$$A_0 = \tfrac{1}{3}(A_x + A_y + A_z) \tag{2.41}$$

which represents the absorbance of the band exclusive of contributions due to orientation of the polymer. This factor is proportional to the amount of chemical structure in the oriented solid giving rise to the IR absorption and is the same quantity measured in gases and liquids, which have no preferred orientation. The difficulty in measuring A_0 in solids is that it is necessary to know the absorbance, A_z, in the thickness direction, which for polymer films is very small. This thickness direction absorbance may be obtained by tilting the sample at some angle, α (Fig. 2.18), and determining the component in the z direction through the relationship [26].

$$A_z = \frac{A_\alpha \cos \alpha_t - A_y}{\sin^2 \alpha_t + A_y} \tag{2.42}$$

A_α and A_y are calculated from the spectra. The true angle, α_t, that the beam makes with the sample is found by correcting the measured angle for the refraction resulting from the refractive index [26].

For three-dimensional measurements, the orientation parameters $A_x/3A_0$, $A_y/3A_0$, and $A_z/3A_0$ can be used to determine the fraction of molecules oriented in the three

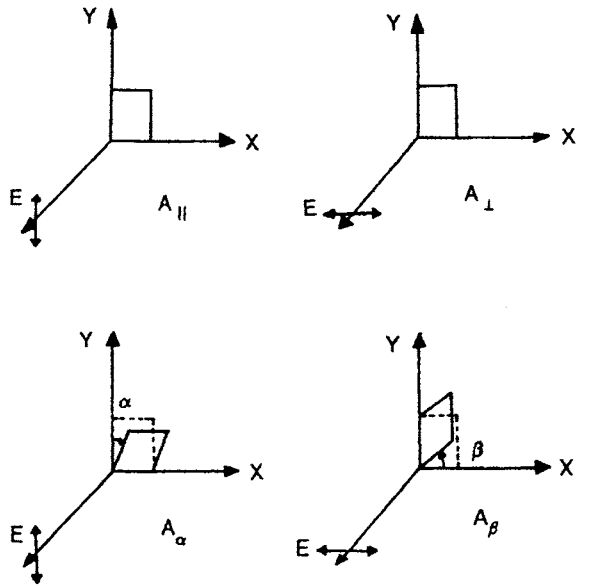

Fig. 2.18. The thickness-direction absorbance may be obtained by tilting the sample at some angle, α, and determining the component in the z direction.

mutually perpendicular directions. In uniaxially oriented samples, which are often encountered by drawing in one direction, the structure factor becomes

$$A_0 = \tfrac{1}{3}(A_{\parallel} + 2A_{\perp}) \qquad (2.43)$$

When a low-molecular-weight liquid substance is adsorbed or mixed into a polymer sample, and the polymer is oriented by stretching or other methods, the entrapped substances become aligned with the polymer chains and exhibit dichroic behavior [30,31], even though these substances may be liquid. The stretched polymers behave as anisotropic solvents, and the polarization properties of the molecules can be determined. Such measurements are useful for determining the structures of organic materials, and should be useful for the study of polymer–solute interactions because increased interaction results in increased orientation in the solute [25].

Characteristic group frequencies in vibrational spectroscopy and interpretation of polymer spectra using group frequencies

Each polyatomic molecule is expected to have $3N$ vibrations (actually $3N - 6$ when the three nonabsorbing or zero energy translations and rotations of the molecule are counted) where N is the number of atoms in the molecule. As indicated previously, these vibrational modes result in a unique spectrum or fingerprint of the molecule. Careful cataloging of the IR spectra reveals an interesting correlation be-

tween the presence of certain chemical groups in the molecules and the appearance of specific IR absorption frequencies.

> *In spite of the apparent complexity of the IR spectrum, whenever some specific chemical groups are present in a molecule, the resulting spectrum has an absorption in a narrow and predictable region. It appears that whenever a specific chemical group is present, it identifies itself. IR spectroscopists started using these 'characteristic group frequencies' as structural probes for chemical groups in newly prepared molecules with unknown chemical structure. How is this possible? The spectrum is highly specific to the molecular framework of the molecule and at the same time is highly reproducible for specific functional groups within the molecular framework. This paradox of IR needs further investigation.*

The vibrational modes of complex molecules fall quite naturally into two distinct categories: internal modes and external modes. As the names imply, the internal modes involve predominantly only a few selected atoms, and the external modes generally involve the motions of all of the atoms in the entire molecule. The internal motions, such as stretching of chemical bonds or bending of bond angles in triatomic groups, are relatively unaffected by the nature of the rest of the molecule and have nearly the same vibrational energy regardless of the attached molecular skeleton. When the internal modes are widely separated from each other and from the external modes, they have a characteristic group frequency that is relatively unaffected by the chemical nature or architecture of the rest of the molecule. In other words, these characteristic group modes are uncoupled from the rest of the molecule and vibrate as if no other atoms were around. When a specific group is found in a number of different molecules, its uncoupled internal vibrations appear in the same narrow frequency region regardless of the type of molecular attachment. For example, a mode appears between 3300 and 2700 cm^{-1} for a C−H bond regardless of the nature of the rest of the molecule. The particular type of C−H bond, that is, aryl or alkane, results in a more specific absorption frequency within this range.

This group frequency concept was embraced by chemists and popularized IR spectroscopy. Catalogs of characteristic group frequencies were reported in the literature, and spectroscopists tried to outdo each other with new and exciting structural assignments of group frequencies. Entire books were written on this subject [32–34], and IR spectroscopy became a valuable tool for determining the chemical structure of molecules. The polymer chemists benefited as well because the characteristic group frequencies generally appear in the same region for polymers as for other molecules [1,7]. Sometimes, specific couplings can occur with regularly ordered chemical functional groups in polymers, and this condition shifts the group frequencies and leads to valuable microstructural information about polymers. This will be covered in de-

tail in the section on 'Coupled infrared vibrations as a polymer structure probe' (page 65).

> *Someone once said that there are three approaches to interpreting the IR spectrum of an unknown material. The 'idiot' approach is to simply plug the spectral data into the computer and let it search the file for a matching spectrum. This works if the unknown is in the file. The 'genius' method is for the spectroscopist to derive the structure from his knowledge of group frequencies. It works well if the spectroscopist is a genius (or at least has an excellent memory). The 'autistic' approach is to send the sample to mass spectroscopy. In practice, a combination of all three works best.*
>
> — A. Lee Smith [4]

The first approach to interpretation of an IR spectrum is to consider the spectrum as the superposition of a number of group frequencies [35]. The second is to confirm the existence of specific chemical groups by looking for other modes of this group, that is, bending, twisting, and wagging modes.

> *It is unlikely that you will be able to identify all of the IR bands in any spectrum of a polymer — there are simply too many. Let me return to our interpretive expert, Professor Bellamy. When he was asked for the assignments of all the bands in an IR spectrum, he responded that the questioner needed a psychiatrist instead of a spectroscopist. Nobody in his right mind expects to know the source of all of the bands.*

Coupled infrared vibrations as a polymer structure probe

To determine the microstructure of polymers, IR modes that reflect the 'connectivity' between the repeating units are necessary, as was indicated in Chapter 1. When chemical groups with the same structure and energy are repeated on a chain in a regular fashion, they are potentially capable of resonating or coupling their vibrational motions. This intramolecular vibrational coupling can lead to the development of a series of resolvable vibrational modes characteristic of the length of the n-ads [36]. This phenomenon has been confirmed by analysis of the spectra of ordered polymers. We will examine briefly the theoretical basis of this experimental result.

Vibrations of the infinite linear monatomic chain

Consider an infinite linear array of atoms of mass m separated by a distance d, as shown in Fig. 2.19.

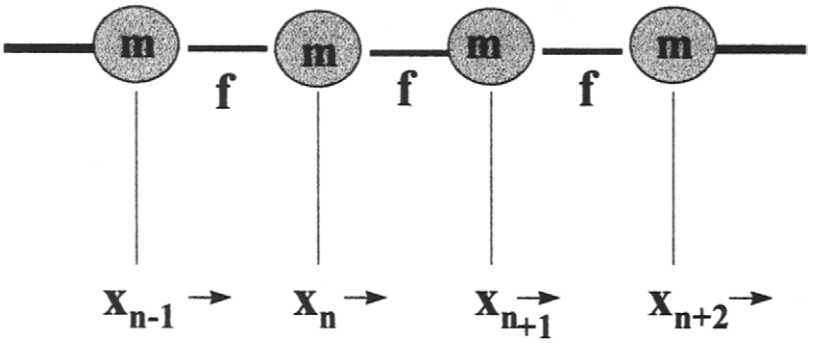

Fig. 2.19. Vibrational model of an infinite monoatomic chain.

Consider the longitudinal displacement of the nth particle from the equilibrium position, and let the potential energy of the displacements of the atoms be determined by the force f acting between adjacent particles. Analysis yields the frequency of the motion as [36].

$$\nu\ (\mathrm{cm}^{-1}) = \left(\frac{1}{c_s \pi}\right)\left(\frac{f}{m}\right)^{1/2}\left|\left(\sin\frac{\phi}{2}\right)\right| \tag{2.44}$$

where ϕ is the phase angle with the range $-\pi < \phi < \pi$. A series of maxima occurs with a period equal to $1/d$.

The phase angle defines the difference in phase between the displacements of particle n and those of particle $n + 1$. The phase angle is also given by

$$\phi = 2\pi \mathbf{k} d \tag{2.45}$$

where $\mathbf{k}$ is the wave vector. The wave vector ranges from $-\frac{1}{2}\phi < \mathbf{k} < \frac{1}{2}\phi$. A plot of Eq. (2.44) ν versus $\mathbf{k}$ or ϕ is called a dispersion curve and is shown in Fig. 2.20.

Only the first mode of the curve is of interest and it produces the plot shown in Fig. 2.21.

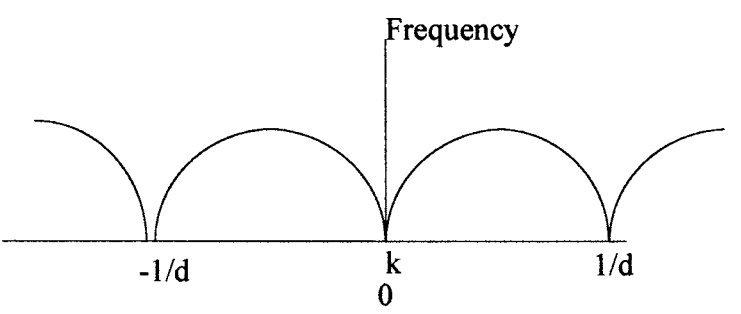

Fig. 2.20. A dispersion curve showing a plot of ν versus $\mathbf{k}$ or ϕ.

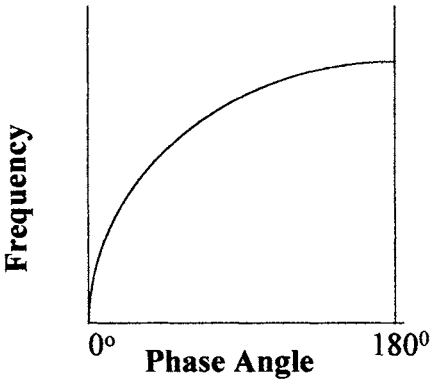

Fig. 2.21. The dispersion curve of frequency versus phase angle

The maximum on the dispersion curve is given by

$$\nu\ (\mathrm{cm}^{-1}) = \left(\frac{1}{c_s \pi}\right)\left(\frac{f}{m}\right)^{1/2} \tag{2.46}$$

which is sometimes referred to in the solid state physics literature as the cutoff frequency because of the analogy between the mechanical system and an electrical low-pass filter.

It is possible to visualize the forms of the vibrations for different values of k. If $k = 0$, the displacements are independent of k and all of the atoms move in phase with the same amplitude and direction as shown in Fig. 2.22. At the maximum frequency, all the atoms are moving with the same amplitude of oscillation but alternate atoms

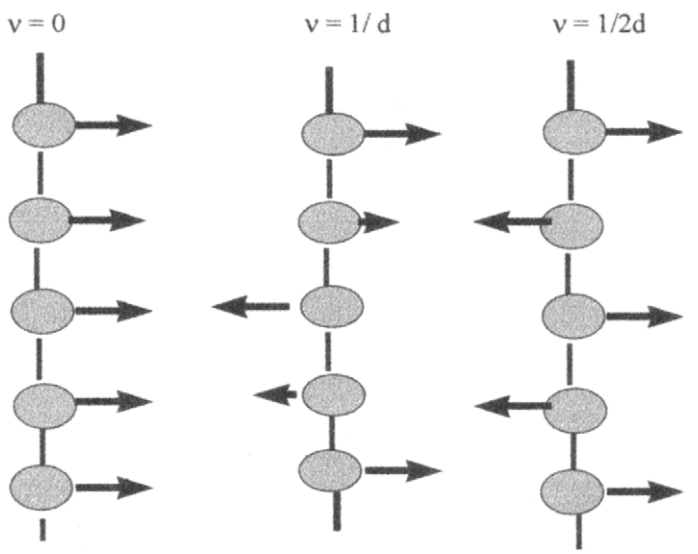

Fig. 2.22. Displacements for various values of ν for an infinite polyatomic molecule

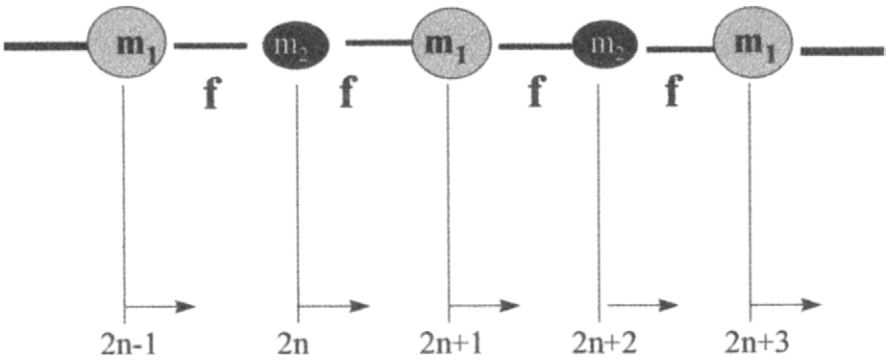

Fig. 2.23. A molecular model of a chain consisting of two different atoms arranged alternately.

are out of phase. At the intermediate frequencies the amplitudes and phases follow a particular pattern.

Vibrations of the infinite diatomic chain

When a lattice consists of two or more types of atoms, new features in the dispersion relationship that appear throw additional light onto the vibrations of polymer chains. Consider a chain consisting of two different atoms arranged alternately as shown in Fig. 2.23.

Assuming only nearest neighbor interactions with a force constant f, one obtains the following equation:

$$\nu^2 = \frac{f}{4\pi^2}\left[\left(\frac{1}{m_1}+\frac{1}{m_2}\right) \pm \left(\frac{1}{m_1}+\frac{1}{m_2}\right)^2 - \frac{4}{m_1 m_2}\sin^2(\pi \mathbf{k} d)\right] \qquad (2.47)$$

where m_1 and m_2 are the masses of the two atoms. The two possible solutions result in two frequency branches of the dispersion relationship, as shown in Fig. 2.24.

A positive sign results in the upper curve, called the *optical* branch because it gives rise to fundamentals in the IR and Raman spectra. Solving the equation by using the negative sign gives the lower curve, called the *acoustic* branch because the frequencies fall in the region of sonic or ultrasonic waves. The acoustic branches are not optically active in the IR or Raman spectra for the infinite chain.

For $k = 0$, the optical branch for the diatomic chain represents the stretching of the bonds between the two atoms with their center of mass fixed. Since the two atoms are different, the oscillating dipole moment can interact with electromagnetic radiation and produce absorption in the infrared. The acoustical branch does not result in a change in dipole moment at $k = 0$.

The displacements observed at various points on the dispersion curve are illustrated (rotated 90°) in Fig. 2.25.

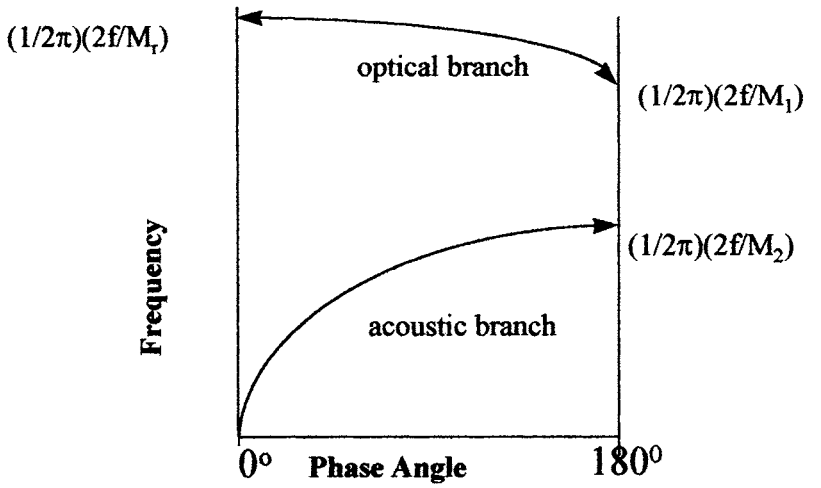

Fig. 2.24. Dispersion curve for the longitudinal vibrations of a diatomic chain.

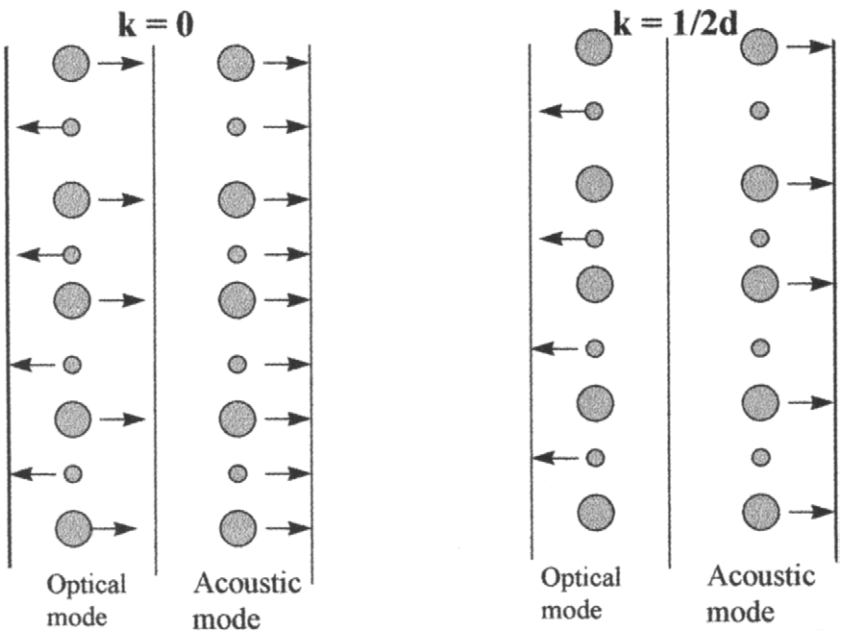

Fig. 2.25. Displacements (rotated 90°) of atoms for the acoustic and optical modes for the infinite diatomic chain.

At $k = 0$, the optical branch has a normal vibration consisting of a simple stretching of the bond between the two atoms. Thus, the center of mass of the two atoms remains fixed and has a frequency equal to $(\frac{1}{2}c_s\pi)(2f/m_r)^{1/2}$, where m_r is the reduced mass $[(1/m_1) + (1/m_2)]$. There is a frequency range between the optical

branch and the acoustic branch that contains no frequencies, corresponding to the region between $(\frac{1}{2}c_s\pi)(2f/m_1)^{1/2}$ and $(\frac{1}{2}c_s\pi)(2f/m_2)^{1/2}$. This region is referred to as the *frequency gap*. A vibrational frequency located in this forbidden region or in the frequency gap must correspond to a normal mode of a defect.

What happens if only weak coupling occurs between adjacent molecules? This condition can be accomplished by simply changing the values of the force constants such that $f_1 > f_2$. The force constant f_1 corresponds to the 'stiffness' of the covalent bond linking pairs of atoms, and f_2 represents the much weaker bonding of the molecules together. Now the frequencies become

$$\nu_{\text{internal}}\ (\text{cm}^{-1}) = \left(\frac{1}{2c_s\pi}\right)\left(\frac{f_1}{m_r}\right)^{1/2} \tag{2.48}$$

$$\nu_{\text{external}}\ (\text{cm}^{-1}) = \frac{1}{c_s\pi}\left[\frac{f_2}{(m_1+m_2)}\right]^{1/2} |\sin \pi \mathbf{k}d| \tag{2.49}$$

For the *internal* vibrations, ν_{internal} is approximately equal to the vibrational frequency of an isolated uncoupled diatomic molecule and is independent of the value of $\mathbf{k}$, and for the *external* vibrations, ν_{external} corresponds to a vibration of the molecules as a whole, each molecule moving as a rigid body against the other. Motions of this type are also referred to as *lattice vibrations* and can be separated into two types: translational-like modes and rotational or vibrational modes.

The above discussion was limited to longitudinal motions. Now consider the situation where displacements can take place perpendicular to the chain. This is accomplished by adding a bending force constant, f_α, the solution to the equations of motion are

$$4\pi^2\upsilon^2 = 2\frac{f_\alpha}{M_1M_2d}\left[(M_1+M_2)(3+\cos 2\pi \mathbf{k}d)\right] \pm [(M_1+M_2)^2(3+\cos 2\pi \mathbf{k}d)^2 - 4M_1M_2(\cos^2 \pi \mathbf{k}d - 2\cos 2\pi \mathbf{k}d + 1)]^{1/2} \tag{2.50}$$

The results are shown in Fig. 2.26. Thus, for the three-dimensional motion of a diatomic chain there is one pair of dispersion curves (one acoustical and one optical branch) for each direction in space. In the three-dimensional motions of a diatomic chain, the transverse directions x and y are equivalent. Consequently, only one transverse optic and acoustic dispersion curve is displayed, as they are degenerate (i.e., have the energy or vibrational motion).

Vibrations of the infinite polymer chain in three dimensions

This simple result in the three-dimensional case [10] can be readily extended to more complicated polymer units. The transverse motions are independent of the longitudinal motions, and in addition, transverse motions at right angles to one an-

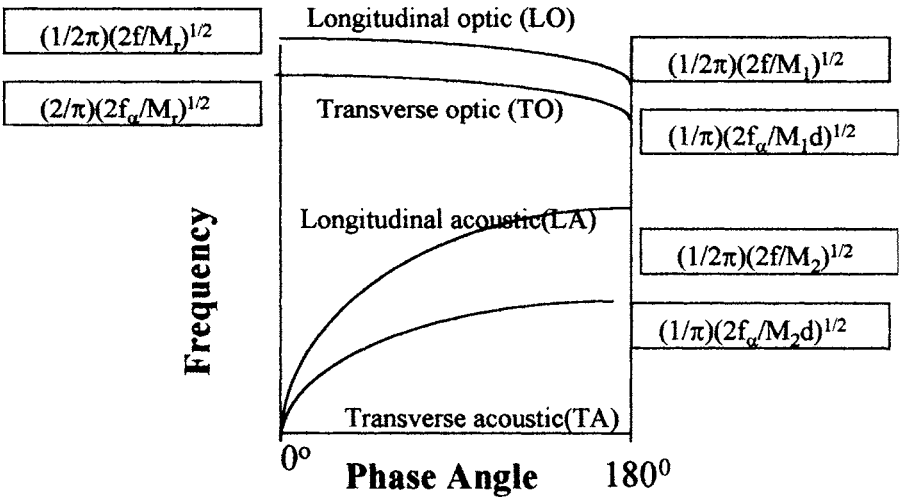

Fig. 2.26. Dispersion curve for the longitudinal and transverse modes of the diatomic molecule.

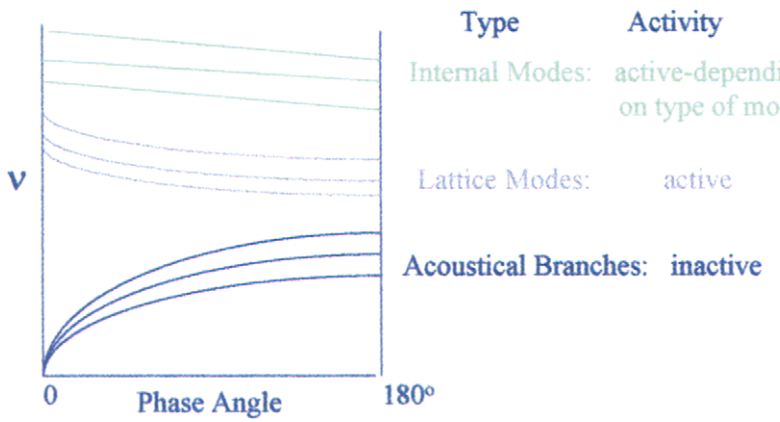

Fig. 2.27. General form of the dispersion curves for a polymer crystal showing type of motion and optical activity.

other are also mutually independent [10]. The resulting dispersion curve is shown in Fig. 2.27.

Considering the vibrations of a three-dimensional lattice, complications arise because the transverse vibrations of molecular crystals are not degenerate. There are three branches for each particle in the unit cell. If there are m_c molecules in the cell, and each molecule is composed of N atoms, then there are $3m_cN$ branches. Three of these branches are acoustic and are inactive in the IR region. In many cases, the vibrations of complex three-dimensional crystals cannot be described as simply longitudinal or transverse because the nature of the waves depends on the details of the intra- and intermolecular forces.

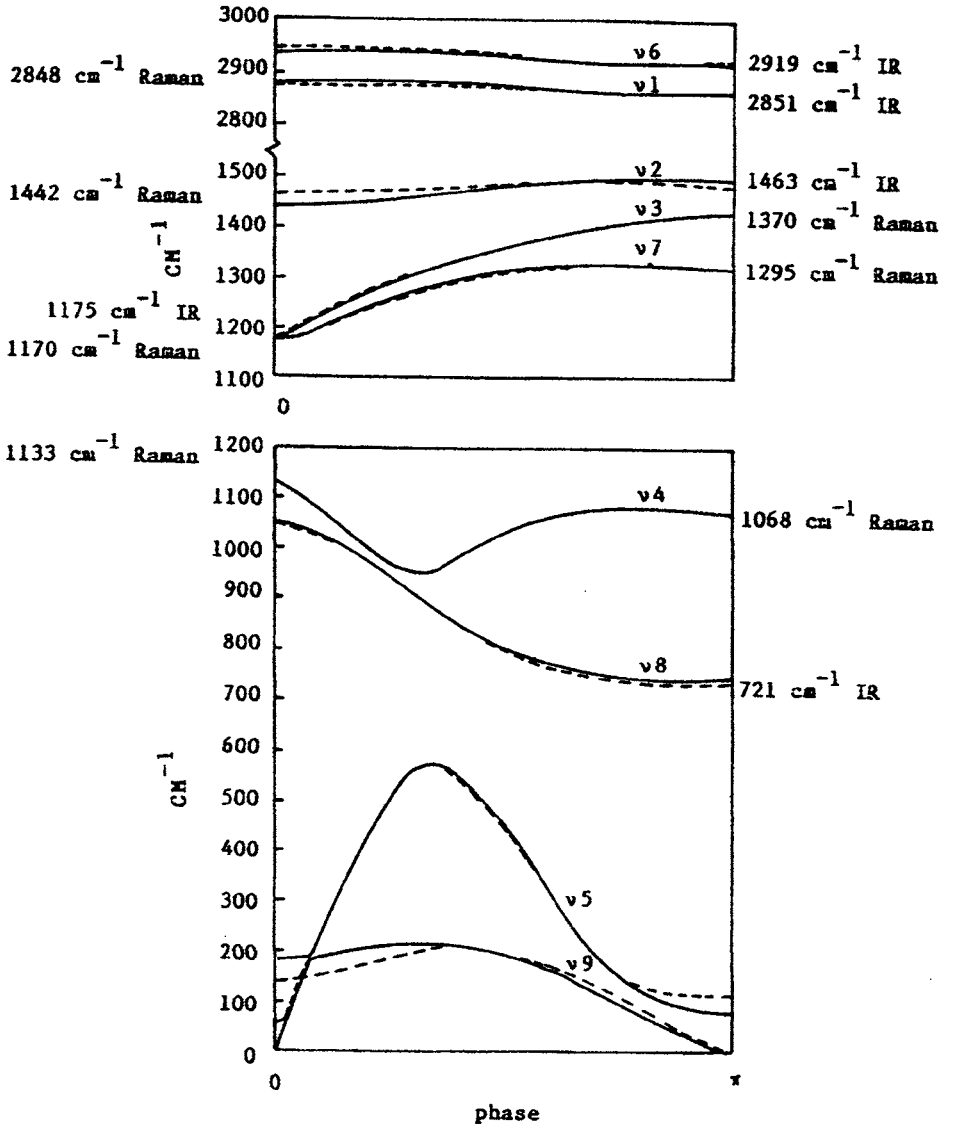

Fig. 2.28. The dispersion curve for an infinite isolated chain of methylene units (crystalline polyethylene).

The dispersion curve for an infinite isolated chain of methylene units has been calculated [36] and is shown in Fig. 2.28.

Because the planar zigzag conformation of polyethylene is a 2_1 helix, the observed IR and Raman lines for the various modes are active at values of $\phi = 0$ and π, respectively, depending on the nature of the motion involved. For the infinite chain, no other modes are observable because for all $\phi > 0$, there is a corresponding $\phi < 0$ somewhere on the chain, and the total change, ϕ, will always be zero. The total sum

of the dipole changes is zero. This result indicates that no total change in the dipole moment will occur for the infinite chain except for vibrational motions with values of $\phi = 0$ and π, respectively. The IR and Raman activity of the various modes depends on the nature of the motion for $\phi = 0$ and π.

Vibrations of finite chains

Theoretically, the simplest finite polymer is a uniform one-dimensional coupled chain of N point masses. The N frequencies for a linear chain of N atoms acting as parallel dipoles with fixed ends (including only nearest neighbor interactions) are given by the following equations [36]:

$$\nu_s^2 = \nu_0^2 + \nu_1^2(1 + \cos\theta) \tag{2.51}$$

where

$$\theta = \frac{s\pi}{(N+1)} \qquad s = 1,\ 2,\ 3,\ \ldots,\ N \tag{2.52}$$

with ν_0 being the frequency of the uncoupled or isolated mode, ν_1 the interaction parameter and s an integer from 1 to N. The phase angles for the oligomers are shown in Fig. 2.29.

The vibrational frequencies are shown in Fig. 2.30.

In addition to the frequency dependence, there is also a dependence of the intensities for the coupled oscillators. Fortunately, in general, only the limiting mode ($s = 1$) is observed, and the remaining oscillator modes are too weak to be observed. The $s = 1$ mode is always the strongest band in the series, and the second strongest ($s = 2$) is calculated to be from 3% to 25% of the strongest. Therefore, under or-

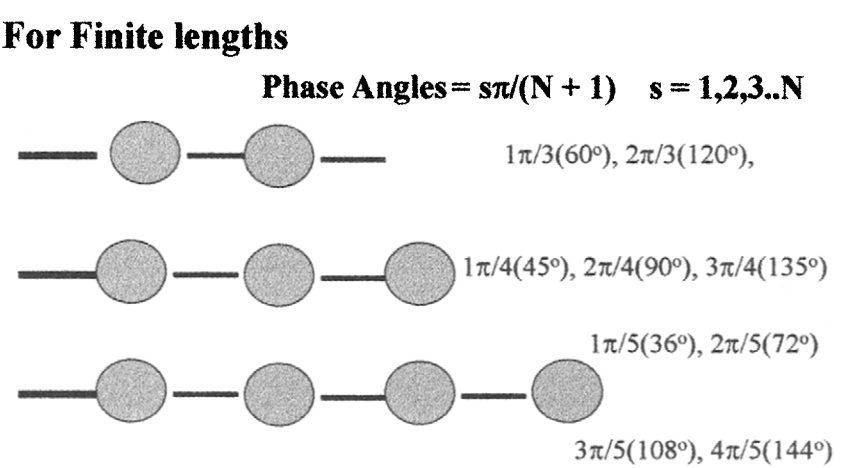

Fig. 2.29. Phase angle of oligomers.

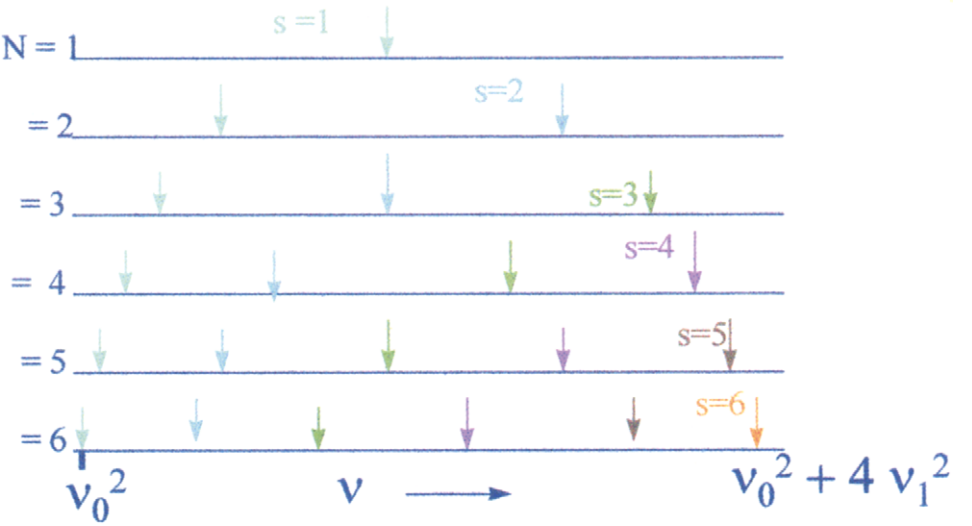

Fig. 2.30. Frequencies for different oligomers.

dinary circumstances, the $s = 1$ mode may be the only one observed. If this is the case, the $s = 1$ mode should be characteristic of the oligomer or sequence length. For strong coupling, the dependence of the modes on the sequence length is shown in Fig. 2.31. This theoretical result of the frequency dependence of the methylene rocking modes is shown in Table 2.1.

The dispersion curve for an isolated polyethylene chain (Fig. 2.29) shows that some of the vibrational motions are uncoupled from their neighbors as indicated by the independence of the frequencies on the phase angle of the C−H stretching and H−C−H bending modes. Other modes such as C−C−C bending and methylene rocking modes are highly coupled to their neighbors and are very sensitive to the phase angle (which can be reduced to a dependence on sequence length). All of the methylene modes of the paraffins fall on the dispersion curve for polyethylene when the appropriate phase factor is used. This confirms the validity of this approach.

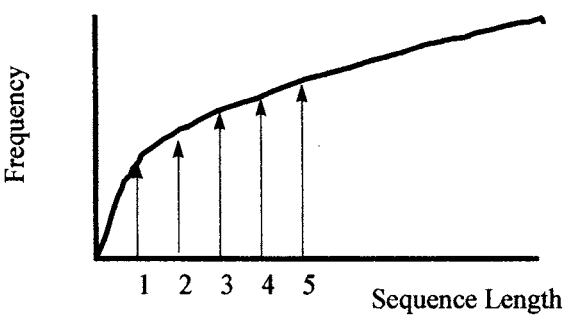

Fig. 2.31. The vibrational frequency as a function of the sequence length.

This simple 'coupled oscillator' approach appears to be quite successful. At a deeper level, it is interesting that the calculated dispersion curve using normal coordinate analysis for an isolated chain of methylene units can be used to predict the frequencies of the spectra of all of the oligomers. It almost makes one want to do normal coordinate analysis! But remember the Bellamy approach.

Distribution of intensities for chain molecules

The intensities of the modes are more sensitive to structural differences in molecules than are the frequencies. For example, the methyl deformation mode at 1378 cm^{-1} has a constant frequency for the methyl, ethyl, propyl, and butyl groups, but the extinction coefficient decreases in going from methyl to butyl groups.

Imagine the difficulty this makes in trying to measure the short-chain branch content of polyethylene when the types of branches present are not known. Think about this the next time you see a report of the branches per 1000 carbons measured by IR spectroscopy.

The sensitivity of the vibrational intensities carries over to chain molecules. The IR and Raman intensities are not linearly related to the degree of disorder [37]. This nonlinearity is a consequence of the fact that the band intensities are associated with modes that are largely delocalized.

Summary

This chapter introduced the basics of vibrational spectroscopy as applied to simple molecules and further extended to polymer molecules. An example demonstrated the method used and the nature of the results that can be obtained. The following chapters will discuss the experimental aspects of IR and Raman spectroscopy and their applications to polymers.

References

[1] Henniker, J.C., Infrared Spectrometry of Industrial Polymers. Academic Press, New York, NY, 1967.
[2] Hummel, D.O., Scholl, F., Infrared Analysis of Polymers, Resins and Additives: An Atlas. Verlag Chemie, Weinheim, 1978.

[3] Colthup, N.B., Daley, L.H., Wiberley, S.E., Introduction to Infrared and Raman Spectroscopy, 2nd edition. Academic Press, New York, NY, 1975.
[4] Smith, A.L., Appl. Spectrosc. 41 (1987) 1101.
[5] Erley, D.S., Anal. Chem. 40 (1968) 894.
[6] Erley, D.S., Appl. Spectrosc. 25 (1971) 200.
[7] Haslam, J., Willis, H.A., Identification and Analysis of Plastics, 2nd edition. Van Nostrand, New Jersey, 1972.
[8] Wilson, E.R., Jr., Decius, J.C., Cross, P.C., Molecular Vibrations. McGraw Hill, New York, NY, 1955.
[9] Thompson, H.W., J. Chem. Soc. (1948) 328.
[10] Painter, P.C., Coleman, M.M., Koenig, J.L., The Theory of Vibrational Spectroscopy and its Application to Polymeric Materials. Wiley, New York, NY, 1982.
[11] Woodward, L.A., Introduction to the Theory of Molecular Vibrations and Vibrational Spectroscopy. Oxford (Clarendon Press), New York, NY, 1972.
[12] Steele, D., Theory of Vibrational Spectroscopy. Saunders, Philadelphia, PA, 1971.
[13] Gribov, L.A., Intensity Theory for Infrared Spectra of Polyatomic Molecules. Consultants Bureau, New York, NY, 1964.
[14] Pacansky, J., England, C., Waltman, R.J., J. Polym. Sci., Polym. Phys. Ed. 25 (1987) 901.
[15] Siesler, H.W., Holland-Moritz, K., Infrared and Raman Spectroscopy of Polymers. Dekker, New York, NY, 1980.
[16] Koenig, J.L., Itoga, M., Appl. Spectrosc. 25 (1971) 355.
[17] Krimm, S., Fortschr. Hochpolym. Forsch. 2 (1960) 51.
[18] Zbinden, R., Infrared Spectrometry of High Polymers. Academic Press, New York, NY, 1964.
[19] Hermans, J.J., Hermans, P.H., Vermaas, D., Weidinger, A., Rec. Trav. Chim. 65 (1946) 427.
[20] Fraser, R.D.B., J. Chem. Phys. 24 (1956) 89.
[21] Siesler, H.W., Adv. Polym. Sci. 65 (1984) 2.
[22] Samuels, R.J., Makromol. Chem. Suppl. 4 (1981) 241.
[23] Mirabella Jr., F.M., J. Polym. Sci., Polym. Phys. Ed. 25 (1987) 591.
[24] Jasse, B., Koenig, J.L., J. Macromol. Sci., Rev. Macromol. Chem. C17(1) (1979) 61–135.
[25] Lefebve, D., Jasse, B., Monnerie, L., Polymer 22 (1981) 1616.
[26] Koenig, J.L., Cornell, S.W., Witenhafer, D.E., J. Polym. Sci. A2 (1967) 301.
[27] Fina, L.J., Koenig, J.L., J. Polym. Sci., Polym. Phys. Ed. 24 (1986) 2509.
[28] Fina, L.J., Koenig, J.L., J. Polym. Sci., Polym. Phys. Ed. 24 (1986) 2525.
[29] Fina, L.J., Koenig, J.L., J. Polym. Sci., Polym. Phys. Ed. 24 (1986) 2541.
[30] Radziszewski, J.G., Michl, J., J. Am. Chem. Soc. 108 (1986) 3289.
[31] Michl, J., Thulstrup, E.W., Spectroscopy with Polarized Light. Solute Alignment by Photoselection in Liquid Crystals, Polymers and Membranes. VCH Publishers, Deerfield Beach, FL, 1986.
[32] Bellamy, L.J., The Infrared Spectra of Complex Molecules. Wiley, New York, NY, 1975.
[33] Bellamy, L.J., Advances in Group Frequencies. Barnes and Noble, New York, NY, 1968.
[34] Dolphin, D., Wick, A., Tabulation of Infrared Spectral Data. Wiley-Interscience, New York, NY, 1977.
[35] Smith, A.L., Applied Infrared Spectroscopy, Fundamentals, Techniques and Analytical Problem-Solving. Wiley-Interscience, New York, NY, 1979.
[36] Snyder, R.G., Schachtschneider, J.H., Spectrochim. Acta. 19 (1963) 85.
[37] Snyder, R.G., Macromolecules 23 (1990) 2081.
[38] Drushel, H.V., Ellerbe, J.J., Cos, R.C., Love, L.H., Anal. Chem. 40 (1968) 370.
[39] Hendra, P.J., Agbenyega, J.L., The Raman Spectroscopy of Polymers. Wiley and Sons, West Sussex, 1992.
[40] Ferraro, J.R., Nakamoto, K., Introductory Raman Spectroscopy. Academic Press, Orlando, FA, 1994.

Chapter 3

Experimental IR spectroscopy of polymers

Introduction

In this chapter, the instrumentation, sampling, and data processing aspects of infrared spectroscopy will be examined in order to develop an understanding of the basis of infrared spectroscopy as a tool in the arsenal of the polymer scientist for the characterization of polymers.

Infrared spectroscopic instrumentation

Infrared (IR) instrumentation has undergone a substantial number of changes as the technique has become more important for materials characterization. Currently, the following IR instrumentation is being utilized:

- Dispersive instruments.
- Multichannel dispersive instruments.
- Multiplex instruments.
- Multichannel/multiplex instruments.

Dispersive infrared instrumentation

Originally, IR spectra were measured using a monochromator which is a scanning dispersive instrument equipped with an optical element of prisms or gratings to geometrically disperse the IR radiation and sequentially present it to the exit slits to isolate the desired frequency domain (Fig. 3.1)

A scanning mechanism passes the dispersed radiation over a slit system that isolates the frequency range falling on the detector [1]. In this manner, the spectrum, that is, the energy transmitted through a sample as a function of frequency is obtained. This dispersive IR method is highly limited in sensitivity because most of the available energy does not fall on the open slits and hence does not reach the detector. Additionally, the accuracy and reproducibility of the frequencies are low due to the mechanical backlash of the scanning mechanism and the effect of variations in laboratory environmental conditions. This poor reproducibility of the frequencies

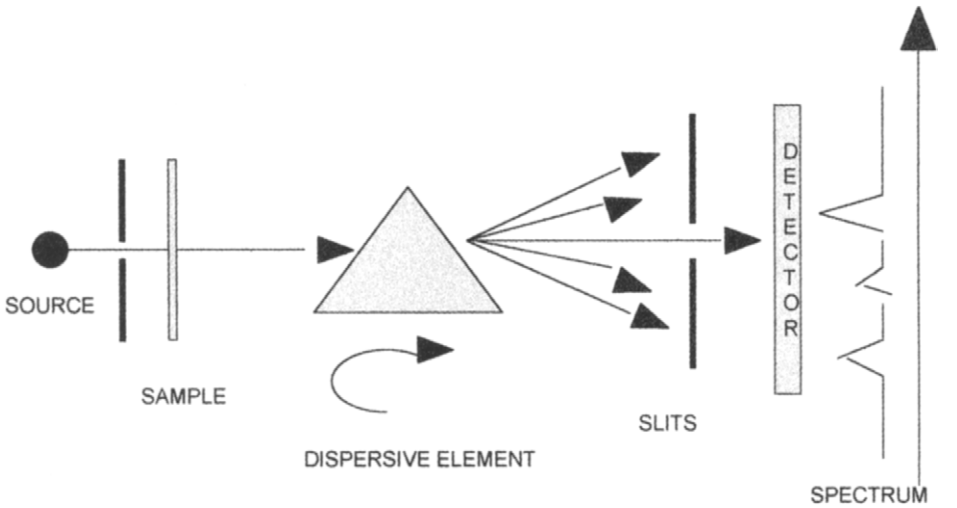

Fig. 3.1. Schematic diagram of the dispersive infrared instrument

complicates the digitization process, which is required for computerization of the system.

Multichannel dispersive instrumentation

Multichannel dispersive IR instruments utilize a multichannel detector (Fig. 3.2). A multichannel detector is an array of many detector elements. Using a multichannel detector improves the signal-to-noise ratio proportional to the square root of the number of detector elements. The use of a multichannel detector has improved the performance of near IR instrumentation.

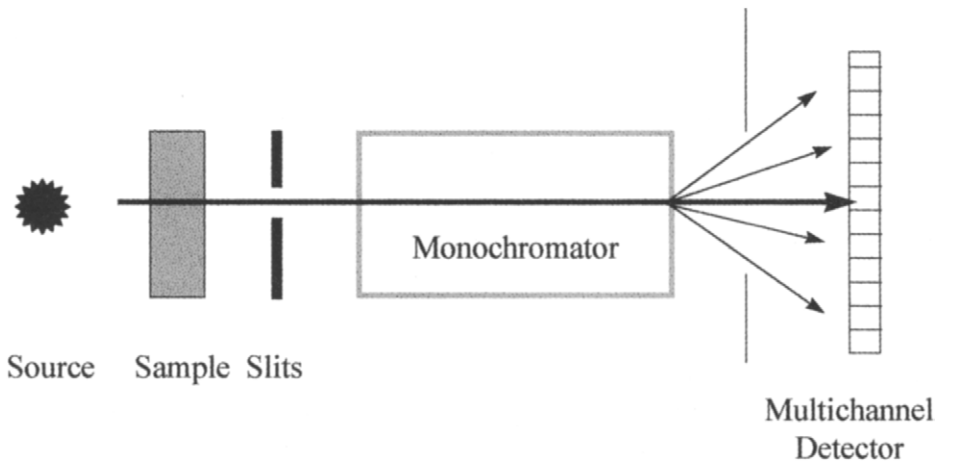

Fig. 3.2. The schematic diagram of a multichannel detector with a dispersive system.

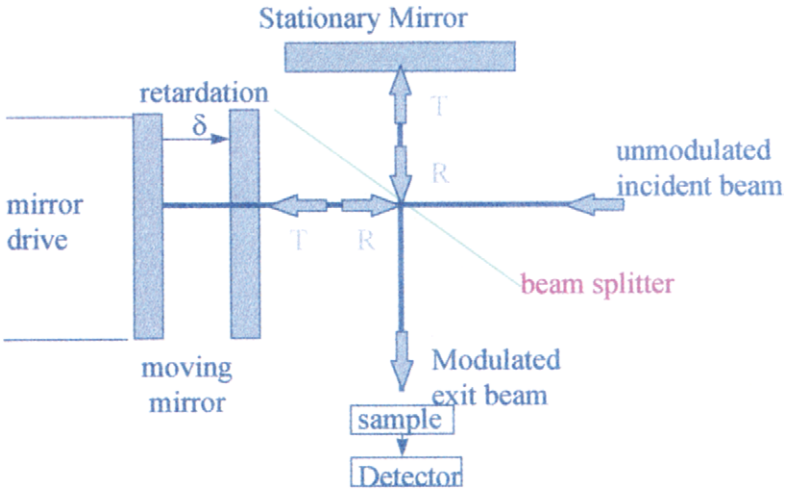

Fig. 3.3. Optical diagram of the Michelson interferometer

Multiplex infrared instrumentation

Fourier transform infrared (FTIR) spectroscopy

Multiplexing is the simultaneous encoding of a number of independent pieces of information in such a way that the information can be received by a single channel system and later decoded into the independent contributing components [2]. A multiplex spectrometer is one that can measure spectral information about the intensities at individual frequencies while measuring the intensities of all frequencies simultaneously with a single detector. The sensitivity of IR spectroscopy is improved with multiplex optical devices such as interferometers due to the continuous detection of all transmitted frequencies simultaneously. The advantages of multiplexing are several including:

- Higher signal-to-noise due to improved detector irradiance.
- Higher energy throughput because no slits are required.
- Accurate wavelength measurement due to calibration with an internal laser.
- High speed as interferometers can be more rapidly scanned than monochromators.
- Signal-to-noise ratio can be improved by signal averaging.

Fourier Transform Infrared (FTIR) spectroscopy uses the Michelson interferometer as the multiplex optical device [3]. The Michelson interferometer has two mutually perpendicular arms, as shown in Fig. 3.3.

One arm of the interferometer contains a stationary plane mirror; the other arm contains a movable mirror. Bisecting the two arms is a beam splitter, constructed from an IR-transparent material, that divides the source beam into two equal beams traversing the two arms of the interferometer. These two light beams travel down their respective arms of the interferometer and are reflected back to the beam splitter

where they recombine. This recombined beam is then reflected to the detector. When the two mirrors are at equal distances from the beam splitter ($x = 0$, where x is the optical path difference), the paths of the light beams are identical. Under these conditions, all wavelengths of radiation striking the beam splitter after reflection combine to produce a maximum flux at the detector.

For a monochromatic source, when the optical path lengths are equal, the two recombined beams constructively interfere at the detector and the signal is at a maximum. If, however, the path lengths in the two arms of the interferometer are not equal, the interference of the recombined beams can be destructive. With a scanning interferometer, the path difference is continuously changed and the signal at the detector varies continuously as a cosine function.

For a white light source (all frequencies), the detector sees the sum of the interferences of the recombined beams. At the zero path point, all the frequencies present in the source interfere constructively and a *center burst* is generated which is the largest signal in the interferogram (Fig. 3.4).

For a monochromatic source of frequency, ν, the interferogram is a cosine function of the frequency and x and the path difference. By extension, the interferogram of a polychromatic source appears as the cumulative sum of many individual cosine interference patterns. The interferogram consists of two parts: a constant (DC) component and a modulated (AC) component. The $I(x)$ or AC component is called the interferogram and is given by

$$I(x) = 2\sum I \cos(2\pi \nu x)\, \mathrm{d}\nu \tag{3.1}$$

where I is the total light flux. An IR detector and an AC amplifier convert this flux

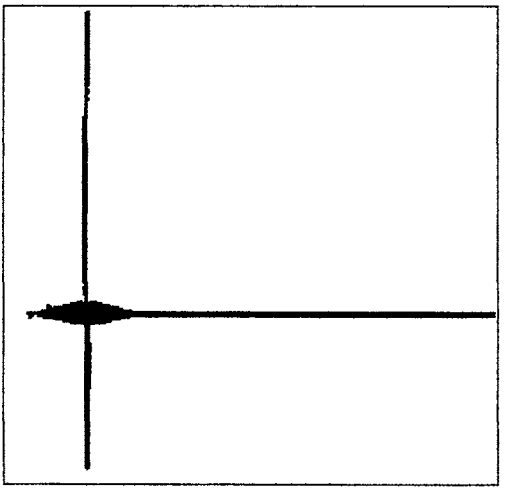

Fig. 3.4. Interferogram showing 'center burst' with signal as a function of time.

into an electrical signal

$$V(x) = re(x) \tag{3.2}$$

in volts, where *re* is the response of the detector and amplifier.

The spectral resolution, $\Delta\nu$, is given by

$$\Delta\nu \sim \frac{1}{\Delta x_{\max}} \tag{3.3}$$

where $\Delta x_{\max}$ is the optical path difference of the interferometer measured from the point of zero-path difference. The nominal resolution (selectable from 0.5 to 16 cm^{-1}) is achieved by changing the optical path variation of the moving mirror.

The moving mirror is generally driven on an air-bearing system. For FTIR measurements to be made, the mirror must be kept in the same plane to within 10 μm-rad for mirror drives up to 10 cm long. It is necessary to have some type of marker to initiate data acquisition at precisely the same mirror displacement every time. The uncertainty in mirror position cannot be greater than 0.1 μm from scan to scan. This precision is accomplished by having a smaller reference interferometer on the moving mirror. A visible white light source is passed through this reference interferometer, to produce a sharp *center burst* or *spike*. Data acquisition is initiated when this center burst reaches a predetermined value.

Digitization of the interferogram at precisely spaced intervals is accomplished by using the interference signal of the auxiliary interferometer. A He–Ne laser is usually used as a distance reference for control of constant scanning velocity and precise equally spaced collection of data points. An auxiliary interferometer is equipped with a He–Ne laser that yields a monochromatic signal to produce a cosine function from the interferometer. The interferogram is sampled at each zero crossing of the laser cosine function. Therefore, the path difference between two successive data points in the digitized interferogram is always a multiple of half wavelengths of the laser, or 0.316 μm. The laser also provides internal calibration of the frequencies. To obtain the greatest accuracy in the digitized signal, the maximum intensity in an interferogram should closely match the maximum input voltage of the analog–digital converter (ADC).

The digitized interferogram for a polychromatic source $A(\nu)$ is given by

$$I(x) = \sum A(\nu)(1 + \cos 2\nu\pi x)\,\mathrm{d}\nu \tag{3.4}$$

Evaluating these integrals involves the determination of the values at zero path length and at very long, or infinite, path length. At zero path length difference

$$I(x = 0) = 2\pi A(\nu)\,\mathrm{d}\nu \tag{3.5}$$

and for a large path length difference

$$I(x = \infty) = A(\nu) = \frac{I(0)}{2} \tag{3.6}$$

Therefore, the actual interferogram, $F(x)$, is

$$F(x) = I(0) - I(\infty) = \sum A(\nu) \cos(2\pi \nu x)\, \mathrm{d}x \tag{3.7}$$

From Fourier transform theory

$$A(\nu) = 2 \sum F(x) \cos(2\pi \nu x)\, \mathrm{d}x \tag{3.8}$$

The Fourier transform process was well known to Michelson and his peers, but the computational difficulty of making the transformation prevented the application of this powerful technique to spectroscopy. An important advance was made with the discovery by Cooley and Tukey of the fast Fourier transform (FFT) algorithm [4]. The discovery of the FFT algorithm breathed new life into the field of spectroscopic interferometry by allowing rapid calculation of the Fourier transform. To Fourier transform a 4096-point array would require $(4096)^2$, or 16.7 million, multiplications. The FFT reduces this to $(4096) \times \log^2(4096)$, or 4096(12), for a total of 49,152 multiplications. The FFT reduces the number of multiplications by a factor of 341. The advantage of the FFT increases with the number of data points. As computers have improved, the time required for a Fourier transform has been reduced to such an extent that with fast array processors the transformation can now be carried out many times per second. Thus the spectra can be calculated during the time needed for the moving mirror to return to its starting position.

There is a modulation of the frequencies, f_{mod}, which is given:

$$f_{\mathrm{mod}} = V_{\mathrm{opt}} \nu \tag{3.9}$$

where V_{opt} is the optical scanning velocity and ν is the frequency.

Traditionally a 256-point Mertz phase correction method is used as the phase varies slowly with wavenumber.

The interferogram as described mathematically is continuous and infinite requiring the Fourier integral to be evaluated over the limits of $\pm\infty$. Since the mirrors cannot move over distances of $\pm\infty$, the actual mirror movement is equivalent to multiplying the infinite interferogram by a boxcar function that has a value at all points between the optical displacement distance, L, and a value of zero everywhere else.

$$D(x, L) = \begin{cases} 1 |x| < L \\ 0 |x| > L \end{cases} \tag{3.10}$$

Boxcar truncation of the interferogram results in a sinc function which has side lobes. The reduction in the side lobes on the spectral lines observed can be accomplished by apodization. Triangular apodization gives a sinc function with the side lobes considerably reduced. The reduction in side lobes is accomplished at the expense of a some loss in spectral resolution.

There are a number of advantages to Fourier Transform IR instrumentation relative to dispersive IR instrumentation including:

- simultaneously records the full spectrum,
- spectral resolution can be adjusted from 0.5 to 16 cm^{-1} according to the application,
- accurate wavelengths based on internal laser calibration,
- large dynamic range: 10^4–10^6,
- high energy throughput,
- signal-to-noise ratio can be improved by signal averaging.

Step-scan FTIR spectroscopy

The advantage of step-scan FT-IR over rapid continuous scanning is that the spectral multiplexing is removed from the time domain [5]. In the rapid-scan operation the moving mirror scans continuously causing modulation of each IR wavelength with a different Fourier frequency. In step-scan operation, the moving mirror is stopped at equally spaced fixed positions (retardation points) during data collections (Fig. 3.5).

Because there is no motion of the mirror at the retardation points, Fourier frequencies are eliminated and do not contribute to the measurement. In this manner, spectral multiplexing is decoupled from the time domain. Thus the entire spectral range is modulated at a single frequency.

In step-scan operation, the interferogram is created point by point which is otherwise equivalent to that created by coaddition of rapid scanning interferograms. By moving the mirror step-wise, one obtains the time courses of the change of the interferogram at each sampling point, and from the data set the spectral changes can be obtained by the Fourier transform at each time of interest. Step-scan FITR can be used to do dynamic spectroscopy, depth profiling in photoacoustic spectroscopy, and improved emission spectra.

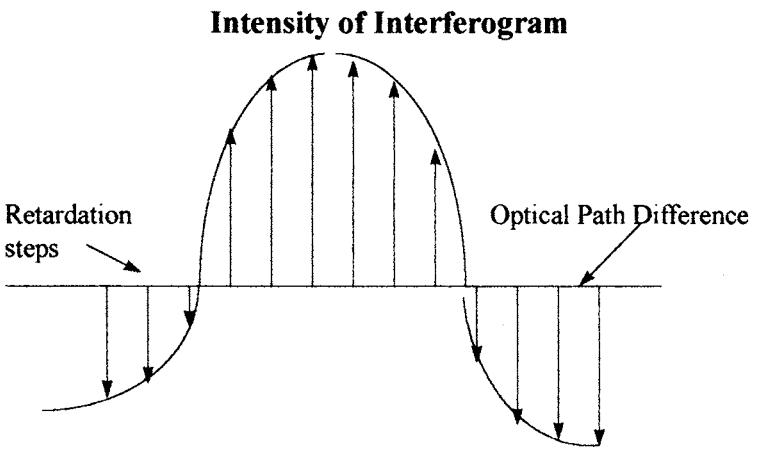

Fig. 3.5. Principle of step-scan interferometry.

Polarization division interferometry

A polarization division interferometer operates on the principle of polarization division of the incoming light. The intensity measured at the detector represents the difference in polarized absorptions. The polarization division interferometer is two times more efficient for dichroism measurements than for the conventional FTIR spectrometers based on the Michelson interferometers [6,7].

Multichannel FTIR spectroscopy

Recently, a multichannel detector has been coupled to a triangular common path interferometer which encodes a spatially distributed interferogram [8]. Such an interferometer requires no mirror scanning but rather utilizes a Fourier mirror to develop a spatially distributed light beam. The infrared multichannel detector for recording the interferogram is a 1024 element PtSi unit with 25 mm × 2.5 mm pixel sizes and a 1 to 4 mm wavelength response. An optical diagram is shown in Fig. 3.6.

With the triangular common path interferometer it is possible to do single-event time-resolved spectroscopy with a time resolution of 5.14 ms for nonrepeatable processes.

Multiplex/multichannel microimaging FTIR instrumentation

A multiplex/multichannel microimaging FTIR system has been developed. The strategy is to combine an IR focal plane array detector with a step-scan interferometer. A InSb focal array detector was used with a 128 × 128 pixel distribution. The detector was interfaced with a with a commercially available step-scan FT-IR interferometer.

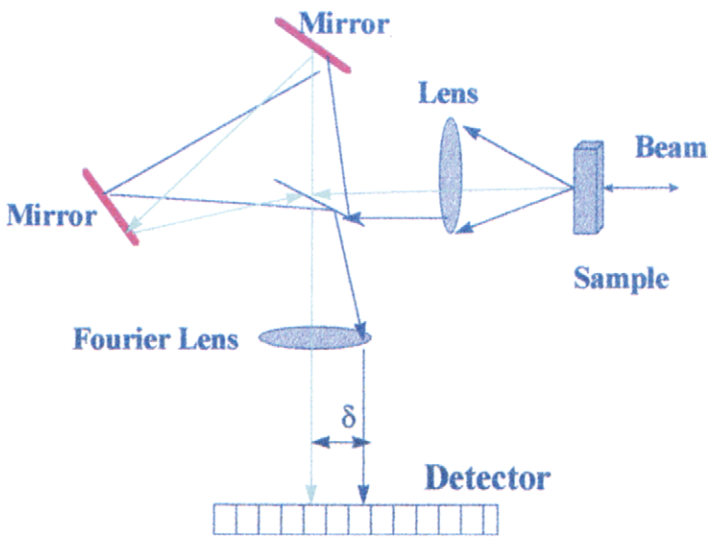

Fig. 3.6. Optical diagram of a triangular common path interferometer which encodes a spatially distributed interferogram.

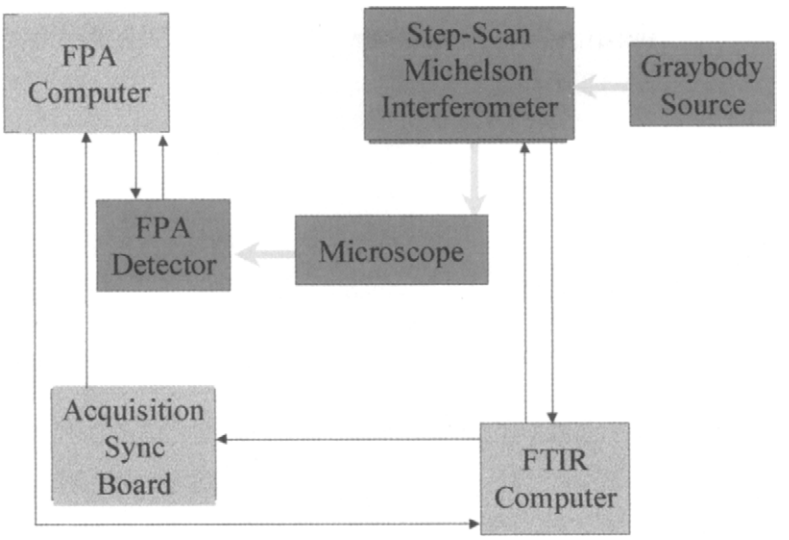

Fig. 3.7. Block diagram of FTIR/multichannel spectrometer.

As a result one achieves a full multiplex/multichannel advantage and 16,384 spatially resolved FT-IR spectra at 16 cm^{-1} with data acquisition time of 12 seconds [9]. A block diagram of this instrument is shown in Fig. 3.7. This instrumentation allows the measurement of spatially-resolved IR spectra of polymer systems.

Sampling methods for IR spectroscopy

Background

The quality of IR spectra is dependent on sample preparation procedures and the performance of the instrumentation. FTIR instrumentation has high-energy throughput and the multiplex advantage coupled with computerized signal enhancement by signal averaging. This FTIR instrumentation allows the use of a number of additional sampling techniques for polymers compared to the traditional dispersion instrumentation [10]. The availability of these newer sampling techniques allows the study of polymeric systems in their final-use state, whether as adhesives, fibers, coatings, or injection-molded articles thus allowing information about effects of processing and engineering environment. The sampling technique selected depends on the geometry of the sample. Thin films of polymers are ideal for transmission while bulkier samples require reflection methods. Extremely small samples require a microscopic approach.

Diagrams of the IR sampling techniques that are currently being used are shown in Fig. 3.8.

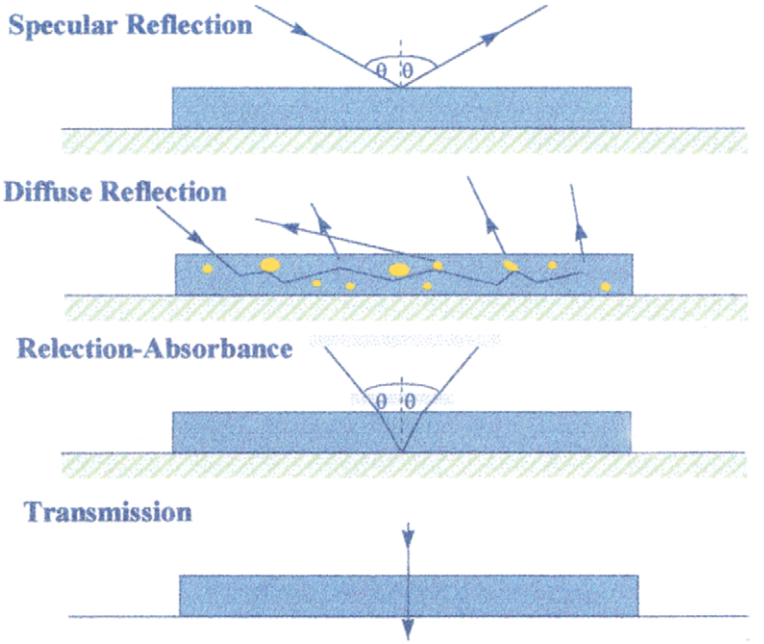

Fig. 3.8. Optical diagram for a number of infrared sampling techniques.

Additionally, photoacoustic and emission spectroscopy is used for polymers. A discussion of these various techniques follows.

IR rays impinging on a sample are reflected, absorbed, transmitted, or scattered. Mathematically,

$$I_0 = I_T + I_R + I_S + I_A \tag{3.11}$$

where I_0 is the intensity of the incident ray, I_R is the intensity of the reflected ray, I_S is the intensity of the scattered ray, I_T is the intensity of the transmitted ray, and I_A is the intensity of the absorbed ray. Experimentally, any of these rays can be used to determine the spectrum of the sample. The differences in the sampling methods depend on the angle of incidence and the magnitude of the change in the refractive index, as shown in Fig. 3.9.

Transmission spectroscopy is observed at a 90° angle (normal) of incidence. Reflectance spectroscopy, including specular, external (both single and multiple), internal (both single and multiple), and diffuse, is observed at smaller angles.

Another factor in sampling is the magnitude of the optical constants of the polymers. A simple diagram of the absorption index and the refractive index is shown in Fig. 3.10.

In transmission measurements, the major contribution is the absorptive index and the refractive index contribution is small. In reflection, the major contributor is the refractive index.

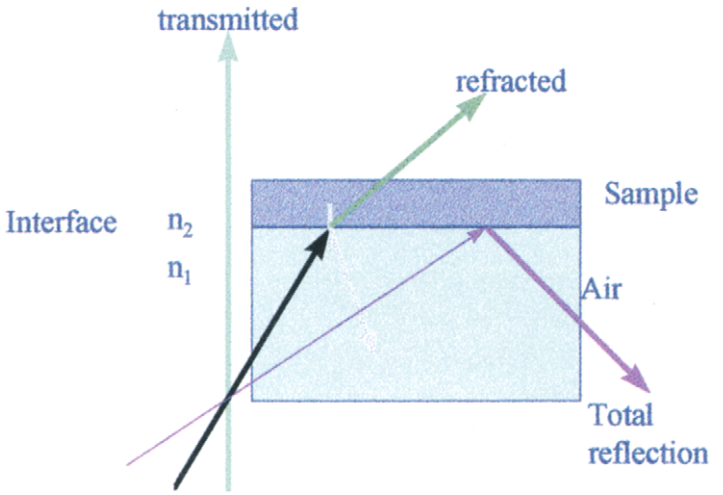

Fig. 3.9. The effect of angle of incidence on transmission and reflection rays.

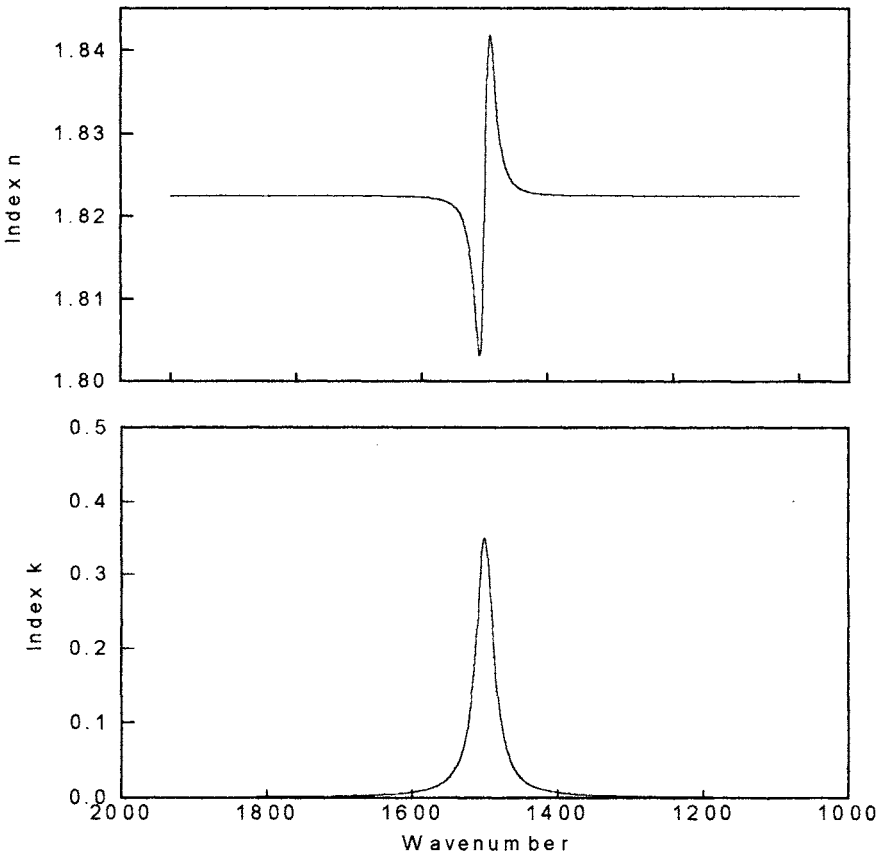

Fig. 3.10. (a) An example of refractive index, and (b) an absorptive index for a single IR band.

For IR measurements, sample preparation has been a labor-intensive operation requiring some measure of skill and experience. Conventional IR spectroscopy is mainly based on transmission measurements except for samples for which the preparation of a thin layer is problematic, inadequate, or prohibited. In these cases other sampling techniques are required.

Transmission spectroscopy

Transmission sampling for IR spectroscopy has several advantages:

- the highest signal-to-noise ratio when the sample has the proper thickness,
- no distortion of the spectra arises due to the sampling technique,
- quantification can be accomplished.

For solids like polymers, a number of methods are available for making the sample sufficiently transparent for transmission measurements.

A thin film can be prepared by solvent casting. Solvent casting requires a solvent, which dissolves the sample, preferably at room temperature, and can be easily removed (high vapor pressure) without formation of bubbles in the sample film. Solvents such as chloroform (BP 61.2°C), acetone (BP 56.2°C), trichloroethanol (BP 151°C), *o*-dichlorobenzene (BP 180.5°C) and water (BP 100°C) can be used and can be selected based on a 'guesstimate' of the nature of the sample. Several drops of the solution are then placed on an inert infrared-transmitting substrate (like KBr or NaCl) and the solvent is evaporated to leave a film of the sample on the substrate. If the film is too thin, an additional deposition on top of the original can be made to increase the thickness. In some cases, the film can be peeled off the substrate, and placed free standing in a film holder in the spectrometer. The limitations of the solvent casting technique are residual solvent interfering with the spectrum of the sample and bubbles in the cast film which produce a nonuniform film.

Thermoplastic polymers can be made into thin films by compression molding. Compression molding requires meltable samples and spacers are used to control the thickness of the sample itself. Teflon-coated Al foil is used over the press platens so the film can be easily removed. The disadvantage of compression molding is the loss of thermal history information of the sample.

Powders or fluff of polymers can be studied with the transmission technique by forming a KBr pellet. This approach disperses the sample in an infrared transparent matrix like KBr or NaCl. These inorganic salts have the property of 'cold flow' so they revert to a glass-like consistency when sufficient pressure (10–15,000 lb/in^2) is applied to a finely divided powder. In this method, KBr is usually mixed with $\sim$1% of a finely ground sample in a special die. Pressure is applied with a press. The sample pellet formed is placed in the spectrometer and measured. The use of an alkali halide matrix to support and surround a solid sample for IR analysis was first presented by Stimson in 1952 [11]. This technique has been used widely because of its general applicability. The limitation of the KBr method (in addition

to the difficulty of making suitable pellets) is that some samples are polymorphic and convert when ground with KBr at high pressures. However, it is very difficult to obtain uniform, transparent KBr pellets. Moisture in the KBr matrix is a problem because it produces pellets which are cloudy and exhibit high scattering. NaCl (cutoff 600 cm^{-1}), KCl (cutoff 400 cm^{-1}), and CeI (cutoff 200 cm^{-1}) have also been used.

Under the usual experimental conditions, preparations of clear neat powder pellets are difficult. Imperfect pellets result in light scattering and base-line problems. Improper sample dispersion can lead to improper absorbance measurements arising from the wedge shape of the sample.

Powdered samples can be ground into a mull such as Nujol (mineral oil) so that the particle size is smaller than the highest frequency of radiation used (typically 4000 cm^{-1}). Nujol has only a limited number of absorption bands so broad windows are available for analysis. However, grinding uniform, small particles in the mull is difficult. For hydrocarbon polymers where the Nujol will interfere, it is possible to do Fluorolube mulling. It is used in the same manner as Nujol but fluorolube has no interfering C−H bands and can be used to obtain information in the 4000–1350 cm^{-1} range.

IR studies on neat liquids and solutions by means of infrared transmission require the use of very thin path lengths (less than 2 μm). It is extremely difficult to construct such cells, and there may be problems with a determination of the exact value of the cell thickness. Commercially, sealed cells with path lengths from 0.015 to several millimeters are available.

Transmission spectroscopy is the traditional sampling method for qualitative analysis for purposes of polymer identification. Nearly all of the spectral catalogs for identifications are based on transmission measurements so for comparison purposes of unknown samples, transmission measurements, when possible, are the most convenient.

Transmission spectroscopy is useful for quantitative measurements only when *uniform* (no holes, no variation in thickness, no orientation) thin films of polymeric samples are available. The polymeric films should be sufficiently thin to allow observation of spectral absorbance values in the linear domain, which is generally an absorbance value of less than 1 for the major portions of the spectra. This is particularly important for those frequencies for which spectral subtractions are anticipated.

For FTIR instrumentation, this absorbance limitation arises from the apodization process. For the common triangular ($\sin c^2$) apodization function, a linear relationship is found between the true absorbance and the apparent (observed) absorbance up to about 0.7 absorbance units. Above 0.7 absorbance units, the apparent absorbance becomes nonlinear, with the amount of decrease depending on the true absorbance and the resolution parameter, r, where r is the ratio of the instrument nominal resolution to the full width at half height. For absorbance values greater than 1, resolution parameters of 0.1 or greater produce nonlinear behavior [12].

This need for thin films for quantitative analysis usually means that polymer film samples should be prepared in the 10–100-μm range of thickness. Solvent casting or compression molding of the samples is usually required to prepare such thin films and, unfortunately, these sample preparation techniques transform the sample through melting or dissolution, with the loss of the thermal and process history of the polymer sample. The film samples must be randomly oriented, because nonrandom chain orientation influences the value of the measured absorbances.

Internal reflection spectroscopy (IRS)

Internal reflection spectroscopy (IRS) (often called *attenuated total reflection* or ATR) is a widely used technique for the analysis of polymer samples with low transmission [13,14]. IRS is a contact sampling method involving a crystal with a high refractive index and with low IR absorption in the IR region of interest.

In the IRS technique a crystalline material of high refractive index is used as an internal reflection element (IRE). The probe beam enters the IRE under an angle that exceeds the critical angle for total internal reflection. At the interface of the highly refractive IRE and the low refractive medium, an evanescent wave evolves which penetrates into the bulk rarer medium. The penetration depth is on the order of the radiation wavelength. The depth of penetration depends on a number of factors, including the angle of incidence and refractive index, but is approximately equal to the wavelength of the IR light. The main advantage of IRS is that spectra of opaque samples can be obtained. The length of the IRS crystal determines the sensitivity of the ATR technique. The signal-to-noise ratio is improved with an increase in the number of reflections, which is a function of the length of the crystal and the angle of incidence.

The mode of interaction is unique because the probing radiation is propagated in a high index-of-refraction internal reflection element (IRE). The radiation interacts with the material of interest, which is in optical contact with the IRE, forming an interface across which a nonpropagating evanescent field penetrates the surface of the material of interest to a depth on the order of one wavelength of the radiation. The electric field at the interface penetrates the rarer medium in the form of an evanescent field whose amplitude decays exponentially with distance into the rarer medium (Fig. 3.11).

The depth of penetration, d_p, of the beam can be calculated by using the following equation:

$$d_p = \frac{\lambda}{2\pi n_1 \left(\sin^2 \theta - n_{21}^2\right)^{1/2}} \tag{3.12}$$

where λ is the wavelength of the radiation in air, θ is the angle of incidence, n_1 is the refractive index of the IRS (ATR) crystal, and n_{21} is the ratio of the refractive index of the sample to that of the IRS (ATR) crystal. The *penetration* of the evanescent wave

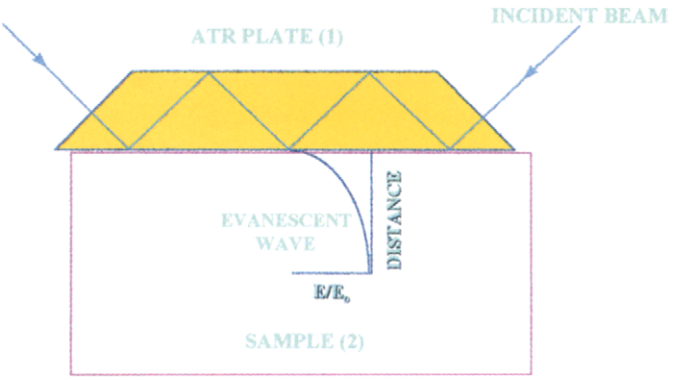

Fig. 3.11. The optical diagram of the Penetration of the light beam into the sample using ATR.

is defined as the distance required for the electric field amplitude to fall to e^{-1} of its value at the surface. For a Ge IRS (ATR) crystal, assuming $\theta = 45°$, $\lambda = 6.1$ μm (the wavelength corresponding to the 1630 cm^{-1} water absorbance band), $n_2 = 4.0$ and $n_{12} = 0.38$ ($n_2 = 1.5$ for water), the effective penetration depth of the electric field is 0.41 μm.

Based on 10 reflections in the IRS (ATR) crystal, the effective transmission-cell path length is 12 μm. The penetration can be further reduced by the addition of a thin metal film on the surface of the IRS (ATR) crystal. This reduction is possible because of the relatively high refractive index and absorptivity of metals with regard to IR radiation [15].

One problem of IRS is the inability to obtain a reproducible pressure and contact area between the sample and the crystal. Reproducible pressure can be placed on the IRS crystal and sample using a torque wrench. One can test the quality of the optical contact by recognizing that for an angle of 45°, it is required that

$$\ln \frac{R_p}{R_s} = 2 \tag{3.13}$$

where R_p is the reflection of the p-polarized light and R_s is the reflection of the s-polarized light.

Another problem with IRS is the fact that the observed frequencies are shifted from those observed in IR transmission spectroscopy, and the relative intensities can be quite different. This problem can be overcome if the optical constants of the polymer are known.

This apparently little-known fact about ATR has led to some interesting reports in the literature. Because ATR is a contact method, it is generally believed that the technique is a surface analysis technique, and if you believe that a penetration of 1 μm is probing the surface, then perhaps ATR is such a method. However, because frequency shifts are observed as a result of the optical physics of the system, it has often been suggested that the IR spectra of some samples have frequencies that are different for the surface species than for the bulk sample. Well, I certainly believe that this is possible, but generally the observations are a result of IRS-induced frequency shifts rather than differences of a chemical nature.

A number of materials are used as ATR elements including ZnSe, KRS-5 and CdTe. Diamond, cubic zirconia and silicon can be used for systems requiring chemical resistance. The advantages of using diamond as a ATR element include:

- excellent inertness to chemicals and abrasion,
- wide range of optical transparency,
- low coefficient of friction so substances do not tend to adhere to the surface,
- can be used at elevated temperature and pressure.

The disadvantages of using diamond as an ATR element include:

- prohibitive cost,
- diamond absorbs nearly all radiation between 2200 and 1900 cm^{-1} which overlaps the triple and cumulated double-bond bands of the fingerprint region.

One of the limitations of most IR sampling techniques is the necessity of placing the sample inside the spectrometer. Fiber optics in the ATR mode can be used to transport a beam of light from a spectrometer to a remote sampling point. A mid-IR-transmitting optical fiber with a 120-μm core of As–Ge–Se glass has been made, and it transmits light down to about 1000 cm^{-1} [16]. The fiber has a 90-μm coating of silicon, which limits the useful spectroscopic range to 3250–1250 cm^{-1}. These fibers have a high light loss (10–15 dB/m), and so the maximum transmission length is 3 m. The fiber is used as its own internal reflection element to obtain a spectrum. The coating is removed over a small section of the fiber, and this section is immersed into the sample of interest, a liquid or viscous mixture such as an uncured resin [17].

An ATR device that has become quite popular is a commercial cell, the ATR Circle Cell (Spectra-Tech), that has a large effective surface area that is approximately 7–8 times greater than that of the ordinary rectangular IRS (ATR) crystal (Fig. 3.12).

It is very useful for studies of aqueous systems because it is possible to subtract the water absorption in a reproducible fashion [18]. The ATR Circle Cell has a large effective surface area that is approximately 7–8 times greater than that of the ordinary rectangular IRS (ATR) crystal. The ATR Circle Cell can be used to study fibers whose circular diameters are ordinarily to large for transmission measurements) by

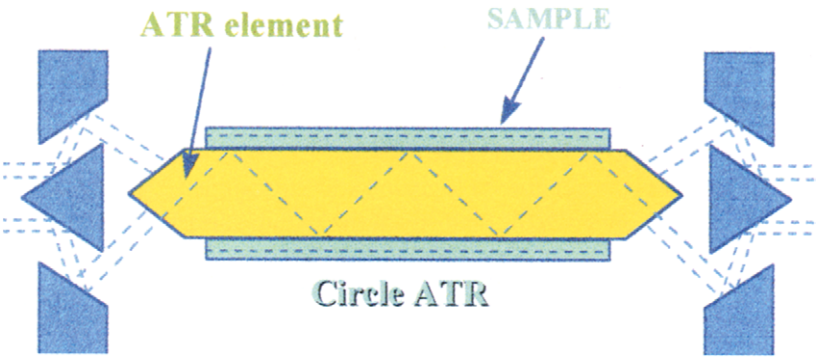

Fig. 3.12. Optical diagram of the ATR Circle Cell.

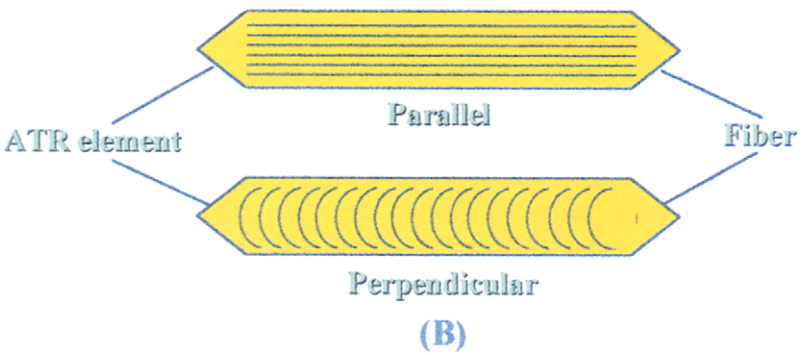

Fig. 3.13. Parallel and perpendicular alignment of fibers with respect to the circle cell ATR axis for the purpose of measuring the dichroic ratio.

wrapping the IRS crystal. As shown in Fig. 3.13, the fibers are wrapped around the ATR cell to enhance the path length and by wrapping in parallel and perpendicular directions in order to measure the dichroic ratio [19].

Variable-angle ATR can be used to determine concentration profiles as a function of depth without disrupting the sample. In general, as the angle of incidence approaches the critical angle, the field strength in the second medium is increased, thereby probing to an increasing depth [20–22]. Thus depth profiling of the sample can be carried out.

For a two-layer system consisting of a thin surface layer on an infinitely thick substrate, the absorbance of a band in the ATR spectrum is related to the thickness of the surface layer. The thickness of the surface layer (t) can be calculated from the ATR spectrum from the absorbance of a band of the substrate $A_s(t)$ according to

$$t = -\left(\frac{d_p}{2}\right) \ln \frac{A_s(t)}{A_s(0)} \tag{3.14}$$

where $A_s(0)$ is the absorbance of the substrate [23].

For microsamples, internal reflection is limited by the size of the illuminated

portion of the internal reflection element. The active area of the crystal should not be significantly larger than the size of the sample. An ATR element has been designed which provides a six times linear reduction of the source image on the sampling surface and thus allows the examination of smaller samples [24].

Recent studies of micro ATR have defined the best experimental conditions for establishing optical contact between the ATR crystal and the sample [25]. This experimental approach has been applied to the analysis of the failure surfaces of adhesively bonded joints. ATR-microscopic measurements have been used for direct measurement and identification of raw materials in textiles coated and impregnated substances on paper [26]. An ATR microscopic probe has been developed which allows one to examine the sample optically through the probe in the microscope. The hemispheric ATR crystal is mounted at the focus of the Cassegrain objective, below the secondary mirror. One can position the crystal in contact with the sample, and run the spectra [27]. In the survey mode, visible light at nearly normal incidence is selected to locate the area of measurement. In the contact mode, low incident angle visible is used to detect contact of the sample to the ATR crystal surface. In the measurement mode, the ATR crystal is slid into position and the incident beam is optimized for total internal reflection. In the Spectra Tech version, all of the available crystals, i.e. ZnSe, Diamond, Silicon, and Germanium can be used. However, Ge and Si are opaque and cannot be used in the survey or contact mode. An optical contact sensor can be used.

External reflection spectroscopy

When the sample is deposited on the surface of a smooth mirror-like substrate, it is possible to use the *specular reflection technique*, or *external reflection spectroscopy* (ERS), which is carried out with the beam at near normal incidence [28]. The specular reflectance is completely governed by Fresnel's formalism and is predominately a function of refractive index. The impinging light reflects from the sample surface and does not penetrate the sample. If the surface is smooth, the reflection and the incidence angles are equal and the reflected beam retains the polarization characteristics of the impinging beam. This type of reflection is called regular Fresnel reflection [29].

In ERS, the beam makes a high-angle reflection of approximately 88° from the sample. Single or multiple reflections can be used. For the analysis of coatings, multiple reflections are generally required. The ERS method has been particularly valuable for examining coatings and adhesives on the surfaces of metals [30]. The problem with the specular reflection technique is that because of the optical requirement of a mirror-like optical substrate, few practical samples can be studied.

When electromagnetic radiation is specularly reflected from a bright surface such as a coated metal, the phase of the wave is shifted as a function of the angle of incidence. For a normal angle of incidence, the phase is shifted by 180°, and the result is a node in the electric field at the surface. Because of this node of zero field strength, it is impossible to couple the radiation to a thin film on the surface.

However, at high angles of incidence and for light polarized in the plane of incidence (p-polarization), the phase shift is such that the optical field strength normal to the surface is high. Light polarized normal to the plane of incidence (s-polarization) remains phase-shifted by 180°. The number of reflections changes with the angle of incidence, and the optimal angle for obtaining IR spectra with this technique is 88°. Under these conditions, the coupling of the field to the film is between 10 and 50 times more efficient than in a normal incidence transmission measurement.

Infrared external reflection spectroscopy is used extensively in the study of thin films on metallic substrates. the incident beam is directly reflected from the metallic surface, and the transmitted beam is attenuated in the regions of substrate absorption for other materials. The reflected beam interacts with molecules situated at the surface of partially transmitting materials. The resulting reflectance spectra are functions of polarization and incidence angle of the incident beam and provide a quantitative measure of the surface concentrations and an indirect measure of the structure and orientation of molecules in the surface layer.

Light polarized with its electric vector parallel to the surface (s-polarized) results in a low-intensity electric field at the film–metal interface at all incident angles, because the electric-field dipole and its image dipole are antiparallel and of equal magnitude, that is, they sum to zero field strength. This situation prevents absorption of s-polarized radiation by a surface-contained vibration.

In contrast, p-polarized light, which has its electric-field vector polarized perpendicular to both the s-polarized electric-field vector and the direction of propagation of the incident light, has a nonzero electric-field vector component perpendicular to the surface. This component is maximized at Brewster's angle [31] which is given by [32]

$$\sin\phi \tan\phi = \frac{2^{1/2}}{[1.05 \times 10^{-6}](\nu\varepsilon\rho)^{1/2}} \tag{3.15}$$

where ν is the frequency of the light, ε is the dielectric constant of the ambient phase, and ρ is the resistivity of the metal. For high conductivity metals, such as aluminum, silver, gold, copper, and platinum, the Brewster's angles are $>89.5°$. This means that optimum spectral sensitivity is achieved at large angles of incidence with p-polarized light [33].

The surface-induced infrared selection rule states that only vibrating dipoles with a nonzero component perpendicular to the substrate surface will be excited by p-polarized infrared radiation. This provides a means for determining the average orientation of surface-confined molecules [34].

It is possible to determine the orientation of the polymer molecules in the coating relative to the metal surface. In the same fashion as dichroic measurements are made, the ratio between a spectrum with parallel-polarized radiation and a spectrum with perpendicular-polarized radiation is calculated in order to determine the molecular orientation. In some cases, this orientation sensitivity is also helpful in making band

assignments to functional groups that exhibit preferred orientations.

The major difficulties with the RA technique are the appearance of asymmetric absorption modes and some shifting of the mode frequencies. Corrections for these spectral differences can be made using the Kramers–Kronig transformation.

Diffuse reflectance FTIR spectroscopy (DRIFT)

Diffuse reflectance results from the incident radiation, which has traveled through some finite thickness of a material and is scattered or reflected from internal surfaces. Diffuse reflection spectra show a reduction in reflectance at frequencies where the absorption bands occur as a result of the radiation penetrating the sample to a distance comparable to its wavelength and being partially absorbed. The optical diagram for the diffuse reflectance experiment is shown in Fig. 3.14.

Diffuse reflectance is an important spectroscopic sampling technique [35]. However, the spectra result from very complex physical processes. One part of the energy is reflected at the surface of the sample without being absorbed and therefore depends on the size and shape of the particles. The other part of the energy penetrates the particles and is partially absorbed. This energy is diffracted or refracted into the particles and then reflected according to the different interfaces encountered. The amount of energy absorbed depends on the concentration and on the absorptivity of the chemical constituents present in the particles.

When highly scattering samples are to be analyzed, diffuse-reflectance spectroscopy is the traditional method of choice. In diffuse-reflectance spectrometry, problems can arise due to sample particle-size distribution, moisture content, and sample packing, which collectively determine the effective optical path length. Additionally, nonlinearities in diffuse-reflectance spectroscopy can occur because of contributions due to specular reflection. Specularly reflected radiation contains very little chemical information about the sample, compared to diffusely reflected radiation.

On a macroscopic scale, the diffusely reflected radiation does not follow the sim-

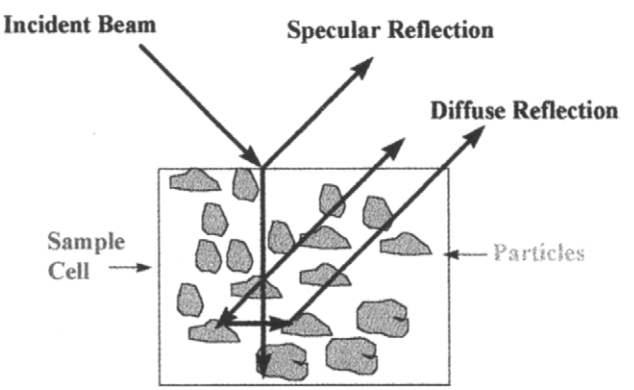

Fig. 3.14. Optical diagram of diffuse reflection sampling.

ple laws of reflection: the angles of diffuse reflections are generally not equal to the angle of incident radiation. Diffuse reflection spectroscopy has been termed DRIFT (diffuse reflectance in Fourier transform). While diffuse reflectance spectra closely resemble absorption spectra, there are fundamental differences. These differences, which include intensification of weaker bands and frequency shifts, are predicted by the Kubelka–Munk theory [36]. It is necessary to apply a Kubelka–Munk correction to diffuse reflection data to create absorption-like spectra [37,38]. Good diffuse reflectors are samples have rough surfaces and high scattering properties.

An IR diffuse reflectance spectrum can be obtained easily if the sample is strongly scattering and weakly absorbing. Spectra of strongly absorbing samples are obtained by diluting the sample with IR-transparent alkali halide powders. The normal sampling technique for DRIFT is to mix the powdered material of interest with a large excess of KBr or similar inert diluent, and place the resulting mixture in a small cup in a special DRIFT accessory. The pure diluent, with no added sample, provides a convenient reference sample, so the effects of atmospheric absorptions and source and detector characteristics can be eliminated. The optical diagram of the DRIFT cell is shown in Fig. 3.15.

The basic problem associated with the design of DRIFT cells is the competition between irradiation and detection for the solid angle. With proper considerations, a diffuse reflectance accessory can be designed with efficiencies larger than 0.3 [39].

The scattering coefficients depend on the particle size distribution of the alkali halide powders and on the nature of the packing of the sample. For quantitative analyses, the dilution requires accurate weighing and perfect mixing. The main drawback of this method is that the signal is not linearly related to the concentration of the sample, but has to be calculated according to the Kubelka–Munk theory [40].

The Kubelka–Munk equation is based on a model where the reflectance properties

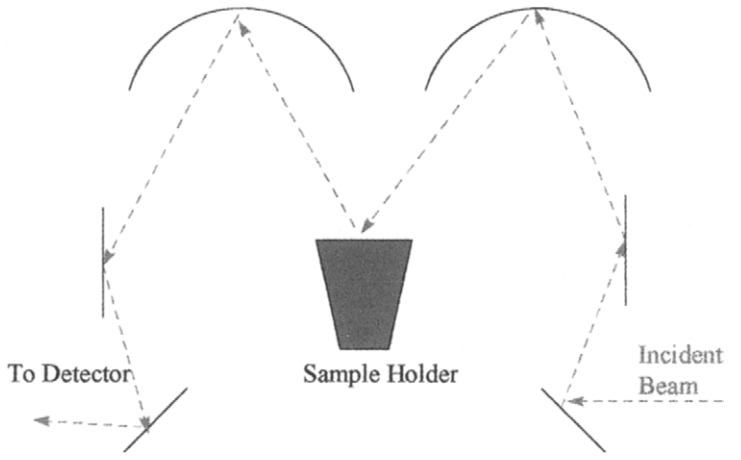

Fig. 3.15. The optical diagram of the DRIFT cell.

are described by differential equations for infinitesimally small layers. The medium is considered homogeneous. The optical inhomogeneities are distributed randomly inside the medium and their lateral dimensions are much smaller than the layer thickness. Isotropic scattering within the sample is assumed and specular reflection is supposed to be negligible [41].

For the propagation of light inside the sample, only two 'flux channels' are assumed: upward and downward. The letters I and J represent radiation in the downward and the upward directions, respectively. The downward flux through a layer of thickness $\mathrm{d}x$ is decreased by absorption and scattering processes and increased by scattering process from the reflected light. As a result the flux equations can be written:

$$\frac{\mathrm{d}I}{\mathrm{d}x} = -(k' + s)I + sJ \tag{3.16}$$

$$\frac{\mathrm{d}J}{\mathrm{d}x} = (k' + s)J - sI \tag{3.17}$$

where k' is a type of absorption coefficient and s is the scattering coefficient. By substituting

$$a = \frac{s + k'}{s} \tag{3.18}$$

one obtains

$$\frac{\mathrm{d}I}{s\,\mathrm{d}x} = -aI + J \tag{3.19}$$

$$\frac{\mathrm{d}J}{s\,\mathrm{d}x} = aJ - I \tag{3.20}$$

The reflectance $R(x)$ is defined by (leaving intensity)/(entering intensity)

$$R(x) = \frac{J(x)}{I(x)} \tag{3.21}$$

Combining into a single differential equation

$$\frac{\mathrm{d}R}{R^2 - 2aR + 1} = s\,\mathrm{d}x \tag{3.22}$$

Integrating between x = 0 and x = x

$$sx = \left[\left\{\frac{1}{(p-q)}\right\}, m\left\{\frac{R-p}{R-q}\right\}\right]_0^x \tag{3.23}$$

where p and q are roots of the equation $(R^2 - 2aR + 1)$

$$p = a + (a^2 - 1)^{1/2} \tag{3.24}$$

$$q = a - (a^2 - 1)^{1/2} \tag{3.25}$$

When the depth of the sample is infinite ($x \rightarrow \infty$), the reflectance at infinite depth R_∞ approaches $q = a - (a^2 - 1)^{1/2}$. This can be solved for a and the Kubelka–Munk function $f(R_\infty)$:

$$f(R_\infty) = \frac{(1 - R_\infty)^2}{2} \qquad R_\infty = a - 1 = \frac{k'}{s} \tag{3.26}$$

At low concentrations the scattering of the absorbing medium can be neglected, then k' will be proportional to the concentration of the sample. In this case, $k' = kc$ where c is the concentration (wt%) and k is the absorptivity of the sample (cm^{-1} $wt.\%^{-1}$).Infinite thickness is defined as the sample thickness beyond which any further increase in thickness causes no change in the measured IR spectrum [42]. In practice, the Kubelka–Munk function is valid only when the amount of *Fresnel reflectance* (defined as radiation that undergoes reflection from the surface of particles but never passes through the particles) is small and the scattering coefficient is independent of the concentration [43]. Because both Fresnel reflectance and scattering are affected by particle size and packing, reproducible diffuse reflectance spectra require good mixing and sieving of the samples to limit the particle size.

It has been demonstrated that samples of the same concentration but different particle sizes give different diffuse reflectance spectra [44]. For polystyrene spheres, the absorbance increases as the particle diameter decreases from 90 to 2 μm. Particles with diameters 2–10 μm give undistorted high-intensity diffuse reflectance spectra that may be used for quantitative analysis.

Bulk polymer samples can be studied by using DRIFT [45,46]. For the study of the surfaces of bulk samples, a DRIFT accessory should perform the following functions:

- reject specularly reflected radiation,
- yield sufficient optical throughput,
- accommodate bulky samples,
- analyze comparatively small areas.

A DRIFT accessory has been developed to examine local areas of bulky samples [47].

Another development in DRIFT is the discovery of a simple spectroscopic method of *depth profiling* the surfaces and interfaces of organic–inorganic materials [48–50]. The new procedure involves the use of a powdered KBr layer on top of the bulk sample to be examined. As the thickness of the overlayer is increased, the ratio of the surface-to-bulk contribution to the recorded spectrum increases. The reflected beam observed at the detector contains contributions from various regions of the sample. By using suitable data processing techniques it is possible to determine the relative contributions of the surface and bulk spectra. This information allows quantitative determinations of differences in structure as a function of depth from the reflecting surface. This technique has been applied to the identification and evaluation of 3-aminopropyltriethoxysilane (γ-APS) coupling agent on E-glass fibers [51]. A circular mat of glass was covered with a uniform layer of KBr, and the DRIFT

spectra were recorded. It was then possible to isolate the spectrum of the absorbed γ-APS coupling agent.

Photoacoustic spectroscopy

Photoacoustic spectroscopy (PAS) is based on the principle that modulated IR radiation striking the surface of a sample will cause the surface to alternately heat and cool with IR absorption [52]. This cyclic heating is conducted to a coupling gas in the photoacoustic cell. A standing sound wave that can be detected by a microphone develops. The diagram of the PAS technique is shown in Fig. 3.16.

The PAS cell must be sealable so that the coupling gas does not leak out of the chamber during the experiment. The leakage leads to exchange with air which has different thermal properties.

PAS signals are generated as a result of the absorption of radiation by the sample, thus causing a periodic temperature fluctuation within the optical absorption depth. Consequently, as the absorbed radiation from within a thermal diffusion length is released to the surface, there is an increase in the pressure of the ambient gas surrounding the sample. The pressure change is then detected by a microphone and subsequently converted to an electric signal.

As only PAS signals generated within the thermal diffusion length are detected, the method can be used to discriminate between the surface and underlying layers of solid materials. PAS is useful for probing penetration of about one micron. In PAS, interferometrically modulated IR radiation impinges upon a sample in a sealed gas-filled chamber. The depth of detection is dependent on the thermal and optical properties of the sample. The scanning depth is conventionally identified with thermal

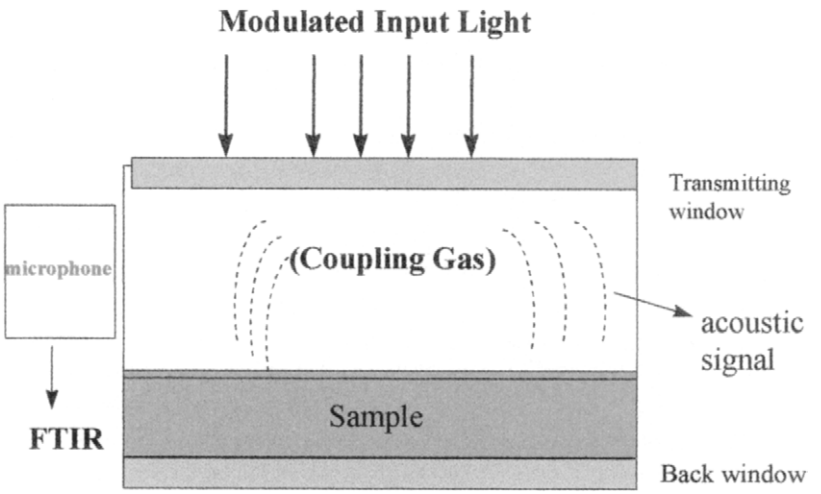

Fig. 3.16. Optical diagram of the PAS technique.

diffusion depth, d_{th}, which is determined by the equation

$$d_{th} = \left(\frac{D}{\pi \nu \omega}\right)^{1/2} \tag{3.27}$$

where D is the thermal diffusivity for the sample, and ω is the modulation frequency of the IR radiation. The modulation frequency, ω, is dependent upon the velocity of the mirror in the Michelson interferometer.

Thus, the sampling depth in PAS is determined by the mirror velocity of the interferometer. Low optical velocities will result in PAS signals from deep within the sample; while high optical velocities will allow thermal diffusion from the surface regions. The dependence of the thermal diffusion length on ν means the d_{th} varies over the frequency region.

The PAS signal is obtained by differentiating the photoacoustic absorption signal of the sample from other sources of acoustical noise. The main sources of noise are absorption signals from the PAS cell walls and window materials, secondary absorption echoes caused by reflected light in the cell, and external sources of acoustic noise or vibrations in the laboratory or spectrometer.

In PAS, signal saturation results in loss of spectral detail, as well as a general broadening of the peaks. These effects occur at low optical scanning velocities, corresponding to large thermal diffusion lengths and in instances where the thermal diffusion depth is larger than the optical depth. As the thermal diffusion length is proportional to the square root of the optical velocity, an increase in optical velocity will decrease the thermal diffusion length and minimize any saturation effects.

Depth profiling using PAS

In PAS, the time-resolved photoacoustic response to sinusoidally modulated incident source radiation has a phase delay. The magnitude of the phase delay depends on the depth in the sample from which the photoacoustic response originates. The square root dependence of the sampling depth on the mirror scanning speed means that a wide range of scanning speeds must be used for depth profiling over a reasonable depth range. For true depth profiling, the modulation frequency of the light source should be the same at all frequencies simultaneously. The sampling depth increases (by a factor of about three across the wavenumber range 400–4000 cm^{-1}) with decreasing wavenumber.

Step-scanning interferometers can enhance the photoacoustic technique, because the variable modulation frequency of the scanning interferometer is decoupled. Thus, a constant modulation frequency is applied to all wavelengths in the spectral range. One can modulate the IR beam via phase modulation in which an interferometer mirror dithers to oscillate the retardation about the set point of each interferometer step. With this approach, all of the frequencies are modulated synchronously, and lock-in modulation can be used to extract the phase-modulation [53]. When phase-

sensitive detection is used, the signal can be represented by its phase and magnitude or in-phase and quadrature components.

The constant modulation frequency also produces a thermal diffusion depth which is independent of wavelength and thus allows more straightforward interpretation of spectral depth profiling data from heterogeneous samples [54].

PAS can be used for layered samples [55]. When a layered sample consists of an absorbing substrate covered with an another transparent layer of another material of thickness b, then the thermal wave at the sample surface will lag behind the creation of the wave at the buried layer by a phase $\Delta\theta$ when using a rapid scan interferometer [56]:

$$\Delta\theta = \frac{b}{d_{\text{th}}} = b\left(\frac{\pi V}{D}\right)^{1/2} \tag{3.28}$$

With a step-scan interferometer, the phase of a substrate absorption band from the layered samples should lag by $\Delta\theta$ behind the phase of the same band from a bare piece of substrate material, so b can be determined from these two phases. It is required that the overlayer be transparent at the wavelength of the substrate absorption. This relation has been tested for a series of samples consisting of a thin PET film on a thick polycarbonate substrate [54].

PAS is now widely used for the detection and analysis of various polymeric materials in liquid and solid phases [57]. PAS is particularly useful in infrared measurements for opaque samples and for cases where sample preparation is not desirable since it may change the process, thermal or environmental history of the sample. The main advantages of PAS are

- minimal sample preparation,
- samples can be examined in their original form,
- capability of studying opaque samples including carbon-black filled,
- capability of depth profiling the sample.

Compared to DRIFT, PAS can analyze the neat sample without dilution with KBr powder, but PAS has a lower inherent sensitivity. The limitations of PAS include

- low signal-to-noise ratio per scan,
- photoacoustic saturation related to high absorption (the use of thin samples minimizes this effect),
- an artificial increase in the signal due to the thermal dilation of the sample (this dilation is sensitive to the absorption of the whole sample; that is, there is an acoustic background between absorption bands),
- an increase in the heat sources (texture or matrix effects) in heterogeneous samples due to light scattering.

PAS is a rapidly growing technique for obtaining IR spectra of samples that are hard to prepare as transparent films, that have high internal light scattering, or that are coated onto opaque or strongly light-scattering substrates. Thus the PAS

technique is complementary to the IRS (ATR) and diffuse reflectance techniques and has the advantage of little or no sample preparation. Typically, only 0.25 ml of sample is required, and the specimen usually can be examined 'as received'. The signal-to-noise ratio for PAS is low, so a longer scanning time (1000–6000 scans) relative to transmission FTIR spectroscopy is required.

In the study of polymer surfaces, PAS can enhance the surface modes by using a highly polarizable inert gas [58,59]. When a highly polarizable coupling gas is used in the photoacoustic cell, useful information can be obtained regarding the species present and their orientation with respect to the surface of the adsorbate. A distinction between the two types of adsorbed molecules on the surface (parallel and perpendicular to the surface) can be made. This technique is simple and nondestructive, and requires a routine photoacoustic setup. It can be applied to virtually any sample, and it represents a new frontier that should expand upon our traditional ideas of the bonding and structure of surface-adsorbed species.

A novel application of PAS is the use of rheophotoacoustic measurements to perform stress–strain studies on polymeric materials [60]. Propagating acoustic waves are detected as a result of the deformation of the sample.

Emission spectroscopy

Emission spectroscopy (EMS) can provide the same information as transmission spectroscopy. When the temperature of any sample is raised, the Boltzmann population of the vibrational energy states is also raised and, upon return to ground state, radiation is emitted. In theory, emission spectra can be measured any time a sample is at a different temperature than the detector. The signal of the emission spectrum increases with the fourth power of the temperature difference between the sample and the detector according to Stefan's law (ΔT^4).

Kirchoff's theorem states that the ratio of a body's spectral luminance to its absorbance, L/a, is a function of the frequency and temperature of the body but not a function of the nature of the body or its geometrical dimensions. This ratio is equal to the spectral luminance of a perfect black body;

$$\frac{L}{a} = L_{\mathrm{BB}} \tag{3.29}$$

By definition, the absorbance of a black body is

$$a_{\mathrm{BB}} = 1 \tag{3.30}$$

The emittance, ε, is defined as

$$\varepsilon = \frac{L}{L_{\mathrm{BB}}} \tag{3.31}$$

and therefore,

$$\varepsilon = a \tag{3.32}$$

In theory, the emittance and absorbance of a sample are equal. Under proper conditions, the emission spectra are the mirror images of the absorbance spectra.

For experimental IR emission spectra there is a large background radiation superimposed on sample emissions restricting the detection limit of infrared emission spectroscopy. Emission spectra are often referenced to the energy emitted by a black body at the same temperature as the sample being studied. In addition, radiation from outside sources such as the heated sample holder, and room lights, must be eliminated. Cooling of the sample chamber and the spectrometer reduces this background. Polarization modulation removes background emission very effectively. Using step-scan instrumentation with polarization modulation, the step-scan mode gives a S/N twice that of the continuous-scan operation. It is thought that the low-velocity operation of the continuous-scan mirror causes instability of data sampling, which affects the spectrum S/N. Using the polarization-modulation technique it is possible to detect the emission spectrum of a 12-nm thick polymer film on a gold evaporated surface [61].

Emission spectroscopy can be used on samples such as metals and opaque substrates that cannot be studied by transmission. The emission technique can sometimes provide a more convenient method of acquiring the same spectral data, because no source other than the heated sample is required and reactions at high temperature can be studied directly. An emission cell has been designed to study samples up to temperatures of 1500°C [62].

Luminance is the intensity of emitted radiance per unit solid angle and frequency. It is sometimes called *spectral radiance*, or *radiant flux. Emissivity* is a property of a sample measured at standard conditions. The sample must be thick enough to be both optically opaque and smooth [63]. In the case of a perfect black body, the sample cannot be reflective. This property is not composition or geometry dependent: even a heated pinhole cavity will show a good black body curve.

On the other hand, *emittance* is a property of the sample dependent on composition and geometry. It contains spectral characteristics and is given as the ratio of a sample luminance to that of a black body. The emittance is the factor by which the black-body radiance of a material must be multiplied in order to obtain its actual radiance.

Kirchhoff's law states that the emittance of any body equals its absorbance, it follows from Beer's law that the emission of a thick non-opaque emitter will approach that of a black body. A black body is defined as a substance which totally absorbs energy (and therefore emits the maximum energy) at any temperature (T) as a function of wavelength. Real objects are compared to this black body through the use of the term *emissivity* (ε). The emissivity of an object varies with wavelength (λ) or frequency (ν) and is defined as:

$$\varepsilon_\nu = \frac{J(\nu, T)}{J_B(\nu, T)} \tag{3.33}$$

where $J(\nu, T)$ is the spectral radiance or radiant flux, $J_B(\nu, T)$ is the radiant flux of

a black body. For a given wavelength, this ratio is equal to one in the case of an ideal black body emitter and is a fraction less than one for non-ideal objects. The only real object, which approximates the ideal emitter, is a black body cavity. These cavities have emissivities of greater than 0.98 over a wide wavelength range. Materials that do not emit as efficiently, but have emissivities that are nearly constant with wavelength, are called gray bodies [64].

In IR emission spectroscopy, however, several forms of distortion can occur and of these background emission is the most important one and requires elimination. Removal of background emission involves measuring the spectra of both the sample and a black body reference material at two temperatures [65]. The measured intensity, $S(\nu, T)$ has several components:

$$S(\nu, T) = R(\nu)[\varepsilon(\nu, T) H(\nu, T) + B(\nu) + I(\nu)\rho(\nu)] \tag{3.34}$$

where $R(\nu)$ is the instrument response function, $\varepsilon(\nu, T)$ is the emittance of the material, $H(\nu, T)$ is the Planck function, $B(\nu)$ is the background radiation, $I(\nu)$ is background radiation reflected off the sample, and $\rho(\nu)$ is the reflectance of the sample. For the black body reference material, $\varepsilon = 1$ and $\rho = 0$. So the intensities measured on the reference material are

$$S_1(\nu, T_1) = R(\nu)[H(\nu, T_1) + B(\nu)] \tag{3.35}$$

$$S_2(\nu, T_2) = R(\nu)[H(\nu, T_2) + B(\nu)] \tag{3.36}$$

For the sample, the measured intensities are

$$S_3(\nu, T_1) = R(\nu)[\varepsilon(\nu, T_1) H(\nu, T_1) + B(\nu) + I(\nu)\rho(\nu)] \tag{3.37}$$

$$S_3(\nu, T_2) = R(\nu)[\varepsilon(\nu, T_2) H(\nu, T_1) + B(\nu) + I(\nu)\rho(\nu)] \tag{3.38}$$

Assuming that the sample emittance and reflectance are independent of temperature over the operating range, the emittance is calculated as

$$\varepsilon = \frac{S_4 - S_2}{S_3 - S_1} \tag{3.39}$$

Subtracting the interferograms rather than the spectra has been suggested to avoid phase corrections.

The IR emittance of a sample relative to a black body is dependent on the reflectivity at the surface of the sample. With a black body as a reference, band distortions such as frequency shifts and false splittings resulting from reflectivity variations in the vicinity of strong bands can still be encountered [66]. Under these circumstances, an opaque sample rather than a black body should be used as a reference.

A pure emission spectrum can originate only from a material that does not have thermal gradients. Re-adsorption of thermal emission can occur when the radiation emitted by a hot portion of the sample passes through a cooler portion of the sample [67]. Self-absorption in optically thick samples can result in emission spectra that

resemble those of a black body, containing no spectral bands characteristic of the material under analysis.

The usual method of reducing self-absorption is to use a thinner sample so that the thermal gradients are smaller. A novel approach to this problem was made by recognizing that it is necessary to reduce the thickness of only the material actually emitting radiation. By using a laser as the heating source, it is possible to generate a thin, transiently heated surface layer of the material and to collect the radiation emitted from only this layer [68]. For the experiments reported, the transiently heated layer was created by using a fixed continuous laser beam that was focused on a rotating sample.

The emission technique is limited to the range of frequencies greater than 2000 cm^{-1} because the low flux of energy in the lower frequency region gives a very weak signal. Measurements down to 400 cm^{-1} are possible if the entire spectrometer and its surroundings are cooled. However, this option is not usually practical. The sample also may be heated to elevated temperatures, but sample decomposition then becomes a problem.

Because emission occurs primarily from the surface of the sample, the EMS technique has potential for surface analysis. The problem with extending the emission technique to surface analysis is the strong background emission that is superimposed on the weak emission of the surface coating. One method of increasing the emission signal is to collect the emitted radiation over a large solid angle by using an ellipsoidal mirror [69]. The maximum emission from a surface occurs when the viewing angle is 70–80° from the normal, and the emission is approximately zero in the direction normal to the surface. This zero emission arises because of destructive interference between emitted and reflected light from the interface to the metal surface.

For surface emission studies, the emittance is defined as

$$\varepsilon = \frac{S_s - S_b}{S_R - S_b} \tag{3.39}$$

where S is the measured intensity, and the subscripts 's', 'R', and 'b' denote the samples, reference substrate, and background emission from the beam splitter, respectively [70]. The emission spectra of different thicknesses of poly(acrylonitrile-*co*-styrene) on aluminum at 150°C are shown in Fig. 3.17.

The intensity is a linear function of thickness up to 1000 Å as illustrated in Fig. 3.18.

A complete analysis of the thermal emission of surface species and their measurements has been reported [71]. A problem of extending the emission technique to surface analysis is that strong background emission can be superimposed on the weaker emission from the surface. Thus the ideal sample for emission studies is a very thin surface layer supported on a perfect reflector. An experimental emission sampling system designed specifically for the study of surface species has been described [72].

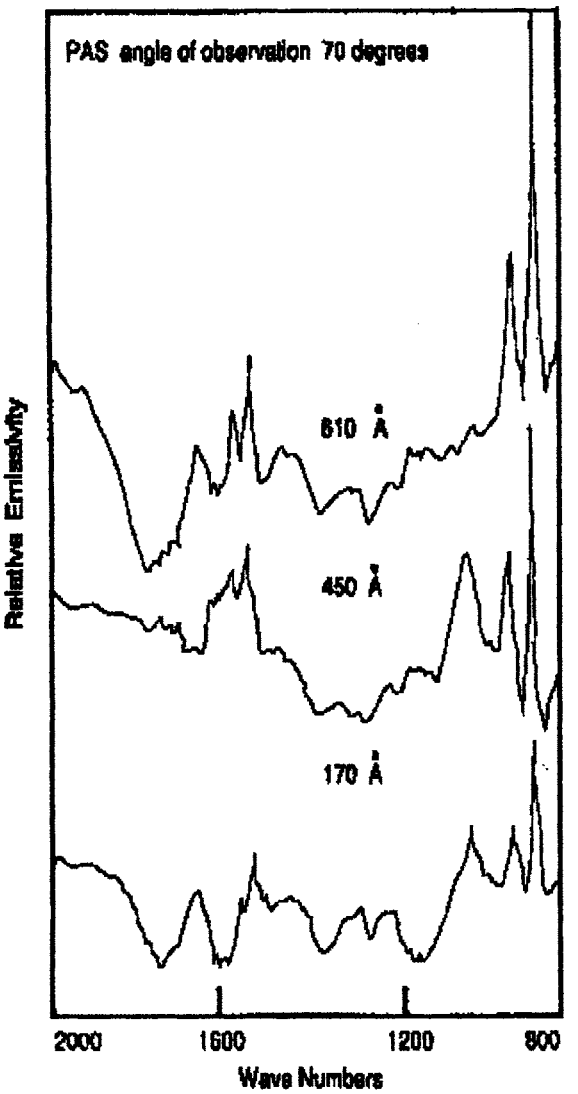

Fig. 3.17. Emission spectra of thin films of poly(acrylonitrile-*co*-styrene) at 150°C. (Reproduced with permission from Ref. [70]. © 1984 Society for Applied Spectroscopy.)

The advantages of emission sampling include:

- simple experimental characteristics (sample is the source),
- noninvasive character,
- in combination with chemometrics, emission promises to be a tool for process monitoring.

An example where emission spectroscopy is very useful is for very thin polymeric coatings on a metal surface. The emission of a thin organic coating is applied

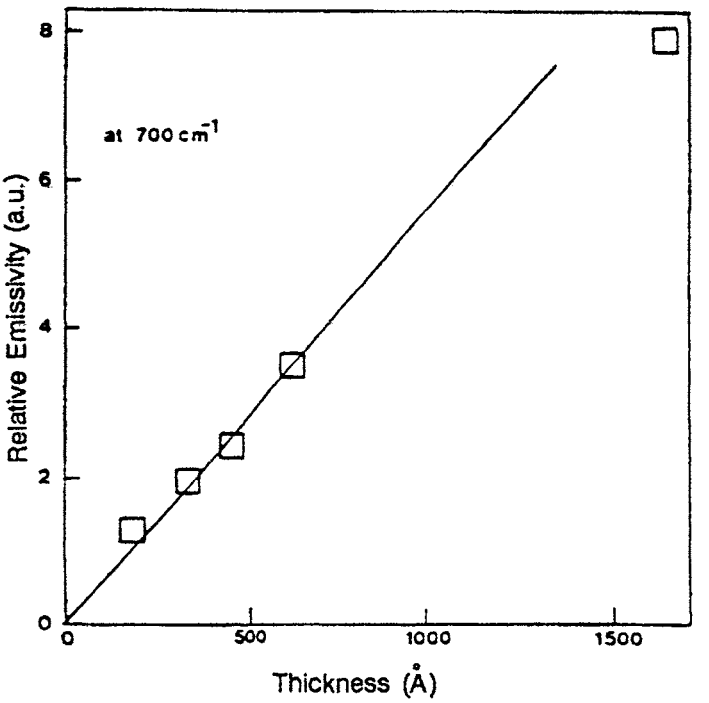

Fig. 3.18. Dependence of emission intensity on the thickness of the thin polymer films on aluminum. (Reproduced with permission from Ref. [70]. © 1984 Society for Applied Spectroscopy.)

on a highly reflecting surface provides good spectral contrast and low background emission.

The disadvantages of emission include:

- other IR sampling techniques in the laboratory are easy to implement, i.e. transmission and reflection,
- other IR sampling techniques have higher signal to noise ratios,
- emission spectra exhibit anomalous behavior arising from temperature gradients in polymeric samples as a result of having to heat the sample and the low thermal conductivity of organic materials,
- complex nonlinear behavior of the emission signal,
- relevant information difficult to extract from emission spectra.

Emission also has the potential for monitoring of samples and plant streams remotely [73]. A report of the monitoring using IR emission of the cure of a commercial paint product has been reported [74].

Microsampling techniques

The applications of IR microspectroscopy have increased as quality IR microscopes with spatial resolution of approximately 50 μm have been developed. IR

microscopes can be used for both transmission and reflection measurements. The characteristics of FTIR spectroscopy that have made these microscopes possible are the energy throughput and multiplex advantages.

A typical IR microscope is all-reflecting, with visible illumination for visual examination of the sample and with a dedicated on-axis small area mercury-cadmium telluride (MCT) detector. The sampling size can vary from less than 50 × 50 μm in linear dimensions to the dimensions of the detector element. The sample is placed on a standard microscope X–Y stage and can be visually examined under a variety of magnifications. The sample area of interest is isolated by placing a variable aperture on an intermediate image of the sample within the barrel of the microscope.

The FTIR microscope is particularly useful for polymer studies because it is relatively easy to obtain a minute polymer specimen, by using a razor blade or a knife, that is thin enough to analyze by transmission. The specimen can be placed in a KBr pellet die or a diamond anvil and pressed to a thickness suitable for analysis.

The IR microscope is a valuable tool for the analysis of fibers, particulates, and inclusions. A dedicated microscope-FTIR instrument with appropriate hardware and software to perform a wide range of microscope experiments has been developed recently.

Recently, IR microspectroscopy has been used to develop two-dimensional functional group images of polymer samples. A two-dimensional computer-restored step-scan was performed on the sample in order to obtain a compositional map. A 250 × 250 μm aperture was used in 250-μm steps in the x and y directions with the aid of a computer-controlled moving stage. Although the technique is powerful, it has two major disadvantages. The resolution is 3 to 10 times less than with Raman and fluorescence microbeam methods, and the time required for data collection and reduction can be as long as 24 h.

Data processing of digitized IR spectra

With the advent of computers and digitized spectra, it is possible to apply a number of signal processing techniques to aid in the interpretation and evaluation of spectra. The universal goal of all signal processing schemes is measurement of the signal in such a manner that the uncertainty introduced by the noise variance is minimized. The choice of a signal processing scheme is generally dictated by the nature of the signal, as well as the statistical behavior of the noise. The proper approach requires a careful analysis of both spectral signal and noise. Spectra are generally processed in some way to

- remove interferences such as background,
- reduce noise,
- extract the information related to the desired signal parameters such as concentration.

Quite commonly, for polymer studies, the desired signal is a single absorbance peak, symmetric or asymmetric, and the desired information is related to some signal parameter, such as its peak height or area.

Elimination of spectral backgrounds

Generally, an extraneous background is present in all types of spectral data, and its elimination or correction is necessary before proceeding to other data manipulation procedures. The background leads to deleterious effects on the fundamental signal-to-noise ratio of the gross signal, since the net absorbing signal must be separated from the background to allow accurate analysis. If the background contribution to the signal is reproducible and can be measured in the absence of the absorbing signal, the background can be removed by subtraction. If the background response is variable and cannot be measured in the absence of the absorbing signal, then it is not possible to remove the background. However, it is necessary to remove or correct as much of the interfering background as possible.

The main source of the background noise in IR spectroscopy of polymers is the partial nonabsorbing scattering of the IR radiation from inhomogeneities in the polymer sample. Other possible sources of background variations include tilting or improper orientation of samples, interference effects, different size sample holders, and imperfect instrumental optics. In most cases, changes in the base line arise from nonabsorptive scattering effects arising from reflections at interfaces. Such scattering is a function of the refractive index differences in the two media as well as the roughness of the reflecting surfaces.

There is no perfect base-line correction, and all corrections are approximates. The simplest base line is a flat line that is parallel to the abscissa axis. Linear base lines with negative or positive slopes have been applied, as well as more complex forms. Several methods are available for base-line correction [75]. As a simple approach, a wedge defined by two points can be subtracted from the absorbance spectrum. Also, the entire spectrum or selected frequency ranges of the spectrum can be fit to a linear least-squares line, repeating the fitting until some predetermined deviation is satisfied. It is important to be able to correct a base line by using a method that avoids as much as possible subjective interaction.

One approach is the explicit measurement of the background at two fixed wavelengths on either side of the desired absorbing wavelength and develop a linear extrapolation. Or a 'piece-wise linear base-line correction' is applied using a number of line segments. An often used route is to subtract a base line by fitting a line (or higher order polynomial curve) to the minima of the signals. This method only works when the minima represent a true 'zero' signal. This method fails when there are interferences with other overlapping peaks or other signals. The method also fails when there are too many broad peaks within the measured range, and the zero signal is not observed.

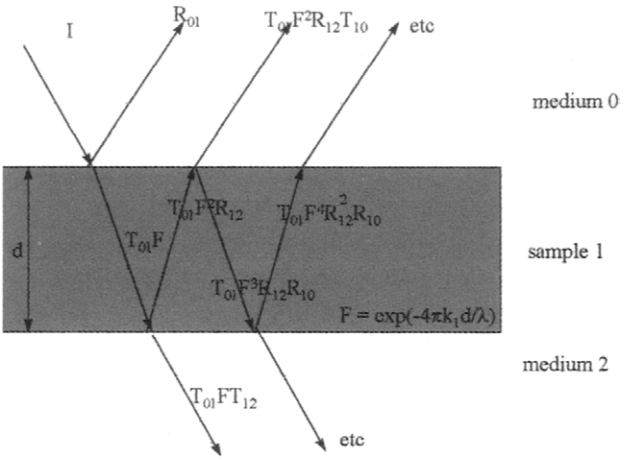

Fig. 3.19. The reflection and transmission of light rays through a film of thickness d.

A base-line correction algorithm that is based on the use of a successive least-squares routine and that includes objective criteria on the convergence of a base line that is either linear or quadratic has been used [75].

When a sample is highly uniform in thickness and has smooth surfaces, another irritating spectral effect, *interference fringes*, can be observed. The basis of the formation of the interference fringes is shown in Fig. 3.19. The reflection patterns of the light rays are shown for a number of reflections, which interfere to form the interference fringes.

FTIR spectroscopy offers some possibilities for eliminating fringes if the 'fringe signature' can be detected in the interferogram. This fringe signature appears as a single spike in the interferogram away from the center burst, and sometimes it can be removed. Consequently, the fringes in the transformed spectra do not appear [76]. Another approach to removing the fringes is to use direct digital subtraction [77].

Reflection interference produces a sine wave in the spectrum. A computer file containing a sine wave of the same amplitude and phase as the experimentally observed curve can be generated, and this computer-generated curve can be subtracted from the observed fringes. However, it often easier to simply make the surface of the films rough by rubbing with KBr powder or steel wool.

Elimination of spectral distortion resulting from sampling technique

As previously discussed, for the analysis of polymers by FTIR spectroscopy various types of optical sampling experiments are used depending on the nature of the sample. Different sampling methods, such as transmission, specular reflection, or attenuated total reflectance, yield spectra that differ in the frequency, shape, and intensity of the bands, even when all of the experiments are performed on the same

sample. In all cases, it would be preferable to obtain an absorbance spectrum that is characteristic of only the chemical structure of the sample without any effects from the optical geometry of the experiment. Furthermore, it is desirable to be able to make direct comparisons between the spectra obtained with different sampling techniques.

The refractive index, n, and absorption index, k, determine the response of a material to incident electromagnetic radiation. Collectively, n and k are referred to as the optical constants; however, they are not strictly constants because they vary with frequency. At the interface between two phases, a propagating electromagnetic wave will be both reflected and transmitted. The magnitude of the signal that is either reflected or transmitted is determined by the relative *optical constants* of the two phases and by the angle of incidence. By using a Kramers–Kronig transformation, the nature of the response can be determined. A algorithm has been developed to simulate ATR and specular reflectance of IR experiments [78]. The results obtained by using these two methods, as well as those obtained by transmission spectroscopy, for a thin film of poly(methyl methacrylate) (PMMA) on a Ge substrate are compared in Fig. 3.20.

The three spectra show differences in the peak position and shape for the identical sample using three different techniques of measurement. The carbonyl band is shifted to higher frequencies by 12 cm^{-1} with specular reflectance and to lower frequencies by 3 cm^{-1} with ATR. The specular reflectance and ATR spectra show an asymmetric carbonyl band, while the transmission spectrum gives the correct profile.

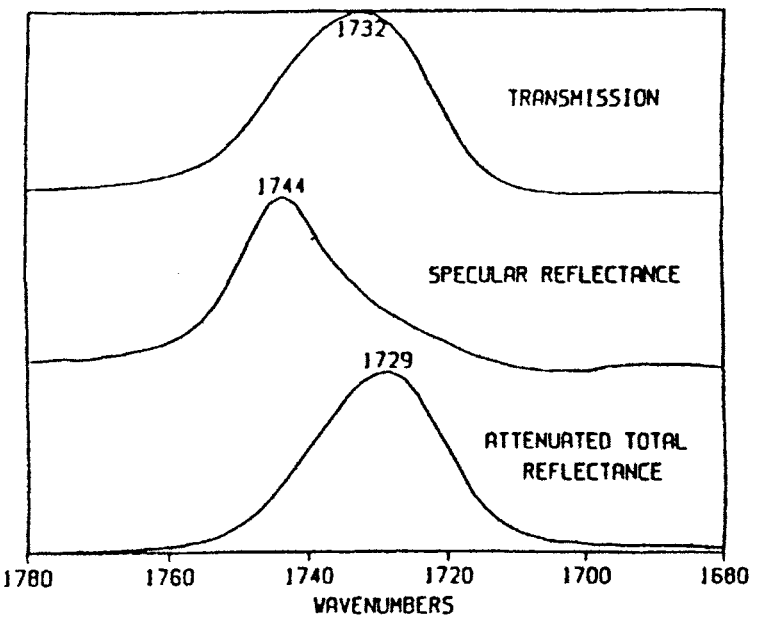

Fig. 3.20. The spectra of a sample of PMMA on a Ge substrate obtained by transmission, specular reflection, and ATR spectroscopy. (Reproduced with permission from Ref. [78]. © 1987 Plenum Press.)

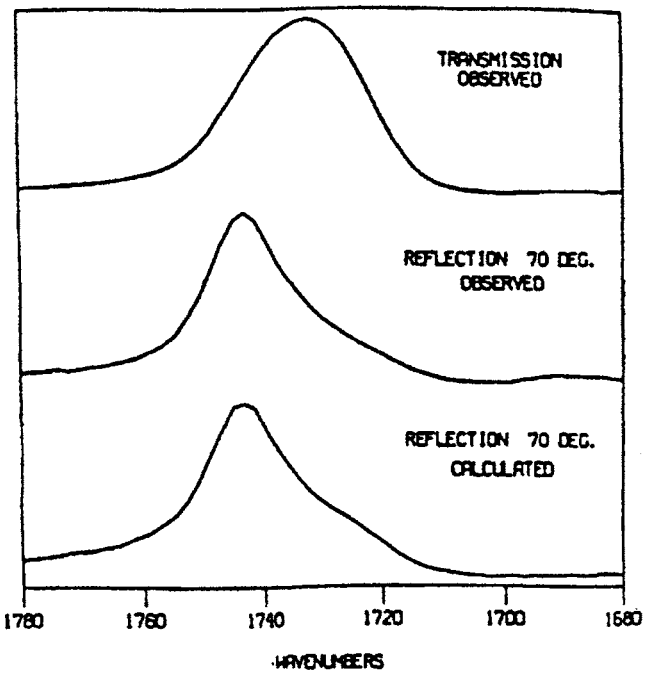

Fig. 3.21. Comparison of the transformed spectrum of the specular reflectance experiment with the transmission and reflection spectra of PMMA on a Ge substrate. (Reproduced with permission from Ref. [78]. © 1985 Society for Applied Spectroscopy.)

By using optical constants previously derived for PMMA, the expected band profiles for specular reflection and ATR experiments were calculated. For the ATR experiment, 13 reflections occur on the face of the Ge element covered by PMMA. For the specular reflectance experiment, all three interfaces (air–film, film–Ge, and Ge–air) must be included in the calculations to obtain the correct band intensities. The results of these calculations are shown in Figs. 3.21 and 3.22.

The peak shifts and shape changes evident in Fig. 3.20 are completely accounted for by the Kramers–Kronig calculation indicating that the frequency and band shape differences are a consequence of the sampling technique.

Spectral subtraction

Spectral subtraction, which has widespread utility, has become an important tool in the arsenal of the spectroscopist. Spectral subtraction allows the study of solid samples with high precision because corrections can be made for differences in sample thickness. Interfering absorbances can be removed. Removing artifacts, solvents, and other impurities with the final result being the pure spectra of the components can purify the spectrum.

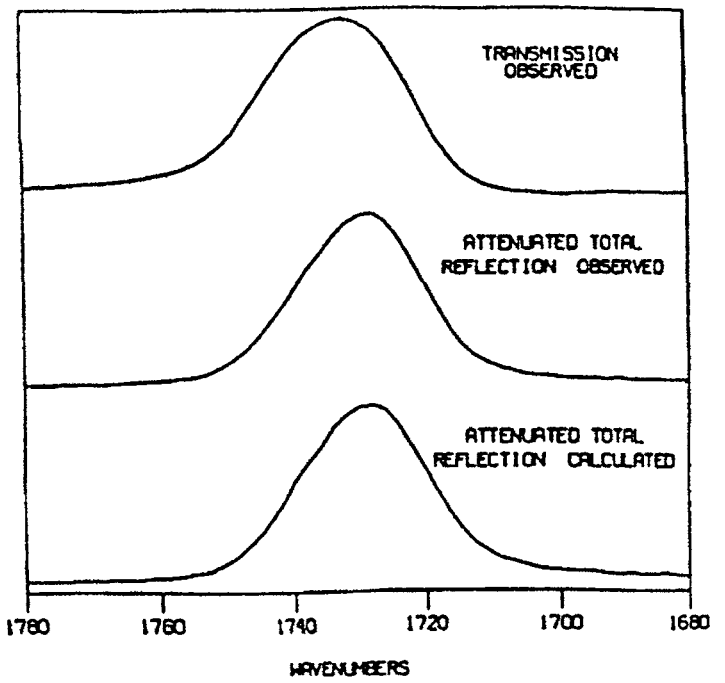

Fig. 3.22. Comparison of the transformed ATR spectrum with the observed transmission and ATR spectra. (Reproduced with permission from Ref. [78]. © 1985 Society for Applied Spectroscopy.)

Absorbance subtraction is based on two fundamental assumptions. First, it is assumed that the absorbance and shape of a band do not change with the optical thickness. Generally, the absorbance values must be less than 1 in order to meet this requirement. The assumption is tested with every subtraction. If the residual absorbance after a subtraction has a different shape than the original absorbance bands, the assumption has been violated, and the procedure or samples should be reexamined for the cause of the nonlinear effects (i.e., holes, nonuniform samples, sample orientation, vignetting, etc.). The second assumption is that the absorbance of a mixture is the linear sum of the absorbances of the components; that is, the components do not interact with each other differently at different relative concentrations. Concentration-dependent interactions will lead to frequency shifts and band shapes changes, but rarely are such effects observed in solids.

In spite of the simplicity of spectral subtraction, there are many problems in applying spectral subtraction. These problems arise because the digital absorbance subtraction is sensitive to changes in intensity, absorption frequency, and linewidths. As a result, even when the samples have perfectly matched thicknesses, a variety of difference spectra can be obtained as is shown in Fig. 3.23.

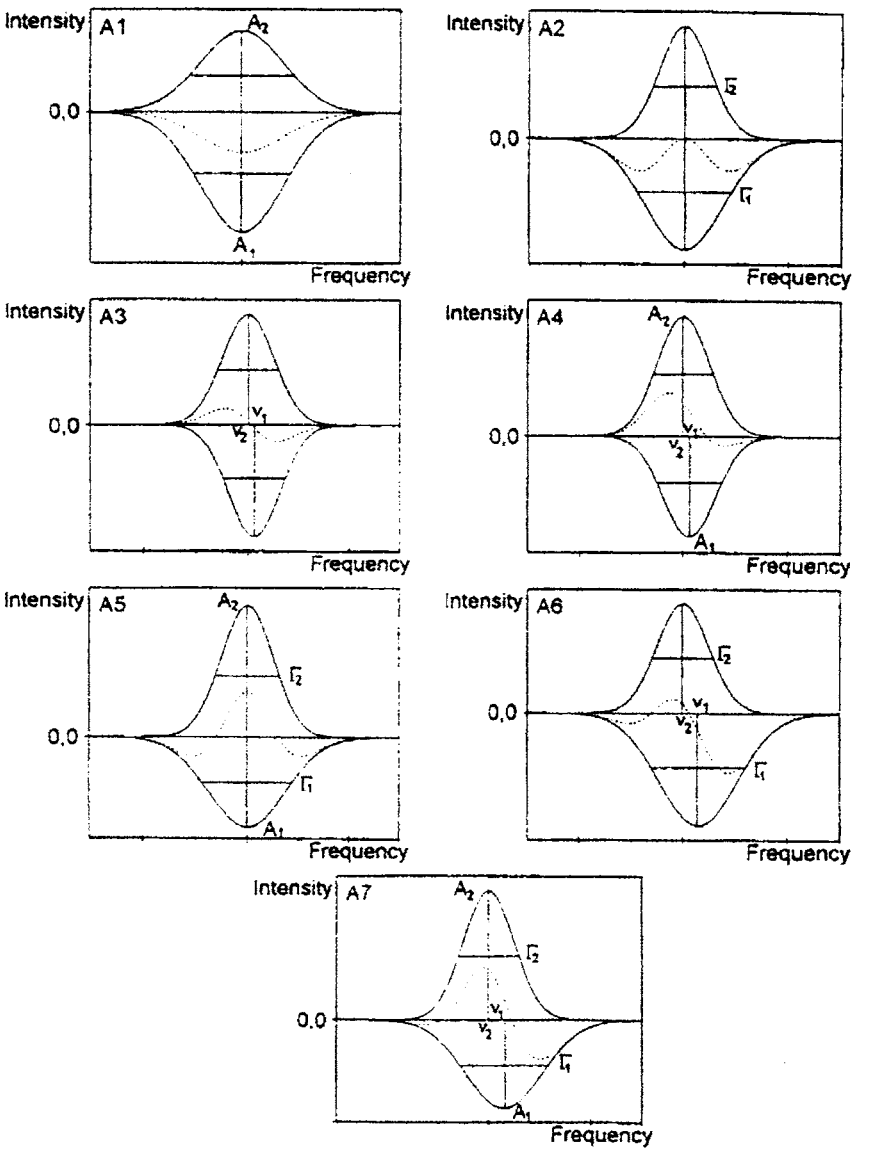

Fig. 3.23. Simulated line shapes due to changes: (A1) intensity only, (A2) linewidth only, (A3) absorption frequency only, (A4) intensity and absorption frequency, (A5) intensity and linewidth, (A6) linewidth and absorption frequency and (A7) intensity, linewidth and absorption frequency. The dashed lines represent the resulting difference bands. (Source: R.A. Ingemey, G. Strohe and W.S. Veeman, Appl. Spectrosc. 50 (1996) 1360.)

All of the changes in the bands to be subtracted can arise due to a variety of sources including the interaction of the individual components with each other to produce frequency shifts and changes in shapes and intensities. Problems in subtraction arise

when the samples are optically too thick or are imperfect (voids, wedgeshaped, etc.) so that the absorbances are not linear.

> *Spectral subtraction is applicable only to spectra obtained in the absorbance mode; that is, spectra plotted in the transmission mode are exponential rather than linear and should never be digitally subtracted.*

Spectral subtraction requires the prior scaling of the spectra to correct for variations in the thicknesses of the samples in the IR beam. The spectroscopy of polymers usually involves solids rather than with solutions or liquids. With solids, it is almost impossible to experimentally prepare samples with identical optical thicknesses in the beam, so a means must be found to correct for this path length mismatch in order to perform spectral subtraction.

If the spectra obtained are in the linear optical range, a reference spectrum can be subtracted from the sample spectrum. The absorbances can be scaled to correct for differences in the amount of sample in the beam if an internal thickness band for the sample can be selected. An *internal thickness band* is a band whose intensity is a function of only the amount of sample in the beam. Generally, isolated bond stretching modes such as the C−H modes have this important property. The absorbance of the internal thickness band for the reference sample can be written

$$A_{ir} = a_{ir} C_i b_r \tag{3.41}$$

where A_{ir} is the absorbance of the internal thickness band of reference sample; a_{ir} the absorptivity coefficient; C_i the concentration of the internal thickness band, i, that is, $C_i = 1$; and b_r is the thickness of the reference sample.

For the sample,

$$A_{is} = a_{is} C_i b_s \tag{3.42}$$

where A_{is} is the absorbance of the internal thickness band of the analytical sample; a_i is the absorptivity coefficient for the analytical sample; C_i is the concentration of internal thickness band, that is, $C_i = 1$; and b_s is the thickness of the analytical sample.

The reference spectrum is scaled by using a scaling factor, k, such that the following equation is satisfied:

$$A_{is} - kA_{ir} = 0 = a_{is} C_i b_s - k(a_{ir} C_i b_r) \tag{3.43}$$

So the scaling factor becomes

$$k = \frac{b_s}{b_r} \tag{3.44}$$

The thickness-scaled reference spectrum can then be subtracted from the spectrum of the analytical sample to produce a difference spectrum. Peak absorbances, integrated

peak areas, or a least-squares curve-fitting method can be used to calculate the scaling factor, k. The method of choice will depend on the system being examined. Remember that the calculation of the scaling factor cannot be done entirely analytically, and the only test of the scaling factor is the resultant difference spectrum, which should be examined carefully before any further analysis is carried out.

If a properly calculated value of k is used, the spectral differences will be independent of sample thickness, and only structural differences will be observed. Additionally, with properly compensated thicknesses and the removal of strong interfering absorbances, the dynamic range of the difference spectrum is large enough to permit the differences in absorbances to be magnified through computer scale expansion, and reveal small details. By using spectral subtraction, the spectral changes that have occurred can be accentuated, and the spectral contributions that did not change can be minimized.

Care must be exercised because the technique is also sensitive to optical spectroscopic errors. It is probably not a misstatement that absorbance subtraction has generated more artifacts than facts because of lack of attention to the proper sample preparation procedures and spectroscopic techniques.

For example, if the sample is nonuniform or wedge shaped, errors can occur. A false difference spectrum will be obtained from two spectra of the same sample with the same mean thickness if the samples are wedge shaped. The severity of the wedging effect depends on the method used to determine the scaling factor and on the optical thickness of the sample.

Another problem often encountered in absorbance subtraction is the preferential orientation of one of the samples relative to the other. Unfortunately, there is no general method or algorithm to eliminate this orientation problem because each band has its own characteristic dichroic behavior. The only solution is to prepare the samples with reproducible or random orientation. Unless this is accomplished, three-dimensional tilted sample methods must be used. The three-dimensional tilted sample method removes the orientation of the sample and generates a pure 'structure-factor' spectrum prior to absorbance subtraction.

Historically, spectral subtraction led to one of the first applications of FTIR spectroscopy to polymers, that is, the study of defects introduced during polymerization at different temperatures [79]. In Fig. 3.24, the FTIR spectra at 70°C in the frequency range of 500–3200 cm^{-1} is shown for *trans*-1,4-polychloroprene polymerized at −20°C (spectrum a) and at −40°C (spectrum b). The b − a difference spectrum, which is also shown, reflects the increased presence of defects in the polychloroprene polymerized at −40°C relative to the sample polymerized at −20°C. The bands exhibited in the difference spectrum (but not visible in the normal spectra) correspond to the *cis*-1,4-polychloroprene structure and reflects the increased amount of these defects.

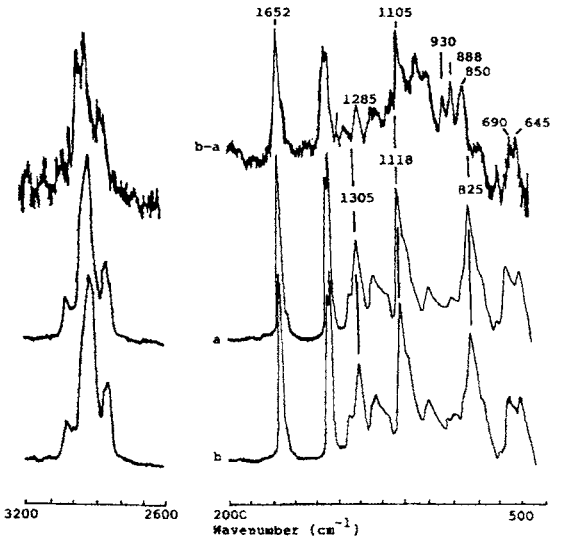

Fig. 3.24. FTIR spectra at 70°C in the range 500–3200 cm^{-1}. (a) *trans*-1,4-polychloroprene polymerized at −20°C, and (b) at −40°C; $_{b-a}$, difference spectrum. (Reproduced with permission from Ref. [81]. © 1975 Wiley and Sons, Inc.)

Absorbance subtraction can be considered a spectroscopic *separation* or *purification* technique for some problems inherent in polymers. An interesting application of FTIR difference spectroscopy is the spectral separation of a composite spectrum of a two-component system. However, complications can arise when there are intermolecular interactions that perturb the frequencies and intensities [80].

One example of the spectral separation approach using absorbance subtraction is a polymer containing two different geometric isomers, G_a and G_b. In general, the IR spectrum of each of these isomers will be different, but because there is a mixture of the two, the spectra of the individual species are difficult to observe. Proper use of subtraction allows the isolation of the spectra of the individual isomers.

The total absorbance, A_t, at a frequency, ν_i, of the polymer may be decomposed into the following contributions

$$A_t(\nu_i)_A = A_a(\nu_i)_A + A_b(\nu_i)_A \quad \text{(thickness compensated spectrum)} \tag{3.45}$$

where $A_a(\nu_i)$ and $A_b(\nu_i)$ are the contributions to the total absorbance at frequency ν_i resulting from the different geometric isomers, G_a and G_b, respectively, in sample A. For sample B, with a different relative amount of the two isomers, a similar equation can be written:

$$A_t(\nu_i)_B = A_a(\nu_i)_B + A_b(\nu_i)_B \quad \text{(thickness compensated spectrum)} \tag{3.46}$$

In order to proceed, isolated bands of both of the geometric isomers must be available for a second subtraction. For this second subtraction, the scale parameter, k_a, is chosen such that

$$A\,(\nu_{ia})_A - k_a A\,(\nu_{ia})_B = 0 \tag{3.47}$$

The resultant difference spectrum is the 'purified' spectrum of the geometric isomer G_b. A similar set of equations holds for the spectrum of the geometric isomer, G_a. This technique can be applied to other separations where a variation in the relative amount of the structural components occurs.

Consider two components, a and b, which are interconverted by some external treatment. In the spectrum of any specimen, the total absorbance of one specimen, A_1, can be expressed as

$$A_1 = A_a + A_b \tag{3.48}$$

With the appropriate treatment (annealing and extraction) of this sample, a certain fraction x of the structure a is converted to b. The total absorbance of this new sample is

$$A_2 = (x)\,A_a + (1 - x)\,A_b \tag{3.49}$$

To remove the characteristic absorptions of structure a subtraction is performed:

$$A_s = A_2 - kA_1 \tag{3.50}$$

When $k = 1 - x$ or $k = x$,

$$A_s = A_a \qquad \text{or} \qquad A_s = A_b \tag{3.51}$$

and the remaining spectrum represents either component a or component b.

This technique was first applied to the isolation of the vibrational bands of the crystalline isomer of *trans*-1,4-polychloroprene [81]. The spectrum of a cast film of predominately (>90%) *trans*-1,4-polychloroprene polymerized at −20°C was compared with the spectrum of the same sample heated to 80°C (above the melting point) for 15 min.

Elimination of the amorphous contribution of the composite semicrystalline spectrum was accomplished by subtracting spectrum b from spectrum a until the bands at 602 and 1227 cm^{-1} were reduced to the base line. The 'purified' crystalline isomer spectrum, spectrum c at the top of Fig. 3.25, exhibits the sharp band structure expected for a regular crystalline array. The interesting aspect of the crystalline isomer spectrum was that when the crystalline component spectra were obtained for samples polymerized at different temperatures through the same procedure, the crystalline isomer vibrational frequencies were different. This should not be the case if the crystalline isomer phase had the same isomeric structure. However, the spectra indicated that structural defects were incorporated into the crystalline domains, and the rate of defect formation increased as the polymerization temperature increased. As a result,

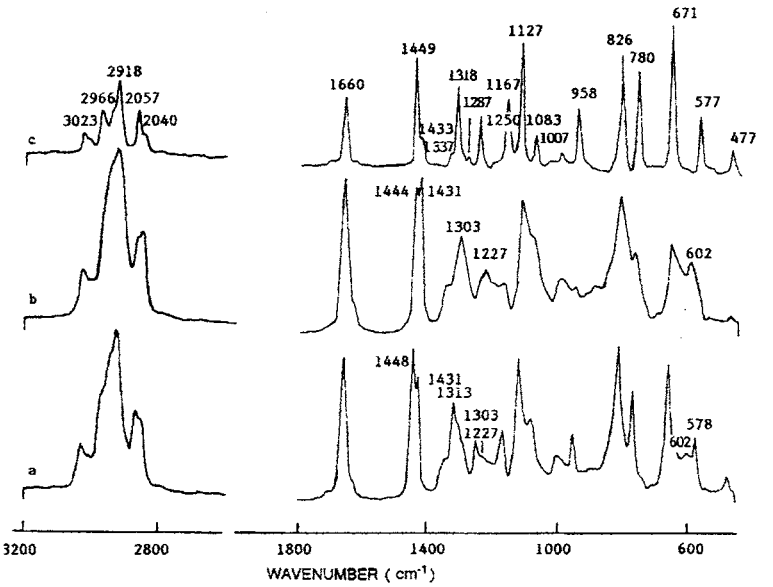

Fig. 3.25. The spectrum of a cast film of predominately (>90%) *trans*-1,4-polychloroprene polymerized at −20°C (spectrum a) is compared with the same sample heated to 80°C (above the melting point) for 15 min (spectrum b). The 'purified' crystalline isomer spectrum (spectrum c) exhibits the sharp band structure expected for a regular crystalline array. (Reproduced with permission from Ref. [81]. © 1975 Wiley and Sons, Inc.)

the defects in the crystalline phase decoupled some of the longer sequences, and the spectrum of the crystalline isomer phase was different.

The separation of the crystalline and amorphous isomeric phases into their respective spectra has been carried out for a number of polymers including poly(ethylene terephthalate) [82], polystyrene [83], poly(vinyl chloride) [84], polyethylene [85,86], polypropylene [87], and poly(vinylidene fluoride) (PVDF) [88].

Digital subtraction of absorbance spectra is often used to reveal or emphasize subtle differences between two samples. When a polymer is examined before and after a chemical or physical treatment, and the original spectrum is subtracted from the final spectrum, positive absorbances in the difference spectrum reflect the structures that were formed during the chemical or physical treatment, and negative absorbances reflect those structures that were lost.

An example of this type of application is shown in Fig. 3.26 in which the difference spectra for polyethylene films irradiated in nitrogen and air for 50 and 100 h are shown [87]. The positive peaks reflect the products of the reaction, including the carbonyl groups formed by oxidation, the methyl groups (1378 cm^{-1}) formed by chain scission, and the isomerization of the vinyl end groups (965 cm^{-1}). The negative peaks are the reactants, including the amorphous methylene groups (1368, 1353, and 1308 cm^{-1}) and the loss of unsaturation of the end groups (991 and 909 cm^{-1}).

Polymer blends can also be studied [89] using subtraction as shown in Fig. 3.27.

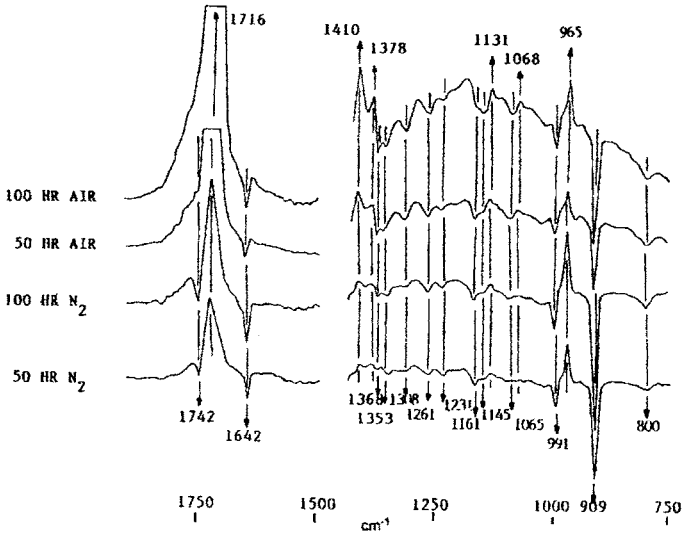

Fig. 3.26. The difference spectra of polyethylene films irradiated in nitrogen and in air for 50 and 100 h. (Reproduced with permission from Ref. [87]. © 1975 Wiley and Sons, Inc.)

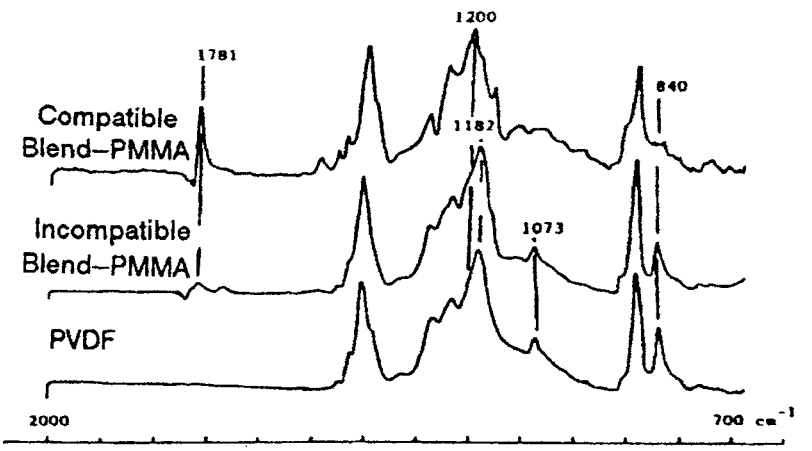

Fig. 3.27. The FTIR spectrum of pure PVDF and the difference spectra of a compatible and an incompatible blend of PMMA-PVDF in the range 700–2000 cm^{-1}. (Reproduced with permission from Ref. [89]. © 1984 Marcel Dekker, Inc.)

The FTIR spectra in the range 700–2000 cm^{-1} are shown for a compatible blend and an incompatible blend of PMMA-PVDF [57]. The top spectrum is the difference spectrum of the compatible blend of PVDF-PMMA (39 : 61) minus PMMA, and the middle spectrum is the incompatible blend of PVDF-PMMA (75 : 25) minus PMMA. The bottom of the figure shows the spectrum of pure PVDF. Comparison of the spectra shows that the spectrum of PVDF is substantially different from that of the

compatible blend but it is very similar to that of the incompatible blend, a result indicating phase separation in the incompatible blend.

Resolution enhancement using curve-fitting methods

One of the problems in polymer spectroscopy is the fact that the IR bands are inherently broad. This fact, coupled with the large number of bands occurring in the spectrum, usually leads to band overlap. Because the bandwidths are usually an order of magnitude greater than the resolution provided by the FTIR instrument, resolution enhancement techniques based on different mathematical procedures are often used [90]. Peak narrowing methods such as derivative spectroscopy [91] and Fourier self-deconvolution [92] are helpful in sharpening the peaks and minimizing the overlap. The computer fitting methods employed generally are all iterative least-squares optimization processes. If the initial choice of parameters is close to the optimum, only two or three cycles of iteration are required.

The first option in fitting IR bands is the selection of the band shape [93]. The common assumption is that vibrational peaks are Lorentzian in shape, although for polymers this is seldom the case. The approximate number of peaks is often determined by visual inspection of the spectral region under examination. Derivative spectra are helpful, as will be demonstrated later. It is recommended that a minimum number of peaks be used to fit the composite profile [94]. As the number of peaks increases, so does the uncertainty.

The remaining problem is bandwidth selection. There appears to be no useful rule for solving this aspect of the curve-fitting problem because the individual bands in a spectrum can have a broad range of bandwidths. Therefore, the bandwidth is often used as one of the variables in the optimization process.

Derivative spectroscopy.

With digitized spectral data and the appropriate computer software, obtaining a derivative spectrum is a simple matter. The even derivatives have sharper peaks at the same frequency values as in the original spectrum. In the case of a Lorentzian profile with unit half-width, the second derivative (for which the peak is negative) has a value that is equal to 0.326 of the original bandwidth [95], and for the fourth derivative, which has a positive peak, the value is equal to 0.208 of that of the original bandwidth. Band sharpening is therefore achieved with the derivative spectra. The resolution enhancement is 2.7 for the second derivative and 3.8 for the fourth derivative.

However, derivative spectroscopy does have some drawbacks. The amplitudes of the peaks in derivative spectra are a function of the widths of the original peaks, and this condition leads to a heavy bias toward the sharper peaks present in the original spectra. The noise peaks are sharper in the derivative spectra than in the spectra upon

which they are superimposed. In addition, peaks located at the same frequency position as one of the lobes in the derivative spectrum can be lost. Also, the signal-to-noise ratio deteriorates as the order, n, of the derivative increases. The rate of deterioration is approximately 2^n and is ultimately the limit to the number of derivatives that can be taken and to the maximum resolution enhancement achievable [96].

An example is the spectrum of the carbon-chlorine region of the highly syndiotactic poly(vinyl chloride) made by the urea-clathrate route [95]. It has two peaks and a high-frequency shoulder. The second derivative spectrum shows two negative peaks at the positions of the two peaks in the original spectrum. There also appears to be a peak at 638 cm^{-1} in the second derivative spectrum; this peak is assigned to long planar syndiotactic sequences. The second derivative spectrum of a commercial poly(vinyl chloride) reveals six peaks.

Fourier self-deconvolution.

> *Deconvolution can be used to extract information about component elements of a data system that are partially or completely overlaid by stronger components so as to be undetectable to the eye in the original curve or other form of visual data plot.* — R. Norman Jones

Another approach to resolution enhancement is the use of Fourier self-deconvolution, which is useful when the spectral features are broader than the instrument resolution [97]. This technique is based on the fact that the breadths of the peaks are the result of the convolution of the intrinsic line shape with a broadening function. Deconvolution allows the removal of the broadening. The broadening function is Lorentzian, and deconvolution with a Lorentzian function will lead to a substantial, physically significant narrowing [98].

The data set is multiplied by the inverse transform of the Lorentzian function, which is the exponential function. The data set is then transformed into the frequency domain to give a conventional, sharpened spectrum. By using spectra from FTIR instruments, resolution enhancement factors of 3 can be obtained [99]. However, no line can be narrower than the original instrument function.

The use of Fourier deconvolution requires knowledge of the half-widths of the peaks to be examined, but in practice the half-widths of the component peaks of overlapping band systems are not known. Underestimation of the bandwidth results in a deconvoluted band that has a shape close to Lorentzian, but that has a lower resolution enhancement than would be achieved with the correct bandwidth. When overestimation occurs, negative lobes flank the deconvoluted band, and the degree of sharpening achieved is greater than expected. Overconvolution also results in serious distortions of the intensities.

Fourier deconvolution is a valuable means for finding peaks in spectra of polymers with extensive overlapping of bands. The Fourier self-deconvoluted IR spectrum of

the urea clathrate type of poly(vinyl chloride) was obtained with a deconvolution function half-width of 11 cm^{-1}. The resolution was increased by a factor of 2.5. The spectrum is similar in quality to the second derivative spectrum. There is, however, no clear indication of a peak in the 650 cm^{-1} region [100].

Fourier self-deconvolution degrades the signal-to-noise ratio of the spectrum. Another problem is that the same deconvolution width is used for the entire spectrum, but individual IR bands have different widths and therefore may not be optimized. In other words, individual bands may be overconvoluted, and overconvolution may lead to the appearance of negative peaks in the final spectrum in much the same manner as with derivative spectroscopy.

Maximum entropy method.

The maximum entropy method approach to resolution enhancement treats the signal and the noise as separate entities [101]. This method sets out to minimize random errors and noise on the basis of two criteria. First, an assumption is made about the shapes of the peaks present. Secondly, the best fit with respect to noise is obtained by maximizing the configurational entropy (negative information content), S, by using the equation

$$S = -\sum p_j \log p_j \tag{3.52}$$

where p_j is the normalized intensity at the spectral frequency j. The maximum entropy method selects the solution that contains the smallest amount of false information from the large number of possible solutions [102]. This method is not used often in IR spectroscopy, but it is used extensively in NMR spectroscopy and NMR imaging.

Quantitative IR spectroscopy of polymers

IR spectroscopy is routinely used to estimate the identity and concentration of absorbing species in multicomponent systems. The standard approach is to measure the spectra of a series of mixtures and use simultaneous equations to extract the desired concentration data.

In the analysis of multicomponent systems, there are four different classes of spectral problems [103]. In the first situation, all of the components and their spectra are known, and calibration data are available. In this case, the method of classical least-squares (see below) is appropriate for finding the quantity of each component. When proper calibration is carried out, this approach yields quantitative data for mixtures. In the second situation, the spectra of the components are not known, but the concentrations of the components of interest are known. This situation requires the use of a cross-correlation procedure. In the third situation, none of the components are

known, and factor analysis is applied. The factor analysis method provides a lower limit to the number of linear-independent components present in the mixture and estimates the spectra when low numbers of components (fewer than three) are present. In the final and most difficult situation, attempting to quantify a number of known components in the presence of a variable background of unknowns, the method of rank annihilation has been developed. When there is only one known component, the amount of that component can be found by iteratively subtracting it from the observed data until the rank of the remaining matrix is reduced by one.

The quantitative relationship between the concentration, c, of a component in a sample and its absorbance, A, is given by the Bouguer–Beer law:

$$A = abc = \log \frac{I_0}{I} \tag{3.53}$$

where the term I_0/I is termed the transmittance. The constant a is the absorptivity, and b is the unit of thickness. Logarithms to the base 10 are ordinarily used, and a factor of 2.3 is incorporated into the constant a. This law assumes photometric linearity and accuracy of the spectrometer. Traditionally, constructing a calibration curve of absorbance of the analytical frequency vs. concentration, and then measuring the concentration of an unknown sample by using either the absorbance peak or the absorbance area carry out quantitative analysis. When two components are involved, absorbance measurements at two frequencies are necessary to estimate the individual concentrations. This method can be extended to more components as required.

When multicomponent systems like polymers are under investigation is assumed that the total signal, $y_T(\nu)$ for each is a linear combination of the individual responses:

$$y_T(\nu) = y_1(\nu) + y_2(\nu) + y_3(\nu) + \ldots + y_m(\nu) \tag{3.54}$$

of the m components. This equation represents the additivity assumption. It is also assumed that the individual response with respect to concentration, c_i, where $i = 1, \ldots, m$ is linear, so

$$A(\nu) = a_1(\nu)c_1 + a_2(\nu)c_2 + a_3(\nu)c_3 + \ldots + a_m(\lambda)c_m \tag{3.55}$$

and a_i are the sensitivity coefficients for the ith component at the νth frequency. This equation reflects the linearity assumption.

For an analysis of multicomponent systems, it is necessary using the analytical method to investigate whether the prerequisites of the additivity of the signal responses and the linearity of the absorbances are fulfilled. This can be accomplished by measuring the signal responses of each pure component and that of synthetic mixtures. The numerical sum expected can be compared with the experimental absorbances to test the additivity assumption. The linearity of the signal intensity can be examined by determining the absorbance response of each pure component at the component-specific wavelengths for several different concentrations involving the

other components. If specific interactions occur between the components, nonlinearity in the signal intensities will occur.

Multivariate linear regression

Multivariate linear regression (MLR) uses absorbances at a number of different frequencies to enhance the precision of the analysis. With digital recording and instrument-based computers, it is possible to process entire spectral regions efficiently making it beneficial to use many frequencies in the calibration and analysis. There are several techniques for multivariate calibration with the most frequently used being classical least squares (CLS), principal component regression (PCR) and partial least squares regression (PLS). Multiple measurements at different frequencies allow:

- higher precision which increases as $(n)^{1/2}$ where n is the number of frequencies used,
- the determination of multiple components in a system,
- the detection of the presence of interferences,
- can treat nonlinearities and background.

Classical least-squares is used for analysis of spectroscopic measurements when the number of components are known and the spectra of the components are available [104–106]. Classical least squares is a full-spectrum method and can yield significant improvements over the use of a single frequency. It also can be used to simultaneously fit spectral base lines [107]. The first condition for using classical least squares for calibration is that the concentrations of all species giving a nonzero response must be included in the calibration step. In classical least squares, the pure component spectra (at unit concentration) are used as standards. Using the full spectral information, the precisions of the measurements are improved considerably. The least-squares method also makes available estimated pure-component spectra and full-spectrum residuals [108]. A major disadvantage of classical least squares is that all interfering chemical components in the spectral region of interest need to be known and included in the calibration. The presence of such interferents leads to bias in the estimation of concentration.

The K-matrix approach

For multivariate linear regression analysis, multiple components are measured for n different frequencies. Assuming a linear model Beer's law between the signal A and the concentration c, one can write

$$A_i = \sum_{j=1} k_{ij} C_j + e_i \tag{3.56}$$

where the terms k_{ij} are the sensitivity coefficients and represent the product of the path length and the absorptivity for component j at frequency i and e_i is the

measurement error in the spectrum. If a well characterized set of j mixtures spectra are obtainable, the sensitivity coefficients can be obtained by ordinary or weighted least squares multiple regression. The normal representation of this problem is

$$\mathbf{A} = \mathbf{KC} + \mathbf{E} \tag{3.57}$$

This method, known as the *K-matrix method* by spectroscopists, minimizes spectral errors [109,110].

In the calibration step with a set of known mixtures, the matrix of absorbances, **A**, is found by experiment, the concentrations are known and **K** can be calculated. Because **C** is not usually square, each side of the equation is multiplied by the transpose of **C**′

$$\mathbf{AC}' = \mathbf{KCC}' \tag{3.58}$$

CC′ is square and invertable, so both sides can be multiplied by $(\mathbf{CC}')^{-1}$. **K** is the least squares fit between the observed and calculated absorbances and is the calibration matrix.

In the analysis step, the absorbances, **A**, of the unknown sample at these same frequencies are measured, and the concentrations of the components are then calculated

$$\mathbf{C} = (\mathbf{K}^{t}\mathbf{K})^{-1}\mathbf{K}^{t}\mathbf{A} \tag{3.59}$$

and **C** is the desired concentration data for the various components in the unknown sample.

There are some limitations to the K-matrix approach. To obtain the matrix of concentration information, **C** must be inverted during the operations. This inversion demands that **C** be nonsingular requiring that there are no linear relationships between its component rows and columns. However, if rows or columns of the matrix have a linear relationship to each other, the determinant will be zero, the matrix singular, and noninvertable. This problem can be avoided by paying careful attention to the makeup of the calibrating standards.

Another problem with the K-matrix approach occurs when the real samples contain impurities that are not in the standards. If an extra component appears in the region of analysis, it is possible to obtain a 'negative' concentration in the unknown sample.

Classical least-squares analysis using spectra of pure components

The classical least squares method is applicable when the number of components and their pure spectra are known, and measurement of the relative concentrations of the components is desired. Beer's law can be applied in matrix form to allow the simultaneous determination of multiple components even when there is no unique set of spectral features for each of the components (i.e., when there is no single band of

one of the components in the system that is not overlapped by one or more of the bands of the other components in the system).

The classical least-squares approach to quantitative analysis considers the complete spectrum with a large number of frequencies simultaneously and uses a least-squares fitting of the pure component spectra and the mixture spectrum to determine the concentrations of the components. This approach has the principle advantage of high precision because an increase in the number of data points improves the precision of the measurement. Other advantages of the method are using all frequencies in each of the spectral peaks (rather than only the peak maximum) performing a weighted least-squares analysis to give greater emphasis to data with higher signal-to-noise ratios fitting a linear or nonlinear base line under each spectral peak [111].

Inverse least-squares method.

The inverse least-squares method for quantitative analysis assumes that concentration is a function of absorbance:

$$\mathbf{C} = \mathbf{AP} + \mathbf{E}_c \tag{3.60}$$

where $\mathbf{C}$ and $\mathbf{A}$ were defined previously, $\mathbf{P}$ is the $n \times l$ matrix of the unknown calibration coefficients relating the l component concentrations to the spectral intensities, and $\mathbf{E}_c$ is the $m \times l$ matrix of the random concentration errors. This representation has the advantage that the analysis is invariant with respect to the number of chemical components, l, included in the analysis [112]. During the calibration,

$$\mathbf{P} = \left(\mathbf{A}'\mathbf{A}\right)^{-1}\mathbf{A}'c \tag{3.61}$$

and the analysis of the unknown is simply

$$\mathbf{C} = \mathbf{AP} \tag{3.62}$$

This means a quantitative analysis can be performed even if the concentration of only one component in the calibration mixtures is known. The disadvantage of the inverse least-squares method is that the analysis is restricted to a small number of frequencies because the matrix that must be inverted has dimensions equal to the number of frequencies, and this number cannot exceed the number of calibration mixtures used in the analysis.

Principal component analysis

Principal component analysis (PCA) is a method of data description which allows one to describe the spectral variance data by means of a small number of uncorrelated variables. PCA transforms the original measurement variables into new, uncorrelated variables called *principal components*. The magnitudes of the individual PCs are

generally referred to as *scores*. Mathematically, PCA examines the data-covariance structure and identifies and quantifies the patterns in the data, which explain its largest variances. The principal components are orthogonal basis vectors, which seek to model the variation in a data set as fully as possible. Each principal component is a linear combination of the original measurement variables. Each of the n spectra may be represented by a point in a ν-dimensional space, where ν is the number of wavelengths. PCA involves rotating and transforming the original ν axes into a new set of axis, α, called the principal components. Using this procedure is analogous to finding a set of orthogonal axes that represent the directions of greatest variance in the data. Often, the two or three largest principal components of the data will capture the bulk of the variance or information: hence, we can use them to generate a plot that represents the structure of the PCA-dimensional measurement space.

Principal component scores are calculated from linear combinations of the spectral data

$$S_1 = G_{11}X_1 + G_{12}X_2 + G_{13}X_3 + \ldots$$

$$S_2 = G_{21}X_1 + G_{22}X_2 + G_{23}X_3 + \ldots$$

where S_i represents the ith principal component score, X_j represents the spectral data at the jth wavelength, and G_{ij} represents the principal component score of the ith component for the data at the jth wavelength.

The principal component regression relates the scores to the dependent variable thusly

$$\overline{Y} = b_0 + b_1S_1 + b_2S_2 + b_3S_3 + \ldots$$

where $\overline{Y}$ is the predicted value of the dependent variable, and the b_i terms are the regression coefficients for the various scores.

We can replace the S_i terms and collect the coefficients for the various S_i

$$\overline{Y} = b_0 + (b_1G_{11} + b_2G_{21} + b_3G_{31} + \ldots)X_1 + (b_1G_{12} + b_2G_{22} + b_3G_{33} + \ldots)X_2 + \ldots$$

Now since all the expressions in the parentheses are constants, this can be written as

$$\overline{Y} = b_0 + k_1X_1 + k_2X_2 + k_3X_3 + \ldots$$

Thus, the results of a principal component regression can be converted into an equivalent set of coefficients of the original data.

If absorbance is measured at k wavelengths for m mixtures containing n analytes ($m > n$), then one has an equation system that can be expressed in matrix form [113] as

$$\mathbf{A} = \mathbf{CK} + \mathbf{E}$$

where $\mathbf{A}(m, k)$ is the absorbance matrix, $\mathbf{K}(n, k)$ the absorptivity coefficient matrix, $\mathbf{C}(m, n)$ the concentration matrix, and $\mathbf{E}(m, k)$ the residuals matrix.

In PCA calibration, the absorbance matrix is broken down into the product of the scores matrix, $\mathbf{T}(m, a)$, and the loadings matrix, $\mathbf{P}(a, k)$:

$$\mathbf{A} = \mathbf{TP} + \mathbf{F}$$

where $\mathbf{F}(m, k)$ is the residuals matrix and a is the number of principal components. Each factor in the model can be thought of as an abstract phenomenon that is a source of variation in the spectra of the calibration samples. The scores for a single factor can be thought of as the 'intensities' of the corresponding abstract phenomenon for each sample, and the loadings for a single factor can be thought of as the 'spectral signature' of the corresponding abstract phenomenon [114].

PCA is based on the singular value decomposition of the spectral data matrix:

$$\mathbf{A} = \mathbf{P\Sigma T}^{\mathrm{t}}$$

The scores matrix $\mathbf{T}$ must satisfy the following:

$$\mathbf{T}^{\mathrm{t}}\mathbf{T} = \mathbf{1}$$

$$\mathbf{T}^{\mathrm{t}}(\mathbf{A}^{\mathrm{t}}\mathbf{A})\mathbf{T} = \mathbf{\Lambda}$$

where $\mathbf{1}$ is an $n \times n$ identity matrix, and $\mathbf{\Lambda}$ is the matrix of the eigenvalues $\mathbf{A}^{\mathrm{t}}\mathbf{A}$. The $n \times n$ matrix $\mathbf{\Sigma}$ is the matrix of the singular values that are the square roots of the eigenvalues:

$$\mathbf{\Sigma}^2 = \boldsymbol{\lambda}$$

The row vectors of $\mathbf{T}$ are orthonormal to each other.

As a result of this transformation, the variances in the spectra are contained in the first k loading orthonormal vectors that correspond to the largest eigenvalues. Therefore, it is possible to separate the signal from the noise, and use a smaller number of components (less than the number of measurements) for the analysis step in PCA.

The individual eigenvalues represent the contribution of each factor to the variance. That is, the factor with the largest eigenvalue represents the spectrum which varies the most from zero. In most circumstances, the mean of the spectra will be the major variations from zero. The factor associated with the largest eigenvalue is almost always a constant multiple of the mean spectrum. The second factor represents the major orthogonal variations of the spectra from the first factor. The smaller eigenvalues represent noise along spectral differences in minor components that are indistinguishable from the noise. By eliminating from the expansion those factors in which the noise contribution outweighs the information about the components in the mixture, the original data can be represented more concisely, without loss of information. This is the implicit noise reduction in the PCA method.

A crucial requirement for the application of PCA is that the acquired experimental data are a linear combination of pure component signals. It is necessary that the ratios of all pure compounds vary between the acquisition of different spectra. In other words, a pair of compounds that appears as a constant ratio in all analyzed spectra, would be detected as one 'pure' component.

Base lines complicate the process as a nonzero base line integrates as a linear increasing offset. This can be minimized by calculating the mean value of each spectra and subtract it from the original spectra. The absorbance vectors should also be normalized.

Partial least-squares method

Partial least-squares regression (PLS) is a multivariate method in which the axes of maximum variance are computed by taking into account both the spectroscopic and the chemical values.

In contrast to PCR, this approach leads to nonorthogonal axes, but uses more information at the calibration step because it takes the chemical data into account. PLS depends on the iterative estimation of a linear combination of spectral features in such a way that the concentrations are optimally predicted [115,116]. PLS is a method in which the calibration and prediction analyses are performed one component at a time. The concentration of only the chemical component of interest is used in the calibration. The calibration spectra can be represented as [117]

$$\mathbf{A} = \mathbf{TB} + \mathbf{E}_a \tag{3.63}$$

where $\mathbf{B}$ is an $h \times n$ matrix, and the rows of $\mathbf{B}$ are the new partial least-squares basis set of h full-spectrum vectors, which are called the loading spectra. The term $\mathbf{T}$ is an $m \times h$ matrix of intensities in the new coordinate system of the h partial least-squares loading vectors for the m sample spectra. In PLS, the rows of $\mathbf{B}$ are eigenvectors of $\mathbf{A'A}$, and the columns of $\mathbf{T}$ are proportional to the eigenvectors of $\mathbf{AA'}$ [118].

By using PLS, it is possible to model complex base lines and some types of nonlinearity in Beer's law. In addition, this method can be used when molecular interactions or reactions are present.

The ratio method for determination of component spectra

Quantitative IR spectroscopy requires determination of the absorptivity by calibration or some other method [119]. For polymers, this aspect of the problem is particularly difficult because usually there is no independent method of calibration. Low-molecular-weight analogs of the structure are often useful for calibration when the structures are similar and the spectral complications of vibrational coupling are not present. Often, however, there are no suitable model systems available (e.g., polymers that exhibit stereoregularity).

The ratio method is one of the techniques available for the extraction of pure-component spectra from mixture spectra [120,121]. The IR spectrum of a two-component mixture can be written as a linear combination of its constituent spectra:

$$[M_1] = [P_1] + [P_2] \tag{3.64}$$

where $[M_1]$ is the spectrum of mixture 1, and $[P_1]$ and $[P_2]$ are the spectra of the pure components. Similarly, the spectrum of a second mixture made up of the same two components but with different relative concentrations can be written as

$$[M_2] = s_1 [P_1] + s_2 [P_2] \tag{3.65}$$

where s_1 and s_2 are the scaling coefficients reflecting the different concentrations of $[P_1]$ and $[P_2]$ in $[M_2]$.

These two equations can be solved for $[P_1]$ and $[P_2]$ in terms of the spectra of the mixtures:

$$[P_1] = \left(\frac{1}{s_1 - s_2}\right)[M_2] - \left(\frac{s_2}{s_1 - s_2}\right)[M_1] \tag{3.66}$$

$$[P_2] = \left(\frac{1}{s_1 - s_2}\right)[M_2] + \left(\frac{s_1}{s_1 - s_2}\right)[M_1] \tag{3.67}$$

The scaling coefficients s_1 and s_2 are derived by calculating the 'ratio spectrum' from the two mixtures:

$$[R] = \frac{[M_2]}{[M_1]} = \frac{s_1 [P_1] + s_2 [P_2]}{[P_1] + [P_2]} \tag{3.68}$$

In a spectral region where $[P_1] \gg [P_2]$, $[R]$ is approximately equal to s_1. Conversely, if $[P_2] \gg [P_1]$, then $[R]$ is approximately equal to s_2. An implicit assumption is that each pure-component spectrum contains a characteristic peak that is not overlapped by peaks appearing in the spectra of other pure components [122]. With the introduction of relative concentrations in the preceding equations, this ratio approach allows quantitative analyses without external calibration [123].

The ratio method has been used to determine the pure spectra of the trans and gauche geometric isomers of PET [124]. The IR spectra of PET films that have been annealed for different times at 230°C are shown in Fig. 3.28.

The ratio spectrum of two of the films is shown in Fig. 3.29, and the computed pure spectra of the trans and gauche isomers are shown in Fig. 3.30.

By using the ratio method in this straightforward fashion, the pure spectra can be obtained.

Factor analysis

Factor analysis is based on the expression of a property as a linear sum of terms, called factors. This method has wide applicability to a variety of multidimensional

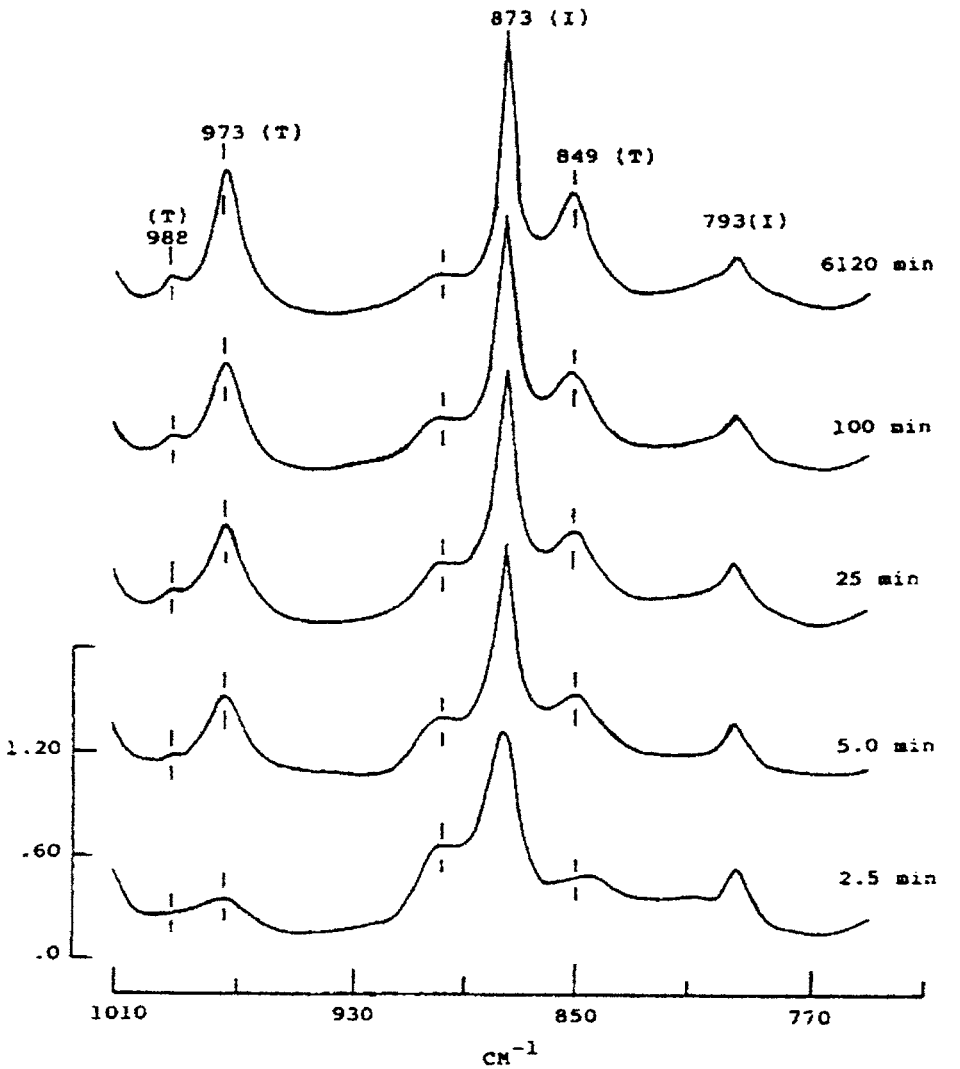

Fig. 3.28. The IR spectra of PET films that have been annealed for different times at 230°C. The letters T, G, and I correspond to trans, gauche, and internal thickness band, respectively. (Reproduced with permission from Ref. [124]. © 1982 Wiley and Sons, Inc.)

problems [125]. The Beer–Lambert law can be written for a number of components over a frequency range as

$$A_i = \sum k_j c_{ij} \tag{3.69}$$

where A_i is the absorbance spectrum of mixture i, k_j is the absorptivity path length product for the jth component, and c_{ij} is the concentration of component j in mixture i. Factor analysis is concerned with a matrix of data points. In matrix notation the

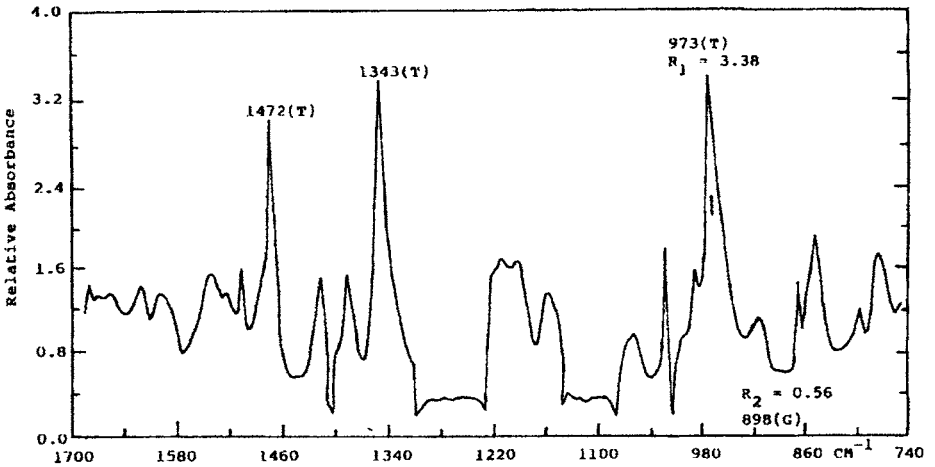

Fig. 3.29. The absorbance ratio spectra of PET for the 1700–750-cm^{-1} region. The spectrum from the sample annealed at 200°C for 102 h was divided by the spectrum from the sample annealed at 75°C for 10 h. The letters T and G correspond to trans and gauche, respectively; R_1 is the maximum absorbance ratio; and R_2 is the minimum absorbance ratio. (Reproduced with permission from Ref. [124]. © 1982 Wiley and Sons, Inc.)

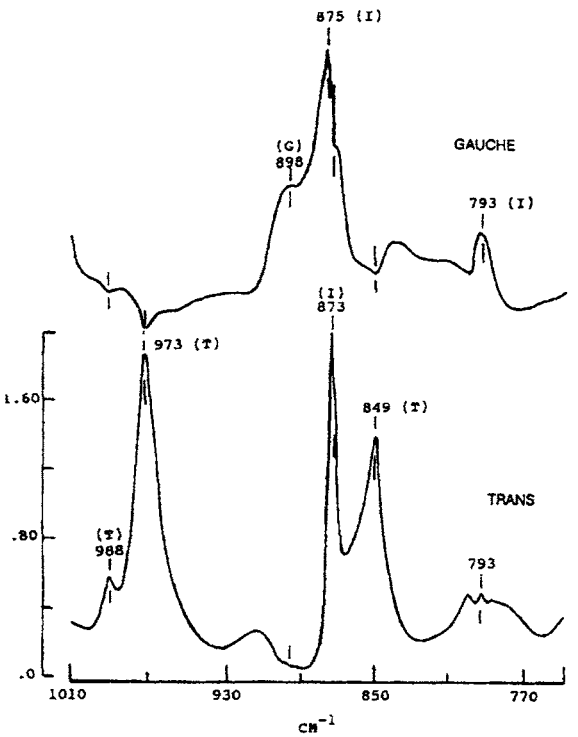

Fig. 3.30. The computed pure spectra of the trans (T) and gauche (G) isomers of PET obtained by the ratio method. The letter I corresponds to an internal thickness band. (Reproduced with permission from Ref. [124]. © 1982 Wiley and Sons, Inc.)

absorbance spectra of a number of solutions can be written as

$$\mathbf{A} = \mathbf{KC} \tag{3.70}$$

where **A** is a normalized absorbance matrix that is rectangular in form. The columns in this matrix contain the absorbance at each wavenumber, and the rows correspond to the different mixtures being studied. The **A** matrix could thus be 400 by 10 corresponding to a measurement range of 400 wavenumbers at one wavenumber resolution for 10 different mixtures or solutions. The term **K** is the molar absorption coefficient matrix, and it conforms with the **A** matrix for the wavelength region but has only the number of rows corresponding to the number of absorbing components. The concentration matrix, **C**, has dimensions corresponding to the number of components and the number of mixtures or solutions being studied. Of course, **K** and **C** are unknown. In principle, factor analysis can be used to generate **K** and **C**, which will allow a complete analysis of a series of mixtures containing the same components in differing amounts.

There are two basic assumptions in factor analysis. First, the individual spectra of the components are not linear combinations of the other components, and second, the concentration of one or more species cannot be expressed as a constant ratio of another species. The different relative concentrations of the components in the mixtures provide the additional information necessary to deconvolute the spectra.

Determination of the number of components in a mixture

Factor analysis initially allows a determination of the number of components required to reproduce the absorbance or data matrix, **A**. The rank of the matrix **A** can be found by using factor analysis, and this rank of **A** is considered equal to the number of absorbing components. To find the rank of **A**, the matrix $\mathbf{M} = \mathbf{A}'\mathbf{A}$ is formed where $\mathbf{A}'$ is the transpose of **A**. This matrix, termed the *covariance matrix*, has the same rank as **A** but has the advantage of being a square matrix with dimensions corresponding to the number of mixtures being examined. In the absence of noise, the rank of **A** is given by the number of nonzero eigenvalues of **M**. In the presence of noise, however, the problem of identifying the number of components is more difficult.

A common method for estimating k (the rank of **M**) is to plot the values of the eigenvalues versus the number of the eigenvalue and to inspect the singular values. If the noise is low compared to the signal, there should be a large drop between the k and $(k + 1)$ values and then much smaller drops between the $k + 1$ value and subsequent values. When the noise level is high, this method is likely to fail, especially when the mixture contains more than two or three individual components. Statistical tests are used to determine how many of the c eigenvalues represent signal $(1, \ldots, n)$ and how many represent noise $(n + 1, \ldots, c)$ [126,127].

With the availability of proper software, the application of factor analysis is straightforward. The normalized spectra of the mixtures to be analyzed are entered into a computer, and the computer calculates the eigenvalues. A plot of the log of the eigenvalues versus the number of components is made. Often, a visual inspection will

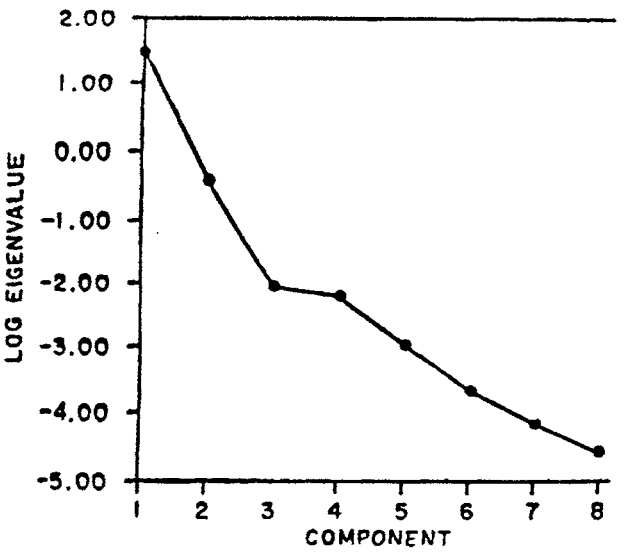

Fig. 3.31. A plot of the magnitude of the eigenvalue versus the number of components for a series of eight PET films that have been annealed for various times. (Source: S.B. Lin and J.L. Koenig, unpublished results.)

reveal the difference between the 'real' eigenvalues and the 'noise or error' eigenvalues. A plot of this type for a series of eight poly(ethylene terephthalate) films that have been annealed for various times is shown in Fig. 3.31.

The plot shows the results using the spectra in the 3120- to 2850-cm^{-1} region. Because of the large drop in the eigenvalues, it is clear that there are only two real eigenvalues, and the remaining eigenvalues correspond to noise [128]. When the eigenvalue differences are not sufficiently large for a visual evaluation, it is sometimes helpful to calculate an *indicator function* [129]. This function reaches a minimum at the point where the principle contribution comes from the real eigenvalues and then increases as the error contribution takes over. An example of the use of the indicator function is shown in Fig. 3.32 for compatible blends of polyoxyphenylene–polystyrene (PPO-PS) and the incompatible blend of polyoxyphenylene–poly(parachlorostyrene) (PPO-P4ClS) [130].

One more component would be expected (the interaction spectrum arising from mixing at the molecular level) for a compatible blend than for an incompatible blend. This is because the incompatible blend would be phase separated and its spectrum should be the simple sum of the spectra of the component homopolymers. The results in Fig. 3.32 suggest such a difference exists for blends made up with different weight fractions.

Determination of the pure spectra of components

If the number of components, n, in a mixture is determined by factor analysis, then the dimension of the vector space in which all spectra of the mixtures can be

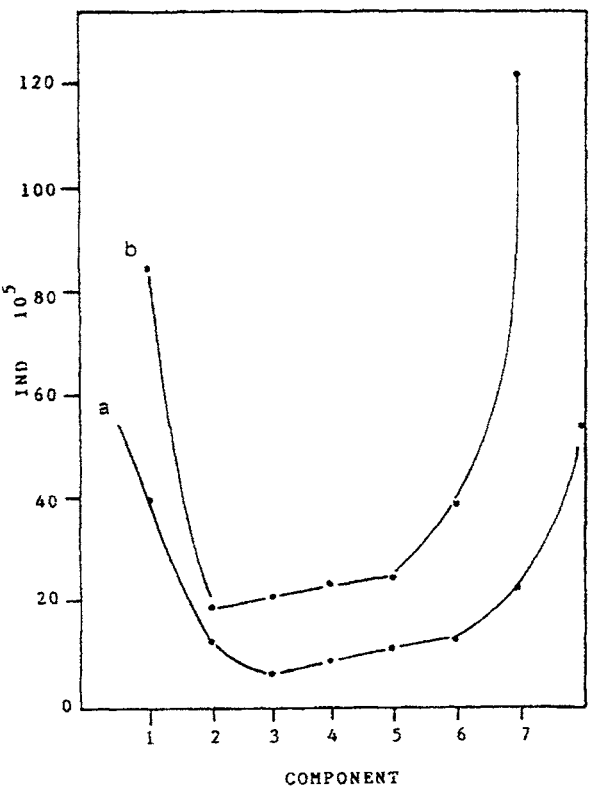

Fig. 3.32. Plots of the indicator function versus the number of components for (a) compatible blends of PPO-PS, and (b) for the incompatible blend of PPO-P_4ClS. (Reproduced with permission from Ref. [130]. © 1981 Society for Applied Spectroscopy.)

represented is known, and a set of mutually orthogonal abstract eigenspectra are obtained. These eigenspectra define an n-dimensional coordinate system within which each data spectrum and each pure component spectrum are represented by points. The coordinate values of the points constitute a transformation vector by which the abstract eigenspectra can be rotated to physically real spectra. The magnitudes of the eigenvalues are a measure of the relative importance of corresponding eigenvectors in data reconstruction. The first eigenspectrum corresponds to the dominant eigenvalue, and hence it contains the maximum information. It represents the spectrum of the system if all the components were to coexist [131]. The first eigenvector is the same line as that obtained from a linear least-squares fit of the data [132]. The first and second eigenvectors are orthogonal by definition, so eigenvector 2 must be orthogonal in information relative to eigenvector 1. Factor analysis constructs eigenvector 2 in order to account for absorbance variations that are not accounted for by the first eigenvector [133]. The information content of the corresponding eigenspectrum can have both positive and negative absorbances. As a result, eigenspectrum 2 resembles a difference spectrum [134].

Special considerations must be made, however, when determining the appropriate linear combinations of these orthogonal spectra to obtain the spectra of the pure components. In two-component systems, it is fairly easy to establish the range of a two-dimensional vector space in which the spectrum of each of the two pure components must fall. For a single spectrum in a two-component mixture, the following equation results:

$$\mathrm{PS} = aV_1 + bV_2 + e \tag{3.71}$$

where PS is the pure component spectrum; a and b are the coordinate values of the solution point; V_1 and V_2 are the first and second eigenvectors, respectively; and e is the error associated with the analysis. The coordinate values a and b, which transform the eigenspectra into the actual spectra, are unknown quantities that must be estimated. Criteria for obtaining an estimate for the location of the vector within the range of possible solutions must be developed. The two basic restrictions are (1) spectra must have positive intensities, and (2) the concentration of the components must be positive. Normalization of the mixture spectra to unit area results in their projections lying on a straight-line segment with the spectra of the purest mixtures located at each end of the line. The projections of the pure spectra also lie on the line and at the intersection of the limits determined by the requirement of positive absorbance.

The classical way of rotating the eigenspectra into physically meaningful spectra requires the restriction that each pure component contains a peak in a region where the other pure components do not absorb. Two- and three-component systems [135, 136] have been analyzed on this basis.

Determining the allowed ranges in higher dimensional vector spaces becomes increasingly difficult with increasing dimensions. For a three-component system, the projections lie on a plane, within a triangular boundary, on a three-axis coordinate system. The vertices of the triangular boundary are the projections of the pure underlying component spectra. Under certain circumstances, the operation that is carried out to obtain the rotation matrix needed to convert the orthogonal eigenspectra to real spectra can use the criterion that each pure component has a unique frequency, called a *pure point*. At the pure point only one component has a definite intensity, and the other components have zero intensity [137]. By using pure points, it is possible to extract spectra and concentrations from a mixture data set of three or four components. One approach is to simplify the spectra by removing contributions from the system one at a time by using *minimum path* or *minimum entropy techniques* [138].

The factor analysis approach to computation of the pure spectra can be illustrated by using computer simulation. Simulated spectra containing two components of Lorentzian line shapes for four different mixtures are shown in Fig. 3.33.

Factor analysis of the covariance matrix indicates two pure components, as anticipated. The two primary eigenvectors for the two real eigenvalues were used to construct the abstract 'eigenspectra' in Fig. 3.34.

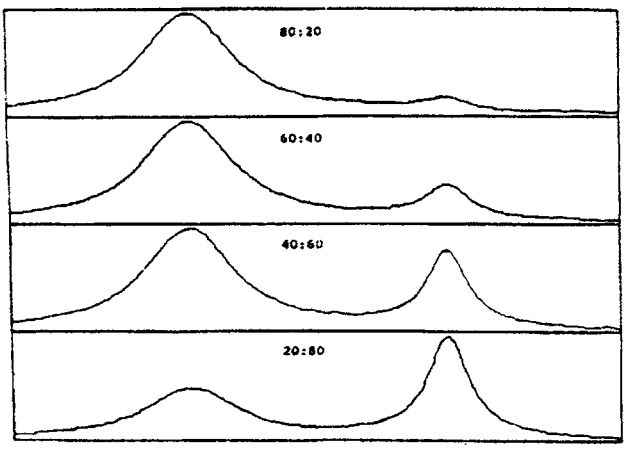

Fig. 3.33. Computer simulated spectra with noise containing two components with Lorentzian peaks for four different mixtures. (Reproduced by permission from Ref. [139]. © 1983 American Chemical Society.)

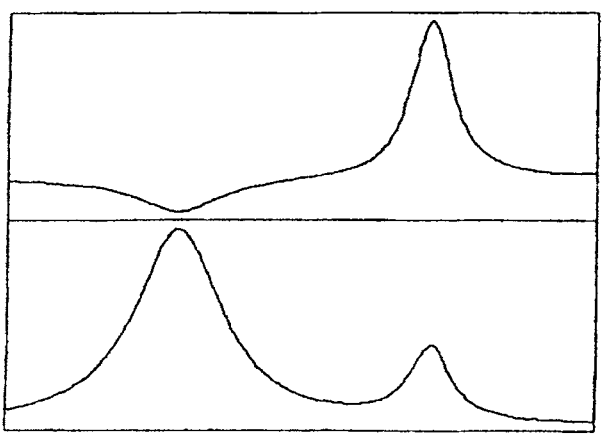

Fig. 3.34. The abstract eigenspectra for the two real eigenvalues. (Reproduced by permission from Ref. [139]. © 1983 American Chemical Society.)

In Fig. 3.35, a plot of the four ordered pairs of the two primary eigenvector mixtures is shown on the eigenvector axis, clearly indicating a linear relationship between the eigenvectors.

The points of intersection of this linear line with the boundary region yield the coefficients by which the abstract eigenspectra are multiplied to obtain the pure component spectra, which are shown in Fig. 3.36 [139].

Rank annihilation

In many quantitative situations, the available sample contains a few known species of interest mixed with other unknowns. In such cases, it would be convenient to be

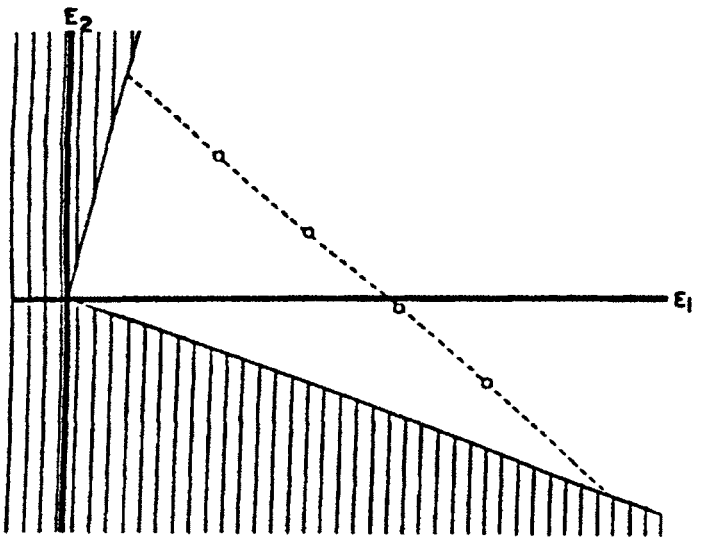

Fig. 3.35. The plot of the four ordered pairs of the two primary eigenvector mixtures is shown on the eigenvector axis. (Reproduced by permission from Ref. [139]. © 1983 American Chemical Society.)

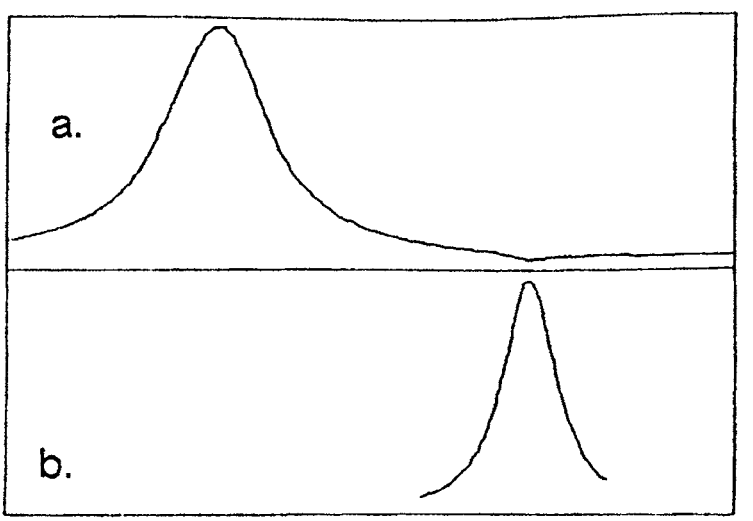

Fig. 3.36. The pure component spectra obtained from the multiplication of the abstract eigenspectra by coefficients obtained from the intersection points of the linear line and the shaded area corresponding to zero absorbance from Fig. 3.35. The spectrum in a is of component 1, and the spectrum in b is of component 2. (Reproduced by permission from Ref. [139]. © 1983 American Chemical Society.)

able to obtain quantitative information for the known compounds without having to consider the other species present. When information is available about only one component in a mixture, the method of rank annihilation has been used successfully to determine the concentration [140]. For a multicomponent system, the rank of

the correlation matrix, **M**, should equal the number of components. If one of the components, N, is known, and the correct amount of N is subtracted from **M**, the original rank of **M** should be reduced by 1. In such an instance, the eigenvalue of **M** corresponding to N should become 0. Given a pure component that is known to be in the mixture, the process of rank annihilation subtracts an amount, β, of the standard from the mixture. The residual matrix **E**, obtained by using this process, can be expressed as

$$\mathbf{E} = \mathbf{M} - \beta N \tag{3.72}$$

where $\mathbf{M}(\mathbf{A}^T\mathbf{A})$ is the correlation matrix. When the correct amount, β, of the pure component, N, is subtracted, the rank of the residual matrix will decrease by 1. This decrease can be monitored by observing the change in the eigenvalues of $\mathbf{E}^T\mathbf{E}$ with various choices of β [141,142]. At the appropriate choice of β, one of the eigenvalues will approach 0. Actually, because of noise, the eigenvalue will show only a minimum [143]. The amount of N subtracted to achieve a minimum in the corresponding eigenvalue will correspond to the relative concentration of the known component in the mixture [144].

Cross-correlation

Cross-correlation is the method of choice for the analysis of one known component in a complex, unknown mixture. The method can be proficient when the background, as well as the number and kinds of components, changes a great deal [145].

The absorbance of all mixtures at a particular frequency can be viewed as the absorbance attributable to the desired pure component multiplied by its fractional concentration plus the absorbances of all other species multiplied by their fractional concentrations. The approach of cross-correlation is to generate 'reference spectra' from knowledge of the sample's quantitative composition, rather than the more traditional method of multilinear regression, which uses the spectra to generate the composition of the mixture.

Cross-correlation is used to evaluate the similarity between the spectra of two different systems, for example, a sample spectrum and a reference spectrum. This technique can be used for samples where background fluctuations exceed the spectral differences caused by changes in composition. The cross-correlation technique also can be used to generate the spectra of the pure components from the mixture spectra when the pure component spectra are not available, or when the pure component spectra differ significantly from the isolated pure spectra because of interaction or matrix effects.

Cross-correlation can also be used for spectral reconstruction. If $a(x)$ is the absorbance or reflectance at a specific wavelength, and $c(x)$ is the concentration of the desired component in the xth sample, then the cross-correlation function, $C_{ac}(d)$,

between signals $a(x)$ and $c(x)$ at zero displacement can be written as

$$C_{ac}(d) = \frac{1}{n}\sum_{n} a(x)c(x \pm d) \qquad d = 0,\ 1,\ 2,\ \ldots,\ n-1 \tag{3.73}$$

where n is the number of samples, x is the sample index, and d is the displacement from the current x index. For each d, the corresponding samples of the absorbance at a specific frequency and the corresponding known concentrations are multiplied, and the products are summed over the entire set to give the value of C_{ac}. When $d = 0$, C_{ac} represents a quantitative measure of the degree of similarity between the functions. Taking products of pairs of points produces a weighted measure. The correlation function has a minimum value at $d = 0$, when the desired component is absent, and increases linearly with increasing concentration of the desired component.

In the absence of noise or other absorbing components in the sample set, the value of $C_{ac}(d)$ at $d = 0$ depends on only the absorbance and concentration of the desired component, and all values of $C_{ac}(d)$ are zero when d does not equal zero. Under these circumstances, repeated application of the cross-correlation function equation at the various IR frequencies will extract the desired spectrum.

In real samples, the problem is complicated by experimental noise sources, the interference of other sample constituents, and a limited number of samples. The cross-correlation function will therefore contain undesired contributions. To overcome these errors, the average of the d values which are not equal to zero is subtracted from the value of $C_{ac}(d)$ at $d = 0$:

$$C_{ac} = \frac{1}{n}\sum_{n} [a(xt) - \bar{a}]\,[c(x) - \bar{c}] \tag{3.74}$$

When this calculation is repeated for a number of frequencies, the resulting spectrum shows the correlation between the sample absorbance and the concentration of the component and should be free of contributions from unwanted sources. The spectrum should be that of the desired component [146].

One of the advantages of the cross-correlation method is that the correlation is less sensitive to background fluctuations because the change may not affect all of the component peaks and will be attenuated accordingly. The correlation scales the noise in proportion to the information, tending to force a constant optimal signal-to-noise ratio over the entire frequency range [147].

Summary

We have examined the IR instrumentation, sampling techniques and data processing. The success of every analysis depends on proper utilization of each of these components in the analysis. The good news is that for IR the state of the art is at an extremely high level, the bad news is that IR is not always performed properly.

It is hoped that the guidelines presented above will help you in making appropriate IR measurements yielding you the analytical information necessary to solve your problems.

References

[1] Potts, W.J., Chemical Infrared Spectroscopy, Vol. 1, Techniques. Wiley, New York, NY, 1963.
[2] Faires, L.M., Anal. Chem. 58 (1986) 1023A.
[3] Griffiths, P.R., de Haseth, J.A., Fourier Transform Infrared Spectrometry. Wiley, New York, NY, 1986.
[4] Cooley, J.W., Tukey, J.W., Math. Comput. 19 (1965) 297.
[5] Palmer, R.A., Spectroscopy 8(2) (1993) 26.
[6] Polavarapu, P.L., Chen, G.-C., Weibel, S., Appl. Spectrosc. 48 (1994) 1224.
[7] Polavarapu, P.L., Chen, G.-C., Deng, Z., Appl. Spectrosc. 48 (1994) 1403.
[8] Hashimoto, M.M., Hamaguchi, H., Appl. Spectrosc. 50 (1996) 1010.
[9] Lewis E.N., Levin, I.W., Appl. Spectrosco. 49 (1995) 672.
[10] Culler, S.R., Ishida, H., Koenig, J.L., Ann. Rev. Mater. Sci. 13 (1983) 363.
[11] Stimson, M.M., O'Donnell, M.J., J. Amer. Chem. Soc. 74 (1952) 1805.
[12] Anderson, R.J., Griffiths, P.R., Anal. Chem. 47 (1975) 2339.
[13] Harrick, N.J., Internal Reflection Spectroscopy. Wiley-Interscience, New York, NY, 1967.
[14] Urban, M., ATR of Polymers. ACS, Washington, D.C., 1996.
[15] Jolley, J.G., Geesey, G.G., Hankins, M.R., Wright, R.B., Wichlacz, P.L., Appl. Spectrosc. 43 (1989) 1062.
[16] IRIS Fiber Optics, Inc., British Telecom Laboratories, Martlesham Health, Ipswich, England.
[17] Compton, D.A.C., Hill, S.L., Wright, N.A., Druy, M.A., Piche, J., Stevenson, W.A., Vidrine, D.W., Appl. Spectrosc. 42 (1988) 972.
[18] Castillo, F.J., Koenig, J.L., Anderson, J.M., Lo, J., Biomaterials 5 (1984) 319.
[19] Urban, M.W., Vibrational Spectroscopy of Molecules and Macromolecules on Surfaces. John Wiley, New York, NY, 1993, p. 86.
[20] Fina, L.J., Chen, G., Vib. Spectrosc. 1 (1991) 353.
[21] Shick, R.A., Koenig, J.L., Ishida, H., Appl. Spectrosc., 47 (1993) 1237.
[22] Huang, J., Urban, M.W., Appl. Spectrosc. 47 (1993) 973.
[23] Ohta, K., Iwamoto, R., Appl. Spectrosc. 39 (1985) 418.
[24] Harrick, N.J., Milosevic, M., Berets, S.L., Appl. Spectrosc. 944 (1991) 45.
[25] Buffeteau, T., Desbat, B., Eyquem, D., Vib. Spectrosc. 11 (1996) 29.
[26] Satou, S., Ikehara, Y., Arime, M., Kanzeri Chuo Bunsekishoho 33 (1994) 93.
[27] Reffner, J., Alexay C.C., Hornlein, R.W., SPIE 1575 (1991) 301.
[28] Kortum, G., Reflectance Spectroscopy. Springer-Verlag, New York, NY, 1969.
[29] Heavens, O.S., Optical Properties of Thin Solid Films. Butterworth, London, 1955, Chap. 4.
[30] Wendlandt, W.W., Hecht, H.G., Reflectance Spectroscopy. Interscience, New York, NY, 1969.
[31] Ishino, Y., Ishida, H., Appl. Spectrosc. 46 (1992) 504.
[32] Harrick, N.J., Am. Lab 18 (1986) 78.
[33] Porter, M.D., Anal. Chem. 60 (1988) 1143A.
[34] Dubois L.H., Nuzzo, R.G., Ann. Rev. Phys. Chem. 437 (1992) 43.
[35] Fuller M.P., Griffiths, P.R., Anal. Chem. 1906 (1978) 50,.
[36] Christy, A.A., Kvalheim O.M., Velapoldi, R.A., Vib. Spectrosc. 9 (1995) 19.
[37] Cheng, H.N., Lee, G.H., Polym. Bull. 13 (1985) 549.
[38] Cheng, H.N., Lee, G.H., Polym. Bull. 12 (1984) 463.
[39] Korte, H., Otto, A., Appl. Spectrosc. 42 (1988) 38.
[40] Kubelka, P., Munk, Z., Z. Tech. Phys., 12 (1931) 593.
[41] Gunde, M., Logar, J., Orei, Z., Orel, B., Appl. Spectrosc. 623 (1995) 49.
[42] Brimmer, P.J., Griffiths, P.R., Appl. Spectrosc. 42 (1988) 242.

[43] Brimmer, P.J., Griffiths, P.R., Harrick, N.J., Appl. Spectrosc. 40 (1986) 258.
[44] Christy, A.A., Liang, Y.-Z., Hui, C., Kvalheim O.M., Velapoldi, R.A., Vib. Spectrosc. 5 (1993) 233.
[45] Chalmers, J.M., Mackenzie, M.W., Appl. Spectrosc. 36 (1985) 634.
[46] Chase, B., Amey, R.L., Holtje, W.G., Appl. Spectrosc. 36 (1982) 155.
[47] Korte, H., Otto, A., Appl. Spectrosc. 42 (1988) 38.
[48] McKenzie, M.T., Culler, S.R., Koenig, J.L., in: H. Ishida (Ed.), Fourier Transform Infrared Characterization of Polymers. Plenum, New York, NY, 1987.
[49] McKenzie, M.T., Koenig, J.L., Appl. Spectrosc. 39 (1985) 408.
[50] Culler, S.R., McKenzie, M.T., Fina, L.J., Ishida, H., Koenig J.L., Appl. Spectrosc. 38 (1984) 791.
[51] McKenzie, M.T., Culler, S.R., Koenig, J.L., Appl. Spectrosc. 38 (1984) 786.
[52] Rosencwaig, A., Photoacoustics and Photoacoustic Spectroscopy. Wiley, New York, NY, 1980.
[53] Jones, R.W., McClelland, J.F., Appl. Spectrosc. 50 (1996) 1258.
[54] Jiang, E.Y., Palmer, R.A., Chao, J.L., J. Appl. Phys. 78 (1995) 460.
[55] Chatzi, E.G., Urban, M.W., Ishida, H., Koenig, J.L., Langmuir 4 (1988) 846.
[56] Adams, M.J., Kirkbright, G.F., Analyst 102 (1977) 281.
[57] Koenig, J.L., Adv. Polym. Sci. 54 (1983) 89.
[58] Urban, M.W., Koenig, J.L., Appl. Spectrosc. 39 (1985) 1051.
[59] Urban, M.W., Koenig, J.L., Anal. Chem. 60 (1985) 2408.
[60] McDonald, W., Goettler, H., Urban, M.W., Appl. Spectrosc. 43 (1989) 1387.
[61] Tochigi, K., Momose, H., Misawa Y., Suzuki, T., Appl. Spectrosc. 46 (1992) 156.
[62] Vassallo, A.M., Cole-Clarke, A., Plang, L.S.K., Palmisano, A.J., Appl. Spectrosc. 46 (1992) 73.
[63] DeBlase, F.J., Compton, S., Appl. Spectrosc. 45 (1991) 808.
[64] Guthrie, J.D., Sparr, B.J., Appl. Spectrosc. 588 (1991) 45.
[65] Chase, D.B., Appl. Spectrosc. 35 (1981) 77.
[66] Hvistendahl, J., Rytter, E., Oye, H.A., Appl. Spectrosc. 37 (1983) 182.
[67] King, V.W., Lauer, J.L., J. Lubrication Tech. 103 (1981) 65.
[68] Jones, R.W., McClelland, J.F., Anal. Chem. 61 (1989) 650.
[69] Handke, M., Harrick, N.J., Appl. Spectrosc. 40 (1986) 401.
[70] Nagasawa, Y., Ishitani, A., Appl. Spectrosc. 38 (1984) 168.
[71] Imhof, R.E., McKendrick, A.D., Xiao, P., Rev. Sci. Instrum. 66(11) (1995) 5203.
[72] Rewick, R.T., Messserschmidt, R.G., Appl. Spectrosc. 45 (1991) 297.
[73] Beer, R., Remote Sensing by Fourier Transform Infrared Spectroscopy. Wiley, New York, NY, 1992.
[74] Pell, R.J., Callis, J.B., Kowoski, B.R., Appl. Spectrosc. 45 (1991) 808.
[75] Liu, J., Koenig, J.L., Appl. Spectrosc. 41 (1987) 447.
[76] Hirschfeld, T., Mantz, A.W., Appl. Spectrosc. 30 (1976) 552.
[77] Clark, F.R.S., Moffatt, D.J., Appl. Spectrosc. 32 (1978) 547.
[78] Graf, R.T., Koenig, J.L., Ishida, H., Appl. Spectrosc. 39 (1985) 405.
[79] Coleman, M.M., Tabb, D.L., Koenig, J.L., Polym. Lett. Ed. 12 (1974) 577.
[80] Hirshfeld, T., Kizer, K., Appl. Spectrosc. 29 (1975) 345.
[81] Koenig, J.L., Tabb, D.L., Coleman, M.M., J. Polym. Sci., Polym. Phys. Ed. 13 (1975) 1145.
[82] D'Esposito, L., Koenig, J.L., J. Polym. Sci., Polym. Phys. Ed. 14 (1976) 1731.
[83] Painter, P.C., Koenig, J.L., J. Polym. Sci., Polym. Phys. Ed. 15 (1977) 1885.
[84] Tabb, D.L., Koenig, J.L., Macromolecules 8 (1975) 929.
[85] Painter, P.C., Koenig, J.L., J. Polym. Sci., Polym. Phys. Ed. 15 (1977) 1223.
[86] Painter, P.C., Koenig, J.L., J. Polym. Sci., Polym. Phys. Ed. 15 (1977) 1235.
[87] Tabb, D.L., Sevcik, J.J., Koenig, J.L., J. Polym. Sci., Polym. Phys. Ed. 13 (1975) 815.
[88] Bachman, M.A., Gordon, M., Koenig, J.L., J. Appl. Phys. 50 (1979) 6106.
[89] Coleman, M.M., Painter, P.C., Appl. Spect. Rev. 20 (1984) 255.
[90] Maddams, W.F., Appl. Spectrosc. 34 (1980) 245.
[91] Vandeginste, B.G.M., De Galan, L., Anal. Chem. 47 (1975) 2124.
[92] Goldman, A., Alon, P., Appl. Spectrosc. 27 (1973) 50.
[93] Baker, C., Cockerill, I.P., Kelsey, J.E., Maddams, W.F., Spectrochim. Acta 34A (1978) 673.
[94] Gillette, P.C., Lando, J.B., Koenig, J.L., Appl. Spectrosc. 38 (1982) 401.
[95] Maddams, W.F., Makromol. Chim. Macromol. Symp. 5 (1986) 38.

[96] Gans, P., Gill, J.B., Anal. Chem. 52 (1980) 351.
[97] Kauppinen, J.K., Moffatt, D.J., Mantsch, H.H., Cameron, D.G., Appl. Spectrosc. 35 (1981) 271.
[98] Kauppinen, K., Moffatt, D.J., Mantsch, H.H., Cameron, D.G., Anal. Chem. 53 (1981) 1454.
[99] Kauppinen, K., Moffatt, D.J., Mantsch, H.H., Cameron, D.G., Appl. Opt. 21 (1982) 1454.
[100] Compton, D.A.C., Maddams, W.F., Appl. Spectrosc. 40 (1986) 239.
[101] Sasaki, K., Kawata, S., Minami, S., Appl. Opt. 23 (1984) 1955.
[102] Friedrich, H.B., Yu, J.-P., Appl. Spectrosc. 41 (1987) 227.
[103] Gillette, P.C., Lando, J.B., Koenig, J.L., in: J.R. Ferraro and L.J. Basile (Eds.), Fourier Transform Infrared Spectroscopy. Academic Press, Vol 4. New York, NY, 1985, p. 1.
[104] Blackburn, J.A., Anal. Chem. (37) (1965) 1000.
[105] Antoon, M.K., Koenig, J.H., Koenig, J.L., Appl. Spectrosc. 31 (1977) 518.
[106] Haaland, D.M., Easterling, R.G., Vopick, D.A., Appl. Spectrosc. 39 (1977) 73.
[107] Haaland, D.M., Thomas, E.V., Anal. Chem. 60 (1988) 1193.
[108] Haaland, D.M., Easterling, R.G., Vopicka, D.A., Appl. Spectrosc. 39 (1985) 73.
[109] Brown, C.W., Lynch, P.F., Obremski, R.J., Lavery, D.S., Anal. Chem. 54 (1982) 1472–1479.
[110] Kisner, H.J., Brown, C.W., Kavarnos, G.J., Anal. Chem. 55 (1983) 1703–1707.
[111] Haaland, M., Easterling, R.G., Vopicka, D.A., Appl. Spectrosc. 39 (1985) 73.
[112] Kisner, H.J., Brown, C.W., Kavarnos, G.J., Anal. Chem. 55 (1983) 643.
[113] Blanco, M., Coello, J., Iturriaga, H., Maspoch, S., Redon, M., Appl. Spectrosc. 48 (1994) 73.
[114] Miller, C.E., Appl. Spectrosc. 47 (1993) 222.
[115] Fuller, M.P., Ritter, G.L., Draper, C.S., Appl. Spectrosc. 42 (1988) 217.
[116] Fuller, M.P., Ritter, G.L., Draper, C.S., Appl. Spectrosc. 42 (1988) 228.
[117] Haaland, D.M., Thomas, E.V., Anal. Chem. 60 (1988) 1193.
[118] Haaland, D.M., Thomas, E.V., Anal. Chem. 60 (1988) 1202.
[119] McClure, G.L. (Ed.), Computerized Quantitative Infrared Analysis. ASTM, Philadelphia, 1987.
[120] Hirschfeld, T., Anal. Chem. 48 (1976) 721.
[121] Koenig, J.L., D'Esposito, L., Antoon, M.K., Appl. Spectrosc. 31 (1977) 292.
[122] Diem, H., Krimm, S., Appl. Spectrosc. 35 (1981) 421.
[123] Koenig, J.L., Kormos, D., Appl. Spectrosc. 33 (1979) 349.
[124] Lin, S.B., Koenig, J.L., J. Polym. Sci., Polym. Phys. Ed. 20 (1982) 2277.
[125] Malinowski, E.R., Howery, D.G., Factor Analysis in Chemistry. Wiley, New York, NY, 1980.
[126] Sekulic, S., Seasholtz, M.B., Wang, Z., Kowalski, B.R., Lee, S.E., Holt, B.R., Anal. Chem. 16 (1993) 835A.
[127] Miller, C.E., Appl. Spectrosc. 47 (1993) 222.
[128] Lin, S.B., Koenig, J.L., J. Polym. Sci., Polym. Phys. Ed. 20 (1982) 2277.
[129] Malinowski, E.R., Anal. Chem. 49 (1978) 612.
[130] Koenig, J.L., Tovar, M.J.M., Appl. Spectrosc. 35 (1981) 543.
[131] Orlando, A., Picollo, M., Radicati, B., Baronti, S., Casini, A., Appl. Spectrosc. 49 (1995) 459.
[132] Rao, G.R., Zerbi, G., Appl. Spectrosc. 38 (1984) 795.
[133] Ge, E., Brown, C., Kisner, H.J., Appl. Spectrosc. 49 (1995) 432.
[134] Tu, X.M., Burdick, D.S., Millican, D.W., McGown, L.B., Anal. Chem. 61 (1989) 2219.
[135] Lawton, W.H., Sylvestre, E.A., Technometrics 13 (1971) 617.
[136] Chen, J.H., Hwang, L.-P., Anal. Chim. Acta. 133 (1981) 271.
[137] Malinowski, E.R., Anal. Chim. Acta. 134 (1982) 129.
[138] Friedrich, H.B., Yu, J.P., Appl. Spectrosc. 41 (1987) 227.
[139] Gillette, P.C., Lando, J.B., Koenig, J.L., Anal. Chem. 55 (1983) 630.
[140] Gillette, P.C., Lando, J.B., Koenig, J.L., Anal. Chem. 55 (1983) 630.
[141] Ho, D.-N., Christian, G.D., Davidson, E.R., Anal. Chem. 52 (1980) 1071.
[142] Ho, D.-N., Christian, G.D., Davidson, E.R., Anal. Chem. 53 (1981) 92.
[143] Gianelli, M., Burns, D.H., Callis, J.B., Christian, G.D., Anderson, N.H., Anal. Chem. 55 (1983) 1858.
[144] Burns, D.H., Callis, J.B., Christian, G.D., Anal. Chem. 58 (1986) 2805.
[145] Horlick, G., Anal. Chem. 45 (1973) 319.
[146] Honigs, D.E., Hieftje, G.M., Hirschfeld, T., Appl. Spectrosc. 38 (1984) 317.
[147] Mann, C.K., Goleniewski, J.R., Sismanidis, C.A., Appl. Spectrosc. 36 (1982) 223.

Chapter 4

Applications of IR spectroscopy to polymers

Structural applications of IR spectroscopy

Many reviews have been published on the application of IR spectroscopy to polymers, and you should examine them if you are concerned with a specific polymer system or application (see the general references at the end of this chapter). The numerous applications of IR spectroscopy to the study of polymers far exceed our limited time and space. The basic IR spectroscopic methods of structural characterization of polymers will be discussed in this chapter, and a few pedagogical examples will be given to illustrate the applications of IR spectroscopy.

Number-average molecular weight by using end-group analysis

IR spectroscopy is a valuable technique for measuring the concentration of end groups in a polymer sample, particularly when the measurement of colligative solution properties is not possible because the sample is insoluble in ordinary solvents at room temperature. From IR measurements, a number-average molecular weight of the polymer can be calculated on the basis of the assumption that the chain is linear (with no branch points). This assumption limits the number of endgroups of a given polymer to either one or two per molecule. When polymers are prepared by addition polymerization, there is always the possibility of branching in the polymer, and in this case, the IR measurement is only a relative number-average molecular weight of the system. For polymers formed by condensation, branching is less likely to occur, and end-group analysis is quite accurate once the chemical nature of the end groups has been determined. Because the end groups are not spectroscopically coupled to the remainder of the chain, low-molecular-weight analogs can be used for calibration. IR spectroscopy is particularly useful for measuring the number-average molecular weight of insoluble systems; it is the standard method used to determine the molecular weights of fluorocarbons.

As an example of the use of IR spectroscopy to determine end-group concentrations and molecular weight, consider poly(butylene terephthalate) (PBT) [1]. In this condensation polymer, the end groups are an alcohol group and an acid, so the

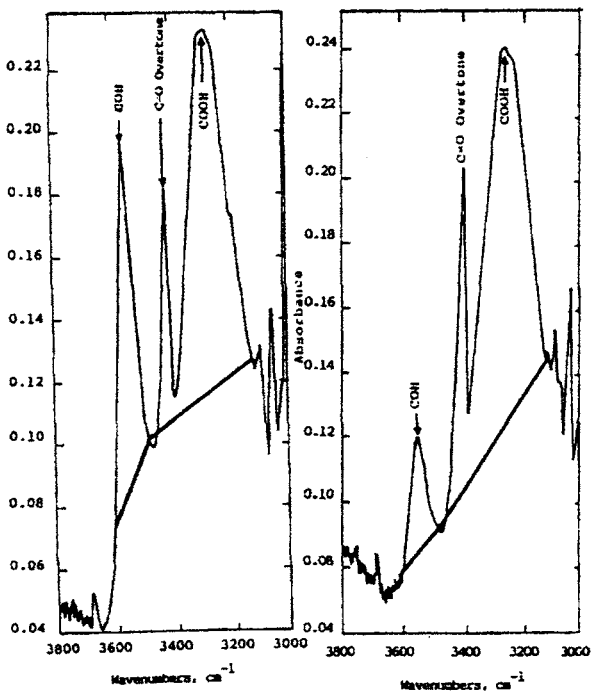

Fig. 4.1. The spectra of two samples of PBT with different molecular weights. (Reproduced with permission from Ref. [1]. © 1985 Society of Plastics Engineers.)

molecular weight, M_n, of the polymer is

$$M_n = \frac{2}{(E_1 + E_2)} \tag{4.1}$$

where E_1 is the equivalents per gram of alcoholic end groups, and E_2 is the equivalents per gram of acid end groups. This equation presumes that no other end groups are present and that no grafting or endgroup degradation has occurred. The IR spectra of two different samples of PBT are shown in Fig. 4.1. The $-$COH end groups absorb at 3535 cm^{-1}, and the $-$COOH end groups absorb at 3290 cm^{-1}.

The extinction coefficients were determined, and the results are as follows: $a_{OH} = 113 \pm 18$ 1/(g-equiv. cm); $a_{COOH} = 150 \pm 18$ 1/(g-equiv. cm). The baseline for the $-$COH is from 3480 to 3600 cm^{-1} tangent to the spectral curves, and for the $-$COOH peak, the baseline is from 3120 to 3480 cm^{-1}. These IR measurements of molecular weight can be correlated with the results from viscosity measurements and can be used to study the changes in molecular weight that are induced by processing the PBT polymer.

Generally, the end groups make only small contributions to the spectra, and in some cases their contributions are more profound. In the case of polyethylene, the bands at 909 and 990 cm^{-1}, which are associated with the terminal vinyl groups,

are intense and readily observable in commercial polyethylene samples. These vinyl end groups are observable because the associated dipole moment is larger than those of the methylene deformations, so the vinyl bands are inherently more intense than the weaker methylene wagging and twisting modes in the same frequency region. Therefore, although the vinyl end groups are very low in concentration, their IR absorptions appear clearly in the spectrum. On the other hand, the methyl end groups at 1378 cm^{-1} are inherently weak like the methylene modes and are difficult to view because they are badly overlapped by the larger number of amorphous methylene modes in this region. However, the methyl end-group absorptions can be used to measure branching in polyethylene.

IR analysis of the polymerization process

IR spectroscopy is a convenient method for studying the curing of polymers. IR spectroscopy can be used to determine the reaction order and the chemical processes that occur in the reactant system. By using thermally controlled cells, the reactions can be studied at temperatures used in the industrial process. One system that has been studied extensively because of its industrial applications is the copolymerization of epoxide resin with cyclic anhydrides or amines. The reaction kinetics of methyl-bicyclo[2.2.1]heptene-2,3-dicarboxylic anhydride (Nadic methyl anhydride isomers or NMA) and diglycidyl ether of bisphenol-A based epoxy (EPON 828, Shell) were followed by means of the 1858-cm^{-1} carbonyl band of the anhydride molecule [2]. For a stoichiometric mixture of the reactants at 80°C, a zeroth-order kinetic plot was obtained up to 55% conversion (130 min). Beyond the gelation, the reaction slows and nearly stops at 71% conversion. A reduction in the polymerization rate is expected when the kinetic processes are slowed by an increase in the viscosity near the point of gelation. Arrhenius plots of the zeroth-order reaction rates in the temperature range of 70–120°C for a 1 : 1 anhydride: epoxy system are quite linear and yield an activation energy of 15.5 kcal/mol.

The extent of crosslinking in the NMA and EPON 828 (with 0.5 wt% benzyl dimethyl amine as a curative in each mixture) can be determined by using IR spectroscopy [3]. The least-squares method was used to fit the spectra of the mixture of NMA and EPON 828. In order to determine the degree of crosslinking, a difference spectrum was calculated by subtracting the spectrum of a stoichiometric mixture of NMA and EPON 828 crosslinked for 37 min at 80°C from the spectrum of the same reactant mixture crosslinked for 83 min at 80°C. The procedure is illustrated in Fig. 4.2 for the 600–2000-cm^{-1} region. The absorbances that are unaffected by the reaction, such as the aromatic ring modes at 1511 and 1608 cm^{-1}, are canceled in the difference spectrum. Bands above and below the baseline represent the ester crosslink formation and the disappearance of anhydride and epoxide groups, respectively. These measurements yielded the following results for different cure times at 80°C.

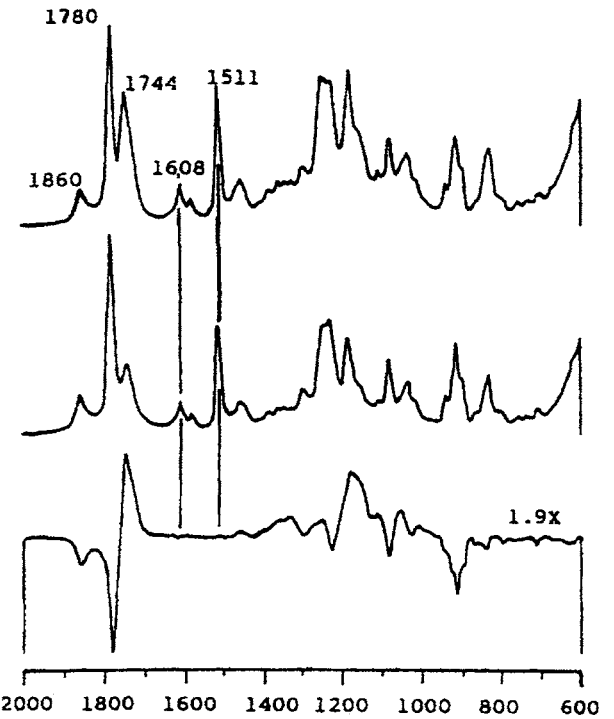

Fig. 4.2. Generation of difference spectrum to characterize crosslinking at 80°C of a stoichiometric mixture of NMA-EPON 828. The samples were crosslinked for 83 min (top spectrum) and 37 min (middle spectrum). The bottom spectrum is the difference spectrum (top – middle).

Time (min)	Degree of cure (%)
30	6.00
60	12.00
90	18.50
120	28.10
360	65.30

(Reproduced with permission from Ref. [3]. © 1981.)

Polymerization processes can be followed in situ using chalcogenide fibers. These chalcogenide fibers are used as ATR elements and can be used to study reactions internal to the sample. They have been used to investigate the polymerization mechanisms involved in the production of polyurethane foams [4]. A 30-cm length of the fiber was stripped of the protective coating and this portion of the fiber was inserted into the foam, which was in a thermostated sample bucket. Spectra were obtained at 8 cm^{-1} spectral resolution and 5 s time resolution for the first three hours and every

hour after that for 16 h. The chemical reaction was as follows:

$$\underset{\text{isocyanate}}{R-N=C=O} + \underset{\text{polyol}}{R'OH} \Rightarrow \underset{\text{urethane}}{R-\overset{H}{\overset{|}{N}}-\overset{O}{\overset{\|}{C}}-O-R'}$$

The consumption of isocyanate was followed by measuring the absorbance of the $-N=C=O$ antisymmetric stretching band at 2275 cm^{-1}. The CH stretching modes were used as an approximate internal standard (systematic changes in the shape of the CH modes were observed). The band at 3350 cm^{-1} was due to the free NH stretching band from the urea and/or urethane groups. The absorbance spectra of the carbonyl region of polyurethane foam from 0.2 to 19.4 min into the reaction are shown in Fig. 4.3.

The broad band around 1640 cm^{-1} is due to water that is present early in the reaction but is completely consumed by 0.5 min. By completion of the mixing, urethane and urea were present as seen from the 1715 and 1730 cm^{-1} bands, respectively. The formation of urethane and urea appears to take place simultaneously as these bands grow in parallel. The doubly hydrogen-bonded bidentate urea carbonyl absorption (1640 cm^{-1}) is observed at about 1.7 min into the process. This band grows as the curing proceeds, which is indicative of phase separation occurring. The isocyanate is not observed until about 5 min after the initial mixing.

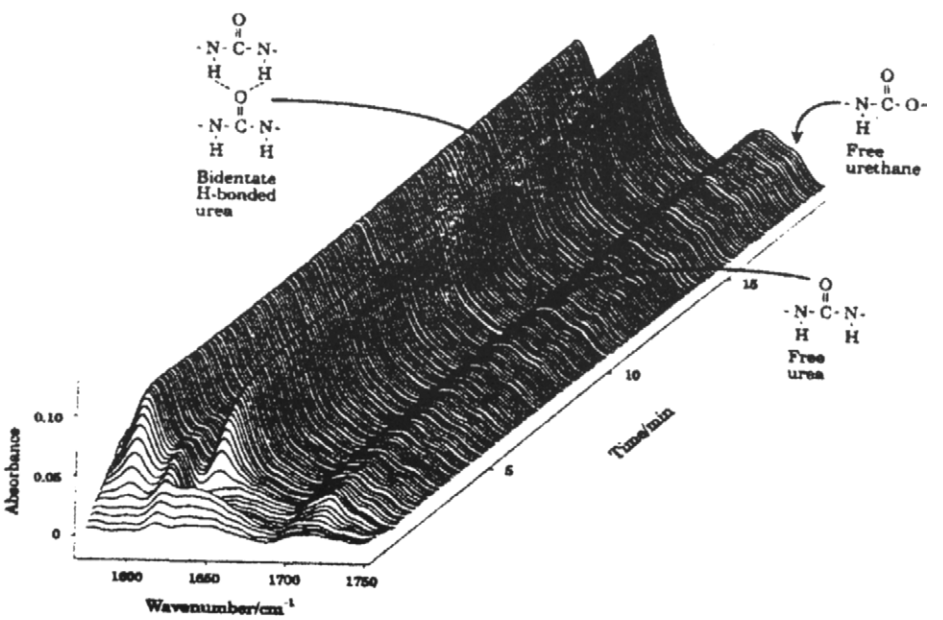

Fig. 4.3. The absorbance spectra of the carbonyl region of polyurethane foam from 0.2 to 9.4 min into the reaction. (Reproduced with permission from Ref. [4]. © 1993 Society for Applied Spectroscopy.)

Chemical transformations in polymers

We are interested in the nature of the structural changes produced by such chemical reactions as oxidation, reduction, and hydrolysis. Because the IR bands of polymers are inherently broad and weak, it is very difficult to detect minor chemical changes occurring on the polymer chain. It is necessary to eliminate from the observed spectrum the interfering absorptions of the unreacted portions of the polymer. This elimination step can be accomplished by using the absorbance subtraction of the spectrum of the control polymer from the spectrum of the reacted system. The resulting difference spectrum contains only those IR bands resulting from the chemical reactions that have occurred. By eliminating the interfering spectra of the unreacted components, the dynamic range is also enhanced, and scale expansion of the difference spectrum up to the limit of the signal-to-noise ratio is possible. By using both spectral subtraction and scale expansion of the difference spectrum, very small chemical changes can be detected. For example, in Fig. 4.4 the spectra of polybutadiene are shown before and after a very mild oxidation, that is, storage in the instrument for 10 h. Visual inspection of the spectrum of the oxidized sample reveals no observable changes, but the subtraction of the spectrum of the unoxidized sample from that of the oxidized sample and scale expansion of the resulting difference spectrum reveals features in the difference spectrum resulting from the onset of oxidation. Absorption in the 1080–1110-cm^{-1} region is characteristic of C–O groups. The negative bands indicate the loss of *cis*-methine groups at 740 and

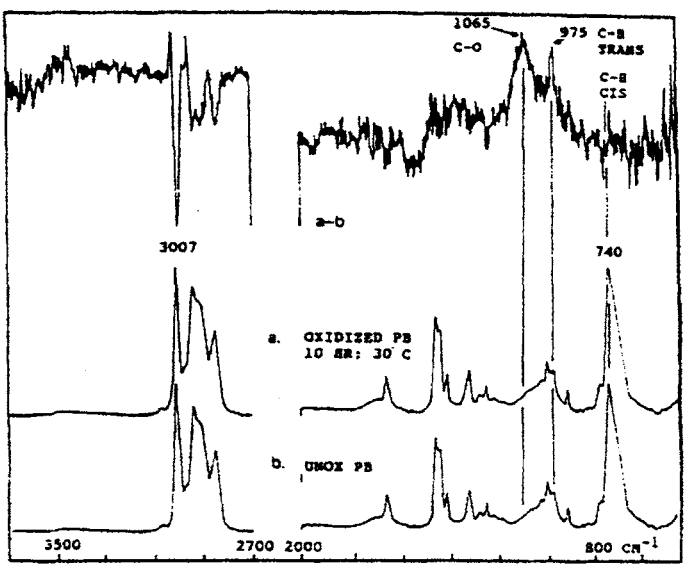

Fig. 4.4. Spectra of oxidized (spectrum a) and unoxidized (spectrum b) samples of *cis*-1,4-polybutadiene and the a – b difference spectrum.

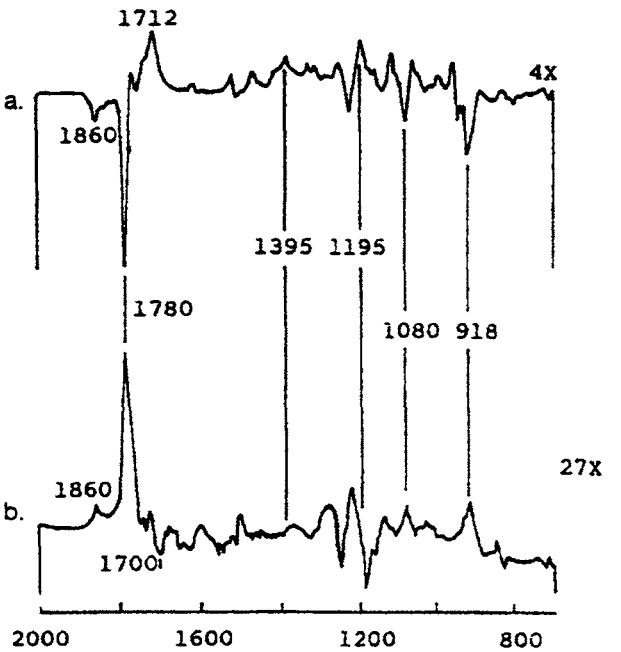

Fig. 4.5. Hydrolysis and leaching of anhydride from epoxy resin exposed to water at 80°C. Film thickness was 11 mm.

3007 cm^{-1}. As the oxidation proceeds, the number of absorbing species increases, as does the complexity of the spectrum. By using absorbance subtraction, the spectral changes can be followed, and the concentration of the various species can be determined [5]. The difference spectrum after 3 h shows formation of *trans*-methine at 975 cm^{-1} and specific carbonyl groups at 1700 and 1727 cm^{-1}. The 34-h difference spectrum shows a broadening of the C−O band. After 640 h, only 27% of the *cis*-methine remains, a result illustrating the need for oxidative stabilizers in rubber samples.

As another example, let us examine the effects of exposing an anhydride-cross-linked epoxy system to moisture [6]. Spectra were obtained after exposure of the epoxy system to water at 80°C for various time periods. The difference spectra obtained after 6.5 days (spectrum b) and 31.5 days (spectrum a) are shown in Fig. 4.5.

A decrease in the anhydride concentration is indicated by decreases in intensity of the vibrations at 1860, 1080 and 918 cm^{-1}. An increase in the concentration of carboxyl groups is indicated by the increases in the intensities of the bands at 1712 cm^{-1} (C=O), 1395 cm^{-1} (O−H) and 1195 cm^{-1} (C−O). These spectral results reflect the initial hydrolysis of the unreacted anhydride (approximately 5% of the initial anhydrides) to the diacid, which is in part leached from the sample by the water. As shown in Fig. 4.5, the water induces some of the diacid molecules to react with the epoxy groups.

This general type of analysis can be used to study chemical reactions of polymers regardless of the specific type of reaction. The ultimate limitation is the sensitivity as determined by the experimental signal-to-noise ratio.

The ability of the spectroscopist to interpret the spectral changes in terms of reactants or products is the principal limitation. With modern instrumentation, interpretation of the nature of the chemical changes is often the final barrier.

Copolymer analysis

One of the more important applications of IR spectroscopy is the characterization of copolymers. The characterization has a simple component that is important. That is, the measurement of the copolymer composition. The complex problem is related to the need to determine microstructure.

Composition of copolymers

The composition of a copolymer can be measured by ratioing an infrared band due to the A-copolymer component (which is not influenced by sequencing effects) to an internal thickness band (which corrects for variations in thickness). It is also advisable to perform the same measurements for the B-copolymer component. As an example, the composition of poly(ethylene-*co*-vinyl acetate) (EVA) can be determined by ratioing the 1740 cm^{-1} band for vinyl acetate to the 1460 cm^{-1} internal thickness band [7].

Microstructure of copolymers

Vibrational coupling complicates the IR analysis of copolymers. The difficulty of the IR analysis is a function of the size of the comonomer repeat units. The magnitude of the vibrational coupling between units is a function of the intramolecular distance. When the repeat units are small, the coupling is large and is a function of the type of vibrational motion. When the repeat units are large, the coupling between units will be zero or very small. For example, the spectrum of the trimer of poly(ethylene terephthalate) (PET) is essentially the same as that of high-molecular-weight PET because the length of the PET repeat unit is so long that the intramolecular interactions between repeat units is essentially zero.

When the repeat units are small (i.e., contain only two carbons, as is the case for vinyl monomers), vibrational coupling can occur between the repeat units. This coupling results in spectral bands that have frequency and absorptivity depending on the length of the ordered sequence. This intensity perturbation by the coupling factor must be taken into consideration when developing a method of spectral analysis. For

large comonomer repeating units, the IR analysis is simplified because the analysis of only the composition is possible, and the copolymer can be considered, from an IR point of view, to be simply a mixture of the two comonomers. Unfortunately, for the case of large repeating units, IR spectroscopy will not yield information about the copolymer sequence distribution.

Consider the case when vibrational coupling occurs; in this case, IR spectroscopy can yield connectivity information about the microstructure of the copolymer. Let us look at the spectra of ethylene–propylene (E-P) copolymers [8]. The structure of the various sequences of this copolymer is shown in the following scheme illustrating the expected origin of the different segments of methylene units.

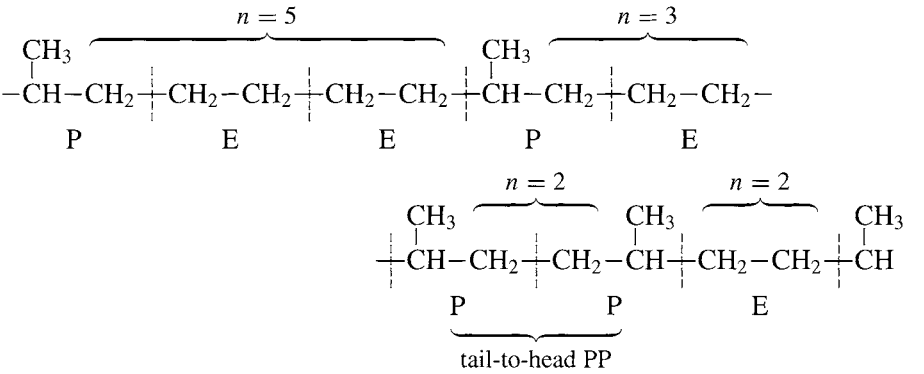

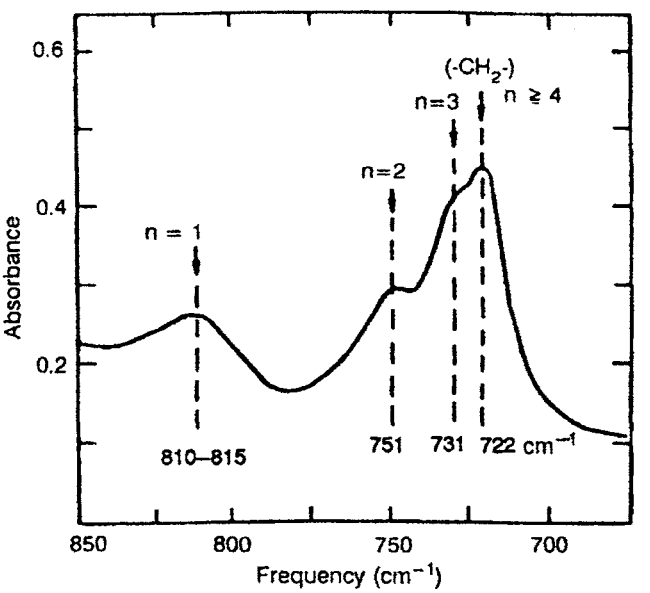

Fig. 4.6. An IR spectrum of the methylene rocking region of an ethylene–propylene copolymer (54.3 wt% C2). (Reproduced with permission from Ref. [8]. © 1968 American Chemical Society.)

An IR spectrum of the methylene rocking region of an E-P copolymer (54.3 wt% C2) is shown in Fig. 4.6.

The assignments of the peaks to the various methylene sequences are also shown. Quantitatively, head-to-tail P—P sequences can be identified by using the 810–815-cm^{-1} absorption band. The tail-to-tail P—P sequence is identified by the presence of the band at 751 cm^{-1}, which is assigned to the methylene sequences with

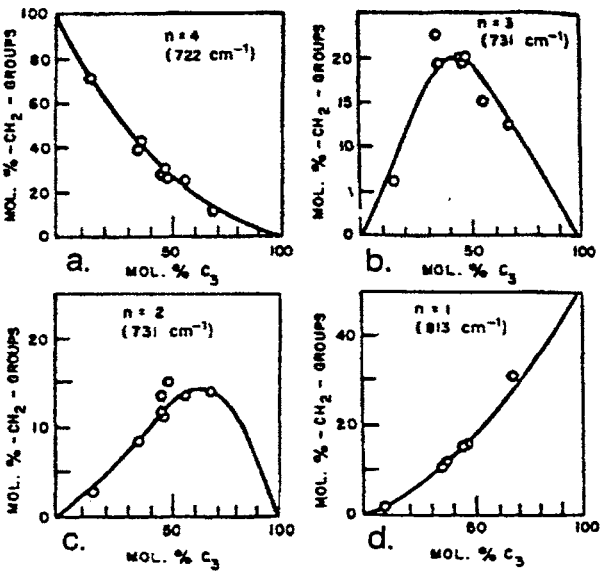

Fig. 4.7. Comparison of the experimental results with the theoretical curves as a function of the mole percent propylene: (a) 4 or more contiguous groups, (b) 3 contiguous groups, (c) 2 contiguous groups, and (d) isolated methylene groups. (Reproduced with permission from Ref. [8].)

Table 4.1
Monad, dyad, and triad probabilities of E-V copolymers

Copolymer	$P_V = 1 - P_E$	P_{VV}	$P_{VE} = P_{EV}$	P_{EE}	P_{EVE}	$P_{VVE} = P_{EVV}$	P_{VVV}
E-V-100	1.0	1.0	0.0	0.0	0.0	0.0	1.0
E-V-85.3	0.853	0.742	0.124	0.011	0.015	0.115	0.619
E-V-84.3	0.843	0.709	0.134	0.023	0.025	0.108	0.615
E-V-70.7	0.707	0.470	0.239	0.052	0.063	0.175	0.310
E-V-62.3	0.623	0.344	0.278	0.099	0.116	0.177	0.177
E-V-61.5	0.615	0.343	0.275	0.107	0.121	0.173	0.198
E-V-50.1	0.501	0.200	0.297	0.205	0.192	0.133	0.073
E-V-45.6	0.456	0.147	0.309	0.235	0.205	0.116	0.037
E-V-37.3	0.373	0.087	0.286	0.342	0.219	0.078	0.012
E-V-34.8	0.348	0.061	0.278	0.383	0.224	0.064	0.015
E-V-21.2	0.212	0.014	0.197	0.593	0.190	0.016	0.0
E-V-13.6	0.136	0.0	0.127	0.746	0.104	0.0	0.0
E-V-2.4	0.024	0.0	0.025	0.950	0.021	0.0	0.0
E-V-0	0.0	0.0	0.0	1.0	0.0	0.0	0.0

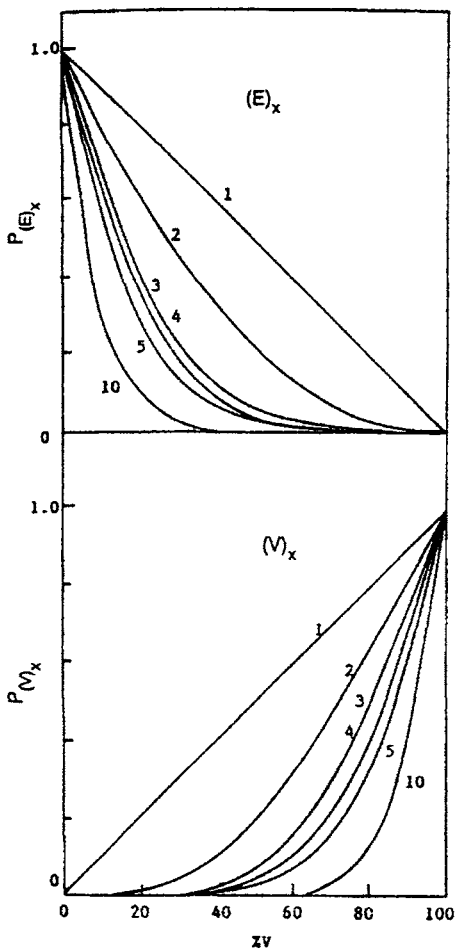

Fig. 4.8. Sequence probability curves vs. concentration of V units for copolymer sequences of various lengths. (Reproduced with permission from Ref. [9].)

$n = 2$. The band at 731 cm^{-1} is assigned to the E−P sequences, and the line at 722 cm^{-1} is associated with the $P(E-E)_{n\geq 2}$ sequences. Quantitative measurements have been made on this system, and the results are shown in Fig. 4.7 as a function of the mole percent of propylene.

The IR spectra of ethylene (E)–vinyl (V) chloride has revealing information. These copolymers were prepared by partial reduction of poly(vinyl chloride) (PVC) with tri-*n*-butyltin hydride [9]. During the reduction of PVC, the reaction rate of tri-*n*-butyltin hydride with the V units depends on the dyad–triad environment of the V unit, with the central unit in the $P_3(VVV)$ being more reactive than the central unit in the $P_3(EVE)$. The mono-ad, dyad and triad probabilities obtained from NMR data for the E-V copolymers are shown in Table 4.1. These results are plotted in Fig. 4.8 for length sequences of 1, 2, 3, 4, 5 and 10.

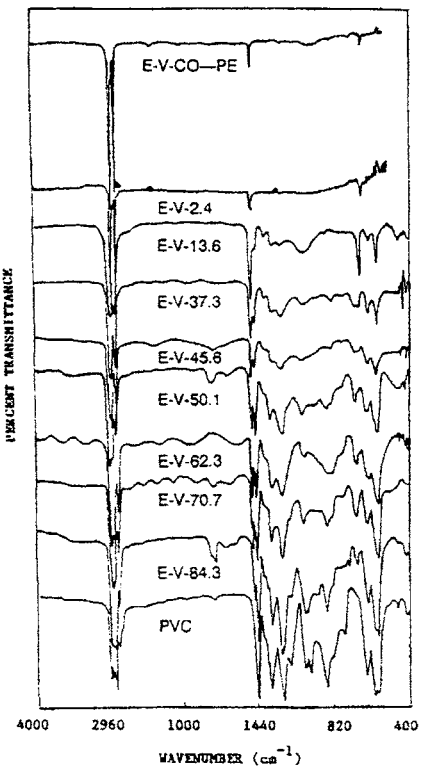

Fig. 4.9. Transmission IR spectra of E-V copolymers. The number adjacent to the spectrum equals the concentration of V units present in the copolymer. (Reproduced with permission from Ref. [9].)

The approach to interpreting the spectra of the copolymers is empirical. First, the copolymer spectra for a wide range of comonomer compositions are obtained, and then the spectra are examined by using the following steps.

Step 1: *Determine whether frequencies are due to the A or B component by determining at what copolymer composition the absorbance peaks disappear.*

The spectra of the copolymers for a range of compositions are shown in Fig. 4.9. The frequencies of the various absorptions are shown as a function of composition in Figs. 4.10 and 4.11. The IR bands resulting from long sequences of either monomer can be assigned by comparing them with the same frequencies in the spectra of the pure homopolymers and with those present predominantly at either end of the copolymer composition scale. These bands are indicated by the assignments given on the right sides of Figs. 4.10 and 4.11. New bands appearing in the spectra most likely arise from short sequences in the copolymer.

Step 2: *Determine which peaks are sensitive to sequence length by determining which peak positions are dependent on composition.*

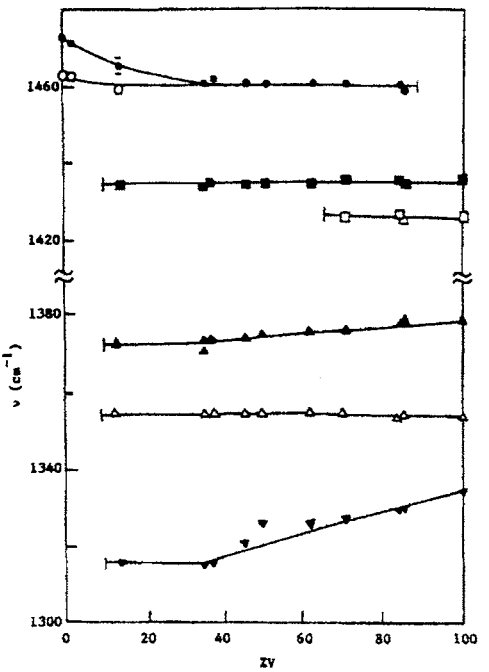

Fig. 4.10. Frequency vs. concentration of V units for the 1300–1480-cm^{-1} absorbance range. The structural assignments are as follows: (•) and ○, 1460 (E) CH_2b; ■, 1434 (V) CH_2b; □, 1426 (V) CH_2b; ▲, 1379 (V) CH_2w; △, 1355 (V) CH_2w; and ▼, 1334 (V) CHb.

For the E-V copolymer, the 700–850-cm^{-1} region had three methylene rocking modes that were found to be sequence dependent. The 850-cm^{-1} band of PVC results from the rocking motion of the methylene group between two methine groups and therefore is proportional to the concentration of VV dyads. A new absorbance band is observed at 750 cm^{-1} as the composition of the copolymer is changed. This band is assigned to the VEV triad and the VEEV tetrad. At the high end of the E concentration scale there are long sequences of E units (E_x, $x > 3$), and as a result, the 750-cm^{-1} band decreases and the 720–730-cm^{-1} band increases. The absorbance intensity–sequence relationships for the various bands are listed in Table 4.2.

Step 3: *Determine the sequence sensitivity of the peaks by correlating the absorbances with the sequence data calculated from approximate reactivity coefficients.*

By using the absorbance areas for the various IR peaks vs. composition and a knowledge of the sequence probabilities, a correlation between the absorbance plots of the various bands and the specific sequences responsible for those absorptions can be established. The C−H stretching resonances at 2800–3000 cm^{-1}, which are proportional to the C−H concentration, are found to be proportional to the mono-ads

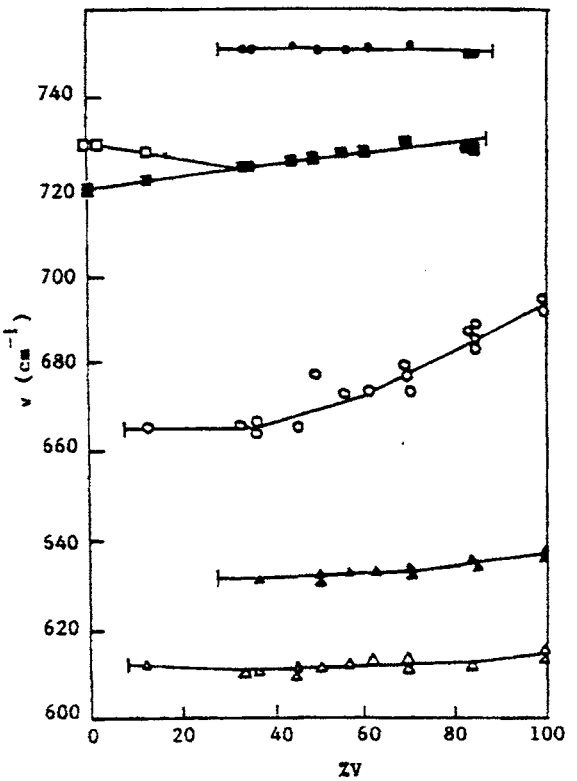

Fig. 4.11. Frequency vs. concentration of V units for CH_2 rocking modes and C–Cl stretching modes. The assignments are as follows: •, 750 (E); □ and ■, 719–730 (E); ○, 665–690 (V); ▲, 630 (V); and △ 611 (V).

of E (Fig. 4.12). The peak at 750 cm^{-1} is sensitive to either P_3(VEV) or P_4(VEEV) (Fig. 4.13). The peak at 728 cm^{-1} results from P_3(EEE) as determined by the comparison of the expected number of P_2(EE) with that of P_3(EEE) (Fig. 4.13).

Step 4: *Determine the extinction coefficients of the bands as a calibration for quantitative analysis.*

Finally, it is necessary to determine the extinction coefficients so that quantitative analysis can be made. In the case of the E-V copolymers, the NMR spectroscopic results can be used for calibration. The extinction coefficients vs. mole percent of V units for several of the absorption bands are shown in Fig. 4.14. As expected, some composition dependence of the absorptivities is observed.

At this point, the assignments and calibrations are complete, and the IR spectra can be used to determine the compositions and microstructures of the copolymers prepared under a variety of conditions. The E-V copolymers under discussion have a 'randomlike' comonomer sequence distribution.

Thus it is clear that FTIR can be used to determine the microsequence structure of copolymers with proper technique and calibration.

Table 4.2
Absorbance intensity–sequence relationship for E-V copolymers

ν (cm^{-1})	A [1]
2800–3000	P(E)
1473–1463	P(E) + P($(E)_x$), $x > 15$
1434–1426	P(V) + P($(V)_x$), $x = 15$
1379→1372	2P(EVE) + P(VVV)
1355	P($(V)_x$), $x = 7 \pm 2$
1334→1316	P(EVE) + P(VVV)
1255 multiplet	P(VVV) + $\frac{1}{2}$P(VVE) + $\frac{1}{2}$P(EVV) + $\frac{1}{4}$P(EVE)
1100 multiplet	P(VVV) + P(EVV) + P(VVE)
960	P($(V)_x$), $x > 5$
915	either (a) P(EVE) + P(VVV) or (b) 2P(EVE) + P(VVV)
860→840	P(VV)
750	P(VEV) or P(VEEV)
728	either (a) P(EEE) or (b) P(EE) + P($(E)_x$), $x > 10$
693→666	P(V)
638, 614	P(V) [+ possible contribution from P($(V)_x$), $x > 15$]

[1] A = absorbance area α (sequence probabilities)

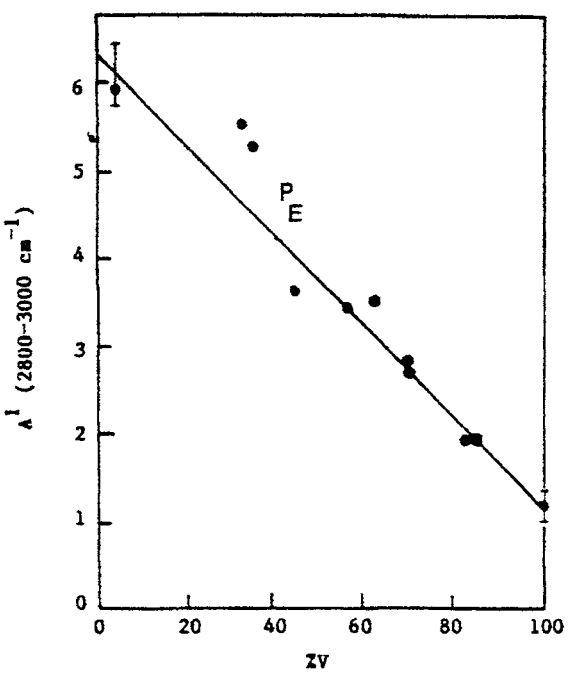

Fig. 4.12. IR intensities vs. concentration of V units for the C–H stretching band from 2800 to 3000 cm^{-1} showing that the band is sensitive to P(E) monads.

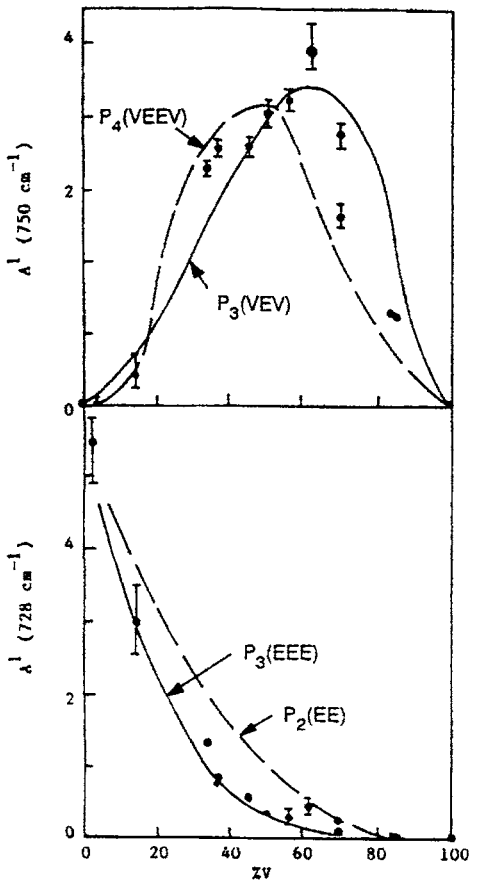

Fig. 4.13. IR intensities vs. concentration of V units for the 750- and 728-cm^{-1} absorbances.

Measurement of stereoregularity

The presence of stereoisomers in polymers is indicated in IR spectra by the appearance of new absorption frequencies, shifting of absorption frequencies, and band broadening. Methods for measuring the stereoisomeric composition of a polymer chain depend on knowledge of the relationship between these spectral properties and the stereoisomer structure.

The assignment of an IR frequency to a particular isomer may be established by:

- synthesis of a polymer containing only one of the stereoisomers,
- correlation with the isomers of low-molecular-weight analogs,
- assignments based on normal coordinate analysis,
- comparison of absorbances with calculated values from other physical techniques such as NMR spectroscopy.

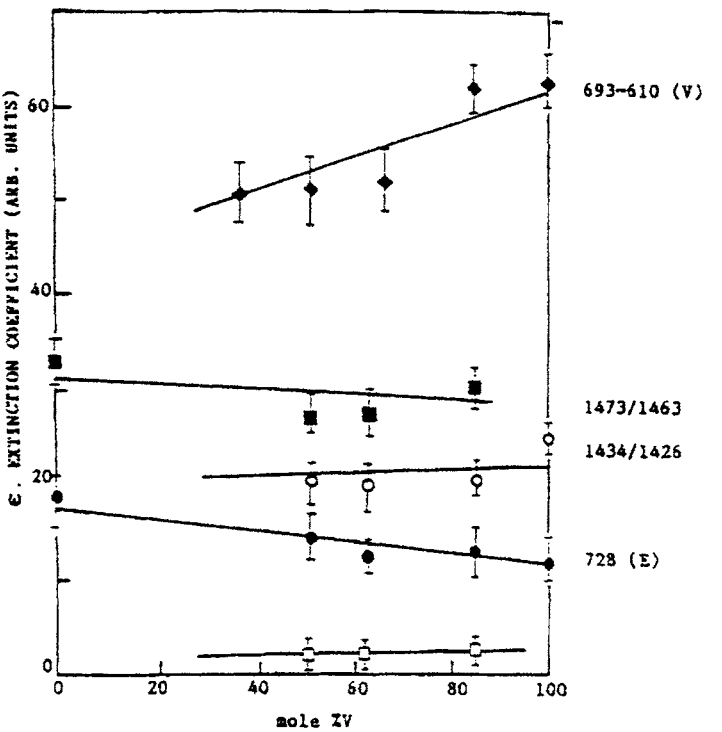

Fig. 4.14. Extinction coefficients for several absorption bands of the E-V copolymer as a function of concentration of V.

The ideal method of determining the spectral differences resulting from syndiotactic or isotactic structures is to prepare the two sterically pure polymers and compare their spectra. Unfortunately, there are few polymers for which the two pure stereoisomers have been prepared. For poly(methyl methacrylate), the spectra of the syndiotactic and isotactic polymers have been reported [10], and the spectra are shown in Fig. 4.15. The frequency differences and the structural assignments are listed in Table 4.3. Similar results have been obtained for polystyrene [11].

Poly(vinyl chloride) has been studied frequently with FTIR spectroscopy because its IR spectrum contains a great deal of information about the configurational and conformational content of the sample (the next section gives definitions of these terms). The vibrations are usually studied by using the C−Cl bonds because they show the greatest sensitivity to the different structural features. The notation developed [12] directly specifies the local tacticity required for a given environment of a C−Cl bond. The notation specifies the environment by the symbol S (implying secondary chloride) with two subscripts, which may be either C or H, to specify the atom trans to the Cl atom across the two neighboring C−C bonds. The symbol S_{HH} is reserved for planar zig-zag structures at least five carbon atoms

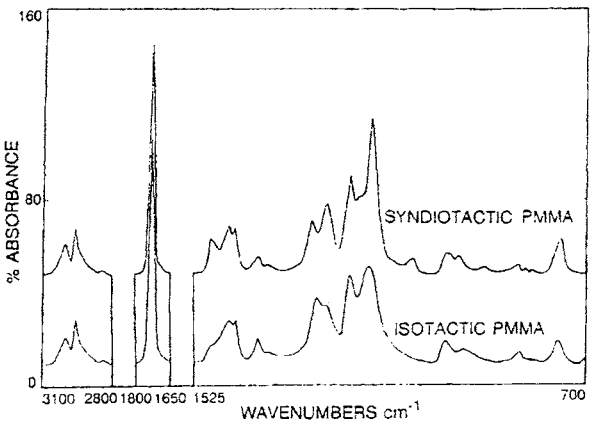

Fig. 4.15. IR spectra of isotactic and syndiotactic poly(methyl methacrylate). (Source: Ref. [10]; © 1981 American Chemical Society.)

Table 4.3
The frequency differences and assignments for poly(methyl methacrylate) for the spectra of syndiotactic and isotactic polymers

Isotactic	Syndiotactic	Assignment
2995		ν(C−H)
2948		ν(C−H)
1750		ν(C=O)
	1485	$\delta_a(\alpha-CH)$
1465	1450	$\delta(CH_2)$, $\delta_a(CH_3-O)$
	1438	$\delta_a(CH_3-O)$
	1388	$\delta_s(\alpha-CH_3)$
	1270	$\delta_s(\alpha-CH_3)$
1260		ν_a(C−C−O)
1252		coupled with
	1240	ν(C−O)
1190	1190	skeletal
1150	1150	
996	998	$\gamma_r(CH_3-O)$
950	967	$\gamma_r(\alpha-CH_3)$
759	749	$\gamma(CH_3)$ + skeletal

long, with the chlorine atom under consideration on carbon atom 3. The symbol S_{HH} reflects nonplanar structures in which the chain bend occurs at carbon atom 2 or 4. From a study of model compounds, the following ranges of frequencies for C−Cl bonds were established: S_{HH}, 608–616 cm^{-1}; S'_{HH}, 627–637 cm^{-1}; $S_{CH'}$, 655–674 cm^{-1}.

The vibration of each C−Cl bond would be expected to depend on the configuration and conformation of the chain on either side of the bond. On this basis, the C−Cl bond can be considered the center of a triad which might be syndiotactic (s),

isotactic (i), or heterotactic (h). Each of these stereoisomers may have more than one rotational isomeric form. Spectral assignments for PVC are given in the following table [13]:

Conformational assignment	Spectral assignments for PVC		
	Peak (cm^{-1})	Isomer	Conformation
TTTT long sequences	602	s	S_{HH}
TTT short sequences	619	s	S_{HH}
TTTT long sequences	639	s	S_{HH}
TTTG syndiotactic	651	s	S'_{HH}
TG*G* syndiotactic	676	s	S_{HC}
TGTG isotactic	697	i	S_{HC}

(Reproduced with permission from Ref. [13]; © 1986 Society for Applied Spectroscopy.)

The assignment of bands to the stereoisomers encourages their use in semiquantitative measurements of differences in the stereoregularity of polymers. Although the validity of such measurements has been questioned, they are nevertheless playing an increasing role in the study of stereospecific polymerization.

Measurement of conformation

The relative geometric arrangement of the chemical groups along the polymer chain, that is, the conformation of the chain is also of interest. In the polymer literature, the terms *configuration* and *conformation* are often used in quite different contexts, but sometimes they are used interchangeably.

> *The term 'configuration' is used for describing an arrangement of atoms that cannot be altered by mere rotation of groups or atoms around single bonds. Configuration is determined during the polymerization process and cannot be altered except by breaking chemical bonds and forming new ones... On the other hand, 'conformation' refers to the relative steric arrangement of atoms or groups that can be altered by rotation of the atoms or groups around a single bond. For example, conformation includes the trans and gauche arrangements of consecutive C−C single bonds and the helical arrangement of several polymers in the crystalline state.* — H. Tadokoro

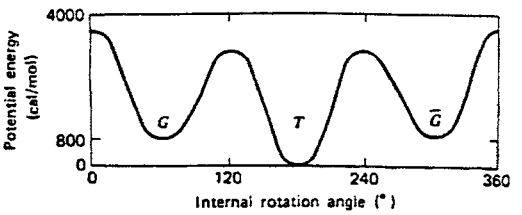

Fig. 4.16. Potential energy curve for internal rotation about the C−C bond of butane. (Source: H. Tadokoro, Structure of Crystalline Polymers. Wiley-Interscience. New York, NY, 1979, pp. 9–10; reproduced with permission from Wiley-Interscience.)

A Nobel Prize winning polymer scientist has the following to say about these two terms:

> *The class of configurations which are generated by executing rotations about single bonds of a molecule often are referred to as conformations. These two terms, configuration and conformation will be used somewhat interchangeably, in keeping with their dictionary definitions and broader usage, with only a minor difference in connotation.*[1] — P.J. Flory

Strong differences of opinion exist. Like Flory, we will use the terms *configuration* and conformation interchangeably and, as in the previous section, the term *stereoconfiguration* will be used for stereochemical systems. The terminology can be made simpler if the isomers are termed *rotamers* when the system under consideration consists of one or more stable isomers resulting from the rotation about a single chemical bond of one or more molecular units.

Polymer chains have a number of possible rotational isomers, depending on the temperature and thermal history of the sample. Rotational potentials for single bonds joining chemical groups such as methylene units are necessarily threefold and symmetric (Fig. 4.16) [14] The energy minima occur when the substituents of the groups, hydrogens in this case, are in the staggered conformations, but maxima occur at the eclipsed conformations. In molecules possessing C−C bonds, the rotation angle values near the potential minima are strongly favored over those near the maxima. However, rapid interconversion is possible among the various forms.

The *trans* form is a staggered conformation in which the internal rotation angle X−C−C−X is 180°. There are two types of *gauche* isomers with an internal angle

[1] *The term conformation connotes form and a symmetrical arrangement of parts. The alternative term, configuration, is perhaps the more general of the two in referring to the disposition of the parts of the object in question without regard for shape and symmetry. Our usage of the latter term may at times violate conventions of organic chemists, who presume to designate the stereochemical arrangement of atoms or groups about the structural element of optical asymmetry in the molecule... Confusion with configuration about an asymmetric center of the kind associated with optical rotation can easily be avoided by use of an appropriate prefix such as stereochemical.*

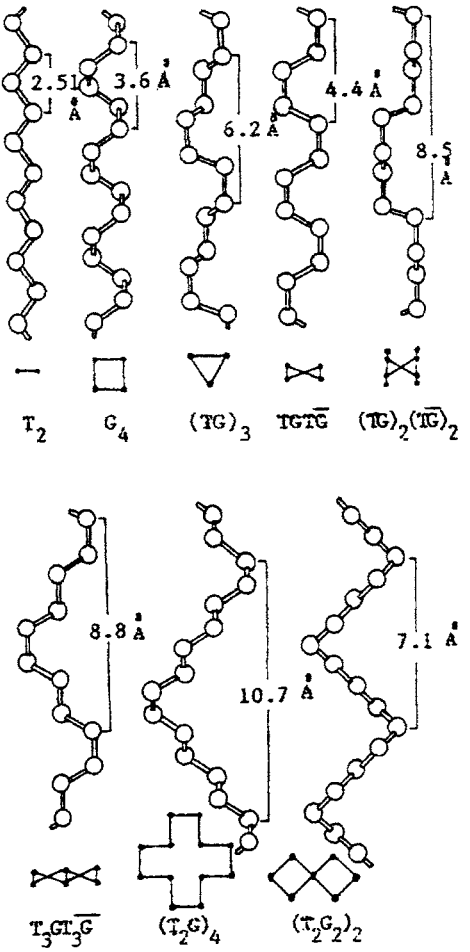

Fig. 4.17. Several possible conformations of a single-bonded carbon chain. (Source: H. Tadokoro, Structure of Crystalline Polymers. Wiley-Interscience. New York, NY, 1979, pp. 9–10; reproduced with permission from Wiley-Interscience.)

of 60°, as shown in Fig. 4.16 [14]. The *cis* conformation of the gauche isomer corresponds to the internal rotation angle of 60° and is the least stable form. Several possible conformations of single-bonded carbon chains can result from these structures, as shown in Fig. 4.17 [14]. The simplest conformation is the planar zigzag (all trans) structure, as exhibited by polyethylene in the crystalline state. A chain of all gauche structures leads to left- or right-handed helices, as in poly(oxymethylene). This discussion has been limited to only two carbon atoms and, of course, more complicated systems give rise to more conformational possibilities. Polymers generally have several different conformations in the solid state depending on their thermal history.

In the crystalline state, the regular structure results in a repeating polymer conformation. This repeating conformation is usually determined by X-ray or electron diffraction methods, but for amorphous and glassy polymers, these diffraction methods are not applicable. Vibrational spectroscopic methods are useful because the vibrational modes are sensitive to differences in internal bond angles. When the polymer chains exhibit extended order, specific vibrational selection rules apply, and these rules can be used to determine the conformation of the isomer [14] as shown in Chapter 3.

In the disordered state, the polymer chain exists in a variety of conformations consisting of combinations of the various rotamers available to the chain. As stated in Chapter 1, it is not possible to determine the position of the atoms in space because there are far too many variations; rather, average values of the isomeric composition can be obtained.

To study rotational isomerism in polymers, the spectroscopic technique must be able to distinguish the spectral features of each identifiable conformer. The vibrational spectrum of a mixture of conformers will exhibit bands arising from the molecular vibrations of all conformers. In general, the conformer bands in a polymer system are observed in pairs that correspond to modes of similar form but slightly different frequencies in the high- and low-energy conformers. When the spectra are obtained as a function of temperature, pairs of bands with one band intensity increasing and the other band intensity decreasing will often be observed. For polymers, there is usually considerable overlap of these band pairs.

Polyethylene (PE) is the most-studied example of rotational isomerism. The crystalline domains are made up of the all-trans conformer structure. Bands that are characteristic of rotamers in the amorphous phase are also present. The most intense of the amorphous absorptions are the methylene wagging modes at 1303, 1353 and 1369 cm^{-1}. The TG conformation is correlated with the bands observed at 1303 and 1369 cm^{-1}. The 1353-cm^{-1} absorption band is assigned to the wagging of the GG structure. When PE is heated through its melting point, the concentration of the TG and GG conformations increases. However, the concentration of the TG conformation increases well below the melting point, and this increase indicates the formation of localized conformational defects in the crystalline polymer.

One method of studying conformations is to selectively substitute deuterium and examine the vibrations of the C−D bonds. When isolated CD_2 groups are chemically substituted in PE, bands at 622 cm^{-1}, which are associated with the rocking mode of an isolated CD_2 group with trans adjacent dihedral angles, are observed. These bands are TT bands. The band observed at 650 cm^{-1} is associated with the isolated CD in the TG structure [15]. Using this topological deuteration approach has made studies of surface melting of stearic acid and *n*-nonadecane [16]. For stearic acid, a premelting process consisting of a conformational disordering of the molecule at either end of the alkyl chain takes place at approximately 7°C below the melting point, and it generates a disorder at the interface between the molecular layers. Such

surface melting coexists with surface domains of ordered material. The longitudinal diffusion process for the chain occurs by a 'conformational soliton' or 'twiston' process.

A problem with these IR techniques is the difficulty in isolating the spectra of each of the 'pure' rotational isomers in the disordered phase. Because there will never be a model polymer of only one rotational isomer, the spectra of the pure isomers must be deconvoluted from the spectra of mixtures containing different amounts of the rotational isomers. Even the preferred isomer found in the crystalline state is contaminated because a polymer sample is never 100% crystalline. The usual procedure is to use spectral subtraction or the ratio method to isolate the spectra of the rotational isomers. Both of these methods have been used in studies of poly(ethylene terephthalate) (PET) [17]. The results of the determination of the spectra of the trans and gauche isomers of PET by using the ratio method were demonstrated in Chapter 3.

Another requirement of the spectroscopic technique for the study of rotamers is the ability to quantitatively measure the concentration of each of the two or more conformers. After the 'pure' spectra have been obtained, least-squares curve fitting can be applied to the mixture spectra to obtain the rotational isomeric composition of the sample. The results for PET that has been annealed at various temperatures are shown in Fig. 4.18 [18].

The conformational structures of polymer melts and solutions are also of interest. Studies of the spectra of molten isotactic polypropylene (PP) have yielded some interesting results [19]. Separation of the spectral components of the ordered and disordered phases permits an accurate determination of the frequencies of the vibrational modes of the polymer chain in the preferred conformation. The amorphous component is determined by obtaining a difference spectrum of two films, one of

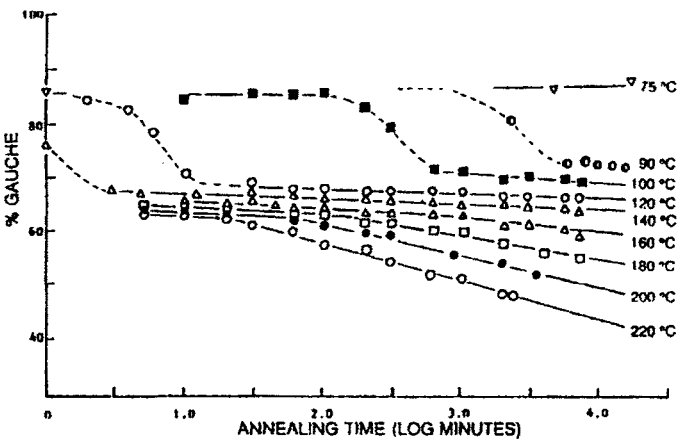

Fig. 4.18. The percent of gauche conformer in PET films as a function of annealing time. (Reproduced with permission from Ref. [18]; © 1983 John Wiley and Sons, Inc.)

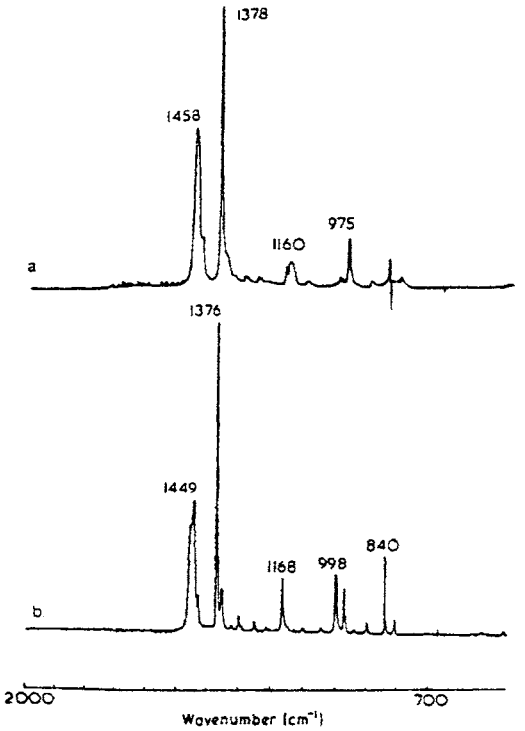

Fig. 4.19. Difference spectra characteristic of the amorphous phase of quenched isotactic polypropylene (spectrum a) and of the ordered phase of the annealed sample (spectrum b). (Reproduced with permission from Ref. [19]; © 1977 Butterworth-Heinemann, Ltd.).

which is annealed. The 'ordered' spectrum is obtained in a similar manner. The results are shown in Fig. 4.19 [20]. The ordered spectrum of isotactic PP shows sharp lines that are well resolved.

This spectrum is precisely what is expected for long lengths of polypropylene chains in the preferred conformation, which is a 3_1 helix. This spectrum might be considered to be a 'crystalline' spectrum because in most polymers such ordered chains are incorporated into a crystal lattice. However, we could detect no differences in the spectra resulting from chain packing. Therefore, we would prefer to refer to this spectrum as a 'helical' spectrum and reserve the term 'crystalline spectrum' for one that reveals intermolecular effects.

Examination of the amorphous spectrum reveals that the bands characteristic of irregular conformation sequences are broader, and a few are also considerably weaker in intensity than those in the ordered spectrum. The spectrum of PP in the melt is compared with the difference spectrum characteristic of the amorphous region in Fig. 4.20.

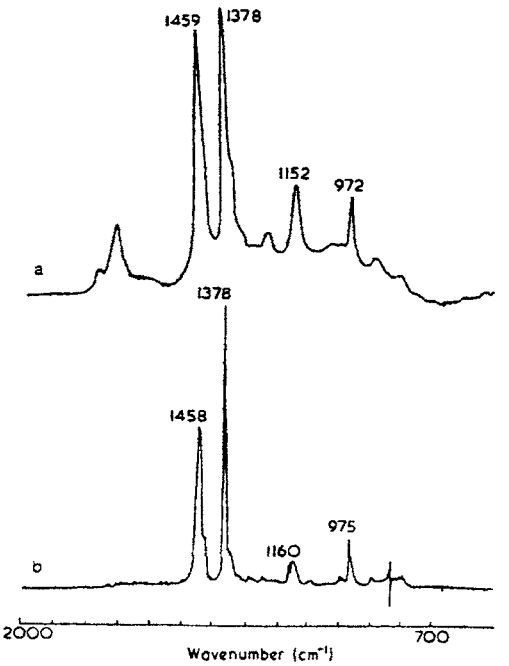

Fig. 4.20. The IR spectrum of polypropylene in the melt (a) and the difference spectrum characteristic of the amorphous phase of polypropylene (b). (Reproduced with permission from Ref. [20]; © 1977 Butterworth-Heinemann, Ltd.)

The bands in the molten spectrum resemble those in the spectrum of the amorphous region, except for the two bands in the 1700-cm^{-1} region, which are characteristic of oxidation occurring in the molten polymer. In terms of the frequencies of many of the bands, the amorphous spectrum is intermediate between the spectrum of the melt and the spectrum of the helical chains. These results indicate that there are helical polymer chain segments in the amorphous phase. The molten spectrum can also be interpreted in terms of residual helical segments occurring in the melt.

The tacticity of PP has been measured by FTIR using the peak at ~1000 cm^{-1} which is sensitive to isotactic helices and ratioing to the internal standard peak ~1170 cm^{-1}. A linear correlation was made with NMR tacticity measurements [21].

Measurement of branching in polymers

One of the most important structural elements of polymers is the nature of the branches or side chains. This subject is particularly important for crystalline polymers, because branches disrupt the crystalline order. It is important not only to establish the number and distribution of branches along the chain but also to determine their distribution between amorphous, interfacial, and crystalline phases and to

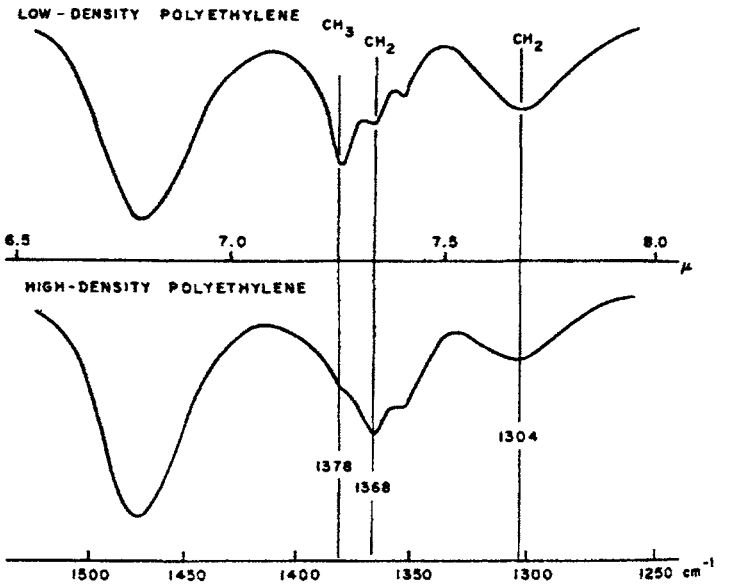

Fig. 4.21. IR spectra of low- and high-density polyethylene in the 1500–1250-cm^{-1} region. (Reproduced with permission from Ref. [22, p. 63]; © 1982 John Wiley and Sons, Inc.)

characterize the degree of disorder introduced into the crystal by their incorporation.

Either a low-pressure catalyzed polymerization or a high-pressure polymerization can make polyethylene (PE). The low-pressure process yields an essentially linear PE chain, and the high-pressure process yields a polymer with a number of short-chain branches, including ethyl and butyl branches, and occasional long-chain branches. PE has been studied extensively by using IR methods, and most commercial lots of PE have a reported branch content that was determined by IR analysis. The spectra of a low-density (branched) and a high-density (unbranched) PE in the region of interest are shown in Fig. 4.21.

The band at 1378 cm^{-1} is due to the methyl capped branches. Unfortunately, the methyl band at 1378 cm^{-1} is badly overlapped by three interfering bands at 1304, 1352 and 1368 cm^{-1} that result from amorphous methylenes. The interference band at 1368 cm^{-1} is particularly strong. By using the spectrum of a linear polymethylene standard, it is possible to obtain a difference spectrum that isolates the 1378-cm^{-1} band of the methyl branch for measurement of its absorbance.

The intensity of the 1378-cm^{-1} band reflects the methyl group concentration. A major complication arises with the IR technique because the absorbances of the methyl groups on the ends of the ethyl branches are greater than the absorbances of methyl groups attached to longer pendant alkyl groups. The differences in the absorptivities of the methyl groups in going from methyl to ethyl to longer branch lengths are 1.55 : 1.25 : 1, respectively [22]. Unfortunately, with an ordinary PE sample it is not possible to separate these absorptivity differences, so the measured absorbance

Table 4.4
Integrated absorptivities and band positions for various branched copolymers

Branch type	Band position (cm^{-1})	Integrated absorptivity (1000C/branch × mm)
Methyl	935	0.049
Ethyl	770	0.649
Butyl	894	0.166
Hexyl	889	0.065
Isobutyl	920	0.317

(Source: J.P. Blitz, PSME Preprints 75 (1996) 65.)

of the 1378-cm^{-1} band is a weighted average of the different branch lengths in PE. As a result, the calculated methyl branch content is not accurate, but it is a scale with which to compare PE samples from similar sources. It is possible to identify the various types of branches and make their measurement. The integrated absorptivities and band positions for copolymers of polyethylene having specific branch lengths are given in Table 4.4.

When an absolute number of the different types of branches is sought, high-resolution solution NMR spectroscopy must be used, as will be discussed in Chapter 8. In practical terms, it is too expensive to use high-resolution NMR spectroscopy for every sample of PE, so the IR scale of branching in PE is accepted and is widely used by manufactures and consumers alike.

Characterization of polymer blends

Polymer blends are used for a variety of reasons. The principal motivation is to enhance the properties of the individual homopolymers in the blend. However, the polymers must be compatible, which means that they must form stable mixtures at the molecular level. The behavior of polymer blends depends, in general, on the degree of mixing of the components and their mutual interaction, as well as on the individual properties of the components. Most pairs of polymers are not miscible on a molecular level, and, in the majority of cases, the mixing of two polymers results in phase separation. Such phase-separated systems exhibit poor mechanical properties. The presence of one polymer in the other polymer phase is commonly demonstrated by experimental observations of the glass transition temperature, T_g, of the coexisting phases. The T_g of one component will be displaced in the direction of the T_g of the second component. For amorphous polymer blends, only a single T_g is observed.

When compatible polymer blends are prepared, the important information is the nature of the interactions leading to compatibility, the reproducibility of the blend interactions, and the changes induced in the interactions with time and temperature after blending. Although a number of methods have been used to establish the

compatibility of blends (e.g., thermoanalysis and NMR spectroscopy), none of the techniques are conducive to rapid analysis of the kinetics of the phase separation process. However, FTIR spectroscopy can be used to establish the nature and level of molecular interactions of blends and the changes in these interactions with aging. From an IR point of view, compatibility of a blend is defined in terms of the presence of a detectable 'interaction' spectrum that arises when the spectrum of the blend is compared to the spectra of the two homopolymers. If the homopolymers are compatible, an interaction spectrum with frequency shifts and intensity modifications that are intrinsic to the system will be observed. If the homopolymers are incompatible, the spectrum of the blend is simply the spectral sum, within experimental error, of the spectra of the two homopolymers.

Factor analysis can be used as a quantitative method to establish the existence of a measurable interaction spectrum [23]. To determine whether the interaction spectrum is a contributing factor to the spectrum of the blend, a series of polymer blends with different volume fractions of each homopolymer is prepared, and the spectrum of each blend is obtained. The number of components present in these blend spectra is then determined by factor analysis. In the case of compatible blends, three components are expected, but for incompatible blends, only two should be observed.

The blends of poly(vinylidene fluoride) (PVF_2)-poly(vinyl acetate) (PVAc) have been studied [24] as a function of composition and temperature during solvent evaporation. Factor analysis was performed on PVF_2-PVAc blends that were heat treated at 75 and 175°C. The minimum indicator function values for both blends correspond to a three-component system, a result indicating that both blends are compatible.

The interaction spectrum was generated by a double subtraction of the spectra of the two homopolymers from the spectrum of the blend. An example of such a subtraction for a 50 : 50 PVF_2-PVAc blend that was heat treated at 75°C is illustrated in Fig. 4.22.

The interaction spectrum shows substantial interaction between the two homopolymers in the blend, as reflected by the shifts in frequencies and intensities. The interaction spectra of several compositions of the PVF_2-PVAc blends that were heat treated at 75 and at 175°C are shown in Figs. 4.23 and 4.24, respectively.

Quantification of changes in the degree of interaction in the blends as a function of blend composition and heat-treatment temperature was determined by the least-squares curve fitting method. The three spectral contributions used in this curve-fitting technique were the spectra of the two homopolymers and the interaction spectrum. In Fig. 4.25, the contribution of the interaction spectrum is shown as a function of weight percent PVF_2 for PVF_2-PVAc blends that were heat treated at 75 and 175°C. As expected, the magnitude of the interaction changes with composition.

Aging studies were performed to monitor changes in the compatibility of these blends with time. As shown in Tables 4.5 and 4.6, the largest changes in the magnitude of the interaction occur during the early stages of aging.

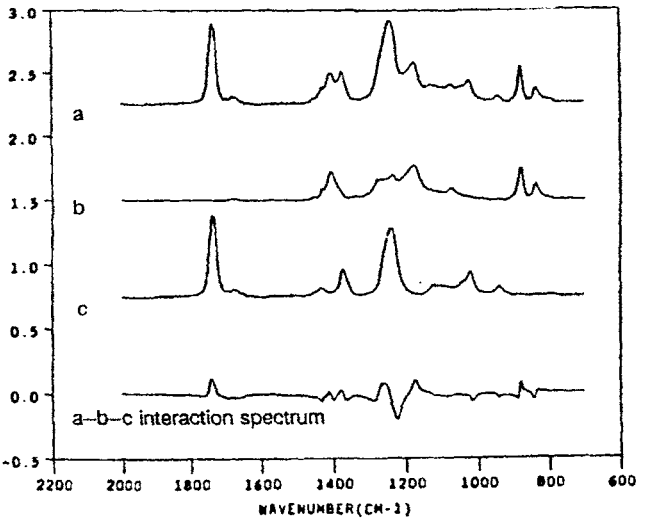

Fig. 4.22. FTIR transmission spectra of 50:50 PVF_2-PVAc (a), PVF_2 (b), PVAc (c), and the interaction spectrum of the 50:50 PVF_2-PVAC blend obtained from the subtraction a – b – c. The spectra were collected immediately after heat treatment at 75°C for 1 h. (Source: Ref. [24].)

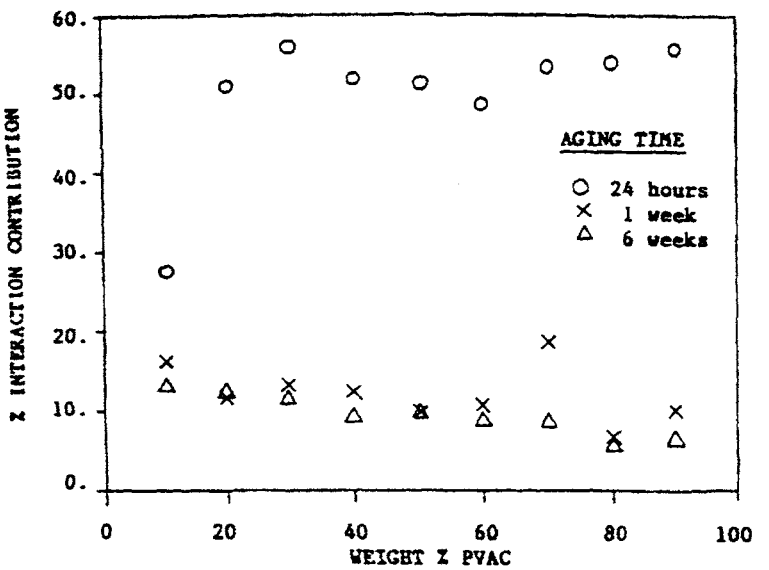

Fig. 4.23. Interaction spectra of PVF_2-PVAc blends obtained immediately after heat treatment at 75°C for 1 h. Spectra were collected for blends having weight percent ratios of 10:90 to 90:10 PVF_2-PVAc. (Source: Ref. [24].)

The most IR-observable effect of molecular interactions in blends occurs when the two components hydrogen bond with each other [25]. An example is given in Fig. 4.26, which shows the IR spectra of poly(vinyl phenol) (PVPh)-PVAc blends

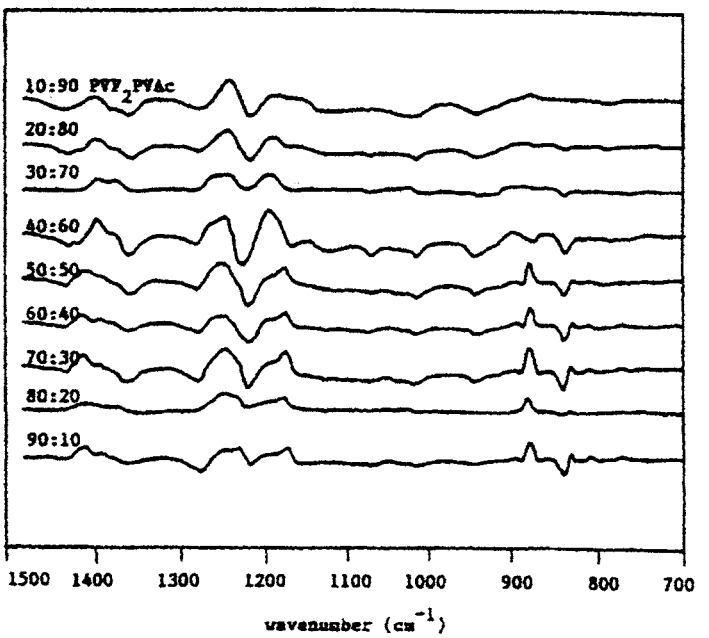

Fig. 4.24. Interaction spectra of PVF_2-PVAc blends heat treated at 175°C. (Source: Ref. [24].)

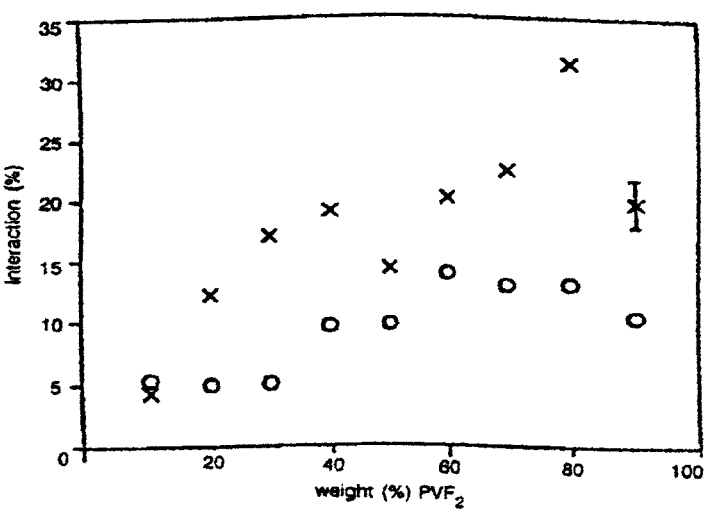

Fig. 4.25. Plot of the percent contribution of the interaction spectrum vs. weight percent PVF_2 for PVF_2-PVAc blends heat treated at 75°C (○) and 175°C (×). (Source: Ref. [24].)

that were cast from tetrahydrofuran (THF) and that contain different amounts of PVAc in the regions from 3800 to 3000 cm^{-1} and from 1800 to 1650 cm^{-1} recorded at room temperature [27]. In this case, the carbonyl and hydrogen bonding IR regions have large spectral differences. Frequency shifts and changes in band inten-

Table 4.5
Interaction contribution (aging time) of PVF_2-PVAc blends heat treated at 75°C

PVF_2-PVAc (wt%)	Time						
	0 h	8 h	16 h	24 h	2 days	7 days	24 days
10:90	5.29	4.43	5.02	4.34	3.87	4.19	4.12
20:80	4.92	3.41	4.11	3.19	2.85	3.21	2.89
30:70	5.04	5.25	6.64	5.40	4.89	5.95	4.96
40:60	9.55	8.35	9.91	7.55	7.48	7.52	6.43
50:50	9.67	8.70	9.56	9.89	8.28	7.93	8.57
60:40	13.89	14.01	12.89	14.88	13.08	12.35	11.44
70:30	12.94	11.90	12.05	13.48	10.98	11.13	9.57
80:20	13.06	12.20	12.25	11.34	11.44	11.59	10.61
90:10	10.36	10.23	9.86	9.12	11.08	9.95	11.37

Note: Experimental error ±2%.

Table 4.6
Interaction contribution (aging time) of PVF_2-PVAc blends heat treated at 175°C

PVF_2-PVAc (wt%)	Time						
	0 h	8 h	16 h	24 h	2 days	7 days	24 days
10:90	4.27	6.81	6.58	4.83	4.49	4.60	5.87
20:80	12.20	14.63	12.65	11.91	12.03	13.01	10.03
30:70	17.05	18.56	15.76	16.88	15.16	13.73	17.12
40:60	19.05	22.27	20.43	20.36	18.84	16.92	19.01
50:50	14.27	14.64	15.79	15.83	14.49	15.35	15.22
60:40	20.10	20.57	20.77	20.81	19.45	19.54	23.00
70:30	22.51	25.00	23.04	22.98	18.76	21.17	21.05
80:20	31.33	28.72	24.94	28.41	29.21	28.95	29.18
90:10	19.80	21.96	16.00	22.52	24.16	24.10	22.58

Note: Experimental error ±2%.

sities show molecular interactions resulting from hydrogen bonding between the chains.

An interesting method of forcing two polymers that do not exhibit hydrogen bonding between each other to be compatible is to introduce into one of the systems a small amount of comonomer that can hydrogen bond and that can act as the chemical link between the polymer chains [26]. The spectra of the styrene (92%)–acrylic acid copolymer, the 89% styrene–acrylic acid (SAAS)–poly(methyl methacrylate) (PMMA) blend (4 : 1), and the interaction spectrum obtained after double subtraction are shown in Fig. 4.27. Hydrogen bonding has been introduced in the blends to make these two polymers compatible.

A note of caution must be inserted here. Allara [27] theoretically investigated the effects of the refractive indices of the component polymers on the IR band shapes associated with strongly absorbing groups. Residual peaks can arise purely

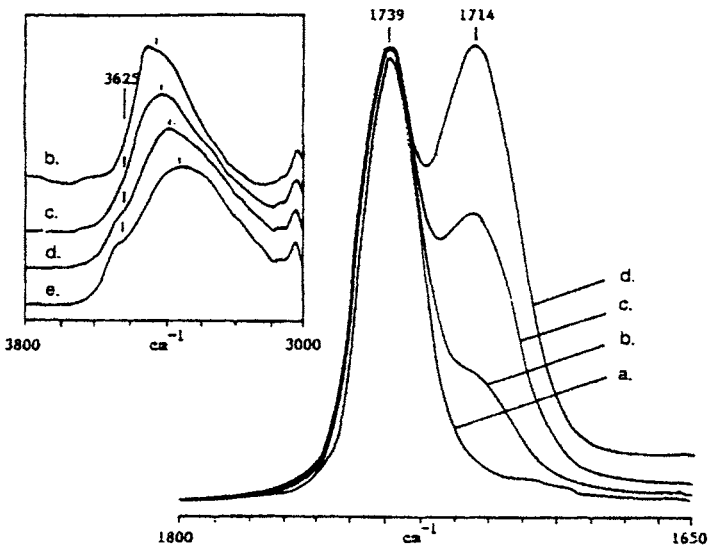

Fig. 4.26. The IR spectra in the regions of 3800 and 1800–1650 cm^{-1} recorded at room temperature of PVPh-PVAc blends cast from THF containing 100 (a), 80 (b), 50 (c), 20 (d), and 0 (e) wt% PVAc. (Reproduced with permission form Ref. [25]; © 1984 Society for Applied Spectroscopy.)

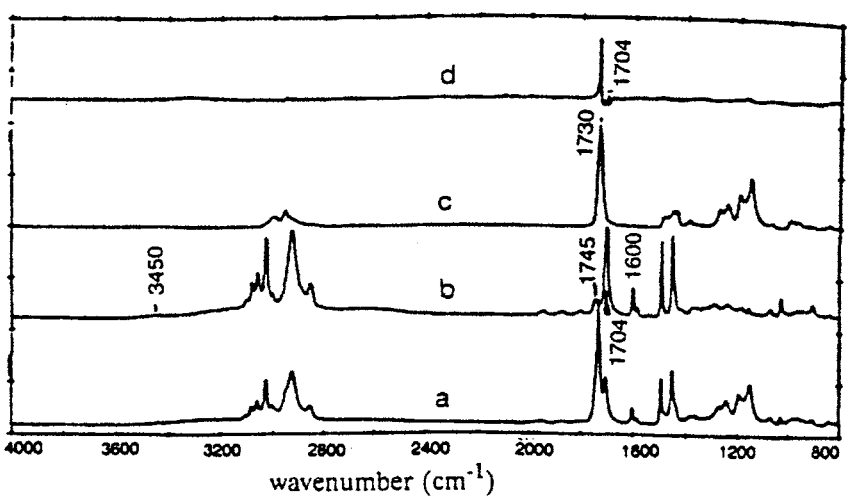

Fig. 4.27. The IR spectra of SAAS-PMMA (4:1) blend (a), pure SAAS (b), pure PMMA (c), and the interaction spectrum (a – b – c). (Reproduced with permission from Ref. [26]; © 1989 John Wiley and Sons, Inc.)

from optical dispersion effects. These residual peaks shift from the absorption peak center in both positive and negative directions with varying intensities. Consider a 10:90 blend of two polymers, A (with a strong absorption band) and B, with refractive indices of 1.5 and 1.4, respectively. Optical dispersion effects will result

in the presence of a large positive peak that has an intensity of about 4% of that of the main blend peak and that is located 12 cm^{-1} from the main blend peak. The higher the concentration of A in the blend or the smaller the difference in refractive index between A and B, the smaller the residual peaks will be. Therefore, it is necessary to recognize whether the observed spectral differences are purely optical artifacts or whether they instead reflect the true intermolecular interactions between the component polymers.

Deformation of polymer systems

The strength properties of synthetic polymers are considerably enhanced by molecular orientation. Therefore, it is desirable to determine the relationship between the molecular orientation and the strength properties. The characterization of orientation effects is difficult because of the multiphase nature of most oriented engineering thermoplastics. For example, X-ray diffraction is an excellent method for determining the orientation of the crystalline regions of the polymer, but it contributes nothing to the knowledge of the disordered or amorphous regions. IR spectroscopy is a particularly useful tool for orientation studies when specific bands from each phase are observed. For this case, IR spectroscopy can reveal the orientation of each of the individual phases. IR spectroscopy is also useful for determining 'internal' orientation, that is, the differences in orientation of the flexible functional groups attached to the polymer chain.

Dichroic IR measurements of orientation in polymers

In general, IR absorption is caused by the interaction between the IR electric field vector and the molecular dipole transition moments related to the molecular vibrations. Absorption is at a maximum when the electric field vector and the dipole transition moment are parallel to each other. In the case of perpendicular orientation, the absorption is zero. Directional absorptions $A_\perp$ and A are measured using polarized light. The terms parallel and perpendicular refer to the orientation of the polarized beam with respect to a reference axis. For deformation studies, the reference axis corresponds to the stretching direction.

The dichroic ratio may be considered to be characteristic of the directional orientation of the segments of the molecule. For a polymer whose molecular axis is oriented parallel to the spectrometer sampling plane, the dichroic ratio, R, is defined as

$$R = \frac{A}{A_\perp} \tag{4.2}$$

where A is the absorbance parallel to the chain axis, and $A_\perp$ is absorbance perpendicular to the chain axis. For highly oriented samples, the dichroic ratio may

approach either infinity or zero, depending on the alignment of the transition-moment vector with respect to the molecular chain axis. The alignment of the chain segments can be determined from dichroic ratio measurements if the inherent polarizations are known [28]. In general, $A_{\parallel}$ and $A_{\perp}$ are determined successively by using a polarizer that is aligned parallel and perpendicular to the stretching direction. For samples that have a low level of orientation, the magnitude of the dichroic ratio is close to 1. In these cases of minimal orientation, it is better to measure the dichroic difference $A_{\parallel} - A_{\perp}$ because it is a more sensitive measurement under these conditions.

Differences in internal orientation of functional groups relative to each other on the polymer chain have been demonstrated by studies of poly(acrylonitrile) [29]. The dichroic behaviors of the nitrile band at 2241 cm^{-1} and the chain methylene band at 1452 cm^{-1}, which represent the orientation of the side groups and the polymer chains, respectively, are shown in Fig. 4.28. Although there is only a small degree of

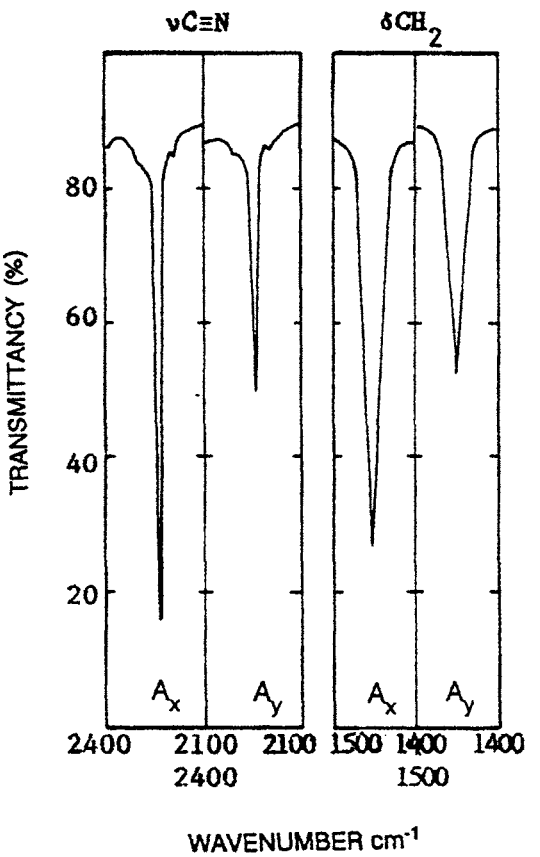

Fig. 4.28. IR dichroism of the nitrile and CH_2 absorption bands of a 3× drawn poly(acrylonitrile) film. (Reproduced with permission from Ref. [29]; © 1970 Marcel Dekker, Inc.)

orientation of the groups, a greater perpendicular alignment of the nitrile transition moments with respect to the chain axis occurs with draw.

IR dichroic measurements have also been made for drawn compatible blends of atactic polystyrene (PS)-poly(2,6-dimethyl-1,4-phenylene oxide) (PPO) [30]. The PPO and PS chains orient in a different manner when subjected to a uniaxial strain on the blend. The PPO orientational behavior does not depend on the PPO concentration, but the PS orientation increases regularly up to 25% PPO and then remains constant. The sensitivity of the orientation of PS to the concentration of PPO is thought to be a result of the hindrance by the PPO of the stress relaxation behavior of PS.

Because IR spectra can be obtained rapidly by using FTIR equipment, the deformation process can be studied while the polymer is being stretched [31]. The dichroic ratio and stress as a function of strain and time for the CH_2 rocking bands between 736 and 726 cm^{-1} and between 726 and 710 cm^{-1} are shown in Fig. 4.29. The CH_2 rocking band between 736 and 726 cm^{-1} has a transition moment that is parallel to the *a*-crystal axis, and the CH_2 rocking band between 726 and 710 cm^{-1} has a transition moment that is perpendicular to the *a*-crystal axis. Before the stretching process, the 730-cm^{-1} band exhibits parallel dichroism, indicating a preferred initial orientation of the *a*-crystal axis along the stretching direction. For small strains, the original orientation increases slightly. With the beginning of the necking process, the dichroic ratio shows the occurrence of a small rotation of the *b*-crystal axis into the

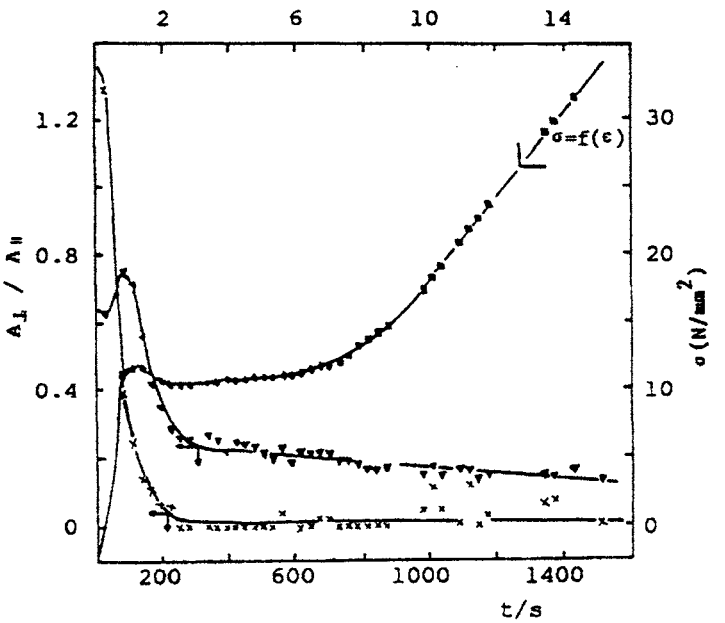

Fig. 4.29. Dichroic ratios and stress as a function of strain and time (stretching velocity) for the CH_2 rocking modes at 730 cm^{-1} (×) and at 720 cm^{-1} (○). The stress–strain diagram is given by (■). (Reproduced with permission from Ref. [31]. © 1981 Hüthig and Wepf Verlag.)

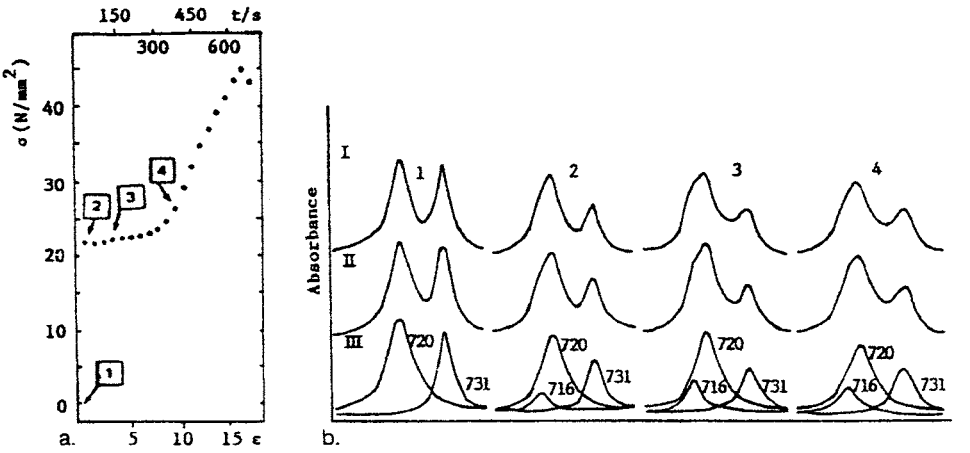

Fig. 4.30. (a) Stress–strain diagram of polyethylene with a draw rate of 0.26 mm/s. (b) Experimental (row I), synthesized (row II), and resolved (row III) bands of the CH_2 rocking modes. The experimental spectra were scanned at the indicated positions (numbers in squares) of the stress-strain diagram. (Reproduced with permission from Ref. [31]. © 1981 Hüthig and Wepf Verlag.)

stretching direction and an opposite movement of the *a* axis. There is a rotation of the *a* and *b* axes into directions perpendicular to the stretching direction when the strain is equal to draw ratios between 1 and 3.

The actual spectra from the various portions of the stress–strain curve of PE are shown in Fig. 4.30, along with the deconvolution of the observed spectra into their individual components. During the stretching process, a new band appears at 716 cm^{-1}. This shoulder is associated with the conversion of the orthorhombic PE modification to the monoclinic structure. As the draw rate is increased, the band at 716 cm^{-1} also increases. From the curve resolution, the amount of the monoclinic form produced is approximately 20% of the total integrated absorbance of the rocking bands in PE [31].

Trichroic IR measurements of orientation

In reality, many polymers have orientation with a three-dimensional character. It is therefore necessary to obtain a structure factor

$$A_0 = \tfrac{1}{3}\left[A_x + A_y + A_z\right] \tag{4.3}$$

in order to determine the relative amounts of the structural components in the sample (*A* is absorbance) in the presence of orientation. The three-dimensional orientation function can be determined by using the ratios A_x/A_0, A_y/A_0 and A_z/A_0. The method of performing such measurements has been described. In Fig. 4.31, the trichroic spectra of uniaxially drawn PET illustrate the differences in the spectra for the directions parallel, perpendicular, and through the thickness direction of the films [32].

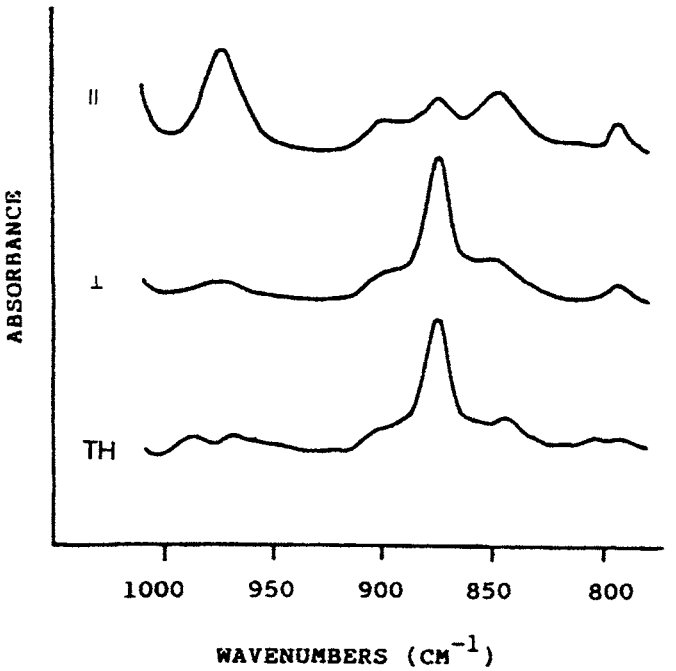

Fig. 4.31. The spectra of one-way drawn PET film in the directions parallel and perpendicular to the direction of draw and through the thickness direction of the film. (Reproduced with permission from Ref. [32]; © 1986 John Wiley and Sons, Inc.)

The isotropic IR spectra of the PET films are obtained from a linear combination of these three spectra. These calculated isotropic spectra for one-way drawn PET are shown as a function of percent elongation in Fig. 4.32 for the frequency region 800–1000 cm^{-1}.

By using the spectra of the pure gauche and trans isomers and the least-squares curve-fitting technique, the conformer composition can be determined as a function of draw ratio. The results are shown in Fig. 4.33.

The orientation parameters for the three different directions can also be calculated as a function of the percent elongation, as shown in Fig. 4.34.

When structural changes occur, the trichroic measurements will reveal frequency shifts as well as changes in relative intensities. This is the case when phase I of poly(vinylidene fluoride) (PVDF) is oriented and annealed both under stress (Fig. 4.35) and without stress (Fig. 4.36) [33].

Frequency differences can be observed at 842 cm^{-1} in the perpendicular direction and at 845 cm^{-1} in the thickness direction in the samples annealed under stress and then relaxed. Similarly, there is a difference in the frequencies at 891 cm^{-1} in the thickness direction and at 882 cm^{-1} in the perpendicular direction. The origin of these shifts has been attributed to defect structures in the phase-I lattice. Defects in the crystal lattice will occur through the introduction of gauche(+) or gauche(−) con-

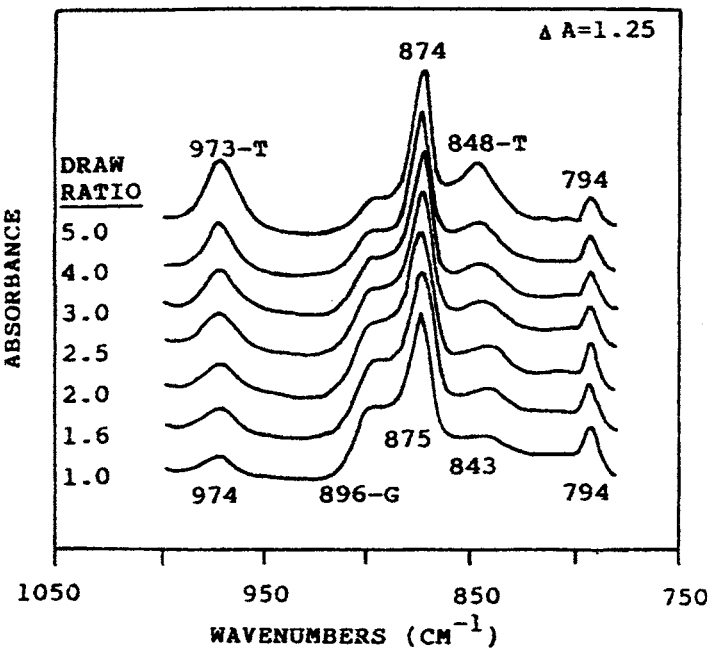

Fig. 4.32. The calculated isotropic spectra of uniaxially drawn PET as a function of percent elongation. ΔA is the absorbance range for each spectrum. (Reproduced with permission from Ref. [32]; © 1986 John Wiley and Sons, Inc.)

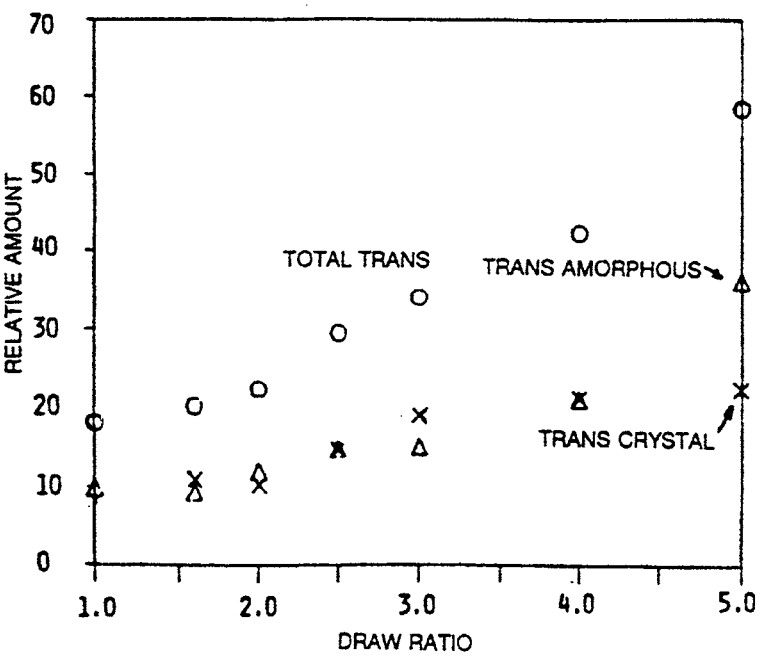

Fig. 4.33. The conformer composition of uniaxially drawn PET as a function of draw ratio. (Reproduced with permission from Ref. [32]; © 1986 John Wiley and Sons, Inc.)

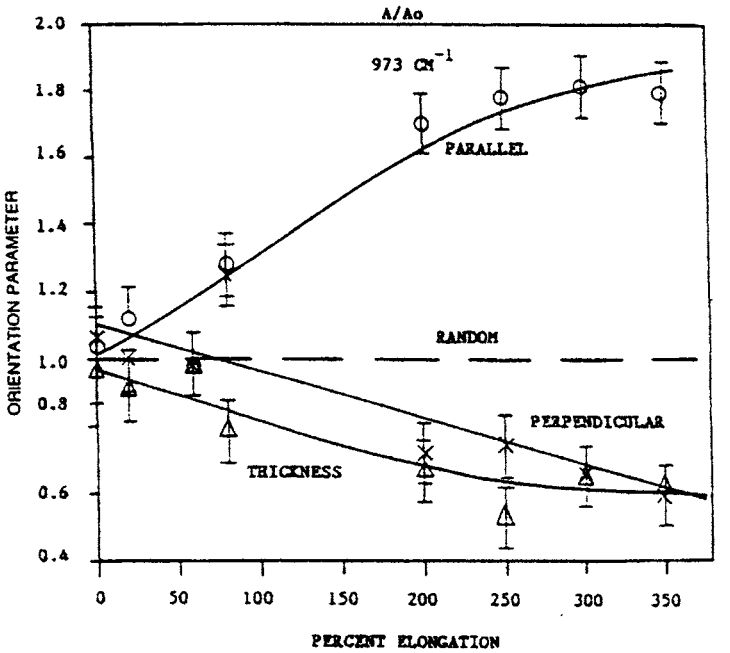

Fig. 4.34. The trichroic orientational parameters for one-way drawn PET as a function of percent elongation. (Reproduced with permission from Ref. [32]; © 1986 John Wiley and Sons, Inc.)

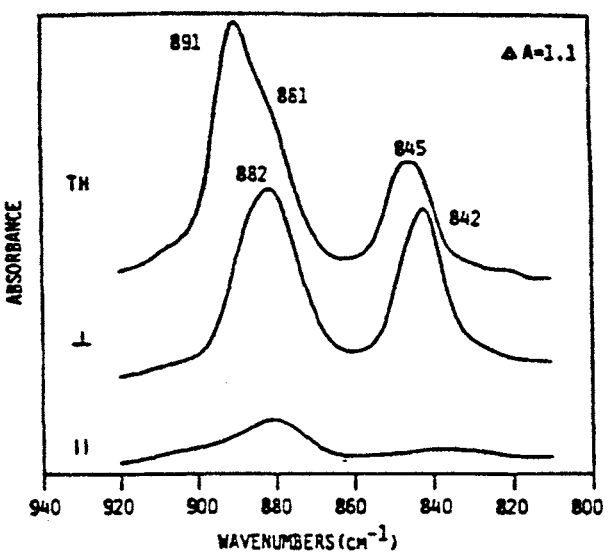

Fig. 4.35. The spectra of oriented phase-I PVDF annealed under tension. Parallel, perpendicular, and calculated thickness-direction spectra are shown. (Reproduced with permission from Ref. [33]; © 1986 John Wiley and Sons, Inc.)

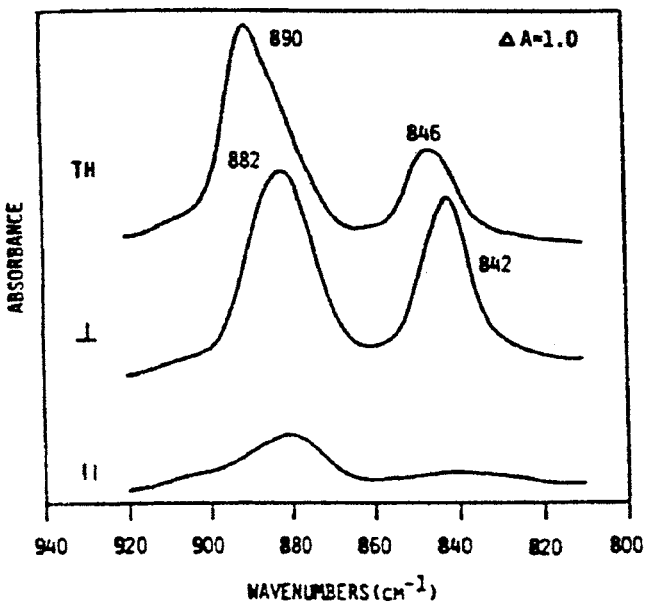

Fig. 4.36. The spectra of oriented phase-I PVDF annealed under strain relaxation. Parallel, perpendicular, and calculated thickness-direction spectra are shown. (Reproduced with permission from Ref. [33]; © 1986 John Wiley and Sons, Inc.)

formations. Nucleation of a transforming chain onto a preexisting defect-containing chain can propagate a kink in a direction-specific manner. Molecular modeling studies suggest a steric feasibility of phase-I crystals with defects aligned approximately perpendicular to the trans lattice. In essence, the vibrations of the defect regions are in register with and at a fixed and defined angle from the defect-free crystal regions. Hence, the orientation dependent frequencies of these defect bands are observed [33].

Mechanically stressed polymer systems

IR spectroscopy can be used to study the effects of applied mechanical stress on highly oriented samples. The goal is to obtain the *molecular stress distribution function*, which is an important quantity for determining the stress relaxation moduli or creep compliances. Shifts in the peak frequencies are observed and an attempt is made to determine the molecular stress distribution by deconvolution [34]. The shifts as a function of stress for the 1168-cm^{-1} band of oriented isotactic polypropylene [35] are shown in Fig. 4.37.

Stress sensitivity typically involves a small shift (0–5 cm^{-1}) to a lower frequency of the band's maximum intensity along with an asymmetric shape change of the entire band. The results are often interpreted in terms of a nonuniform distribution of external load, resulting in a nonsymmetrical displacement of the individual bond absorption frequencies. The shift appears as a linear function of stress and can be

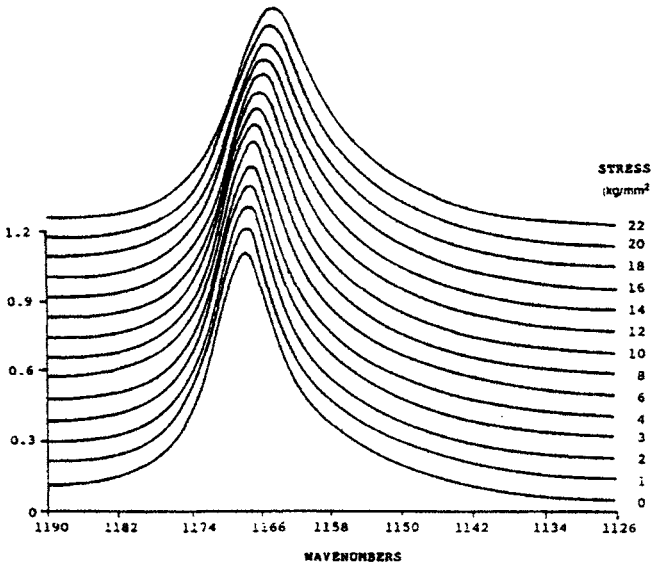

Fig. 4.37. Parallel-polarized 1168-cm^{-1} band of oriented isotactic polypropylene at successive stress levels. The average stress application rate was 0.5 (kg/mm^2)/min. The spectra were obtained at 4-cm^{-1} resolution, and the profiles of successive levels were vertically offset by 0.09 absorbance units. The peak frequency varies from 1167.72 cm^{-1} at $\sigma = 0$, to 1164.90 cm^{-1} at $\sigma = 22$ kg/mm^2. (Reproduced with permission from Ref. [35]; © 1984 John Wiley and Sons, Inc.)

expressed by

$$\Delta\nu_\sigma = \nu(\sigma) - \nu(0) = \alpha_x\sigma \tag{4.4}$$

where $\Delta\nu_\sigma$ is the mechanically induced peak frequency shift; $\nu(\sigma)$ is the frequency of the bond under a stress, σ; $\nu(0)$ is the frequency of the bond without stress; α_x is the mechanically induced frequency shifting coefficient at constant temperature, T; and σ is the applied uniaxial stress. The value of α_x is an approximate measure of the stress distribution asymmetry for a band whose IR intensity is independent of conformation and molecular environment. If the band is associated with a particular conformational isomer, variations in α_x can occur. The magnitude of a frequency shift resulting from stress depends on the draw ratio, annealing treatments, and thermal history of the sample. This dependence has been demonstrated particularly for PET [36]. There is also a threshold stress below which no shift in frequency will occur. The threshold stress effect may be related to the ability of the disordered amorphous chains to sustain the load before appreciable strains are transferred to the crystalline chains.

The vibrational frequency shifts and α_x are significantly affected by temperature. An increase in temperature is accompanied by an increase in the magnitude of the frequency shift.

For some polymers, poly(butylene terephthalate) (PBT) in particular, the application of stress leads to a nearly reversible crystalline-phase transformation. The

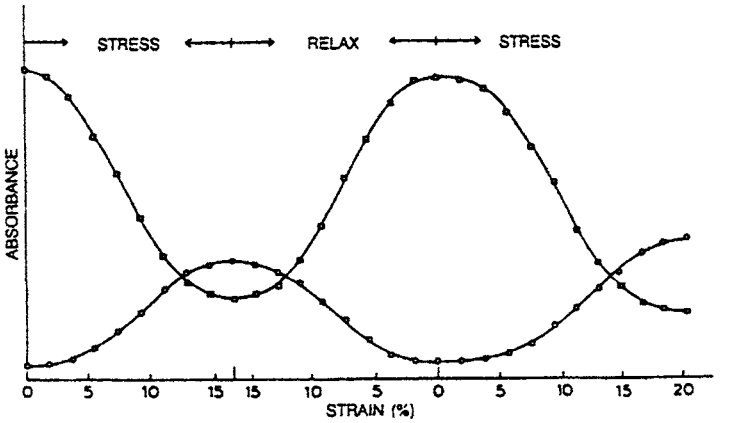

Fig. 4.38. Absorbance of the poly(butylene terephthalate) (PBT) methylene absorption of bands at 1460 (□) (relaxed form) and 1485 (○) cm^{-1} (stressed form) as a function of reversible stress and strain. The absorbances have been corrected for changes in sample thickness by using the aromatic ring band at 1510 cm^{-1} as a reference internal-thickness band. (Reproduced with permission from Ref. [37]; © 1979 Steinkopff Verlag Darmstadt.)

crystal structure of the unstressed PBT has a crumpled gauche–trans–gauche conformation of the aliphatic chain segments. Under stress, the crystal structure changes to a strained form in which the polymer chains are essentially fully extended with an all-trans sequence of aliphatic segments. The sensitivity of IR spectroscopy to this phase change arises primarily from the conformational changes of the aliphatic segments. The simplest representation of the dependence of the transformation on strain and the reversible nature of the transformation is a plot of the absorbance variations of the CH_2 modes at 1485 cm^{-1} (stressed form) and bands at 1460 cm^{-1} (relaxed form) [37] that are shown in Fig. 4.38.

The decrease in absorption that occurs at about 2–3% strain coincides with the onset of the crystalline-phase transition. The PBT system has been studied extensively because of its interesting phase transformation as well as its industrial value as a stretchable fiber for blue jeans.

Dynamic IR linear dichroism spectroscopy

Dynamic mechanical techniques are important in the characterization of the rheological properties of polymers. In dynamic mechanical analysis, a small-amplitude oscillatory strain is applied to a sample, and the resulting dynamic stress is measured as a function of time. The dynamic mechanical technique allows the simultaneous measurement of both the elastic and the viscous components of the stress response. Typically, the temperature and deformation frequencies are changed in order to determine the mechanical relaxation spectrum of the system. The molecular basis of changes in the dynamic mechanical properties can be investigated using dynamic IR dichroism.

In dynamic IR dichroism experiments, a change of the dipole transition moments of functional groups is induced by a small external time-dependent mechanical perturbation. In order to ensure a linear viscoelastic response, the oscillatory strain amplitude is typically well below 1.0%. When the perturbation is small, the time-dependent IR $A(\nu, t)$ can be written as a sum of two independent absorptions:

$$A(\nu, t) = A_s(\nu) + A_t(\nu, t) \tag{4.5}$$

where $A_s(\nu)$ is the static component due to the unperturbed sample and $A_t(\nu, t)$ describes the absorption response to the perturbation and is a measure of the dynamic absorption.

The sinusoidal strain, $\varepsilon(t)$, can be written:

$$\varepsilon(t) = \varepsilon + \varepsilon' \sin \omega_s t \tag{4.6}$$

where ε is the static strain, ε' is the strain coefficient, ω_s is the frequency, and t is the time. The time-dependent stress response to the strain, $\sigma(t)$, is given by

$$\sigma(t) = \sigma + \sigma' \sin(\omega_s t + \delta) \tag{4.7}$$

where δ is the loss angle. This dynamic stress response, $\sigma(t)$ can be separated into two orthogonal components that are in phase and quadrature ($\pi/2$ out of phase) with the dynamic strain, $\varepsilon(t)$:

$$\sigma(t) = E'\varepsilon' \sin \omega_s t + E''\varepsilon' \cos \omega_s t \tag{4.8}$$

The coefficients E' and E'' are the in-phase and quadrature components of the time-dependent stress and are referred to as the *dynamic tensile storage modulus* and *loss modulus*, respectively. They are related to the loss angle, δ, and the amplitudes of the dynamic stress and strain by

$$E' = \left(\frac{\sigma'}{\varepsilon'}\right) \cos \delta \tag{4.9}$$

and

$$E'' = \left(\frac{\sigma'}{\varepsilon'}\right) \sin \delta \tag{4.10}$$

The storage modulus, E', represents the ability of the material to elastically store the absorbed mechanical energy as potential energy. The loss modulus, E'', represents the ability to dissipate the absorbed energy as heat. The ratio between the dissipated and stored mechanical energy is referred to as the *mechanical dissipation factor.*

$$\tan \delta = \frac{E''}{E'} \tag{4.11}$$

This quantity is a convenient index for characterizing the viscoelastic state of the material because the onset of a new type of dissipation process for mechanical energy often results in a change in $\tan \delta$. This dissipation factor is used to detect various transition phenomena in polymers [38].

The polarization modulation requires a photoelastic modulator (PEM) so that the plane of the polarization of the light can alternate rapidly between two directions that are parallel and perpendicular to a fixed reference axis taken as the direction of strain. Like the stress response discussed previously, the time-dependent dichroic difference signal, $\Delta A(t)$, is written

$$\Delta A(\nu, t) = \Delta A_0(\nu) + \Delta A'[\sin \omega_s t + \beta(\nu)] \tag{4.12}$$

Because the molecular orientation is a rate-dependent process, there is an optical phase-loss angle, β, between the dynamic dichroism and the strain signals.

Like the dynamic loss, the dynamic dichroism signal can be separated into two orthogonal components:

$$\Delta A(\nu, t) = \Delta A'(\nu) \sin(\omega_s t) + \Delta A''(\nu) \cos(\omega' t) \tag{4.13}$$

Here the terms $\Delta A'(\nu)$ and $\Delta A''(\nu)$ are referred to as the in-phase spectrum and the quadrature spectrum of the dynamic IR linear dichroism, respectively. The two orthogonal spectra are related to the amplitude, $\Delta A(\nu)$, and loss angle, $\beta(\nu)$ by

$$\Delta A'(\nu) = \Delta A(\nu) \cos \beta(\nu) \tag{4.14}$$

$$\Delta A''(\nu) = \Delta A(\nu) \sin \beta(\nu) \tag{4.15}$$

The $\Delta A'(\nu)$ in-phase spectrum is proportional to the extent of instantaneous strain. The $\Delta A''(\nu)$ quadrature spectrum represents the component of reorientation proportional to the rate of strain that is out-of-phase with the strain by $\pi/2$. A *dichroic dissipation factor*

$$\tan \beta = \frac{\Delta A''}{\Delta A'} \tag{4.16}$$

is also defined in a way analogous to the mechanical dissipation factor, $\tan \delta$. Because ΔA and $\Delta A''$ are measured as a function of frequency, it is possible to compare the responses of specific functional groups to each other as well as to the macroscopic strain signal.

The dynamic spectra, $\Delta A'$ and $\Delta A''$, and the absorbance spectrum of an atactic polystyrene film [39] in the region between 1425 and 1525 cm^{-1} are shown in Fig. 4.39.

The DIRLD spectrometer used in this study was constructed around a Dynastat dynamic mechanical analyzer and dispersion IR instrument [39]. The 1490-cm^{-1} absorption band of polystyrene is assigned to the coupling of the aromatic ring and the aromatic CH deformation and is polarized in the plane of the ring perpendicular to the bond between the phenyl group and the backbone aliphatic chain. This band has a significant signal in the quadrature component that is shifted to a higher frequency, but the rest of the spectrum is nearly in phase with the applied strain. This variation in dynamic dichroism for different absorption bands suggests that some fraction of the aromatic side chains in the sample are responding to the applied strain at a rate that is different from that of the polymer backbone.

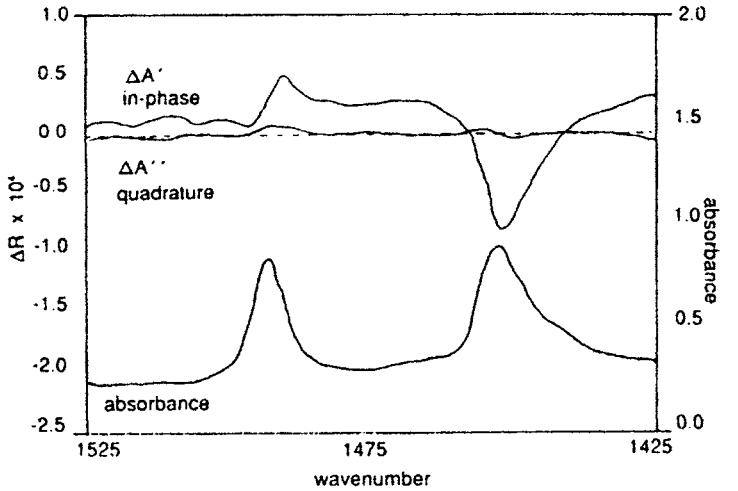

Fig. 4.39. The DIRLD spectra, $\Delta A'$ (in-phase) and $\Delta A''$ (quadrature), and the absorbance spectrum of an atactic polystyrene film in the region between 1525 and 1425 cm^{-1}. (Reproduced with permission form Ref. [39]; © 1988 Society for Applied Spectroscopy.)

Dynamic IR linear dichroism (DIRLD) studies have been made using a rapid-scan interferometer system. For dynamic strain frequencies achievable are between 0.1 Hz and 10 kHz step-scan interferometers are useful.

Recent work examined the DIRLD spectra of pre-stretched polypropylene (PP) [40,41]. The DIRLD spectra are shown in Fig. 4.40.

Spectra a and b in Fig. 4.40 represent the in-phase and quadrature spectra of i-PP prestretched four times its original length, respectively. Spectrum c is the dichroic

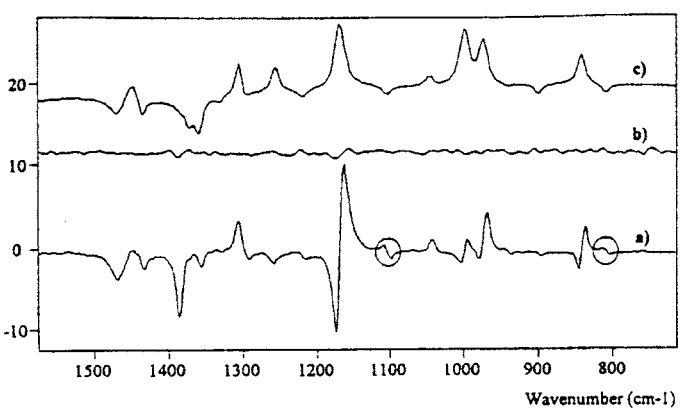

Fig. 4.40. DIRLD spectra of a prestretched I-PP sample. Collected at a stretching frequency of 20 Hz. (a) In-phase spectrum; (b) quadrature spectrum; (c) dichroic spectrum. The inversion of the sign of the dipolar bands at 809 and 1103 cm^{-1} (see the circles) relative to those of 842, 975 and 1168 cm^{-1} is due to a different dichroism. (Source: Ref [41, fig. 2].)

spectrum of the sample. Only, the in-phase spectrum exhibits measurable signals as the quadrature spectrum is essentially noise. The in-phase spectrum shows monopole bands (monopole bands show differences in absorption maxima with stress) positive and negative intensities and bipolar bands (bipolar bands which show a frequency shift in the absorption maximum with stress) at 1170, 970 and 840 cm^{-1}. These bipolar bands all show frequency shifts towards small wavenumbers with increasing stress. Frequency shifts occur when internal bond angles and bond lengths are changed in the sample with stress. The monopole bands show differences in the absorption maxima arising from changes due to change in the magnitude of the transition moment vector.

Dynamic two-dimensional IR spectroscopy

Linear dynamic perturbations of a polymer sample will generate directional changes in the transition moments of functional groups. The relaxation of this perturbation depends on the intra- or intermolecular couplings of the functional groups. DIRLD and dynamic absorbance spectra, which vary sinusoidally at a fixed frequency, are plotted as two separate spectra one with an in-phase and the other with the quadrature with respect to the applied strain. This presentation contains all of the time-resolved information about the system. However, by constructing 2D-IR correlation spectra, a cross-correlation function can be derived from time resolved DIRLD spectra over an averaging period T to obtain correlation intensities as a function of two independent wavenumbers. For a given correlation time τ, this function is uniquely specified by the two independent wavenumbers, ν_1 and ν_2. One of the benefits of 2D-IR is the improvement in resolution, which is enhanced when time-dependent responses of overlapped peaks are different. The correlations of the specific fluctuation rates of the individual dipole transition moments can be used as spectroscopic labels to differentiate the relationships between highly overlapped IR bands. This improved resolution occurs because the dynamic strain selectively perturbs the IR signals [42].

From the cross-correlation function, two types of 2D correlation spectra, synchronous and asynchronous spectra can be obtained. The synchronous spectrum shows a strong correlation intensity at wavenumber coordinates where the IR signal responses are fluctuating in phase with each other. Some peaks will be observed on the diagonal in the synchronous 2D spectrum. A peak observed along the diagonal of a synchronous 2D spectrum indicates that that particular absorbance changes as a result of the applied perturbation. In the asynchronous spectrum, a strong correlation intensity occurs where the IR signal responses are in-phase with each other.

Atactic polystyrene has been studied near its glass transition using 2D-IR [43]. Fig. 4.41a shows the time-resolved spectrum of atactic polystyrene under a 0.1% 23-Hz oscillatory strain. Fig. 4.41b shows the in-phase and quadrature DIRLD spectrum and the normal IR absorbance spectra. The IR signals in the in-phase and quadrature spectra are four orders of magnitude smaller than the normal IR ab-

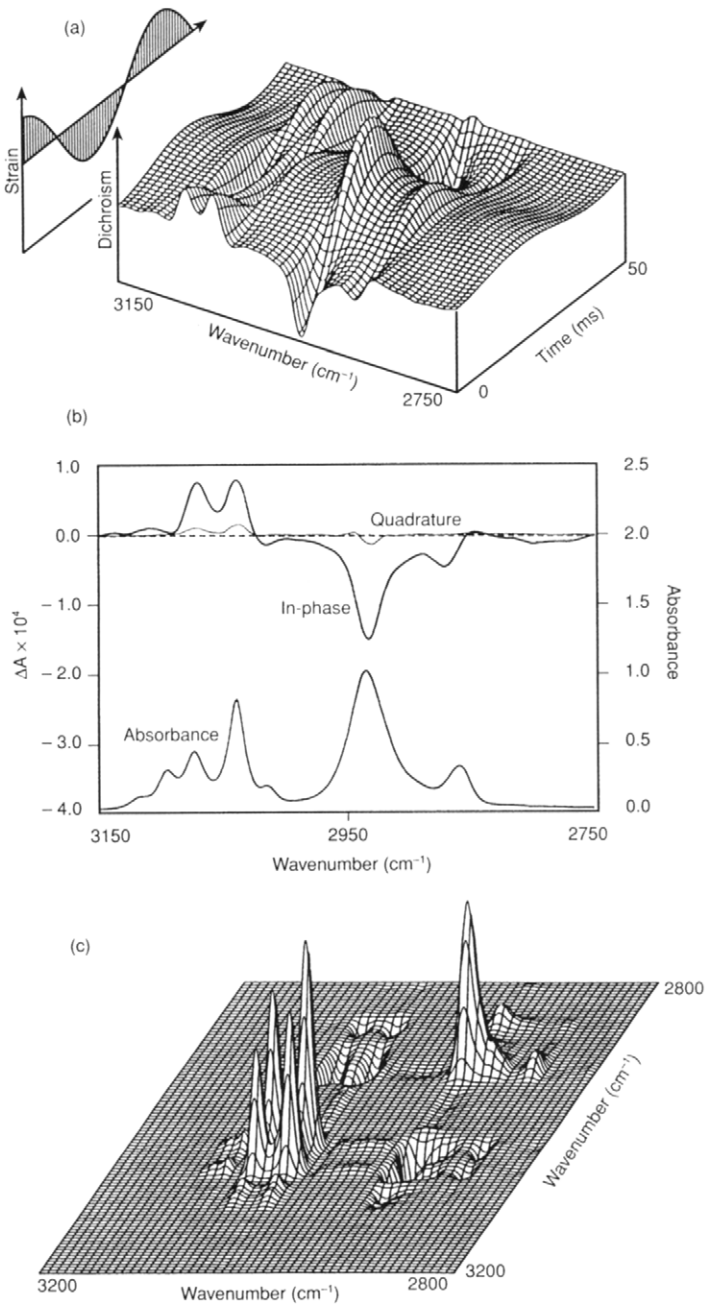

Fig. 4.41. Dynamic 2D-IR spectra of atactic polystyrene in the CH-stretching region. (a) Time resolved DIRLD spectrum. (b) In-phase and quadrature components of the DIRLD spectrum along with the normal IR absorbance spectrum. (c) Fishnet representation of the synchronous 2D-IR correlation map of the DIRLD spectrum. (Source: Ref. [43, fig. 3].)

sorbances. In Fig. 4.41c, a fishnet representation map of these data is shown. The negative in-phase DIRLD signals associated with the two CH_2 stretching modes is indicative of the polymer chains tending to align with the stretch direction with the small amplitude strain.

Dynamic 2D-IR studies were also made of atactic polystyrene at room temperature and at 125°C [44]. The in-phase dynamic dichroism signals associated with the phenyl CH-stretching vibration above 3000 cm^{-1} change from being all positive at room temperature to being entirely negative at 125°C. This result indicates that the local reorientation of some of phenyl groups is different in the glassy and rubbery states of atactic polystyrene. The spectra suggest that the reorientation mobility changes observed for the backbone CH_2 groups do not occur at precisely the same temperature as the phenyl side groups.

Polymer blend systems have been studied by dynamic 2D-IR methods by this same group. In particular, they have examined a polystyrene/polyethylene blend, a polystyrene/polytetrafluoroethylene blend and a polystyrene/poly(vinyl methyl ether) blend. Information about the sites of interaction and the relative influence of the blend components on their respective mobilities is obtained.

Measurement of morphological units in polymers

The structure and organization of the macromolecules ultimately determine the mechanical, physical, and chemical properties of polymers. In the crystalline regions, the polymer chains are highly ordered and immobile. These regions give the thermoplastic material its mechanical strength. In the amorphous layers, the polymer chains are mainly disordered and mobile. These disordered regions allow plastic deformation of the material. Thus the precise characterization of molecular order is a primary prerequisite to understanding the macroscopic properties of polymeric materials.

The crystallization conditions directly affect the structure and properties of the polymer. A knowledge of the arrangement of molecular chains within the lamellae of a semicrystalline polymer should be valuable in understanding the properties. Most polymers crystallize into folded chain crystals. Semicrystalline polymers exhibit a lamellar morphology when crystallized both from the melt and from dilute solution. The lamellae are typically 100–500 Å thick, with the amorphous polymer interspersed between the crystalline regions. The molecular chains are normal to the lamellae and have lengths that are much greater than the lamellar thickness. Thus the molecular chains can traverse one or more lamellae several times. A considerable fraction of the chains must return to the same crystal; that is, they are folded. Whether the molecule returns with a reentry that is either predominantly adjacent or random to the crystallite stem of origin is a matter of debate. Vibrational spectroscopy can contribute to our knowledge of the nature of the order in polymers and is useful in such determinations.

This fold problem has been studied in polyethylene (PE) by using deuterium isotopic labeling [45,46]. The orthorhombic unit cell of crystalline PE contains two symmetrically nonequivalent chains. These two chains give rise to both in-phase and out-of-phase modes whose frequency differences are the correlation splitting. When deuterated PE and normal PE are crystallized together, bands from both species give rise to correlation splittings. The observed resolved doublet splitting is evidence of adjacent reentry along a (110)-fold plane because the magnitude of the splitting was found to agree with calculated values for highly extended (110)-fold planes.

The chain fold in PE must contain TG (trans–gauche) sequences, and probably six TG bond sequences are required per fold. Although the number of TG bond sequences in a solution-crystallized sample can be calculated directly, the number of folds is not available because the TG conformation can be found in cilia and other defects as well as in folds. Relative changes in the number of TG units can be observed in a sample that has been annealed because annealing reduces the number of folds and therefore increases the stem length [47,48].

Intermolecular interactions in polymers

Vibrational spectroscopy can be used to study intermolecular effects in the solid state and the changes produced by temperature effects. If the intermolecular forces are sufficient, the fundamental modes of the single chain are split into different spectral components in the crystal.

The number of theoretically expected bands depends on the number of molecules in the unit cell. Polyethylene (PE) has a planar conformation and an orthorhombic unit cell containing two molecules. Each group mode of the isolated PE molecule is predicted to be split into two components for crystalline PE.

This crystal field splitting has been observed for the methylene rocking mode at 720 cm^{-1} and for the methylene bending mode at 1460 cm^{-1} in spectra of crystalline PE. Although other modes should also exhibit such splitting, their inherent bandwidth prevents the observation of separate components. When PE is melted, the crystal field splitting disappears. Consequently, a measure of the relative intensities of the 720- to 730-cm^{-1} bands can be used to rank the relative crystallinity of PE samples.

This crystalline result for PE is known to nearly everyone in the polymer field. It has caused untold misery for practising polymer spectroscopists because they have been asked to perform IR crystallinity measurements on all of the semicrystalline polymers of interest to their colleagues. Crystallinity plays a major role in the determination of the physical and mechanical properties of semicrystalline polymers, and a simple, rapid, and cheap method to measure crystallinity is desired.

My belief is that the density of the sample is such a measure of crystallinity. But such a simple measurement gets little respect and requires a knowledge of the density of the crystalline and amorphous phases, and therefore, one is often reluctant to use it. Crystallinity should probably be measured by X-ray diffractometry whenever possible because this is the final test of crystallinity. IR analysis is usually required of most samples for reasons of chemistry or impurities, so the IR spectroscopist is asked, "Why don't you measure the crystallinity while you are at it?" After all, we can measure a lot of things, so why not do it all!

The problem is that very few polymers exhibit the crystal field splittings observed for PE. The explanation is that the crystal field splitting is very sensitive to the distance of separation of the polymer chains. The intermolecular interaction forces fall off at a rate of r^6, where r is the distance between chains. A very small difference in separation results in a large difference in the magnitude of the interactions, and consequently, in the frequency separation of the bands. In fact, the PE chains are closer together than chains of any other polymer, so the crystal field splitting is the largest for PE.

For polypropylene (PP), on the other hand, it has not been possible to observe any IR splittings resulting from intermolecular or crystalline packing. In fact, there are many features in the PP spectrum that look like pairs of bands, and indeed they are. However, the band pairs arise from *intramolecular helical splitting*, not from *intermolecular crystalline splitting*. Actually, intermolecular packing influences the IR spectrum of PP very little. In Fig. 4.42, the X-ray patterns of the monoclinic α phase and the smectic δ phase are shown. The monoclinic α phase consists of well-ordered crystalline 3_1 helices, while the smectic δ phase consists of 3_1 helices that are out of register with each other. The smectic phase will convert with time to the

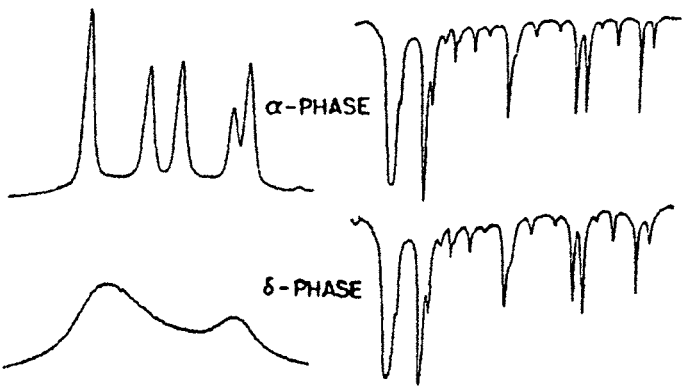

Fig. 4.42. A comparison of the IR spectra and the X-ray diffraction patterns of the monoclinic α phase and smectic δ phase of isotactic polypropylene.

monoclinic α phase at a rate that is a function of temperature. The IR spectra of these two phases are also shown in Fig. 4.42, and the spectra are strikingly similar [49].

Only minor differences in intensities are observed in the IR spectra, yet from the X-ray point of view, the smectic phase is noncrystalline. The reason for these small differences is that the helices are far apart (relative to the distance in PE), and consequently, the intermolecular forces are much lower, and the intermolecular splitting is below the resolution of the instrument. Unfortunately, the spectral results for PP are typical for most semicrystalline polymers.

Generally, the chains are simply too far apart and the intermolecular forces are so small that crystal field splitting is not observed!!

Even the experienced IR spectroscopist may be confused at this point. There are a number of reports in the polymer literature of correlations of spectral features with crystallinity or density. However, *these IR correlations are based on the measurement of the amount of the rotational isomer preferred in the crystalline state*, which, on the average, may correlate with the crystallinity or density. Two different measurements of crystallinity here are being considered here. X-ray diffraction measures the *long-range order* or *inter*molecular order as a result of chain packing. IR spectroscopy measures the concentration of the crystalline isomer, which is a *short-range order* or *intra*molecular phenomenon. These two physical methods do not necessarily determine the same crystallinity. The short-range intramolecular order is a necessary condition for the occurrence of long-range intermolecular order, but the short-range order can exist without the presence of the long-range order. For example, in the cilia connecting one lamella to another, the short-range order can be high. However, there is little possibility of intermolecular order because the cilia can be completely isolated from each other. IR spectroscopy would detect these repeat units in the crystalline domain, but in X-ray diffraction they would go undetected. Consequently, the IR spectroscopic and X-ray diffraction measurements of crystallinity can be different, and this result is often the case. This does not mean either measurement is wrong. The two methods simply measure different phenomena that are generally lumped into the term 'crystallinity'. IR spectroscopy measures short-range crystallinity, and X-ray diffraction measures long-range crystallinity.

Another technique for measuring crystallinity is the differential scanning calorimeter (DSC) measurement of the heat of fusion. The DSC measures the amount of heat required to melt a sample, and by using a knowledge of the heat of fusion of a 100% crystalline sample, the percent crystallinity is calculated. DSC measures yet another type of crystallinity — the *meltable* portion. The meltable crystalline portion represents a degree of order less than that of the long-range X-ray order because some crystallites can melt but are too small to be observed with X-rays. Yet, DSC does not measure the contributions of cilia and other isolated ordered chains to short-range

order. Again, correlations can be made for PET [50], but careful annealing conditions are required to establish such correlations.

Therefore, the method used to measure crystallinity, whether by density, IR spectroscopy, X-ray diffraction, or DSC, needs to be specified in order for the results to be meaningful.

Structural changes and transitions as a function of temperature

The intensity, band shape, and frequency of an IR absorption band can change as a result of a change in the temperature of the sample. There are two extremes of interpretation of the effects of temperature on spectroscopic results. Either thermal expansion affects the inherent nature of the dipole moment change as a result of changes in the intermolecular forces or the concentration of the absorbing species changes with temperature. These two effects can occur simultaneously, and this event often precludes a straightforward analysis.

With increasing temperature, intermolecular expansion reduces the electric dipole moment of the interaction and therefore reduces the intensity of the absorption band. The temperature effect on band intensity is most pronounced for bands that arise from very polar chemical groups. Changes in band shape can also result from changes in temperature. These changes are the result of additional thermal energy being imparted to the multiplicity of vibrational energy levels available to the polymer. The effects of thermal broadening are most easily observed in the IR spectra of molten polymers.

At cryogenic temperatures, no concentration changes are expected; thus IR spectroscopy can be used to detect transitions in polymers by recording abrupt or discontinuous changes in intensities as a function of temperature. This IR type of molecular dilatometry should indicate the same transitions that are observed in bulk thermal expansion measurements. If certain IR absorptions are related to the various components or morphological structures present, then a probe of the thermal responses of these structures is available. Multiphase and copolymer systems can be easily studied by using IR spectroscopic analysis.

Conformational analysis of polymers

IR spectroscopy can be used to characterize the different conformers in a polymer. The criteria for identifying the absorption bands of the conformers are based on the following observations. As the temperature of the sample is increased, the relative intensities of the absorption bands of the high-energy conformers increase, and those of the lower-energy conformers decrease. When the sample is cooled rapidly to form a stable crystalline form, the bands of the stable conformers dominate and those of the high-energy conformers essentially disappear. Conformer bands should be ob-

served in pairs corresponding to the same vibrational modes in both the high-energy conformer and the low-energy conformer.

The equilibrium between two conformers A and B, where A $\Leftrightarrow$ B is dependent on temperature. The concentration of the high-energy A conformer, C_A, relative to the concentration of the low-energy form, C_B, is given by the van't Hoff expression

$$\frac{C_A}{C_B} = \exp\left[-\frac{\Delta G}{RT}\right] \tag{4.17}$$

where R is the gas constant, T is the temperature, and ΔG is the Gibbs free energy difference between conformers, given by the expression

$$\Delta G = \Delta H - T\Delta S \tag{4.18}$$

The standard enthalpy difference, ΔH, is the difference in enthalpy of the two conformers, and ΔS is the difference in entropy.

The vibrational band intensities of the conformer bands, A_A and A_B, are related to the concentration of each conformer as follows:

$$A_A = a_A C_A b \tag{4.19}$$

$$A_B = a_B C_B b \tag{4.20}$$

where a is absorptivity and b is path length.

Substitution of these relationships into the van't Hoff relation yields

$$\frac{A_B a_A}{A_A a_B} = \exp\left[-\frac{\Delta H}{RT_e} + \frac{\Delta S}{R}\right] \tag{4.21}$$

This may be expressed as

$$\ln\left[\frac{A_B}{A_A}\right] = -\frac{\Delta H}{RT} + \frac{\Delta S}{R} - \ln\frac{a_A}{a_B} \tag{4.22}$$

If it is assumed that ΔS and the ratio a_A/a_B are constant with temperature, it is possible to determine ΔH by making a series of measurements of A_B/A_A at various temperatures. On this basis, the van't Hoff energy is defined as

$$\Delta H = h_+ - h_- \tag{4.23}$$

with

$$h_\pm = \frac{-R\,\partial \ln A_\pm(\nu)}{\partial\,(1/T)} \tag{4.24}$$

where the bands that increase in intensity, $A_+(\nu)$, or decrease in intensity, $A_-(\nu)$, yield the energies h_+ and h_-, respectively. Then

$$\Delta H = \frac{R\partial\left[\dfrac{\ln A_+(\nu)}{A_-(\nu)}\right]}{\partial\,(1/T)} = R\partial\left[\frac{\ln K}{\partial\,(1/T)}\right] \tag{4.25}$$

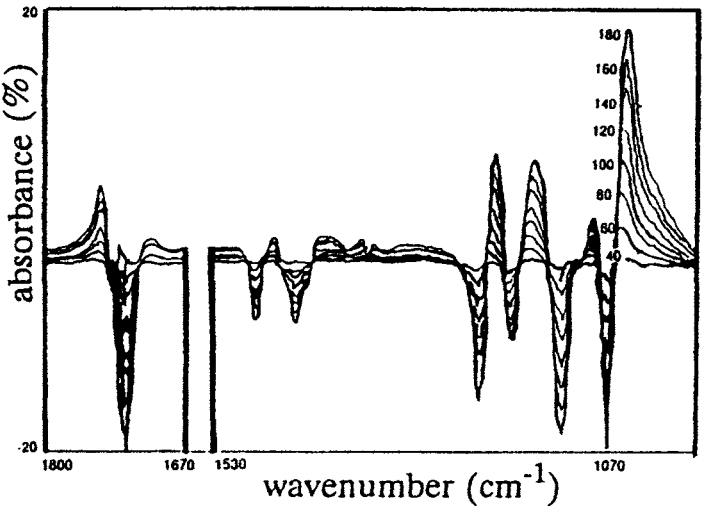

Fig. 4.43. The FTIR difference spectra of syndiotactic PMMA obtained at 20-degree intervals starting at 30°C. (Reproduced from Ref. [10]; © 1981 American Chemical Society.)

where the equilibrium constant, K, is defined by

$$K = \frac{A_+ (\nu)/a_+}{A_- (\nu)/a_-} \tag{4.26}$$

where $A_\pm$ and $a_\pm$ are the peak absorbances and extinction coefficients, respectively, of the increasing and decreasing bands.

The FTIR spectrum of syndiotactic PMMA was obtained at 20-degree intervals starting at 30°C [10]. The difference spectra of syndiotactic PMMA are shown in Fig. 4.43.

These differential absorbances were analyzed by using the van't Hoff equation and were plotted as shown in Fig. 4.44.

The conformational energies are largest (2000 cal/mol) for the 1276–1264-cm^{-1} bands and range from 1080 to 1283 cal/mol for the 1195–1168- and 1152–1140-cm^{-1} bands. These data have been interpreted in terms of the rotational isomeric state theory. The IR spectroscopic approach is straightforward and is useful for obtaining information of this type.

Time-dependent phenomena in polymers

One of the major advantages of FTIR spectroscopy is its rapid scanning capability, which has opened new applications of IR spectroscopy. These new applications require continuous monitoring in short time intervals and extremely small differences between spectra. With currently available commercial instrumentation, inter-

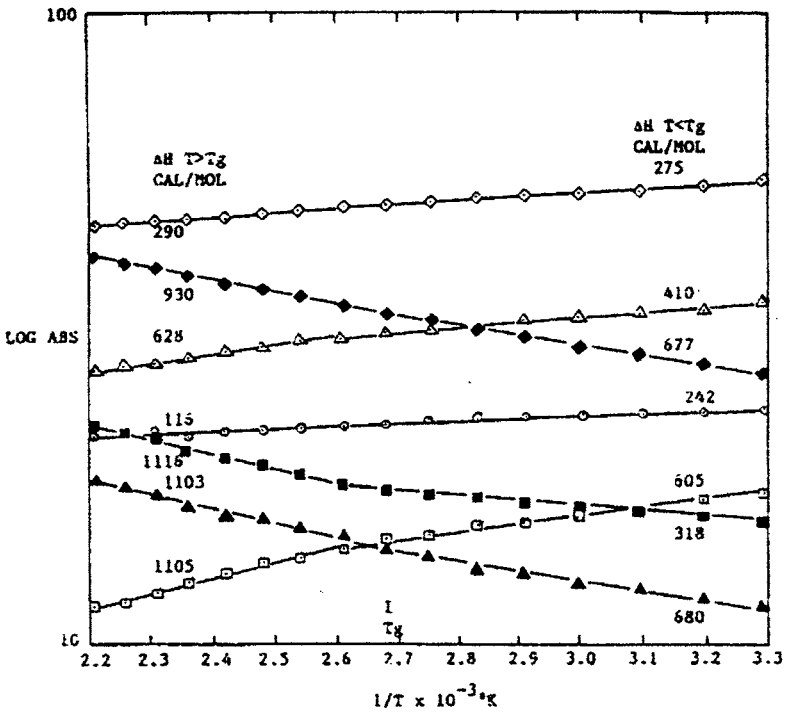

Fig. 4.44. The differential absorbances of PMMA analyzed by using the van't Hoff equation. The activation energy, ΔH, is given in calories per mole. The IR band frequencies (cm^{-1}) are as follows: ◇, 1152; ◆, 1136; △, 1195; ■, 1260; ○, 1246; ▲, 1224; and □, 1276. (Reproduced from Ref. [10]; © 1981 American Chemical Society.)

ferograms may be collected and stored at a rate of 50 to 85 scans per second to give a time resolution of 12–20 ms. If the time frame of the transient phenomenon is long with respect to the mirror scan time, and if the signal is sufficiently large, single interferograms may be transformed in a rapid-scan instrument to yield essentially instantaneous incremental spectra.

Kinetic studies of polymerization reactions

From the study of time-dependent intensity changes of absorption bands characteristic of the polymerization reactants and reaction products, the order and specific rate, k, of a reaction can be derived. Also, the activation energy can be calculated when studies of absorption are made as a function of temperature.

With the rapid-scanning capability of FTIR spectroscopy, the chemical changes of a sample in a heated cell can be monitored, provided that the spectral sampling interval is shorter than the interval during which the change occurs. Conversion curves as a function of time and temperature for each species involved in the cure process can be generated from the IR absorbances. The determination of the kinetic parameters

from a single dynamic scan is based on the general nth-order rate expression in which the conversion, F, as a function of time, t, and temperature, T, is given by

$$\frac{\mathrm{d}F(t,T)}{\mathrm{d}t} = k\left[1 - F(t,T)\right]^n \tag{4.27}$$

where n is the reaction order. Assuming that the temperature dependence of the rate constant is described by the Arrhenius equation

$$k = A\exp\left[-\frac{E}{RT}\right] \tag{4.28}$$

where E (kcal/mol) is the activation energy, and A (s^{-1}) is the *Arrhenius frequency factor*. The conversion curve can be used to determine the reaction kinetic parameters, E, n and $\ln A$.

The rapid-scan FTIR technique has been applied to the study of the cure kinetics of isocyanate coatings [51]. The reaction can be followed by monitoring the absorbance of the peak at 2256 cm^{-1}, which results from the isocyanate functionality, as a function of time. Film thickness can be monitored using the band at 1446 cm^{-1}. The fractional conversion as a function of temperature and time is calculated by

$$F(t,T) = \frac{[A_f - A(t,T)]}{A_f - A_0} \tag{4.29}$$

where A_0 is the initial absorbance, $A(t,T)$ is the absorbance at temperature T and time t, and A_f is the final absorbance. The kinetic parameters were determined by using a simplex fitting procedure.

The polymerization of methacrylates has been studied in real time using rapid scan FTIR [52].

A rather new approach to time-resolved spectroscopy that uses modern optoelectronic-controlled step-scan methods of Fourier transform interferometry has been suggested [53]. When using step-scan interferometry, the initiation of a reversible event must occur at each mirror position. The time evolution at each mirror position subsequent to initiation is then measured at discrete time intervals. Data processing involves sorting by time in order to produce an interferogram for each sampling time. These interferograms are subsequently Fourier transformed to yield a set of time-resolved spectra. To quote the authors:

> *It is anticipated that, given sufficient source intensity, and with the availability of fast mercury cadmium telluride (MCT) detection and transient digitizing electronics, time intervals down to ~10 ns should be accessible.*
>
> — R. A. Palmer et al.

Step-scan FTIR has been successfully used to study electric field reorientation of nematic liquid crystals [54] as well as the phase separation process in polymer

dispersed liquid crystals [55]. The orientation of strands in polymeric liquid crystals has also been studied [56].

Characterization of surfaces

IR spectroscopy has been shown to be an effective means for the study of surface species [57] and reactions occurring at interfaces [58]. These results can be reflected in the nature of interfacial bonding and the role of adhesion in property determination.

Infrared studies of absorbed systems have been very useful particularly when (1) the substrate has a simple spectra, and (2) when the surface area of the substrate is very high. For example the surface area probed by an IR beam when using silica particles is about 4 orders of magnitude greater than when using flat surfaces [59]. Under these circumstances it is easy to detect the IR bands due to an adsorbed species and allows a convenient and reliable measurement of polymer/surface interactions. Further more, the bands can be easily quantified to determine the adsorbed amount.

The vibrational frequencies of each of the adsorbed molecules are determined by the electric field of surrounding dipoles due to the vibrational Stark effect:

$$\nu_I = \nu_0 - K_{ST}\mu_0 \sum r_{ij}^{-3} \tag{4.30}$$

where K_{ST} is the vibrational Stark constant, r_{ij} is the distance between interacting molecules, ν_0 is the frequency of isolated adsorbed molecule and μ_0 is its effective dipole value [60]. Thus on a theoretical basis, frequency shifts of absorbed molecules on polymer surfaces may be observed.

Theoretical studies have been made on the nature of surface sites for polymer adsorption [61]. There is a depletion of polymer segments on the surfaces. This effect is purely entropic, arising from restrictions imposed by the solid surfaces on chain conformations and persists even when attractive surface-chain end interactions are included. There is an increase in the fraction of absorbed chains with the number of weakly adsorbing chain ends. The fraction of surface sites occupied by chain ends for both ends adsorbing is 0.082 for zero adsorption energy, 0.144 for weakly adsorbing ends and 0.282 for strongly adsorbing ends. As a result chains form more brush-like conformations with an increased frequency of long loops and tails.

Significant bond orientation parallel to the surface exists only in the surface layers [62]. Attractive surface-chain ends have little influence on the degree of bond orientation or the persistence of orientation from the surface.

The nature of the chain conformations of the absorbed polymer chain has also been examined [58]. The average length of loops increases considerably as the number of attractive ends increases. As the density of chain ends on the surfaces increases, segments away from the ends are forced into loops (including bridges) and tails. As the number of attractive ends increases, there is a decrease in the fraction of segments involved in trains and the average size of trains. Bridges are statistically rare.

These theoretical results have been verified by FTIR measurements [63]. The adsorption of copolymers [64] and comb polymers have been examined [65].

FT-IR studies of diffusion

Diffusion of penetrants in polymers is an important industrial problem as their resistance to sorption can influence the engineering usefulness of polymers. Using FTIR-ATR has several advantages for such studies:

- can study gases, liquids and solids into polymers,
- penetrants with strong absorbances can be detected at very low levels,
- concentration profiles can be determined as measurements are rapid [66],
- can measure accurately diffusion coefficients based on tested theoretical models,
- can examine multicomponent diffusion with ease as each species has its fingerprint spectrum,
- can show the presence of molecular association between penetrants themselves and between the penetrant and the polymer.

In recognizing these benefits, a number of FTIR/ATR studies have been made. The diffusion of additives in polyolefins have been studied [67] through a measurement of their infrared absorbances as a function of mass uptake. Environmental penetrants have been studied [68]. The mutual interdiffusion of polymers has also been studied using the FTIR/ATR method [69]. The interpenetration of semicrystalline polymers such as poly(ether imide/poly(aryl ether ketone) has been examined [70]. The interdiffusion of polystyrene and poly(methyl ether) has also been studied and diffusion coefficients measured which agreed with other approaches [71].

Summary and conclusions

Every polymer system of industrial interest has, at some stage, been subjected to IR examination. Whether to identify the chemical nature of the polymer or to determine its composition, IR is a useful highly specific tool. For quantitative analysis of microstructure, stereoregularity, branching or crosslinking, in many cases, IR analysis is the simplest and most sensitive method. Consequently, IR analysis is a popular tool in the arsenal of the polymer scientist. It will continue to be!

Where do we go from here?

The applications of IR spectroscopy seem to be limited only by the imagination of the spectroscopist. The quality of the instrumentation is continuing to improve, and the cost is decreasing so that quality instrumentation is available to laboratories of all sizes. Therefore, the number of applications of IR spectroscopy will continue to

grow. IR instrumentation is moving into the quality control laboratory because of its sensitivity to small differences in samples. It is also being used in the chemical plant as a process monitoring device because of its capability of continuously monitoring a large variety of structural aspects in a process stream. Growth in these areas will continue as instrumentation is specifically designed for these applications.

> *Our modern instruments are capable of giving signal/noise ratios greater than one part in 10^5 which means if your chart paper is over 60 m tall, it would display the data appropriately.* — Tomas Hirshfeld

References

[1] Kosky, P.G., McDonald, R.S., Guggenheim, E.A., Polym. Eng. Sci. 25 (1985) 389.
[2] Antoon, M.K., Koenig, J.L., J. Polym. Sci., Part A: Polym. Chem. 19 (1981) 549.
[3] Antoon, M.K., Zehner, B.E., Koenig, J.L., Polym. Compos. 2 (1981) 81.
[4] deHaseth, J.A., Andrews, J.E., McClusky, J.V., Priester Jr., R.D., Harthcock, M.A., Davis, B.L., Appl. Spectrosc. 47 (1993) 173.
[5] Pecsok, R.L., Painter, P.C., Shelton, J.R., Koenig, J.L., Rubber Chem. Technol. 49 (1976) 1010.
[6] Antoon, M.K., Koenig, J.L., J. Polym. Sci., Part B: Polym. Phys. 19 (1981) 197.
[7] Mirabella Jr., F.M., Spectroscopy 5 (1991) 20.
[8] Drushel, H.V., Ellerbe, J.J., Cos, R.C., Love, L.H., Anal. Chem. 40 (1968) 370.
[9] Bowmer, T.N., Tonelli, A.E., J. Polym. Sci., Part B: Polym. Phys. 24B (1986) 1681.
[10] O'Reilly, J.M., Mosher, R.A., Macromolecules 14 (1981) 602.
[11] Zimba, C.G., Rabolt, J.F., English, A.D., Macromolecules 32 (1989) 2867.
[12] Shipman, J.J., Folt, V.L., Krimm, S., Spectrochim. Acta, 18 (1962) 1603.
[13] Compton, D.A.C., Maddams, W.F., Appl. Spectrosc. 40 (1986) 239.
[14] Koenig, J.L., Appl. Spectrosc. Rev. 4 (1971) 233.
[15] Snyder, R.G., Poore, M.W., Macromolecules 6 (1973) 708.
[16] Zoppo, M.D., Zerbi, G., Polymer 31 (1990) 658.
[17] Lin, S.B., Koenig, J.L., J. Polym. Sci., Polym. Symp. 71 (1984) 121.
[18] Lin, S.B., Koenig, J.L., J. Polym. Sci., Part B: Polym. Phys. 21 (1983) 2365.
[19] Painter, P.C., Watzek, M., Koenig, J.L., Polymer 18 (1977) 1169.
[20] Painter, P.C., Watzek, M., Koenig, J.L., Polymer 18 (1977) 1169.
[21] Blitz, J.P., PSME Preprints 75 (1996) 65.
[22] Koenig, J.L., Chemical Microstructure of Polymer Chains. Wiley, New York, NY, 1982, p. 63.
[23] Koenig, J.L., Tovar, M.J.M., Appl. Spectrosc. 35 (1981) 543.
[24] Sargent, M., Koenig, J.L., Vib. Spectrosc. 2 (1991) 21.
[25] Coleman, M.M., Painter, P.C., Appl. Spectrosc. Rev. 20 (1984) 255.
[26] Jo, W.H., Cruz, C.A., Paul, D.R., J. Polym. Sci., Part B: Polymer Phys. 27 (1989) 1057.
[27] Allara, D.L., Appl. Spectrosc. 33 (1979) 358.
[28] Jasse, B., Koenig, J.L., J. Macromol. Sci., Rev. Macromol. Chem. C17(1) (1979) 135.
[29] Wolfram, L.E., Koenig, J.L., Grasselli, J.G., Appl. Spectrosc. 24 (1970) 263.
[30] Lefebvre, D., Jasse, B., Monnerie, L., Polymer 22 (1981) 1616.
[31] Holland-Moritz, K., van Werden, K., Makromol. Chem. 182 (1981) 651.
[32] Fina, L.J., Koenig, J.L., J. Polym. Sci., Part B: Polym. Phys. 24 (1986) 2525.
[33] Fina, L.J., Koenig, J.L., J. Polym. Sci., Part B: Polym. Phys. 24 (1986) 2541.
[34] Bretzlaff, R.S., Wool, R.P., Macromolecules 16 (1983) 1907.
[35] Lee, Y.-L., Bretzlaff, R.S., Wool, R.P., J. Polym. Sci., Part B: Polym. Phys. 22 (1984) 681.

[36] Wool, R.P., Polym. Eng. Sci. 20 (1980) 805.
[37] Siesler, H.W., in: D. Hummell (Ed.), Proceedings of the 5th European Symposium on Polymer Spectroscopy. Verlag Chemie, Weinheim, 1979.
[38] Noda, I., Appl. Spectrosc. 44 (1990) 550.
[39] Noda, I., Dowrey, A.E., Marcott, C., Appl. Spectrosc. 42 (1988) 203.
[40] Budveska, B.O., Manning, C.J., Griffith, P.R., Roginski, R.T., Appl. Spectrosc. 47 (1993) 1843.
[41] Ingemey, R.A., Strohf, G., Veeman, W.S., Appl. Spectrosc. 50 (1996) 1360.
[42] Palmer, R.A., Manning, C.J., Chao, J.L., Noda, I., Dowrey, A.E., Marcott, C., Appl. Spectrosc. 45 (1991) 12.
[43] Marcott, C., Dowrey, A.E., Noda, I., Anal. Chem. 66 (1994) 1065A.
[44] Noda, I., Dowrey, A.E., Marcott, C., Polym. Prepr. 33(1) (1992) 70.
[45] Tasumi, M., Krimm, S., J. Chem. Phys. 46 (1967) 755.
[46] Tasumi, M., Krimm, S., J. Polym. Sci., A-2, 6 (1968) 995.
[47] Painter, P.C., Havens, J., Hart, W.W., Koenig, J.L., J. Polym. Sci. 15 (1977) 1223–1236.
[48] Painter, P.C., Havens, J., Hart, W.W., Koenig, J.L., J. Polym. Sci. 15 (1977) 1237–1249.
[49] Koenig, J.L., unpublished results, 1963.
[50] Lin, S.-B., Koenig, J.L., J. Polym. Sci. 71C (1984) 121.
[51] Provder, T., Neag, C.M., Carlson, G., Kuo, C., Holsworth, R.M., in: J.F. Johnson and P.S. Gill (Eds.), Analytical Calorimetry. Plenum, New York, NY, 1984, p. 377.
[52] Dietz, J.E., Elliott, B.J., Peppas, N.A., Macromolecules 28 (1995) 5163.
[53] Palmer, R.A., Manning, C.J., Rzepiela, J.A., Widder, J.M., Chao, J.L., Appl. Spectrosc. 43 (1989) 193.
[54] Gregoriou, V.G., Chao, J.L., Toriumi, H., Palmer, R.A., Chem. Phys. Lett. 179 (1991) 491.
[55] Snively, C., Chen, P.Y., Palmer, R.A., Koenig, J.L., Mol. Cryst. Liq. Cryst. 289 (1996) 11–23.
[56] Kaito, A., Kyotani, M., Nakayama, K., Macromolecules 24 (1991) 3244.
[57] Urban, M.W., Vibrational Spectroscopy of Molecules and Macromolecules on Surfaces. Wiley, New York, NY, 1993.
[58] Suetaka, W., Surface Infrared and Raman Spectroscopy: Methods and Applications. Plenum Press, New York, NY, 1995.
[59] Tripp, C.P., Hair, M.L., Langmuir 9 (1993) 3523.
[60] Yu, A.E., Tsyganenko, E.T., Tsyganenko, A.A., Smirnov, K.S., Vib. Spectrosc. 6 (1993) 15.
[61] Smith, G.D., Yoon, D.Y., Jaffe, R.L., Macromolecules 25 (1992) 7011.
[62] Fleer, G.J., Cohen Stuart, M.A., Scheutjens, J.M.H.M., Cosgrove, T., Vincent, B., Polymers at Interfaces. Chapman and Hall, New York, NY, 1993.
[63] Frantz, P., Granick, S., Macromolecules 28 (1995) 6915–6925.
[64] Green, P.F., Russell, T.P., Macromolecules 25 (1992) 7.
[65] van der Linden, C.C., Leermakers, F.A.M., Fleer, G.J., Macromolecules 29 (1996) 1000.
[66] Hsu, S.C., Lin-Vien, D., French, R.N., Appl. Spectrosc. 46 (1992) 225.
[67] Schlotter, N.E., Furlan, Y.P., Vib. Spectrosc., 3 (1992) 147.
[68] Fieldson, G.T., Barbari, T.A., Polymer 34 (1993) 1146.
[69] Van Alsten, J.G., Lustig, S.R., Macromolecules 25 (1992) 5069.
[70] Lustig, S.R., Van Alsten, J.G., Hsiao, B., Macromolecules 26 (1993) 3885.
[71] Jabbari, E., Peppas, N.A., Macromolecules 26 (1992) 2175.

Chapter 5

Raman spectroscopy of polymers

In the previous chapters, IR spectroscopy of polymers was discussed. In this chapter, a complementary technique that also measures the vibrational energy levels, Raman spectroscopy, will be examined. As discussed in Chapter 2, there is a fundamental difference in the IR and Raman techniques. IR spectroscopy depends on a change in the permanent dipole moment of the chemical bond or molecule with the vibrational normal mode in order to produce absorption. Raman spectroscopy, on the other hand, depends on a change in the induced dipole moment or polarization to produce Raman scattering. This difference in the physical nature of the selection rules may seem minor, but it plays a major role in the manner in which the two vibrational techniques are used for the study of polymers.

The nature of Raman scattering spectroscopy

In the first paragraph of the paper by C.V. Raman and K.S. Krishnan [1] in which they introduce this technique, they state

> *If we assume that the X-ray scattering of the 'unmodified' type observed by Professor Compton corresponds to the normal or average state of the atoms and molecules, while the 'modified' scattering of altered wavelength corresponds to their fluctuations from that state, it would follow that we should expect also in the case of ordinary light two types of scattering, one determined by the normal optical properties of the atoms or molecules, and another representing the effect of their fluctuations from their normal state. It accordingly becomes necessary to test whether this is actually the case...*

The results of these tests led to the following statement later in the paper:

> *Some sixty different common liquids have been examined in this way, and every one of them showed the effect in greater or less degree.*

Thus, the technique we now call the *Raman effect* was first observed.

Spectral differences between IR and Raman spectroscopy

The Raman effect is produced by the exchange of energy between the incident photons and the vibrational energy levels of the molecule and is unique to each molecule. In many instances, the magnitudes of the Raman shifts in frequency correspond exactly to the frequencies of IR absorption. As a result, the information obtained from IR measurements can also be found in the Raman spectra. Some vibrational modes appear only in the IR spectrum, and other modes appear only in the Raman spectrum. The differences in the vibrational patterns of IR and Raman spectroscopy can be used to a great advantage in the determination of the structure of molecules and these differences represent one of the prime reasons for interest in Raman spectroscopy. Generally, the more symmetric the molecule is, the greater the differences will be between the IR and Raman spectra. Strong Raman scattering arises from nonpolar molecular groupings, and strong IR absorption occurs when the molecule contains polar groups [2]. In chainlike polymer molecules, the vibrations of the substituents on the carbon chain are most easily studied by using IR spectroscopy, and the vibrations of the backbone carbon chain can be studied by using Raman spectroscopy [3].

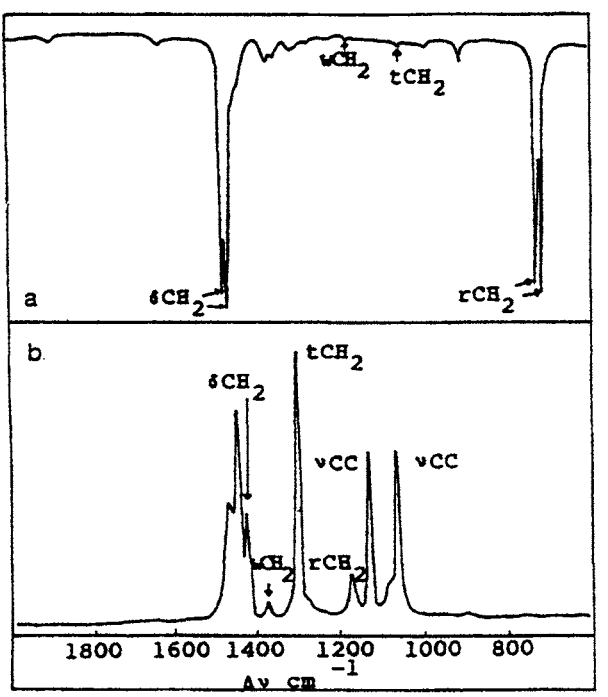

Fig. 5.1. The Raman and IR spectra of linear polyethylene. (Reproduced with permission from Ref. [4, p. 15]. © 1979 Steinkopff Verlag Darmstadt.)

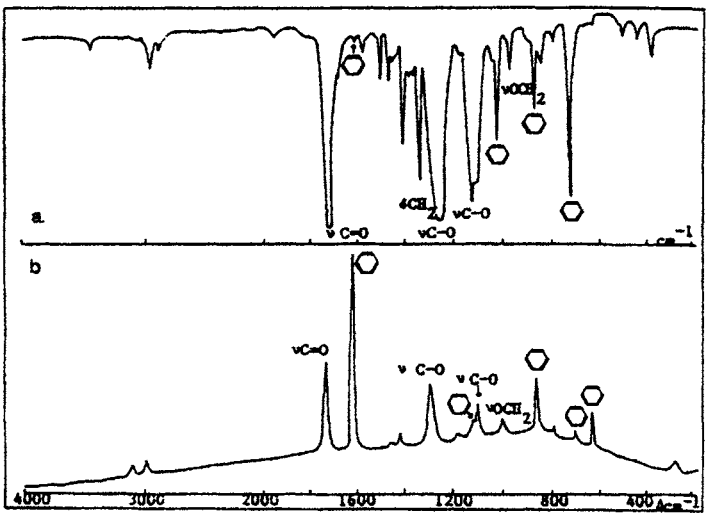

Fig. 5.2. (a) FTIR Spectra of poly(ethylene terephthalate) (b) Raman spectra of poly(ethylene terephthalate). (Reproduced with permission from Ref. [4, p. 15]. © 1979 Steinkopff Verlag Darmstadt.)

These differences between Raman and IR spectroscopy for polymers can be illustrated. The Raman and IR spectra of linear polyethylene are shown in Fig. 5.1 [4].

The polyethylene molecule has a center of symmetry and the IR and Raman spectra should exhibit entirely different vibrational modes due to the mutual exclusion rule. Examination of the spectra reveals that this is the case. In the IR spectrum, the methylene modes are clearly the strongest, but the C−C modes dominate the Raman spectrum. The IR and Raman spectra of poly(ethylene terephthalate) (PET) are shown in Fig. 5.2.

The C−C stretching modes of the aromatic ring clearly dominate the Raman spectrum, and the C−O modes are strongest in the IR spectrum. The Raman spectrum has a fluorescence background that makes the dynamic range of the spectrum less than is desirable. The Raman lines are weak when superimposed on the broad background. The IR and Raman spectra of poly(methyl methacrylate) (PMMA) are compared in Fig. 5.3.

The Raman spectrum is particularly rich in the lower frequency range, where there is little absorbance in the IR spectrum. The C=O and C−O bands dominate the IR spectrum, and the C−C modes dominate the Raman spectrum.

Compared to IR spectroscopy, Raman spectroscopy has a number of advantages, and these advantages are as follows:

- Raman spectroscopy is a scattering process, so samples of any size or shape can be examined.
- Very small amounts of materials can be examined without modification (sometimes localized degradation can occur with high laser power).

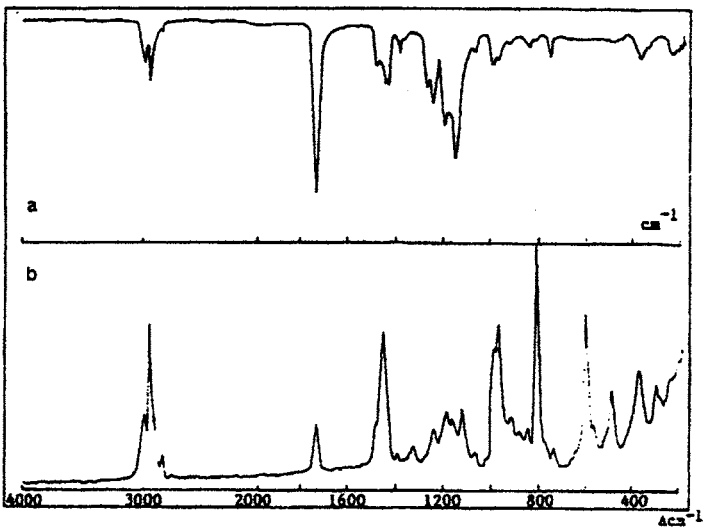

Fig. 5.3. Upper spectrum is FTIR of PMMA and lower spectrum is the Raman spectrum. (Reproduced with permission from Ref. [4, p.15]. © 1979 Steinkopff Verlag Darmstadt.)

- Glass and closed containers can be used for sampling.
- Fiber optics can be used for remote sampling.
- Aqueous solutions can be analyzed.
- The low frequency (10–500 cm^{-1}) region is available on the same instrument.
- Small samples can be studied since the laser beam can be focused down to about a spot with a diameter of 100 μm.
- Less restrictive selection rules apply, so richer spectra are obtained.

Because the Raman effect is a scattering process, it does not have the problems associated with the requirement of light transmission. Raman front-surface reflection allows the examination of a sample of any size or shape. If the sample can be hit with the laser beam, a Raman spectrum can usually be obtained.

Raman spectroscopy has an inherent microsampling capability because the laser beam has a small diameter, and the beam can be focused to an even smaller size.

Because the Raman effect can be successfully integrated with fiber optics, remote sampling is possible. IR spectroscopy can also be interfaced with fiber optics, but the loss of light in the IR region is much higher than the loss in the visible region, and the maximum distance between the sample and the instrument is much smaller for IR spectroscopy than for Raman spectroscopy.

Because water is a highly polar molecule, it is a strong IR absorber. By the same token, it is a weak Raman scatterer. Therefore, the Raman effect can be used to study aqueous solutions, and this fact has been beneficial for the study of water-soluble polymers and to the biological field. Studies of water-soluble polymers such as surfactants can be successfully carried out with Raman spectroscopy.

As will be demonstrated later in our discussion of Raman instrumentation, a single instrument can be used to scan the region from (depending somewhat on the scattering power of the sample) to 4000 cm^{-1}. FTIR spectroscopy, on the other hand, requires changing the beam splitter and detector to reach this low frequency, or *far*-IR, region of the spectrum. Raman spectroscopy has been used to detect the low-frequency acoustic modes of polymers, and the frequencies of these modes have been used to measure the dimensions of crystals.

For polymers and most other molecules, the Raman selection rules are less restrictive than the IR selection rules, so the Raman spectra are richer in vibrational information than the IR spectra. Ideally, a spectroscopist would like to have both the IR and Raman spectra of a sample. Recent developments in Fourier transform instrumentation now make this a real possibility.

There are differences in the instrumentation needed to make IR and Raman measurements. These differences in instrumentation are compared in Table 5.1 [5].

Rapid changes are taking place in Raman instrumentation, but the general character remains the same. The major difference between the two spectroscopic techniques is the need for a laser light source for Raman spectroscopy compared to a black-body source (usually a heated wire) for IR spectroscopy. The Raman detector for the visible light range is a photomultiplier tube, which has a much higher level of sensitivity than the thermal or pyroelectric detectors used in IR spectroscopy. Although energy is the limitation for both techniques (as it is eventually for all forms of spectroscopy), inefficient scattering (1 photon in 10^8) is the limiting factor in Raman spectroscopy, and the low power level of the black-body source is the limiting factor in IR spectroscopy.

These differences between Raman and IR spectroscopy lead to different sample handling techniques (Table 5.2).

Instrumentation and sample handling considerations are reflected in the applications of IR and Raman spectroscopy. Raman spectroscopy is effective for aqueous solutions and in low-frequency ranges.

Table 5.1
Comparing Raman and IR experiments instrumentation

Factor	Raman	IR
Relative complexity	moderate	slightly greater
Source	laser	black-body or diode laser
Detector	photomultiplier tube	thermal, pyroelectric, bolometers
Resolution	ca. 0.25 cm^{-1}	ca. 0.05 cm^{-1}
Principle limitation	energy	energy
Wavenumber range	10–4000 cm^{-1}	180–4000 cm^{-1} (one instrument)
Purge requirement	no	yes
Photometry	scattering single beam	absorption double beam

(Source: Ref. [5].)

Table 5.2
Comparing Raman and IR experiments applications

Feature	Raman	IR
General applicability	95%	99%
Sample limitations	color, fluorescence	metals, aqueous solutions
Ease of sample preparations	very simple	variable
Liquids	very simple	very simple
Powders	very simple	more difficult
Single crystals	very simple	very difficult
Polymers	very simple	more difficult
Single fibers	possible	difficult
Gases and vapors	now possible	simple
Cells	very simple (glass)	alkali halide
Micro work	good (<1 μg)	good (<1 μg)
Trace work	sometimes	sometimes
High and low temperature	moderately simple	moderately simple

(Source: Ref. [5].)

Raman and IR spectroscopy in combination to determine polymer conformation

When IR and Raman spectroscopic techniques are used in combination, the results are much greater than with the use of either technique individually. The combined use of IR and Raman spectroscopy extracts most of the obtainable information (silent, or optically inactive, modes and extremely weak modes are not detected). The complementary nature of the IR and Raman data has important practical applications. This complementary nature arises from the differences in selection rules governing the vibrational energy levels. For molecules with a center of symmetry (there are identical atoms on either side of the center of symmetry), no vibrational frequencies are common to the IR and Raman spectra. This principle is called the *mutual exclusion principle*. Although symmetry might be considered important for low-molecular-weight substances like ethylene and benzene (both of which have a center of symmetry), polymers are not usually expected to have a center of symmetry. Polyethylene has a center of symmetry, and the observed IR and Raman lines do not coincide in frequency (see Fig. 5.1). Theory predicts that eight modes for polyethylene are active in the Raman while only five in the infrared.

Consider this result from a point of view of structural determination; that is, if the Raman and IR lines are mutually exclusive in frequency, a center of symmetry must exist in the polymer. Consider polyethylene sulfide (PES), which contains of succession of $(-CH_2CH_2SCH_2CH_2S-)$ repeat units. The conformations about the CC, CS, SC, CC, CS, and SC bonds, are *trans*, *gauche* (right), *gauche* (right), *trans*, *gauche* (left), and *gauche* (left), respectively. This structural model of PES has a center of symmetry, and theory predicts that the observed IR and Raman frequencies are mutually exclusive.

If PES exists in a helical form like polyethylene oxide (PEO), it does not have a center of symmetry, and theory would suggest that there are many frequencies that would be coincident in the Raman and IR spectra. PEO has 20 coincident Raman and IR bands, but PES has only two coincident frequencies, and these coincident bands are the result of 'accidental' degeneracies. Accidental degeneracies arise when the frequency differences between modes are too small to be resolved within the instrument. Thus, the configuration of PES is opposite to that of PEO. In PEO, the C−C bond takes the gauche form, and the C−O bond takes the trans form; but in PES, the C−C bond takes the trans form, and the C−S bond takes the gauche form [6].

This mutual exclusion rule for molecules with a center of symmetry is one example of the manner in which symmetry within a molecule can influence the selection rules for vibrational spectroscopy. All elements of symmetry influence the selection rules. The selection rules can be evaluated by using the structural models of the molecules, and the proper structural model for a molecule can be determined by comparing the experimental results with the theoretical results. This approach to structure determination has been a valuable tool for the study of the various geometric structures of low-molecular-weight substances. This approach can also be used in the study of polymer conformation.

For polymers, the additional measurements of polarization in Raman spectroscopy and dichroic behavior in IR spectroscopy can be used to aid in the classification of the vibrational properties. In combination, the two techniques can be used to measure the vibrational modes and to classify these vibrational modes into types that are unique to the molecular symmetry of the polymer chain.

A general example is the monosubstituted vinyl polymers $(CH_2-CHX)_n$, which can exist in two possible stereoregular forms — *isotactic* (substitution on the alternate carbons on the same sides of the chain) and *syndiotactic* (substitution on the alternate carbons on the opposite sides of the chain). These ordered stereoregular forms can assume either planar or helical conformations. Each of these ordered structures has well-defined, unique selection rules for IR and Raman activity. These various structures can be distinguished on the basis of spectral properties without a detailed knowledge of the molecular motions or energies, that is, without normal coordinate analysis.

Any observed vibrational spectra can be classified into sets of modes that are defined as follows:

- [R, IR] Frequencies coincident in both Raman and IR spectroscopy.
- [R, 0] Frequencies active in Raman spectroscopy, but inactive in IR spectroscopy.
- [0, IR] Frequencies inactive in Raman spectroscopy, but active in IR spectroscopy.

In addition to these three general classifications, each set of IR and Raman polymeric frequencies can be subclassified according to their individual Raman polarizations and IR dichroic behaviors. The Raman lines may be polarized or depolarized,

and the IR bands may have parallel or perpendicular dichroism with respect to the polymer chain axis. The terminology for describing the observed frequencies in the IR and Raman spectra is based on the general expression $[a, b]$, where a indicates the polarization properties of the Raman lines, and b indicates the dichroic behavior of the IR bands. On this basis, a may be p (polarized), d (depolarized), or 0 (inactive), and b maybe σ (perpendicular), π (parallel), or 0 (inactive). Therefore, the expression $[p,\sigma]$ indicates that the observed frequency is found in both the Raman and IR spectra and is polarized in the Raman spectrum and has perpendicular dichroism in the IR spectrum. On this basis, all observed frequencies in the IR and Raman spectra must fall into one of the following classifications: [p,0], [d,0], $[0,\pi]$, $[0,\sigma]$, $[p,\pi]$, $[p,\sigma]$, $[d,\pi]$, and $[d,\sigma]$.

Any spectrum can consist of any or all combinations of the aforementioned mode types. The range of possibilities for a given ordered polymer structure is determined solely by the symmetry properties of the polymer. However, the picture may be distorted by the limited spectral sensitivity of the Raman and IR instrumentation (in other words, a Raman or IR vibrational mode can be expected theoretically, but the intensity of the mode is so low that it is not observed experimentally). Instruments yielding high signal-to-noise ratios will minimize this problem. Another complication is the presence of multiple or disordered structures (which have no specific selection rules) that cause deviations from the pure mode selection rule requirements of the perfect chain. The spectral bands that are associated with minor amounts of irregular structures are weak and variable in intensity from sample to sample, which makes their detection possible in some cases.

The band classification for each type of polymer chain stereoconfiguration and conformation for monosubstituted vinyl polymers can be calculated, as shown in Fig. 5.4.

Selection Rules for Monosubstituted Polyvinyl Polymers

	STRUCTURE	SYMMETRY	OPTICAL ACTIVITY R: p p d d / iR: σ π σ π	OPTICAL ACTIVITY p d: 0 0	OPTICAL ACTIVITY 0 0: π σ	EXAMPLE
	CENTER OF SYMMETRY	D_{2h} C_{2h}		XX	XX	PE PES
	ATACTIC		XXXX			PVF
SYNDIOTACTIC	HELIX>3$_1$	D_n	X	XX	X	PEO
SYNDIOTACTIC	HELIX 3$_1$	D_3	X	X	X	
SYNDIOTACTIC	HELIX 2$_1$	D_2	XX	X		
SYNDIOTACTIC	PLANAR	C_{2v}	XXX	X		PVC
ISOTACTIC	HELIX>3$_1$	C_n	X X	X		POLYBUTENE
ISOTACTIC	HELIX 3$_1$	C_3	X X			PP
ISOTACTIC	PLANAR	C_s	X X			

Fig. 5.4. The IR and Raman polarizations for monosubstituted vinyl polymers. (Source: Ref. [2].)

Every polymer structure possesses a unique collection of spectroscopic vibrations, and on this basis, the stereoconfiguration and conformation of the polymer chain in the solid state can be determined by measuring of the properties of the spectroscopic vibrations.

A specific example is poly(vinyl chloride) (PVC), which is a monosubstituted vinyl polymer that has a syndiotactic-rich character and a conformation that can be either an extended all-trans structure or a folded syndiotactic structure. The vibrational modes of these conformational models obey different selection rules and have different dichroic properties that can be used to spectroscopically test these structures [7]. The folded syndiotactic model of PVC has the [p,0] classification that requires unique Raman lines (no coincident IR frequency) that are polarized. The extended syndiotactic model has the two unique classifications of [d,0] and [p,σ], which means that the unique Raman lines are depolarized, and the Raman lines that are polarized have perpendicular dichroism in the IR spectrum. In the Raman spectrum of PVC [8], polarized lines are observed at 363, 638, 694, 1172, 1335, 1430 and 1914 cm^{-1}, and IR bands are also observed at each of these frequencies. This result rejects the folded syndiotactic structure, because this structure requires the polarized lines to be unique. In addition, each of these frequencies is perpendicularly dichroic in the IR spectrum, a fact that supports the planar syndiotactic structure.

This structural determination method, which is based on differences in the IR and Raman frequencies, is a general method for ordered polymer structures in the solid state. This approach is particularly useful for noncrystalline and insoluble systems.

Limitations of Raman spectroscopy resulting from fluorescence

One of the principal problems in Raman spectroscopy is *fluorescence.* Fluorescence occurs when the excitation line is partially absorbed and remitted. *Phosphorescence* is luminescence that is emitted for a significant period of time (in the millisecond to second time regime) after excitation. Many compounds that do not fluoresce do exhibit phosphorescence.

The principle limitation of Raman spectroscopy in the visible region is that of fluorescence and Raman spectra cannot be obtained from many samples because of the curtain of fluorescence that hides them. Even if the fluorescence is assumed to arise from an impurity that is present at the parts-per-million level, with a fluorescent quantum yield of only 0.1, 10 fluorescent photons will be produced for every Raman photon. In the visible excitation region, 95% of polymers are not amenable to Raman analysis because of unquenchable fluorescence.

> *It is also safe to say that the more desperately that you need the Raman spectrum, the more likely it is that unquenchable fluorescence will raise its ugly head.*

A number of methods to remove fluorescence resulting from impurities have been attempted [9].

> *If the fluorescence is not the result of an impurity but rather from the sample itself, the sample will usually burn up very quickly in the laser beam, and a neat looking hole in the sample will result. Under these circumstances, you have removed the fluorescence along with the sample, and you can't obtain a Raman spectrum.*

The most convenient and often-used method of fluorescence removal is photobleaching, that is, exposure of the sample to the laser beam until the fluorescence decays. In many cases, a few minutes of exposure to the laser beam will cause the fluorescence to decay sufficiently that a Raman spectrum can be observed. Sometimes, exposure of the sample to the laser beam for several hours is required. The decay of the fluorescence is easily detected by driving the recorder as a function of time without scanning the monochromator. A perceptible 'bleaching' of the sample at the spot of the laser focus can sometimes be observed.

Removal of the colored impurities by exposure to activated charcoal columns (the old sugar chemist's trick) or by extraction has proven to be a successful purification method for some samples.

Sometimes, it is possible to change the laser frequency so that excitation occurs outside the absorption envelope of the fluorescent impurity. Because most fluorescence emission occurs between 270 and 700 nm, one can excite in the near IR at wavelengths longer than 700 nm, or in the UV at wavelengths shorter than 250 nm. Occasionally, changing the frequency from blue to red excitation improves the Raman signal by decreasing the fluorescence level. The laser excitation frequency can be decreased below the critical value by using a Krypton laser at 6471 Å rather than an Argon laser at 4880 Å. With UV laser light it is possible to induce photochemical changes which should be avoided.

A more drastic approach is to use an exciting frequency in the IR region that is well below the absorbing electronic frequencies. This technique has been termed the Fourier transform Raman technique. In this case shifting the Raman excitation wavelength into the near-IR means that insufficient energy is available for electronic excitation. Most materials do not show strong fluorescence in the NIR region. In addition, NIR Raman spectroscopy can avoid photodecomposition and/or photoinduced transformation. Some sample heating can occur due to absorption of the IR energy from the laser.

Fluorescence and Raman scattering can be distinguished on the basis of the duration of the two processes. In fluorescence, the system absorbs radiation and is excited to a higher electronic state. After approximately 10^{-9} s, the system re-emits radiation. Raman scattering involves no absorption of radiation. The scattering system is never in an excited electronic state, and the whole process takes place in less than 10^{-12} s. Therefore, another approach may be used to obtain the Raman spectra. *Time-resolved gated detection* recognizes that the fluorescence has a finite delay time and the Raman signal does not, and so the detection is gated to observe the immediate Raman signal and to suppress the latent fluorescence signal. This technique is very sophisticated and demanding experimentally, and unfortunately, does not completely eliminate the fluorescence signal. Consequently, it is not widely used.

Resonance enhancement can be used to remove fluorescence by making the Raman signal much more intense than the fluorescence signal. The UV-resonance Raman method can be used to enhance the Raman signal above the fluorescence signal if the sample has the proper electronic structure for resonance enhancement and if the proper UV frequency source is available. The resonance Raman technique is discussed in the section "Resonance Raman Spectroscopy" (p. 229) in this chapter.

A recent approach is the use of anti-Stokes Raman spectroscopy [10]. The advantage of this anti-Stokes measurement is that it does not restrict the Raman excitation wavelength as does FT-Raman. The disadvantage of the anti-Stokes method is the extremely weak signal obtained. In order to surmount this problem, a new instrumental system was devised which increases the density of the anti-Stokes lines by using a chromatic aberration focal lens with a highly sensitive spherical integration cell and finally with a laser power reference system.

In summary, there is no universally adequate solution to the fluorescence problem in Raman spectroscopy. All polymer samples will fluoresce, and the concern is a matter of how much fluorescence and for how long. However, with modern techniques such as FT-Raman and resonance Raman spectroscopy, there is considerable optimism that this problem can be overcome.

Experimental Raman spectroscopy

The problem facing the development of Raman spectroscopic instrumentation is the inherent weakness of the inelastic scattering. The sample has a characteristic Raman intensity, S, with units of photons s^{-1} cm^{-2} sr^{-1} which is given by

$$S = K P_D \left(\frac{d\sigma}{dO}\right)_o D_n \tag{5.1}$$

where P_D is the laser power density (photons s^{-1} cm^{-2}), $(d\sigma/dO)_0$ is the differential Raman Cross section (cm^2 $molecule^{-1}$ sr^{-1}) and D_n is the number of density (molecule cm^{-3} for liquids. K is a constant which depends on the geometry of the

experiment. As an example, benzene has a cross section for Raman scattering of 1.6×10^{-29} (cm^2 $molecule^{-1}$ sr^{-1}). If one assumes standard collection optics, the scattering efficiency is calculated to be approximately 1 in 10^{-10}. Therefore to produce a detectable Raman signal a high powered light source is needed. In addition, Raman requires a spectrometer with a very high degree of discrimination against the Rayleigh elastic scattered light. Finally, since very few Raman photons are generated, the detection system must be very sensitive to detect the Raman signal over the dark noise background [11].

In facing this challenge three general types of Raman spectrometers have evolved:
(1) conventional single-channel Raman spectrometers,
(2) optical multichannel-detector spectrometers,
(3) Fourier transform Raman spectrometers.

In addition to ordinary inelastic Raman scattering, two additional resonance enhancement forms of Raman spectroscopy have proven useful for the study of polymers: UV resonance Raman spectroscopy and surface-enhanced Raman spectroscopy. These two resonance techniques use conventional instrumentation but exhibit useful enhancement effects.

Each type of Raman spectrometer has been designed to optimize certain aspects of the Raman experiment. Conventional Raman spectrometers are designed to generate the Raman signal and differentiate it from the unwanted stronger Rayleigh-scattered light from the weaker Raman signal and count the Raman photons. These conventional Raman spectrometers are the simplest and are readily available for routine work when interfering fluorescence is not a major problem. Optical multichannel detectors for conventional Raman measurements use the multichannel advantage to increase the sensitivity and speed of acquisition of Raman spectra. Fourier transform Raman spectrometers are designed to deal with interfering fluorescence by using low-energy laser excitation. Modifications have been made to the FTIR instruments to convert them to Fourier transform Raman spectrometers. All of these instruments will be discussed briefly.

Experimental conventional Raman spectroscopy

The experimental apparatus for conventional Raman spectroscopy, outlined in block form in Fig. 5.5, includes:

- a powerful laser irradiating in the visible-wavelength region,
- an illuminating chamber for the sample,
- a high-performance light-dispersion system to resolve the more intense, elastically scattered light from the weak, inelastically scattered Raman signal,
- a light detection and amplification system capable of detecting weak light levels,
- a recorder.

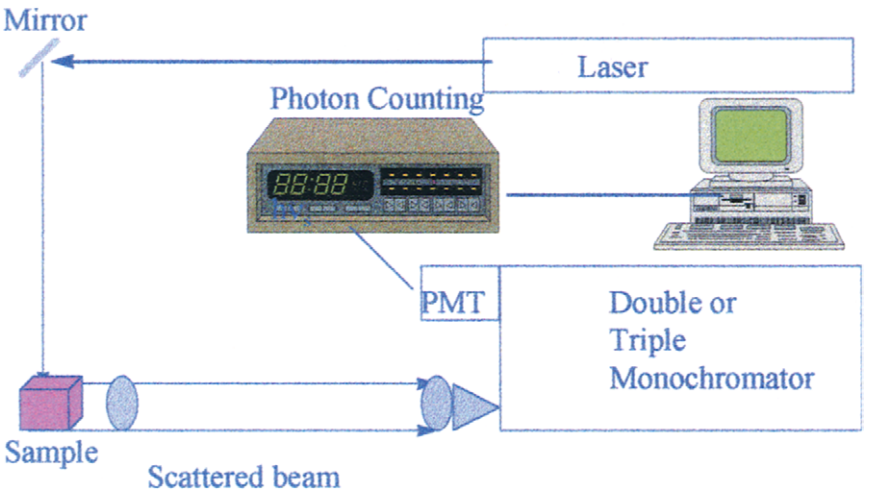

Fig. 5.5. Diagram of the components of a conventional Raman spectrometer.

Raman illumination sources

The first source for Raman spectroscopy was the sun, which is not a very intense spectroscopic source. A helical mercury arc (the Toronto arc) that surrounded a cylindrical sample was developed later and was the only source used for many years. In order to obtain a Raman spectrum with a Toronto arc, the samples had to be colorless and free of dust and fluorescence. This requirement for the samples was a major restriction for the study of polymers at the time. With the advent of the laser light source, Raman spectroscopy underwent major growth as Raman spectra with a high signal-to-noise ratio could be obtained in a reasonable measurement time. Additionally, the frequency of the laser source could be selected to avoid adsorption of the laser by the sample (leading to sample destruction) and to minimize the fluorescence (going to lower energies). With modern Continuous Wave (CW) gas lasers can be operated in a stabilized output called 'light mode'. In this light mode, the photon flux of the laser can be kept constant for several hours, yielding a constant incident signal.

The main advantages of a laser light source for Raman spectroscopy are:

- directionality which makes focusing simple,
- coherency which enhances the usable power,
- intensity which yields a high power density,
- monochromaticity which eliminates multiple Raman lines,
- inherent linear polarization which yields quality polarization measurements.

Typically, the focused laser spot produces a high-power density of the order of 10^4 to 10^6 W cm^{-2}. Power-densities of this magnitude can produce heating and decomposition of sensitive, especially absorbing, samples. The laser can heat up the sample

substantially. If the incident laser beam of radiance I_0 (W/cm^2) radiates a sample of radius, r (cm) in contact with a substrate of thermal conductivity (K/cm/K) with efficiency E, then the temperature rise, T, is given by:

$$T = \frac{EI_0 r}{4K} \tag{5.2}$$

For a typical transparent material, E is approximately 1×10^{-4} so if the sample is in contact with air having thermal conductivity, $K = 2.6 \times 10^{-4}$ W/cm/K, the temperature of the sample potentially could rise ~200°C. Defocusing of the beam or the use of less laser power can minimize these effects but at the expense of lower S/N ratio.

Improvements in lasers as the technology has evolved has resulted in a large array of available frequencies ranging from the UV to the infrared and Raman spectroscopy has been the beneficiary of these advances. Particularly, in the reduction of flores-cence where near infrared lasers can be used with energies below the electronic energy levels of most molecules.

The choice of laser excitation frequency depends on the type of sample being examined. In most cases, the laser wavelength is chosen to avoid any absorption by the sample as it may be destroyed by photodecomposition. Visible excitation may produce a large background of fluorescence. Sometimes, for particular samples, exciting at longer wavelengths can decrease the fluorescence. Occasionally, a particular exciting wavelength may reasonably enhance certain features of the spectrum. In a resonance Raman experiment where the laser is absorbed by the sample, certain vibrational modes, which are coupled to the absorbing chromophore, are enhanced in the Raman. In some cases the Raman scattering cross section can be orders of magnitude larger, making the Raman signal greatly enhanced. However, there is also a high risk of the sample being destroyed by photochemical effects or thermal heating under resonance Raman conditions.

Using lasers as spectroscopic sources requires that short term fluctuations be minimized or eliminated. Most of the current lasers have feed-back systems which control the fluctuations.

A monochromatic laser light beam is characterized by its wavelength (λ), power, and polarization. The frequency, ν, is given by

$$\nu = \frac{c}{\lambda} \tag{5.3}$$

where c is the speed of light (2.9981010 cm/s in a vacuum), λ is expressed in centimeters, and ν is expressed in Hertz, or cycles per second.

The wavelength of light is commonly expressed in angstroms (Å), and 10 Å = 1 nm = 10^{-9} m. The wavelength (or frequency) of light is related to the energy, E, by

$$E = h\nu \tag{5.4}$$

Table 5.3
The wavelengths and typical powers of common lasers used in Raman spectroscopy

Laser	Wavelength (nm)	Wavenumber (cm^{-1})	Power (mW)
Ar-ion	488.0 (blue)	20491.8	1500
	514,5 (green)	19436.3	2000
Kr-ion	413.1 (violet)	24297.2	1800
	530.9 (green-yellow)	18835.9	1500
	647.1(red)	15453.6	3500
Kr-ion	206.5 (UV) [1]		4
(frequency doubled)	234 (UV) [1]		8
He–Ne	632.8 (red)	15802.8	50
Nd–YAG	1064 (near-IR)	9398.0	500000
Ti : sapphire	1300 (near-IR)		750
Diode lasers	785 (near IR)	12740	500
	840 (near IR)	11900	500

[1] J.W. Holtz, R.W. Bormett, Z. Chi, N. Cho, X.G. Chen, V. Pajcini, S.A. Asher, L. Spinelli, P. Owen and M. Arrigoni, Appl. Spectrosc. 50 (1996) 1459.

where h is Planck's constant. The energy of a single photon in Joules, E_p, is

$$E_p = \frac{1.986 \times 10^{-16}}{\lambda \text{ (nm)}} \tag{5.5}$$

where λ is the wavelength.

The photon energy available from 1 mol of photons can be calculated as joules Avogadro's number (in kilocalories per mole), where 1 cal (thermochemical) = 4.184 J. Because Avogadro's number is equal to 6.02210^{23}, the energy of 1 mol of photons at 500 nm can be calculated as

$$\frac{(3.973 \times 10^{-19}) \times (6.022 \times 10^{23})}{4.184 \times 10^{3}} = 57.18 \text{ kcal/mol} \tag{5.6}$$

Table 5.3 shows the wavelengths and typical powers of common lasers used in Raman spectroscopy.

Dispersing optical elements: monochromators

Raman spectral measurements require the detection of a small Raman signal in the presence of a much stronger elastically scattered Rayleigh signal. Liquid samples of high purity show Rayleigh intensities that are 10^6 stronger than the Raman signal. In normal Raman measurements, the conventional approach to reducing the amount of Rayleigh signal reaching the detector is to use multiple stages of dispersion at the cost of greatly reducing the overall throughput. Double and triple monochromators are used to reduce the intense elastically scattered light to a low enough level that

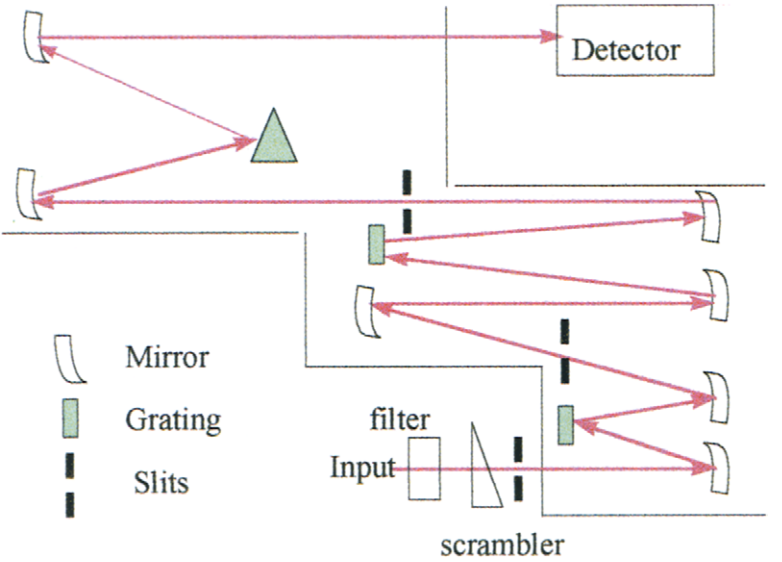

Fig. 5.6. The optical diagram of a triple monochromator.

the extremely weak Raman signal can be detected. Because the Raman signal is only 10^{-9}–10^{-6} as strong as the Rayleigh line, two and three grating monochromators are used in tandem to reduce the Rayleigh-scattered light to an acceptable level. The stray light rejection is basically a function of the quality of the gratings. A typical single-stage monochromator provides stray light rejections of 10^{-5} to 10^{-6}. A double monochromator will reduce the stray light at the detector to 10^{-10} and a triple will yield a stray light level of 10^{-15}. Unfortunately, double or triple grating systems results in 1–7% transmission efficiency because of reflection losses and grating efficiencies.

The triple monochromator shown in Fig. 5.6 has three slits with one between each monochromator and three gratings with the necessary reflecting mirrors. Stray light performance is further improved by minimizing the Rayleigh light entering the monochromator by using narrow-band rejection filters such as holographic edge and notch filters, absorption of an atomic or molecular vapor, placed in front of the monochromator. The perfect rejection filter would have a cutoff of ± 30 cm^{-1} from the excitation line, a large optical density (approx. 6.0) in the cutoff region and 100% transmission outside the cutoff region [12]. Supernotch Holographic filters approach this ideal behavior.

The illuminating chamber is simple and is built to facilitate the focusing of the beam on the sample. A long focal length lens is used in order to vary the spot size on the sample.

The laser beam is first filtered to remove the plasma lines and then passes through a beam rotator and then focused on the sample. The beam is scattered from the

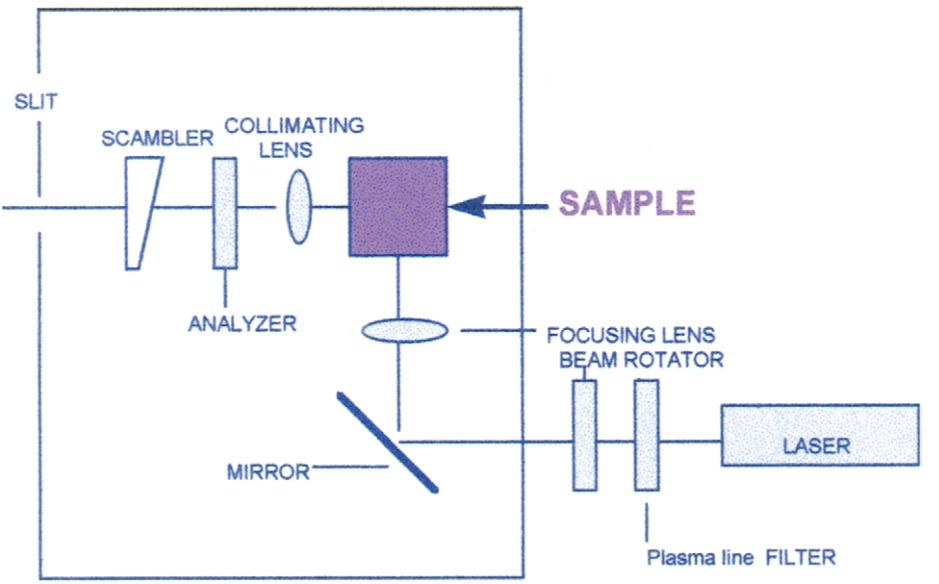

Fig. 5.7. Optical diagram of the Raman sampling chamber.

sample. The scattered light is condensed by using a lens system and is focused on the slits of the light-dispersion system. A lens focuses the light on the dispersive slits after passing through a polarization analyzer and then through a scrambler, which depolarizes the light before it, enters the monochromators (Fig. 5.7).

The sample is placed at the focal region of the laser beam and it is desirable to collect all of the Raman radiation emerging from the sample. The collection optics for the Raman experiments are shown in Fig. 5.8 for the forward scattering of 90° and a backscattering of 180°. The optical conductance of the collection optics should be the same as for the monochromator. These illuminating systems consist of two lens with the first lens having a short focal length with a low f number in order to collect the largest possible amount of light from the scattering due to the sample. The second lens is a collection objective, which focuses the image of the sample scattering on the monochromator slit. This lens should have an f number matching the monochromator. The forward scattering 90° system is simple and versatile. The 180° backscattering system has a small prism on the front of the first lens, which causes some loss of signal due to the obstruction caused by the prism.

The detector for conventional Raman instrumentation involves photon counting by photomultiplier tubes (PMTs). A phototube consists of an evacuated glass envelope containing a surface coated with an active metal. Incident radiation causes emission of electrons from this surface by the photoelectric effect; a positively charged plate termed dynodes collects these electrons. The plate current is proportional to the intensity of the radiation. The photomultiplier effect arises when the electrons emitted from the cathode of a phototube are accelerated by a large potential and then allowed

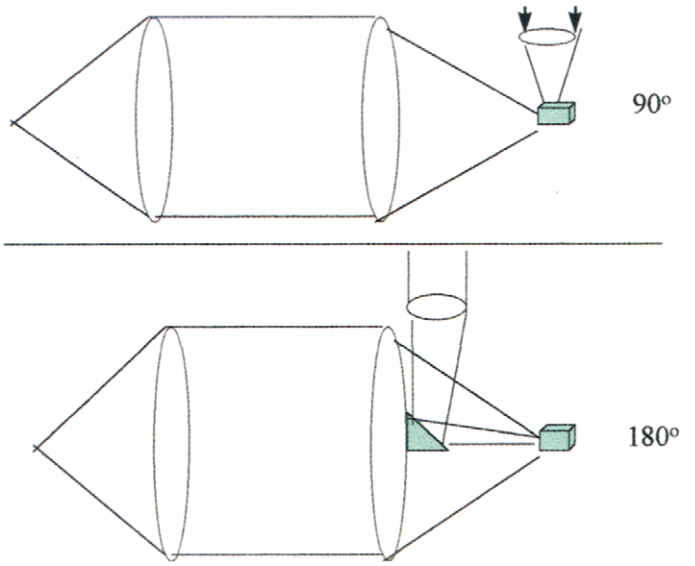

Fig. 5.8. The illuminator system showing optics for 90° and 180° scattering.

to strike another active surface; it is possible to get multiple emission of electrons from the second surface for each of the original electrons. These secondary electrons may, in turn, be accelerated, and upon striking the next surface, give rise to a larger number of electrons. By combining ten or twelve such amplification stages, it is possible to get stable amplification of the original signal by a factor of a million or more.

PMTs are used because of their large internal gain and low noise readout. The noise arises mainly through the dark current due to the random thermal excitation of electrons. The PMT has a $D^* \simeq 10^{16}$ at room temperature. By cooling of the PMT, the dark current can be made negligible, so that then $D^* \simeq 10^{19}$, which corresponds to about 1 false photon/second. For detecting low-intensity visible light, nearly ideal performance (i.e., limited only by light fluctuations) can be achieved by using a cooled PMT with a high quantum efficiency for the spectral region of interest. For detection of Raman signals, the PMTs must exhibit extended red response.

The disadvantages of these devices include the following: the peak quantum efficiency of PMTs rarely exceeds 20%; only one wavelength can be monitored at a time, and they are difficult to use in a multichannel configuration. PMTs also can be damaged by exposure to high light levels. The cost of PMTs is high and they are mechanically fragile.

The output from the photomultiplier is fed to a discriminator amplifier that detects only electron bursts originating on the photocathode and in this way produce counting statistics which are limited only by shot noise.

Optical multichannel Raman spectrometers

Raman instruments have been developed which utilize a polychromator or spectrograph and a multichannel detector instead of the monochromator and single channel detector (a photomultiplier tube). The entire Raman spectrum is collected simultaneously using an array of detectors in which each element of the multichannel detector is of comparable sensitivity to a single photomultiplier. The assumption is that all light incident on the detector is correctly positioned with a single wavelength incident upon each single detector. In this way the measurement time needed to record a spectrum is reduced by a factor of 10–200. Additionally, the simultaneous detection of the spectrum increases the accuracy of intensity measurements of different Raman bands and avoids errors in interpreting accidental changes in the background due to laser fluctuations. The ideal Raman spectrometer would consist of a high-dispersion, low-stray-light single monochromator with a multichannel detector. A diagram of a multichannel Raman instrument is shown in Fig. 5.9.

When a multichannel detector is used, only a limited wavelength range can be observed at any one time. This range is determined by the size of the detector, the spectrometer position (or spectrometer wavelength) and the linear dispersion of the grating at the detector. The wavelength at a particular detector element is determined by the position of that element at the focal plane of the monochromator, (the grating position). However, due to the small size of the detector elements (typically 20–30 μm) and the large number of variables affecting the dispersion of the light at the focal plane, calibration of the spectrometer is required and such calibration needs to be performed often. Ultimately, it is the accuracy of the calibration, which determines the reproducibility of the spectrometer [13,14].

Multichannel Raman spectrometers are similar to the conventional systems except that the photomultiplier tube is replaced with an optical multichannel detector

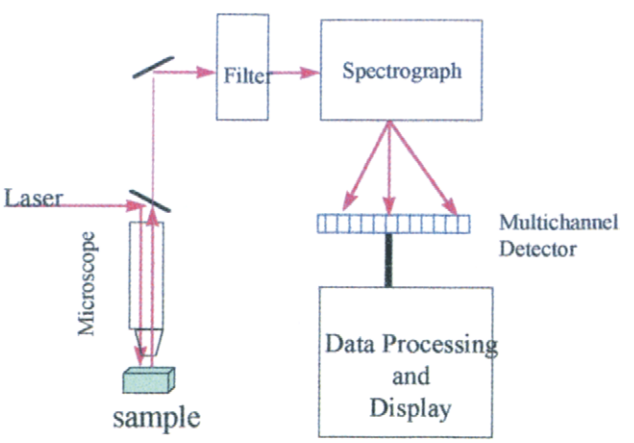

Fig. 5.9. Optical diagram of a multichannel Raman spectrometer.

(OMD). The OMD consists of many (500–1000) photosensitive elements, each monitoring a different wavelength at the focal plane. Instead of scanning the wavelengths across the exit slit, the dispersed spectrum is focused onto an OMD at the focal plane. An intensified photodiode array can monitor 1000 wavelengths simultaneously.

Multichannel Raman spectrometers have a number of advantages compared to conventional Raman spectrometers [15]. First, OMDs allow a substantial segment of the Raman spectrum to be recorded simultaneously without scanning the spectrometer's wavelength setting. This capability of simultaneous analysis of multiple data points makes it possible to record an image (10^3 channels) rather than an average light intensity of a single frequency. Thus, the instrument can be operated as a spectrograph rather than as a scanning monochromator. Typically the multichannel detector can monitor a frequency range of 600 cm^{-1}.

Sensitivity is the primary advantage of the OMD. The sensitivity of the photodiode for an area of 25 × 2.5 μm is similar to that of a good photomultiplier tube. The OMD also has a short response time that permits the storage of all the spectral elements in 'single-exposure' duration of as short as a few milliseconds. Each element, or pixel, of the photodiode array stores a charge proportional to the integral number of photons striking the element. At intervals of 10 ms or more, the stored charge from all pixels is read, and the pixel is reset. With this repetitive integration and readout, a series of spectra can be generated, and each of these spectra represents a Raman scattering during a 10-ms segment of time. In this manner, time-resolved Raman spectra can be obtained.

Multichannel detectors offer new possibilities for investigation of photolabile systems since less laser power is required to obtain a high S/N.

The limitations of the OMDs involve a resolution/bandwidth trade-off. If high bandwidth or spectral coverage is required, then resolution must be sacrificed. In addition, there is some cross-talk between the adjacent elements which further reduce the resolution. There is also a limitation which arises primarily from the fact that the maximum spectral region that can be measured at one time is limited by the active area of the detector and the available dispersion of the grating. The connection of two or more separately measured spectral regions is a prerequisite for obtaining a complete Raman spectrum. There are also the inevitable channel-to-channel differences in sensitivity, particularly at the edges of the array. Because detector sensitivity falls off at each end of the active area, it is necessary to make a sensitivity calibration to generate a smoothly connected spectrum [16].

Today, CCDs are thinned and back-side illuminated and have quantum efficiencies of greater than 70% and a spectral range from 350 to 1000 nm. The response of these detectors is quite good in the red, and with quantum efficiencies peaking near 700 nm.

Fourier transform Raman spectroscopy

Fourier transform Raman spectroscopy is designed to eliminate the fluorescence problem encountered in conventional Raman spectroscopy [17]. Fluorescence can be avoided by using an excitation frequency below the threshold for any fluorescence process. The most common excitation frequency for FT-Raman spectroscopy is the Nd : YAG laser source at 1.064 μm (9398 cm^{-1}). Consequently, the Raman scattering occurs in the 5398–9398-cm^{-1} (near-IR) region, and conventional FTIR instrumentation can be used with slight modification. Rejection of the Rayleigh line is accomplished by using absorption filters (dielectric interference filters) that are designed to pass wavelengths that are longer than the laser wavelength. The sharpness of the cutoff determines the low-frequency limit (200 cm^{-1}) of the FT-Raman spectrometer.

FT-Raman also benefits from advantages inherent to interferometry: high collection efficiency, excellent wavelength precision, easily variable resolution, spectral coverage, and software developments in FTIR. The restrictions of FT-Raman arise from the low signal to noise ratio. This is because the SNR is limited by detector noise rather than signal shot noise. The result is a SNR comparable to that for a single-channel dispersive system with equal measurement time [18].

The FT-Raman instrument has the following components:

(1) a near IR laser excitation source (typically Nd : YAG at 1.06 μm),
(2) a Fourier transform interferometer equipped with the appropriate beam splitter (quartz) and a detector (InGaAs or Ge) for the near-IR region,
(3) a sample chamber with scattering optics that match the input port of the Fourier transform instrument,
(4) an optical filter for rejection of the Rayleigh-scattered light.

A diagram of such an instrument is shown in Fig. 5.10.

The notch filter minimizes the amount of Rayleigh scattered light entering the interferometer and is essential for FT-Raman spectroscopy. All of the collected light strikes the detector simultaneously including the elastically scattered component, which is more intense than the Raman components by many orders of magnitude. This tests the dynamic range of the system and small errors in the measurement of the center burst are distributed over all of the Raman frequencies. In some cases, this can amount to 2–5%.

Typically, a visible He : Ne laser beam is coaligned with the invisible Nd : YAG laser beam to make it possible to align and focus the Nd : YAG beam. Another option is to use fiber optics [19]. With fiber-optic components, optical alignment is virtually eliminated which allows rapid switching from one sample to another.

The spectral advantage of FT-Raman spectroscopy is the removal of fluorescence. The FT-Raman technique is specifically designed to eliminate fluorescence, and in some cases, the effects are quite dramatic. The spectra of a highly fluorescing dye

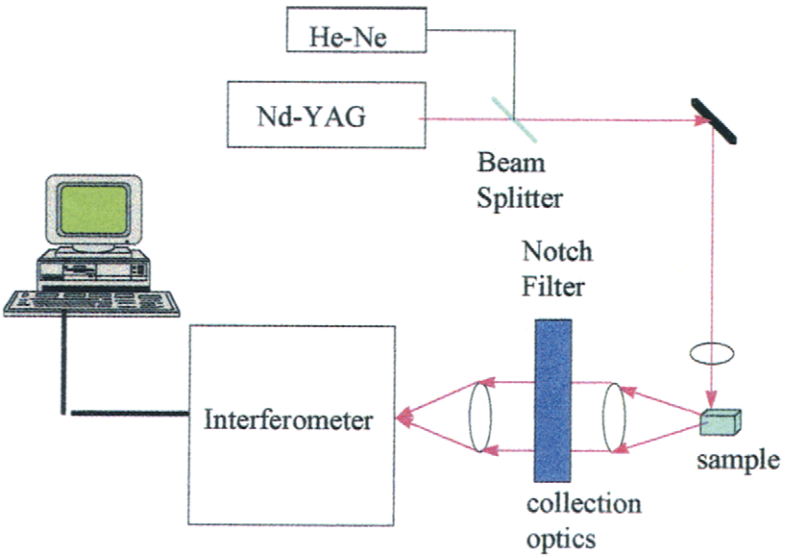

Fig. 5.10. Optical diagram of a Fourier transform Raman instrument.

shown in Fig. 5.11 were obtained with conventional visible Raman and FT-Raman spectroscopy [20].

The resulting spectra suggest that the effort required to accomplish the FT-Raman method is rewarding.

The advantages of collecting Raman spectra by using Fourier-transform techniques are counterbalanced by potential difficulties that arise primarily from the distinction between inherently weak Raman signals and extraordinarily strong, undesired Rayleigh scattering. The noise associated with an intense Rayleigh line is redistributed across the entire spectrum by the Fourier transform process creating an increase in multiplicative noise (often termed the *multiplex disadvantage*) which is distributed over the entire Raman spectrum [21]. Thus, effective use of the FT-Raman technique requires a reduction in the intensity of the Rayleigh line so that the energy reaching the detector is primarily Raman-scattered radiation. Notch filters and colloidal-gel-diffracting filters are currently being used for this purpose, and the laser line is Bragg-diffracted so that its transmission through the filter is less than 10^{-10}. The notch filter transmits Raman-shifted lines with greater than 50% efficiency.

FT-Raman spectroscopy using FTIR instrumentation solves another problem frequently encountered in conventional Raman spectrometers, which is the lack of sufficient frequency precision required to perform spectral subtractions. This poor precision arises from back-lash in the mechanical drive and fluctuations in the laboratory environment which causes changes in alignment.

FT-Raman spectroscopy does have some disadvantages, as might be expected. The cross section for Raman scattering at the IR excitation wavelength of 1.06 μm is

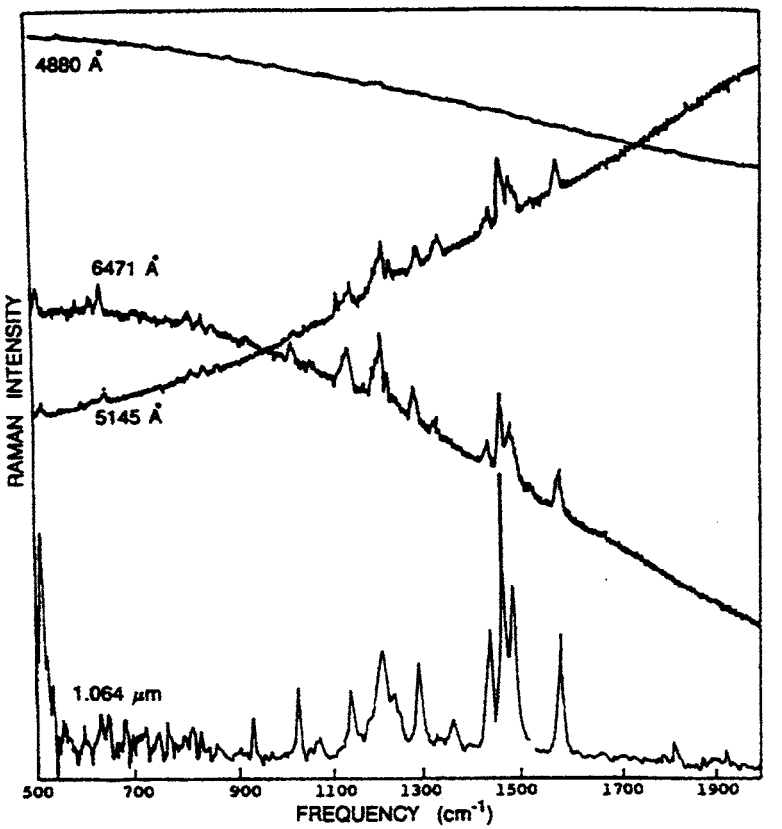

Fig. 5.11. Raman spectra of a cyanine dye, 3,3-dioctadecyl-2,2′-methylene-bis(benzothiaxole) perchlorate, recorded at different wavelengths throughout the visible and into the near-IR. (Reproduced with permission from Ref. [17]. © 1987 Society for Applied Spectroscopy.)

reduced by a factor of 16 from that of the visible excitation wavelength of 5145 Å. The result is a considerable loss in sensitivity because the small Raman scattering cross sections of molecules.

Recently, Ti : sapphire lasers which excite at 1.3 μm show beneficial for further minimization of fluorescence [22].

Improved detectors (i.e., near shot noise limited) for the IR regions are necessary. Because the process requires IR radiation, absorption can result in local heating, particularly for black samples.

Resonance Raman spectroscopy

Resonance Raman takes place when the frequency of the exciting lines is near the absorption frequency of a chromophore in the sample [23,24]. The Raman signal

from the corresponding chromophore can be enhanced by seven or eight orders of magnitude. Resonance Raman occurs when the energy of the exciting beam is close to an electronic energy level of the molecule and the excitation makes one term in the sum of eigenstates dominate over all others. When this occurs, the electron cloud surrounding the molecule is more readily distorted by the electric field of the incident light. The transition has a higher probability, and there is an enhancement of the Raman process. The vibrational modes enhanced are generally totally symmetric and distort the molecule along directions of electron density changes between the ground and the resonant electronic excited state.

When the laser wavelength used to excite the Raman effect lies under an intense electronic absorption band of a chromophore, this condition will lead to a considerable resonance enhancement of the Raman signal by a factor of 10^3 to 10^6. With resonance Raman in the absence of fluorescence, detection limits for an individual component can be less than one femtogram [25].

A tunable pulsed-UV laser source (frequency-doubled Nd : YAG laser) that pumps a dye laser can produce radiation from 217 to 450 nm and will allow the observation of the resonance Raman effect. Contrary to the high power required by conventional Raman and FT-Raman spectroscopy, the typical power requirement for resonance Raman spectroscopy is only a few milliwatts. The resonance Raman spectrometer and detectors are the same as for the conventional or multichannel Raman systems.

The most obvious advantage of resonance Raman spectroscopy is the enhancement of the observed UV excitation by 6 to 7 orders of magnitude. These high intensity enhancements allow trace analysis at the 20-ppb level. The enhanced vibrational modes are generally totally symmetric and are associated only with the electronic chromophore being excited. This condition results in a considerable simplification of the Raman spectrum and allows a selected chromophore to be used as a probe in the molecule.

Exciting higher electronic states sometimes eliminates fluorescence interference and makes resonance Raman spectroscopy a viable method when fluorescence is a problem in the conventional Raman experiment [26].

There are some inherent disadvantages in resonance Raman spectroscopy. The observed modes are associated only with the excited chromophore, and in some cases, this may not be the chromophore of interest. Because irradiation occurs at an absorption frequency of the sample, undesirable photochemistry may destroy the species under investigation. For quantitative analysis, there is the possibility of nonlinear variations in intensities that depend in a complex way on the proximity of the laser excitation wavelength to the electronic maximum of the sample [27].

The availability of a range of excitation frequencies from the laser source makes exploitation of this form of Raman scattering possible. There are currently available laser systems that can be easily operated at many discrete excitation lines in the UV.

Detection of UV-RR spectra is complicated by a number of experimental difficulties: the photo-oxidation and photodestruction of molecules, distortion of spectral information due to optical saturation phenomena and photo-induced transients, and fluctuations of the scattered light intensity in inhomogeneous samples.

At this stage it may be desirable to compare resonance Raman spectroscopy with FT-Raman spectroscopy. FT-Raman spectroscopy allows vibrations that are not associated with the electronic chromophore to be observed. Additionally, FT-Raman spectroscopy exhibits linear scattering intensities that allow quantitative analysis. On the other hand, resonance Raman spectroscopy is much more sensitive than FT-Raman spectroscopy [28].

UV-excited Raman spectra of a number of synthetic polymers have been reported [29]. Raman spectra using pulsed laser output between 218 and 242 nm can be generated with very low power (<1 mW) but care must be taken to prevent photo-oxidation and thermal degradation. UV resonance Raman spectra will be most valuable in the generation of fluorescence-free spectra for UV transparent polymers.

Surface-enhanced Raman scattering

It has been observed that the Raman effect for molecules in contact with noble metal surfaces is resonantly enhanced by several orders of magnitude [30,31]. In order to achieve large surface Raman signals, it is necessary that the metal surfaces be specially prepared in one of several ways, which renders them rough or finely divided on a length scale comparable to optical wavelengths. Under favorable conditions, SERS-active metals enhance the surface Raman intensity by up to ca. 10^5-fold, giving strong Raman signals.

When the incident radiation interacts with the surface, it causes the free electrons to oscillate with the incident electric field and polarizes the noble metal particles [32]. This creates a strong local electric field at the particle surface known as a *surface plasmon*. When a molecule is in close proximity to a noble metal particle the molecule is polarized by the electric field of the noble metal particle. This leads to an enhancement of the Raman signal because the Raman scattering is proportional to the square of the local electric field. The enhancement originates, in part, from the interaction of the optical frequencies with the electric field of the noble metal particles.

However, the Raman resonance enhancement due to the surface decreases very quickly as a function of distance, and little enhancement is obtained for molecules a few monolayers away from the surface. As a result, SERS is *surface selective*. The scattering from a polymer film on a SERS-active substrate arises almost entirely from the first few molecular layers adjacent to the substrate as long as the film is less than 1000 Å in thickness. Thus SERS can be used for in situ nondestructive characterization of polymer interfaces [33]. SERS is ideal for the study of polymer–metal

composites since it enhances almost exclusively the first monolayer of molecules adjacent to the surface [34].

SERS offers considerable promise for the study of polymers for several reasons. The enhancement effect can increase Raman scattering by a factor of 10^3–10^6. Adsorption of molecules on the SERS-active metal surface causes fluorescence quenching in highly fluorescent compounds. In addition, surface-enhanced resonance Raman scattering can further enhance the Raman scattering efficiency by a factor of 10^3–10^5 above that observed under resonance or surface-enhanced conditions alone.

Local electromagnetic field effects on certain roughened materials (e.g., Ag, Au, and Cu) enhance the Raman signal by factors of up to 10^6 and make detection of monolayers straightforward [35]. Enhanced Raman spectra that are 10^5–10^6 as strong as normal Raman scattering were reported for pyridine [36].

Sampling techniques in Raman spectroscopy

The sampling techniques used in Raman spectroscopy are shown in Fig. 5.12. A sample in any state can be examined without difficulty by using Raman spectroscopy. The laser beam is narrow, collimated, and unidirectional, so it can be manipulated in a variety of ways depending on the configuration of the sample.

For liquids, a cylindrical cell of glass or quartz with an optically flat bottom is positioned vertically in the laser beam. For solids, the particular method used depends on the transparency of the sample. For clear pellets or samples, right-angle scattering is used. With translucent samples, it is helpful to drill a hole in the sample pellet. Powdered samples can be analyzed by using front-surface reflection from a sample holder consisting of a hole in the surface of a metal block inclined at 90° with respect to the beam. Injection-molded pieces, pipes, and tubing; blown films; cast sheets; and monofilaments can be examined directly. One of the advantages of Raman sampling is that glass containers can be used which can be sealed if desired [37].

Raman spectroscopy can be used to examine samples contained inside polymeric packages. The pharmaceutical industry takes advantage of this Raman internal package analysis in order to examine pills which are mixtures in which the active component is distributed in an excipient [38]. Analysis of samples directly in gel capsules is possible. For forensic purposes, drugs can be examined without opening the evidence bags. Samples like sugars and artificial sweeteners can be identified in paper packets.

An FT-Raman bottle holder accessory was recently announced that allows samples to be analyzed directly in their sample bottles. Bottles can be as large as the two-liter plastic bottle or as small as a sample vial [39].

Filled polymers can be studied by using Raman spectroscopy because the fillers such as glass, clay, and silica are weak Raman scatterers and do not interfere with the Raman spectrum of the polymer matrix.

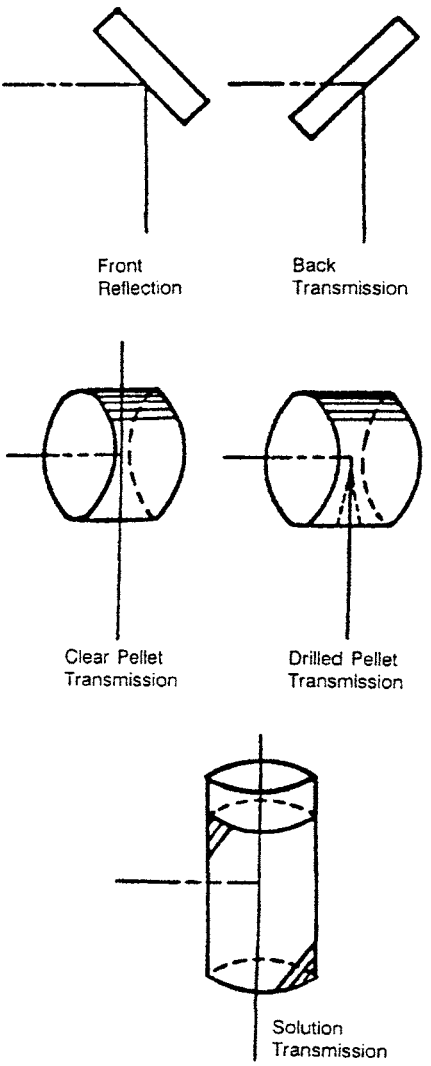

Fig. 5.12. Raman sampling techniques for polymers.

Carbon-black-filled samples present a problem for Raman spectroscopy because the carbon black will totally absorb the laser beam. The subsequent heating of the sample can lead to destructive results, including loss of sample. But it is fun watching it smoke!

Strongly absorbing samples may heat up due to absorbance of the laser beam. Rotating cells have been designed so that the exposure of any single portion of the

sample is very short. The rotating sample cell is also of use if the sample is inhomogeneous because this rotation assures that a number of regions of the specimen is sampled.

Raman studies can be carried out at high pressure, using a diamond-anvil cell [40]. To calibrate the pressure, a small piece of powdered ruby can be enclosed in a metal gasket. Using the 514.5-nm line of an Ar laser, the sharp ruby R_1 fluorescence line can be excited. This line exhibits a pressure-dependent shift (-0.753 cm^{-1}/kbar) [41]. The diamond-anvil cell is used in the 180° backscattering geometry.

Fiber-optic sampling in Raman spectroscopy

One of the advantages of Raman spectroscopy is that remote sampling can be accomplished using fiber-optic sampling [42,43]. A block diagram of a remote sampling probe using fiber optics is shown in Fig. 5.13.

An optical fiber has a transparent amorphous and homogeneous core (which is generally silica) surrounded by a cladding. Finally, there is a protective sheath around the fiber optic system. The light propagates in the core via a total internal reflection process [44].

In the original Raman applications of optical fibers, a fiber bundle was used to deliver the excitation beam to the sample and a second bundle to collect and return the scattered radiation to the spectrometer. Currently a single excitation fiber is used in the fiber-optic probe as there is less loss in radiation intensity in a single core optic cable. The efficiency of the fiber-optic probe is improved by surrounding a single excitation fiber with a number of equal-sized collection fibers ordered. A diagram of such a fiber-optic probe is shown in Fig. 5.14.

A theoretical evaluation of the parameters involved in probe designs of this type has been reported [45].

Probes have been designed with multiple excitation fibers surrounded by multiple collection fibers.

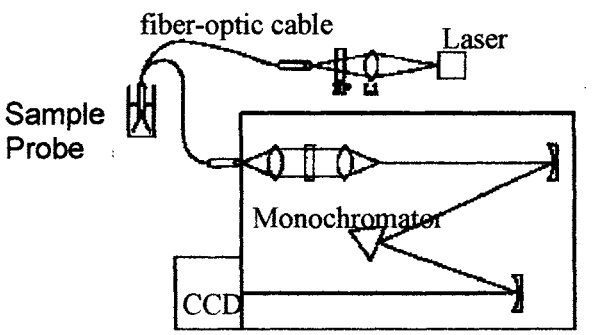

Fig. 5.13. Diagram of a Raman spectrometer with a fiber-optic remote probe. (Source: Ref. [43].)

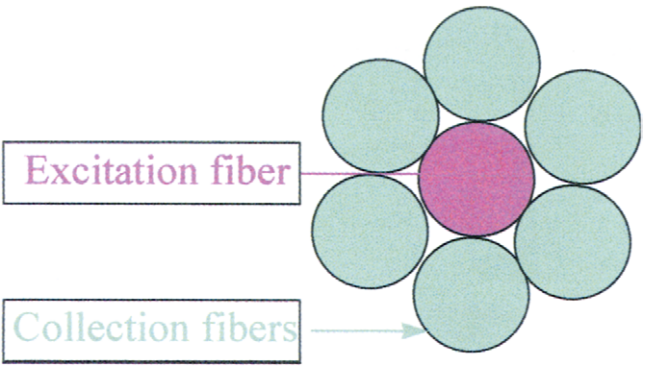

Fig. 5.14. Diagrammatic representation of 6-around-1 optical fiber system.

One of the basic problems with fiber-optic probes is the need to reduce the Raman spectra of the silica which is inevitably generated. One approach has been the development of externally filtered probes that utilize optical filters to remove the silica Raman background [46].

One of the early disadvantages of using an optical fiber is that the polarization of the Raman signal is scrambled so it was not possible to measure depolarization ratios. However, currently an enlarged fiber-optic coupling system has been designed by Kaiser Optical system, Inc. (Ann Arbor, Michigan) that allows polarization measurements.

A single-mode fiber can be used as a point detector or a pinhole [47]. Using this approach, a fiber-optic-coupled Raman microscope has been developed which facilitates focusing of the beam on the sample [48]. In another version, a fiber-optic bundle is placed in the imaging plane of a microspectrometer and functions as a variable pinhole. This arrangement allows confocal measurements to be made [49]. A primary benefit of the fiber-bundle functioning as a variable-size pinhole is it requires no physical manipulation to alter depth resolution. This fiber-optic collection system has been termed as 'super-focal' imaging as the imaging depth is considerably higher than with conventional imaging configurations. This microspectrometer was used to examine a sample consisting of three layers: diamond, 5P4E lubricant and a 100 μm thick polyester film (3M PP2500 plain paper copier film) which was translated through the laser focus at 10-μm intervals. At each point, a spectrum was taken. Fig. 5.15 shows the spectra as a function of depth.

Clearly, depth resolution is being observed with diamond appearing in the regions of 955–1014 cm^{-1}, the lubricant at 1314–1346 cm^{-1}, and the polyester at 1690–1762 cm^{-1}. The depth resolution for the confocal arrangement was determined to be 60 μm while for the superfocal configuration it was 22 μm.

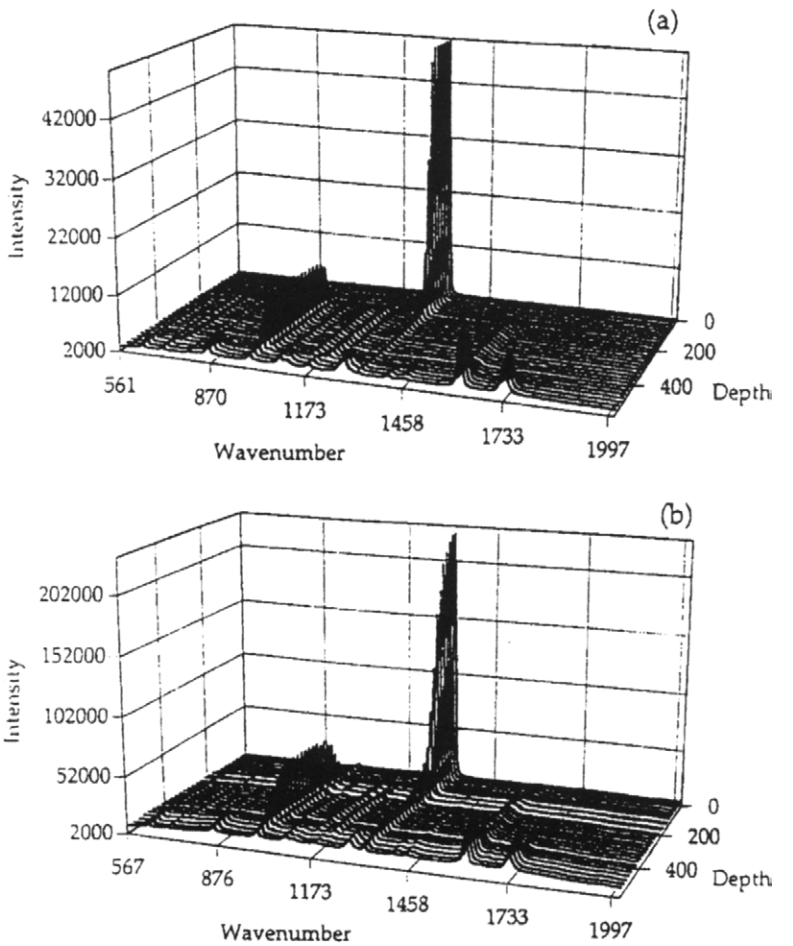

Fig. 5.15. The spectra of a three layered sample as the sample is translated axially through the laser focus. (a) Confocal configuration; (b) super-focal configuration. (Reproduced with permission from Ref. [49]. © 1996 Society for Applied Spectroscopy.)

Quantitative analysis using Raman spectroscopy

It is desirable to use Raman spectroscopy to make quantitative measurements of functional groups. The relationship between concentration (g/ml) and intensity of the Raman scattering is linear. With absorption IR, this relationship is logarithmic, and so as less radiation passes through the sample due to strong absorption bands, the measurement of absorbance is less reliable.

Quantitative measurements can be made using Raman spectroscopy and the chemometric techniques which were described for IR quantitative analysis. The demanding aspect of quantitative analysis is the fact that Raman spectroscopy is a single beam

method and fluctuations in source, optics, and sample are a problem. Raman spectra can show unpredictable shifts in absolute intensity and baseline stability. Double beam methods have an inherent method of dealing with such sources of noise. However, with proper technique and appropriate analysis of the data, a Raman-based analysis can be achieved with an uncertainty of about the one percent relative level.

One of the inherent problems in dispersive Raman spectroscopy is the problem of errors in frequency due to the resetting of the position (backlash) of the monochromator. Corrections in frequency can be made to compensate for this effect. One approach is to record a neon spectrum for which the frequencies are known. A linear regression between the pixel positions and wavelengths can be used for shifting the spectra [50].

In quantitative Raman spectroscopy of solids, the 'internal standard' technique must be used because the number of scattering sites in the laser beam cannot be determined. For solutions, a known amount of a standard can be added to determine the relative amount of the unknown material in solution.

With single beam methods, the use of an internal standard can partially compensate for some of the uncontrolled fluctuations in the measurements. One possible internal standard is water. Water has characteristic peaks, is stable and readily available (as well as cheap).

Deconvolution is a procedure for obtaining the original signal from the observed signal. In the case of Raman spectroscopy, the observed spectrum is a convolution of the original signal spectrum and the slit function of the spectrometer. The slit function affects information about the resolution, peak position, and intensity in the observed spectrum. In deconvolution, the slit function is eliminated from the observed spectrum and the original signal spectrum is obtained. The Gauss–Seidel method is a procedure which isolates the original spectrum $\mathbf{x}$ by repeating calculations of the equation

$$\mathbf{y} = \mathbf{H}\mathbf{x} \tag{5.7}$$

to fit the observed spectrum vector $\mathbf{y}$. In this equation $\mathbf{H}$ is the instrument function.

Chemical structure and composition

The choice of Raman spectroscopy for analysis of chemical composition and structure is based on the high specificity and sensitivity of the Raman effect for certain nonpolar chemical groups. In polymers, these groups are primarily the nearly homonuclear single and multiple C−C bonds that are weak or absent in the IR spectra. The characteristic group frequencies for Raman spectroscopy have been tabulated [51–53]. The Aldrich FT-Raman library contains over 14,000 compounds and has the OMNIC™ library search capability.

For polymers, Raman spectroscopy is particularly useful for characterizing the unsaturation in the monomers and polymers. The general nature of the polymerization

process can be written:

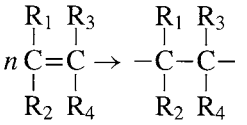

where R_1, R_2, R_3, and R_4 represent different functional groups [54]. In any case, monomers of this type show a very strong C=C stretching mode in the range from 1620 to 1680 cm^{-1} and are quite specific to the chemical nature of the substituted functional groups and to the internal structure (i.e., cis or trans).

Raman spectroscopy can differentiate between internal and external bonds as well as cis and trans isomerism and conjugation in compounds with ethylenic linkages. The type of unsaturation in butadiene and isoprene rubbers can be determined from the intense Raman scattering of the C=C stretching modes [55]. The *trans*- and *cis*-1,4-polybutadiene structures scatter at 1664 and 1650 cm^{-1}, respectively. The 1,2-vinyl structure of polybutadiene scatters at 1639 cm^{-1}, and this scattering is well-resolved from that of the 1,4-polybutadiene structures. For polyisoprene, a slightly different situation prevails. The *cis*- and *trans*-1,4-polyisoprene structures are not resolved, and they scatter at 1662 cm^{-1}, but the 3,4-polyisoprene structure scatters at 1641 cm^{-1}, and the 1,2-vinyl structure scatters at 1639 cm^{-1} [56,57].

Raman scattering of other functional groups, which give strong and specific scattering, include C≡C, C≡N, C−N, C−S, S−S, O−O, N−N, C−O, and cyclic structures. The Raman spectra of ring and aromatic compounds are also intense and highly specific to the nature of the substitution. The polymerization of styrene has been studied by monitoring the C=C stretching mode of the exocyclic vinyl group at 1631 cm^{-1} [58]. At 100°C, the bulk polymerization is first order up to about 80% conversion.

Raman spectroscopy has also been used to study urea–formaldehyde resins [59]. The important moieties in the cured resins are $-CH_2OH$ and $-CH_2OCH_2-$. The Raman line occurs at 1450 cm^{-1} for the $-H_2OH$ moiety and at 1435 cm^{-1} for the $-H_2OCH_2-$ moiety. The concentration of −NCH2N− groups increases with cure relative to the concentration of $-CH_2O-$ groups. These results support the acid-catalyzed mechanism in which methyl groups are lost by reaction with $-NH_2$ to form $-NCH_2OCH_2N-$ linkages. This latter type of $-CH_2O-$ moiety is also removed by the loss of formaldehyde to yield additional $-NCH_2N-$.

Monitoring of polymerization using Raman spectroscopy

The emulsion polymerization of methyl methacrylate (MMA) has been studied using water as an internal standard [60]. MMA has a >C−C< stretching mode which appears near 1640 cm^{-1} which overlaps the water peak at 1636 cm^{-1}. The peaks of

MMA are broader than those of the neat liquid. The reference spectrum for MMA was obtained by subtracting the spectra of water and surfactant from the spectra of MMA, surfactant and water. The reference spectrum for PMMA was prepared by subtracting the spectra of water, surfactant, and silica from the final spectrum of a reaction run. The limit of detection was 0.12% with a correlation coefficient of 0.996. These same authors have reported a similar study of the polymerization of styrene [61].

Monitoring residual monomer in polymer dispersions

Due to the high sensitivity of the Raman $-C{=}N$ stretching mode, it is possible to make an in situ determination of the distribution of acrylonitrile (AN) in rubber latex [62]. The addition of AN to an aqueous rubber latex leads to a partitioning of the monomer between the dispersion medium (water) and the polymer phase. This partitioning is directly demonstrated by the change in shape of the $\nu(C{\equiv}N)$ stretching mode which becomes a superposition of two bands at 2230 cm^{-1} (AN in the polymer phase) and 2237 cm^{-1} (AN in the continuous water phase) (Fig. 5.16). A deconvolution of this band leads directly to a determination of the amounts of AN in both phases. The intensities of the $\nu(C{=}C)$ of AN can be used as an internal standard for calibration. The partition coefficient K_{AN} of the monomer is defined as:

$$K_{AN} = \frac{m_{AN}(\text{polymeric})}{m_{AN}(\text{water})} \tag{5.8}$$

where m_{AN}(polymeric) and m_{AN}(water) are the total masses of AN in the polymeric and aqueous phases, respectively. It was determined that K_{AN} increases with increasing total monomer concentration from about 0.56 (1.3 wt% AN) up to 1.12 (9.9 wt% AN).

Degradation of polymers

One of the advantages of Raman sampling is that a complete reaction system can be studied in situ in a glass container. Thus, running the sample with water in a sealed glass container facilitates the study of hydrolysis reactions with Raman spectroscopy. Such studies have been carried out for the hydrolysis of a polyamide in a sealed glass container. Initially, the polyamide exhibited as strong band at 865 cm^{-1} characteristic of the amide group. The cell containing the sample was heated for long periods of time at temperatures up to 200°C and spectra taken at intervals. As the hydrolysis proceeded, the band at 865 cm^{-1} decreased and a new band at 925 cm^{-1} appeared which was due to the hydrolysis product [63].

Resonance Raman has also proved useful for degradation studies of a special class of polymers. PVC dehydrochlorinates when exposed to heat, the process involves the

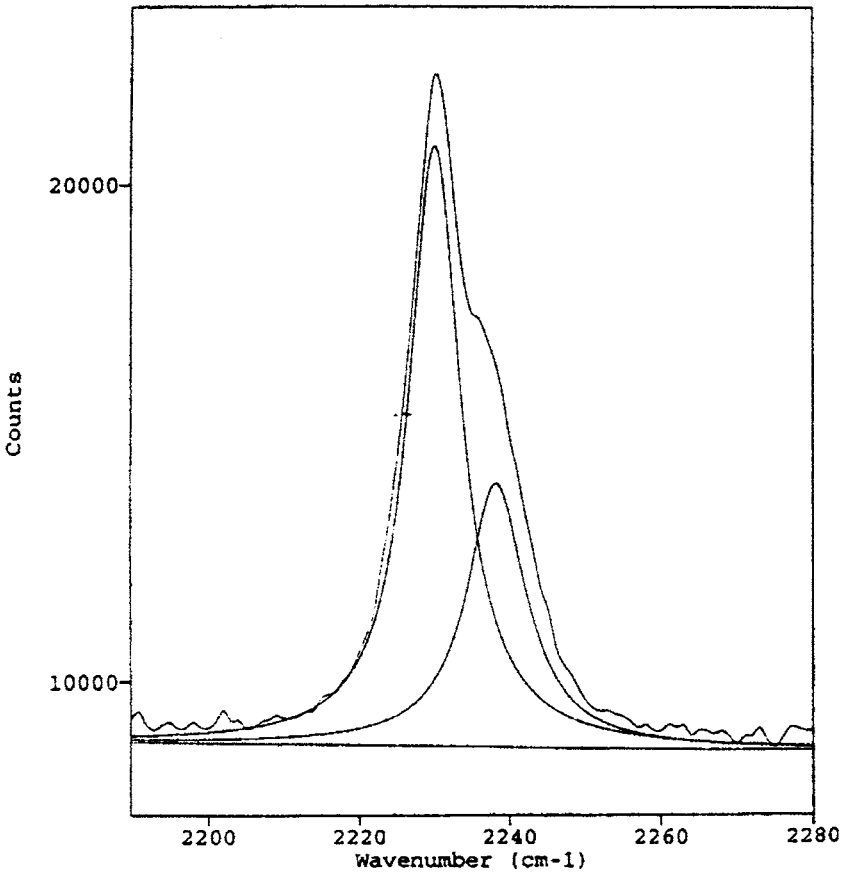

Fig. 5.16. Raman spectrum of the C=N stretching region of rubber latex saturated with AN. (Reproduced with permission from Ref. [62]. © 1994 Society for Applied Spectroscopy.)

elimination of HCl and the formation of a double bond in the polymer chain.

$$\sim(CH_2CHCl)_n\sim \rightarrow \sim(CH{=}CH)_n + n\text{HCl} \tag{5.9}$$

The double bond acts as a site for subsequent rapid elimination of HCl and a conjugated polyene is formed via the so-called unzipping reaction. The presence of these polyenes causes the PVC to darken in color. This observed color change is due to the polyenes exhibiting a UV-visible absorption and Raman spectroscopy makes use of this property. As the value of n reaches 4–5, even though the total extent of dehydrochlorination may be less than $10^{-2}\%$, the absorptions of the polyenes extend into the visible and the polymer becomes colored.

No resonance Raman spectra are observed for uncolored PVC films. The polyene chains, of varying chain length, have a broad electronic absorption in the visible region which supports a strong resonance Raman enhancement of vibrations associated with the $-C-C-C-$ backbone [64]. The resonance Raman spectrum of degraded

PVC shows two intense bands around 1100 cm^{-1} and 1500 cm^{-1} originating from the $\nu_1(=C-C=)_n$ and $\nu_2(-C=C-)_n$ stretching vibrations, respectively. Bands due to PVC itself are also observed at 650, 1440, and 2800 cm^{-1}. In particular the C=C stretch near 1500 cm and the C−C stretch near 1500 cm are enhanced sufficiently to allow detection of PVC degradation at 10^{-3}% levels. The degree of resonance enhancement is determined by the proximity of the laser excitation wavelength to the electronic absorption band profile maximum. This is in turn determined by the polyene chain length distribution in the sample.

Maximum resonance enhancement will occur when the laser wavelength is closest to the absorption maximum. Hence the longer the wavelength of the laser excitation the greater will be the contribution to the resonance Raman spectrum of the longer polyenes. Similarly, for shorter laser wavelengths there will be a greater contribution from shorter polyenes. Therefore, for any particular laser wavelength the resonance Raman spectrum will be a mean of the overall distribution of polyenes weighted towards those polyenes which have an absorption maximum closest to the laser wavelength being used. For polyenes, the excitation wavelength, λ_{exc}, for which the optimum resonance effect occurs follows the following relationship:

$$\lambda_{exc} = 700 - 537.7 \exp[-0.0768n] \tag{5.10}$$

Less than 0.0001% dehydrochlorination of PVC can be detected. The relationship between the conjugated polyene sequence length (n) and the value [65] of $\Delta\nu_2$

$$\Delta\nu_2 = 1461 + 151.2 \exp(-0.07808n) \tag{5.11}$$

Raman profiles were obtained for samples exposed to triethylenediamine for 21 days. Bands at 1436 and 1602 cm^{-1} with a weak shoulder at 1574 cm^{-1} are due to plasticizer and serve as an internal standard [66].

However, more recent data suggest that when samples are measured without dissolving them, the distribution of polyenes decreases *during* the resonance Raman experiment when power densities above 20 W/mm^2 are used. This decay is a result of either laser-induced crosslinking or chain scission, since both result in a shorter conjugation length. The photoinitiated reaction of polyenes with oxygen was determined not to be the basis of the decrease as the same results were obtain in air and in vacuum.

In order to avoid these resonances Raman induced effects, it is necessary to operate at low laser powers and exposure times of less than a minute. It was observed that if the polymer is dissolved in tetrahydrofuran, the degradation during the Raman experiment is minimal. But, the solution process results in an altered polyene sequence distribution and the samples must be stored in a cooled state and in the dark.

The direct method (no dissolution) can be used for lightly degraded PVC samples while the dissolution method is best for more highly degraded samples [67].

The catalytic degradation of PVC using metal chlorides ($FeCl_3$, $SbCl_3$ and $ZnCl_2$) has been studied to produce high concentrations of polyene sequences [68]. These catalytically degraded samples are than doped to produce a material that is electri-

cally conducting. One example is the doping with iodine [69]. The addition of the I_2 dopant resulted in a shortening of the polyene sequences due to chain disruption. It was also observed that FT-Raman reveal different domains than the visible excitation resonance Raman. In previous work, the near-IR excitations are in resonance with the same doped domains, but near-IR excitation preferentially enhances the features due to the domains with longer conjugation lengths. However, with I_2-doped samples the opposite is observed, that shorter effective sequence lengths are preferentially observed with the near-IR excitation compared to the 488-nm spectra.

Conformation of polymer chains in the solid state

One of the important applications of Raman spectroscopy (with IR spectroscopy) is the determination of the configuration and conformation of polymer chains in the solid state. As will be discussed in Chapter 6, high-resolution NMR spectroscopy of polymers in solution is a powerful technique for determining stereoregularity, but it is not useful for solids. The applications of NMR spectroscopy to polymeric solids will be discussed in Chapter 7.

When molecules possess symmetry, this symmetry restricts the types of vibrational modes that can be observed in the IR and Raman spectra (see Fig. 5.4). For polymers with C−C backbones, the Raman spectra are dominated by the strong lines arising from the C−C skeletal modes. These skeletal modes are sensitive to the conformation because they are highly coupled, and any change in the conformation will vary the coupling and shift the frequencies accordingly. Additionally, for the planar 2_1 and 3_1 helices, differences in selection rules for Raman and IR spectra allow a determination of the conformation. For helical conformations with a pitch higher than that of a 3_1 helix, the selection rules do not change.

When a polymer chain coils into a helix, a characteristic splitting of nearly all of the IR and Raman modes is observed. Theory offers an explanation of these observations. All monosubstituted vinyl helical polymers have [p,π] vibrational modes, which are termed the A modes, and [d,σ] modes, which are termed the E modes. Theoretically there are two different E modes for each helix, but they are degenerate in frequency and do not appear separately. The frequencies of the helical A and E modes depend on the helix angle. The normal modes of a helical chain can be represented by a dispersion curve of frequency vs. a phase angle, θ. Each pitch of the helix will have a characteristic dispersion curve, and similar motions will have similar energies. On the dispersion curve, the A-mode vibrations occur at $\theta = 0$, and the E-mode vibrations occur at $\theta = \varphi$, where φ is the helix angle. Thus for a polymer with the same chemical repeat units, differences in conformations will be reflected in the modes because the different helical conformations will depend on only energy considerations, and the phase-angle difference is the same. The E-mode shifts from one helical form to another depend on the energy differences and on φ

differences corresponding to the different helix angles. The helical modes should be slightly more sensitive to the changes in conformation [70].

Some branches of the dispersion curve of the helical conformations will be insensitive to the environment of the chemical groups. These are referred to as the *characteristic* modes, and they correspond to the uncoupled vibrational modes. These characteristic modes have a very flat dispersion curve, and their frequencies do not depend on the phase angle (i.e., the conformation). Other branches of the dispersion curve are sensitive to the phase angle, and the frequencies of the modes depend on the pitch of the helix of the repeating units. Generally, the observed spectra will have modes that have the same frequency (characteristic modes) regardless of the helix type, as well as modes that have different frequency positions because of the helix form. These latter modes are useful for characterizing the helical conformation of a polymer in the solid state.

Raman spectroscopy will not supplant X-ray diffraction for the determination of the conformation of a polymer in the solid state, but Raman spectroscopy can be useful for those systems that are unstable and cannot be satisfactorily oriented to give a proper X-ray pattern. Poly(butene-1) is an example where Raman spectroscopy has been of value for the determination of the conformation of the polymer in the solid state.

Poly(butene-1) exists in at least three crystalline forms. Form I has a hexagonal unit cell with 3_1 helices. Form II is prepared by casting a film from different solvents, but it will transform slowly and irreversibly into form I at room temperature, so X-ray diffraction patterns of form II are difficult to obtain. Form III of poly(butene-1) transforms to form II upon heating, and then spontaneously transforms to form I. The Raman spectra of forms II, III, and I are substantially different because of differences in the conformations [71]. Detailed analysis (including the dreaded use of normal coordinate analysis) can establish the conformation of poly(butene-1) from the Raman spectra.

Conformation of polymers in solution and in the melt

Spectroscopic studies of polymers in solution are of interest primarily to relate the structure in solution to other solution properties. In many cases, the conformation of the polymer changes upon dissolution or melting, or undergoes transformation with changes in the pH, ionic strength, or salt content of the solution. The preferred solvent for Raman spectroscopy is water because the scattering of water is very weak except for the regions of 1650 and 3600 cm^{-1}. As a consequence, Raman spectroscopy is quite useful for studying the secondary and tertiary structures of biological molecules, including carbohydrates, proteins, and nucleic acids. For synthetic polymers, the spectral results are less dramatic but nevertheless revealing.

There are substantial differences in the Raman spectra of a flexible polymer in its ordered conformational state compared to its disordered state. Generally, the spectra

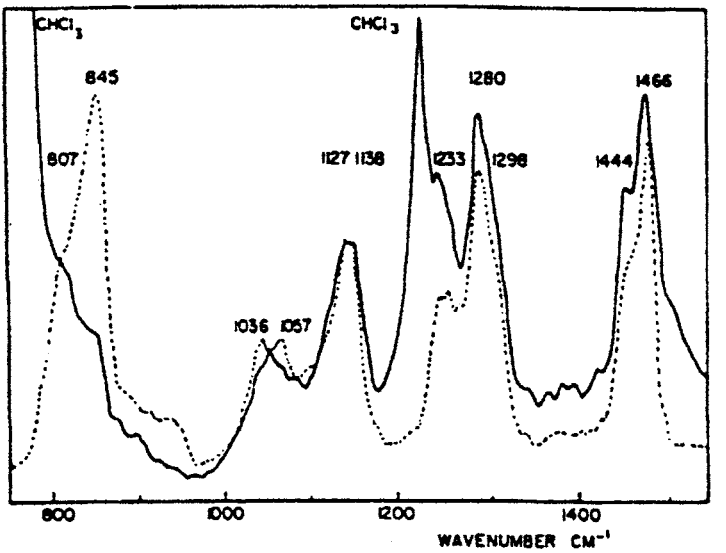

Fig. 5.17. Raman spectra of PEG in aqueous solution (dashed line) and in chloroform (solid line). (Reproduced with permission from Ref.[2]. © 1970 John Wiley and Sons, Inc.)

of the disordered state are quite complex and it is difficult to establish a theoretical basis for interpretation except in a few isolated cases [72]. and limited primarily to short alkane chains [73]. Consequently, the interpretation of conformationally disordered spectra is largely empirical.

The Raman spectra of poly(ethylene glycol) (PEG) in aqueous and chloroform solutions are shown in Fig. 5.17. Comparison of the Raman spectrum of PEG in aqueous solution with that of PEG in the melt indicates that the changes that occur on dissolution in water are considerably less dramatic than the changes observed upon melting. On the other hand, the spectrum of PEG in chloroform is very similar to the spectrum of PEG in the melt. The half-widths of the Raman lines of the spectrum of the aqueous solution are considerably narrower than those of the spectrum of the molten state, a result indicating fewer energy states are available to the molecule in the aqueous solution than in the melt [2].

In the Raman spectra of conformationally disordered polyethylene, the D-LAM mode found at a frequency (near 200 cm^{-1}) that is proportional to the concentration of gauche bonds [74]. This D-LAM mode is also observed in other molten vinyl polymers including polypropylene, polybutene and polystyrene. The presence of this Raman line in these polymers suggests a common structural basis although the chains themselves have different side chains [75]. In the vinyl polymers the band may appear as a doublet. For polypropylene, for example, there is a line near 200 cm^{-1} and 400 cm^{-1} and it is suggested that these two components are associated with the conformationally ordered $(gt)_4$ polypropylene.

Conformation of polymers at interfaces

SERS measurements probe the Raman spectrum of a polymer molecule at the interface of the metal surface. An important aspect of SERS is its potential for probing the interactions between various adsorbates and metallic surfaces as SERS enhances almost exclusively the first monolayer adjacent to the surface.

The selection rules for the SERS intensities indicate that since the local fields are highest normal to the surface, normal modes of the polymer involving changes in the molecular polarizability with components normal to the surface are subject to the greatest enhancements. Thus it is possible by knowing the molecular polarizability of functional components of a polymer to elucidate the surface orientation of the adsorbed molecules.

The surface geometry of polybenzimidazole on silver has been determined by observing the relative intensity change of the out-of-plane and the in-plane lines of the aromatic rings of the polymer. The normal mode of the out-of-plane vibrations involves a change in polarization perpendicular to the plane of the molecule. The in-plane mode is parallel to the plane of the molecule. The polymer shows two different orientations on the silver surface depending on the method of deposition. By slow evaporation, the aromatic rings are deposited lying down flat on the surface while dipping in a warm solution resulted in perpendicular orientation of the rings. The flat bonding geometry arises from a π-bonding of the aromatic ring to the surface. The standing bonding geometry is bonding through the nitrogen pair (N-bonded through σ-donation). With heating, the chains originally parallel to the surface transform to the perpendicular orientation indicating that the N-bonding geometry is more stable than the π-bonding for the silver surface [76].

Crystalline dimensions

Graphite is the most stable phase of carbon at low temperatures and pressure. Graphite has found wide spread use because of its unique properties. Raman spectroscopy has become the standard method for determining the planar coherence lengths in graphitic carbon. For these materials, a broad band is found at $\sim$1360 cm^{-1} which is attributed to disorder-induced Raman activity. The Raman line at 1581 cm^{-1} is due to highly ordered crystalline graphite due to an in-plane stretching mode. Using concurrent X-ray diffraction, it was shown that the ratio of the 1360 peak to the 1581 peak is inversely proportional to the coherence lengths in a range of 2.5–1000 nm [77].

Measuring the crystalline chain segment length

The longitudinal acoustic mode (LAM) is found in a number of semicrystalline polymers. The LAM mode for the all-trans *n*-alkanes is a symmetric accordion-like

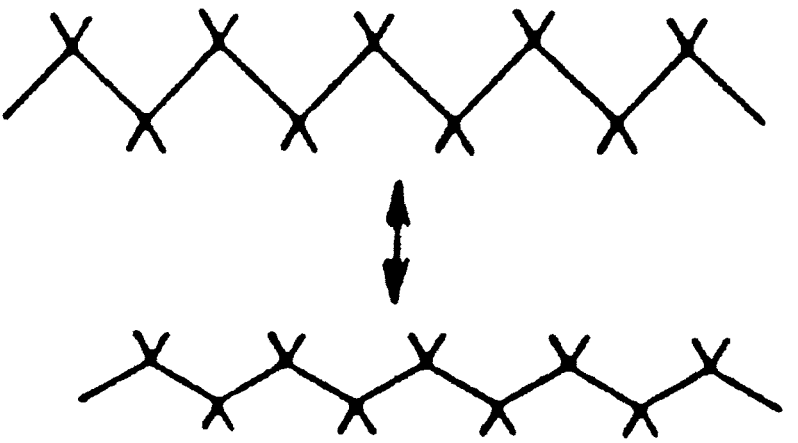

Fig. 5.18. The LAM mode for polyethylene.

longitudinal vibration. The LAM mode occurs at very low frequency (Fig. 5.18).

It has been observed that this skeletal vibration of the crystalline stems within a lamella is a function of the stem length [78]. For polyethylene and *n*-alkanes, the frequency of the LAM, ν_m, is described by the relation

$$\nu_m = \frac{m}{2cL}\left(\frac{E}{\rho}\right)^{1/2} \tag{5.12}$$

where m is the integer order of the mode, c is the speed of light, L is the length of the vibrating chain segment, E is the elastic modulus of the chain and ρ is the single chain density. Since Raman activity is associated with a change in polarizability, even values of m give no such change so only modes of odd m are Raman active. The LAM mode has a characteristically high intensity apparently due to the large change in polarization associated with the long-chain motion of this mode and the Boltzmann factor associated with frequencies of low wavenumber. Finally, the elastic modulus can be estimated from the slope of the curve ν_m vs. $1/L$. This quantity represents the maximum attainable elastic modulus of a polymer (defect-free) [79]. However, longitudinal interactions may modify this relation [80]. For helical polymers, significant lateral interchain interactions affect the LAM frequency. Another variation can result from changes in the crystalline arrangement. Since the lattice modes represent vibrations in which the chains in the unit cell undergo motions with respect to each other, changes in the crystalline arrangement will cause shifts in the frequencies.

This relationship provides an unusual morphological tool for the study of crystalline lamella. The LAM mode has been observed in a number of semicrystalline polymers including PTFE, PP, POM and PEO as well as in linear aliphatic polyesters. However, attempts at identifying the LAM mode in polypeptides have not been successful. However, the LAM mode has been identified in poly(β-hydroxybutyrate)

(PHB) in the 15 cm^{-1} region. This Raman mode exhibits an inverse relationship between the long period measured by small-angle X-ray scattering and the line frequency [81]. The range of lamellar thickness for PHB consisted of only 6–11 repeat units/fold stem in single crystals. The elastic modulus can be calculated from measurements of the LAM frequency and in the case of PHB has a value of 29.6 GPa that is consistent with that of a helix.

A fascinating example of the use of the LAM to investigate the chain folding process is the study of polyethylene oxide (PEO) (Fig. 5.19) [82].

PEO is known to exhibit a simple integer-fold structure, in which the lamellar thickness is expected to be close to an integral fraction of the extended chain length. The low frequency Raman spectrum of a well-crystallized PEO 3000 fraction shows several bands in the frequency region below 100 cm^{-1}. There is a sharp band at 5.5 cm^{-1} which is assigned to the fully extended crystalline stem length (209 Å). Another LAM mode appears at 11.6 cm^{-1} corresponding to once-folded chains (99 Å). When this PEO fraction crystallizes, it initially shows a LAM mode at 9.1 cm^{-1} (120 Å) which is between the LAM of the extended chain and the mode of the once-folded chains which corresponds to a non-integer-fold. This LAM mode at 9.1 cm^{-1} shifts to a slightly higher frequency during the early stages of crystallization. Thus, although integer fold structures eventually develop, the initial lamellae consist of well-defined non-integer-fold chain stems. The non-integer-fold to integer folding is a solid state process that can eventually proceed to the extended chain structure.

Molecular orientation in polymers

Polarized Raman spectroscopy can be used to probe the molecular orientation in polymers. The advantages of using Raman polarization are that it can be used for thick samples if care is taken not to scramble the polarization in the sample. This generally means that the sample must not be turbid. Secondly, Raman can determine both the second and fourth moments of the orientation distribution function while IR and birefringence measurements only report the second moment. Thirdly, Raman spectroscopic measurements (like IR) can reveal the orientation of not only the crystalline phase but also the amorphous phase. Raman polarizations can be made on polymeric fibers that are difficult with IR. Polyethylene [83,84]. and poly(ethylene terephthalate) have been studied [85].

One of the major problems is the difficulty of determining that the polarization is scrambled whether by scattering inhomogeneities in the sample itself or the birefringence of the sample itself. Many spectra show evidence of extensive depolarization of both the incident and scattered light. Each spectrum is an indeterminate mixture of four different polarizations: the intended polarization, the one resulting from depolarization of the incident light, the one resulting from depolarization of the scattered light, and (to a lesser extent) the one resulting from depolarization of both the inci-

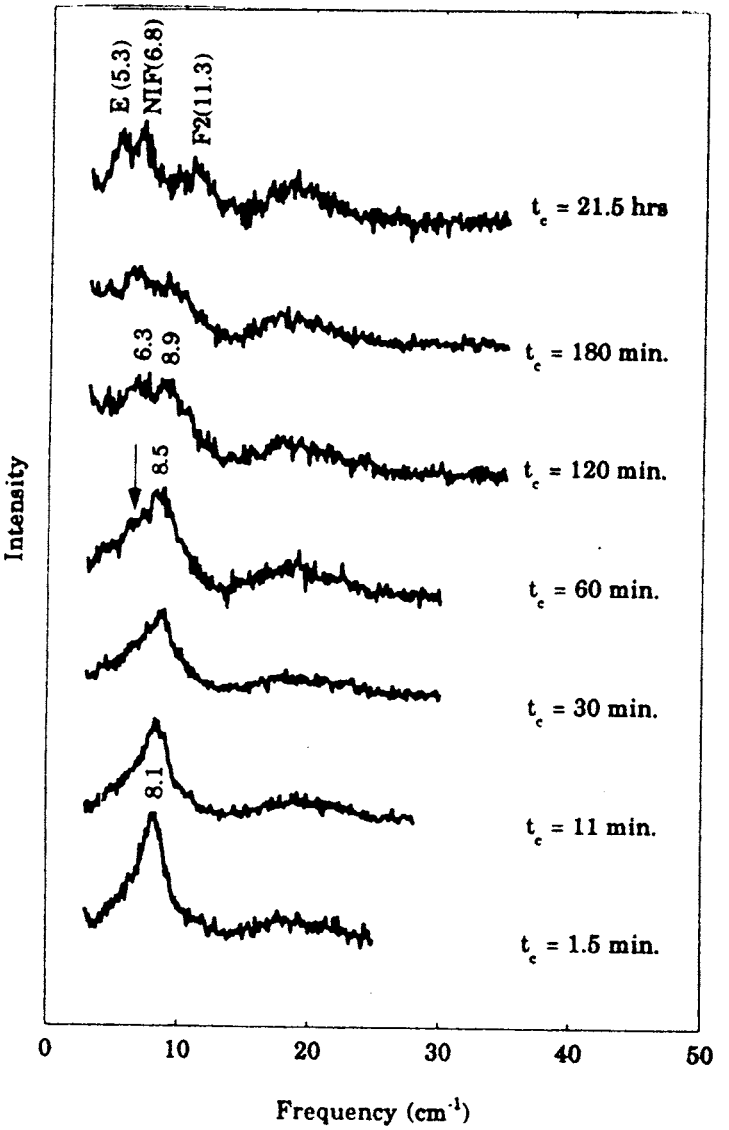

Fig. 5.19. The low frequency Raman LAM mode for PEO. (Reproduced with permission from Ref. [82]. © 1996 American Chemical Society.)

dent and scattered light. Any light depolarization due to optical inhomogeneity will lower the apparent orientation. In some cases, this polarization scrambling occurs to the extent that little useful information is available from the individual polarized spectra. Polarization scrambling can probably be reduced by using a backward scattering experimental geometry since the scattered light arises from a small scattering volume near the surface of the sample.

The Raman scattering intensities, I_s, are given by quadratic expressions of all components of the Raman tensor for the vibration studied, α_{ij} ($i, j = 1$–3), the coefficients being the direction cosines I_i and I'_j defining respectively, the polarization direction of the incident and scattered light with respect to a set of axes fixed in the sample. Thus,

$$I_s = I_0 \sum \left(\sum_{ij} I_i I'_j \alpha_{ij} \right)^2 \tag{5.13}$$

where I_0 is a constant depending on instrumental factors and the incident light intensity. The sum outside the parentheses indicates that the observed intensity results from a sum over all of the scattering units. The direction cosines I'_i and I_j relate the polarization vector of the incident and scattered radiation respectively to a set of axes, $O{-}X_1\,X_2\,X_3$ fixed within the sample. The term α_{ij} represents the ijth component of the Raman tensor of a particular structural unit.

Each α_{ij} can be expressed as a linear combination of the principal components α_1, α_2 and α_3 of the derived polarizability or Raman tensor of the vibration investigated. The experimental values of the scattered intensities are of the form $I_0 S \alpha_{ij} \alpha_{pg}$.

In the case of uniaxial symmetry, it can be shown that

$$\sum \alpha_{ij} \alpha_{pg} = 4p^2 N_0 \sum M_{100} A_{100}^{ijpg} \tag{5.14}$$

where A_{100}^{ijpg} is the sum of terms in α_1, α_2 and α_3. M_{100} is expressed in terms of Legendre polynomials $\langle P_l(\cos\theta)\rangle$ by

$$M_{100} = \frac{1}{4\pi^2} \left[\frac{2l+1}{2} \right]^{1/2} \langle P_l(\cos\theta)\rangle \tag{5.15}$$

where $\langle P_l(\cos\theta)\rangle$ is the coefficient of the lth term in the expansion of the orientation distribution function for a set of symmetry axes. θ is the angle between the chain axis of the structural unit and the unique axis of the sample. It can be shown that

$$M_{000} = \frac{1}{4\pi^2} \left(\frac{l}{2} \right)^{1/2} \tag{5.16}$$

$$M_{200} = \frac{1}{4\pi^2} \left(\frac{5}{2} \right)^{1/2} \langle P_2(\cos\theta)\rangle \tag{5.17}$$

$$M_{400} = \frac{1}{4\pi^2} \left(\frac{9}{2} \right)^{1/2} \langle P_4(\cos\theta)\rangle \tag{5.18}$$

For a sample with uniaxial symmetry, there are five unknowns, α_1, α_2 and α_3, and the orientation parameters $\langle P_2(\cos\theta)\rangle$ and $\langle P_4(\cos\theta)\rangle$ [86]. Therefore, five independent nonzero sums $\alpha_{ij}\alpha_{pg}$ are needed. These five independent $I_0 S \alpha_{ij} \alpha_{pg}$ are $I_0 S \alpha_{33}^2$,

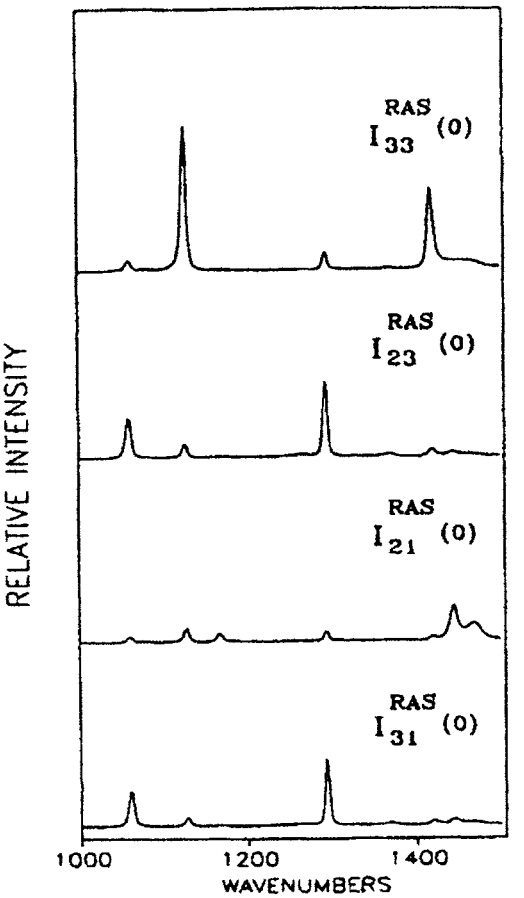

Fig. 5.20. Four polarized spectra of polyethylene fibers obtained with right angle scattering experimental configuration. (Source: Ref. [83, fig. 2].)

$I_0 S\alpha_{32}^2$, $I_0 S\alpha_{21}^2$, $I_0 S\alpha_{22}^2$ and $I_0 S\alpha_{22}\alpha_{33}$. For uniaxial alignment, the order parameters are calculable from the Raman data. The five independent $I_0 S\alpha_{ij}\alpha_{pg}$ spectra for polyethylene fibers are shown in Fig. 5.20.

For uniaxial alignment, the order parameters are given as:

$$\langle P_2(\cos\theta)\rangle = \tfrac{1}{2}\langle 3\cos^2\theta - 1\rangle \tag{5.19}$$

$$\langle P_4(\cos\theta)\rangle = \tfrac{1}{8}(35\langle\cos^2\theta\rangle - 30\langle\cos^2\theta\rangle + 3) \tag{5.20}$$

where θ is the angle between the molecular z-axis and the macroscopic Z-axis. The '$\langle\ \rangle$' denote the average over all angles θ. $\langle P_2(\cos\theta)\rangle$ varies from -0.5 for perfect alignment perpendicular to Z (all $\theta = 90°$) through 0 for random alignment, to 1 for perfect alignment along Z (all $\theta = 0$). The behavior of $\langle P_4(\cos\theta)\rangle$ is more complex but also takes the value of 1 for perfect alignment along Z.

The Raman tensor is not cylindrical (a_1/a_3 not equal to 1) as expected from the planar zig-zag structure of polyethylene. The sign changes demonstrate that the polarizability changes during the vibrations have opposite sign in the plane or perpendicular to the plane of the chains. The values of $\langle P_2(\cos\theta)\rangle$ increase with the draw ratio. The values obtained for $\langle P_4(\cos\theta)\rangle$ show that the distribution of crystal orientation is narrower at higher draw ratios and falls within the range of the most probable ones.

The values obtained by Citra et al. [83] using the crystalline 1418 cm^{-1} line gave a $P_2\langle(\cos\theta)\rangle$ value of 0.82 and $P_4\langle(\cos\theta)\rangle = 0.53$ indicating the orientation in the crystalline phase for PE fibers. Concurrent X-ray data gave a $P_2\langle(\cos\theta)\rangle = 0.84$. The slight discrepancy between the two values is attributed to imperfect alignment of the fiber with respect to the laboratory axes.

Generally, it is difficult to find 'pure' amorphous bands for some polymer systems. So an approach to measuring the amorphous phase orientation in semicrystalline polymers is to introduce a molecular probe into the amorphous phase and follow its orientation [87,88]. The limitation of this approach is that the exact relationship

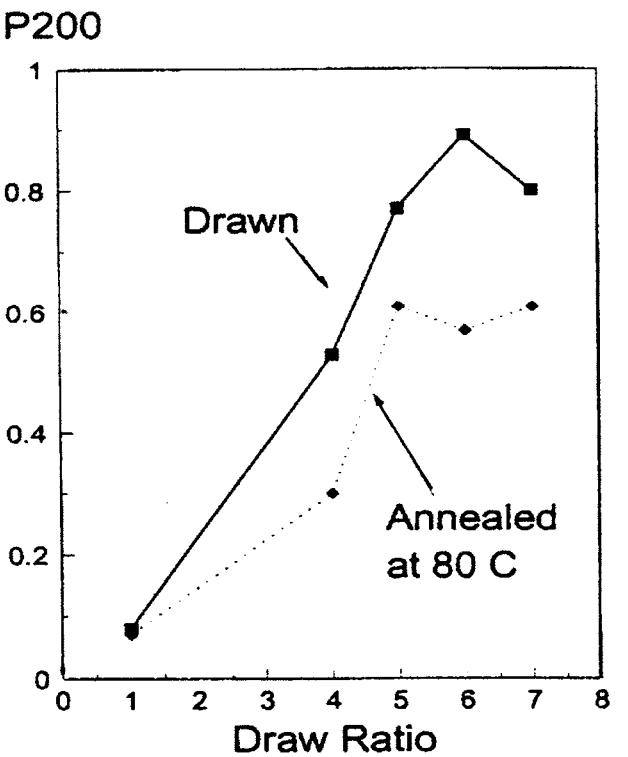

Fig. 5.21. $P_2\langle\cos\theta\rangle$ as a function of draw ratio for polyethylene before and after annealing at 80°C showing that annealing introduces a randomization of the amorphous region. (Reproduced with permission from Ref. [88]. © 1996 Society for Applied Spectroscopy.)

between the orientation of the probe molecule and the polymer chains in the amorphous region is uncertain — the probe merely acts as an indicator of orientation of the amorphous phase. The linear (all trans) biphenyl polyene $[\Phi-(C=C-)_n-\Phi]$, where Φ represents a phenyl ring has been dispersed in poly(ethylene) by melt mixing. This polyene has a resonance-enhanced C=C stretch at $\sim$1574 cm^{-1} and the motion is dominated by only one component (α_{zz}) which simplifies the analysis of the polarized intensities. Fig. 5.21 shows $P_2\langle\cos\theta\rangle$ as a function of draw ratio for polyethylene before and after annealing at 80°C showing that annealing introduces a decrease in the orientation of the amorphous region through relaxation.

Summary, conclusions and forecast

It is proper to say that the rate of improvement in Raman instrumentation is extremely fast. With the development of improved near-IR lasers, the fluorescence problem is diminishing. With the development of multichannel detectors, the sensitivity of the Raman measurement is improving. With the development of notch filters, the need for multi-monochromators is decreasing. With the development of tunable filters like the AOEF, the portability of the Raman equipment itself is increasing. With the development of improved fiber optical materials, the capability of doing remote Raman spectroscopy is improving. So, as is clear from the current literature, the utility and applications of Raman spectroscopy to structure problems in polymers is growing at an astronomical rate. This is good!

Raman spectroscopy will never replace infrared, but it is taking its place as an equal partner in vibrational spectroscopy.

References

[1] Raman, C.V., Krishnan, K.S., Nature 121 (1928) 501.
[2] Koenig, J.L., Angood, A.C., J. Polym. Sci. A8 (1970) 1787.
[3] Koenig, J.L., Appl. Spectrosc. Rev. 4 (1971) 233.
[4] Willis, H.A., in: D.O. Hummel (Ed.), Proceedings of the 5th European Symposium on Polymer Spectroscopy. Verlag Chemie, Weinheim, 1979, p. 15.
[5] Grasselli, J.G., Snavely, M.K., Bulkin, B.J., Chemical Applications of Raman Spectroscopy. Wiley, New York, NY, 1981.
[6] Koenig, J.L., Angood, A.C., J. Polym. Sci. A8 (1970) 1787.
[7] Angood, A.C., Koenig, J.L., J. Macromol. Sci. (Phys.) B3 (1969) 323.
[8] Koenig, J.L., Druesdow, D., J. Polymer. Sci. A-2 (1969) 1075.
[9] Mosier-Boss, P.A., Lieberman, S.H., Newbery, R., Appl. Spectrosc. 49 (1995) 630.
[10] Dou, X., Yamaguchi, Y., Yamamoto, H., Uenoyama, H., Ozaki, Y., Appl. Spectrosc. 50 (1996) 1301.
[11] Chase, D.B., in: J.G. Grasselli and B.J. Bulkin (Eds.), Analytical Raman Spectroscopy. Chemical Analysis Series, Wiley, New York, NY, 1991.
[12] Schoen, C.L., Sharma, S.K., Helseley, C.E., Owen, H., Appl. Spectrosc. 47 (1993) 305.
[13] Carter, D.A., Pemberton, J.E., Appl. Spectrosc. 49 (1995) 1550.
[14] Carter, D.A., Pemberton, J.E., Appl. Spectrosc. 49 (1995) 1561.

[15] Champion, A., Woodruff, W.H., Anal. Chem. 59 (1987) 1299A.
[16] Iwata, K., Hamaguchi, H., Tasumi, M., Appl. Spectrosc. 42 (1988) 12.
[17] Hirschfeld, T., Chase, B., Appl. Spectrosc. 40 (1986) 133.
[18] Zhao, J., McCreery, R.L., Appl. Spectrosc. 50 (1996) 1209.
[19] Zimba, C.G., Hallmark, V.M., Swalen, J.D., Rabolt, J.F., Appl. Spectrosc. 41 (1987) 722.
[20] Hirschfeld, T., Chase, B., Appl. Spectrosc. 40 (1986) 133.
[21] Hendra, P.J., Jones, C.H., Warnes, G., Fourier Transform Raman Spectroscopy: Instrumentation and Chemical Analysis. Ellis Horwood, Chichester, 1992, p. 89.
[22] Chase, B., Appl. Spectrosc. 48 (1994) 14A.
[23] Asher, S., Ann. Rev. Phys. Chem. 39 (1988) 537.
[24] Asher, S., Anal. Chem. 65 (1993) 59A.
[25] Dalterio, R.A., Baek, M., Nelson, W.H., Sperry, J.F., Purcell, F.J., Appl. Spectrosc. 41 (1987) 241.
[26] Dudik, J.M., Johnson, C.R., Asher, S.A., J. Phys. Chem. 89 (1985) 3805.
[27] Asher, S.A., Johnson, C.R., Science 225 (1984) 311.
[28] Asher, S.A., Anal. Chem. 56 (1984) 720.
[29] Chadha, S., Ghiamati, E., Manoharan, R., Nelson, W.H., Appl. Spectrosc. 46 (1992) 1176.
[30] Chang, R., Furtak, T.E. (Eds.), Surface Enhanced Raman Spectroscopy. Plenum, New York, NY, 1982.
[31] Fleischmann, M., Hendra, P., Mcquillan, A., Chem. Phys. Lett. 26 (1974) 163.
[32] Laserna, J.J., Cabalin, L.M., Montes, R., Anal. Chem., 64 (1992) 2006.
[33] Boerio, F.J., Tsai, W.H., Montaudo, G., J. Polym. Sci., Part B: Polym. Phys. 27 (1989) 2477.
[34] Xue, G., Dong, J., Polymer 33 (1992) 643.
[35] Angel, S.M., Katz, L.F., Archibal, D.D., Lin, L.T., Honigs, D.E., Appl. Spectrosc. 42 (1988) 1327.
[36] Angel, S.M., Myrick, M.L., Anal. Chem. 61 (1989) 1648.
[37] Compton, D.A.C., Compton, S.V., Appl. Spectrosc. 45 (1991) 1587.
[38] Hendra, P.J., American Lab., December 1996, p. 17.
[39] Nicolet FT-IR Customer Newsletter, 9, December 1996, p. 3.
[40] Ferraro, J.R., Vibrational Spectroscopy at High Pressures. Academic Press, New York, NY, 1984.
[41] Song, K., Miller, R.D., Wallraff, G.M., Rabolt, J.F., Macromolecules 25 (1992) 3629.
[42] Lewis, I.R., Griffiths, P.R., Appl. Spectrosc. 50 (1996) 12A.
[43] Newman, C.D., Bret, G.G., McCreery, R.L., Appl. Spectrosc. 46 (1992) 262.
[44] Halley, P., Fiber Optic Systems. Wiley, Chichester, 1987.
[45] Chong, C.K., Shen, C., Fong, Y., Zhu, J., Yan, X., Brush, S., Mann, C.K., Vickers, T.J., Vib. Spectrosc. 3 (1992) 35.
[46] Myrick, M.L., Angle, S.M., Appl. Spectrosc. 44 (1990) 565.
[47] Kimura, S., Wilson, T., Appl Optics 30 (1991) 214.
[48] Everall, N., Davis, K., Owen, H., Pelletier, M.J., Slater, J., Appl. Spectrosc. 50 (1996) 5389.
[49] Schrum, K.F., Ko, S., Ben-Amotz, D., Appl. Spectrosc. 50 (1996) 1150.
[50] Wang, C., Vickers, T.J., Mann, C.K., Appl. Spectrosc. 46 (1992) 772.
[51] Dollish, F.R., Fateley, W.G., Bentley, F.F., Characteristic Raman Frequencies of Organic Compounds. Wiley-Interscience, New York, NY, 1974.
[52] Schrader, B., Raman/Infrared Atlas of Organic Compounds. VCH Publishers, New York, NY, 1989.
[53] Stadler Standard Raman Spectra, Philadelphia, Sadtler Research Labs, Inc., 1976.
[54] Gerrard, D.L., in: J.G. Grasselli and B.J. Bulkin (Eds.), Analytical Raman Spectroscopy. Wiley, New York, NY, 1991.
[55] Cornell, S.W., Koenig, J.L., Rubber Chem. Technol. 43 (1970) 313.
[56] Cornell, S.W., Koenig, J.L., Rubber Chem. Technol. 43 (1970) 322.
[57] Coleman, M.M., Shelton, J.R., Koenig, J.L., Rubber Chem. Technol. 46 (1973) 938.
[58] Gulari, E., McKeigue, K., Ng, K.Y.S., Macromolecules 17 (1984) 1822.
[59] Hill Jr., C.G., Hedren, A.M., Meyers, G.E., Koutsky, J.A., J. Appl. Polym. Sci. 28 (1984) 2749.
[60] Wang, C., Vickers, T.J., Mann, C.K., Appl. Spectrosc. 47 (1993) 928.
[61] Wang, C., Vickers, T.J., Schlenoff, J.B., Mann, C.K., Appl. Spectrosc. 47 (1993) 928.
[62] Heregeth, W.D., Codella, P.J., Appl. Spectrosc. 48 (1994) 900.
[63] Gerrard, D.L., in: J.G. Grasselli and B.J. Bulkin (Eds.), Analytical Raman Spectroscopy. Wiley, New York, NY, 1991, p. 282.

[64] Gerrard, D.L., Maddams, W.F., Macromolecules 8 (1975) 54.
[65] Bariua, A., Gerrard, D.L., Maddams, W.F., Macromolecules 16 (1983) 578.
[66] Gerrard, D.L., Maddams, W.F., Macromolecules 14 (1981) 1352.
[67] Kip, B.J., van Aaken, S.M., Meier, R.J., Williams, K.P.J., Gerrard, D.L., Macromolecules 25 (1992) 4290.
[68] Owen, E.D., Maayib, K.J., J. Polym Sci., Part A: Polym. Chem. 27 (1989) 1833.
[69] Owen, E.D., Shah, M., Everall, N.J., Twigg, M.V., Macromolecules 27 (1994) 3436.
[70] Koenig, J.L., Raman Spectroscopy of Biological Molecules: A Review, J. Polym. Sci., Part D, 6 (1972) 59–177.
[71] Cornell, S.W., Koenig, J.L., J. Polym. Sci. A7 (1969) 1965.
[72] Snyder, R.G., Strauss, H.L., J. Chem. Phys. 87 (1987) 3779.
[73] Snyder, R.G., Kim, Y., J. Phys. Chem. 95 (1991) 602.
[74] Mandelkern, L., Alamo, R., Mattice, W.L., Snyder, R.G., Macromolecules 19 (1986) 2404.
[75] Hallmark, V.M., Bohan, S.P., Strauss, H.L., Snyder, R.G., Macromolecules 24 (1996) 4025.
[76] Xue, G., Dong, J., Zhang, J., Macromolecules 24 (1991) 4195.
[77] Tuinstra, F., Koenig, J.L., J. Chem. Phys. 53 (1970) 4713.
[78] Mizushima, S., Shimanouti, T., J. Am. Chem. Soc. 71 (1949) 1320.
[79] Song, K., Krimm, S., J. Polym. Sci., Polym. Phys. Ed. 28 (1990) 35.
[80] Song, K., Krimm, S., J. Polym. Sci., Polym. Phys. Ed. 28 (1990) 51.
[81] Chien, B., Hsu, S., Stidham, H.D., Macromolecules 29 (1996) 4247.
[82] Kim, I., Krimm, S., Macromolecules 29 (1996) 7186.
[83] Citra, M.J., Chase, D.B., Ikeda, R.M., Gardner, K.H., Macromolecules 28 (1995) 4007.
[84] Pigeon, M., Prud'homme, R., Pezolet, M., Macromolecules 24 (1991) 5687.
[85] Huijts, R.A., Peters, S.M., Polymer 35 (1994) 3119.
[86] Bower, D.I., J. Phys. B: Atom. Mol. Phys. 9 (1976) 3275.
[87] Margulies, L., Stockburger, M., J. Raman Spectrosc. 8 (1979) 26.
[88] Everall, N., Chalmers, J., Mills, P., Appl. Spectrosc. 50 (1996) 1229.

Chapter 6

High resolution NMR spectroscopy of polymers in solution

Elements of nuclear magnetic resonance spectroscopy

Perhaps, the Nobel prize winner for NMR achievements, Dr. Ernst, said it best when he was describing the utility of nuclear magnetic resonance (NMR) in his Nobel lecture [1]:

> *Nuclear spin systems possess unique properties that predestine them for studies of molecules:*
>
> *(1) The atomic nuclei serving as sensors are extremely well localized, with a diameter of a few femtometers, and can report on local affairs in their immediate vicinity. It is thus possible to explore molecules and matter in great detail.*
>
> *(2) The interaction energy of the sensors with the environment is extremely small, less than 0.2 $Jmol^{-1}$, corresponding to the thermal energy at 30 mK^o. The monitoring of molecular properties is thus virtually perturbation-free. Nevertheless, the interaction is highly sensitive to the local environment.*
>
> *(3) Information on the structure of molecules can be obtained from nuclear pair interactions: magnetic dipole–dipole interactions provide distance information, while scalar J couplings allow one to determine dihedral angles.*

NMR spectroscopy is the experimental study of the energy levels of certain atomic nuclei of molecules in a magnetic field [2,3]. In a magnetic field, the magnetic properties of the nuclei dominate. All atomic nuclei possess a characteristic known as *nuclear spin*. Certain atomic nuclei that have an odd number of either protons or neutrons possess a nonzero spin. Examples are the principal isotopes of hydrogen, sodium, and phosphorus. As the positively charged nucleus spins on its axis, the moving charge creates a magnetic moment, μ, that tends to align in a magnetic field. Actually, the thermal motion of the molecule makes the magnetic moment wobble. The torque makes the magnetic moment act like a child's top, and it precesses about the axis of the external magnetic field at a frequency that depends on the strength of the field. Quantum mechanics indicates that a nucleus with spin I_s is characterized by

an angular momentum with a spin quantum number I and is related to the magnetic moment, μ, by:

$$\mu(\text{nuclear magnetos}) = \gamma \hbar I \tag{6.1}$$

where γ is the gyromagnetic ratio (rad/G-s), and $\hbar$ is Planck's constant divided by 2π.

> *Subatomic particles spin about a theoretical kind of axis like a spinning top. One big difference between a spinning top and a spinning particle, however, is that a top can spin either faster or slower, but a subatomic particle always spins at exactly the same rate.* — Gary Zukav [4]

Nuclei with a spin number of zero ($I = 0$) are not observable in NMR experiments, but there are 118 nuclei that have been studied by NMR [5]. The nuclei of primary interest to polymer chemists are the proton (^{1}H, $I = 1/2$), deuteron (^{2}H, $I = 1$), ^{13}C ($I = 1/2$) (for the more common ^{12}C isotope, $I = 0$), and ^{19}F ($I = 1/2$). The two primary factors that determine the sensitivity and utility of a nucleus for NMR spectroscopy are the natural abundance and the magnitude of the gyromagnetic ratio. For example, the ^{1}H isotope is 100% naturally abundant and has a high gyromagnetic ratio. As a consequence ^{1}H is the most sensitive nucleus in terms of the magnitude of the NMR signal. On the other hand, the ^{13}C nucleus is present in natural abundance at a level of only 1.1% and has a gyromagnetic ratio that is 1/4 that of hydrogen to make it 1.610^{-2} less sensitive than hydrogen for NMR study. Properties of nuclei that are useful for the study of polymers by NMR spectroscopy are listed in Table 6.1.

Table 6.1
NMR properties of nuclei of interest in polymers

Isotope	Natural abundance	Resonance frequency (MHz) for field of 10 KG (1 T)	Relative sensitivity for equal number of nuclei at constant H_0	Magnetic moment (units of nuclear nuclear magnetons)	Spin I in multiples of $\hbar$
^{1}H	99.9844	42.577	1.000	2.79270	1/2
^{2}H (D)	0.0156	6.536	0.00964	0.85738	1
^{13}C	1.108	10.705	0.0159	0.70216	1/2
^{14}N	99.635	3.067	0.00101	0.40357	1
^{15}N	0.365	4.315	0.00104	−0.28304	1/2
^{17}O	0.037	5.772	0.0291	−1.8930	5/2
^{19}F	100.0	40.055	0.834	2.6273	1/2
^{29}Si	4.70	8.460	0.0785	−0.55477	1/2
^{31}P	100.0	17.235	0.0664	1.1305	1/2
^{35}Cl	75.4	4.172	0.00471	0.82089	3/2
^{37}Cl	24.6	3.472	0.00272	0.68329	3/2

(Source: J.C. Randall, in: A.E. Woodward and F.A Bovey (Eds.), Polymerization Characterization by ESR and NMR. ACS Symposium Series 142, American Chemical Society, Washington, DC, 1980, p. 100. © 1980 American Chemical Society.)

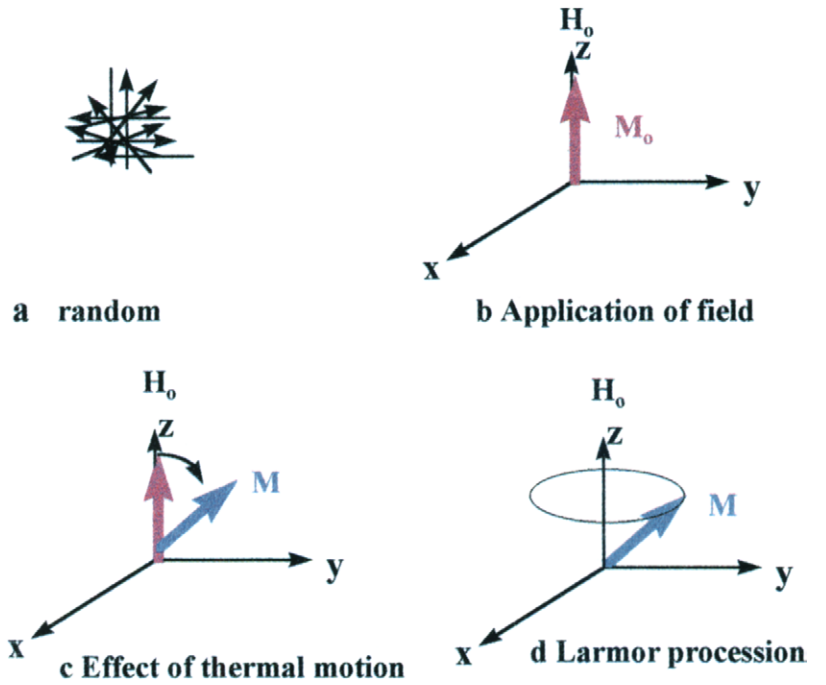

Fig. 6.1. The nuclear spin generates a small magnetic field, and in the absence of an applied magnetic field, the orientation of these dipoles is random (a). When a sample is placed in a homogenous magnetic field, the dipoles will align themselves with the lines of induction or force of the applied magnetic field (b). However, thermal motion does not allow the alignment to remain, and the average alignment is at a small angle to the magnetic field (c). The magnetic moment precesses about the magnetic field at the Larmor frequency (d).

Possession of both charge and spin makes some nuclei magnetic which affects their behavior in an external magnetic field (H_0). The nuclear spin generates a small magnetic field, and in the absence of an applied magnetic field, the orientation of these dipoles is random (Fig. 6.1a).

In NMR, the nuclei are subjected to a constant external magnetic field, H_0. It causes them to progressively take up one of the two allowed orientations, parallel or anti-parallel to the direction of H_0 (Fig. 6.1b). Because the nuclei have angular momenta and thermal motions, they will not align completely parallel to the field (Fig. 6.1c). The torque from the applied field causes the magnetic moments to precess about the field direction with a characteristic angular frequency. The precession frequency is known as the *Larmor frequency*, ω_0, and is proportional to the applied magnetic field, H_0 (Fig. 6.1d) and is given by

$$\omega_0 \text{ (rad/s)} = \gamma H_0 \tag{6.2}$$

or in MHz

$$\nu_0 \text{ (MHz)} = \left(\frac{\gamma}{2\pi}\right) H_0 \tag{6.3}$$

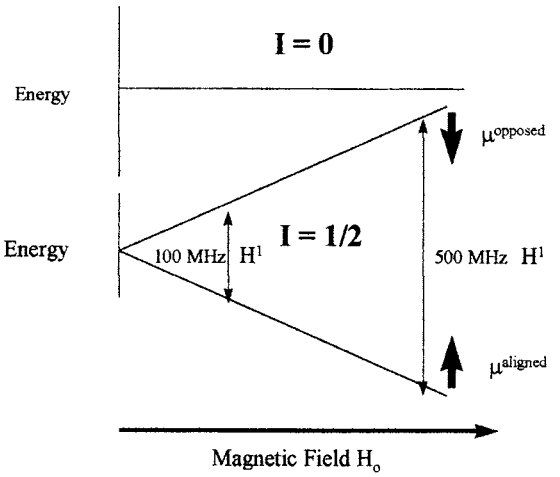

Fig. 6.2. Quantized energies of nuclei in a magnetic field for values of the spin quantum number of 0, and 1/2 . The alignment of the magnetic moment is shown with the μ^{opposed} corresponding to the higher energy and μ^{aligned} corresponds to the lower energy. The energy differences are shown for a magnetic field corresponding to 100 MHz and 500 MHz for H^1.

The nuclei with a spin quantum number of 1/2 have two energy states; aligned with the field (lower energy) and aligned against the field (higher energy). The energy levels that occur in the presence of a static magnetic field appear as shown in Fig. 6.2.

> *Spin is quantized just like energy and charge. It comes in chunks. Like charge, all of the chunks are the same size. In other words, when a spinning top slows down, its rotation does not diminish smoothly and continuously, but in a series of tiny steps.* — Gary Zukav [4]

The energy levels of the nuclei with a spin of 1/2 in the presence of a magnetic field are given by

$$\Delta E \text{ (MHz)} = \gamma \hbar H_0 \tag{6.4}$$

At equilibrium, the spins are distributed between the two corresponding quantum energy levels following a Boltzmann distribution. Because molecules are constantly in thermal motion, and because the molecules interact with each other, the thermal motion will cause the magnetic moments of most of the protons to point randomly. However, the average or net magnetization will be preferentially aligned along the magnetic field. The average of all these magnetic moments is called the *thermal equilibrium magnetization*, $\mathbf{M}_0$, and is given by

$$\mathbf{M}_0 = \left(\frac{N_1}{3kT}\right)\gamma^2\hbar^2 I(I+1)H_0 = \chi_0 H_0 \tag{6.5}$$

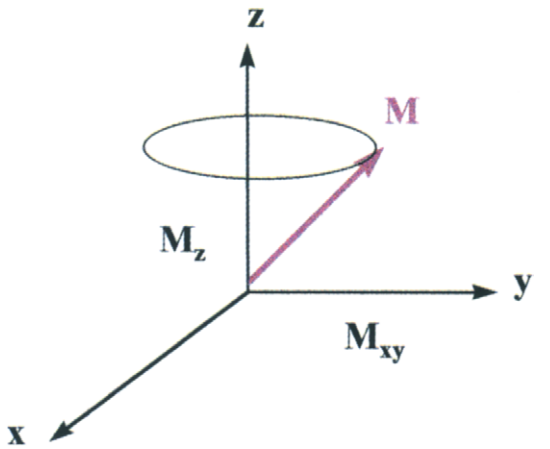

Fig. 6.3. Schematic representation of the macroscopic nuclear magnetization **M** precessing about the magnetic field along the z-axis after being tipped from its equilibrium value along z by a radiofrequency field, H_1.

where N_1 is the number of spins per unit volume, k is Boltzmann's constant, T is temperature, χ_0 is the static magnetic susceptibility, and H_0 is the applied magnetic field. The net magnetization is approximately 1.4 ppm, which means that there are only 1.4 excess aligned protons per million protons. The intensity of the NMR signal is proportional to $\mathbf{M}_0$ and is directly related to the magnitude of the applied field. The *macroscopic nuclear magnetization*, **M**, is the vector sum along H_0 of the individual spin moments (Fig. 6.3).

The very small differences in size of the two opposing populations give rise to a net magnetization vector **M** in the direction of H_0. For spin 1/2 systems, such as the proton, at normal temperatures, this resultant equilibrium magnetization closely follows Curie's law: increases with the B_0 field strength, and is inversely proportional to the absolute temperature. As the Z axis, along H_0, is the only privileged direction, the spins are randomly oriented with respect to the perpendicular XY plane. Therefore, there is no net magnetization in that plane.

If one changes to a rotating frame of reference, xyz, turning at the Larmor frequency and with z collinear with Z, the spins appear to be immobile and subject to 'zero external magnetic field'. This is analogous to the 'zero gravity' experienced by someone inside a falling elevator. The consequence of this apparent disappearance of H_0 is that if a second, less intense magnetic field H_1 is applied along x (produced, for example, by a radiofrequency electromagnetic field tuned to the Larmor frequency), the spins will start to precess about x at a frequency:

$$\Delta E_0 = \hbar \nu_0 \text{ (MHz)} \tag{6.6}$$

Expressed in terms of the applied magnetic field, the frequency of the rf field is

$$\nu_0 \text{ (MHz)} = \gamma H_0 \tag{6.7}$$

This equation describes the resonance condition for the NMR experiment and shows that the 'resonant' radiofrequency must correspond to the Larmor frequency for the applied magnetic field. Because the gyromagnetic ratio is different for each nuclear isotope, different nuclei resonate at widely different frequencies in a given applied magnetic field. In a magnetic field of 1 T, ^{1}H has a frequency of 42.5759 MHz, and ^{13}C a frequency of 10.705 MHz.

If the short rf pulse at the Larmor frequency is applied, all the spins are simply rotated together around x as a coherent packet. By adjusting the duration, t_p, of the radiofrequency pulse, it is possible to rotate $\mathbf{M}_0$ by any given angle. The usual NMR experiment uses a 90^0_x rf pulse along x, to flip $\mathbf{M}_0$ over the z axis to the y axis where it can then be detected.

> *Every subatomic particle has a fixed, definite, and known angular momentum, but nothing is spinning! If you don't understand it, don't worry. Physicists don't understand these words either. They just use them.* — Gary Zukav [4]

This radiofrequency (rf) is generated by using an alternating current of variable frequency that is passed through a coil whose axis lies in the xy plane perpendicular to the applied magnetic field. This current gives rise to an oscillating magnetic field that is also perpendicular to the applied field. As the frequency of the oscillating rf field is varied, there is a point at which it exactly matches the precessional frequency of the nuclei, and energy from the radiofrequency is absorbed by the nuclei. When this absorption occurs, the system is said to be in *resonance*. This absorption of energy is the resonance phenomenon. In resonance, energy is transferred from the rf radiation to the nuclei, which causes a change in the spin orientation of the nuclei or, in other words, a change in the spin populations in the higher energy levels.

The applied rf field, H_1, provides the nuclei with the quanta of energy necessary to move to the higher energy levels. The need for a time-dependent H_1 results from the fact that H_1 is active only if it can 'chase' the spins at the frequency at which they are rotating. When the proper rf pulse is applied, the nuclei begin to precess in phase. As the rf pulse continues, more and more nuclei fall in line and precess in phase with the rf magnetic field. After a certain period of rf exposure, the magnetization becomes *coherent*. The protons then precess as a coherent group in the xy plane rather than as randomly phased individuals in the z direction. Just as the synchronization of randomly phased light waves forms a coherent laser, synchronization of radiowaves produces a coherent rf signal that is detectable over the random background.

After the rf field is turned off, the magnetization returns to its original equilibrium value by emitting energy or by transferring energy to the surrounding molecules. However, the probability of spontaneous emission depends on the frequency to the third power, and at radiofrequencies this term is too small to be significant. Thus, all NMR transitions are *stimulated*. The stimulated process by which the energy is lost to the environment is called *relaxation*.

Pulsed NMR Fourier transform spectroscopy

> *A major improvement in the signal-to-noise ratio of NMR spectra was achieved in 1964 by the conception of Fourier transform (FT) spectroscopy. The basic principle — parallel data acquisition, leading to the multiplex advantage — was already applied by Michelson in 1891 in optical spectroscopy and explicitly formulated by Fellgett in 1951. However, the approach used in optics, spatial interferometry, is unsuited for NMR spectroscopy, since an interferometer with the necessary resolution would require a path length of at least* 3×10^8 *m.* — Richard R. Ernst [1]

Basis of the Fourier transform NMR experiment

Let us investigate the pulsed NMR Fourier transform experiment further. In order to understand the pulsed NMR experiment, one must recognize that the magnetization vector, $\mathbf{M}_0$, is resolved into a component, M_z, along the z axis, and a component, M_{xy}, perpendicular to the field. The M_z component is called the *longitudinal magnetization*, and the M_{xy} component is termed the *transverse magnetization*. At thermal equilibrium, M_z is equal to $\mathbf{M}_0$ (the initial magnetization), and M_{xy} is zero. When the sample is irradiated with the rf pulse (from the $+x$ direction), M_z decreases, and M_{xy} increases. Note that the NMR signal is detected in the xy plane. The 90°_x rf pulse, also known as the read pulse, is generated by passing an oscillating electric current through the transmitting coil that surrounds the sample. A short pulse of rf radiation of t seconds duration is equivalent to the simultaneous excitation of all the frequencies in the range $\mathrm{rf}_0 \pm t - 1$, where rf_0 is termed the *carrier frequency* of the nuclei under study. Because the pulse duration is only microseconds, the bandwidth is sufficiently large to excite all of the resonant nuclei in the sample. By adjusting the duration of the pulse, t_p, it is possible to rotate $\mathbf{M}_0$ for any given angle:

$$\theta = \gamma H_1 t_\mathrm{p} \tag{6.8}$$

As the nuclei receive the pulse, they come into phase with each other and become a bundle of precessing nuclei that has a net magnetization in the xy plane (Fig. 6.4).

Following the pulse, the nuclear spins initially precess about the static field and are coherently in phase (Fig. 6.4b). Because of the inhomogeneities in the static magnetic field and the local magnetic fields of adjacent molecules, the nuclei start to precess at different frequencies and quickly lose their coherence (become out of phase) (Fig. 6.4c,d). The precession phase of the nuclei is not totally random, and a net component of magnetization is generated in the xy plane. This rotating M_{xy} component induces a voltage in the receiving coil that surrounds the sample.

The pulse diagram for the 90° read sequence is given in Fig. 6.5.

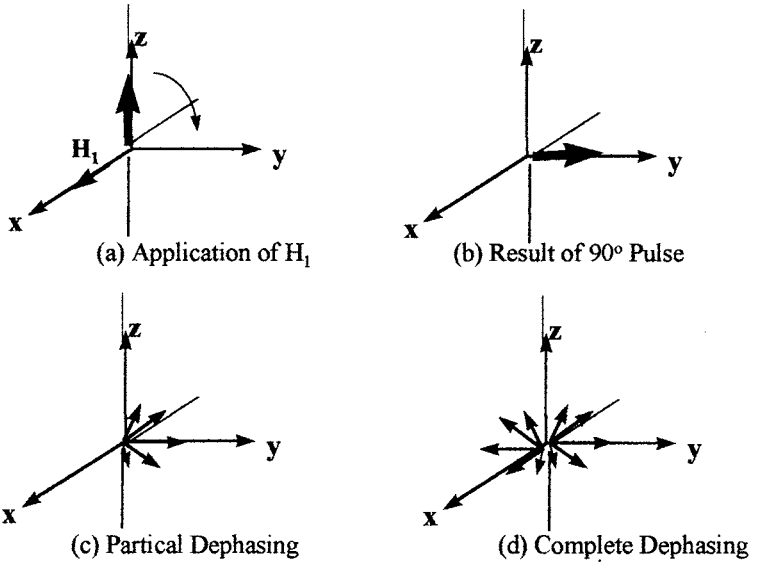

Fig. 6.4. (a) Effect of the 90° rf pulse on the magnetization vector; (b) magnetization vector in the xy (rotating frame); (c) dephasing of the magnetization vector; (d) complete dephasing.

The observed signal in the time domain is called a *free induction decay* (FID) because it is measured 'free' of a driving rf field. It is a 'decaying' voltage because the net nuclear magnetic field decays as the nuclei return to their equilibrium value (Fig. 6.5).

The term 'induction' is used because a current is induced in the receiver coil. This signal is collected as a function of time, amplified, and processed to give the detected NMR signal.

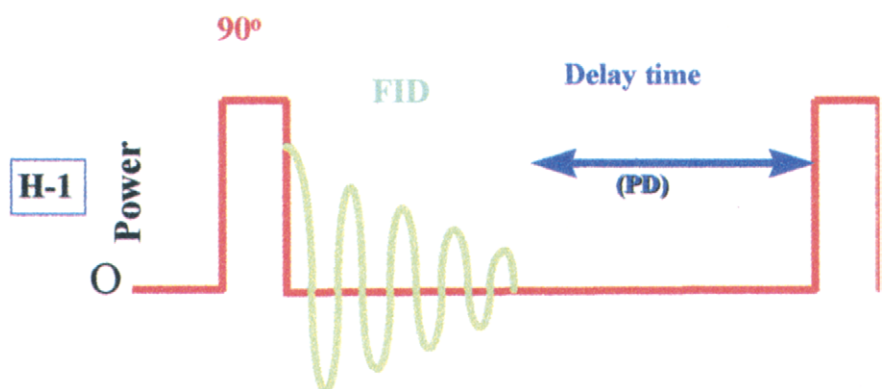

Fig. 6.5. The pulse diagram to read the NMR signal. A 90° pulse is applied sufficiently long to produce a rotation of the magnetization vector into the M_{XY}. The pulse is turned off and the free induction decay is recorded. After an appropriate delay time the sequence is repeated.

The FID signal for the nuclei can be expressed as

$$\text{FID} = A \cos \omega_0 t \exp\left(\frac{-t}{T_2^*}\right) \tag{6.9}$$

where A is the amplitude. The term T_2^* is the experimental *transverse relaxation time* and includes contributions resulting from the inhomogeneity of the static magnetic field as well as from the T_2, which is the *spin–spin relaxation time*. The FID observed in pulsed NMR spectroscopy can be described as a linear combination of damped oscillations characterized by a complex frequency. FID signals in NMR data usually consist of several groups of wave elements distributed within narrow-frequency bands. The spectrum in the frequency domain is obtained by taking the Fourier transform of this response:

$$F(\omega) = \gamma_0 A \cos \omega_0 t \exp\left(\frac{-t}{T_2^*}\right) \exp(i\omega t)\, \mathrm{d}t \tag{6.10}$$

where ω is the Larmor frequency and i is the square root of (-1). Integration yields

$$F(\omega) = \frac{A}{2}\left(\frac{T_2^*}{1 + T_2^* (\omega - \omega_0)^2}\right) \tag{6.11}$$

This function is termed a *Lorentzian line shape* and is the NMR spectral result for a single nuclear type. For actual chemical systems, a number of different nuclear types will be present, and the FID are quite complicated [6]. The Fourier transform process separates the different contributions and produces the proper spectrum in the frequency domain [7]. This is the pulsed NMR Fourier transform experiment.

Experimental considerations for the FT NMR experiment

In recording the FID, the *pulse width* and *read pulse* (90°) must be set properly to assure highest possible sensitivity. Then the *pulse delay time* must be determined. It is normally set at 5× the longest T_1. Next the *spectral width* (SW) is set. In ^{13}C NMR, the chemical shift range is 250 ppm, so at 50 MHz, the resonances will lie within 12,500 Hz which is the required SW. The number of data points (DP) must be 2^n (from the FT algorithm) For ^{13}C NMR, 16K or 32K are usually considered sufficiently high. The *digital resolution* (DR) is calculated:

$$\text{DR} = \frac{\text{SW}}{(\text{DP}/2)} \tag{6.12}$$

where DP is total number of data points but only DP/2 are real (also from the FT algorithm). So for a 32K spectrum at 50 MHz is

$$\text{DR} = \frac{2 \times 12,500}{32,768} = 0.76 \text{ Hz } (\sim 0.015 \text{ ppm}) \tag{6.13}$$

which determines the accuracy of the resonance positions to ±0.76 Hz (±0.015 ppm) as well as the resolution limitations which requires that resonances have chemical shifts must be separated by 1.54 Hz (~ 0.03 ppm) to be resolved [8].

In NMR spectroscopy, high applied magnetic fields are desirable, not only because of an increase in the signal-to-noise, but also because the resonance peaks are spread over a wider frequency range, allowing for greater resolution in the spectrum (i.e. separation between the peaks).

Improved sensitivity in NMR

> *Under optimum conditions with modern high-field spectrometers, 10^{14}–10^{15} spins of one kind are needed to detect a signal within a measurement time of one hour. The low-signal to noise ratio is the most limiting handicap of NMR. Any increase by technical means would significantly extend the possible range of NMR applications.* — Richard R. Ernst [1]

NMR is considered to be one of the most powerful methods for structural elucidation of material. Unfortunately, NMR has a number of limitations including low sensitivity. With the advent of Fourier Transform methods in the 1980s, NMR spectrometers with an increased dynamic receiver range became available; thus observation of signals from samples diluted up to 1 : 10,000 in protonated solvents became possible. Increasing the signal-to-noise ratio of the spectra was responsible for this improvement.

To increase the signal-to-noise ratio (SNR), the spectra are signal-averaged by collecting a large number of pulses. The NMR signal adds coherently, whereas the random noise adds only as the square root of the number of scans accumulated. Thus, the improvement in the signal-to-noise ratio is proportional to the square root of the number of transients accumulated. However, on the down side, improvement in SNR by a factor of 2 requires a 4-fold prolonged acquisition time.

During this summation process, the interval between pulses (the PD or pulse delay) must be sufficient for the system to return to equilibrium; otherwise, the signal can become saturated. The time required to return to equilibrium is the *longitudinal relaxation time* (which will be discussed later) and the general practice is to make $PD = 5T_1$ to ensure a return ($\approx 98\%$) to equilibrium [7].

The limit of detection (LOD) in NMR experiments depends on a variety of parameters. The signal corresponds to the number of protons within the detection cell and therefore increases with the cell volume at constant concentration of the unknown. The SNR ratio is improved by the power of 3/2 with the magnetic field strength, so optimum performance is obtained with modern superconducting magnets.

An essential component of the NMR system is the sampling probe. The performance of the probe is highly dependent upon the performance of the rf coil and upon the material properties of the sample fixture, and circuitry. The magnitude of the signal detected by the radiofrequency coil (rf) is directly proportional to the filling volume and the sensitivity of the rf coil. A high SNR is generally achieved using an

optimized winding geometry of the coil (e.g., wire diameter, interturn spacing, and number of turns). An important factor in the design of detector cells is the filling factor, a measure of the fraction of coil volume occupied by the sample. Theoretically, maximum sensitivity would be attained when the total coil volume is filled with sample.

High resolution measurements concentrates the signal in a narrow frequency range and enhances the signal. The resolution is determined by the line widths obtained. The uniformity of the magnetic field is important in determining the inherent line widths. Conventional NMR systems decrease the line widths by spinning the sample to reduce the effects of magnetic field inhomogeneities. Higher magnetic fields also improve the resolution. A separation of 1 ppm between two peaks at 25 MHz is 25 Hz whereas at 125 MHz, it becomes 125 Hz. The 900-MHz (21.1 T) magnet is the highest field strength that current superconducting materials can achieve.

Nuclear spin relaxation

After the resonance rf pulse has been applied, a higher energy excited state exists. This higher energy level corresponds to the nuclei that are elevated to the antiparallel position. To return to the equilibrium or ground state, this excess energy is passed to the surroundings by stimulated emission, and some of the antiparallel nuclei return to the parallel or low-energy state. The rate of this process is determined by two external factors or relaxations: the spin–lattice relaxation time, T_1, and the spin–spin relaxation time, T_2.

The spin–lattice relaxation time

The rate of return to equilibrium along the static field (z axis) depends on the rate of exchange of energy between the nuclei and the environment or, *lattice* in NMR terminology. The longitudinal magnetic relaxation time, T_1, is often called the *spin–lattice relaxation time* and depends on the effectiveness of energy transfer from the excited nuclei to the lattice. Just as resonance requires stimulation by rf energy at a particular frequency, return to the ground state is enhanced by the presence of rf energy in the lattice at the resonant frequency (*stimulated emission*). This rf energy comes from fluctuating magnetic nuclei and electrons in the lattice. Magnetic fluctuations that are at or near the resonant Larmor frequency generate rf magnetic fields that stimulate the transition from the high-energy to the low-energy states. This coupling mechanism allows the energy initially added by the rf pulse to be dissipated to the lattice.

The spin–lattice or longitudinal relaxation time, T_1, which characterizes the time needed to establish equilibrium between the spin system and the medium (termed the lattice in this field). Thermal agitation creates molecular motions that give rise to a wide frequency range of oscillating magnetic fields. If some of the components

of this 'magnetic noise' are correctly oriented and oscillate at the Larmor frequency, energy transfers occur between the nuclear spins and their environment and spins relax from the higher quantum energy level to the lower. This irreversible energy loss leads to a decrease in the total energy of the spin system.

The T_1 will be shorter for molecular movements with frequencies close to the resonance frequency (Larmor frequency), as these near resonance frequencies favor transitions between the quantum energy levels. Therefore, T_1 is relatively long for solids, where the movements are very slow, and in very fluid samples, where the movements are rapid.

The basic pulse sequence for spectrum editing based on T_1 is the inversion–recovery sequence (180°–t_r–90°–FID), where the 180° pulse causes inversion of the magnetization and the FID is collected after a suitable recovery time t_r. Assuming perfect inversion, the signal intensity is proportional to $[1 - (2\exp(-t_r/T_1)]$; thus spins with $T_1 > 1.44t_r$ will give rise to negative peaks and spins with $T_1 < 1.44t_r$ will give rise to positive peaks, and those spins with $T_1 \sim 1.44t_r$ will have peaks at the null point.

The T_1 is specific for each molecule and its environment and gives information about the molecular dynamics of the magnetic moments and the molecules around them. When the nuclear magnetization rotates at the Larmor frequency, local fluctuating magnetic fields (perpendicular to the rf axis) lead to a decay of the longitudinal spin magnetization. The local fluctuating magnetic fields are generated primarily by molecular motion. Thus when the lattice exhibits considerable molecular motion at the appropriate frequency, the energy coupling is effective, and the T_1 is short. On this basis, the T_1 is short for liquids where the molecular motion is extensive over a broad range of frequencies but is quite long for solids where the motion is restricted and occurs over a narrow range of frequencies. When a solid is heated to a viscous liquid, the T_1 shortens. Initially, thermal energy transfer improves as the molecular motion increases. An optimum is reached in a viscous liquid state, and T_1 is minimized. Additional heating results in molecular motions that are too rapid for efficient thermal energy transfer, and the T_1 value again increases.

The spin–spin relaxation time

The transverse magnetization decays by a different relaxation process than the spin–lattice process and involves the return to equilibrium by the loss of coherence of the transverse magnetization of the nuclei. The magnetization dephases in the xy plane because of differences in the individual precession frequencies of adjacent nuclei. The energy is transferred adiabatically between the nuclei as they are jostled between high- and low-energy positions. These internal differences introduce a 'flip-flop' process and a loss of coherence. Because this internal adiabatic exchange occurs between two different spins, the transverse magnetic relaxation time, T_2, is also called the *spin–spin relaxation time*.

A simple pulse sequence using transverse relaxation is the spin-echo (90°–t_s–180°–t_s–FID) and here the signal intensity is proportional to $\exp(-2t_s/T_2)$. Unlike the inversion-recovery method, the spin-echo method can allow the spectra to be phased to give positive peaks for all spins, but phase distortion is expected for homonuclear coupled spin systems when longer spin-echo times are used or where larger coupling constants are present in this method.

The T_2 gives information about the distribution of resonant frequencies and about the local fields experienced by the magnetic moments of the nuclei. Local fields are related to the structure and to the chemical nature of the environment around the nuclei. Because the local magnetic fields in liquids fluctuate very rapidly and can average to zero, the internal local fields are weak and yield long T_2s or narrow resonance lines. The atoms in solids are in nearly fixed positions, and the internal fields are significant and contribute to the rapid loss of coherence. Therefore, the T_2 in solids is very short (microseconds), and the resonance lines are very broad.

There is an additional contribution to T_2 that is not molecular in origin. The rate of decay of transverse magnetization is influenced by any inhomogeneity of the external static magnetic field. The inhomogeneity of the magnetic field across the sample causes the nuclei in different parts of the sample (called *isochromats*) to precess at different rates, which leads to additional irreversible destruction of the coherence. The experimentally observed T_2^* is the sum of the actual internal molecular T_2 and the contribution resulting from the nonuniformity of the magnetic field.

Application of an rf pulse along the x axis rotates $\mathbf{M}_0$ about the x axis through an angle θ given by

$$\theta = \gamma H_1 t_p \tag{6.14}$$

where H_1 is the intensity of the rf pulse, and t_p is the length of the pulse (generally in the range of microseconds). Thus, the appropriate values of H_1 and t_p can be combined to make $\theta = 90°$ and to rotate $\mathbf{M}_0$ through 90°. For ^{1}H, γ is 6.2577 kHz G^{-1}, and for an H_1 field of 50 G, t_p is 1.17 μm. The magnetization becomes colinear with the y axis and thus gives rise to a signal. Such a pulse is called a 90° *pulse*. In similar fashion, a pulse that will invert the magnetization vector can be generated, and this pulse is called a 180° or *inversion pulse*.

The principal source of external relaxation or coherence in the transverse plane for liquids and solutions is inhomogeneity in the static magnetic field. Using a spin-echo sequence (Fig. 6.6) can eliminate this source of loss.

After the 90° pulse, the individual nuclei precess around the z axis at different rates because of the inhomogeneity of the magnetic field and lose phase coherence (Fig. 6.6c). A 180° rf pulse reverses the y components of the individual vectors so that after the pulse they start to come back into coherence (Fig. 6.6d) to form an echo. Coherence is achieved when the individual vectors realign to produce maximum magnetization (Fig. 6.6e). The echo is then detected as the FID with an increased signal.

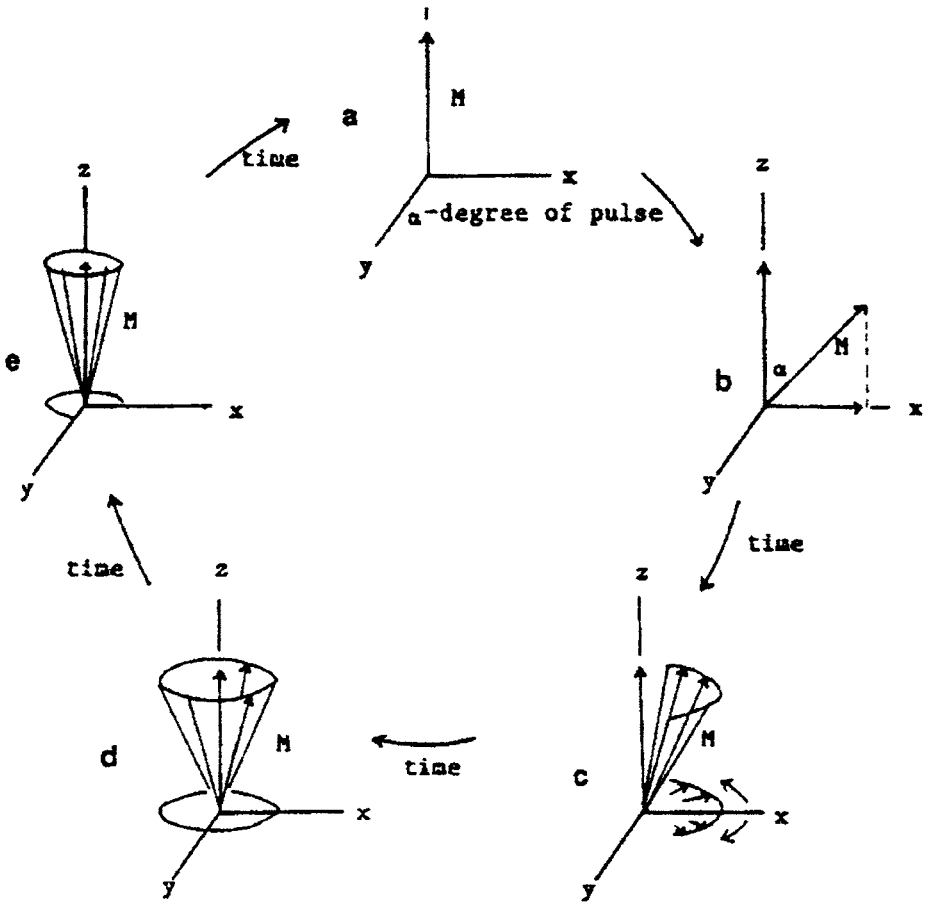

Fig. 6.6. The spin-echo sequence.

Magnetic interactions between nuclei

> *One of the most striking and characteristic features of nuclear magnetic resonance (n.m.r.) is that the spectra from solids are so very much broader than those from liquids. An excellent example is provided by water, whose proton n.m.r. linewidth at room temperature is about 0.1 Hz, while for ice at low temperatures it is about 10^5 kHz, six orders of magnitude broader.*
>
> — E. R. Andrew [9]

All nuclei are surrounded by magnetic dipoles that are associated with neighboring nuclei. The effective field, H_{eff}, at a particular nucleus may be either larger or smaller, depending on the relative orientation of these neighboring nuclei with respect to the static magnetic field. For solids, these orientations are fixed, and the nuclei may

come into resonance over a broad range of frequencies ($\approx$ 1–100 kHz). In liquids or solutions, the effects of the magnetic dipoles are mutually canceled if the Brownian motion is sufficient to rapidly change the relative orientations of the molecules with respect to each other in a time shorter than the lifetime of a spin state. The result is to average the local field of the magnetic dipoles to zero. The width of the resonance line for samples of this kind decreases to a value (0.1–1 Hz) that depends primarily on the inhomogeneity of the applied magnetic field. For polymers, the rotational and translational motions of the chain segments may be hindered because the motions of neighboring segments are correlated with each other [10]. The result is a broadening of the resonance peaks up to 10–50 Hz, particularly if the chains are stiff and the motion is anisotropic.

Interactions between nuclei and their environments

The nuclei not only interact with the magnetic field but also with the surrounding nuclei and their electrons. The result has important implications for the study of molecules by NMR.

Observation of chemical shifts in proton resonances

The discussion to this point has focussed on individual nuclei and as such the expectation is that a molecule with a number of chemically different nuclei would have a single resonance for the protons. However, when the NMR spectra of molecules in liquids and solutions are obtained at sufficiently high field strengths, multiple resonances are observed [11]. The first observed spectrum of ethyl alcohol, showing three different lines resulting from the three different types of protons, is shown in Fig. 6.7.

The ratio of the intensities is 3 : 2 : 1 immediately suggests to the chemist that the assignment on the basis of the number of protons was to the CH_3, CH_2, and

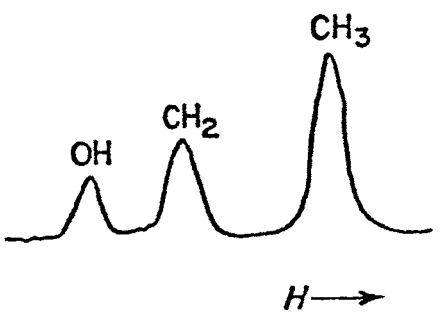

Fig. 6.7. The NMR spectrum of ethyl alcohol at low magnetic field. This was the first NMR observation of different chemical shifts in the same molecule. (Reproduced with permission from Ref. [11]. © 1951 American Institute of Physics.)

hydroxyl protons, respectively. These multiple resonances arise from differences in the electronic environments of the different protons in ethyl alcohol. The source of the change in resonance is the shielding effect by the electron orbitals of the nuclei from the applied magnetic field. The external field, H_0, induces orbital currents that produce a small local magnetic field, H_{loc}, which is opposed to H_0. The nucleus inside the electron cloud experiences an effective field, H_{eff}, that is slightly smaller than H_0, and therefore comes to resonance at a lower Larmor frequency. Since the electron cloud for each of the chemically different protons in ethyl alcohol generates different electronic shielding, the different protons exhibit three different resonances. This effect is known as *chemical shielding*. The observation of chemical shifts has broad applications to the study of molecules by NMR.

> *With the observation of three magnetically nonequivalent types of protons in ethyl alcohol, nuclear magnetic resonance began to be primarily the province of the chemist, as it is today.* — F. A. Bovey [10]

Origin of chemical shifts

The Larmor equation accounting for electronic shielding is written:

$$\omega = \gamma H_{eff} \tag{6.15}$$

describes the relationship among the Larmor precession (resonance) frequency of a magnetic nucleus, ω, the gyromagnetic ratio of the nucleus, γ, and the strength of the effective magnetic field surrounding the nucleus, H_{eff}. The field of interest, H_{eff}, the local field in which the nucleus is immersed, is different from the field caused by the magnet alone, H_0. This difference is caused by nearby nuclei and electrons having associated magnetic fields that contribute to the total field surrounding the nucleus of interest. Since surrounding electrons have associated magnetic fields that give rise to diamagnetic effects (i.e. they generate opposing magnetic fields), their effect is an apparent shielding of the nucleus from the applied magnetic field. Thus, a particular nucleus of a given isotope (which has a characteristic gyromagnetic ratio) placed in a known magnetic field can have different resonance frequencies, depending on its chemical environment.

In the case of motional averaging in solutions or liquids, sharp narrow resonances are observed in the NMR spectra. The appearance of different resonances for the observed nuclei in a given molecule arises from differences in the shielding effect, which is modified by the electron-withdrawing or electron-donating effects of neighboring groups. The electron-withdrawing or donating effect is proportional to the field strength, H_0, and the shielding field, H_s, is

$$H_s = -\sigma H_0 \tag{6.16}$$

or

$$H_{\text{eff}} - H_0 + H_s = H_0(1 - \sigma) \tag{6.17}$$

where σ is a proportionality factor called the *screening constant* and is characteristic of the shielding effect caused by the chemical surroundings of a given isotope.

Ideally, we would like to know the absolute magnitude of shielding constants but this is not practical experimentally. The susceptibility variation in the materials near the sample can lead to localized distortions in the static magnetic field in the sample region. As a consequence, the absolute value of the effective magnetic field at a nucleus cannot be determined, so in order to obtain a point of reference for the different effective fields, a standard substance is used as an internal reference. Generally, tetramethylsilane (TMS) is chosen as the standard reference for proton NMR spectroscopy. The screening constants are found to be approximately 10^{-5} or less, and the factor 10^6 transforms δ to the units of parts per million (ppm). Chemical shift values are generally expressed in terms of parts per million (ppm) relative to a reference

$$\text{Chemical shift (ppm)} = \frac{10^6(\nu_{\text{sample}} - \nu_{\text{reference}})}{\nu_0} \text{ at constant } H_0 \tag{6.18}$$

where ν_{sample} and $\nu_{\text{reference}}$ are the sample and reference frequencies and ν_0 is the spectrometer operating frequency. While the actual frequency differences in Hz depend on the magnetic field strength, the differences in ppm do not. The total frequency range of the chemical shifts for a particular nucleus depends on both the field strength and the isotope being studied.

NMR spectra are plotted with decreasing frequency to the right with the origin being the reference value (usually TMS). If one nucleus is more shielded than another, its signal will be shifted to lower frequency (or up field). By convention, it will have a more negative chemical shift and will appear further toward the right side of the spectrum.

This chemical shielding property allows the observation of a spectrum of resonance frequencies for a given molecule, which is the basis of spectroscopy. Chemical shifts are an extremely important tool in NMR since chemical shifts can reveal changes in the chemical and physical environment of a molecule. Of course, the magnetic field must be sufficiently homogeneous to allow resolution of the various spectral components.

The primary benefit of chemical shifts is that nuclei exhibit specific resonances that depend on the chemical nature of the nuclei [12]. Like characteristic group frequencies in IR and Raman spectroscopy, similar molecular groups have similar chemical shifts. Measurements of chemical shifts have generated catalogs of correlations between the magnitudes of these chemical shifts and the chemical nature of the resonating nuclei [13]. Consequently, measurements of the chemical shifts of nuclei in different molecules allow a determination of the chemical nature of the nuclei involved. This method of chemical structure determination using ^{1}H-, ^{19}F-, ^{29}Si- or

^{13}C-NMR spectroscopy is widely used to determine the chemical structures of small molecules and polymers [14,15].

Through-bond interactions with other nuclei

> *Compilations of proton and carbon NMR chemical shifts are a means of drawing correlations between different compounds. Spin coupling data, whether homo- or heteronuclear, extend the elucidation process a step further, providing connectivity information for structural fragments rather than just plausible identities of isolated atoms.* — Gary E. Martin [16]

At higher resolution (i.e., at higher magnetic fields), the proton resonances can split into patterns reflecting the environments of the nuclei. When the resonating homonuclear nuclei are in the same molecule, spin–spin interactions via bonding electrons will occur. To first order, these scalar interactions are normally observed through three chemical bonds. The scalar interactions occur only when the interacting protons are magnetically and chemically distinguishable.

There is also an orientation-dependent dipole–dipole interaction that occurs through space between both bonded and nonbonded nuclei. When rapid motion occurs, as in liquids and solutions, the effects of these through-space dipolar nuclear interactions average to zero. The *scalar* through-bond interactions are independent of the orientation of the chemical bonds with the magnetic field and are not averaged to zero by molecular motion. Thus, the scalar spin-spin interactions persist even in the presence of molecular motion.

The scalar bond-coupling pathway is used to transmit information concerning the spin states through the electron orbitals of the bonds to the neighboring nuclei. The result is a splitting of the energy levels to produce new resonances that appear as perturbations of the original energy levels.

One of the first ^{1}H-NMR spectra of ethyl alcohol is shown in Fig. 6.8.

At a higher magnetic field, the resonances split into interesting patterns. The interpretation of the new lines is given in Fig. 6.9, which shows the various orientations and the corresponding energy levels of the methyl and methylene protons.

These NMR results can be summarized in the following fashion. A nucleus, X, with a spin of $1/2$ has spin states of either $+1/2$ or $-1/2$. A second adjacent homonucleus, A, in the same molecule will be able to recognize the two different spin states of the nucleus X through the scalar coupling of intervening bonds. Consequently, the coupled nucleus will resonate at two different frequencies corresponding to the upper- and lower-energy levels of the interacting nucleus. Because of the large number of nuclei present and the small differences in the populations of the two levels, the two coupled resonances of nucleus A will have nearly equal intensities, that is,

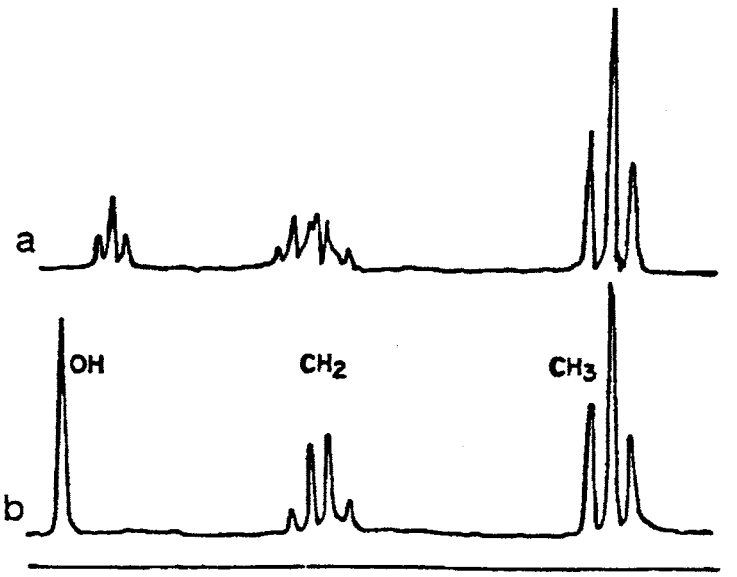

Fig. 6.8. NMR spectra of pure dry ethyl alcohol (a) and slightly acidic alcohol (b). The slightly acid environment causes rapid exchange of the hydroxyl group between neighboring molecules. This exchange is sufficiently rapid to "average" the electronic environment. (Reproduced with permission from Ref. [11]. © 1951 American Institute of Physics.)

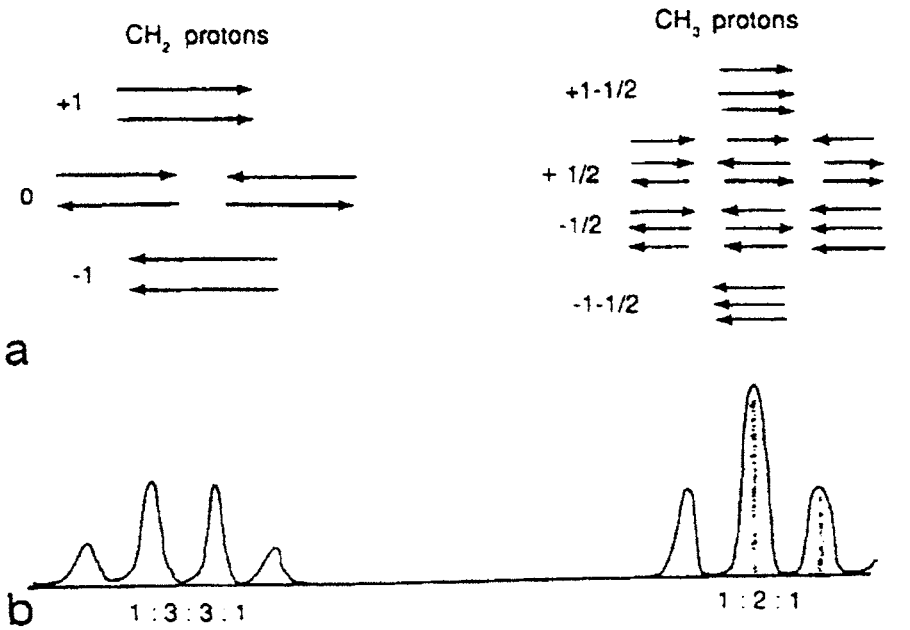

Fig. 6.9. Spin–spin coupling diagrams showing the possible spin orientations of the methyl and methylene protons (a) and the corresponding spectrum with these functionalities as neighboring groups (b). (Reproduced with permission from Ref. [11]. © 1951 American Institute of Physics.)

1 : 1. Similarly, two resonances of equal intensity, with a frequency separation corresponding to J_{AX}, will be observed for nucleus X. The magnitude of the frequency difference is determined by the strength of the scalar coupling and is specific for the chemical nature of the two interacting nuclei. Consequently, the magnitude of the coupling is given by a specific coupling constant J_{AX} (Hz), where A and X are the homonuclear coupled nuclei. Measurement of J_{AX} from the NMR spectrum is useful for determining the presence of the coupled A and X nuclei, that is, the chemical environment of the A and X nuclei [17].

When there are two nuclei (A_2) with magnetically equivalent surroundings in a molecule, the nuclei will influence a scalar-interacting nucleus, X, in this molecule via bonding electrons. The following spin-state combinations will be possible: $(+1/2, +1/2)$, $(+1/2, -1/2)$, $(-1/2, +1/2)$, and $(-1/2, -1/2)$. The net effect of the two energy-state combinations $(+1/2, -1/2)$ and $(-1/2, +1/2)$ is energetically the same. Hence, the resonance of the neighboring nucleus is split into three equally spaced peaks with a separation of J_{AX} and with an intensity ratio of 1 : 2 : 1.

The spectra obtained are a direct result of these different energy levels being available to the nuclei. The intensities of the lines are a function of the number of available states for each energy level. The magnitude of the splitting for the methylene protons is the same as for the methyl protons, and the magnitude of the separation is termed the *J-coupling constant.*

When the ethyl alcohol is neat, there is no exchange of the slightly acidic protons on the hydroxyl group, and the methylene resonances are further split as a result of the presence of this proton on the hydroxyl group. The methyl protons are not affected (to first order) because they are more than three chemical bonds away from the hydroxyl protons, and the interaction effect is too small to observe at this level of resolution.

As the number of equivalent nuclei increases, the number of lines increases. In general, the multiplicity of the splitting is given by $2NI_s + 1$, where N is the number of magnetically equivalent nuclei with spin I_s (Fig. 6.10).

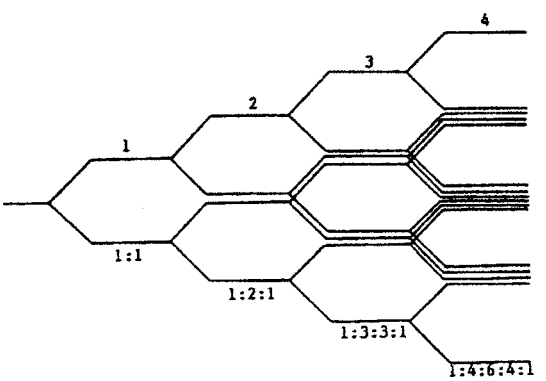

Fig. 6.10. The spin–spin coupling effect for increasing numbers of equivalent nuclei showing the number of lines and their relative intensities.

The intensity distributions of these lines are specific, and a general prediction for the intensities can be made on the basis of the coefficients of the binomial expansion $(a + b)^n$. The intensity ratio of the multiplet is given by the corresponding row of Pascal's triangle, with the first row corresponding to $N = 0$ (no interacting nucleus). These intensity ratios extend to five equivalent nuclei as represented in the sixth row in the triangle.

1
1 1
1 2 1
1 3 3 1
1 4 6 4 1
1 5 10 10 5 1

These rules are valid only when the chemical-shift differences between the coupled protons are much greater than the coupling constants. The spectra are then said to obey the *first-order approximation*. When the chemical shift differences become smaller, more complex spectra are obtained. Such spectra are said to be *second order* [18].

Vicinal coupling constants can vary in both sign and magnitude depending on a number of structural parameters, and particularly on the dihedral angle between the C−H protons. If one looks down the C−C bond between the carbon atoms to which two coupled vicinal protons are attached, the angle the protons make with one another is known as the *dihedral angle*. The dependence of the coupling constants of vicinal protons on the dihedral angle, ϕ, is given by the Karplus equation (Fig. 6.11):

$$J = \left(8.5\cos^2\phi\right) - 0.28 \qquad \text{for } \phi = 0\text{–}90^\circ \tag{6.19}$$

$$J = \left(9.5\cos^2\phi\right) - 0.28 \qquad \text{for } \phi = 90^\circ\text{–}180^\circ \tag{6.20}$$

This dependence of the coupling constants on bond angle is particularly useful for studying the stereochemistry in biopolymer systems [19].

The preceding discussion has particular relevance for ^{1}H-NMR spectra, but similar effects are observed for other nuclei. For example, heteronuclear ^{1}H–^{13}C scalar decouplings can be observed. Because these ^{1}H–^{13}C scalar decouplings lead to additional resonances and further decrease the ^{13}C signal, it is the usual practice to 'decouple' these ^{1}H–^{13}C scalar decouplings (see the section "Experimental ^{13}C-NMR spectroscopy", p. 277).

In a manner similar to the spin–spin couplings apparent in the ^{1}H-NMR spectra, ^{13}C–^{13}C scalar couplings are present in ^{13}C-NMR spectra. The one-bond carbon–carbon couplings ($^1J_{CC}$) are typically 30–40 Hz for C−C single bonds and 50–60 Hz for C=C double bonds. The one-bond C−C couplings are about an order of magnitude larger than typical two- and three-bond C−C couplings ($^2J_{CC}$, $^3J_{CC}$) [17]. Unfortunately, because of a low natural abundance, ^{12}C surround most of the ^{13}C, and

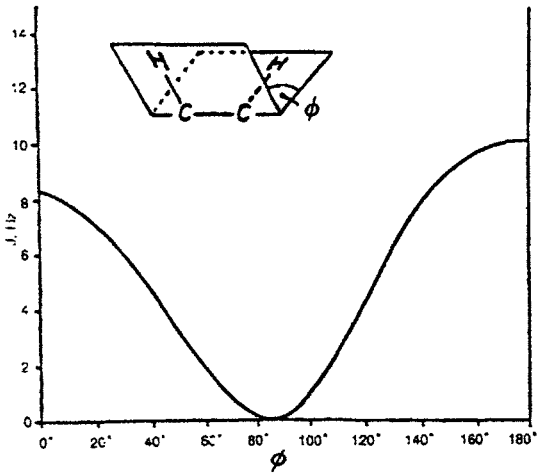

Fig. 6.11. The dependence of the scalar coupling constants, J, of vicinal protons on the dihedral angle ϕ.

no coupling occurs. However, a small fraction ($\approx 10^{-4}$) of ^{13}C–^{13}C pairs exists at natural abundance for each C–C bond in the polymer. Moreover, these pairs are isolated from all other pairs and exhibit simple AX or AB patterns. However, the intensity of these ^{13}C–^{13}C scalar coupling resonances is very weak, and it is generally necessary to enrich the sample with 13C isotopes in order for these C–C couplings to be observed.

By using chemical shifts and spin coupling patterns, neighboring atoms in a molecule can be determined unambiguously. The coupling constant depends on the chemical structure of the moiety that contains the coupling nuclei. The notation for a system of nuclei coupling with each other is characterized by capital letters. Each set of magnetically equivalent nuclei is represented by one capital letter, with the number of the nuclei in the set as a subscript. Sets of magnetically equivalent nuclei whose differences in chemical shifts are comparable to the coupling constants to yield higher-order spectra are designated by A, B, C. Other sets of magnetically equivalent nuclei with chemical shifts comparable to the coupling constants, but differing greatly from A, B, or C in chemical shift, are written X, Y, Z. Thus, the three aliphatic protons in styrene and vinyl chloride yield ABC spectra, and the four protons of 1,1-dichloroethane yield an A_3X spectrum. As will be demonstrated later, these proton interactions are valuable in the determination of stereoregularity in some polymer systems.

Through-space interactions with other nuclei

In addition to the scalar couplings, there are also through-space interactions arising from dipolar interactions. In solution NMR, the molecular motion is sufficient to

average these dipolar interactions to zero so narrow lines are obtained. However, these interactions are particularly important in the NMR spectroscopy of solids.

Experimental proton NMR spectroscopy

Experimentally, proton (^{1}H) NMR spectroscopy generates the largest signal because of the nearly 100% natural abundance and high gyromagnetic ratio of the proton. However, from the point of view of chemical spectroscopy, proton NMR spectroscopy suffers from the disadvantage of a small chemical-shift with a total range of only 10 ppm. On the other hand, the proton spin–spin coupling constants yield useful information about the chemical environment of the resonating proton.

High-resolution proton NMR spectroscopy can furnish valuable information about the chemical structure, regiochemistry, stereochemistry, and conformation of a polymer. Model compounds are helpful for assigning peaks in the NMR spectra of polymers. Although data from the monomer and dimer models can be presumed to be transferable to the polymers, some unique features in the proton spectra of the polymers can give insight into the polymer structure.

Experimental ^{13}C-NMR spectroscopy

> *Thanks to the development of Fourier transform instruments with spectrum accumulation, carbon spectroscopy, despite the low natural abundance of ^{13}C (1.1%), has become a method of fairly high sensitivity, able to establish the presence of structural features at a level of less than one carbon per 10,000.* — Frank Bovey [10]

In spite of improvements in the homogeneity and field strength of superconducting magnets, NMR transitions are still of very low energy ($\sim 10^{-25}$ J/spin). Because the transition energy is small with respect to kT (Boltzman constant $\times$ temperature) at room temperature, the population difference between the upper and lower energy states represents <0.01% of the total number of molecules. So NMR is a relatively insensitive detection method. This low sensitivity has precluded the use of NMR in trace analysis and minor components in polymers.

There are several aspects of ^{13}C-NMR spectroscopy that contribute to the low sensitivity. The low natural abundance of the ^{13}C nucleus (1.1%), the relatively small magnetic moment (1.59×10^{-2} for ^{13}C compared to 1.0 for ^{1}H), and the long ^{13}C relaxation times (limiting the frequency of pulsing or signal averaging) all contribute to a low NMR signal. The ^{13}C signal is 1/5700 as strong as the ^{1}H-NMR signal, but modern FT NMR machines allow the detection of the ^{13}C in natural abundance.

The advantage of using ^{13}C-NMR spectroscopy is that the ^{13}C nucleus is sensitive to subtle changes in its immediate electronic environment and insensitive to long-range effects, such as solvent effects and diamagnetic anisotropy of neighboring groups. The resonances of ^{13}C nuclei occur over a broad range of approximately 250 ppm (compared to 10 ppm for protons); generally the result is a separate resonance for every carbon atom in the molecule. Within a series of compounds (e.g., alkanes), the chemical shifts can be predicted with a high degree of accuracy. In compounds with high C/H ratios, much of the molecule is invisible in proton NMR spectroscopy. Quaternary carbons (those not bearing protons) are readily observed in ^{13}C spectra.

The low concentration of adjacent ^{13}C nuclei has the advantage that no homonuclear dipolar coupling occurs because the probability of two ^{13}C nuclei being adjacent in natural abundance is 1.1% of 1.1%, or 1 : 8264.

When protons are bonded to carbon, ^{13}C spectra show multiple lines resulting from spin–spin coupling to ^{1}H. This coupling is often of the same order (120–250 Hz) as the chemical-shift differences between the carbon nuclei, and complex spectra occur. As a result of spin–spin C–H interactions, a CH_3 signal is split into a quartet of peaks with intensities of 1 : 3 : 3 : 1. A CH_2 signal is split into a triplet with intensities of 1 : 2 : 1. A CH signal is split into a doublet with intensities of 1 : 1, and the quaternary carbon appears as a singlet. The frequency separation in Hertz between the multiplets is the *spin–spin heteronuclear coupling constant*, J_{CH}.

This multiplet structure weakens the signal for the ^{13}C spectra and, in the case of many resonances, complicates the spectra beyond recognition. For ^{13}C solution NMR spectroscopy it is desirable to eliminate the multiplet fine structure arising from the J coupling of the carbons to the protons. Spin decoupling causes the vectors of a multiplet to be static in the rotating frame because their Larmor frequencies become

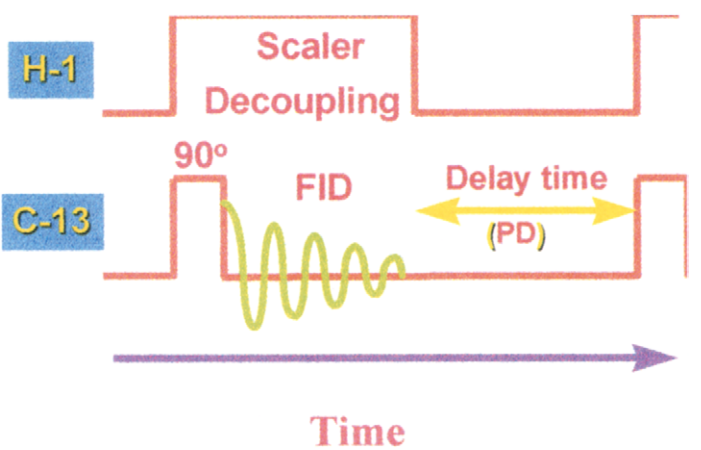

Fig. 6.12. The scalar decoupling (SD) pulse sequence for ^{13}C-NMR spectra.

identical if $\delta_A = \delta_B$. This scalar decoupling is accomplished by the use of broad-band proton decoupling shown in Fig. 6.12.

In a double-resonance experiment, in addition to the carrier frequency of the ^{13}C, there is resonant irradiation of the protons that coherently signal-averages the scalar couplings to 0. This is called *scalar decoupling*. The ^{13}C resonance is measured at the carbon resonance frequency. Because the ^{1}H–^{13}C scalar couplings are less than 200 Hz, an rf decoupling strength of ≈ 0.7 G ($\gamma H_1/2\pi = 3$ kHz) is sufficient. The magnitude of the scalar decoupling proton rf field is such $\gamma_H H_1 \gg J_{CH}$, where J_{CH} is the spin–spin coupling constant for the carbon and proton. The magnitude of the field is ~ 4 kHz. The pulse duration time, t_p, must meet the condition that $t_p \ll (1/4)\Delta - 1$, where Δ is the total range of frequencies from the rf pulse. For ^{13}C at 2.3 T, $\Delta = 4$ kHz, so $t_p \ll 60$ μs. In order to irradiate all the protons as one regardless of their chemical shifts, the irradiating rf field is modulated with random noise.

For a methyl carbon with scalar-proton decoupling, the intensity of the resulting single line is 24 times greater than the outer lines in the 1 : 3 : 3 : 1 quartet that would be observed without decoupling. For ^{13}C-NMR spectra, which are recorded for the low natural abundance of carbon, scalar decoupling can be used to obtain better signal-to-noise ratios and to improve the sensitivity.

The application of this scalar broad-band rf proton field causes the lifetime of the particular state to be short relative to $1/J_{CH}$ and thus collapses the coupling to produce a singlet for every CH_x signal. The signal-to-noise ratio in such spectra is enhanced because the individual peaks of a multiplet collapse into a single line at the center of the multiplet. Additionally, the line widths in broad-band decoupled spectra are narrower because the broadening resulting from long range C–H interactions is also destroyed.

As a result of the scalar decoupling experiment, high-resolution proton-decoupled ^{13}C spectra of liquids exhibit only single resonances for each magnetically distinct carbon if the spectral resolution is high enough. The continuous irradiation or decoupling of the protons in a sample disturbs the Boltzmann distribution of the upper and lower ^{1}H energy levels. The carbon nuclei react to the change in ^{1}H-energy-level populations by changing their own energy-level populations. This change results in an equilibrium excess of nuclei in the lower ^{13}C energy level relative to that specified by a Boltzmann distribution. Therefore more energy will be absorbed because of the excess population in the lower energy level. This enhancement is termed the *nuclear Overhauser effect* (NOE). The maximum signal gain or enhancement, E_s, that is obtained is

$$\Delta E_s = 1 + \left(\frac{\gamma_H}{2\gamma_C}\right) \tag{6.21}$$

so the maximum NOE for ^{13}C-NMR spectroscopy is 2.99. However, this NOE enhancement can be a mixed blessing, particularly if quantitative measurements are made. The NOE may be variable for the different resonances, which makes quantitative measurements difficult unless due consideration is given to this effect.

Experimental NMR spectroscopy of polymers

> *Advances in both liquid and solid NMR techniques have so changed the picture that it is now possible to obtain detailed information about the mobilities of specific chain units, domain structures, end groups, branches, run numbers, number-average molecular weights, and minor structural aberrations in many synthetic and natural products at a level of 1 unit per 10,000 carbon atoms and below.* — J. C. Randall [20]

The ^{1}H- and ^{13}C-NMR spectra of a polymer can be obtained in solution if the polymer is soluble. The experimental high-resolution NMR techniques used for polymers are similar to those used for low-molecular-weight compounds.

The most obvious experimental differences between solution NMR spectra of low-molecular-weight compounds and polymers are the greater line widths of the signals in the polymer spectra. The line widths of the NMR signals depend on the T_2 relaxation time of the nucleus, which in turn depends on the rate and nature of motion of the nucleus. For low-molecular-weight molecules, the rates of motion are rapid, the relaxation times are longer, and the line widths are narrow. Because of the high viscosity of the polymer solutions, the rates of motion of the polymers are slower, and hence the relaxation times are shorter, and the line widths are broader.

The overall rotational mobility of the polymer, rather than segmental motions, is primarily responsible for the motional averaging of the dipolar and chemical-shift interactions to their isotropic values. The viscosity can be decreased and the motion can be increased by making more dilute polymer solutions and by increasing the measurement temperature. In this manner, narrower lines for high-resolution spectra can be obtained for polymers in solution. Special techniques are required to obtain high-resolution spectra of polymeric solids [21,22].

Another approach to wrestling the chemical-shift information from the polymer systems and to improving the NMR spectra of polymers is to use high-field magnets. The most important advantage of a high static magnetic field is that the chemical-shift dispersion is proportional to the field strength, and potentially more chemical-shift information is available at a higher field strength if the line widths do not increase at the same time. For studies of configuration and conformation of homopolymers and of sequencing in copolymers, the higher field strengths allow the observation of the chemical shifts of longer sequences, which yield more structural information. This is illustrated in Fig. 6.13 where the sensitivity for adjacent repeating units is shown.

The second advantage of a high-field magnet is that the sensitivity is proportional to the magnetic field to the 7/4 power. For polymers measured in very dilute solutions in order to obtain narrow-line high-resolution spectra, the increased sensitivity decreases the required measurement time. Finally, for quadrupolar nuclei, the

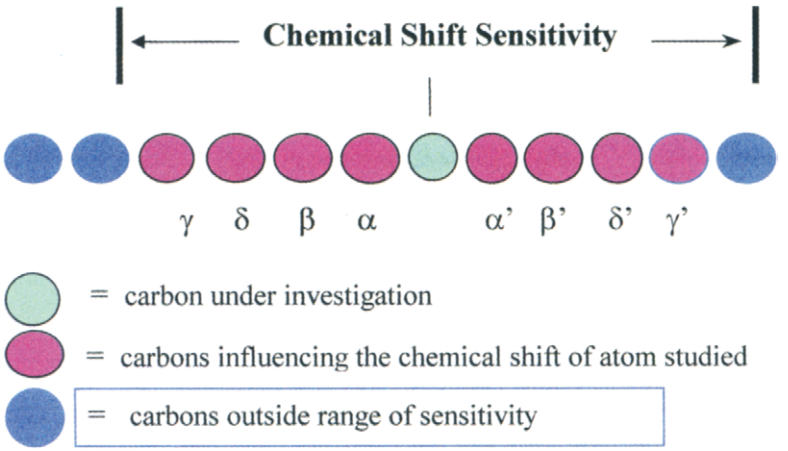

Fig. 6.13. Sensitivity range of chemical shifts in NMR.

lines tend to become narrower at higher fields because the second-order quadrupolar broadening is inversely proportional to the magnetic-field strength.

NMR method of structure determination for polymers

Structural elucidation is dependent upon establishing the nature of the chemical bonds between the various atoms in the polymer. Sometimes, bonding can be inferred from the ^{1}H and ^{13}C chemical shifts and from the spin–spin couplings between nuclei. The first step in any NMR study of a polymer is to assign the NMR resonances to specific structural features of the polymer. Using one or more of the methods in the following list makes most structural assignments:

- comparison of the observed polymer chemical shifts with those observed for analogous low-molecular-weight model compounds,
- estimation of the polymer chemical shifts using additivity relationships, particularly for ^{13}C,
- synthesis of polymers with known specific structural or compositional features to establish chemical shift resonance–structure relationships,
- synthesis of polymers with selectively enriched ^{13}C sites or deuterium substitution for protons to highlight specific sites on the polymer chain,
- computer simulation and comparison of the intensities of structural sequences with predicted intensities calculated on the basis of assumed polymerization kinetics and statistical models,
- one-dimensional spectral-editing techniques such as selective-spin-decoupling experiments for the determination of the proton bonding of the carbons,
- two-dimensional techniques revealing correlations between the nuclei.

However, all these methods have limitations, and it is generally necessary to use a combination of these methods, as well as other physical and chemical techniques.

Recently developed two-dimensional (2D) NMR techniques can be used to determine the coupling between nuclei and to reveal the chemical shifts of these nuclei [23,24]. These new techniques largely replace a wide variety of selective spin-decoupling experiments.

The use of chemical shifts to determine polymer structure

Electronic shielding consists of two different contributions, termed *diamagnetic* and *paramagnetic effects*. The overall effect is the sum of both diamagnetic and paramagnetic contributions to the electron circulation. The local shielding fields that are induced by circulations resulting from spherical electron distributions are termed *diamagnetic* (*dia* meaning opposite) because these currents oppose the applied H_0. A perfectly spherical electron distribution will produce a larger local shielding than one that is distorted from spherical symmetry. The shieldings arising from distortions of the spherical electronic distributions are termed *paramagnetic* because they act to produce induced local fields in the same direction as H_0. The result is that the distorted electron distributions appear to have fewer electrons surrounding the nucleus than the corresponding spherical distributions.

Measurement of chemical shifts

Because chemical shifts in high-resolution solution NMR spectroscopy are very small and depend on H_0, the magnetic field must be stabilized in order to make accurate measurements of the chemical shifts. This stabilizing is done with a lock system that uses the resonance of a nucleus (usually deuterium from a deuterated solvent) to continuously adjust the magnetic field so that the resonance of the lock substance remains constant. A number of different factors can modify the values of the frequencies used to measure chemical shifts, including the magnetic susceptibility (χ), solvent effects, and temperature effects. The applied magnetic field inside the sample depends on its bulk magnetic susceptibility according to the following equation:

$$H_{\text{eff}} = (1 - k\chi)H_0 \tag{6.22}$$

where k is a shape factor. This correction is usually small, that is, 1 ppm or less. Chemical shifts also depend on the nature of the solvent used, and therefore a knowledge of the solvent effect on the reference material is necessary for accuracy. The temperature of the measurement also influences the value of the chemical shift, although this effect is also quite small. For protons, the temperature effect is approximately 10^{-3} ppm K^{-1}.

Interpretation of chemical shifts

The ^{13}C nucleus has a large range of chemical shifts (250 ppm), which offers an excellent opportunity for chemical characterization of the different carbons. Carbons that differ only by a substituent that is four or five bonds away can be distinguished from each other [25]. Carbons with sp^3 tetrahedral hybridization are highly shielded and exhibit chemical shifts in the range of 0–80 ppm. Carbons with sp^2 trigonal hybridization are less shielded, and their chemical shifts fall in the range of 100–200 ppm; and carbons with sp hybridization have intermediate shielding and have chemical shifts in the range of 70–130 ppm. Electronegative substituents on a carbon tend to deshield that particular carbon. Extensive tables that correlate the chemical shifts with the chemical nature of the carbons have been published [25]. A useful handbook with 58,000 ^{13}C-NMR reference spectra has been published [26].

The ^{13}C-NMR spectra of organic compounds can be interpreted by using two different approaches. In the first, the spectrum of the unknown substance is compared with those of familiar compounds, and the degree of correlation is assessed. A very useful feature of ^{13}C-NMR chemical shifts is their additivity that can be divided into the contributions of different substituents. So, the second approach is to use empirical generated additivity rules to assign the observed resonances to different structures. The magnitude of the chemical shift for a carbon in a given molecular structure can usually be estimated. Simple additive substitution rules have been empirically generated to estimate the structural dependence of the chemical shifts [27,28]. For example, in hydrocarbons, each carbon substituent in the α or β position deshields the observed carbon to produce a downfield shift of approximately $+10$ ppm relative to an unsubstituted carbon. Carbon substituents in the γ-positions shield the observed carbon, and the result is upfield shifts of approximately -2 to -3 ppm.

In order to be useful for structure analysis, the observed resonances must be assigned to chemical structures. For copolymer analysis, the enormity of the problem of assigning the observed resonances can be recognized by the following simple considerations. For the 21 most common vinyl and vinylidene monomers, there are a total of 210 possible binary copolymers and 1330 ternary copolymers [29]. These copolymer combinations can also have an alternating, random, or block sequence structure so that the total number of possible copolymers is quite large. Experimentally, only about 30 of these copolymers have been studied. This extremely complex situation suggests that computer simulation of the spectra of the copolymers is helpful in the interpretation of the NMR spectra [30].

One approach to ^{13}C-NMR simulation involves the construction and use of linear models to relate numerically encoded structural features to the observed ^{13}C-NMR chemical shifts [31]. These models have the general form:

$$S_{cs} = b(0) + b(1)X(1) + b(2)X(2) + \ldots + b(p)X(p) \tag{6.23}$$

where S_{cs} is the predicted chemical shift of a designated carbon. The $X(i)$ terms

encode structural features of the chemical environment of the atom and indicate the presence or absence of substituents at certain positions (position parameter). The $X(i)$ terms can assume values of 0, 1, or 2, depending on the number of substituents present at the ith carbon. The $b(i)$ terms are coefficients representing substituent-induced shift increments. They are determined from a multiple-linear-regression analysis of a library of unambiguously assigned chemical shifts. The term p denotes the number of descriptors in the model and is seldom greater than 5 because the shielding is nearly zero at this distance from the specified carbon.

The common notation in the literature uses Greek letters to show the distance from the designated carbon (α = on the next carbon, β = on the vicinal carbon, etc.). A number after the Greek letter refers to the number of substituents at that carbon.

Linear and branched alkanes, as well as heterocyclics and unsaturated molecules [27] have been examined using this approach. More recently, computer techniques have been developed to calculate the chemical shifts of complex molecules [32–34], including copolymers.

Although theoretical treatments of the chemical shift factors have been attempted, these treatments have not been satisfactory. For the ^{13}C shifts additive empirical equations have been developed for the presence of attached or nearby carbon atoms [34].

For paraffins the chemical shift is calculated assuming that the carbon of interest is an alkyl-substituted methane molecule. First, a constant is used which nearly corresponds to that of methane (−1.87 ppm). Then chemical shift contributions are added for each carbon up to five carbons adjacent to the specified carbon. These contributions are described by constants α for the first bonded carbon, β for the second carbon, which is two bonds away, γ for the third, δ for the fourth, and ε for the fifth. If there are two α, β, or other carbons, the constant is multiplied by the appropriate number of adjacent carbons of the type. Values of α through ε were obtained by Grant and Paul from a regression analysis of a series of paraffins. The results are shown in Table 6.2. For branched alkanes upfield shifts are observed for branched carbons and carbons next to branches, so corrective terms are required to account for chemical shifts of carbons associated with branching. Quaternary, tertiary, secondary, and primary carbon atoms are designated by 4°, 3°, 2°, and 1°, respectively. In the cor-

Table 6.2
Grant and Paul parameter values of α through ε [1] for paraffins

α	8.61 ± 0.18 ppm	3° (2°)	-2.65 ± 0.08 ppm
β	9.78 ± 0.16	2° (3°)	-2.45 ± 0.17
γ	-2.88 ± 0.10	1° (3°)	-1.40 ± 0.38
δ	0.37 ± 0.14	$\delta \sim (CH_4)_{R_{sub}}$ [2]	−1.87 ppm
ε	0.06 ± 0.13	Number of observations 56	

[1] Measured from polymers in 1′,4-trichlorobenzene solutions at 125°C.
[2] With respect to an internal TMS standard.

rective terms the carbon of interest is tested first and the adjacently bonded carbon is placed in parenthesis. Thus the 3°(2°) term gives the corrective contribution to the methine carbon chemical shift associated with an adjacent methylene group. Table 6.2 shows the chemical shift parameters for a series of ethylene-1-olefin copolymers and hydrogenated polybutadiene. This equation can be used to predict chemical shifts with a standard error of 0.8 ppm. Consider calculating the ^{13}C chemical shift of the methyl, methylene, and methine carbons for polypropylene. For the methine the shift contributions are as follows:

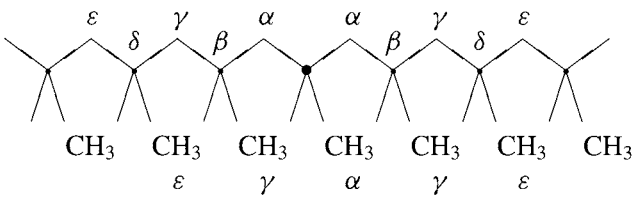

The additivity relationship is given by

$$\begin{aligned}\delta_{CH} &= 3\alpha + 2\beta + 4\gamma + 2\delta + 4\varepsilon + 2[3°(2°)] + (-1.87)\\ &= 3(8.61) + 2(9.78) + 4(-2.88) + 2(0.37) + 4(0.06) + 2(-2.65)\\ &= 27.68 \text{ ppm (26–29 ppm observed).}\end{aligned}$$

In a similar fashion, for methylene and methyl the relationship is

$$\begin{aligned}\delta_{CH_2} &= 2\alpha + 4\beta + 2\gamma + 4\delta + 2\varepsilon + 2[2°(3°)] + (-1.87)\\ &= 45.41 \text{ ppm (44–47 ppm observed),}\end{aligned}$$

$$\begin{aligned}\delta_{CH3} &= \alpha + 2\beta + 2\gamma + 4\delta + 2\varepsilon + 1°(3°) + (1.87)\\ &= 20.74 \text{ ppm (20–22 ppm observed).}\end{aligned}$$

For atactic polypropylene the configurational contribution adds additional splittings of 1–2 ppm in the vicinity of each carbon, but these contributions have not been included.

Spectral editing techniques for structural assignments

Spectral editing involves determining the responses of the various resonances to different experimental conditions or pulse sequences. Differences in the responses of the resonances can be used as a basis for their structural assignments. For example, with the use of proper experiments, resonances can be assigned to methyl, methylene, methine, and quaternary carbon sites on the polymer chain. These assignments can be accomplished by generating subspectra associated with the different protonated carbon species.

The term 'pulse sequence' has come to symbolize the recipe for preparing a nuclear spin system in a desired fashion [35,36]. Special pulse sequences have been designed for particular tasks, including resolution enhancement, selective pulse excitation, selective suppression, sensitivity enhancement, multiplicity selection, and connectivity [37,38]. These special pulse sequences utilize the influence of a variety of interactions on the spin systems. They are designed to differentiate between resonances on the basis of position, line width, multiplicity, magnitude of spin–spin coupling, magnitude of dipolar coupling, exchange rates, or relaxation times [37]. The resultant spectra yield information concerning the spectral origin of the resonances lines.

Special multiple-pulse sequences are designed to enhance or suppress certain interactions by using spin manipulation. The most important common feature of these special pulse sequences is the addition of an evolution time, τ_e, during which the spin system evolves under the selected interaction.

pulse	τ_e	90°	
preparation	evolution	detection	time →

The preparation time is designed to place the spins in a specified state, which is most often a relaxation to thermal equilibrium state. The evolution time allows for the phase modulation of the spins by J coupling or other interactions. The evolution time is selected to optimize the information content of the resultant spectra and generally corresponds to the magnitude of the selected interaction, that is, $\tau_e = 1/J$ or some multiple depending on the nature of the experiment. The read pulse terminates the sequence and is followed by detection of the FID.

Spectral assignments using decoupling techniques

> *The most common problem in NMR spectroscopy is not a lack, but an overabundance, of information. For very complex molecules with many nuclei in subtly different environments, the spectra may consist of hundreds of lines, the assignments of which are exceedingly difficult. If there were some way to simplify the spectrum so that it depended only on the chemical shift, then it would be possible to assign the gross features of the spectrum, after which the couplings among the nuclei could be specified, with the known chemical shifts of the various nuclei as a guide. This is one of the goals of double-resonance experiments.* — M.D. Bruch et al. [39]

Double-resonance (decoupling) techniques generally result in a simplification of the NMR spectrum and yield information relative to the relationships between the resonances. This latter information reveals the internal chemical bonding of the sample under investigation.

To demonstrate these decoupling techniques, butyl rubber will be used as a simple and useful example. Butyl rubber is the generic name for a family of isobutylene–

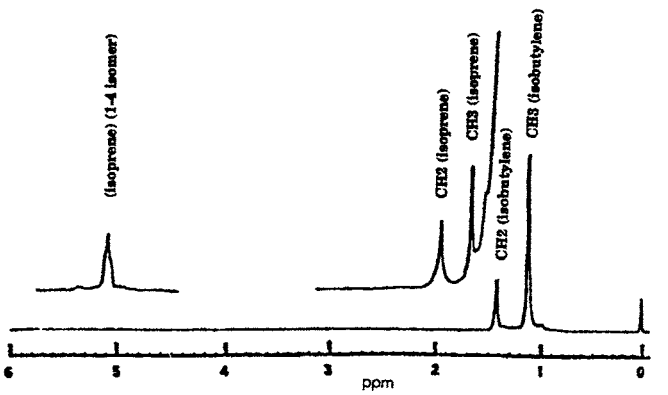

Fig. 6.14. ^{1}H-NMR spectrum of butyl rubber at 250 MHz in $CDCl_3$. (Reproduced from Ref. [40]. © 1985 American Chemical Society.)

isoprene copolymers that usually contain less than 3% isoprenyl groups. Butyl rubber exhibits a number of structural facets, including directional isomerism of the butyl and isoprenyl units and chemical isomerism of the isoprenyl groups, that is, 1-4, 1-2, and 3-4 structures and geometric isomerism (Z or E, which are cis and trans, respectively) [40]. The 250-MHz ^{1}H-NMR spectrum of butyl rubber in $CDCl_3$ is shown in Fig. 6.14.

The resonances at 1.11 and 1.41 ppm are assigned to the methyl and methylene protons, respectively, of the isobutylene units of butyl rubber. The isoprenyl units have resonances at 1.65, 1.94, and 5.05 ppm. A comparison of this spectrum with that of the model compound, 2,2,4,8,8-pentamethyl-4-nonene, shows that the isoprenyl units of butyl rubber are in a single isomeric form. The corresponding regions of the spectrum of the model compound (which is known to be a mixture of isomers) contains a pair of signals. The single triplet at 5.05 ppm suggests the incorporation of the isoprenyl units in the 1-4 mode. If 1-2 or 3-4 incorporation occurred, additional signals would appear. When butyl rubber is prepared with deuterated isoprene, the signal at 1.65 ppm is absent, and the signal at 1.94 ppm is reduced to half of its original size. On the basis of these observations, the signals at 1.65 and 1.94 ppm are assigned to the methyl and methylene protons of the isoprene units, respectively. The isoprenyl groups can be in either Z (cis) or E (trans) form. The ^{1}H-NMR spectroscopic results suggest that whereas the model compound has two sets of signals for most of the protons of isoprenyl residues, only one set is present in butyl rubber. The close agreement between the chemical shifts of the butyl rubber with the E isomer of the model compound suggests that the predominant geometry of the isoprenyl groups of the polymer is E. However, the Z isomer can be observed by using spectral subtraction as shown in Fig. 6.15.

The weak line at 1.70 ppm suggests the presence of the Z isomer at a level of approximately 10% [40].

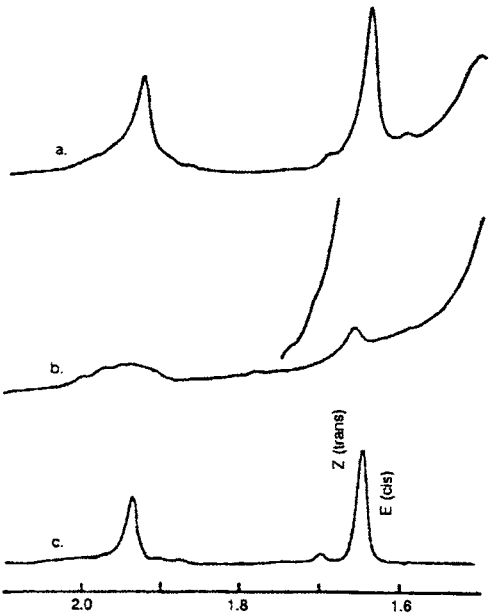

Fig. 6.15. High-field region of the ^{1}H-NMR spectrum of butyl rubber (at 250 MHz in $CDCl_3$). Spectrum a is of commercial butyl rubber, spectrum b is of specifically deuterated butyl rubber, and c is the a – b difference spectrum. The signal at 1.65 results from the E isomer, and the weak signal at 1.70 results from the Z isomer. (Reproduced from Ref. [40]. © 1985 American Chemical Society.)

Selective scalar–spin decoupling

A powerful short pulse (broad frequency range), which affects all of the nuclei in the sample, is termed a *nonselective* or *hard pulse*. If only those nuclei corresponding to one resonance in the spectrum are to be disturbed, a much weaker and longer pulse (narrow frequency range) is used, and this pulse is termed a *selective* or *soft pulse*. The selectivity of a pulse increases with its length. In order to achieve a selectivity of 1 Hz, a pulse length of about 1 s must be used. The spectral response to selective decoupling is generally quite specific and is invaluable for making assignments.

For the assignment of resonances, a *single* nucleus or spectral line can sometimes be selectively decoupled without perturbing the rest of the spectrum. Selective positioning of the proton frequency is used to remove a particular scalar-bond interaction. By using selective irradiation of specific protons, the coupling effects between the protons and carbon atoms to which they are attached can be eliminated. When the assignments of the proton spectrum are known, selective decoupling allows the assignment of a signal to a particular carbon atom in the ^{13}C-NMR spectrum.

For samples with well-resolved lines, the selective-decoupling method involves placing the rf field at the exact resonance frequency of the chosen resonance. Low rf power is used under these conditions so that only the selected resonance is affected. All other lines are far enough from resonance that their excitation is negligible. Be-

cause each line must be excited individually, the total time required for the selective-decoupling experiment can be long if there are a large number of lines in the spectrum.

One of the problems with selective decoupling is that the rf field actually irradiates a range of frequencies. When other resonances are within this frequency range, complete selectivity is not possible. In many cases, one spin cannot be irradiated independently of the others. Another limitation is that relaxation occurs during the pulse and limits the detectable signal.

The spectrum of butyl rubber can also be used to illustrate selective decoupling. The assignment of the signal at 1.65 ppm to the methyl group of the isoprene residue in butyl rubber was confirmed by a selective spin-decoupling experiment. When the olefinic proton at 5.05 ppm is irradiated, the signal at 1.65 ppm becomes considerably sharper because of the removal of long-range coupling effects.

The off-resonance spectrum in the 0–60-ppm region of the ^{13}C-NMR spectrum of butyl rubber is shown in Fig. 6.16.

Selective decoupling by irradiation of the isoprenyl methylene proton resonance at 1.94 ppm causes the two triplets at 23.37 and 55.87 ppm to collapse to two singlets (Fig. 6.16). This observation indicates that these two signals result from the methylene carbons of the isoprenyl units of butyl rubber. On the basis of differences in chemical shifts, these signals are assigned to C-4 and C-1, respectively. By using the methylene

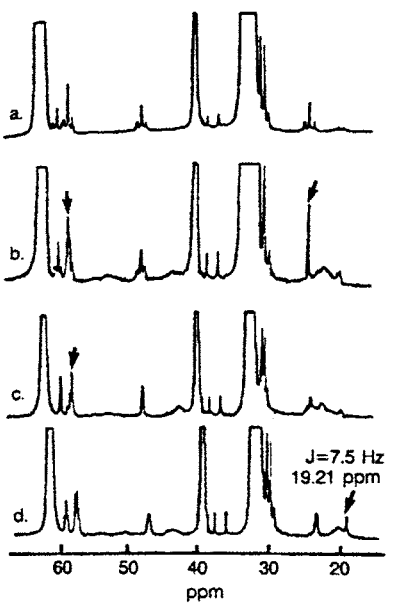

Fig. 6.16. Amplified expanded ^{13}C-NMR spectra of butyl rubber (at 62.8 MHz in $CDCl_3$). The expanded off-resonance decoupled spectrum is shown in a. Spectra b, c, and d are the same as a except that the irradiation for the three spectra was 1.94, 1.41, and 1.65 ppm, respectively. The arrows indicate peaks that have collapsed. (Reproduced from Ref. [40]. © 1985 American Chemical Society.)

proton signals, which resonate at 1.41 ppm, of the isobutylene blocks selective spin decoupling collapses the resonances at 55.75 and 57.34 ppm into singlets (Fig. 6.16). Hence, these two resonances can be assigned to the methylene carbons from the neighboring isobutylene groups. Selective decoupling of the methyl group resonance of the isoprenyl group at 1.65 ppm collapses the methyl carbon signal at 19.21 ppm from a quartet to a doublet with residual splitting (Fig. 6.16). This residual coupling suggests the presence of long-range coupling. The measured coupling constant of 7.45 Hz for this resonance agrees with that measured for polyisoprene ($J = 7.44$ Hz).

Sometimes, one or more multiplets can be observed in a group of overlapping multiplets. The most direct method for selectively observing one of the multiplet patterns makes use of gated decoupling to selectively null the other multiplets. This nulling is accomplished by gating the decoupler during acquisition at the chemical shift of those protons that cause the splitting of the multiplet, which causes the splitting to be nulled. For example, by gating the decoupler on during acquisition, a doublet will be converted to a singlet with an intensity that is equal to the sum of the intensities in the rotating-frame projection [41].

Off-resonance decoupling

Off-resonance decoupling is a more general and rapid procedure than selective decoupling because the entire spectrum is displayed. Off-resonance decoupling produces a coupled ^{13}C-NMR spectrum having collapsed multiplets and shows only the couplings to attached protons. Long-range C−H couplings are suppressed. Off-resonance decoupling reduces the J coupling to a fraction of its actual value. The signal multiplicities in the off-resonance spectrum can be used to discriminate between methyl, methylene, methine, and quaternary carbons. When the J_{CH} and the ^{1}H-NMR chemical shifts are known, specific assignments can be made on the basis of the magnitude and multiplicity of the residual splittings.

Several disadvantages must be taken into consideration when using the off-resonance experiment. It is not completely successful in those cases where the signals appear as ill-defined, second-order multiplets. Also, severe overlap of resonance lines and slight changes in the ^{13}C shieldings resulting from temperature effects can limit the value of the off-resonance experiments, especially when the spectral region contains a number of resonances. Finally, coherent off-resonance decoupling suffers from an effective loss of sensitivity that is more than an order of magnitude lower than ordinary proton-decoupled ^{13}C-NMR spectroscopy.

An example of the use of off-resonance decoupling is shown in Fig. 6.17 for the decoupled ^{13}C-NMR spectrum of butyl rubber [40].

The signal at 31.28 ppm is associated with the methyl group carbon, the signal at 38.26 ppm is associated with the quaternary carbon bearing two methyl groups, and the signal at 59.28 ppm is associated with the carbon atom of the methylene groups.

The off-resonance experiment allows the assignment of the olefinic carbon atoms of the isoprenyl units in butyl rubber. The signal at 129.98 ppm appears as a doublet

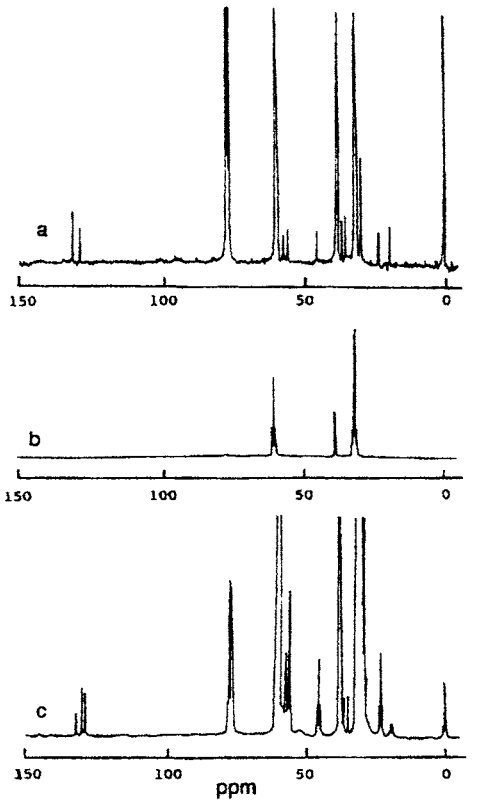

Fig. 6.17. Off-resonance decoupling spectra of ^{13}C-NMR spectrum of butyl rubber (at 62.8 MHz in $CDCl_3$). (Reproduced from Ref. [40]. © 1985 American Chemical Society.)

and is assigned to the olefinic (C-3) carbon. In a similar manner, the signal at 132.36 ppm, which remains a singlet in the off-resonance-decoupling spectrum, is assigned to the quaternary carbon (C-2). Additionally, the off-resonance experiment allows the assignments of the methyl and methylene groups. The resonance at 19.21 ppm results from the carbon atom of a methyl group. In the same manner, resonances at 23.37, 45.63, and 55.81 ppm may be assigned to the methylene groups of isoprenyl groups and the isobutylene group attached to them [40].

The problem with coherent off-resonance decoupling is that the signals often appear with overlap or as ill-defined second-order multiplets, especially when the spectral region of interest contains a number of resonances.

Selective excitation of ^{13}C resonances

Selective excitation of individual ^{13}C resonances is difficult because of the broad spectral window. Selective excitation can be achieved by using a tailored excitation procedure that involves the application of a *pulse train* (20–60 pulses). The pulse

train is a series of m pulses with very small pulse angles, α, and small pulse delays, t_r, such that $m\alpha = 90°$. By using the proper values for α and t_r, ^{13}C resonances can be selectively excited. The delays are set to the inverse of the separation of the chosen resonance line from the carrier frequency position. The chosen line precesses 360° during each of the delays. The pulses therefore have a cumulative effect and turn this magnetization component down to align the y axis of the rotating frame. The remaining resonances do not have this exact synchronization. These sequences are called DANTE (*d*elays *a*lternating with *n*utations for *t*ailored *e*xcitation) sequences and give the individual fully proton-coupled multiplets as separate spectra [42,43]. However, in complex spectra where extensive overlap of the lines occurs, it is difficult to distinguish the multiplets from each other.

Selective multiplet acquisition

A suggested alternative to DANTE is based on *selective acquisition* of the desired signals rather than on selective excitation [44]. A single hard excitation pulse is applied at the chemical-shift frequency of the carbon resonance whose multiplet is to be selectively observed. After a short delay time, τ, the FID is then acquired. Broad-band proton decoupling is applied during the pre-excitation period and also during excitation, but is turned off during the data acquisition. The delay time, τ, is incremented regularly, and as a result, the phase of the signal located at the pulse is unaltered. However, the off-resonance signals are altered and consequently decrease. Good selectivity is achieved if more than 25 increments are used.

Selective-frequency polarization transfer

Consider the mechanism of the selective polarization-transfer (SPT) experiment using a ^1H–^{13}C spin system [45]. Such a weakly coupled spin system has four energy levels: one doublet each for the ^1H and the ^{13}C. The low-frequency line, H_α, in the proton spectrum arises from those molecules in which the proton is bonded to a ^{13}C in the α-spin state (lower energy). The high-frequency proton line, H_β, arises from those molecules in which the proton is bonded to a ^{13}C in the β-spin state (higher energy). A similar situation applies for the ^{13}C-NMR spectral lines.

At thermal equilibrium, the polarization depends on the differences in the populations of the various levels. Because γ_H is approximately equal to $4\gamma_C$ the population differences for the carbon and proton transitions may be taken as 1 and 4 arbitrary units, respectively. Coupling of the nuclei implies that the state of the nucleus depends on the state of the coupled nucleus. When a $90°_x$ ^1H pulse is applied to the sample, the proton magnetization is rotated about the 90° axis. For the H_α resonance line, the magnetization will precess slowly in the rotating frame, and the H_β resonance line will precess more rapidly (further from the carrier frequency). These coupled spin states can be mixed by the action of an rf pulse. A 180° frequency-selective pulse can be applied to the H_α proton transition without affecting the other transition. This soft or selective 180° pulse simply interchanges the populations of

the α and β levels. Inverting the H_α-proton line causes the proton populations of the energy levels associated with the proton H_α-transition to be interchanged. This interchange affects the intensities of the carbon transitions associated with these same energy levels. A measurement of the ^{13}C-NMR spectrum shows intensities corresponding to population differences across the carbon transitions. The intensity of the C_α and C_β signals is not a 1 : 1 doublet. Instead it is a doublet with intensities of -3 and $+5$ units, respectively. The polarization transfer shows a fourfold enhancement of the normal ^{13}C signal. In addition to this fourfold enhancement, further signal enhancement occurs because the repetition rate for signal averaging depends on the shorter ^{1}H T_1 rather than on the longer ^{13}C T_1.

Experimentally, the population inversion can be achieved by using a selective 180°_x pulse applied at the frequency of *any* selected ^{1}H line. The SPT experiment is carried out with the ^{1}H decoupler applied immediately after the ^{13}C pulse at the frequency of one of the ^{13}C satellite lines. The limitation of the SPT experiment is that only one line can be enhanced at a time.

Unfortunately, there are a number of difficulties with this experiment. The precise positions of the ^{13}C satellite lines (i.e., lines arising from the 1% of protons that are spin coupled to ^{13}C nuclei) in the ^{1}H-NMR spectrum must be known. A soft pulse that is exactly centered on the chosen satellite line must be used. However, the principle of polarization transfer is used in a number of NMR experiments.

The SPT experiment also provides evidence of a connected proton transition. Therefore, this technique can be used to pick out the resonant frequencies of proton transitions while observing the connected ^{13}C nuclei.

General polarization-transfer methods

There is also a pulse sequence that results in general polarization enhancement rather than the selective enhancement of the SPT experiment. The basic INEPT (*i*nsensitive *n*uclei *e*nhancement by *p*olarization *t*ransfer) pulse sequence for nonselective polarization transfer is as follows [46]:

$$\begin{array}{lllll} ^1\text{H} & 90^\circ_x\text{–}\tau\text{–}180^\circ\text{–}\tau\text{–}90^\circ_x & & \tau = \dfrac{1}{4J_{\text{CH}}} & \\ ^{13}\text{C} & \qquad\qquad 180^\circ & 90^\circ & \text{acquired FID} & \end{array} \tag{6.24}$$

This special pulse sequence uses strong nonselective pulses and gives general enhancement rather than specific sensitivity enhancement, as in SPT. The pulse sequence has a basic polarization-transfer portion that produces a net inversion of one of the proton spin states. Proton transverse magnetization is created by the initial proton 90° pulse and precesses for a period τ. The magnetization is then refocused as a spin echo at a time 2τ by the action of a 180° proton pulse. Application of a ^{13}C 180° pulse at the midpoint of the 2τ delay ensures that the echo is modulated by the scalar coupling, J_{CH}. If τ is chosen to be equal to $1/(4J_{\text{CH}})$, then at time 2τ, the

two proton magnetizations are completely out of phase as required for polarization transfer. The second proton 90°_y pulse, which is phase shifted to give a rotation about the y axis, then rotates one magnetization to lie along the $+z$ and $-z$ axes. Because of the relatively small range of values for J_{CH}, a single experiment produces enhanced signals from all protonated ^{13}C sites in a molecule. Following a simultaneous ^{13}C 90° pulse, there exists enhanced magnetization in the ^{13}C multiplet. The ^{13}C doublet has equal but opposite intensity components with values of 1 and -1 to give a characteristic 'up-down' pattern, or an intensity ratio of $1:-1$. This inverse character can be removed by addition of an extra delay, 2Δ, after the 90° ^{13}C pulse, which allows the ^{13}C to realign to give a net signal.

Determination of proton multiplicity of carbons

> *Many of the new NMR methods rely on the fact that it is possible to modify the Hamiltonian almost at will to extract desired information... The Hamiltonian can be manipulated to such an extent that some experiments border on sorcery.* — R.R. Ernst et al. [37]

The INEPT experiment

The INEPT sequence for polarization transfer just described can also be used with slight modification to determine the multiplicity of the bonding of the carbons [47]. If a delay, Δ, is introduced prior to simultaneous decoupling and data acquisition, then selective nulling or inversion can be accomplished depending upon the number of protons coupled to the nucleus being studied. Thus, if $\Delta = (2J)^{-1}$, where J is the heteronuclear coupling constant between ^{13}C and ^{1}H, then only signals from carbons bearing a single proton are observed in the ^{13}C-INEPT spectrum. In contrast, if $\Delta = 3(4J)^{-1}$, then the ^{13}C signals for CH_3 and CH groups appear normal, and the CH_2 carbon resonances are inverted.

For example, the INEPT technique has been applied to low-density polyethylene and ethylene–propylene copolymers [48]. The results of the ^{13}C-INEPT experiment at 125.77 MHz for the methine and methylene regions are shown in Fig. 6.18.

The delay time for the INEPT experiment was $3/(4J)$, so methyl and methine carbon resonances appear positive and methylene carbon resonances appear negative. The observed 15 different methine carbons suggest that at least 15 different branch types exist. In addition, ethylene-1-hexene copolymers were studied with the INEPT method, and similar results were obtained [49]. Chemical-shift assignments of regioirregular polypropylene have been verified by using the INEPT experiment [50]. Weak lines corresponding to carbons located in the inverted portion of the chain can be assigned by using this technique.

The INEPT experiment often provides too much information. When a molecule has a large number of carbons, the spectrum can be rather complex because of all

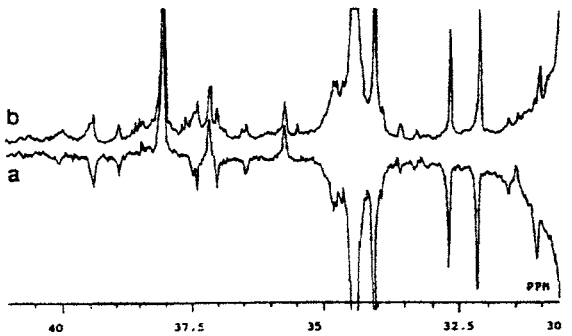

Fig. 6.18. ^{13}C-INEPT spectrum (a), and the proton-decoupled spectrum at 125.77 MHz (b) of LDPE. (Reproduced from Ref. [48, p. 119]. © 1984 American Chemical Society.)

the proton-coupled fine structure. A major disadvantage of the INEPT technique is that it can lead to severe distortions of the intensities of the components of a coupled multiplet. There is also a strong dependence on J, and as a result, signals that should be null may not be, a result that leads to extraneous lines. Because variable delay times are used for multiplicity selection, variations in T_2 can cause additional problems [48].

The DEPT experiment

The DEPT (*d*istortionless *e*nhancement by *p*olarization *t*ransfer) experiment was designed to eliminate many of the difficulties encountered in the INEPT experiment [51,52]. DEPT requires fewer pulses than INEPT and therefore is less sensitive to pulse missettings and inhomogeneities. DEPT is more sensitive to the spin-relaxation rate than the INEPT experiment because the relevant delay in DEPT is of the magnitude $3/(2J)$, and corresponding periods in INEPT typically range from $1/J$ to $5/(4J)$.

The pulse sequence is shown in Fig. 6.19.

By choosing the proton nutation angles of $\theta_1 = 45°$, $\theta_2 = 90°$ and $\theta_3 = 135°$ in separate spectra, CH, CH_2, and CH_3 subspectra can be obtained from proper

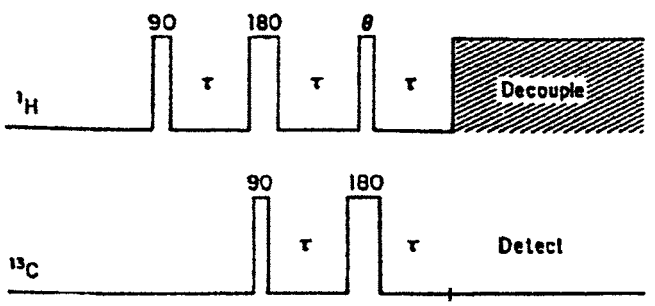

Fig. 6.19. Pulse sequence for DEPT spectroscopy. The third ^{1}H pulse is variable with $\theta = 45°$, 90° and 135°. The delay time τ is set to $(2J_{CH})^{-1}$. (Reproduced from Ref. [52]. © 1986 American Chemical Society.)

combinations of the spectra.

$$CH = \theta_2 - c\,(\theta_1 + a\theta_3) \tag{6.25}$$

$$CH_2 = \theta_1 - a\theta_3 \tag{6.26}$$

$$CH_3 = \theta_1 + a\theta_3 - b\theta_2 \tag{6.27}$$

where a, b, and c have theoretical values of 1.0, 0.707, and 0, respectively. Slightly different values may be required because of experimental factors such as the probe and spectrometer setups.

DEPT was used to generate subspectra of copolymers of styrene (S) with maleic anhydride (MAn) [53]. The normal spectrum of an S-MAn copolymer with a composition of 52% styrene consists of three broad resonances that display fine structure (Fig. 6.20).

The three subspectra show good separation (Fig. 6.20). In the CH spectrum, the multiplet at 29 ppm is a solvent impurity. The peaks at 44 and 52 ppm result from methine carbons. From the CH_2 subspectrum, the signal at 35 ppm is associated with the methylene carbons. Methylene subspectra were obtained from four copolymers with different compositions to allow the comonomer sequence assignments to be made for the observed resonances.

DEPT is a very simple and useful sequence for the determination of the proton multiplicity of carbons and is of considerable value for the study of polymer systems in solution and in the solid state [54,55].

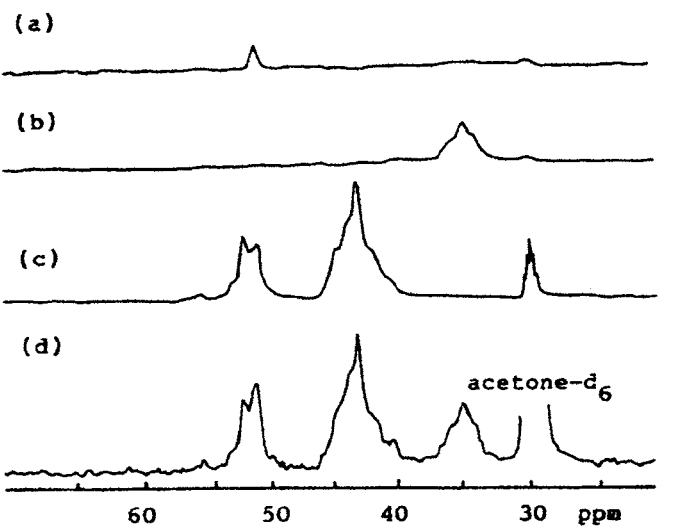

Fig. 6.20. Aliphatic region of the ^{13}C-NMR spectra at 75.46 MHz of S-MAn. The subspectra generated by the DEPT sequence are CH_3 (a), CH_2 (b), and CH (c); (d) is the normal spectrum obtained with gated decoupling to remove nuclear Overhauser enhancement. (Reproduced from Ref. [53]. © 1984 American Chemical Society.)

Determination of carbon connectivity — the INADEQUATE experiment

NMR spectroscopy can be used to determine the connectivity between adjacent carbon atoms on a polymer chain. This information is usually obtained from ^{13}C–^{13}C spin–spin couplings that are ordinarily lost in the NMR spectrum because the signals due to ^{13}C–^{13}C couplings are 1/200th the intensity of the signal from a single ^{13}C. However, a pulse sequence that has been developed suppresses the normal ^{13}C-NMR signal compared to the coupled ^{13}C–^{13}C signals on the basis of the presence or absence of the homonuclear spin–spin coupling, J_{C-C}. This experiment is termed INADEQUATE, which stands for incredible natural abundance double quantum transfer experiment [56]. This experiment takes advantage of the phase differences between single- and double-quantum coherences. The unwanted signals are removed through phase cycling. The pulse sequence for INADEQUATE is given as

$$90^\circ_x - \tau - 180^\circ_y - \tau - 90^\circ_x \tag{6.28}$$

Discrimination between single- and double-quantum coherence is accomplished by setting τ equal to $1/(4J_{C-C})$.

Two-dimensional NMR experiments

> *Two-dimensional spectroscopy should not be dismissed as merely an alternative (and quite complicated) display mode, for it has some inherent operating advantages. The first is the possibility of disentangling spectra that are complicated by extensive and multiple overlapping of spin–multiplet structure — the problem that eventually makes very large molecules intractable for NMR.* — G. Bodenhausen et al. [57]

High-resolution NMR spectroscopy is a highly sensitive tool for the study of polymers. But NMR spectroscopy is often limited because of the considerable overlap arising from the multiplicity and relative broadness of resonances. The usual methods of off-resonance and selective decoupling to determine the multiplicity of carbon bonding are not effective because of the inherent limitation of selectivity in the presence of the large number of overlapping resonances. Consequently, structure assignments to resonances lines are often difficult and arbitrary.

One method that can be used to overcome these limitations is the 2D NMR experiment [58]. To make a 2D experiment out of a 1D experiment, the evolution time must be stepped incrementally through a range of values, and a series of FIDs is stored, each with a different evolution time. After the first Fourier transformation, the resulting first-domain spectra are aligned parallel to one another to form a matrix of data points. Transposition of the matrix gives a new series of data points that can be subjected to a second Fourier transformation. This process is done for each data point of the original first-domain spectrum. When the resulting spectra from the

second Fourier transformation are again arrayed in a matrix, the chemical shifts can be aligned along one axis, and the frequency, which is dependent on the phase or amplitude modulation that developed during the evolution period, can be aligned on the other axis. Thus the scale could be spin–spin coupling. The resolution in the 2D spectrum is better than in either the ^{13}C or ^{1}H spectrum alone, but the sensitivity is lower. In 2D NMR experiments, the resolution increases as the square of the field strength. At the higher static field strengths that are available on modern NMR instruments, the advantages of 2D NMR experiments further increase.

In 2D NMR spectroscopy, the raw data are a function of two time periods, an evolution time (t_e), which may also include a mixing period (t_m), and a detection time (t_d), both of which are preceded by a preparation time as shown in the following diagram [58]

$$\begin{array}{cccc} & t_e & t_m & t_d \\ \text{preparation} & \text{evolution} & \text{mixing} & \text{detection} \end{array}$$

The preparation period involves preparing the reservoir of nuclei in a known state by using T_1 processes or saturation pulses. The evolution period, t_e, (including the mixing period for some 2D experiments) is the time in which the spins are subjected to a preselected interaction as a result of designed pulse sequences. The evolution time is systematically incremented throughout the course of the experiment to accommodate the desired spin interactions. During the detection period, t_d, a second selected interaction or combination of interactions occurs. Double Fourier transformation yields a 2D NMR spectrum with two frequency axes

$$S(t_e, t_d) = FT^2 = S(\omega_e, \omega_d) \tag{6.29}$$

In 2D NMR spectroscopy, the experimental conditions (i.e., the pulse sequences) can be arranged such that only one interaction is operative during the evolution time and a second or combined interactions are predominant during the detection period. 2D FT-NMR spectroscopy is possible if a systematic variation of the evolution period results in a modulation of the spin system, such as through spin–spin interactions, chemical-shift interactions or dipolar interactions.

In principle, the three classes of 2D spectra are *coupling-resolved*, *coupling-correlated*, and *exchange* 2D spectra. A coupling-resolved spectrum is characterized by one frequency axis (F_1) containing the coupling information and the other axis (F_2) containing the chemical shifts. In the coupling-correlated type of spectrum, both frequency axes contain chemical shifts. The connection between the F_1 and F_2 axes is established through homonuclear or heteronuclear scalar coupling or through dipolar coupling. In exchange 2D spectroscopy, the interaction is the magnetization exchange resulting from either chemical exchange, conformational or motional effects, or the Overhauser effect arising from nonbonded protons.

Unfortunately, the sensitivity in 2D experiments is a factor of 3 less than in a regular dipolar-decoupled ^{13}C experiment. Because of the large volume of data

required, the acquisition times are quite long. Furthermore, large data matrices are required for the 2D experiment, and the processing time is tedious. Another concern is 't_1 noise', which generates phantom peaks in the 2D spectra. These phantom peaks occur because of spectrometer instabilities resulting from the extended acquisition times needed for these measurements (7–14 h). Further limitations can arise when extensive overlap makes assignments difficult in the 2D maps.

2D experiments utilize a particular class of pulse sequences in which the selected interaction modulates the magnitude of the resonance. Under this circumstance, when the height of any peak is plotted as a function of τ, this height will vary *sinusoidally* rather than exponentially. That is, the peak height will *oscillate* (and decay) as a function of τ. This oscillatory behavior can be analyzed to determine the frequency or frequencies contributing to the oscillations. The frequencies are determined by taking a second Fourier transform as a function of τ.

Consider the example termed 2D J-resolved spectroscopy. Spin echoes, which are generated by the pulse sequence $90°$–τ–$180°$–τ–$180°$–$90°$, are modulated by spin–spin coupling. If the peak heights are extracted from each of the spectra and plotted as a function of t, an interferogram that is the superposition of the contributing frequencies is obtained. When analyzed by Fourier transformation, this interferogram determines the contributing frequency or frequencies of oscillation. Double transformation generates a J spectrum for each chemically shifted resonance and displays this multiplet structure in the second dimension — "an operation similar to the opening of a Venetian blind" [58].

In the actual 2D procedure, the first interferogram is formed from the first data point from each of the original spectra, and the second interferogram is formed from the second data point from each of the original spectra. Mathematically, this process is a simple matrix transposition. In fact, if these spectra are thought of as the rows of the data matrix $S(t_e, F_2)$ then the columns represent the variation of the intensity of a given frequency component F_2 as a function of τ. The result of this complete process is a 2D frequency map, on which the data are plotted in the form of a series of spectra (stacked or 'white-washed' plot) or in the form of a contour plot in which each successive contour represents a higher intensity.

Because the process begins with a series of 'normal' 1D spectra, the normal spectral axis will be on one axis of a 2D plot. This axis represents the signals actually detected in the receiver of the spectrometer during a time conventionally labeled t_2, and hence this axis becomes the F_2 axis. The second axis (or *domain*), known as the F_1 axis, is the axis along which the frequencies of oscillation of the original peaks will appear following the second Fourier transformation.

An overwhelming number of 2D experiments have been described. Here, the information available from selected basic 2D experiments will be summarized; I will neglect, for the moment, methods of dynamic chemical and conformational exchange.

For macromolecules, which typically have broad resonances and appreciable spectral overlap, 2D experiments are sometimes difficult. Additionally, macromolecules

Table 6.3
Information content of the various 2D NMR experiments

Experiment	F_1	F_2	Information
Heteronuclear J-resolved	J_{CH}	δ_C	Heteronuclear coupling constants
Homonuclear J-resolved	J_{HH}	δ_H	Homonuclear J and δ
Heteronuclear chemical shift	δ_H	δ_C	Correlation δ_J and δ_C
Correlation vis homonuclear scalar coupling (COSY) interactions	δ_H	δ_C	Correlation of all scalar coupling
NOE (NOSEY)	δ_H, J_{HH}	δ_H, J_{HH}	Spatial proximity of nonbonded protons
INADEQUATE	$\delta_A + \delta_X$	δ_X	Heteronuclear activities

have long correlation times, and dipolar ^1H–^{13}C interactions make considerable contributions to both ^1H and ^{13}C line widths. Consequently, the sensitivity of the 2D experiment is low for polymer systems. A 2D experiment may be impossible to interpret because of the rapid ^1H relaxation during the evolution period, or impractical because of the insensitivity of ^{13}C detection. The types of information that can be obtained from the various 2D experiments are summarized in Table 6.3.

2D correlation via heteronuclear chemical shifts

A 2D experiment has been designed to correlate the chemical shifts of protons with the corresponding directly bonded carbons [59]. As a correlation experiment, the ^1H spin serves as a spy nucleus for its attached ^{13}C nucleus. The information obtained from these experiments is the resonance frequency of the proton(s) coupled directly to the various ^{13}C nuclei in the molecule (i.e., which carbon resonance is correlated with which proton resonance) [60,61]. Because the ^{13}C chemical shifts are generally better known with respect to their structural origin, this 2D method permits the interpretation of the ^1H-NMR spectra. With this knowledge, the highly sensitive ^1H-NMR spectra can be used to determine the polymer microstructure. The main limitation of this 2D correlation experiment is that it functions only for carbons that have directly bonded protons.

The description of the 2D ^1H–^{13}C correlated spectroscopy experiment is given by Bax [62]. Consider the case of a single ^1H–^{13}C system whose spectrum consists of two doublets, one in the ^{13}C spectrum and one in the ^1H spectrum. A differential proton-spin inversion is first accomplished by using two 90° proton pulses applied along the x axis of the rotating frame and separated by a time t_e. The proton signal is allowed to precess after a 90° rf pulse for an evolution time t_e, with the extent of this precession being proportional to the extent to which the peak of interest is off resonance from the ^1H transmitter frequency. This step makes the phase of the ^{13}C signal dependent on the ^1H chemical shift. Intensity is transferred from the protons to the observed nucleus by simultaneous 90° pulses.

The longitudinal proton magnetizations are proportional to $-\cos(\Omega_H + \pi J)t_e$ and $-\cos(\Omega_H - \pi J)t_e$, where Ω_H is the proton frequency offset resulting from the chemical shift, and J is the C−H coupling constant. The changes in longitudinal ^{13}C magnetizations, ΔI_1 and ΔI_2, are

$$\Delta I_1 = \cos(\Omega_H + \pi J)\, t_e - \cos(\Omega_H - \pi)\, t_e \tag{6.30}$$

$$\Delta I_2 = \cos(\Omega_H - \pi J)\, t_e - \cos(\Omega_H + \pi)\, t_e \tag{6.31}$$

for the two ^{13}C doublet components, respectively. As a result, the phases of the individual ^{13}C signals are coded with the ^1H chemical shift. These changes in longitudinal ^{13}C magnetization are observed by using the application of a 90° ^{13}C pulse after the second proton pulse. The amplitudes of the two ^{13}C doublet components are modulated in amplitude with the proton frequencies but in an opposite manner.

By using 2D ^1H–^{13}C correlated spectroscopy, a 2D data matrix with the carbon chemical shifts along one axis (F_2) and the proton chemical shifts along the other (F_1) is obtained. The projections onto the two axes give the corresponding full signal, except that resonances having no corresponding shift for the other nucleus (e.g., nonprotonated carbons or hydroxyl protons) do not appear. Connectivities are established by noting the frequencies at which the peaks appear along both the carbon and the proton axes. The intensities of the (^1H, ^{13}C) cross peaks are proportional to the number of protons attached to the specific carbon atom. Correlations via the C−H bond are most efficient when the evolution period t_e is equal to $1/(2J_{CH})$ (125–160 Hz), where J_{CH} is the one-bond C−H coupling constant. The value of t_d is set to $1/(3J_{CH})$ when proton-decoupled spectra are recorded. When long-range (vicinal) couplings are being studied, longer delays are required.

The 2D heteronuclear chemical-shift correlation experiment just described is most easily understood in the simplified-doublet form that was presented. The multiplet structure complicates the results, and the protons must be decoupled from the ^{13}C nucleus by application of a 180° ^{13}C pulse at the midpoint of the evolution period. Proton decoupling can be applied during the detection period as well.

Bax [62] gives a detailed discussion of the experimental aspects of this 2D heteronuclear chemical-shift correlation experiment and suggests methods for the suppression of the axial peaks as well as of errors resulting from quadrature ^1H detection.

For the application of this heteronuclear 2D technique to polymers, there is the usual problem of low sensitivity resulting from limited solubility and excess viscosity of the resulting solutions. For polymers, additional problems arise because of the low ^{13}C sensitivity, the rapid relaxation of the ^1H nucleus during the evolution time, and large line widths that limit the resolution. The major consequence of long polymer-correlation times is that dipolar ^1H–^{13}C interactions may make considerable contributions to both ^1H and ^{13}C line widths. Thus, even in the 2D experiments with polymers, considerable overlap can occur.

Because of the short relaxation times, the signal may decay to an unacceptable

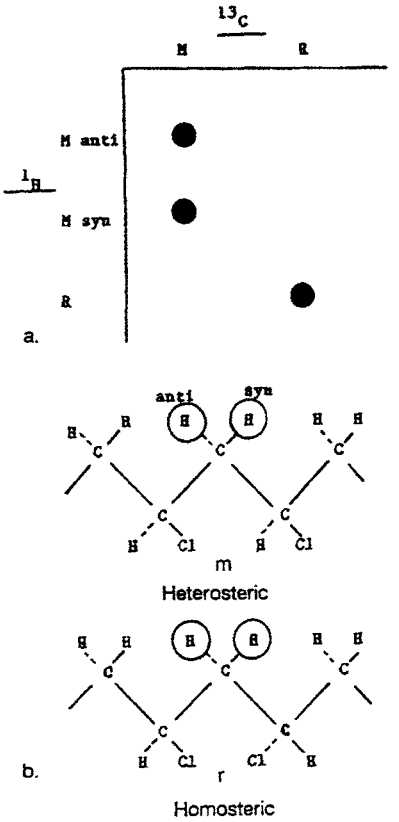

Fig. 6.21. The pattern resulting from $^{1}H-^{13}C$ correlations of methylene dyads (a) and the heterosteric and homosteric configurations (b). (Reproduced from Ref. [64]. © 1986 American Chemical Society.)

level before acquisition has occurred. Solutions to this problem are to use high static magnetic fields and ^{13}C enrichment. Alternatively, a large amount of sample can be used or the data collection can be limited to a small portion of the ^{1}H spectrum in order to decrease the total experimental time while maintaining the digital resolution in the second dimension [63].

For studies of the tacticity of polymers, the heteronuclear 2D technique can be used to make absolute configurational-sequence assignments for the ^{1}H spectra based on the connectivity with the carbon chemical shifts. The theoretical basis of the assignment procedure for methylene systems arises from the patterns that result from the presence of homosteric and heterosteric methylene protons. Fig. 6.21 shows the pattern resulting from $^{1}H-^{13}C$ correlations of methylene dyads [64].

A single carbon shift correlated to a single proton shift indicates a sequence with equivalent or homosteric methylene protons. A single carbon shift correlated to two proton shifts indicates a sequence in which the methylene protons are nonequivalent or heterosteric. This property can be used to distinguish certain stereosequences.

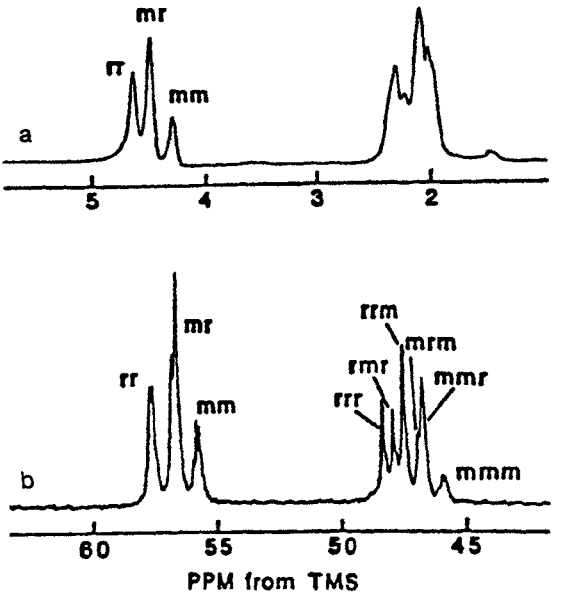

Fig. 6.22. The 125-MHz ^{13}C (a) and 500-MHz ^{1}H (b) NMR spectra of PVC at 65°C. (Reproduced from Ref. [65]. © 1986 American Chemical Society.)

An excellent demonstration of the power of 2D heteronuclear chemical-shift correlations to determine tacticity has been given for polyvinyl chloride (PVC) [65]. The 500-MHz ^{1}H and 125-MHz ^{13}C spectra of PVC at 65°C are shown in Fig. 6.22.

The methylene region is not resolved in the 500-MHz 1H spectrum, but in the ^{1}H–^{13}C 2D correlation spectrum, separate proton resonances are observed for each stereosequence Fig. 6.23.

For PVC, the rmr, rrm, and mmr methylene sequences are correlated with more than one proton resonance. Thus the proton methylene stereosequences can be correlated by using a knowledge of the ^{13}C assignments and the correlation with one or two proton shifts of the corresponding ^{13}C sequence. In Fig. 6.23, the methine and methylene assignments for both the carbons and the protons are indicated. In the methylene region, there is no simple relationship in the ordering between the chemical shifts of the stereosequences in the ^{13}C and ^{1}H spectra. However, with a knowledge of the ^{13}C triad assignments, as is the case with PVC, the proton assignments can be made. In the methine region, the rr, mr, and mm triads have the same relative ordering along both the ^{13}C and ^{1}H axes. These differences in the ordering of the chemical shifts for the ^{13}C and the ^{1}H spectra indicate that different factors influence the ^{13}C and ^{1}H chemical shifts. Mirau and Bovey [65] suggest that: "The ^{1}H chemical shifts are determined by the carbon type (methyl, methine, or methylene) and the inductive effects due to substituents and ionizable groups. ^{13}C chemical shifts are sensitive to these factors but also to the rotational isomeric state of the polymer."

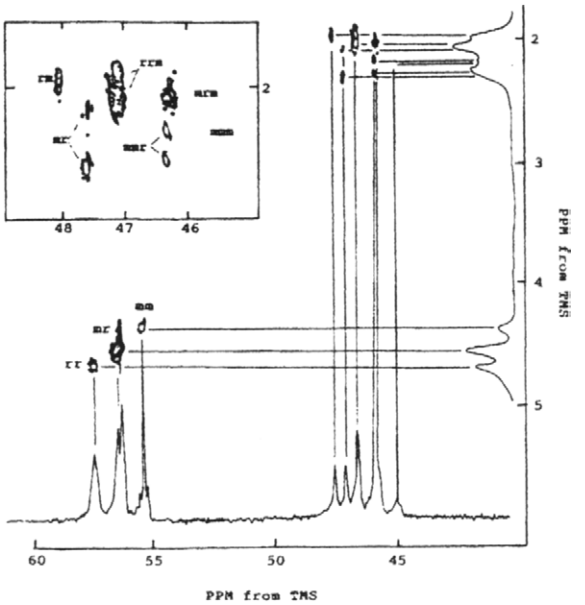

Fig. 6.23. ^{1}H–^{13}C heteronuclear-shift 2D correlation NMR spectrum of PVC at 65°C. The insert shows an expansion of the methylene region. (Reproduced from Ref. [65]. © 1986 American Chemical Society.)

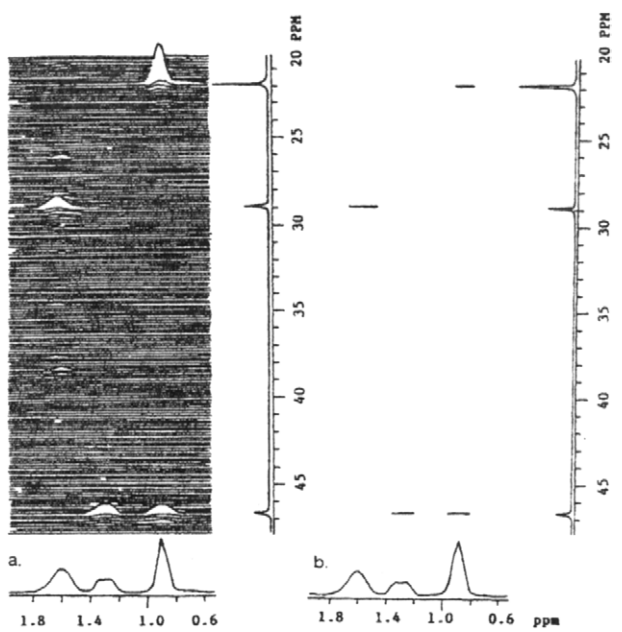

Fig. 6.24. The ^{1}H–^{13}C heteronuclear-shift correlation map for isotactic PP: (a) correlation map, (b) contour plot. (Reproduced with permission from Ref. [67]. © 1985 Springer-Verlag.)

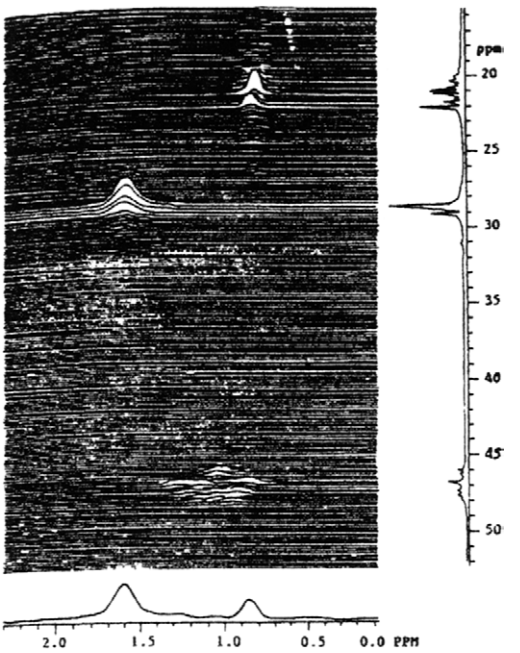

Fig. 6.25. The ^{1}H–^{13}C heteronuclear-shift correlation map for atactic PP. (Reproduced with permission from Ref. [67]. © 1985 Springer-Verlag.)

The ^{1}H–^{13}C heteronuclear-shift correlation has been used to assign the tactic sequences observed in the ^{1}H-NMR spectrum of polypropylene (PP) [66]. The ^{1}H–^{13}C heteronuclear-shift correlation map is shown in for isotactic PP [67] in Fig. 6.24.

The correlated assignments for both the ^{13}C and ^{1}H spectra of isotactic PP are given in Table 6.4.

The ^{1}H–^{13}C heteronuclear-shift correlation map for atactic PP is shown in Fig. 6.25.

This correlation map is considerably more complicated. The methine and methyl portions of the ^{1}H–^{13}C heteronuclear-shift correlation map are given in Fig. 6.26.

For the methine region, even the 2D technique does not resolve all the resonances, and individual assignments cannot be made. However, the chemical shifts for the pen-

Table 6.4
NMR spectral assignments for isotactic polypropylene

Group	^{13}C shifts (ppm)	^{1}H shifts (ppm)	^{1}H coupling constants (Hz)
CH_3	21.8	0.87	$J_3(CH_3-CH) = 6.56$
CH	28.7	1.60	$J_3(CH-CH_2, s) = 6.9$; $J_3(CH-CH_2, a) = 6.1$
CH_2	46.6	0.89 (syn)	$J_2(CH_2, gem) = -13.6$

(Reproduced with permission from Ref. [67]; © 1985.)

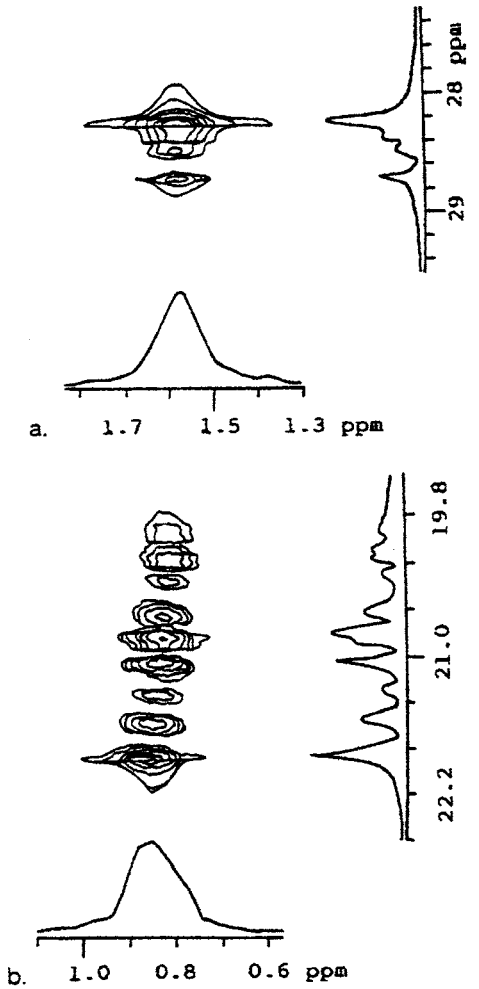

Fig. 6.26. The contour plots of the methine portion (a) and the methyl portion (b) of stereoirregular PP. (Reproduced with permission from Ref. [67]. © 1985 Springer-Verlag.)

tads of the methyl groups occur in the same order in the ^{13}C and ^{1}H spectra. Therefore, the correlations and assignments can be made, and these are given in Table 6.5.

The methylene region of the contour plot of stereoirregular PP is very complex, and correlations of the ^{13}C hexads with the ^{1}H tetrads have been made [67]. This 2D technique was also used for ethylene–propylene copolymers [68].

2D correlation via homonuclear scalar coupling (COSY)

The first 2D NMR experiment was based on phase modulation by the spin–spin coupling [69]. The standard sequence is $90°–t_1–90°–t_2$. After the preparation period, a 90° pulse causes the protons to precess and acquire phases that differ according to their

Table 6.5
Methyl assignments for stereoirregular polypropylene

Pentad	^{13}C shifts	^{1}H shifts
mmmm	21.8	0.871
mmmr	21.6	0.867
rmmr	21.4	0.859
mmrr	21.0	0.856
mrmm	20.8	0.852
rmrr	20.8	0.852
mrmr	20.6	0.846
rrrr	20.3	0.845
rrrm	20.2	0.837
mrrm	19.9	0.835

Note: All values are given in parts per million.
(Reproduced with permission from Ref. [66]; © 1985.)

differences in chemical shifts and the homonuclear J interactions. The final 90° pulse samples the orientations of the various magnetization components and records them by the spectrum in t_2. Because each proton in the spectrum has its own chemical shift as a modulation in t_e, the resulting doubly transformed data has peaks with identical ω_1 and ω_2 values, which are further modulated in ω_1 by the homonuclear J coupling. The correlated spectroscopy (COSY) spectrum shows all the proton resonances correlated with themselves (i.e., autocorrelated) along the diagonal. The off-diagonal peaks or cross-correlated peaks show which protons are spin coupled to one another. In this fashion, it is possible to trace the vicinal and geminal coupling interactions between protons. The pattern of the cross-peak network is unique for the connectivity of the protons. This technique provides a map of the J-coupling network within the polymer.

The 500-MHz COSY spectrum of PVC [65] at 65°C is shown in Fig. 6.27.

The solid lines show the correlation between triad and tetrad resonances. When the methylene protons are equivalent, two correlations are expected for rr (rrr and mrr) and mm (mmm and mmr), and four correlations are expected for mr (mrr, mrm, rmr, and mmr). Some assignments can be made from the correlation spectrum. For example, the resonance at the highest field triad has a single cross peak in the methylene region and must result from the mm–mmr interaction. The largest number of cross peaks is in the middle triad sequence, so this resonance must be assigned to mr. The lowest field methine peak results from rr and is expected to show cross peaks to mrr and rrr. However, because of the missing cross peaks and the extensive overlap, the proton spectrum of PVC cannot be completely assigned by using the COSY spectrum alone.

2D homonuclear J-resolved spectroscopy

Coupling constants that cannot be measured from the conventional ^{1}H-NMR spectrum of a polymer can often be measured from the 2D Jresolved spectrum. This

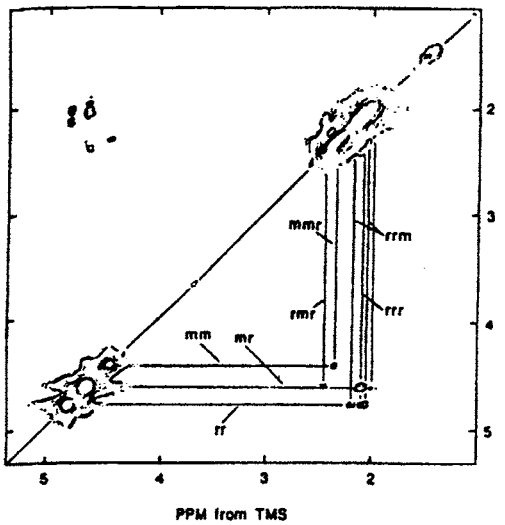

Fig. 6.27. The 500-MHz COSY spectrum of PVC at 65°C. (Reproduced from Ref. [65]. © 1986 American Chemical Society.)

technique separates the effects of the chemical shift and J coupling along two frequency axes in the 2D spectrum and allows the coupling constants to be measured, even in the case of severe spectral overlap. The power of homonuclear 2D J-resolved spectroscopy is in the separation of overlapping resonances in the proton spectrum of a polymer in order to determine the sequence-length sensitivity of the spectrum.

The basis of the method can be illustrated by the following simple example. In proton NMR spectroscopy, the lines in the individual patterns are phase modulated by the spin–spin coupling during the spin-echo experiment by using variations in t_e. For example, the two components in a first-order doublet of a two–spin system are phase modulated at a frequency of $J/2$. The phase modulation of the resonance intensity results from the fact that the spin states of the protons producing the multiplet pattern are different. If a methyl proton is interacting with a methine proton, a doublet is observed because there are two possible energy orientations of the methine proton relative to H_0.

The preparation period is a relaxation delay to ensure that the spin system is in equilibrium. Following a 90° pulse, the magnetizations from each of the lines of the doublet are colinear. If the carrier frequency is equal to the frequency midway between the two lines, then during the delay period immediately following the 90° pulse, the higher-frequency component of the doublet will move ahead of the carrier frequency, and the lower-frequency component will fall behind. At time t_e, a broad-band 180° pulse is applied to reverse the orientation of the methyl protons. Because it is a broad-band pulse, however, it simultaneously reverses the orientation of the methine proton. Thus, those methyl protons that were originally coupled to

a methine proton of the original orientation (which gives rise to the faster rotating component of the doublet) are now coupled to a proton of the opposite orientation. Therefore the magnetization from this component precesses more slowly during the second delay period, and consequently does not refocus at time $2t_e$. Likewise, the slower component will be out of phase with the carrier frequency at time $2t_e$, giving rise to the phase modulation. For example, if $J = 6.25$ Hz for the methyl doublet, the component that was precessing more rapidly immediately following the 90° pulse will be 90° out of phase when $2t_e = 0.08$ s ($t_e = 0.04$ s). The other component will be $-90°$ out of phase. When $2t_e$ is 0.16 s, the two components will be 180° and $-180°$ out of phase, respectively. When $2t_e$ is 0.32 s, the two components will be 360° and $-360°$ out of phase. As t_e is increased, this phase modulation is repeated at a frequency of J. Thus, in general, a doublet will be inverted when $t_e = 1/(2J)$, $3/(2J)$, and $5/(2J)$. The doublet will be positive when $t_e = 1/J$, $2/J$, and $3/J$. In 2D spin-echo FT-NMR experiments, FIDs are obtained at a series of closely spaced t_e values. Each FID is Fourier transformed to give spectra that are arranged as a function of t_e at particular frequencies over the chemical-shift region of interest. The amplitude in the *echo interferogram* at a particular chemical shift is modulated at frequencies that are determined by the nature of the resonance patterns at that particular chemical shift. Thus, Fourier transformation of the echo interferogram separates overlapping resonances in the J dimension according to their modulation frequency.

The results of 2D J-resolved spectroscopy can be plotted in two dimensions, with F_1 representing the J dimension and F_2 representing the chemical-shift dimension. Projection of the individual spectra on the F_2 axis gives the completely proton–proton decoupled spectrum of the sample. Hence, the projection can be used to determine the number of distinct spin species in a molecule and to measure the chemical shift of each of these species. Projection onto the F_1 axis gives the J spectra from which the homonuclear J couplings can be measured. The individual components of a given multiplet appear at frequencies in the F_1 and F_2 dimension such that the individual lines of a given multiplet overlap for a projection at an angle of 45° relative to F_1 and F_2. The important result is that single lines are obtained for the chemically shifted protons rather than the multiplet patterns of normal spectra.

The intensities of the cross peaks depend on a number of features, including the coupling constants, the complexity of the coupling pattern, the relaxation rates, and the relative abundance of the coupled moieties. A number of variations of the 2D J-resolved experiment have been suggested, including one designed particularly for macromolecular systems to yield increased sensitivity and resolution [70].

Poly(propylene oxide) has been studied by using 2D J-resolved NMR spectroscopy [71]. The scalar coupling is observed only between protons of the same monomer unit because the oxygen atom separates the monomer units in the chain. The 500-MHz proton NMR spectrum of a commercial atactic poly(propylene oxide) is shown in Fig. 6.28.

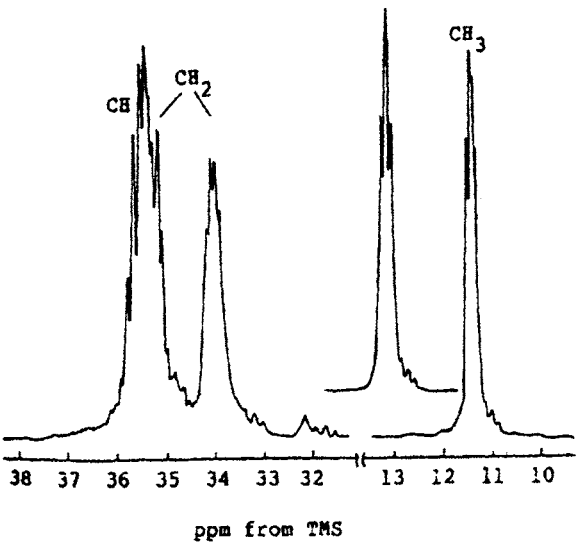

Fig. 6.28. The 500-MHz proton NMR spectrum of a commercial atactic poly(propylene oxide) in $CDCl_3$ at 25°C showing extensive overlap resulting from the presence of stereosequences. The simulated spectrum (inset) was calculated by using the values of the J couplings that were obtained from the 2D spectrum. (Reproduced from Ref. [71]. © 1985 American Chemical Society.)

Extensive overlap resulting from the presence of stereosequences is apparent. In Fig. 6.29, an expansion is shown of the 500-MHz 2D J-resolved spectrum of the methyl region of poly(propylene oxide).

Five main doublets are apparent in this region, and at least five very weak doublets appear at higher shielding. The five major doublets correspond to different stereosequences, and the weak doublets correspond to inverted units [72]. Interestingly, although all of the sequences have different chemical shifts the same coupling constant of 6.5 Hz is observed for all sequences.

The homonuclear 2D J-resolved experiment was also used as an aid in assigning the copolymer sequences in poly(ethylene-*co*-vinyl alcohol) [72]. The problem is that the coupling constants are of the same order of magnitude as the chemical-shift differences between the coupled methylenes. The EEE (ethylene) sequences give rise to a singlet because all neighboring methylenes are equivalent, and these sequences can be assigned from the 2D spectrum. Methylenes in other sequences are coupled to neighboring methylenes that have similar, yet different chemical shifts. The CH−OH coupling constants are sequence dependent. The coupling constant is large (5.8 Hz) when the neighboring units are either ethylene or both racemic vinyl alcohol. The coupling constant drops to 3.9 Hz for any sequence containing at least one meso VV (vinyl alcohol) dyad, which indicates that the average dihedral angle between the methine and hydroxyl protons is different for these sequences.

The homonuclear 2D J-resolved experiment was also used as an aid in assigning resonances in the epoxy resin diglycidyl ether of bisphenol-A [73] and the com-

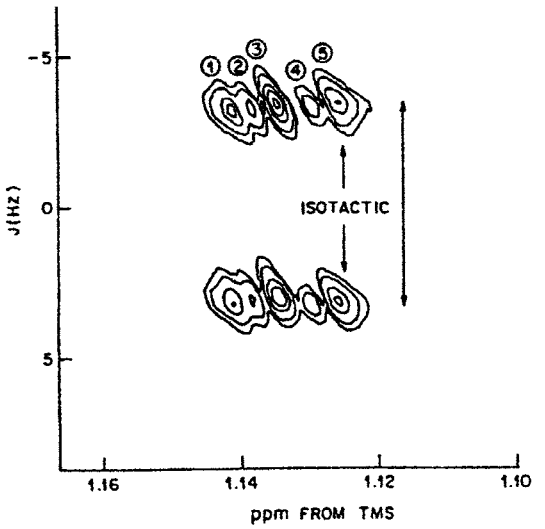

Fig. 6.29. Expansion of the 500-MHz 2D *J*-resolved spectrum of the methyl region of atactic poly(propylene oxide). The circled numbers correspond to the five main doublets. The splittings due to the *J* coupling can be observed in the upper and lower portions of the figure. The measured J_{CH3-CH} value of 6.5 Hz corresponds to the expected value for this system. (Reproduced from Ref. [71]. © 1985 American Chemical Society.)

posite of bis[*N,N*-bis(2,3-epoxypropyl)-4-aminophenyl]methane and the curing agent bis(4-aminophenyl)sulfone [74]. The complex proton spectrum resulting from the glycidylamine moiety can be completely elucidated in this manner.

Expectations

There is a continuing need for more rapid, precise and accurate analyses of the chemical composition of polymers. The special editing techniques described simplify and correlate the complex and multiline experimental NMR spectra. The resulting spectra are considerably easier to use to obtain the structural information. Progress in this field has been rapid as the NMR instrumentation, computer speed and capacity as well as software has improved. In the future, we will see considerably more use of the 2D (3D and 4D as well) methods in the study of synthetic polymer systems.

References

[1] Ernst, R.R., Angew. Chem., 31 (1992) 805.
[2] Pople, J.A., Schneider, W.G., Bernstein, H.J., High Resolution Nuclear Magnetic Resonance. McGraw-Hill, New York, NY, 1959.
[3] Abragam, A., The Principles of Magnetic Resonance. Oxford, New York, NY, 1961.
[4] Zukav, G., The Dancing Wu Li Masters. Morrow, New York, NY, 1979.

[5] Harris, R.K., Mann, B.E., NMR and the Periodic Table. Academic, London, 1978.
[6] Farrar, T.C., Becker, E.D., Pulse and Fourier Transform NMR. Academic Press, New York, NY, 1971.
[7] Shaw, D., Fourier-Transform NMR Spectroscopy. Elsevier, Amsterdam, 1976.
[8] Pham, Q.T., Petiaud, R., Waton, H., Proton and NMR Spectra of Polymers. CRC Press, London, 1991.
[9] Andrew, E.R., Phil. Trans. R. Soc. London, A: 299 (1981) 505.
[10] Bovey, F.A., Nuclear Magnetic Resonance Spectroscopy, 2nd edition. Academic Press, San Diego, CA, 1988.
[11] Arnold, J.T., Dharmatti, S.S., Packard, M.E., J. Chem. Phys. 19 (1951) 507.
[12] Stothers, J.B., Carbon-13 NMR Spectroscopy. Academic Press, New York, NY, 1972.
[13] Wehrli, F.W., Wirthlin, T., Interpretation of Carbon-13 NMR Spectra. Heyden, Philadelphia, PA, 1978.
[14] Levy, G.C., Lichter, R.L., Nelson, G.L., Carbon-13 Nuclear Magnetic Resonance Spectroscopy. Wiley, New York, NY, 1980.
[15] Silverstein, R.M., Bassler, G.C., Morrill, T.C., Spectrometric Identification of Organic Compounds. Wiley, New York, NY, 1981.
[16] Martin, G.E., Org. Magn. Reson. 7 (1975) 2.
[17] Atta-ur-Rahman, Nuclear Magnetic Resonance: Basic Principles. Springer-Verlag, New York, NY, 1986.
[18] Ando, I., Webb, G.A., Theoretical Aspects of NMR Parameters. Academic Press, London, 1983.
[19] Wuthrich, K., NMR of Proteins and Nucleic Acids. Wiley, New York, NY, 1986.
[20] Randall, J.C., Zoepfl, F.J., Silverman, J., in: J.C. Randall (Ed.), NMR and Macromolecules. ACS Symposium Series 247, American Chemical Society, Washington, DC, 1984, p. 245.
[21] Schaefer, J., Stejskal, E.O., J. Am. Chem. Soc. 98 (1976) 1031.
[22] Komoroski, R.A. (Ed.), High Resolution NMR of Synthetic Polymers in Bulk. VCH Publishers, Deerfield Beach, FA, 1986.
[23] Bax, A., Two-Dimensional Nuclear Magnetic Resonance in Liquids. Reidel, Boston, MA, 1982.
[24] Schmidt-Rohr, K., Spiess, H.W., Multidimensional Solid-State NMR of Polymers, Academic Press, Orlando, FL, 1994.
[25] Bremser, W., Franke, B., Wagner, H., Chemical Shift Ranges in Carbon-13 NMR Spectroscopy. Verlag Chemie, Weinheim, 1982.
[26] Bremser, W., Ernst, L., Franke, B., Gerhards, R., Hardt, A., Carbon-13 NMR Spectral Data. Verlag Chemie, Weinheim, 1981.
[27] Grant, D.M., Paul, E.G., J. Am. Chem. Soc. 86 (1964) 2984.
[28] Lindeman, L.P., Adams, J.G., Anal. Chem. 43 (1971) 1245.
[29] Cheng, H.N., Bennet, M.A., Anal. Chem. 56 (1984) 2320.
[30] Cheng, H.N., Transition Metal Catalyzed Polymerizations. Alkenes and Dienes, MMI Press. Harwood Academic Press, New York, NY, 1983, p. 617.
[31] Jurs, P.C., Sutton, G.P., Ranc, M.L., Anal. Chem. 61 (1989) 1115A.
[32] Small, G.W., Jurs, P.C., Anal. Chem. 55 (1983) 1121.
[33] Small, G.W., Jurs, P.C., Anal. Chem. 56 (1984) 1314.
[34] Kalchhauser, H., Robien, W., J. Chem. Inf. Comput. Sci. 25 (1985) 103.
[35] Slichter, C.P., Principles of Magnetic Resonance. Harper and Row, New York, NY, 1980.
[36] Derome, A.E., Modern NMR Techniques for Chemistry Research. Pergamon Press, New York, NY, 1987.
[37] Ernst, R.R., Bodenhausen, G., Wokaun, A., Principles of Nuclear Magnetic Resonance in One and Two Dimensions. Oxford University Press, Oxford, 1991.
[38] Bovey, F.A., Nuclear Magnetic Resonance Spectroscopy, 2nd edition. Academic Press, New York, NY, 1988.
[39] Bruch, M.D., Dybowski, C., Lichter, R.L., in: C. Dybowski and R.L. Lichter (Eds.), NMR Spectroscopy Techniques. Marcel Dekker, New York, NY, 1987, p. 170.
[40] Chu, C.Y., Vukov, R., Macromolecules 18 (1985) 1423.
[41] Rabenstein, D.L., Nakashima, T.T., Anal. Chem. 51 (1979) 1465A.
[42] Bodenhausen, G., Freeman, R., Morris, G., J. Magn. Reson. 23 (1976) 171.
[43] Morris, G., Freeman, R., J. Magn. Reson. 29 (1978) 433.
[44] Sadler, I.H., J. Chem. Soc., Chem. Commun. (1987) 321.

[45] Sorensen, S., Hansen, R.S., Jakobsen, H.J., J. Magn. Reson. 14 (1974) 243.
[46] Morris, G.A., Freeman, F., J. Am. Chem. Soc. 101 (1979) 760.
[47] Doddrell, D.M., Pegg, D.T., J. Am. Chem. Soc. 102 (1980) 6388.
[48] Hikichi, K., Hiraoki, T., Takemura, S., Ohuchi, M., Nishioka, A., in: NMR and Macromolecules. ACS Symposium Series 247, American Chemical Society, Washington, DC, 1984, p. 119.
[49] Gray, G.A., in: J.C. Randall Jr. (Ed.), NMR and Macromolecules, Sequence, Dynamic and Domain Structure. ACS Symposium 247, American Chemical Society, Washington, DC, 1984.
[50] Asakura, T., Nishiyama, Y., Doi, Y., Macromolecules 20 (1987) 616.
[51] Bendall, M.R., Pegg, D.T., Doddrell, D.M., Field, J., J. Am. Chem. Soc. 103 (1981) 936.
[52] Dodrell, D.M., Pegg, D.T., Bendall, M.R., J. Magn. Reson. 48 (1982) 323.
[53] Barron, P.F., Hill, D.J.T., O'Donnell, J.H., O'Sullivan, P.W., Macromolecules 17 (1984) 1967.
[54] Bruch, M.D., Bonesteel, J.K., Macromolecules 19 (1986) 1622.
[55] Komoroski, R.A., Shockcor, J.P., Gregg, E.C., Savoca, J.L., Rubber Chem. Technol. 59 (1985) 328.
[56] Bax, A., Freeman, R., Kempsell, S.P., J. Am. Chem. Soc. 102 (1980) 4849.
[57] Bodenhausen, G., Freeman, R., Niedermeyer, R., Turner, D.L., J. Magn. Reson. 26 (1977) 133.
[58] Van de Ven, F.S.M., Multidimensional NMR in Liquids: Basic Principles and Experimental Methods. VCH Publishers, Inc., New York, NY, 1995.
[59] Sarkar, S.K., Bax, A., J. Magn. Reson. 62 (1985) 109.
[60] Maudsley, A.A., Ernst, R.R., Chem. Phys. Lett. 50 (1977) 368.
[61] Bodenhausen, G., Freeman, R., J. Magn. Reson. 28 (1977) 471.
[62] Bax, A., in: G.C. Levy (Ed.), Topics in Carbon-13 NMR Spectroscopy, Vol. 4. Wiley, New York, NY, 1984.
[63] Westler, W.M., Ortiz-Polo, G., Markley, J.L., J. Magn. Reson. 58 (1984) 354.
[64] Crowther, M.W., Szeverenyi, N.M., Levy, G.C., Macromolecules 19 (1986) 1333.
[65] Mirau, P.A., Bovey, F.A., Macromolecules 19 (1986) 210.
[66] Cheng, H.N., Lee, G.H., Polym. Bull. 13 (1985) 549.
[67] Cheng, H.N., Lee, G.H., Polym. Bull. 12 (1984) 463.
[68] Cheng, H.N., Lee, G.H., J. Polym. Sci., Part B: Polym. Phys. 25 (1987) 2355.
[69] Jeener, J., Meier, B., Bachmann, P., Ernst, R., J. Chem. Phys. 71 (1979) 4546.
[70] Macura, S., Brown, L.R., J. Magn. Reson. 53 (1983) 529.
[71] Bruch, M.D., Bovey, F.A., Cais, R.E., Noggie, J.H., Macromolecules 18 (1985) 1253.
[72] Bruch, M.D., Macromolecules 21 (1988) 2707.
[73] Jagannathan, N.R., Herring, F.G., J. Polym. Sci., Polym. Chem. 26 (1988) 1.
[74] Herring, F.G., Jagannathan, N.R., Luoma, G., J. Polym. Sci., Polym. Chem. 23 (1985) 1649.

Chapter 7

Applications of high-resolution solution NMR

Introduction

^{13}C- and ^{1}H-NMR spectroscopy are powerful methods to directly observe the chemical species and types of molecular connections existing in polymeric materials. The information obtainable from high-resolution NMR spectroscopy include chemical composition of the main chain, microstructural defects, distribution of defect structures along the chain, comonomer composition and sequence, terminal end-group structures, branching, abnormal structures (cyclic and isomerized structures), nature of the monomer enchainment and tacticity.

The main advantages of using NMR compared to the other analytical techniques are the high spectral selectivity and the capability of measuring quantitatively the structural components in the sample without using external calibration. The spectral sensitivity is more pronounced in ^{1}H NMR due to the high natural abundance and higher gyromagnetic ratio of hydrogen relative to ^{13}C. However, ^{13}C NMR has a greater spectral selectivity due to the larger dispersion of the chemical shifts compared to ^{1}H NMR, enabling more detailed structural characterization. ^{13}C NMR is a very specific probe of the local environment, often capable of distinguishing between two carbons in structural moieties that differ in structure four bonds away from the site of interest. The quantitative nature of the results can be compromised in conventional solution ^{13}C NMR by the presence of heteronuclear spin coupling, but it can be overcome in the gated decoupling pulse mode with some sacrifice in the sensitivity. In the ^{13}C NMR of polymer solutions, high-resolution spectra with very narrow line widths are obtained because rapid, random molecular motions in the solution average the line-broadening interactions to zero.

Only a few selected examples of the application of high-resolution NMR spectroscopy will be given in this chapter. Several excellent monographs on the application of NMR spectroscopy to polymers are available, and one cannot do better than to read Bovey [1], Tonelli [2], and Bovey and Mirau [3] but for pedagogical reasons and completeness, some recent results will be given here.

Determination of structure of the repeating unit

The chemical structure of the repeating unit can be directly determined by NMR if spectra with adequate signal-to-noise can be obtained and suitable structural assignments made for the recorded resonances.

As an example, let us consider the structure of X-ray-irradiated poly(methyl methacrylate) (PMMA) [4]. The proposed structural changes occurring with X-ray-irradiated are shown in Chart 7.I.

It is postulated that there is an initial formation of the alkene degradation products **1**–**4**. Chain-scission products (**1** and **2**) appear as end groups and chain intact products

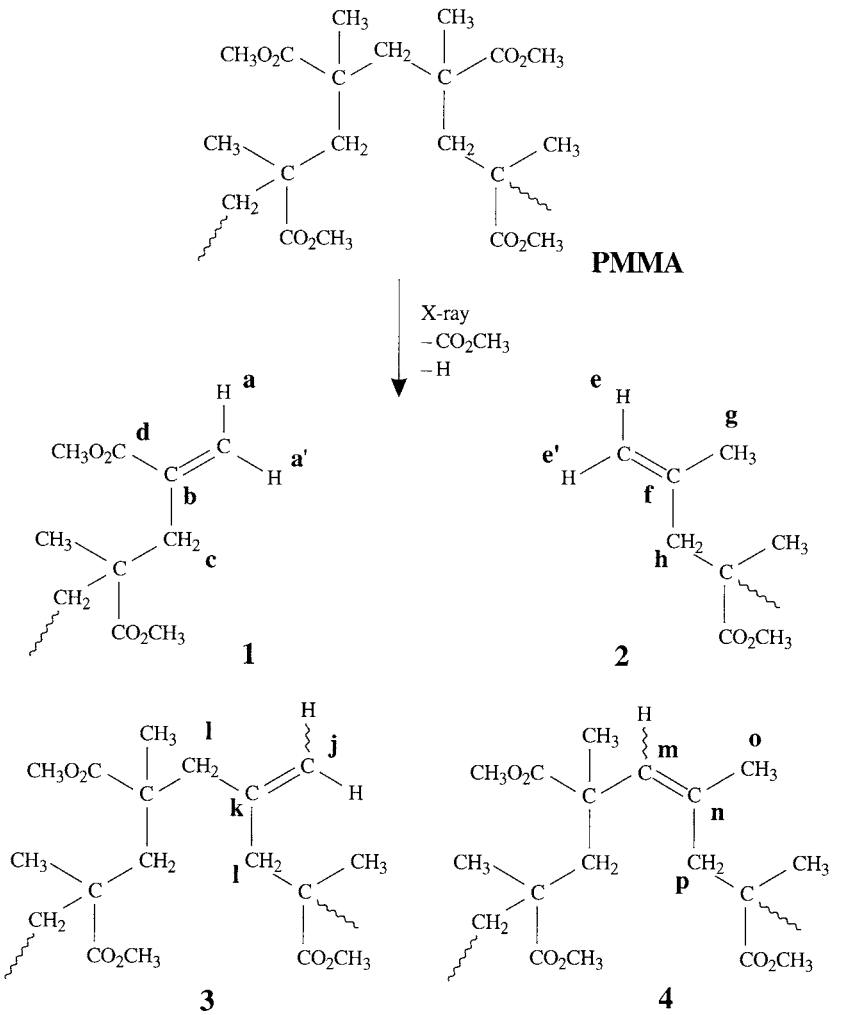

Chart 7.I.

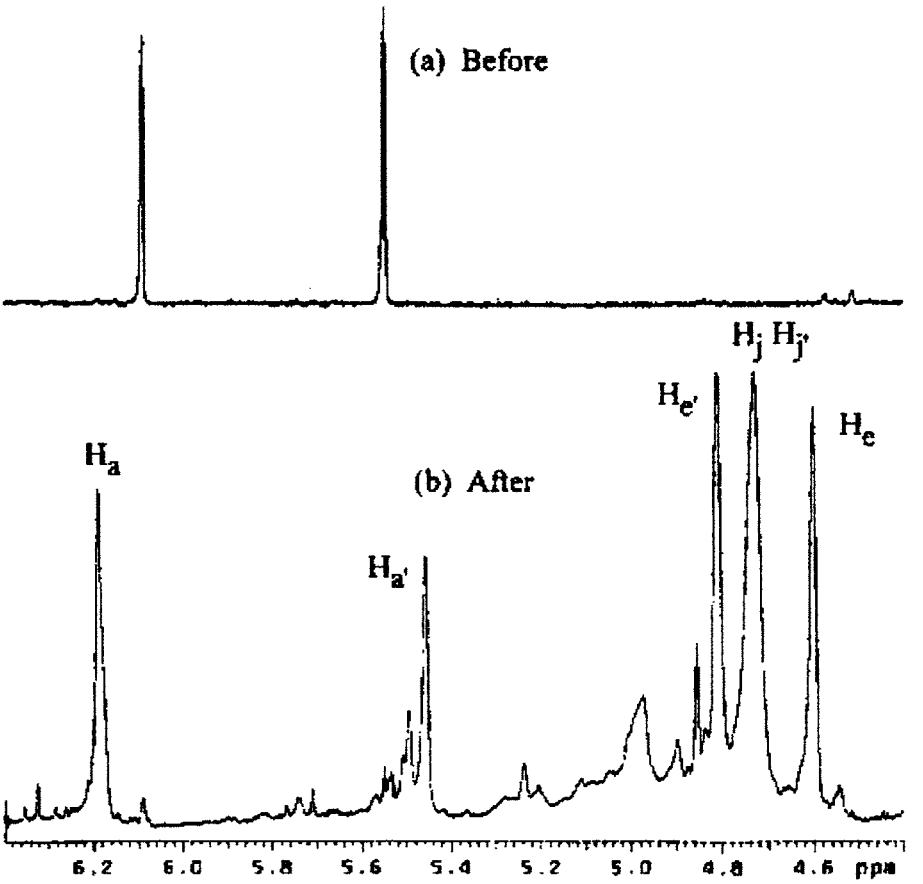

Fig. 7.1. The 400-MHz ^{1}H-spectra of PMMA in the alkene region (a) before X-ray exposure showing the 0.5% methyl methacrylate impurity in the bulk material; (b) after X-ray exposure. See the test for the labeling of the hydrogen resonances. The relative intensities of signals in (a) have no relationships to those in (b). (Reproduced with permission from Ref. [4]. © 1997 American Chemical Society.)

(**3** and **4**) result from the elimination of methyl formate. The 400-MHz ^{1}H spectra of PMMA before and after X-ray irradiation are shown in Fig. 7.1.

Degradation products are identified by the formation of upfield signals at ~0.96, 1.1, 1.6, and 2.1–2.5 ppm. The carbon and hydrogen resonance assignments were made using the one dimensional hydrogen and carbon spectra with two dimensional H, HCOSY, HMQC, and HMBC spectra, as indicated in Table 7.1.

The alkene hydrogen shifts at 5.46 (H_a) and 6.19 ($H_{a'}$) ppm are coupled as indicated by the delayed COSY experiment and this results supports the α,β-unsaturated carbonyl structure for product **1**. The alkene hydrogen peaks at 4.60 (H_e) and 4.81 ($H_{e'}$) are correlated with one another and with the allylic methyl hydrogens (H_g) (1.59 ppm) for product **2**. Delayed COSY shows correlations with the alkene hydrogens at

Table 7.1
Hydrogen and carbon NMR chemical shifts for the X-ray-degradation products of PMMA

Product (Chart 7.I)	Nucleus (Chart 7.I)	Observed chemical shift (ppm)	Predicted chemical shift (ppm)
1 (0.50%)	H_a	6.19	6.15 (alkene)
(chain scission)	$H_{a'}$	5.46 (and 5.48)	5.58 (alkene)
	H_c	2.43	(methylene)
	$H_{c'}$	2.60	(methylene)
	C_a	128.2	130.3 (terminal alkene)
	C_b	143.6	144.2
	C_c	43.6	38.7 (allylic methylene)
	C_d	167.3	165.0 (conjugated carbonyl)
2 (0.47%)	H_e	4.60	4.75 (alkene)
(chain scission)	$H_{e'}$	4.81	4.75 (alkene)
	H_g	1.59	(allylic methyl)
	H_h	2.35	(methylene)
	$H_{h'}$	1.95	(methylene)
	C_e	115.6	114.4 (alkene)
	C_f	141.1	143.7 (alkene)
	C_g	23.6	23.6 (methyl)
	C_h	51.2	46.4 (methylene)
	C_i	176.2	176.0 (methoxy-carbonyl)
3 (0.52%)	H_j, $H_{j'}$	4.73	4.75 (alkene)
(chain intact)	H_l	1.77	(methylene)
	$H_{l'}$	2.23	(methylene)
	C_j	118.6	114.4 (alkene)
	C_k	Not observed	
	C_l	49.5	44.5 (allylic)
4 (0.18%)	H_m	5.0	5.20 (alkene)
(chain intact)	H_o	1.35	(allylic methyl)
	H_p	Not observed	
	C_m	135.8	132.5 (allylic methyl)
	C_n	Not observed	
	C_o	17.7	17.7 (methyl)
	C_p	45.6	46.5 (methylene)

1.77 and 2.24 consistent with the diastereotopic methylene hydrogens product **3**. The broad peak observed at 5.0 ppm is correlated with the allylic methyl hydrogen at 1.35 and this is consistent with a double bond capable of cis/trans isomerism for product **4**.

Determination of end-group structure

The chemical nature of the polymer end groups is determined by the initiation and termination steps and therefore represents a history of the polymerization process. Identification of the end groups by NMR is facilitated when the molecular weight of the polymer is low as the concentration of end groups is higher. Due to the higher

sensitivity of proton NMR it is advantageous to use this NMR technique whenever possible since the concentration of end groups is low.

For addition polymerizations, the end groups generally fall into two general classes: saturated and unsaturated. The saturated end groups arise from the initiator fragments and the unsaturated from disproportionation occurring in the termination step. The saturated endgroups can be studied using ^{1}H and ^{13}C NMR while insufficient resolution exists for ^{1}H NMR for the unsaturated groups. For olefin polymerizations, signals for vinylene, trisubstituted, vinyl and vinylidene double bonds are expected in the ^{1}H-NMR spectrum at 5.5–5.3, 5.3–5.1, 5.1–48, and 4.8–4.6 ppm, respectively [5].

As an example, let us consider, the end groups of ethylene-*co*-1-butene copolymers. Experimentally, the ^{1}H-NMR signals for the major vinylidene end group are observed as a doublet at 4.74 and 4.68 ppm [6]. These signals correspond to vinylidene end groups which have either an ethylene penultimate unit (4.68 ppm) or a 1-butene penultimate unit (4.74 ppm). The ^{13}C-NMR signals for the vinylidene with a 1-butene penultimate unit occur at 150.2 and 109.1 ppm and for the vinylidene with a ethylene penultimate unit the signals occur at 151.5 and 107.4 ppm. It was further observed that the signals for the vinylidene end groups with the 1-butene penultimate group were further split into a pair of resonances as a result of differences in the penpenultimate unit. The vinylidene end groups are formed by β-hydride transfer from propagating 1-butene terminal units. The ethylene terminal units are much more reactive and prefer to propagate rather than terminate. The chemical shift differences are determined by the identity of the penultimate and penpenultimate units. Hence, the excess of the butyl penultimate vinylidene end group over the ethyl penultimate end group arises from propagating chains rich in 1-butene units.

In the case of the trisubstituted double bond end groups, the ^{13}C-NMR analysis showed the presence of at least six different double bond end groups. Again, the two different penultimate groups give rise to separate signals but also the cis and trans placements contribute to different resonances.

Nomenclature for end-group resonances of α-olefin-co-ethylene copolymers

There are a total of 77 different end-group structures which can arise as a result of copolymerization and subsequent mechanochemical degradation of poly(ethylene-*random-co*-propylene) polymers [7]. There are 29 possible saturated structures generated by random placements of ethylene and propylene near the chain ends. However, many of these structures are spectroscopically degenerate resulting in 32 distinguishable structures (Table 7.2). Needless to say, some type of nomenclature must be developed.

Each saturated chain end is designated by a three-character code. The rightmost character is a number representing the distance from the first methyl substituent to the chain end. The first Greek letter to the left represents the distance from the first methyl substituent from the chain end to the second methyl substituent and the left-

Table 7.2
Olefin chain ends of ethylene/propylene copolymers and their chemical shifts [1]

No.	Code	Chain structure	Chemical shifts (ppm)			Present?
			C3	C2	C1	
1	$\omega 0'$	~0000000		139.1	114.2	+
2	$\omega 1'$, $\omega\delta 1'$, $\omega\varepsilon 1'$	~0000010		145.8	110.3	+
3	$\omega 2'$, w$\gamma 2'$,$\omega\delta 2'$,$\omega\varepsilon 2'$, $\varepsilon\gamma 2'$	~0000100		145.1	112.3	+
4	$\omega 3'$, $\omega\beta 3'$, $\omega\gamma 3'$, $\omega\delta 3'$, $\delta\beta 3'$	~0001000		137.8	115.4	+
5	$\omega 4'$,$\omega\beta 4'$, $\omega\gamma 4'$, $\omega\delta 4'$ $\delta\beta 4'$	~0010000		139.3	114.1	+
6	$\omega 5'$	~0100000		137.1	114.1	+
7	$\omega 6'$	~1000000		138.5	113.6	+
8	$\omega\beta 1'$, $\delta\beta 1'$, $\varepsilon\beta 1'$	~0001010		144.6	111.8	+
9	$\omega\beta 2'$, $\delta\beta 2'$, $\varepsilon\beta 2'$	~0010100		144.8	112.3	+
10	$\omega\gamma 1'$, $\varepsilon\gamma 1'$	~0010010		146.2	110.3	+
11	$\omega 0''$(E)	~0000000	131.8	124.6	17.9	+
12	$\omega 0''$(Z)	~0000000	131.2	123.8	12.8	+
13	$\omega 1''$	~0000000	125.2	131.1	17.6	+
14	$\omega 2'$, $\omega\delta 2,'$, $\omega\varepsilon''$(E)	~0000100	135.9	118.4	13.3	–
15	$\omega 2'$, $\omega\delta 2''$, $\omega\varepsilon''$(Z)	~0000100	136.1	119.2	13.3	–
16	$\omega 3''$, $\omega\gamma 3''$, $\omega\delta 3''$(E)	~0001000	137.1	123.0	18.0	–
17	$\omega 3''$, $\omega\gamma 3''$, $\omega\delta 3''$(Z)	~0001000	137.3	122.4	13.0	–
18	$\omega 4''$, $\omega\beta 4''$, $\omega\gamma 4''$, $\omega\delta 4''$, $\delta\beta 4''$(E)	~0010000	130.4	125.8	17.9	–
19	$\omega 4''$, $\omega\beta 4''$, $\omega\gamma 4''$, $\omega\delta 4''$, $\delta\beta 4''$(Z)	~0010000	129.7	124.4	12.8	–
20	$\omega 5''$(E)	~0100000	132.5	124.7	17.7	+
21	$\omega 5''$(Z)	~0100000	131.7	123.8	12.8	–
22	$\omega 6''$(E)	~1000000	132.1	124.7	17.5	+
23	$\omega 6''$(Z)	~1000000	131.2	123.8	12.3	–
24	$\omega\gamma 1''$, $\varepsilon\beta 1''$	~0001010	133.0	128.9	25.7	+
25	$\omega\beta 2''$, $\delta\beta 2''$, $\varepsilon\beta 2''$(E)	~0010100	135.5	118.8	9.3	–
26	$\omega\beta 2''$, $\delta\beta 2''$, $\varepsilon\beta 2''$(Z)	~0010100	135.7	119.5	9.3	–
27	$\omega\beta 3''$, $\delta\beta 3''$(E)	~0101000	138.0	123.0	19.2	–
28	$\omega\beta 3''$, $\delta\beta 3''$(Z)	~0101000	137.7	122.5	7.8	–
29	$\omega\gamma 1''$, $\varepsilon\gamma$ $1''$	~0010010	123.9	131.7	25.8	+
30	$\omega\gamma 2''$, $\varepsilon\gamma$ $2''$	~0010010	139.5	118.8	15.8	–
31	$\omega\delta 1''$	~1000010	125.3	130.8	25.7	+
32	$\delta\beta 1''$	~0101010	129.7	129.8	25.7	–

[1] A '1' in the structure column represents a methyl group attached to a methine carbon, while a '0' represents a methylene. The two carbons connected by the double bond are underlined. The carbons are numbered from the chain end. A '+' in the 'present' column indicates that resonances which may indicate the presence of this structure are observed in the ^{13}C spectra.
(Source: Ref. [7].)

most character represents the distance of the first methyl substituent to the third one. If no such third methyl group exists or if its presence is irrelevant, this is designated by the letter ω. For simplicity, the unsubstituted straight chain is designated $\omega 0$.

For the case of unsaturated chain ends, the addition of a (′) or (″) represents the position of the double bond, originating at either the C-1 position, the chain end, or the C-2 position, one carbon from the end. Thus the three main structural families, vinyl, vinylidene and vinylene are designed $\omega 0'$, $\omega 1'$ and $\omega 0''$, respectively.

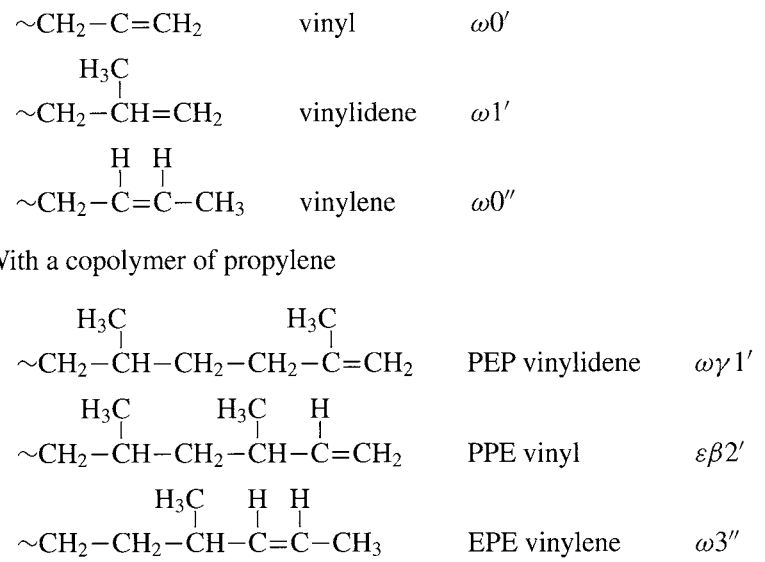

With a copolymer of propylene

In high temperature extrusion for ethylene-*co*-propylene copolymers, vinyl, *t*-vinylene and vinylidene chain ends were observed. The mechanism of polymer shearing appears to be C−H scission followed by disproportionation to form olefins. The methine proton is preferentially abstracted by a ratio of more than 6 to 1, relative to a proton on a secondary carbon. Following chain scission, there is a preference toward main chain scission at the β-position.

Identification of end groups in PMMA at high field

One strategy for increasing the sensitivity of ^{1}H NMR for the detection of end groups is to make the measurements at higher field strengths. For example, the signal-to-noise ratio with a 750 MHz spectrometer is 4 times higher than that with a 500 MHz spectrometer under the same conditions [8]. The higher field of the 750 MHz suggests a higher potential for observation of the weaker signals of end groups in high molecular weight polymers. This prediction has been validated by studies of the end groups of PMMA initiated with benzoyl peroxide using a 750 MHz spectrometer (Fig. 7.2). Resonances due to end groups resulting from initiation, chain transfer and termination reactions were observed and assigned. The 750 MHz ^{1}H-NMR spectrum of PMMA prepared with BPO in toluene at 100°C is shown with the proton assignments for the various end groups.

In Chart 7.II is shown the elementary reactions and possible terminal structures in the polymerization of MMA with BPO in toluene.

The initiation reaction with BPO gives structures **I** and **II**. Chain transfer to toluene forms benzyl radicals which initiate the polymerization of MMA leading to the formation of structure **III**. Termination with primary radicals of BPO gives structures

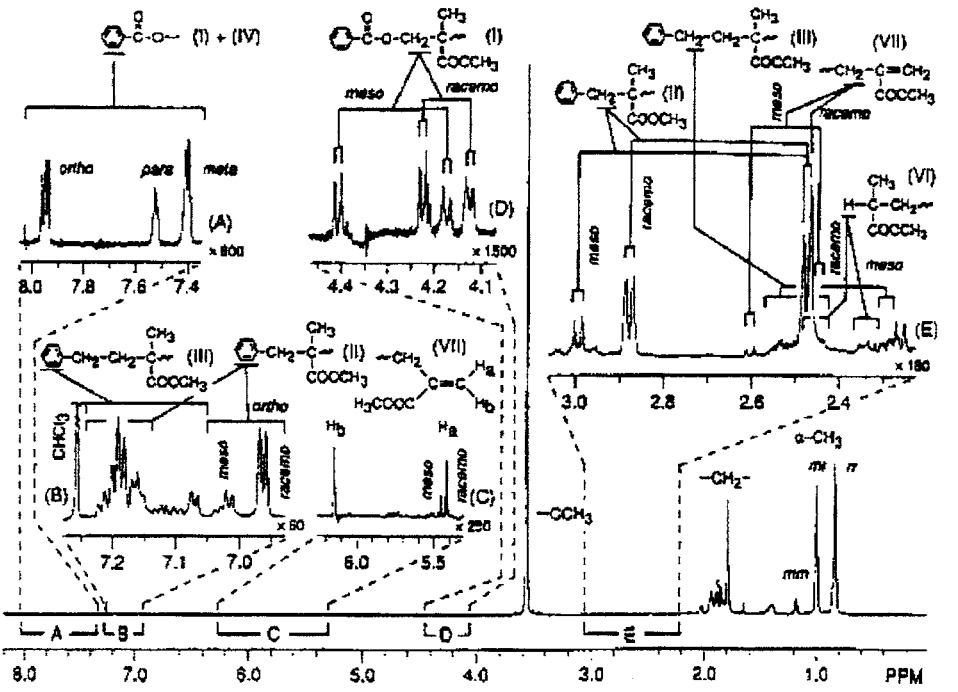

Fig. 7.2. The 750-MHz ^{1}H-NMR spectrum of PMMA prepared with BPO in toluene at 100°C is shown with the proton assignments for the various end groups. (Reproduced with permission from Ref. [8]. © 1997 American Chemical Society.)

IV and **V**. Chain transfer to BPO also forms structure **IV**. Termination of the propagating radicals by disproportionation gives end groups **VI** and **VII**. Termination by combination forms structure **VIII** in the middle of the polymer chain. Table 7.3 gives the numbers of end groups per chain for the polymerization of PMMA with BPO in toluene at 100°C.

Determination of branching in polyethylene.

By using the chemical shielding factors, the chemical shifts can be determined for a number of structural entities found in polyethylene (PE) [9], including the products of oxidation processes [10], and the types of branching [11] and crosslinking [13].

Polyethylenes prepared conventionally are structurally complex and have many versatile properties. These unusual features result from the type and concentration of the branch groups associated with a given polymer. Thus a quantitative analysis of the branching characteristics is useful. The thermodynamic, morphological, and physical properties should depend on the kind, distribution, and concentration of the branches. The ^{13}C-NMR spectra can be used to determine the nature of the branches in PE [12].

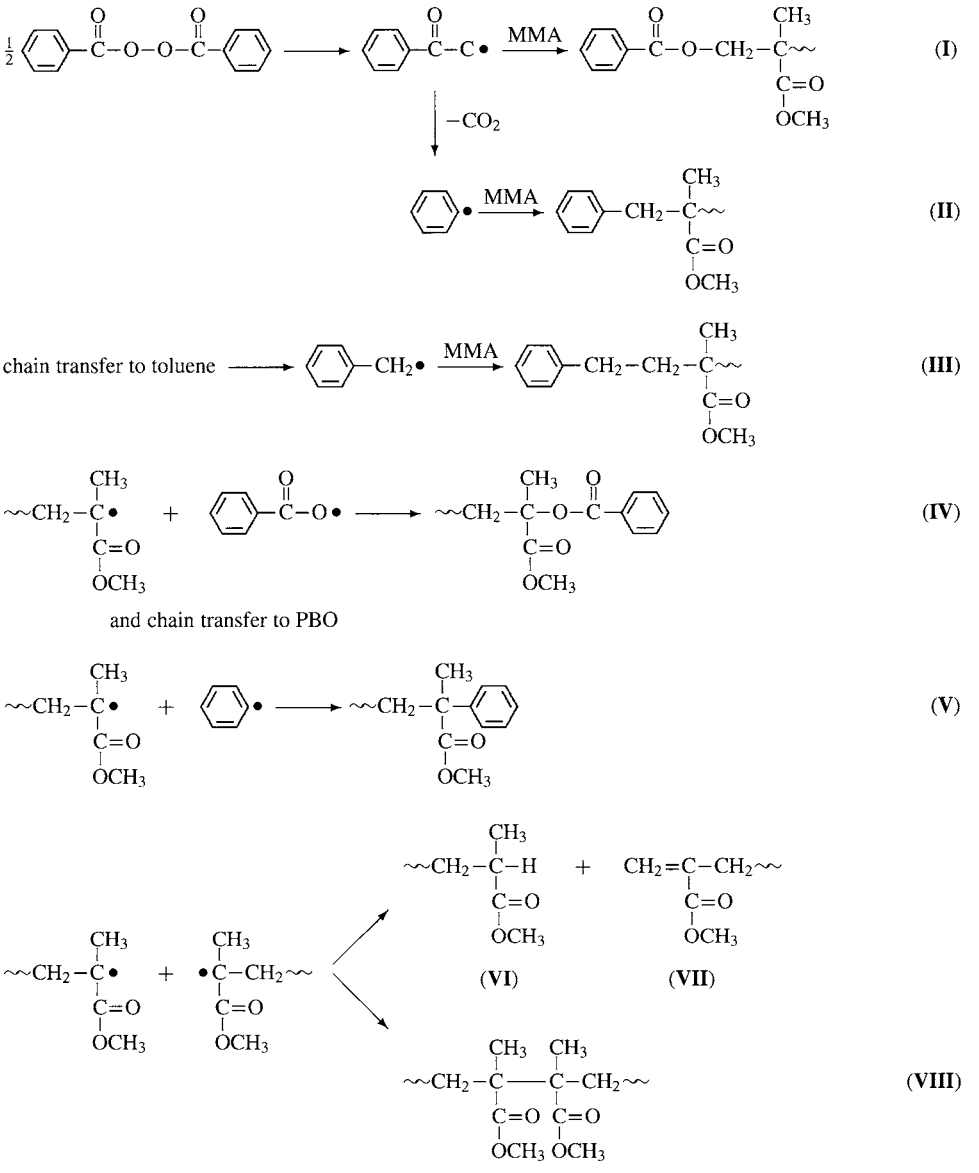

Chart 7.II. (Source: Ref. [8, scheme 1].)

Nomenclature for branch carbon resonances

The nomenclature used to designate the polymer backbone and branch carbon resonances discriminated by ^{13}C-NMR spectroscopy is as follows [12].

Branch carbon resonances, xB_y: B_y is a branch of length y carbons; x is the carbon being discussed, with the methyl at the end of the branch numbered as 1. Thus, the

Table 7.3
Numbers of end groups per chain for the polymerization of PMMA with BPO in toluene at 100°C

End group	No. of end groups per chain [1]
I	0.08_6
II	0.86_1
III	0.29_5
(I + II + III)	1.24_2
IV	0.01_4
VI	0.40_4
VII	0.19_3
Total	1.85_3

[1] Calculated from intensities of each signal and the methoxy-proton signal and the molecular weight of the PMMA sample.

resonance for the second carbon from the end of a buty branch is designated $2B_4$. xB_y^+ refers to branches of length y and longer including end-of-chain (EOC) contributions.

The methylene backbone carbons are designated by Greek symbols. The first Greek letter gives the distance in carbon atoms to the nearest branch; thus β refers to a backbone CH_2 two carbons away from a branch point. If two letters are given, the second refers to the distance from a second branch point in the opposing direction. γ^+ refers to methylenes three or more units away from a branch. The resonances are different and can be used to identify branch lengths up to six carbons, but a

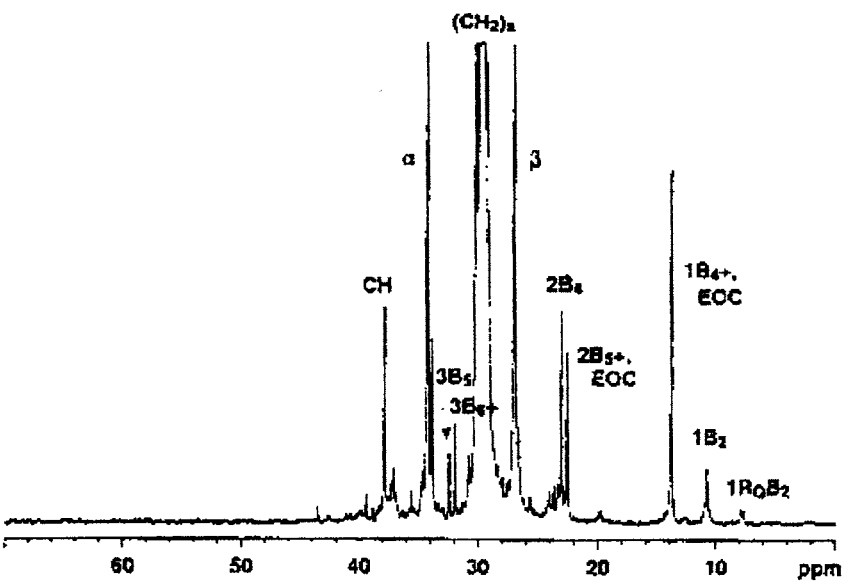

Fig. 7.3. The ^{13}C-NMR spectrum at 100 MHz of a low-density PE produced by a high-pressure process at 270°C. (Reproduced with permission from Ref. [12]. © 1997 American Chemical Society.)

six-carbon branch produces the same ^{13}C pattern as any subsequent branch of greater length. Therefore, NMR spectroscopy is not useful for the detection of long-chain branches.

For copolymers, xA_zB_y, refers to a branch containing a comonomer unit A, where z is the carbon carrying the comonomer functional group. xA_QB_y indicates that the comonomer unit is located off the backbone carbon at the branch point making it quaternary.

The ^{13}C-NMR spectrum at 100 MHz of a low-density PE produced by a high-pressure process at 270°C is shown in Fig. 7.3 [12].

The resonance assignments of the branches are given in the figure. A determination can be made of the number of each type of branch length from measurements of the areas of the respective branch peaks and are reported as number of branches per 1000 CH_2. The level of short-chain branches (branches of length 5 or shorter) increases from 6 per 1000 CH_2 at a polymerization temperature of 165°C to 20 branches for polymer prepared at 270°C. The typical short-chain branching mechanisms for ethylene homopolymerization are shown in Fig. 7.4.

The butyl branch formed from a single backbite is designated xB_4 in the spectra with x being the carbon number in the branch. The butyl and amyl$^+$ branch carbons appear in the 21–24 ppm region with the $2B_4$ peak appearing at 23.1 ppm and the $2B_5^+$ amyl peak at 22.6 ppm. The ethyl branch structures must always occur in pairs and

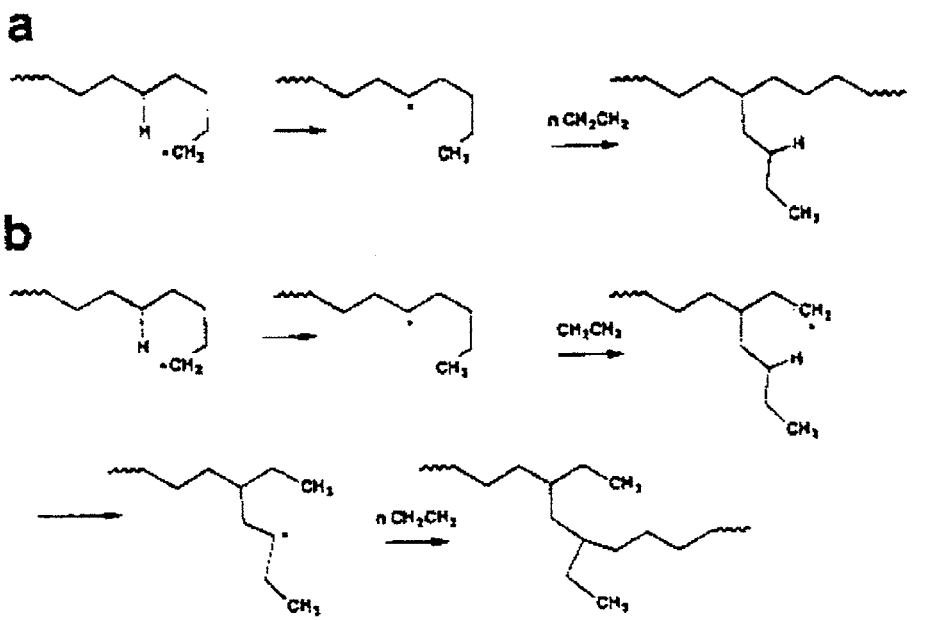

Fig. 7.4. Typical short-chain branching mechanisms for ethylene homopolymerization: (a) formation of a butyl branch (single backbite); (b) formation of paired ethyl branches (double backbite). (Source: Ref. [12, fig. 1].)

appear in the 7–12 ppm region with the ethyl $1B_2$ appearing at 10.8 ppm. The spectra reveal that only trace quantities of methyl and propyl branches are observed. This is consistent with the intramolecular H-abstraction backbiting mechanism favoring six-membered rings rather than seven-membered rings.

In addition to the ethylene homopolymers, copolymers of varying composition of *n*-butyl acrylate (*n*BA), methyl acrylate (MA), vinyl acetate (VAc), *n*-butyl methacrylate (*n*BMA) acrylic acid (AA) and methacrylic acid (MAA) were also studied for short-chain branch content. The expected types of backbiting mechanisms that may occur during copolymerization are shown in Fig. 7.5.

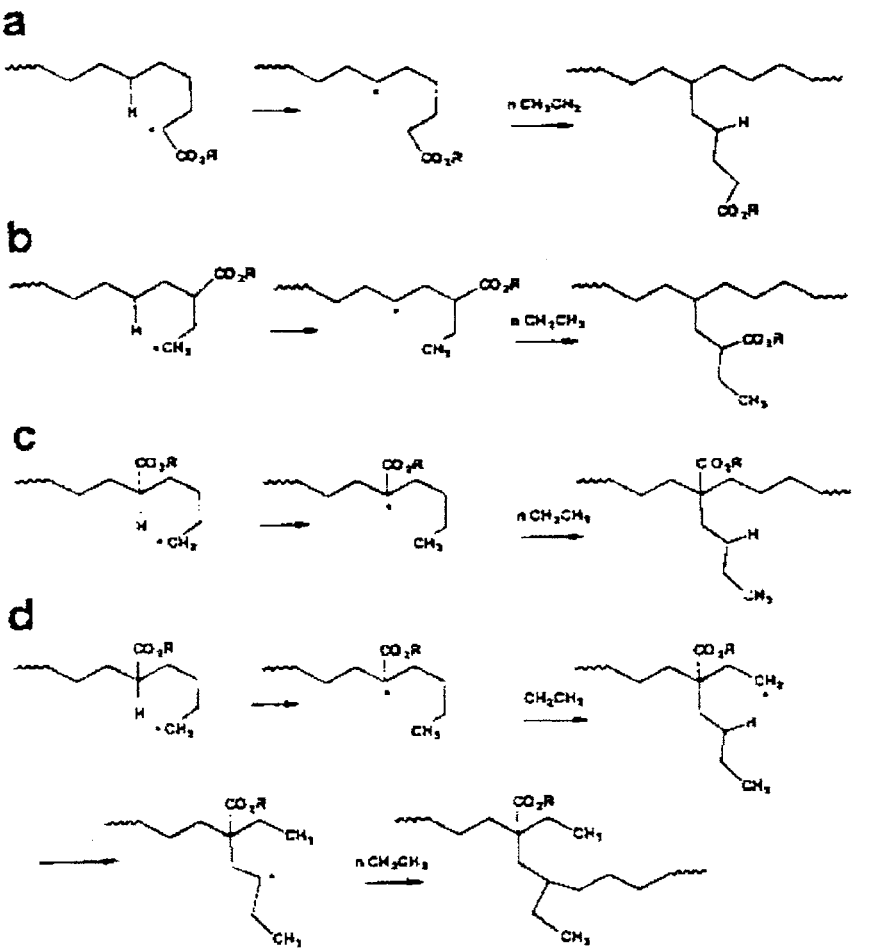

Fig. 7.5. Possible short-chain branching mechanisms involving polymerization of ethylene with an acrylate comonomer: (a) H-abstraction by a comonomer radical (formation of A_1B_4 branch); (b) H-abstraction across a comonomer unit (formation of A_3B_4 branch); (c) H-abstraction from a comonomer unit to form A_QB_4 butyl branch (single backbite); (d) double-backbite mechanism involving H-abstraction from a comonomer unit, to form paired A_QB_2-B_2 branches. (Source: Ref. [12, fig. 2].)

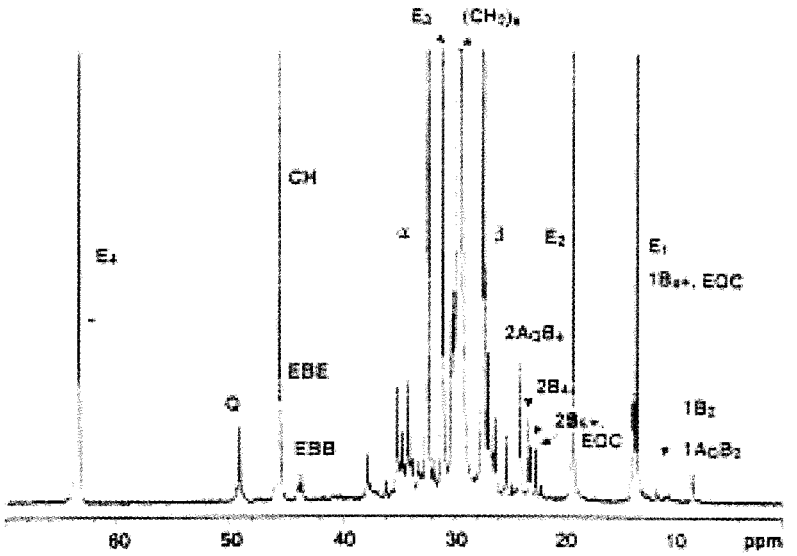

Fig. 7.6. The ^{13C}-NMR (100-MHz) spectrum of E/*n*BA copolymer (34 wt% *n*BA) synthesized at 200°C. (Reproduced with permission from Ref. [12]. © 1997 American Chemical Society.)

A considerable increase in the number of branch structures is indicated as well as contributions arising from the comonomer sequences. Therefore, the ^{13}C-NMR spectra are more complicated as indicated in Fig. 7.6.

The short-chain branch assignments are shown as well as an indication of the *n*BA sequences in the 40–50 ppm shift region including *n*BA-centered triads EBE and EBB. It was found that the ethyl and butyl branch structures increase with *n*BA content. The bulk of the evidence suggests that the H-abstraction from the *n*BA group through backbiting occurs frequently. However, within the detection limits of the NMR, *n*BA radicals do not participate in the backbiting short-chain branching mechanism. For all the copolymer systems studied by this group, there is evidence that A_3B_4 structures are formed indicating that the comonomer unit does not prevent the formation of the six-membered ring structure required for backbiting. Short-chain branches originating from comonomer units (A_QB_4 and A_QB_2) and containing comonomer units (A_3B_4) are formed.

Determination of crosslinking in polyethylene

High resolution ^{13}C NMR in solution can be used to measure the type and number of crosslinks in polymers [13]. The ^{13}C-NMR techniques possesses the required sensitivity to detect concentrations of long-chain branches (Y-type) and H-type crosslinks as low as approximately 0.5 structural units per 10,000 carbon atoms [14]. The limitation of the NMR technique is the limiting solubility arising from gel for-

mation during the crosslinking process. The NMR technique has recently been used to study the photoinitiated crosslinking of LDPE using a 100.6 MHz ^{13}C-NMR instrument. The 100.6 MHz ^{13}C-NMR spectra of unirradiated and irradiated LLLDPE samples are shown in Fig. 7.7.

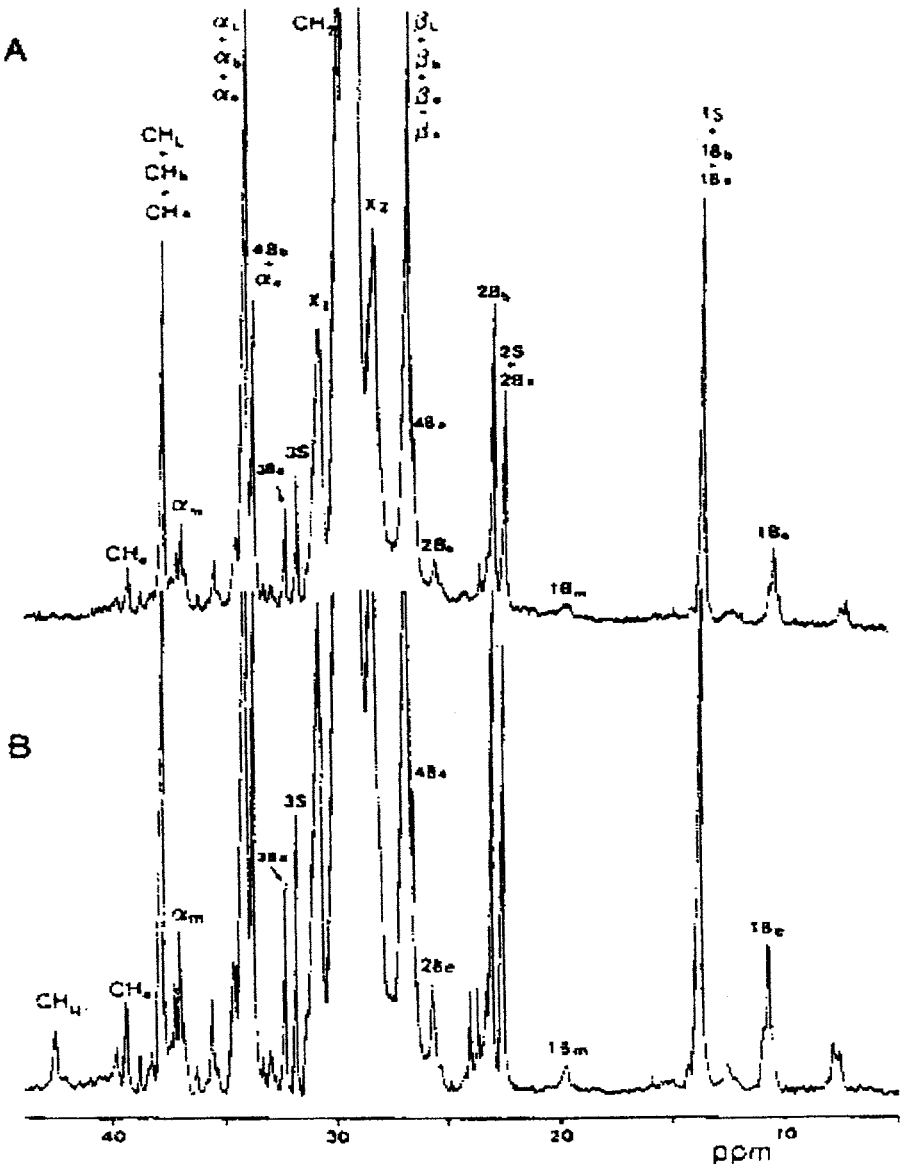

Fig. 7.7. The 100.6-MHz ^{13}C-NMR spectra of: (A) unirradiated LDPE samples measured in 20% 1,2,4-trichlorobenzene/benzene-d_6 (TCB/C_6D_6 = 80/20 v/v) and at 125°C; (B) UV-irradiated for 10 s under a nitrogen atmosphere. (Reproduced with permission from Ref. [14]. © 1997 American Chemical Society.)

Table 7.4
The ^{13}C-NMR spectral assignments for the main components of unirradiated and irradiated LDPE samples

Chemical shifts for unirradiated sample 1 (ppm)	Assignment[a]	Chemical shifts for unirradiated sample 3 (ppm)
	CH_H [b]	42.50
39.38	CH_e	39.33
37.86	CH_L [c] + CH_b + CH_a (+ CH_Y)	37.90
37.04	α_m	36.98
34.24	$\alpha_L + \alpha_b + \alpha_a (+\alpha_Y)$	34.24
33.86	$4B_b + \alpha_e$	33.74
32.39	$3B_a$	32.36
31.82	3S	31.82
30.78	$\gamma_L + \gamma_b + \gamma_a + \gamma_e (+\gamma_Y)$	30.76
29.69	$-(CH_2)_n-$	29.68
28.30	$4S + 3B_b + 3B_a$	28.17
26.98	$\beta_L + \beta_b + \beta_e + \beta_a (+\beta_Y)$	26.98
26.53	$4B_a$	26.46
25.56	$2B_e$	25.69
22.85	$2B_b$	22.78
22.47	2S	22.33
19.86	$1B_m$	19.73
13.79	$1S + 1B_b$	13.78
10.63	$1B_e$	10.62
7.78	$1B_{ee}$	7.78
7.50	$1B_{be}$	7.50

[a] L, S, and B refer to long branches, saturated end groups, and short branches; m, s, b, and a represent methyl, ethyl, butyl, and amyl groups, respectively; the Greek letter describes the position along the chain of the nearest substituent; CH_H and CH_Y represent the H-links and Y-type branche produced by UV irradiation, respectively.

[b] Abbreviations according to the following structure:

$$-\overset{\gamma}{CH_2}-\overset{\beta}{CH_2}-\overset{\alpha}{CH_2}-\overset{CH_H}{CH}-\overset{\alpha}{CH_2}-\overset{\beta}{CH_2}-\overset{\gamma}{CH_2}-$$
$$-CH_2-CH_2-CH_2-CH-CH_2-CH_2-CH_2-$$

[c] Abbreviations according to the following structure:

$$\overset{\gamma}{CH_2}-\overset{\beta}{CH_2}-\overset{\alpha}{CH_2}-\overset{CH_L}{CH}-\overset{\alpha}{CH_2}-\overset{\beta}{CH_2}-\overset{\gamma}{CH_2}-(CH_2)_n-\overset{3S}{CH_2}-\overset{2S}{CH_2}-\overset{1S}{CH_2}$$
$$\alpha\ CH$$
$$\beta\ CH$$
$$\gamma\ CH$$

(Source: Ref. [14, table 1].)

The resonance lines at 39.38 and 37.86 are assigned to ethylene branches CH_e and butyl, amyl, long chain branches (CH_b + CH_a + CH_L), and Y-type branches (CH_Y) respectively. A new resonance line at 42.50 ppm produced by irradiation is assigned to the H-links (CH_H). Table 7.4 shows the spectral assignments for the main components of unirradiated and irradiated LDPE samples.

The number of H-links was determined by ratioing the area of the 42.50 ppm resonance to the area of the rest of the spectrum. The number of Y-links was calculated as the increase in long chain branches before and after irradiation. The results are shown in Table 7.5.

As can be seen, the H-links and Y-branches are of the same order of magnitude in the irradiated samples. For the 5 and 10 s irradiation times in vacuum or N_2, the number H-links and Y-branches are 5.7–16.9 and 7.6–21.6 per 10 000 carbon atoms, respectively. Thus, in the photoinitiated crosslinking of LDPE in the melt, the

Table 7.5
Photoinitiated crosslinking yields of H-links and Y-branches for different UV-irradiated LDPE samples

Sample No.	Irradiation conditions	No. of units per 10,000 carbon atoms	
		H-links	Y-branches
2	5 s in vacuum	5.7 ± 0.5	12.6 ± 0.5
3	10 s in N_2	12.6 ± 0.5	14.7 ± 0.5
4	10 s in vacuum	16.9 ± 0.5	21.6 ± 0.5

(Source: Ref. [12, table 4].)

Y-branches are formed as efficiently as the H-links. This is in contrast to the results for γ-irradiation of HDPE where the H-links were dominant [15].

A mechanism for of photoinitiated crosslinking of LDPE has been proposed [14]. The triple state $^3(BP)^*$ abstracts hydrogen from the LPDE chain forming the following radicals:

$$-CH_2-\bullet C-CH_2-, \quad -CH_2-\bullet\underset{\displaystyle CH_2-}{CH}-CH_2-, \quad -\bullet CH_2-CH=CH_2$$

When these radicals undergo combination with each other, the H-links are formed as follows:

$$-CH_2-\underset{\displaystyle -CH_2-}{\underset{|}{CH}}-CH_2-, \qquad -CH_2-\underset{\displaystyle -CH-CH=CH_2-}{\underset{|}{CH}}-CH_2-,$$

$$-CH_2-\underset{\displaystyle -CH_2-}{\underset{|}{CH}}-CH_2-, \qquad -CH_2-\underset{\displaystyle -CH_2-}{\underset{|}{\overset{\displaystyle CH_2-}{\overset{|}{C}}}}-CH_2- \quad \text{etc.}$$

$$\qquad\qquad\quad -CH_2-\underset{\displaystyle CH_2-}{\overset{|}{C}}-CH_2-$$

The Y-branches are formed by addition of the above radicals to vinyl end groups that are formed during the photoinitiated free-radical process except for the original ones in the LPDE sample.

Determination of thermal oxidation in polyethylene

NMR spectroscopy is very useful for the study of polymer degradation. NMR spectroscopy can be used to distinguish between the various degradation products at an early stage of degradation and to produce detailed chemical identification and quantification of the oxidized species. The chemical shifts of the CH_2 groups that are α and β to carbons bearing oxygen can be used to identify the oxidation sites. The types of spectral differences are shown in Fig. 7.8.

The NMR results indicate the following distribution of oxidation products for the polyethylene sample that initially had 17.7 branches per 1000 CH_2 groups: ketone,

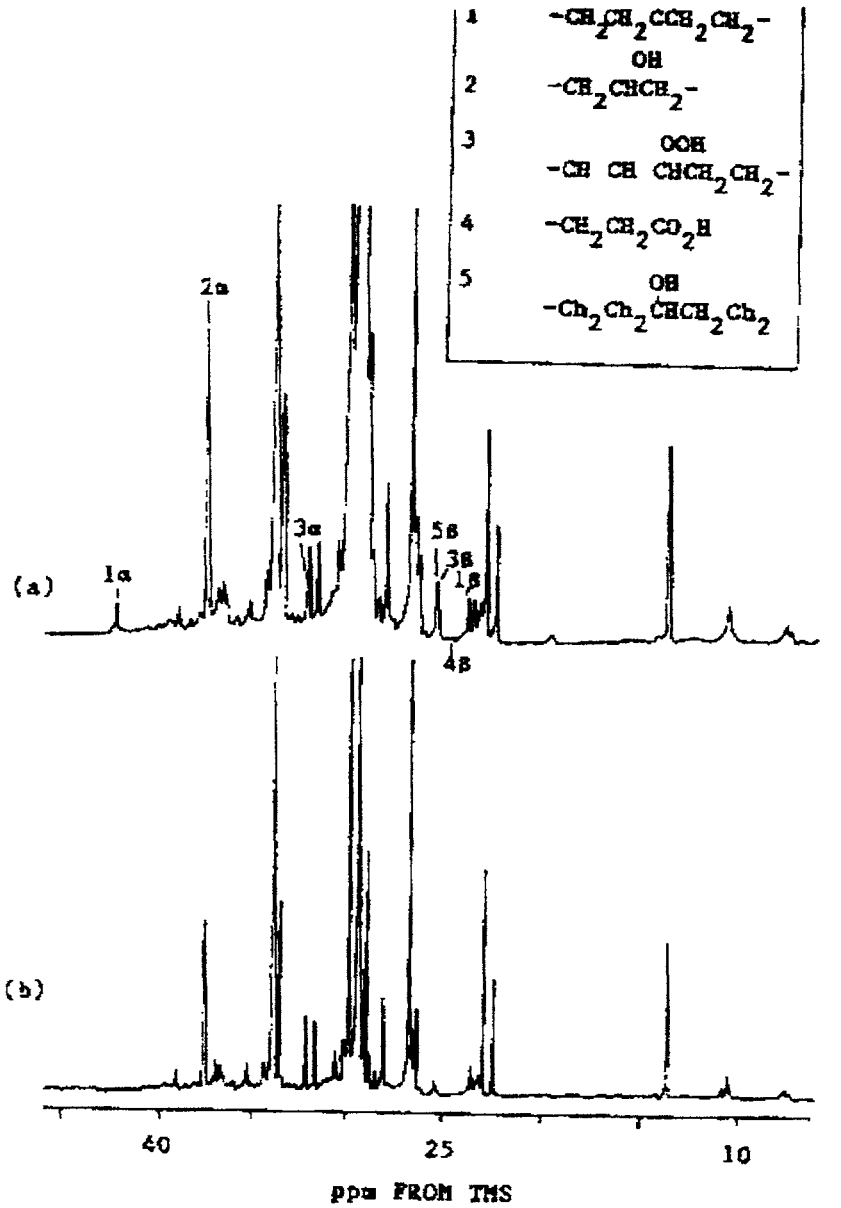

Fig. 7.8. ^{13}C-NMR spectra of the CH_2 region of an oxidized PE sample (a) and a control sample (b). The peak assignments are shown in the insert. (Reproduced from Ref. [10, fig. 1]. © 1984 American Chemical Society.)

18%; secondary alcohol, 40%; tertiary alcohol, 7%; carboxylic acids, 4%; and secondary hydroperoxides, 32%. The total amount of oxygen was 0.6%. Some conversion of hydroperoxide to secondary alcohol occurs during the process of dissolution and recording of the NMR spectra.

Determination of stereoregularity of polymers

> *A polymer chain is a permanent record of the statistical chain of events which constituted the polymerization process. From its microstructure, it is possible to identify the various monomer reactions modes, to measure their relative rates, and even — at least in principle — to infer their interdependence: the longer the chain segment that can be examined, the richer is its message.*
>
> — Busico et al. [20]

The stereoregularity of virtually all commercially available polymers has been determined by high-resolution ^{1}H- and ^{13}C-NMR spectroscopy [16,17] and the importance of tacticity in establishing the properties of polymers is well established.

Nomenclature for NMR resonances for stereoregular polymers

Tacticity in NMR is represented by the relative configuration of pair wise units. A typical ^{13}C-NMR spectrum of an atactic vinyl polymer in solution consists of numerous relatively sharp lines, that are assigned to the various sequences of *meso* (*m*) and *racemic* (*r*) dyads. These new lines are a result of *configurational* splitting. *Meso* (*m*) or *isotactic* dyads have the same optical configurations (dd or ll). *Racemic* (*r*) or *syndiotactic* dyads are pairs of adjacent asymmetric centers that have opposite optical configuration (dl). Triads, tetrads, pentads, etc., are denoted by a succession of dyads.

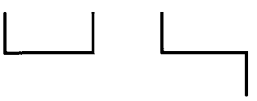

meso (m)	*racemic (r)*
isotactic	syndiotactic

In ^{1}H-NMR spectroscopy, molecules having CM_2 groups (where M is an observable nucleus) are termed *geminally heterosteric* when the M groups can be differentiated because of differences in their average environments and are termed *geminally homosteric* when the M groups are equivalent. For the isotactic placement, or meso dyad (m), the protons of each methylene group do not experience the same average environment and have different chemical shifts. The methylene protons are heterosteric, and the AB quartet of lines is observed (Fig. 7.9).

For a syndiotactic placement of a vinyl monomer, the protons in the methylene groups are racemic and have the same average environment and, in the absence of vicinal coupling, are not distinguishable. Consequently, a single line resulting from the syndiotactic placement or racemic dyad (r) is observed. On this basis,

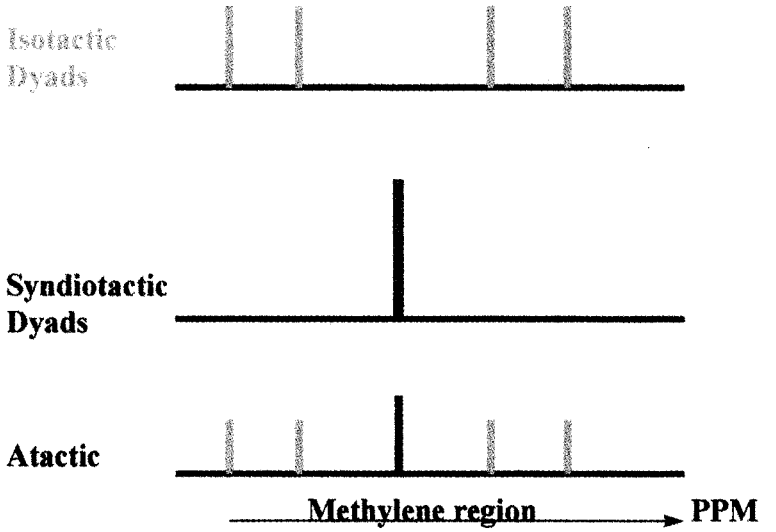

Fig. 7.9. The methylene regions shows the AB quartet of lines for the isotactic configuration and a single line for the syndiotactic configuration. The atactic structure exhibits all the lines as it is a combination of syndiotactic and isotactic dyads.

^{1}H-NMR spectroscopy can be used to distinguish on an absolute basis the isotactic and syndiotactic dyads of some vinyl polymers. The atactic polymer is a combination of isotactic and syndiotactic dyads and so all five lines appear.

Poly(methyl methacrylate) (PMMA) was the first polymer studied in this manner and the interpretation of the corresponding ^{1}H-NMR spectra illuminated the nature of the tacticity. The methylene proton spectrum of the anionically initiated polymer exhibits an AB quartet (J_{gem} = 14.9 Hz) centered 1.86 ppm and therefore this polymer is predominately isotactic. In the spectrum of the free-radical polymer, the methylene-proton resonance is a broad singlet, and so this polymer is predominately syndiotactic. This interpretation of the stereoregularity of these two polymers is a direct result of the expectations illustrated in Fig. 7.9.

Additionally, three resonances are observed for the α-methyl proton resonances which exhibit substantially different relative intensities between the two polymers. These three resonances are assigned to the stereoregular triad sequences. Those monomer units that are flanked on both sides by units of the same configuration are termed *isotactic triads* (*i*). Those monomer units that have units of opposite configuration on both sides are *syndiotactic triads* (*s*). Those monomer units that have a unit of the same configuration on one side and a unit of opposite configuration on the other side are *heterotactic triads* (*h*). These three triad α-methyl resonances have the same chemical shifts in the spectra of the different stereoregular polymers but have very different intensities in each spectrum. The relative intensities of these α-methyl proton triad resonances provide a measure of the triad probabilities.

As the magnetic strength is increased, longer configurational sequences can be

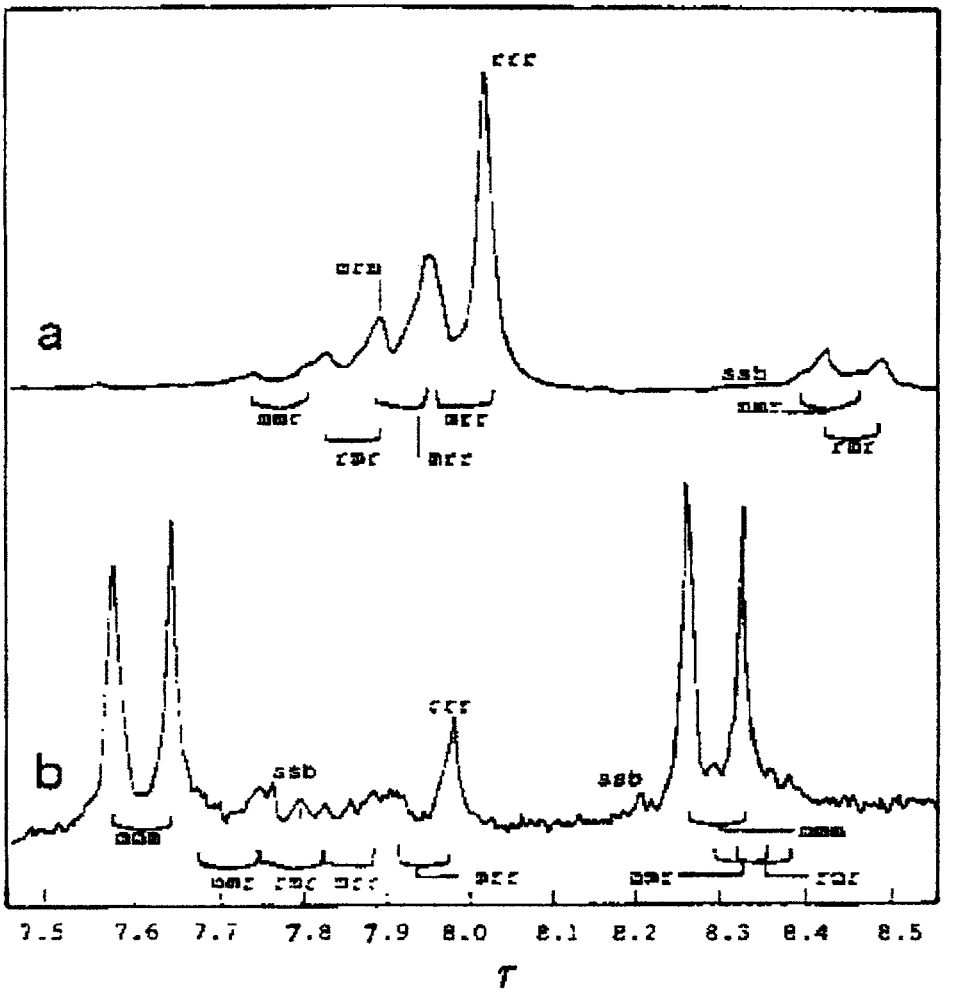

Fig. 7.10. The proton resonance spectra of the β-CH_2 units of syndiotactically rich (a) and isotactically rich (b) samples of PMMA at a high-field strength of 220 MHz. (Source: Ref. [1].)

observed. The proton-resonance spectra of the β-CH_2 units of the two samples of PMMA at a high-field strength of 220 MHz are shown in Fig. 7.10.

For the β-methylene groups, the tetrad (and perhaps even the hexad) resonances appear as fine structure on the m and r dyad resonances. The assignments are superimposed on the spectra. The m peak shows additional resolved resonances resulting from mmm, mmr, and rmr placements. Substitution of an outside m with an r results in a downfield shift. When adding placements on either side, the change in chemical shift on substituting an m for an r is just the opposite.

For the α-methyl groups, pentad and heptad sequences may be observable at high resolution (Fig. 7.11).

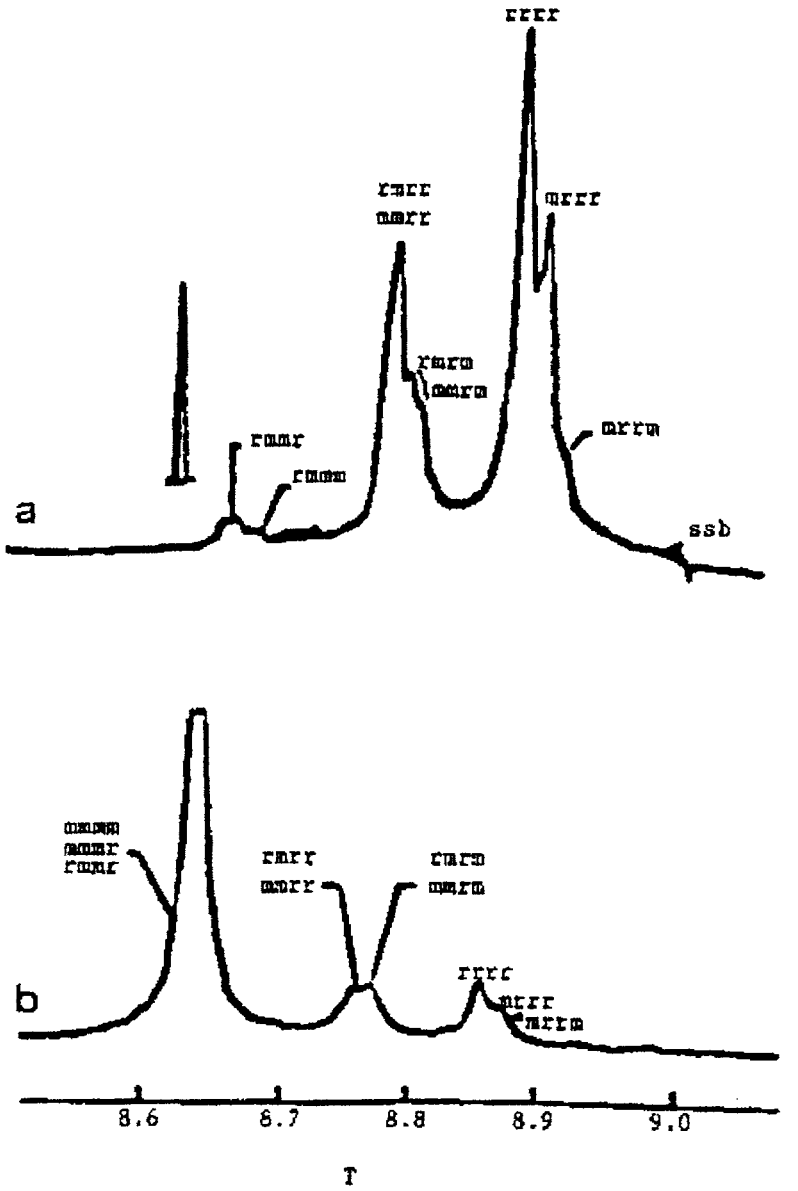

Fig. 7.11. The high-field resonance spectra of the α-CH_3 groups of syndiotactically rich (a) and isotactically rich (b) samples of PMMA at a high-field strength of 220 MHz. (Source: Ref. [1].)

The relative concentrations of the longer configurational sequences can be calculated by using probability theory and the appropriate polymerization model. The manner in which the relative proportions of the various sequences can be calculated for the Bernoullian or terminal model of the stereochemical polymerization is shown in Table 7.6.

Table 7.6
Stereochemical sequence designation and Bernoullian probabilities

Designation	Projection	Bernoullian probability
α-CM_3 substituent,	triad	
isotactic, mm	(i)	P_m^2
heterotactic, mr	(h)	$2P_m(1 - P_m)$
syndiotactic, rr	(s)	$(1 - P_m)^2$
	pentad	
mmmm		P_m^4
mmmr		$2P_m^3(1 - P_m)$
rmmr		$P_m^2(1 - P_m)^2$
mmrm		$2P_m^3(1 - P_m)$
mmrr		$2P_m^2(1 - P_m)^2$
rmrm		$2P_m^2(1 - P_m)^2$
rmrr		$2P_m(1 - P_m)^3$
mrrm		$P_m^2(1 - P_m)^2$
rrrm		$2P_m(1 - P_m)^3$
rrrr		$(1 - P_m)^4$
β-CM_2 substituent,	dyad	
meso, m		P_m
racemic, r		$(1 - P_m)$
	tetrad	
mmm		P_m^3
mmr		$2P_m^2(1 - P_m)$
rmr		$P_m(1 - P_m)^2$
mrm		$P_m^2(1 - P_m)$
rrm		$2P_m(1 - P_m)^2$
rrr		$(1 - P_m)^3$

Similar calculations can be performed for more complex mechanisms such as the penultimate and penpenultimate models.

The differences in stereoconfiguration between odd and even numbers of units in vinyl polymers like PVC are reflected in the splitting of the CH and CH_2 carbon resonances. The number of signals from CH and CH_2 groups is shown in Table 7.7

Table 7.7
Numbers of signals of CH and CH_2 groups for monosubstituted vinyl systems in ^{13}C-NMR spectra

CH group (triad)	Pentad	Heptad	CH_2 group (tetrad)	Hexad	Octad
rr	3	10	rrr	3	10
rm	4	16	rmr	3	10
mm	3	10	rrm	4	16
			mrm	3	10
			mmr	4	16
			mmm	3	10

for the various sequences. As the magnetic field strength increases, the resolution increases and longer sequences can be observed so the amount of available information improves.

A particularly good example is atactic polypropylene (PP) for which 20 heptad resonances out of a possible 36 have been clearly resolved. The 90-MHz ^{13}C-NMR spectrum of atactic polypropylene is shown in Fig. 7.12.

The lines on the figure represent the positions of the CH_3, CH_2, and CH sequences that were calculated by using the γ-gauche effect, which will be discussed later.

When the resonance assignments to the stereoconfigurational sequences have been made the stereoconfigurational propagation mechanism can be determined. Accurate peak areas must be obtained. The unconditional probability of occurrence of any

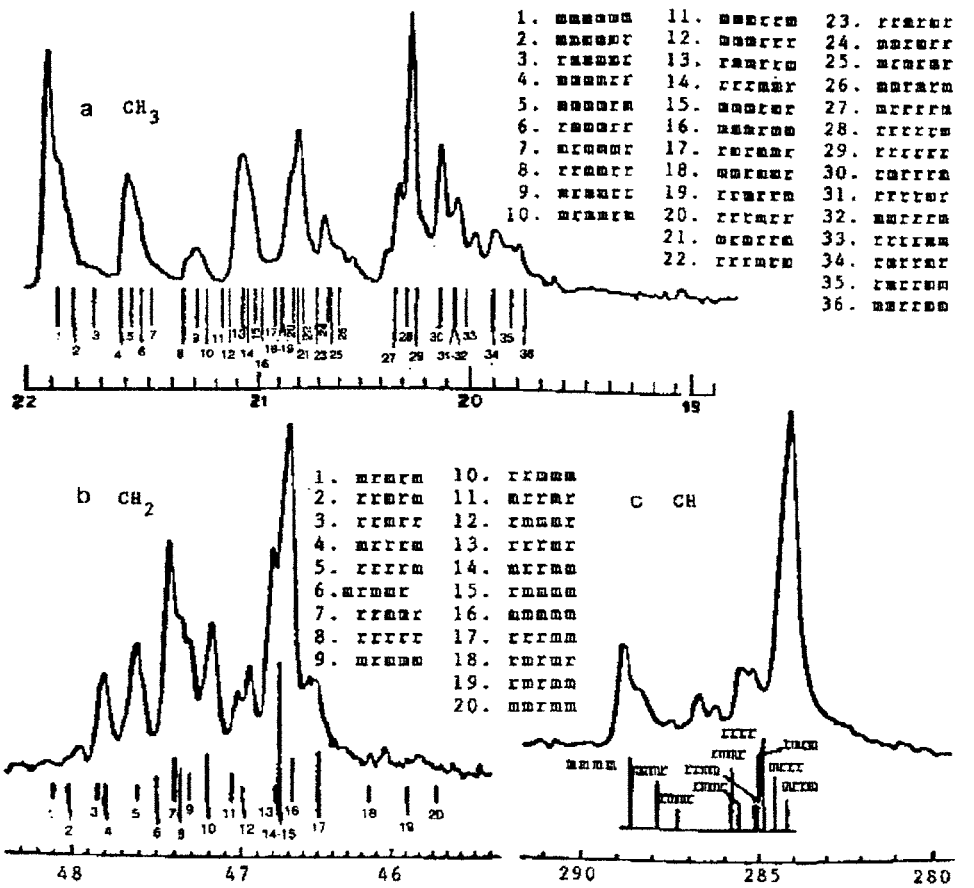

Fig. 7.12. The 90-MHz ^{13}C-NMR spectra of atactic polypropylene in a 20% (w/v) solution of heptane at 67°C; (a) CH_3, (b) CH_2, and (c) CH. Line spectra appearing below the experimental spectra correspond to theoretically calculated resonance positions for (a) heptad, (b) hexad, and (c) pentad configurational sequences. (Reproduced with permission from Ref. [1]. © 1988, Academic Press.)

Table 7.8
The peak intensities for stereo sequences in PMMA from a free-radical polymerization

	Stereochemistry	Observed	Bernouilli trial, $P_m = 0.24$
Dyad	(m)	0.24	
	(r)	0.76	
Triad	(mm)	0.04	0.06
	(mr)	0.36	0.36
	(rr)	0.60	0.58
Tetrad	(mmm)	~0.00	0.01
	(mmr)	0.07	0.09
	(rmr)	0.19	0.20
	(mrm)	0.04	0.04
	(mrr)	0.23	0.23
	(rrr)	0.43	0.44
Pentad	(mmmm)	~0.00	0.003
peak 1	(rmmr)	0.05	0.03
peak 2	(mmmr) (rmrr)	0.02	
peak 3	(mmrr)	0.25	0.27
peak 4	(rmrm)	0.06	0.07
peak 5	(mmrm)	0.02	0.02
peak 6	(rrr)	0.40	0.39
peak 7	(mrrr)	0.14	0.16
peak 8	(mrrm)	0.05	0.03

(Source: Ref. [3, table 2.1].)

particular sequence S is simply its peak area, $A(S)$, divided by the total resonance area of the carbon under observation.

Triad data are necessary and sufficient to test for conformance to Bernoullian statistics, but tetrad data are required to test first-order Markov statistics if the former treatment is inappropriate. For Bernoullian statistics, P_m can be calculated directly from the ratio of the areas, $A(rr)/A(rm)$, which is equal to $(1 - P_m)/P_m$.

By comparing the NMR resonance intensities with the predicted values given by the Bernoullian and first-order Markov (or higher), one can investigate the stereospecific polymerization mechanism. This approach has been used to define the mechanism for the free radical and anionically polymerized PMMA. The peak intensities for the measured stereosequences in PMMA from a free-radical polymerization are shown in Table 7.8. Using a probability of isotactic addition (P_m) equal to 0.24, the fraction of the triad, tetrad and pentads was compared with the measured values. The agreement suggests that the Bernoullian mechanism applies.

In similar fashion the peak intensities for the measured stereosequences in PMMA from an anionic polymerization are shown in Table 7.9.

In this case the results are compared for the first-order Markov, second-order Markov and the Coleman Fox model. For the first-order Markov, the sequence intensities are calculated from the values of the conditional probability obtained from the

Table 7.9
The peak intensities for stereo sequences in PMMA from a free-radical polymerization

	Stereochemistry	Observed	Markov		Coleman–Fox
			first-order	second-order	
Dyad	(m)	0.82			
	(r)	0.18			
Triad	(mm)	0.75			
	(mr)	0.14			
	(rr)	0.11			
Tetrad	(mmm)	0.70	0.69	0.70	0.70
	(mmr)	0.09	0.13	0.09	0.09
	(rmr)	0.03	0.006	0.03	0.02
	(mrm)	0.04	0.03	0.04	0.04
	(mrr)	0.06	0.09	0.06	0.06
	(rrr)	0.07	0.07	0.07	0.08
Pentad					
peak 1	(mmmm) (mmmr) (rmmr)	0.75	0.75	0.77	0.74
peak 2	(rmrr) (mmrr)	0.07	0.09	0.06	0.07
peak 3	(rmrm) (mmrm)	0.07	0.05	0.08	0.08
peak 4	(rrr)	0.07	0.04	0.05	0.07
peak 5	(mrrr) (mrrm)	0.04	0.07	0.05	0.05

(Source: Ref. [3, table 2.2].)

triad analysis. For the second-order Markov model, the conditional probabilities were calculated from the observed triad and tetrad intensities. The Coleman–Fox model is a two state model and the method computation is slightly complex [18]. For our purposes, it is only necessary to observe that the agreement of the Coleman–Fox model is at least as good as that of the second-order models.

The differences between the activation enthalpies and entropies for meso and racemic placement can be obtained from a plot of $\ln(P_m/P_r)$ against reciprocal temperature. Thus,

$$\ln\left(\frac{P_m}{P_r}\right) = \ln\left(\frac{k_m}{k_r}\right) = \left(\frac{\Delta S^m}{R}\right) - \left(\frac{\Delta H^m}{RT}\right)$$

where k_m and k_r are the rates of meso and racemic addition, respectively.

In general, polymers prepared by using free-radical initiators are predominantly syndiotactic, and the tendency to form syndiotactic sequences increases as the polymerization temperature is lowered. The propagation reaction can be regarded as being subdivided into two fundamental reactions, that is, isotactic and syndiotactic propagations. In this way, the placement of a given unit (isotactic or syndiotactic) is not determined until after the next unit has been added to the end of the growing radical. This is because the end unit itself, being a free radical, is unable to maintain asymmetry and is either planar or oscillating rapidly between the two possible tetrahedral

configurations. Therefore, there is not a permanent spatial position for the terminal carbon radical. However, the α-substituted atom of the penultimate unit does take up a single tetrahedral configuration and must be either isotactic or syndiotactic with respect to the previous asymmetric carbon. Theoretically, syndiotactic propagation should be slightly favored energetically (for steric reasons) over isotactic propagation in the free species.

More detailed studies have revealed that the stereochemical propagation can occur by several different mechanisms. Two general kinds of mechanisms can be identified: one is chain-end controlling and the other is catalytic-site controlling. Free radical, anionic and most cationic polymerizations are chain end controlled, whereas many Ziegler–Natta polymerizations are catalytic-site controlled [19].

In catalyst systems developed for polypropylene like the 'single site' metallocene catalysts, highly isotactic polypropylene structures with configurational defects are obtained by a chain-end mechanism of stereocontrol. For catalytic polymerizations where the tacticity is high, configurational defects can be recognized.

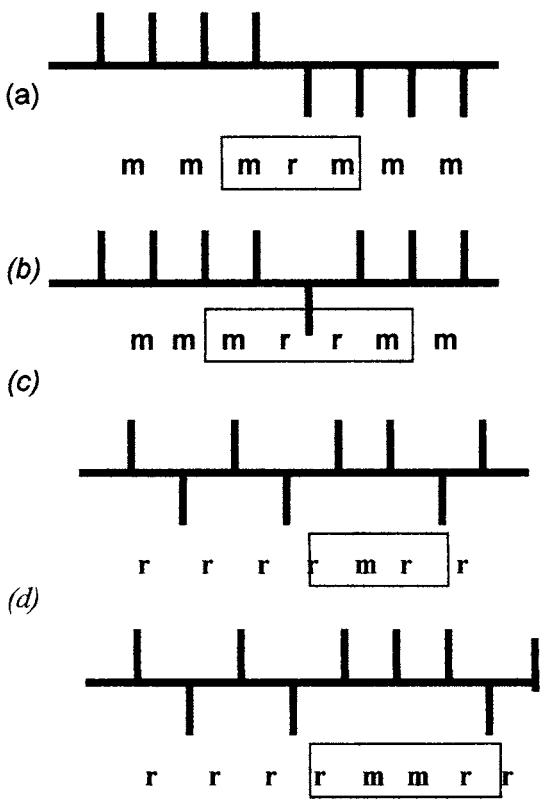

Fig. 7.13. Diagram of types of stereodefects existing in highly stereoregular polymers (see text for details of mechanisms for the formation of the different types of defects).

As shown in Fig. 7.13a, an isotactic structure with isolated stereodefects of the type ... mmmrmmm ... which results from a chain-end mechanism using single site metallocene catalysts. In Fig. 7.13b, an isotactic structure is made with randomly distributed stereodefects of the type mmmrrmm ..., which can be described in terms of enantiomorphic-site statistics. In Fig. 7.13c, there are rrrmrr stereoeffects as a result of a chain migratory propagation mechanism. In Fig. 7.13d, a rrmmrr structure occurs arising from occasional monomer misinsertions.

Using high-field NMR it is possible to detect the presence of these defects in isotactic and syndiotactic polypropylene prepared with special catalyst systems [20]. The 150-MHz ^{13}C-NMR spectra (Fig. 7.14) are shown of the methyl region of four model polypropylene samples A–D dissolved in 1,1,2,2-tetrachloroethane-d_2 at 70°C. Polymer A was obtained in the presence of the catalyst system bis(cyclopentadienyl)-$TiCl_2$/methylalumoxane at low temperature (m $\sim$ 0.80) (see also Table 7.10). Polymer B was prepared with the catalyst system *rac*-ethylenebis(4,5,6,7-tetrahydro-1-indenyl)$ZrCl_2$ (m $\sim$ 0.70). Polymer C was prepared in the presence of (methyl)$_2C$(cyclopentadienyl)(9-fluorenyl)$ZrCl_2$ (r $\sim$ 0.80). Polymer D is a hemiisotactic polypropylene obtained from the catalyst system (methyl)$_2C$(cyclopentadienyl)(9-fluorenyl)-$ZrCl_2$/methylalumoxane.

The agreement between the calculated positions of the resonances for the different sequences is excellent. The relative fractions calculated from the chain-end model with $P(\mathrm{m}) = 0.79_9$ also shows good agreement with the experimental values. It is clear that the high field measurements are revealing new and valuable information about the stereospecific polymerization of polypropylene.

Determination of directional isomerism in polymers

There is a directional form of structural isomerism due to the enchainment in polymers, namely *regioisomerism*, that is isomerism arising from head–tail, head–head, and tail–tail additions of an asymmetrical monomer unit (Fig. 7.15).

Nomenclature for regioisomerism

The simplest example is the addition of a vinylidene monomer, M, such as poly(vinylidene fluoride), which is directional by virtue of an asymmetrical arrangement of substituents about the double bond (i.e., protons at one end and X atoms at the other). The head will be designated as the substituted end ($=CX_2$), and the other end will be designated as the tail, that is, the CH_2 portion of the unit. Thus a sequence of M units may have head–head (CX_2-CX_2), head–tail (CX_2-CH_2), or tail–tail (CH_2-CH_2) junctions. A given structure is designated *isoregic*, *syndioregic*, and *aregic* for sequences in which the directional sense of successive monomer units is the same, alternating, or random, respectively [21].

Table 7.10
Assignments of the methyl resonances in the 150-MHz ^{13}C spectrum of polymer A obtained in the presence of the catalyst system bis(cyclopentadienyl) $TiCl_2$/methylalumoxane at low temperature ($m \sim 0.80$)

Range/peak number	Assignment	δ(exp) ppm (TMS)	δ(calc) ppm (TMS)	% fraction	
				expected	calculated [1]
I	mmmm	22.0–21.7		40.0	40.8
1	mmmmmmmm	21.94	21.933		16.6
2	mmmmmmmmrm	21.92	21.899		5.3
3	mmmmmmrr	21.89	21.834		2.1
5	mmmmmmmrmr	21.87	21.819		1.3
6	mmmmmmmrmm	21.84	21.811		5.3
	+ rmmmmmmrmm		21.798		1.3
8	rmmmmmrm	21.82	21.773		2.1
9	mrmmmmrm	21.75	21.685	1.0	1.0
II	mmmr	21.7–21.4		20.9	20.5
10	mmmmmrrm	21.61	21.660	1.8	2.1
13	mmmmmrmr	21.58	21.596		2.1
	+ mmmmmrmm		21.574		8.4
14	rmmmmrmm	21.56	21.538		2.1
15	rmmmrr	21.52	21.538		0.8
	+ rrmmmrmm		21.474	1.8	0.5
	+ mrmmmrmr		21.472		0.5
16	mrmmmrmm	21.49	21.450	2.4	2.1
III	rmmr	21.4–21.2		2.5	2.6
20	mrmmrr	21.30	21.298		0.8
21	mrmmrm	21.28	21.230		1.7
IV	mmrr	21.2–21.0		4.7	5.2
22	mmmrrm	21.13	21.183	3.3	3.3
V	mmrm + rmrr	21.0–20.7		22.8	21.8
24	mmmrmr	20.97	21.030	3.2	3.4
25	mmmmrmmr	20.91	21.005	2.0	2.1
26	mmmmrmmm	20.86	20.986		8.4
	+ rmmmrmmm		20.947		2.1
30	mrmmrmmm	20.77	20.848	2.1	2.1
VI	rmrm	20.7–20.5		4.8	5.2
31	rrmrmr	20.67	20.730	0.3	0.2
32	rrmrmm	20.63	20.672	1.0	0.8
33	mrmrmr	20.60	20.652	1.0	0.8
34	mrmrmm	20.55	20.592	2.5	3.3
VII + VIII	rrrm + rrrr	20.5–20.0		1.7	1.5
40	mrrrmm	20.07	20.083	0.6	0.8
IX	mrrm	20.0–19.7		2.5	2.6
45	mmmrrmmr	19.8	19.773	0.5	0.5
46	mmmrrmmm	19.75	19.743	1.1	1.0

[1] According to the chain-end model with $P(\mathrm{m}) = 1 - P(\mathrm{r}) = 0.79_9$.
(Data taken from Ref. [20, table 1].)

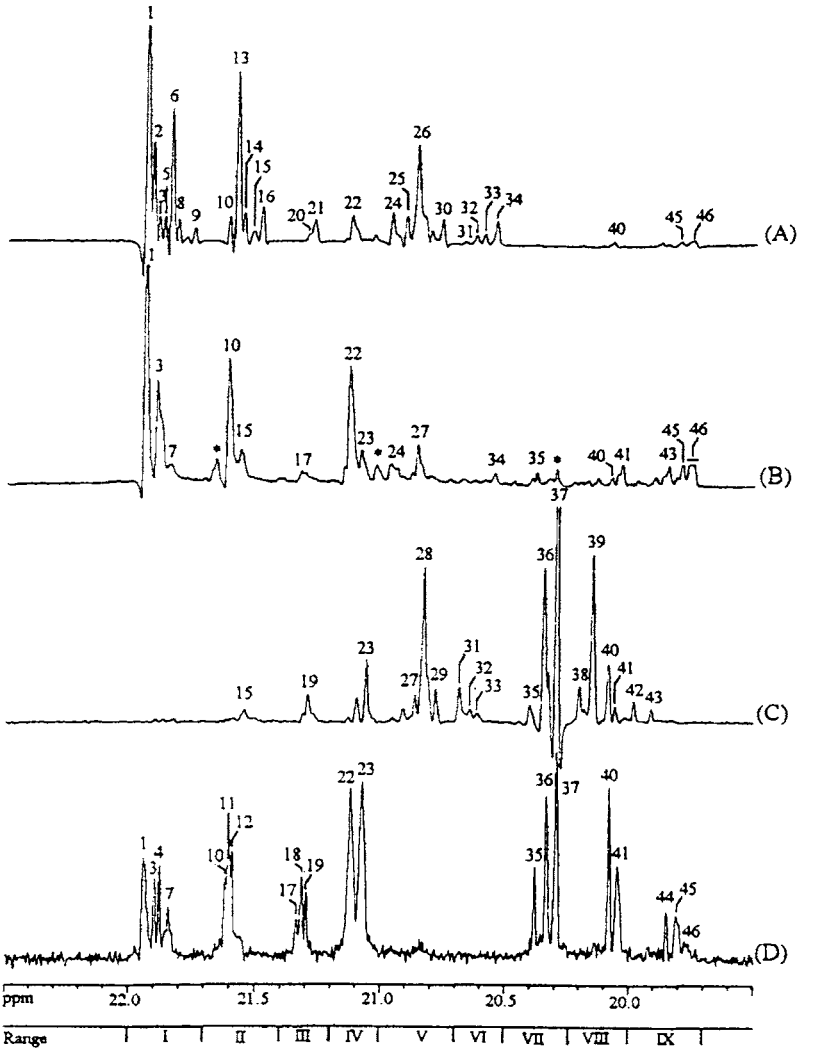

Fig. 7.14. The 150-MHz ^{13}C-NMR spectra are shown of the methyl region of four model polypropylene samples A–D dissolved in 1,1,2,2-tetrachloroethane-d_2 at 70°C. Polymer A was obtained in the presence of the catalyst system bis(cyclopentadienyl)$TiCl_2$/methylalumoxane at low temperature ($m \sim 0.80$). Polymer B ws prepared with the catalyst system *rac*-ethylene-bis(4,5,6,7-tetrahydro-1-indenyl)$ZrCl_2$ ($m \sim 0.70$). Polymer C was prepared in the presence of (methyl)$_2C$(cyclopentadienyl)(9-fluorenyl)$ZrCl_2$ ($r \sim 0.80$). Polymer D is a hemiisotactic polypropylene obtained from the catalyst system (methyl)$_2C$(cyclopentadienyl) (9-fluorenyl)$ZrCl_2$/methylalumoxane. The Roman numerals at the bottom of the spectra represent the regions of the pentad resonances and the numbers on the peaks are for the heptad resonances. (Source: Ref. [20, fig. 1].)

Regioisomerism studies

Poly(vinylidene fluoride) (PVF_2) is a simple example of regioirregular sequences in homopolymers, because PVF_2 does not have the stereoconfigurational irregularity

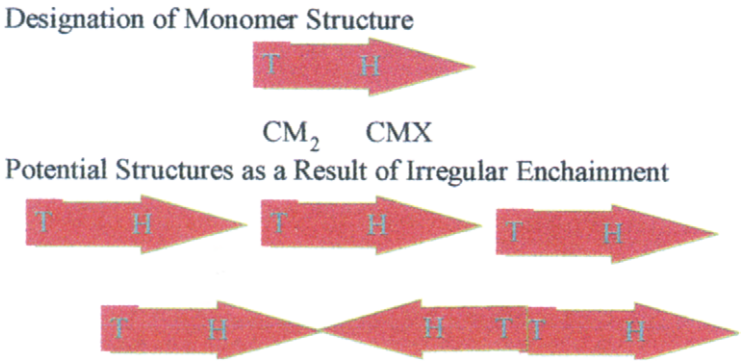

Fig. 7.15. Designation of vinyl monomer repeating unit as head (CMX) and tail (CM_2) and the resulting irregular enchainment structures which can occur.

that complicates the spectra of other polymers. The 188.22-MHz ^{19}F-NMR spectrum of PVF_2 dissolved in dimethylformamide is shown in Fig. 7.16.

The resonances can be assigned to heptad sequences, and for convenience, the head of M will be represented by 1 and the tail will be represented by 0. The resonance assignments are listed in Table 7.11.

The relative intensities of the resonances can be used to determine the nature of the mechanism for regiospecific addition. In the case of PVF_2, the data are highly

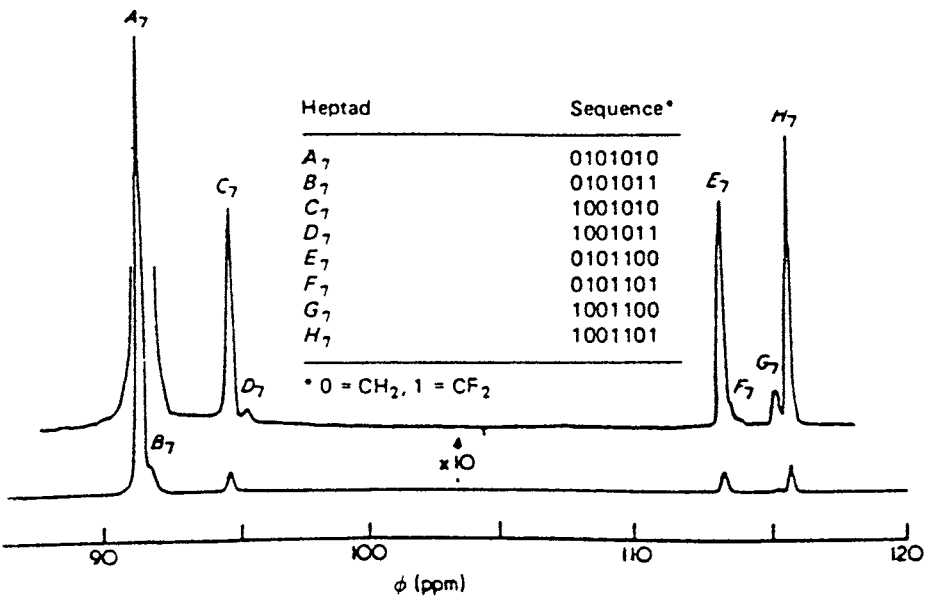

Fig. 7.16. The ^{19}F-NMR spectrum of PVF_2 dissolved in dimethylformamide is shown with the heptad assignments (insert). (Reproduced with permission from Ref. [1]. © 1988, Academic Press.)

Table 7.11
Assignments of heptad sequences for the ^{19}F-NMR spectrum of PVF_2

Heptad	Sequence [1]	Chemical shift (±0.05)
A_7	0101010	91.31
B_7	0101011	91.79
C_7	1001010	94.43
D_7	1001011	95.37
E_7	0101100	113.33
F_7	0101101	113.62
G_7	1001100	115.34
H_7	1001101	115.76

[1] 1 = head, 0 = tail.

suggestive of a first-order Markov-enchainment mechanism rather than a Bernoullian mechanism.

Determination of copolymer structure

As a technique for the analysis of sequence distribution in copolymers, high-resolution NMR spectroscopy is particularly useful when the spectral resolution is sufficient to resolve the resonances of the specific sequences. A number of copolymer structural problems can be elucidated by using NMR spectroscopy. The composition of the copolymer can be quantitatively determined. The detection of compositional dyads can be used to determine the distribution of composition, that is, whether the sample is a mixture of homopolymers, a block copolymer, an alternating copolymer, or a random copolymer (see Chapter 1). If resonances are resolved due of the triad sequences of the copolymer, sequence distributions can be determined, and the mechanism of the copolymerization can be tested in terms of Bernoullian, first-order Markov, second-order Markov, or non-Markovian statistics. In rare circumstances, the tactic nature of the copolymer can be determined if distinguishable syndio- and isotactic *n*-ad resonances are resolved. Such an analysis has been carried out for copolymers of methyl methacrylate–methacrylic acid, for which the α-CH_3 resonances of all 20 triads have been assigned and have been used to determine the cotacticity of the copolymer [22].

A number of examples may be found in the literature. The polymerization of ethylene with α-olefins is a particularly simple example as it obeys the ideal copolymerization model. For the polymerization of ethylene-1-butene produced by zirconocene/methylaluminoxane catalysis [23], the triad concentrations measured by ^{13}NMR are shown in Table 7.12.

This catalyzed ethylene-1-butene system shows *ideal* behavior: r_E is large while r_B is small, and the product of the reactivity ratios is near unity. The copolymer has a random distribution with short sequence lengths of each monomer.

Table 7.12
Comonomer distribution statistics for the polymerization of ethylene-1-butene by zirconocene/methylaluminoxane catalysis

Sequence	^{13}C-NMR resonance (ppm)	Triad fractions		Terminal model	
		sample 1	sample 2	statistics #1	statistics #2
EEE	39.2	0.04	0.19	0.03	0.21
EEB + BEE	33.6	0.12	0.26	0.12	0.30
BEB	33.8	0.16	0.14	0.15	0.11
EBE	39.0	0.11	0.20	0.06	0.18
BBE + EBB	36.4	0.22	0.13	0.29	0.16
BBB	34.0	0.36	0.08	0.35	0.04
SUM		1.01	1	1	1
E		0.32	0.59	0.30	0.62
B		0.68	0.41	0.70	0.38
n_E		1.5	3.2		
n_b		2.2	1.6		
r_E				30	83
r_B				0.034	0.0078
$r_E \times r_B$				1.02	0.65

(Source: Ref. [6].)

Another simple example is the NMR analysis of vinyl chloride (VC)–vinyl acetate (VA) copolymers [24]. The 300-MHz ^{1}H-NMR spectra of VC-VA copolymers are shown in Fig. 7.17.

The resonances are assigned on the basis of analogy with the assignments for PVC and PVA and are listed in Table 7.13.

The methylene-proton resonances centered at 1.96,.14, and 2.34 ppm result from the three compositional dyads. The lines are broad because of a combination of spin–

Table 7.13
Spectral assignments for VC-VA copolymers as measured by 300-MHz ^{1}H-NMR spectroscopy

Chemical shift [1] (ppm)	Protons	Dyads or triads
2.01	methyl	(VA, VA, VA)
		(VA, VA, VC)
		(VC, VA, VC)
1.96	methylene	(VA, VA)
2.14	methylene	(VA, VC)
2.34	methylene	(VC, VC)
4.03	methine	(VA, VC, VA)
4.23	methine	(VC, VC, VA)
4.45	methine	(VC, VC, VC)
4.86	methine	(VA, VA, VA)
5.07	methine	(VA, VA, VC)
5.27	methine	(VC, VA, VC)

[1] Chemical shift is given with respect to internal $(CH_3)_2SO$-d_5H (2.50 ppm).
(Reproduced from Ref. [24]. © 1983 American Chemical Society.)

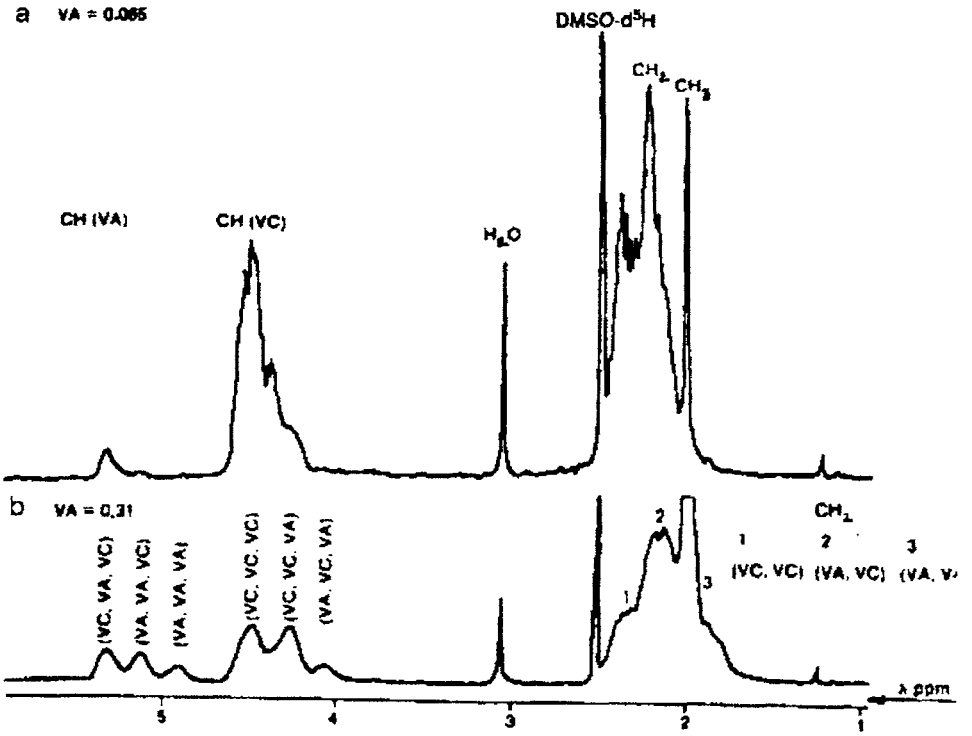

Fig. 7.17. 300-MHz ^{1}H-NMR spectra of VC-VA copolymers containing 0.065% VA (spectrum a) and 0.31% VA (spectrum b) in $(CH_3)_2SO$-d_6 at 85°C. (Reproduced from Ref. [24]. © 1983 American Chemical Society.)

spin coupling and configurational splitting. There are six methine resonances in two separate groups of three lines each. All six of these methine resonances are assigned to the six compositional triads. The composition and the number-average sequence length of the acetate and chloride sequences can be calculated by using the integrated areas of the triads. The results for composition, dyad, triad, and number-average sequences are shown in Table 7.14 for the VA-VC sample with VA = 0.31%.

The Bernoullian model and the first-order and second-order Markov models of the copolymerization mechanism can be tested by using the observed distribution of the triads. The results for the three models are shown in Table 7.15 for the sample with VA = 0.31%.

The conclusions were stated as follows:

> *It is evident that for polymer B (VA = 0.31), the Bernoullian model can be abandoned and that a significant amelioration of the results is achieved by going from first-order Markov to second-order Markov analysis. Thus the propagation statistics of polymer B is adequately described by a second-order Markov process.* — G. van der Velden [24]

Table 7.14
Composition and mole fraction of dyads and triads as measured and calculated by ^{1}H-NMR spectroscopy of a VC-VA copolymer (VA = 0.31)

Dyads and triads	^{1}H NMR [1]	^{13}C NMR [2]
(VC, VC, VC)	0.329	
(VC, VC, VA)	0.302	
(VA, VC, VA)	0.055	
(VC, VA, VC)	0.139	
(VA, VA, VC)	0.116	
(VA, VA, VA)	0.055	
(VC, VC)		0.47
(VA, VC)		0.40
(VA, VA)		0.13
n_0^{VA}	1.57	1.65
n_{2+}^{VA}	2.95	
n_0^{VC}	3.34	3.35
n_{2+}^{VC}	4.18	
(VA)	0.31	0.32

[1] In $(CH_3)_2SO$-d_6.
[2] In C_6D_6.
(Reproduced from Ref. [24]. © 1983 American Chemical Society.)

This copolymer system demonstrates the nature of the information obtained from high-resolution NMR spectra of copolymer systems. Unfortunately, many of the copolymers do not have well-resolved resonances that can be easily integrated and used for quantitative analysis. However, as the applied magnetic fields increase, the resolution will also increase, and more copolymer systems will become tractable. An alternate approach that is proving to be helpful in this regard is the two-dimensional NMR technique.

Compositional heterogeneity of copolymers as determined by NMR

Most copolymers exhibit compositional heterogeneity. When the comonomers have different reactivity ratios, they polymerize at different rates and the compositions of the polymer chains are functions of conversion. This has been termed conversion heterogeneity [25]. Other kinds of heterogeneity have also been described [26]. To treat compositional heterogeneity, an exponentially modified Gaussian (EMG) function has been used. The advantage of the EMG is its ability to describe band broadening [25]. The Markovian model is perturbed using the EMG. Essentially, this changes the terminal conditional probabilities $P(\mathrm{A/B})$ and $P(\mathrm{B/A})$ allowing them to take on a distribution of probability values. An average $P'(A/B)$ and $P'(B/A)$ are used. The width of the EMG is given by σ. An exponential modifier, τ, allows the distribution to become skewed. Approaches of this type have proven useful in understanding compositional heterogeneity for NMR data. An analysis of two different

Table 7.15
Calculated and observed triad comonomer distributions for VC-VA copolymers

Triad	Distribution	Observed Bernoullian [1]	Markov	
			first-order [2]	second-order [3]
VCVCVC [4]	0.814	0.817		
VCVCVA	0.121	0.114		
VAVCVA	0.000	0.004		
VCVAVC	0.055	0.057		
VAVAVC	0.010	0.008		
VAVAVA	0.000	0.000		
VCVCVC [5]	0.329	0.328	0.316	0.332
VCVCVA	0.032	0.295	0.284	0.299
VAVCVA	0.055	0.066	0.064	0.053
VCVAVC	0.139	0.148	0.125	0.143
VAVAVC	0.116	0.133	0.160	0.117
VAVAVA	0.055	0.030	0.051	0.056

[1] $\alpha = 0.935$ (0.065% VA), $\alpha = 0.69$ (0.31% VA).
[2] $\alpha = \gamma = 0.69$, $\beta = \delta = 0.61$.
[3] $\alpha = 0.69$, $\beta = 0.71$, $\gamma = 0.74$ and $\delta = 0.51$.
[4] The copolymer contained 0.065% VA.
[5] The copolymer contained 0.31% VA.
(Reproduced from Ref. [24]. © 1983 American Chemical Society.)

degrees of conversion of styrene (S)/butyl acrylate (A) for the triad data are shown in Tables 7.16 and 7.17.

The copolymer of styrene and butyl acrylate was polymerized in the batch mode and the NMR triad data obtained [27]. The analysis shown in Tables 7.16 and 7.17 clearly indicates the existence of compositional heterogeneity for these copolymers.

Table 7.16
Analysis of the conversion to 5% of styrene (S)/butyl acrylate (A) for the NMR triad data [25]

Sample (conversion 5%)	Observed intensities	Calculated intensities	
		no compositional heterogeneity	with compositional heterogeneity
SSS	1.5	1.3	1.5
SSA	12.2	12.4	11.8
ASA	29.1	29.1	29.1
SAS	21.8	21.81	22.2
AAS	25.8	27.0	25.7
AAA	9.7	8.4	9.7
P'(A/S)		0.824	0.839
P'(S/A)		0.617	0.626
σ		0	0.095
τ		0	−0.004
MD [1]		0.49	0.16

[1] Mean deviation.

Table 7.17
Analysis of conversion to 63% of styrene (S)/butyl acrylate (A) for the NMR triad data [25]

Sample (conversion 63%)	Observed intensities	Calculated intensities	
		no compositional heterogeneity	with compositional heterogeneity
SSS	0	0.5	0.1
SSA	7.0	7.0	7.0
ASA	24.8	24.8	24.8
SAS	12.6	11.8	12.6
AAS	31.4	32.9	31.4
AAA	24.2	22.9	24.2
P'(A/S)		0.876	0.890
P'(S/A)		0.418	0.432
σ		0	0.0016
τ		0	−0.0107
MD [1]		0.68	0.02

[1] Mean deviation.

The lower standard deviations for the calculated NMR triad intensities are indicative of the presence of compositional heterogeneity.

Summary

High resolution solution NMR is a most important tool for the structural characterization of polymers. The spectral selectivity is the most important advantage of NMR. Unfortunately, the spectral sensitivity is low. The S/N can be increased by signal averaging and the use of higher magnetic fields. However, both of these techniques are costly. It is clear that we will continue to see an increase in the applications of NMR to the characterization of polymers.

References

[1] Bovey, F.A., Nuclear Magnetic Resonance Spectroscopy, 2nd edition. Academic Press, San Diego, CA, 1988.
[2] Tonelli, A.E., NMR Spectroscopy and Polymer Microstructure. The Conformational Connection. VCH, New York, NY, 1989.
[3] Bovey, F.A., Mirau, P.A., NMR of Polymers. Academic Press, San Diego, CA, 1996.
[4] Waali, E.E., Scott, J.D., Klopf, M.M., Vladimirsky, Y., Vladimirsky, O., Macromolecules 30 (1997) 2386.
[5] Silverstein, R.M., Bassler, G.C., Morrill, T.C., Spectrophotometric Identification of Organic Compounds, 5th edition. Wiley, New York, NY, 1991, pp. 215, 237–238.
[6] Rossi, A., Zhang, J., Odian, G., Macromolecules 29 (1996) 2331.
[7] Kolbet, A.C., Didier, J.G., Macromolecules 29 (1996) 8591.
[8] Hatada, K., Kitayama, T., Ute, K., Terawaki, Y., Yanagida, T., Macromolecules 30 (1997) 6754.
[9] Randall, J.C., Zoepfl, F.J., Silverman, J., in: J.C. Randall (Ed.), NMR and Macromolecules. ACS

Symposium Series 247, American Chemical Society, Washington, DC, 1984, p. 245.
[10] Jelinski, L.W., Dumais, J.J., Luongo, J.P., Cholli, A.L., Macromolecules 17 (1984) 1650.
[11] Randall, J.C., Ruff, C.J., Kelchtermans, M., Gregory, B.H., Macromolecules 25 (1992) 2624.
[12] McCord, E.F., Shaw Jr., W.H., Hutchinson, R.A., Macromolecules 30 (1997) 246.
[13] Randall, J.C., Zoepfl, F.J., Silverman. J., in: J.C. Randal (Ed.), NMR and Macromolecules: Sequence, Dynamic and Domain Structure. ACS Symposium Series 247, American Chemical Society, Washington, D.C., 1984, p. 245.
[14] Qu, B, Qu, X, Xu, Y, Jacobsson, U., Ranby, B., Russell, K.E., Baker, W.E., Macromolecules 30 (1997) 1408–1413.
[15] Horii, F., Zhu, Q.R., Kitamara, R., Yamaoka, H., Macromolecules 23 (1990) 977.
[16] Bovey, F.A., Chain Structure and Conformation of Macromolecules. Academic Press, New York, NY, 1982.
[17] Tonelli, A.E., NMR Spectroscopy and Polymer Microstructure. The Conformational Connection. VCH, New York, NY, 1989, Chapter 6.
[18] Frisch, H.L., Mallows, C.L., Heatley, F., Bovey, F.A., Macromolecules 1 (1968) 533.
[19] Cheng, H.N., in: H.G. Barth and J.W. Mays (Eds.), Modern Methods of Polymer Characterization. John Wiley, New York, NY, 1991, Chapter 11.
[20] Busico, V., Cipullo, R., Monaco, G., Vacatello, M., Segre, A.L., Macromolecules 30 (1997) 6251.
[21] Cais, R.E., Sloane, N.J.A., Polymer 24 (1983) 179.
[22] Klesper, E., in: D.O. Hummel (Ed.), Polymer Spectroscopy. Steinkopff Verlag, Darmstadt, 1976, p. 197.
[23] Rossi, A., Zhang, J., Odian, G., Macromolecules 29 (1996) 2331.
[24] van der Velden, G., Macromolecules 16 (1983) 1336.
[25] Cheng, H.N., Macromolecules 30 (1997) 4117.
[26] Cheng, H.N., Tam, S.B., Kasehagen, L.J., Macromolecules 25 (1992) 3779.
[27] Llauro-Darricades, M.F., Pichot, C., Guillot, J., Rios, G.L., Cruz E., Gizman, C.C., Polymer 27 (1986) 889.

Chapter 8

High-resolution NMR spectroscopy of solid polymers

> *The history of high-resolution NMR in solids has been, inter alia, a quest for narrow spectral lines.* — A. N. Garroway et al. [1]

Introduction

The differences in the NMR spectra measured under Fourier Transform conditions with scalar decoupling of the same substance, say water and ice, boggle the mind. The proton NMR spectrum of the water is sharp and narrow with a band width of one Hz, while the proton NMR spectrum of ice is extremely broad with a band width of 20 KHz. This is totally unexpected. In the early days of experimental NMR, the NMR lines of solids were so broad that no measurable signal could be obtained related to chemical structure.

We now know the sources of the differences in the NMR spectra of solids and liquids [2,3]. In liquids and solutions, sharp NMR lines are obtained because the local interacting fields are averaged to zero by the rapid isotropic motions of the nuclei (termed incoherent averaging). Anisotropic interactions, such as dipolar and quadrupolar interactions, are averaged to zero by the molecular motions to effectively remove them from broadening the spectra. As a result, narrow lines are obtained for liquids and solutions.

Generally, in solids, there is not sufficient motion to average the anisotropic interactions and extremely broad lines are present. Because the incoherent averaging (molecular motion) do not narrow the NMR lines, coherent-averaging techniques such as dipolar decoupling and magic-angle spinning must be used to produce narrow line widths [4]. For solids, the low sensitivity of the ^{13}C nucleus is improved by transferring polarization from the magnetization-rich protons to the ^{13}C nuclei by using cross-polarization. By combining high-power decoupling (DD), magic-angle spinning (MAS), and cross-polarization (CP) experiments into one grand experiment [5], narrow lines and enhanced sensitivity can be obtained for polymers in the solid state. As a consequence, high-resolution NMR spectroscopy has become an important tool in the structural investigation of polymers in the solid state [6–9].

The dipolar-decoupling experiment (DD)

> *Proton dipolar broadening in ^{13}C spectra of solids can be removed by a high-power version of the decoupling technique used in solution NMR spectroscopy.* — C.Y. Yannoni [10]

The major contributions to the line widths in ^{13}C-NMR spectra of organic solids are the interactions arising from heteronuclear dipolar broadening by protons [11]. Consider the general model of a rigid isolated pair of nuclei, designated μ_1 and μ_2 with spin 1/2, interacting through their dipoles (Fig. 8.1). The dipole resulting from μ_1 processes at the Larmor frequency about the applied magnetic field, H_0, to create a static component along the field direction and a rotating component in the plane perpendicular to the static-field direction. The static component of μ_1 produces a small static field at the site of the dipole μ_2. The magnitude of this local field, H_{loc} depends on the relative positions of the spins and their orientations with respect to the applied magnetic field. If a sample containing this isolated pair of nuclei is placed in a static magnetic field, H_0, each nucleus then experiences an effective magnetic field (H_{eff}):

$$H_{\text{eff}} = H_0 \pm H_{\text{loc}} \left(\frac{\mu}{r_{ij}^3} \right) (3\cos^2 \theta_{ij} - 1) \tag{8.1}$$

where θ_{ij} is the angle between the internuclear vector, r_{ij} and the direction of the external magnetic field μ is the magnetic moment.

For a large H_0, only the components parallel or antiparallel to H_0 cause significant changes in the net static field. The resulting line width should be approximately equal to the magnitude of the local static field, thereby contributing to substantial line broadening.

For unlike spins, the rotating field is off resonance, and thus the interaction is less. The ^{13}C spin experiences a force due to the z component of the magnetic field, H_z^1, generated by the ^{1}H spins. This component may add or subtract from the applied external field and results in the appearance of a doublet. In the NMR spectrum, a doublet will be centered around the ^{13}C Larmor frequency ($\Delta\nu_{\text{CH}}$) with a splitting in Hz (Fig. 8.2) equal to [12]

$$\Delta\nu_{\text{CH}} = \left(\frac{\gamma_{\text{C}}}{\pi} \right) H_z^1 \tag{8.2}$$

with

$$H_z^1 = \left(\frac{\mu_z^{\text{H}}}{r_{\text{CH}}^3} \right) \langle 1 - 3\cos^2 \theta \rangle \tag{8.3}$$

where r_{CH} is the internuclear carbon-to-hydrogen distance and μ_z^{H} is the z component of the dipole of the ^{1}H nucleus.

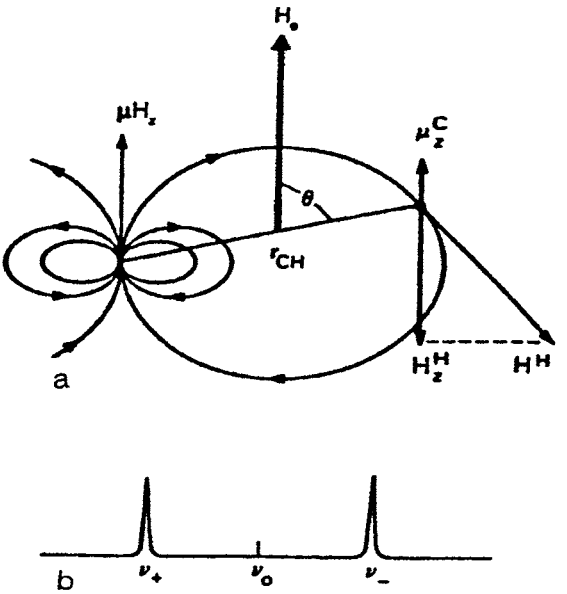

Fig. 8.1. Proton–carbon dipolar coupling in an isolated C−H bond. (a) Lines of force from the proton magnetic moment (shown here in the + state, parallel to the external field H_0) generate a static local field H^H at the ^{13}C nucleus. Because $H_H \ll H_0$, the ^{13}C experiences only H_z^H, the component of H^H that is antiparallel to H_0. (b) The resulting ^{13}C spectrum for a sample of isolated C−H fragments with a single orientation, θ, is shown.

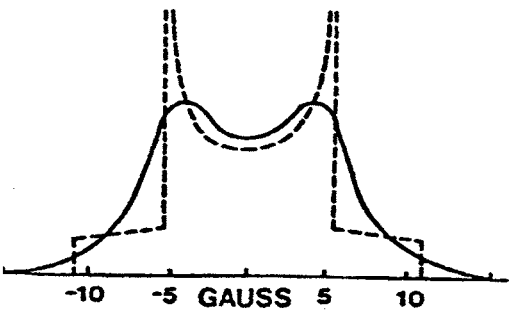

Fig. 8.2. The absorption curve of a two-spin system for dipolar interactions. The dotted curve gives the absorption for an isolated pair of nuclei. The solid curve shows the effect of neighboring nuclei on the isolated system. In the NMR spectrum, a doublet will be observed, with a spacing determined by the length and orientation of the internuclear vector. (Reproduced with permission from Ref. [12]. © 1948 American Institute of Physics.)

The angular brackets denote an average that depends on the molecular motion. For dipolar ^1H–^{13}C splittings, values as high as 40 kHz are possible. However, a doublet is not observed for semicrystalline polymers. The observed result is generally a broad Gaussian-shaped resonance. The dipolar spectrum is featureless because of the many interactions of all of the spins with each other. Because of the distance dependence of

the dipolar interactions, only spins within a radius of $\leq$20 Å contribute, but for most polymer systems there are still 10–100 dipolar interactions [13].

When a strong decoupling field is applied in the solid state, there are rapid transitions or mutual spin flips that occur at a rate approaching that of the inverse of the line width of the proton resonance. The time constant for this process is T_2 (the spin–spin relaxation time), which ranges from 10 to 100 μs for rigid solids [12].

There is a distinction between scalar coupling and dipolar effects. Decoupling eliminates both, but the sources of the effects are different. Scalar coupling arises from the coupling of the internal C–H energy levels, and dipole–dipole effects arise from changes in the local magnetic field due to the dipoles present. Scalar coupling is eliminated by relatively low-power decoupling, and dipole–dipole effects require high-power decoupling.

Dipolar decoupling (DD) with high-powered proton decoupling can be used to coherently average the heteronuclear dipolar interactions to zero [12]. The DD forces the proton spins to change energy states at a fast rate compared to the frequency of the dipolar ^{1}H–^{13}C interactions. Under these circumstances, the local dipolar fields at the ^{13}C nucleus are reduced to zero [14]. To decouple protons from carbons in solids, the magnitude of the decoupling field must be capable of exciting all proton transitions within a bandwidth of 40–50 kHz, which is large compared to the proton–proton dipolar coupling.

The DD experiment can be applied either continuously or gated [15]. In the latter experiment, often termed *inverse-gated decoupling*, broad-band irradiation is applied only during acquisition. In this manner, the total power consumption is smaller, and this condition leads to less heating of the sample.

The required decoupling field can be calculated. Consider a system with chemically shifted resonances that occur in a frequency range of ΔH_z, following the method of Lyerla [16]. The effective field in the rotating frame is given by

$$H_{\text{eff}} = \left(H_0 - \frac{\omega}{\gamma}\right) z + H_1 x \tag{8.4}$$

or in terms of interest here

$$H_{\text{eff}} = \left(\frac{1}{\gamma}\right) [(\omega_1 - \omega)^2 + (\gamma H_1)^2]^{1/2} \tag{8.5}$$

This is the relationship between the precession frequency ω_1 and the effective field when H_1 is applied at ω. If H_1 is large enough to meet the condition $\gamma H_1 \gg \pi \Delta'$, where Δ' is the total range of frequencies from the rf, then the first term in Eq. (8.4) can be neglected, and

$$H_{\text{eff}} = H_1 \tag{8.6}$$

The magnetizations of all the nuclei in the frequency range Δ' precess about H_1 or all $\mathbf{M}_i$ are rotated through the same angle θ. By using short, intense pulses, the entire range of resonance frequencies for the protons can be simultaneously decoupled.

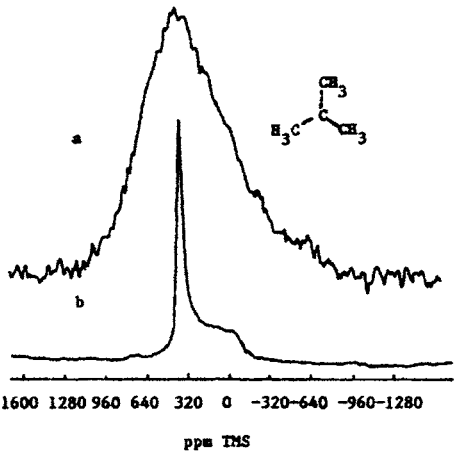

Fig. 8.3. The effect of high-powered proton decoupling is shown for the ^{13}C spectra at $-180°C$ of the central carbon of the *tert*-butyl cation prepared from [2-^{13}C]2-chloro-2-methylpropane and SbF_3. Spectrum a was obtained without decoupling and spectrum b was obtained with strong (43 kHz) ^1H and ^{19}F decoupling. (Reproduced from Ref. [10]. © 1982 American Chemical Society.)

The required decoupling power also depends on the sample size. The ^1H power in a sample coil is given approximately by

$$^1H = 3\left(\frac{PQ}{\omega_0 V}\right)^{1/2} \tag{8.7}$$

where P is the transmitter power in watts, Q is the quality factor of the probe circuit, ω_0 is the Larmor frequency (MHz), and V is the sample volume (cm^3). Thus, doubling the sample volume requires a corresponding doubling of the rf power level to keep a constant ^1H field or 90° pulse width.

The effect of high-powered proton decoupling is shown in Fig. 8.3 for the ^{13}C spectra at 180°C of the central carbon of the *tert*-butyl cation prepared from [2-^{13}C]-2-chloro-2-methylpropane and SbF_3 [17].

Spectrum a was obtained without decoupling, and spectrum b was obtained with strong (43 kHz) ^1H and ^{19}F decoupling. The spectral contribution from the methyl carbons was subtracted from these spectra [10]. The residual resonance line shape observed is due to the chemical-shift anisotropy of the central carbon in a powdered sample. The effects of chemical-shift anisotropy will be discussed in later in this chapter.

Heteronuclear decoupling using spin-locking techniques

Decoupling by spin locking has the advantage of developing longer relaxation times so that additional pulse sequences can be used. For spin-lock decoupling, a 90°_x pulse is applied, followed by a $\pi/2$ phase shift of the rf field, which is then left

on. From the perspective of the rotating frame, this spin-locking experiment has the effect of aligning **M** along the rf field H_1 [18]. As long as H_1 is large compared to the local dipolar field, the system cannot relax by a T_2 process because the spin-flip mechanism does not conserve Zeeman energy along H_1.

At resonance, the rotating frame is a coordinate system moving in synchronism with the precession of the proton moments around the static field at a frequency

$$\nu_0^{\mathrm{H}} = \left(\frac{\gamma_{\mathrm{H}}}{2\pi}\right) H_0 \tag{8.8}$$

In this rotating reference frame, the proton spins are stationary, but in the presence of the rf field, $H_{1\mathrm{H}}$, the proton spins precess at a frequency

$$\nu_{1\mathrm{H}} = \left(\frac{\gamma_{\mathrm{H}}}{2\pi}\right) H_{1\mathrm{H}} \tag{8.9}$$

While spin locked, the z components oscillate at a frequency $\nu_{1\mathrm{H}}$. The ^{13}C spins experience this field as a coherently averaged z component $\langle \mu_z^H \rangle$. For sinusoidal variation,

$$\langle \mu_z^{\mathrm{H}} \rangle = 0 \tag{8.10}$$

so that the ^{1}H–^{13}C dipolar couplings are removed. For effective decoupling, $\nu_{1\mathrm{H}}$ must be much greater than $\Delta\mu_{\mathrm{HH}}$, where $\Delta\mu_{\mathrm{HH}}$ is the homogenous proton line width. Thus, high-power heteronuclear decoupling requires spin-lock fields of 1 mT (43 kHz) or more [13].

Homonuclear decoupling using multipulse methods

The previous decoupling methods involved coherent spatial averaging to remove the heteronuclear dipolar coupling. The dominant line-broadening mechanism in the ^{1}H magnetic resonance of solids is normally the ^{1}H–^{1}H homonuclear dipolar interaction, which cannot be removed by the double-resonance experiment if the ^{1}H spectrum is to be observed. In order to obtain narrow ^{1}H resonances of solid samples, the line-broadening effects of the homonuclear dipolar interactions must be eliminated while the chemical-shift interactions are retained.

The homonuclear dipolar ^{1}H–^{1}H interactions can be removed by modulating the spin states rather than the spatial factors [19]. This multipulse sequence reduces the line widths in rigid solids from 10^2 to 10^4 Hz. The multiple-pulse sequence used is the WAHUHA sequence (after the initials of the originators) and is

$$\mathrm{P}_{-y}\text{–}\tau\text{–}\mathrm{P}_{-x}\text{–}2\tau\text{–}\mathrm{P}_{x}\text{–}\tau\text{–}\mathrm{P}_{y}\text{–}2\tau\text{–}\mathrm{P}_{-y} \tag{8.11}$$

The cycle time, $t_n = 6\tau$, can be considered as a rotation period. If the pulses are short enough and the delays τ are kept to a minimum, the 'rotation rate' of the process can be made fast enough to effectively decouple homonuclear dipole–

dipole interactions. During the multiple pulse sequence, the evolution of the nuclear spins in the magnetic field is not a free precession. Under multiple-pulse decoupling, the proton signal is acquired while the multiple-pulse train drives the spin states. The apparent evolution is determined by the internal interactions modulated by the rf excitation. Experimentally, the system is examined stroboscopically at such times that the detected signal is not influenced by the dipolar interactions. As a consequence of this process, the chemical shift is reduced by a factor of $3^{1/2}$.

Unfortunately, the WAHUHA sequence does not completely eliminate dipole–dipole interactions because the applied pulses have finite widths [20,21]. To minimize these effects, more complex sequences have been developed.

Limitations of the dipolar decoupling process

In the heteronuclear double-resonance dipolar decoupling process, residual line broadening will occur when the proton rf field is off resonance or when the decoupling field is low. For solids, the proton irradiation is always off resonance because the protons have anisotropic chemical-shift tensors. It has been suggested [22] that the off-resonance effect (assumed to be 4 ppm) can contribute a broadening of 1.0–2.4 Hz at a field of 1.4 T.

Line broadening can occur because of incomplete decoupling when the molecular motion has correlation frequencies that are near the frequency of the decoupling field [23]. An example is the molecular reorientation of polymeric methyl groups [24]. Incomplete decoupling arises when the methyl group motion about the C_3 axis is comparable to the strength of the decoupling field. Under experimental conditions, when the temperature of the polypropylene sample is decreased, the methyl resonance broadens significantly, and at −143°C, the methyl resonance completely disappears. Similar phenomena have been observed for methyl groups in epoxy resins [23] and in poly(tetrafluoroethylene) (PTFE) (CF_3 in this case) [25].

Chemical-shift anisotropy (CSA) in solids

> *A complete chemical-shift tensor gives information about the local symmetry of the electron cloud around the nucleus and therefore presents a much more detailed picture of the chemical bonding of a certain atom than the isotropic chemical shift measured in solution.* — W.S. Veeman [26]

Basis of chemical-shift anisotropy

The resonance frequency of a nuclear spin is determined by the shielding of the static magnetic field by the surrounding electrons. When a magnetic field is applied to the sample, a secondary magnetic field is generated by the motion of the electrons,

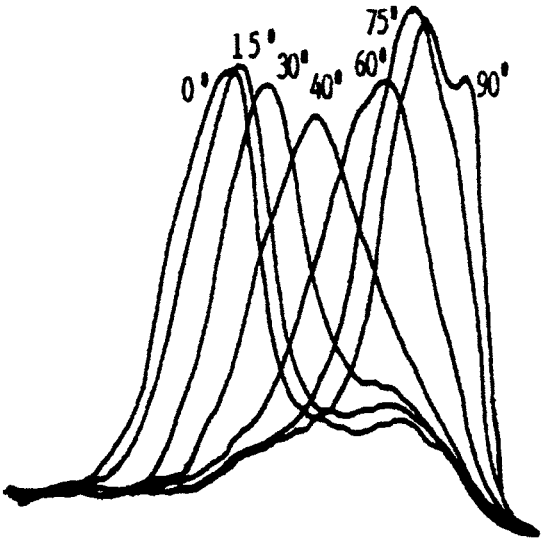

Fig. 8.4. ^{19}F-NMR spectra of oriented PTFE fibers at −108°C for various angles between the fiber direction and the magnetic field. (Reproduced from Ref. [27]. © 1980 American Chemical Society.)

and this secondary magnetic field partially shields the nucleus from the applied magnetic field. This shielding due to the electrons, as observed in solid-state NMR spectroscopy, is *anisotropic*.

An example of the anisotropic behavior of the chemical shift of the resonating nucleus [27] is demonstrated in Fig. 8.4.

For the multiple-pulse decoupled ^{19}F-NMR spectra of oriented PTFE fibers at −108°C, the observed chemical shift depends on the orientation angle between the fiber direction and the applied magnetic field [27]. The PTFE fiber exhibits only one ^{19}F resonance (the CF_2), and this resonance shifts with the angle of alignment of the fiber with the magnetic field. These experimental observations, along with many others, indicate that the electron cloud surrounding the nuclei in most chemical bonds does not have spherical symmetry. That is, the shielding due to the electrons is anisotropic, and this anisotropic shielding causes a resonance shift that depends on the orientation of the chemical bond in the applied magnetic field. In solutions, the random molecular motions are fast on the NMR time scale. The anisotropic portion of the chemical shift is therefore averaged out to leave only the isotropic part of the chemical shift. In rigid solids, where molecular motion is highly restricted, the spatial dependence of this shielding determines the resonance line shape.

The chemical-shift anisotropy (CSA) is the chemical shift difference with the orientation of the bond in the static magnetic field. The ranges of chemical-shift anisotropies of several useful nuclei are listed in Table 8.1.

The CSA range is much larger than the range of the isotropic chemical shift because solution measurements reflect the average value.

Table 8.1
Typical chemical-shift anisotropy values

Nucleus	Chemical-shift anistropy extremes	Typical line width	Isotropic chemical-shift range, σ
^{1}H	100	10	20
^{13}C	425	120	250
^{19}F	1150	150	100
^{31}P	500	250	200

Note: The anisotropy values are given in parts per million (ppm).

The anisotropic nature of the chemical-shift tensor reflects the local symmetry of the electron cloud around the nucleus. The nuclei are shielded not only by their electrons, but also by the polarized electron clouds of the neighboring chains. Because of the existence of neighboring molecules, the electron cloud of the observed nucleus is modified through van der Waals interactions. Consequently, the CSA depends on the intermolecular distances as well as on the intramolecular environment. A summary of the available CSA data can be found in the recent literature [26,28].

Description of chemical-shift anisotropy

The chemical shift of a nuclear spin depends on the relative spatial orientation of the external magnetic field and on the molecule to which the spin belongs. The directional nature of this chemical-shift interaction can be described in the following manner. The local field, H_{loc}, is given by

$$H_{\text{loc}} = \boldsymbol{\sigma} H_0 \tag{8.12}$$

where $\boldsymbol{\sigma}$ is a dimensionless second-rank tensor that represents the anisotropic shift of the resonance frequency with respect to a bare nucleus. This tensor can be written as the sum of a symmetric and an antisymmetric component. The antisymmetric component affects only the NMR line positions to the second order and can therefore be neglected.

In a coordinate axis system, with x, y and z related to the frame of the molecule, the chemical-shift tensor has nine elements but only six unique components:

$$\sigma = \begin{bmatrix} \sigma_{xx} & \sigma_{xy} & \sigma_{xz} \\ \sigma_{yx} & \sigma_{yy} & \sigma_{yz} \\ \sigma_{zx} & \sigma_{zy} & \sigma_{zz} \end{bmatrix} \tag{8.13}$$

where $\sigma_{xy} = \sigma_{yx}$, $\sigma_{xz} = \sigma_{zx}$, and $\sigma_{yz} = \sigma_{zy}$. A special molecular-based axis system, known as the principal axis system x', y', z', can be constructed, and in this system,

the chemical-shift tensor is diagonal:

$$\sigma = \begin{bmatrix} \sigma_{x'x'} & 0 & 0 \\ 0 & \sigma_{y'y'} & 0 \\ 0 & 0 & \sigma_{z'z'} \end{bmatrix} \tag{8.14}$$

where $\sigma_{x'x'}$, $\sigma_{y'y'}$, and $\sigma_{z'z'}$ are the principal or diagonal elements of the tensor. In this molecular reference system, the chemical-shift tensor is completely determined by three principal elements and by the direction cosines (θ_{ij}) of these three principle axes with the applied magnetic field. By convention the nomenclature is as follows: the principal elements are ordered according to the amount of shielding, so that σ_{11} is the least-shielded element, and σ_{33} is the most-shielded element. When the magnetic field points along the least-shielded direction, the nuclear spin resonates at the lowest field strength. Depending on the molecular symmetry, σ_{11} may be equivalent to $\sigma_{x'x'}$, $\sigma_{y'y'}$, or $\sigma_{z'z'}$ where x', y', and z' are determined by symmetry. Therefore,

$$\sigma_{zz} = \theta_1^2\sigma_{11} + \theta_2^2\sigma_{22} + \theta_3^2\sigma_{33} \tag{8.15}$$

The isotropic average of each θ_i^2 is $\frac{1}{3}$, so the average of σ_{zz} is the isotropic average

$$\sigma_{zz} = \sigma_1 = \tfrac{1}{3}[\sigma_{11} + \sigma_{22} + \sigma_{33}] \tag{8.16}$$

Effect of chemical-shift anisotropy on line shapes

The molecules in a powder are randomly oriented. Therefore, the observed spectrum is the superposition of the signals from molecules having all possible orientations ranging from σ_{xx} to σ_{zz}. The line shape of the powder pattern $I(\sigma)$ is given by [29]

$$I(\sigma) = \left[\frac{K(\theta)}{\pi \Delta_1}\right] \arcsin\left(\frac{\Delta_2}{\Delta_1}\right)^{1/2} \tag{8.17}$$

with

$$\Delta_1 = \left[\left(\sigma_{zz} - \sigma_{yy}\right)\left(\sigma - \sigma_{xx}\right)\right]^{1/2} \tag{8.18}$$

$$\Delta_2 = \left[\left(\sigma_{zz} - \sigma\right)\left(\sigma_{yy} - \sigma_{xx}\right)\right]^{1/2} \tag{8.19}$$

where $K(\theta)$ is the complete elliptic integral of the first kind. This equation holds for $\sigma_{xx} < \sigma_{yy} < \sigma_{zz}$. A broad asymmetric powder pattern is observed when σ_{11} is not equal to either σ_{22} or σ_{33} (Fig. 8.5).

This broad but highly characteristic band shape has break points that can be used to extract the tensor principal values of each chemically unique spin, as shown in Fig. 8.5. The line shape can be usefully be discussed in terms of its width and asymmetry. The width, δ, is given as

$$\delta = \sigma_{33} - \sigma_i \tag{8.20}$$

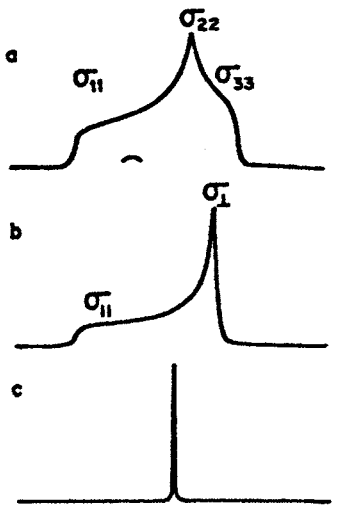

Fig. 8.5. Line shapes in solid-state NMR spectroscopy: (a) axially asymmetric CSA, (b) axially symmetric CSA, and (c) solution.

and the asymmetry, η, is given by

$$\eta = \frac{\sigma_{22} - \sigma_{11}}{\delta} \tag{8.21}$$

In a polycrystalline spectrum, the three principal elements can be determined, but the direction of the principal axis (which can be determined only for single crystals) cannot.

For uniaxial symmetry, $\sigma_{11} = \sigma$, and $\sigma_{22} = \sigma_{33} = \sigma_{\perp}$

$$\sigma = \sigma \cos^2 \phi + \sigma_{\perp} \sin^2 \phi \tag{8.22}$$

The resulting polycrystalline pattern for a nucleus with an axially symmetric CSA has the shape shown in Fig. 8.6.

A number of factors complicate the experimental measurements of CSA. These include a distribution in the values of the CSA; nonrandom orientation of the chains in the sample; inhomogeneous interactions, such as residual line broadening due to incomplete proton decoupling and carbon–carbon dipolar coupling; and molecular motion [30].

First, the shielding tensor, σ, of a nucleus may differ slightly from those of the other nuclei. In polymers, the CSA reflects a distribution of structural parameters such as variations in chain conformation and intermolecular distances. A range of CSA values is expected, and this spread in principal values will affect the line shapes.

Second, if the molecules are oriented, the line shape will be modified in a characteristic way that is determined by an orientation distribution function [31]. When there is axial symmetry in the molecules and the sample, the spectral intensity at any

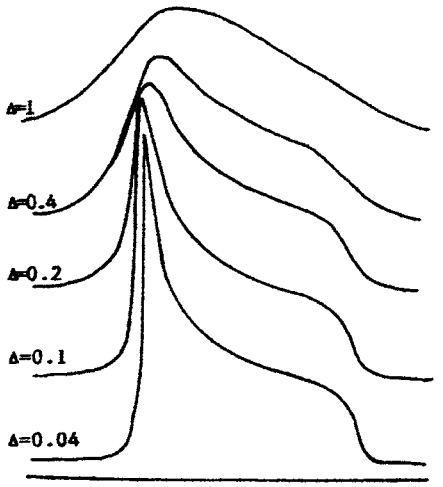

Fig. 8.6. The powder line shapes of an axially symmetric chemical-shift tensor. (Reproduced with permission from Ref. [26]. © 1984 Pergamon Press, Inc.)

given frequency is directly proportional to the population of molecules in a particular orientation [32]. From the observed line shape, information about the distribution or orientation of the sample can be obtained.

This derivation of the theoretical line shapes assumes that the NMR lines of each spin are infinitely narrow. The introduction of a broadening function that arises from the experimental limitations makes the detection of singularities in the pattern difficult. The powder line shapes of an axially symmetric chemical-shift tensor [26] are shown in Fig. 8.6.

These powder line shapes have been convoluted with Lorentzian broadening functions of different widths of $A = [\sigma_{11} - \sigma_{22}]\omega_0$, where ω_0 is the NMR frequency.

Experimental determination of the chemical-shift anisotropy

The NMR experiments that can be used to measure CSA are the following [26]:

- the angular dependence of the chemical-shift shielding in single crystals,
- the observed shift of molecules oriented in a liquid crystal,
- the line shape of a powder,
- reconstruction from side band intensities observed with magic-angle spinning,
- 2D experiments.

In most molecules, there are direct and indirect couplings between the ^{13}C and other spins such as ^{1}H. When the shift of a resonance line is the result of two tensorial interactions, the problem becomes more complicated. For polymers, the ^{13}C chemical-shift interactions can be isolated from the dipolar interactions by removal of the proton interaction with high-powered dipolar decoupling.

When the molecule contains several chemically different carbons, the powder pattern is a superposition of powder line shapes of the individual carbons. This overlap causes additional problems.

For single crystals sufficiently large to be precisely oriented with respect to the magnetic field, the six components of the chemical-shielding tensor can be determined [33]. In the most general case, the orientations of the principal axes in the molecular frame must be specified. Because of the inversion symmetry of the magnetic interactions, the single-crystal spectrum is the same for two oppositely directed magnetic-field vectors. It is thus necessary to cover only half of all directions to obtain the correct result.

The chemical shift for six orientations of the single crystal with respect to the magnetic field must be measured. The change in frequency of each resonance can be determined as the sample is rotated. Analysis of rotation plots of the chemical shift yields the required information. From these measurements, the six unknowns can be determined. This method has low precision. A better approach is to rotate the crystal around three axes and to measure the shift as a function of θ. A problem with this approach for polymers is that large single crystals are not available.

In some cases, the CSA can be determined from the line shapes of a powder spectrum. The NMR spectrum of a powder is the sum of the resonance lines resulting from all possible orientations of the nuclear sites. Such powder spectra often have characteristic band shapes with well-defined features from which the NMR parameters can be directly read. In a single isolated nucleus, the three principal values of the chemical-shift tensor can be obtained directly from the frequencies of the two shoulders and the peak in the spectrum. A least-squares curve-fitting procedure has been described [34] in which a set of theoretical points is produced by calculation from a set of adjustable parameters, and the theoretical points are compared to the corresponding set of experimental points.

Unfortunately, for systems with a number of different carbon nuclei, there is usually extensive overlap of the CSA signals, and the analysis of the powder pattern is difficult, if not impossible. Therefore, other techniques that partially narrow the lines must be used. Three different experiments can be used to determine chemical-shift anisotropies for powders:

(1) slow magic-angle sample spinning [35–37],
(2) off-angle magic-angle spinning [35,38],
(3) rotation-synchronized rf pulse techniques [39,40].

When the spinning speed of the sample is less than the CSA, rotational echoes appear as spinning sidebands that flank the averaged isotropic main peak. These echoes are spaced at the inverse of the spinning frequency. A graphical procedure has been described [41] for extracting the principal components of the chemical-shielding tensor from the intensities of the spinning sidebands. This method has been used for poly(butylene terephthalate) (PBT) [42] and dimethyl terephthalate (DMT), and the results are listed in the following table.

Sample	Carbonyl carbon	Nonprotonated aromatic carbon
DMT	137 ± 4	201 ± 4
PBT [1]	127 ± 5	202 ± 4

Note: the values shown were obtained as $|\sigma_{33} - \sigma_{11}|$ and are in parts per million.
[1] From Ref. [42].

The limitation of the slow magic-angle spinning (MAS) method is the difficulty of obtaining accurate measurements of the sideband intensities for complex systems in which there is extensive overlap. All sidebands must be resolved and properly assigned to use this method.

Rapid off-magic-angle spinning (OMAS) yields a scaled powder pattern that can be analyzed to determine the individual chemical-shielding tensors. The isotropic chemical shift must be known, and can be determined separately. The relation can calculate the tensor components from the OMAS-scaled components:

$$\sigma_{\mathrm{I}} = \frac{\sigma_{i'} - \sigma_{\mathrm{ave}}}{C} + \sigma_{\mathrm{ave}} \tag{8.23}$$

where

$$C = \frac{3\cos^2\theta - 1}{2} \tag{8.24}$$

where θ is the angle between the rotational axis and the static magnetic field, σ_i is one of the three tensor components, $\sigma_{i'}$ is one of the OMAS-scaled components, and σ_{ave} is the isotropic value of the three tensor components. OMAS is used to generate the tensor information at both positive and negative offsets of the magic angle because the sign of the shielding anisotropy inverts. OMAS has been used to study poly(ethylene terephthalate) (PET) [38] and PBT [43]. The experimental values of the chemical-shift tensors were used to simulate the OMAS spectra. The values that were measured are listed in the following table.

Carbon type	σ_{11}	σ_{22}	σ_{33}
Carbonyl			
$\theta = 56.3°$	165.8	165.8	165.0
$\theta = 57.6°$	167.1	167.1	158.4
Nonprotonated aromatic			
$\theta = 56.3°$	137.6	133.0	129.9
$\theta = 57.6°$	140.9	132.6	127.0
Protonated aromatic			
$\theta = 56.3°$	133.5	128.2	125.9
$\theta = 57.6°$	136.9	127.4	123.3

Note: all values are given in parts per million.
(Source: Ref. [43].)

The CSA can also be determined by using 2D techniques [39,44,45]. The 2D experiment results in a plot on which one axis is the anisotropic shift and the other axis corresponds to the isotropic shift. If the FID is sampled at times $t_n = n(2\pi/\omega_r)$, where ω_r is the rotor frequency, the FID represents the isotropic spectrum. If the FID is observed at different times $t, \ldots, t_n$, and the FIDs are Fourier transformed, the 2D spectrum will be observed [46].

The aforementioned methods for determining the CSA are applicable only for samples without dipolar-modulated chemical-shift powder patterns [47]. Under these circumstances, the analysis problem becomes quite difficult. Sample-spinning NMR techniques must be used to measure the heteronuclear dipolar–chemical-shift 2D powder patterns [48,49].

CSA for hydrogen nuclei in various environments

Sufficient results have been obtained from CSA measurements to allow a comparison of the principal values of the shielding tensors for hydrogen nuclei in various environments.

CSA for carbon nuclei in various environments

The CSA patterns for the various types of carbons have been determined. The CSA for carbons with sp^3 hybridization are shown in Fig. 8.7, those for carbons with sp^2 hybridization are shown in Fig. 8.8, and those for carbons with sp hybridization are shown in Fig. 8.9 [28].

The high sensitivity of the CSA to the nature of the carbon is reflected in these CSA patterns. The width of the CSA for a given carbon can be quite narrow, as shown for the methyl carbon of ethyl alcohol, or can be very wide, as for the aromatic carbons of benzene and toluene.

Of particular interest to polymer scientists is the CSA of methylene carbons. For the methylene carbon, the values of the chemical-shift tensors are as follows: σ_{11}, which bisects the H−H bond, has a value of 50.5 ± 15 ppm; σ_{22}, which bisects the H−C−H angle, has a value of 37 ± 10 ppm; and σ_{33}, which is perpendicular to the H−C−H plane, has a value of 16 ± 17 ppm. The three elements of the chemical-shielding tensor and their assignments in an all-trans methylene chain [50] are shown in Fig. 8.10.

For the methylenes in polyethylene (PE), $\sigma_{11} = 49$ ppm, $\sigma_{22} = 35$ ppm and $\sigma_{33} = 12$ ppm. On the basis of these assignments, the carbons of a PE chain with its axis aligned along H_0 will resonate at 12.9 ppm.

Effect of motion on chemical-shift anisotropy

Changes in the NMR line shapes can define the geometry of the dominant motions in the polymers. Motionally averaged powder patterns reflect the rates, amplitudes,

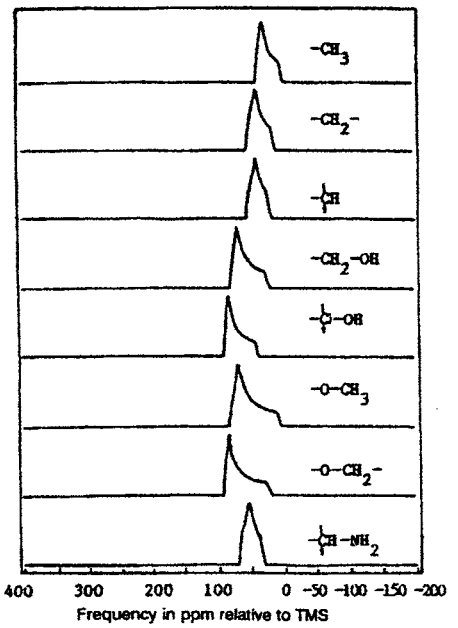

Fig. 8.7. The CSA for carbons with sp^3 hybridization. (Reproduced with permission from Ref. [28]. © 1987 American Institute of Physics.)

and angles of the motions involved. Rapid rotation about one bond axis of a molecule causes a partial averaging of the shielding tensor, and the average shielding tensor displays axial symmetry about the rotation axis. Consider the simple case of rotation of a CF_3 group around the C−C axis (Fig. 8.11).

The CSA changes from an asymmetric pattern to a uniaxially symmetric pattern as a result of the averaging of σ_{11} and σ_{22} because of rotation about the σ_{33} axis, and the line shapes are characterized by only two values of the chemical-shift tensor.

The rate and type of motion that takes place in the sample influence the chemical line shape. Three types of motions make important contributions to the line shapes, and these are macroscopic sample rotation, molecular reorientation, and molecular conformational changes.

Macroscopic sample rotation is performed in a variety of ways, including magic-angle spinning (MAS), which is discussed later in this chapter. When the solid sample undergoes magic-angle spinning, the average shift over one cycle of rotation becomes independent of orientation and is given by the isotropic shift [51]. However, the sample rotation must be rapid compared to the anisotropy spread ($\sigma_{33} - \sigma_{11}$) in order for the coherent averaging to occur. This condition means that a polycrystalline sample will have only a single narrow line for each magnetically inequivalent nucleus. Chemical shifts observed in the solid state are usually within a few parts per million of those observed in solution.

When the rate of molecular motion is much faster than the spectroscopic time scale

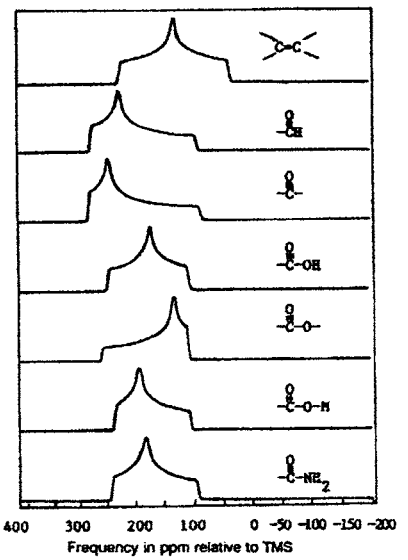

Fig. 8.8. The CSA for carbons with sp^2 hybridization. (Reproduced with permission from Ref. [28]. © 1987 American Institute of Physics.)

(the *fast-exchange limit*), only the angles are needed for line-shape calculations. For example, the effect of fast-diffusional rotation about an arbitrary axis is calculated by transforming the static tensor to a rotationally averaged tensor. Spiess has reviewed the method of calculating the chemical-shift line shapes in the presence of rotational motion of molecules [52].

Consider the example of motions of phenyl rings [53]. Two different motional models are possible. Reorientation about the chain ring $C_\beta - C_\nu$ bond axis may occur either by 180° flips (jumps between two indistinguishable conformations) or by fast-diffusional rotational motion with small angular displacements. The principal axis system is shown in Fig. 8.12.

The chemical-shielding tensor for aromatic-ring carbons has σ_{zz} bisecting the C−C−C angle, σ_{yy} perpendicular to the plane of the ring, and σ_{xx} orthogonal to these two axes. With this orientation, $\sigma_{yy} > \sigma_{zz} > \sigma_{xx}$, and their sum equals zero. Consequently,

$$\sigma_{zz} = -\tfrac{1}{2}(1 + \delta)\sigma \tag{8.25}$$

$$\sigma_{xx} = -\tfrac{1}{2}(1 - \delta)\sigma \tag{8.26}$$

$$\sigma_{yy} = \sigma \tag{8.27}$$

with $\delta = (\sigma_{xx} - \sigma_{zz})/\sigma_{yy}$; the powder pattern calculated for $\sigma = 3.87$ kHz and $\delta = 0.73$.

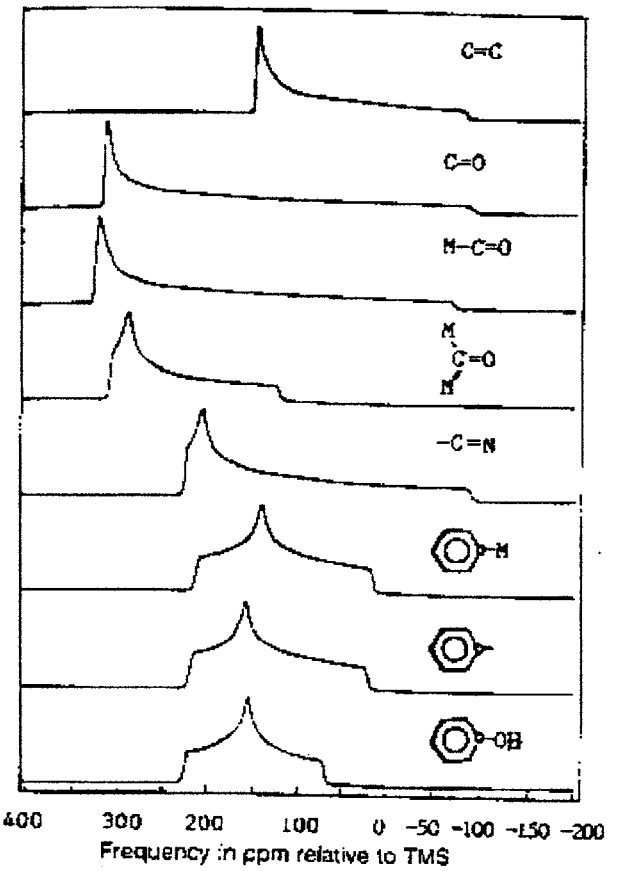

Fig. 8.9. The CSA for carbons with sp hybridization. The circle in the structures represents the carbon that is being observed. (Reproduced with permission from Ref. [28]. © 1987 American Institute of Physics.)

The effects of fast-diffusional rotation have been calculated by transforming the tensor from the static system to a rotating system. For comparison, the motional model that considers rapid jumps between two equivalent sites is calculated by using rotation matrices to construct an average flipping-frame tensor from the static one.

NMR studies of the motions of the aromatic amino acids of the fd bacteriophage protein were made, and the results are shown in Fig. 8.12. The experimental spectrum fits the calculated flip-averaged spectrum better than it fits the rotationally averaged spectrum. Therefore the rings are executing 180° flips in less than 1 ns, and probably in less than 0.01 ns. Additionally, the experimental spectrum is narrower than expected from the static chemical-shift tensor, and so additional molecular motion of the main chain is also involved.

NMR line-shape experiments of molecular motion have been made for the polycarbonates of bisphenol-A (BPA-PC) [54–56]. Two motional processes occur: (1) restricted rotational diffusion over a limited angular amplitude around the carbon-

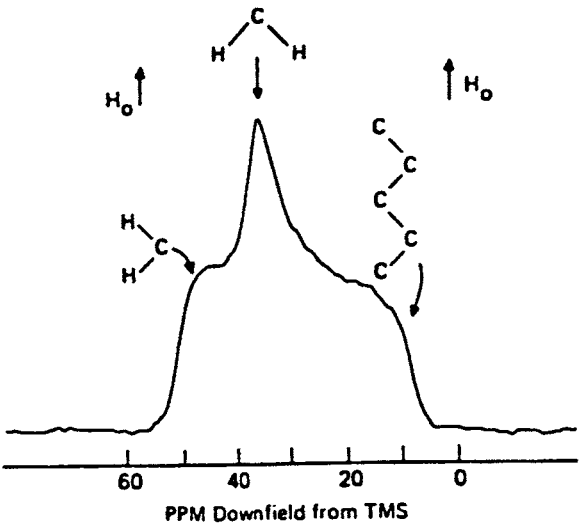

Fig. 8.10. The DD-CP ^{13}C spectrum of polycrystalline PE. All-trans methylene chain, three elements of chemical-shielding tensor and their assignments are shown. (Reproduced with permission from Ref. [50]. © 1976 Academic Press.)

ring bond axis, and (2) 180° flips between two potential minima around the same axis; these 180° flips constitute the primary motion. These motions correlate well with mechanical and dielectric results for this polymer.

Structural applications of chemical-shift tensors

A number of applications of CSA have been developed with the experimentally determined band shapes. Differences in the CSA band shapes are a consequence of changes in the electronic environment associated with the chemical nature of the carbon site, and these differences can be used to determine the amount of the unique carbon in the sample. In practice, powder patterns are simulated and compared with the experimental spectra to obtain structural information or the relative fractions of the carbon types.

CSA analysis of coal samples

CSA line shapes were used for the analysis of carbon types in coal samples. The derived experimental line shapes were fit to the experimental coal spectra for samples with high and low oxygen contents, and the fractions of the different types of carbons in the coal were determined. Differences in the CSA band shapes for aromatic compounds are due to differences in the bond orders of the aromatic-ring carbons. Aromatic carbons can be classified into three different subgroups according

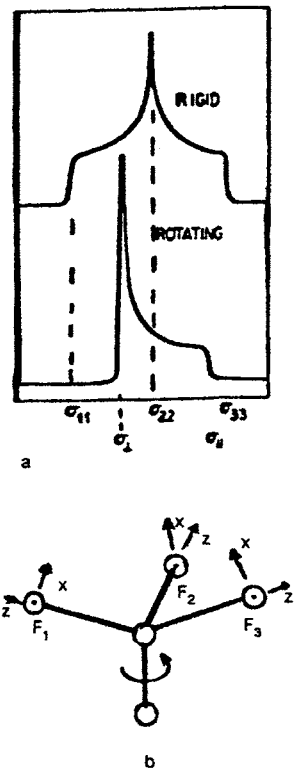

Fig. 8.11. (a) The ^{19}F chemical-shift spectra of polycrystalline CF_3COOAg for rigid and rotating $-CF_3$. (b) Diagram of rotation of the CF_3 group about the C−C axis.

to distinct chemical environments. These groups are benzene-like sp^2 hybridized protonated carbons on the periphery of the aromatic ring, substituted peripheral carbons (e.g., alkylated carbons), and condensed inner and bridgehead carbons. Protonated benzene-like carbons are characterized by a highly asymmetric powder pattern. Upon substitution of an aliphatic group, the two in-plane tensor components move closer to reduce the asymmetrical features of the band. The inner carbons in a large polycondensed aromatic system have nearly axial symmetry, and the band shape is nearly axially symmetric [57]. These band shapes were used to analyze the different carbon types in fusinite and anthracite coals.

CSA determination of crystallinity

The CSA line shapes of the crystalline and amorphous portions of polymers are substantially different from each other and can be used to determine the crystallinity of polymer systems. An analysis of the NMR crystallinity of poly(tetrafluoroethylene)

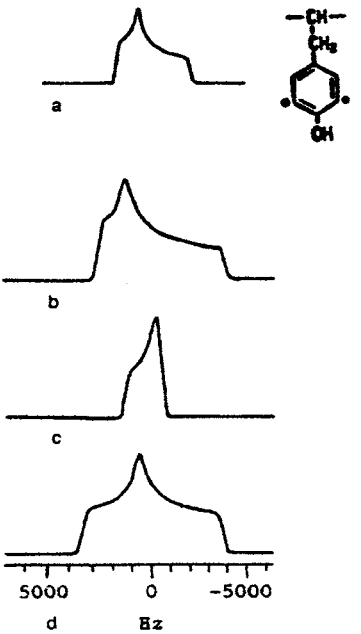

Fig. 8.12. The observed spectra of the phenyl ring (a), and the simulated spectra for motion involving ring flips (b), rapid rotation (c), and a static system (d). The principal axis is the C−C−phenyl ring bond axis. (Reproduced with permission from Ref. [53]. © 1982.)

(PTFE) was accomplished by using ^{19}F CSA line-shape analysis with multiple-pulse techniques for the removal of dipolar effects. The ^{19}F spectral changes of PTFE as the crystalline content is varied are shown in Fig. 8.13.

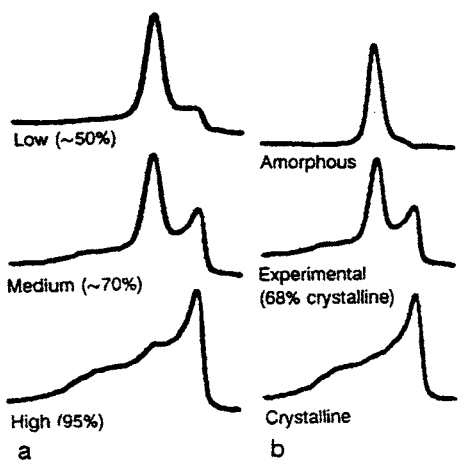

Fig. 8.13. (a) The ^{19}F REV-8 chemical shift of PTFE samples of varying crystallinity obtained at 259°C. (b) The ^{19}F REV-8 chemical shift of a PTFE sample with 68% crystallinity, showing the decomposed line shapes of the amorphous and crystalline fractions. (Reproduced from Ref. [27]. © 1980 American Chemical Society.)

The analysis of the ^{19}F spectrum was accomplished by decomposing the line shapes into the amorphous and crystalline fractions.

CSA determination of orientation

A number of methods are available for the determination of the degree of molecular orientation in solid polymers. Techniques that selectively give information about the molecular orientations in the crystalline and amorphous regions are especially valuable. A potential method for measurement of orientation is the determination of the CSA.

This approach has been used to study the uniaxial drawing of PTFE. The ^{19}F multiple-pulse spectrum of semicrystalline PTFE samples as a function of the angle, β, between the direction of stress and the magnetic field [58] is shown in Fig. 8.14.

By varying the moments of these spectra about the isotropic chemical shift, an approximate orientational probability distribution of the chain axes about the direction of stress can be determined. These results are shown in Fig. 8.15 for samples with different draw ratios [58].

The increase in the intercept reflects the greater alignment of the chains with the draw direction.

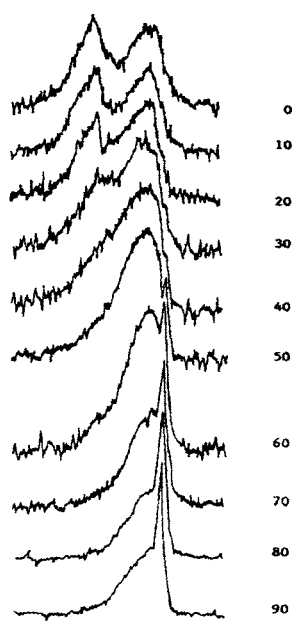

Fig. 8.14. The ^{19}F NMR chemical-shift spectra of deformed PTFE samples as a function of the orientation, β, of the stretch axis relative to the static magnetic field. (Reproduced with permission from Ref. [58]. © 1982 Butterworth and Co., Ltd.)

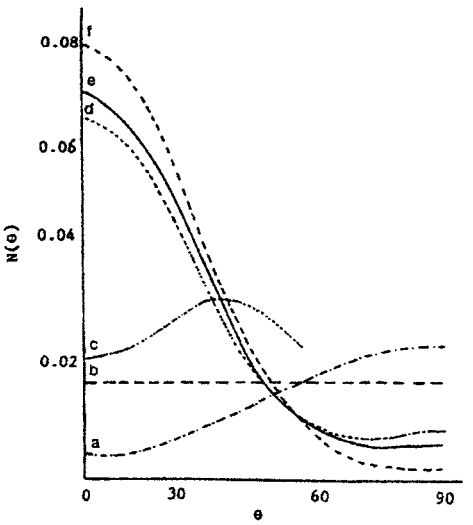

Fig. 8.15. The distribution function, $N(\theta)$, derived from the ^{19}F-NMR spectrum of PTFE at different draw ratios. (a) $\lambda = 0.82$, (b) $\lambda = 1.0$ (unoriented), (c) $\lambda = 1.40$, (d) $\lambda = 1.75$, (e) $\lambda = 2.10$, and (f) $\lambda = 2.40$. (Reproduced with permission from Ref. [58]. © 1983 John Wiley and Sons, Inc.)

Biaxial films of poly(ethylene terephthalate) (PET) were studied by using the NMR CSA technique [59]. There is a highly ordered component of the film in which the planes of the aromatic rings lie close to, but not in, the plane of the film. There is also a fast-relaxing component that is much less oriented and results from polymer chains that are relatively mobile, that is, the amorphous phase.

The magic-angle spinning (MAS) experiment

As suggested by Andrew [14], for solids in which the molecular motion is insufficient, "one may seek to emulate nature by imposing a motion on the nuclei". This was first accomplished by rapidly spinning the solid sample at 57.4° (the *magic angle*) [60,61]. Under this circumstance, each molecule experiences a continuous series of orientations with respect to the external magnetic field. The result is an isotropic average of the chemical shift for the solid similar to that observed for the same sample in solution.

Utility of MAS

MAS can potentially remove any of the magnetic interactions responding to the $(\cos^2 \beta - 1)$ geometrical dependence. These interactions include dipolar interactions, CSA, and quadrupole interactions. However, there are severe limitations to the use of MAS. First, the spinning rate must exceed the magnitude of the interactions to be removed. Because of the large magnitude of some of these interactions, sufficiently

high spinning rates are difficult to achieve. The magnitude of the homonuclear dipolar field for protons is approximately 20 kHz, and generally, it is not practical to spin at such high speeds. High-speed spinners are now commercially available, and in the future it may be possible to use MAS to remove the proton dipolar interactions. Currently, homonuclear dipolar interactions for protons are generally removed by using multipulse techniques. For ^{13}C nuclei, the homonuclear dipolar effects are much smaller because of the large distances between the ^{13}C nuclei resulting from the low natural abundance of the ^{13}C. MAS will therefore remove the ^{13}C homonuclear dipolar interactions.

The substantial removal of anisotropic-broadening interactions from the NMR spectra of solids by rapid rotation about the magic angle reveals the chemical shift and spin-multiplet fine structures for solids, and these are similar to those obtained in

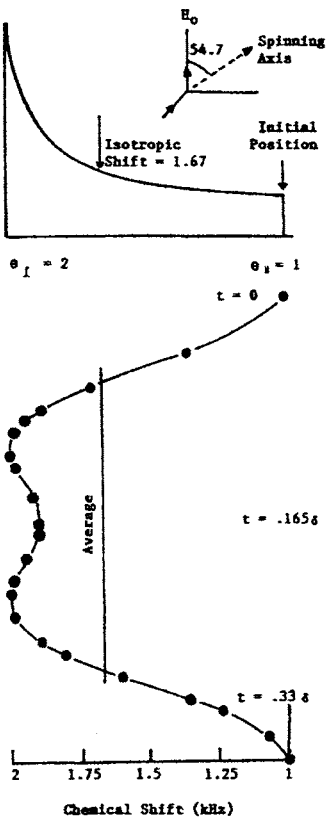

Fig. 8.16. The change in chemical shift with rotation is shown for a uniaxial chemical shift. In this case, an average isotropic shift of 1.67 will be measured when the anisotropy range is 1–2. The top figure is the powder pattern for a CSA going from 2 to 1. The bottom figure shows the specific shift as a function of rotation angle. These measurements should agree very closely with the value measured for the corresponding carbon in the liquid or solution state if other solid-state effects are neglected. (Reproduced with permission from Ref. [62]. © 1983 Plenum Publishing Corporation.)

the high-resolution NMR spectra of liquids. The MAS NMR method is used when a material must be studied in the solid state in order to examine the solid-state structure, or in cases where the material will not dissolve in a suitable solvent or melt without decomposition.

Removal of chemical-shift anisotropy

Because CSA has the same angular dependence as the dipolar interactions, but the magnitude of the effect (1–3 kHz) is much smaller, MAS is a viable technique for the removal of CSA.

The chemical shift can be written as follows:

$$\sigma_{zz} = \langle\sigma\rangle + \sigma^{a} \tag{8.28}$$

where $\langle\sigma\rangle$ is the isotropic part that is equal to $\frac{1}{3}Tr(\sigma)$ and σ^{a} is the anisotropic part. For a uniaxially symmetric tensor, the anisotropic part can be written

$$\sigma^{a} = \tfrac{1}{3}[\sigma_1 - \sigma_2(3\cos^2\theta - 1)] \tag{8.29}$$

and when the sample is rotated at the magic angle ($\theta = 57.4°$)

$$\langle\sigma^{a}\rangle = 0 \tag{8.30}$$

Under these circumstances, the CSA is removed, and only the isotropic average is measured. This is illustrated in Fig. 8.16, where the changes in the chemical shifts with rotation are shown for a uniaxially symmetric CSA [62].

In this case, an average isotropic shift of 1.67 ppm will be measured when the anisotropy ranges from 1 to 2 ppm.

However, another complication is observed in the spectra obtained with MAS. When the sample spinning speed is less than the CSA, rotational echoes appear as spinning sidebands that flank the isotropic peak. These echoes are spaced at the inverse of the spinning frequency. The effects of spinning on the ^{31}P spectra are shown as a function of the spinning rate [63] in Fig. 8.17.

As the rate of rotation increases, the rotational spinning sidebands move further out and become weaker. At very high spinning speeds, the intensities of the sidebands become negligible, and the spectrum consists of the narrowed central line at the Larmor frequency, ω_0. The intensities of the first satellites are expected to decrease at a rate of ω_r^{-2}, thus preserving their contributions to the second moment of the entire spectrum. Indeed, the magnitude of the second moment of the spectrum should be invariant with respect to rotation. The intensities of the second and higher satellites fall even more rapidly with an increase in ω_r, as ω_r^{-2n} for the nth satellite.

Setting the magic angle is very critical to the success of the MAS experiment. If the error in setting the magic angle is 0.1° for a shielding anisotropy of 200 ppm (not uncommon for ^{13}C in organic solids) this misalignment error results in a line

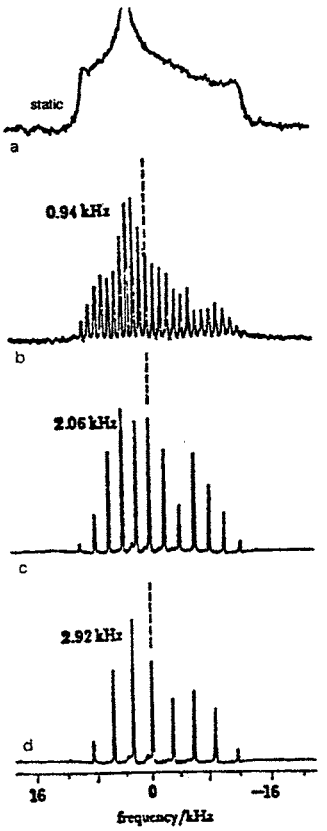

Fig. 8.17. ^{1}H-decoupled ^{31}P-MAS spectra of BDEP. The powder pattern in (a) is approximately 23 kHz wide and narrows to a spectrum exhibiting sidebands of 60 Hz full width at $n_r = 2.92$. The dashed line marks the isotropic shift. (b–d) The effects of spinning on the ^{31}P spectra as a function of spinning rate. (Reproduced with permission from Ref. [63]. © 1980 The Royal Society of Chemistry.)

broadening of 1.02 ppm [64]. The effect on the measured spectra of misalignment of the magic angle is shown in Fig. 8.18.

In the case of polycrystalline sucrose, the nonspinning spectrum is shown as well as the spectra for a misadjustment of the magic angle [65] by 0.7°. The line width increases and a loss of resolution occurs with the magic-angle misadjustment, although the lines are clearly narrowed by the spinning. A series of spectra of a single crystal of sucrose are shown in Fig. 8.19.

These spectra were obtained with misadjustment of the magic angle [65]. In this case, chemical-shift differences for a single crystal are observed with the missetting of the magic angle.

MAS is most effective in narrowing the resonances of carbons in solids with a narrow CSA. For aliphatic carbons, the CSA is small, and moderate spinning speeds suffice. For carbons with multiple bondings, the CSA is much larger, and

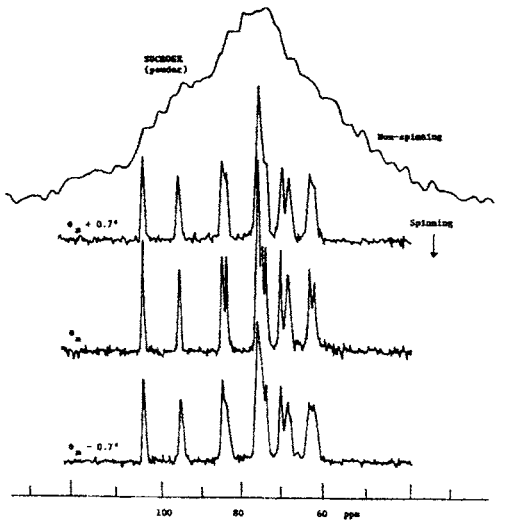

Fig. 8.18. The effect on the measured spectra of misadjustment of the magic angle. (Reproduced with permission from Ref. [64]. © 1982 Academic Press.)

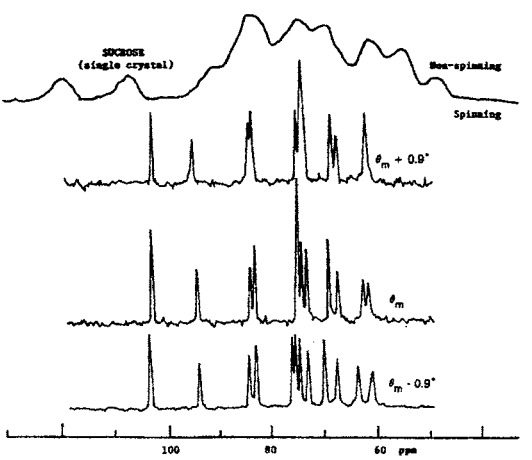

Fig. 8.19. A series of spectra of a single crystal of sucrose obtained with misadjustment of the magic angle. (Reproduced with permission from Ref. [65]. © 1982 Academic Press.)

higher spinning speeds are required to coherently average the CSA. For aromatic carbons, the CSA is nearly 150 ppm. At a carbon Larmor frequency of 15 MHz, this CSA corresponds to 2.25 kHz, and the sample must be rotated at this frequency to coherently average the CSA. Because the magnitude of the CSA increases with the applied magnetic field, higher spinning speeds are required for higher applied magnetic fields.

The ^{13}C isotope presents a challenge for NMR spectroscopy because of its inherent low sensitivity. The low natural abundance, the low gyromagnetic ratio, and the long

spin–lattice relaxation time of the ^{13}C nucleus limit the observable ^{13}C signal. The sensitivity must be increased for the detection of the resonances of the ^{13}C nuclei. In response to this need, polarization-transfer methods are used to transfer the large spin-state polarization of the protons to the weakly polarized ^{13}C nuclear species. Perfect transfer of polarization from protons to ^{13}C would improve the ^{13}C signal by a factor of $\gamma_C/\gamma_H = 4$.

In NMR spectroscopy, improvements in the signal-to-noise ratio are often accomplished by signal averaging through the coadding of the FIDs. The delay between pulse sequences that can be coadded is limited by the time required to repolarize the nuclear spin system ($\sim 5 \times T_1$). The $^{C}T_1$ spin–lattice relaxation times for solids are significantly longer than the $^{H}T_1$ times, so the maximum number of pulses that can be used is less. However, with polarization transfer, the delay time between cross-polarization pulse sequences depends on the shorter $^{H}T_1$ times, and further gains in signal enhancement occur to the extent of $(^{C}T_1/^{H}T_1)^{1/2}$.

Experimental implementation of cross-polarization

Cross-polarization (CP) is a double-resonance experiment in which the energy levels of the ^1H and ^{13}C spins are matched to the Hartman–Hahn condition [66] in the rotating frame. Under this condition, energy may be exchanged between the two coupled spin systems. The result is a growth of the ^{13}C magnetization at the expense of the ^1H magnetization. The method involves four steps [67]:

(a) polarization of the ^1H spin system,
(b) spin-locking of the protons in the rotating frame,
(c) establishment of contact between the carbons and the protons,
(d) measurement of the magnetization of the carbon nucleus.

The basic pulse sequence used for the cross-polarization experiment is shown in Fig. 8.20. The application of a 90° ^1H pulse rotates the ^1H longitudinal magnetization into transverse magnetization (the xy plane is in the rotating reference frame as shown in Fig. 8.20a). The second step is the nearly immediate (within microseconds) application of a 90° phase-shifted proton pulse, which makes the effective field colinear with the proton magnetization and results in *spin locking* (Fig. 8.20b). Spin locking is used because the magnetization of the protons in the spin-locked state decays by a rotating frame spin–lattice relaxation time, $^{H}T_{1\sigma}$, at a rate that is orders of magnitude slower than the ordinary spin–spin relaxation (T_2) process. Thus, the magnetization loss of the protons resulting from relaxation effects during the contact time is small.

Simultaneously with the spin locking of the protons, in the third part of the experiment (Fig. 8.20c), a pulse is applied in the ^{13}C channel, and this pulse is carefully adjusted so that the energy gap for spin flips corresponds exactly to that of the protons. This pulse is maintained for a time, t_{CP}, and is the contact time. This *contact time* allows for the exchange of energy between the abundant proton-spin reservoir and the rare carbon-spin system. This exchange, called *cross-polarization*,

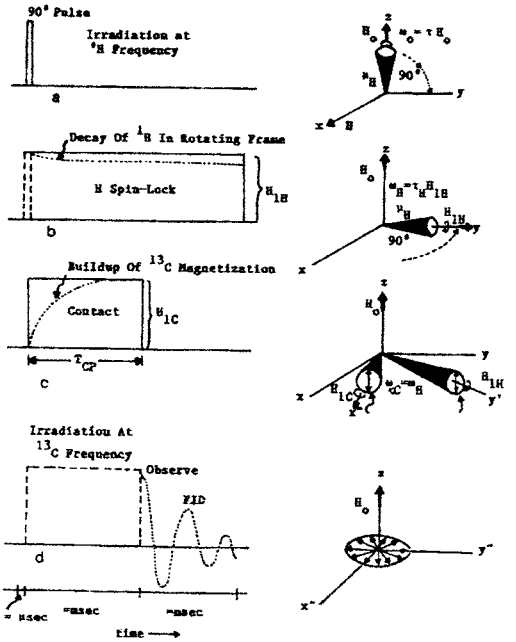

Fig. 8.20. The timing sequence for the cross-polarization experiment. (Reproduced with permission from Ref. [67]. © 1979 International Scientific Communications, Inc.)

occurs when the Hartmann–Hahn match [68], which is defined as

$$\omega_h = \omega_c \tag{8.31}$$

is satisfied in the rotating frame.

The fourth part of the CP experiment (Fig. 8.20d) is to terminate the ^{13}C pulse and to observe the FID while the ^{1}H field is used for decoupling. The resulting FID is Fourier transformed to give the frequency-domain spectrum.

In the CP experiment, the ^{13}C spin system is polarized by the ^{1}H spin system under the Hartmann–Hahn condition. Therefore, the longer $^{C}T_1$ (1–1000 s) is replaced by the shorter $^{H}T_1$ spin–lattice time (1–100 ms). The optimum recycle delay has been calculated, and it is 1.25 $^{H}T_1$ for the situation in which spin diffusion dominates the spin system [69]. For the case in which spin diffusion is not efficient, the optimum recycle delay must be longer (4–5 $^{H}T_1$) to avoid saturation.

Dynamics of the CP experiment

A typical increase in carbon magnetization with contact time is shown in Fig. 8.21.

In the CP experiment, polarization is transferred from the magnetically rich protons to the magnetically poor carbons via their static dipolar interactions. When both

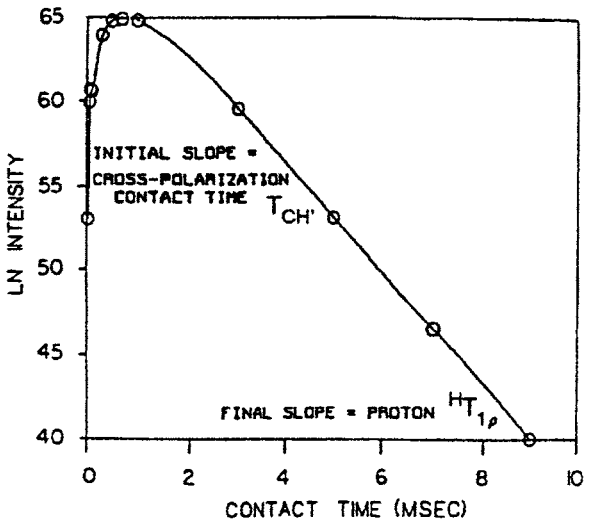

Fig. 8.21. The change in carbon magnetization with contact time for the cross-polarization experiment. The initial rise is due to the cross-polarization contact time, T_{CH}, and the relaxation decrease is governed by the $^{H}T_{1\sigma}$.

spins are locked in the rotating rf fields and their amplitudes are matched by using the Hartmann–Hahn condition, the time constant for the transfer of polarization under conditions of spin locking is called the T_{CH} relaxation time. This transfer is a spin–spin process, and it generally has a magnitude in the range of 100 μs. In polymers, the T_{CH} for methine and methylene carbons ranges from 15 to 50 μs and from 45 to 100 μs for protonated aromatic carbons. These T_{CH} values are essentially independent of the rate of sample rotation in the MAS experiment.

The result of CP is an initial growth of the ^{13}C magnetization at a rate that is inversely proportional to the cross-polarization transfer-rate constant (T_{CH}) (Fig. 8.21). After a suitable period (typically 1–10 ms), a maximum ^{13}C magnetization is reached, after which the ^{13}C signal begins to decay at a rate proportional to the inverse of the $^{H}T_{1\sigma}$ time. The carbon magnetization, S, is given by

$$S = \exp\left(\frac{t_m}{^{H}T_{1\rho}}\right) 1 - \frac{\exp(-t_{CP})}{T_{CH}} \tag{8.32}$$

where t_{CP} is the contact time. Thus two opposing relaxation mechanisms operate during the contact time. For short contact times, the T_{CH} process dominates, and the carbon magnetization increases exponentially. At longer contact times, the process is dominated by the $^{H}T_{1\sigma}$ process, and the magnetization decreases exponentially because of the proton spin–lattice relaxation in the rotating frame. $^{H}T_{1\sigma}^{-1}$ is approximately proportional to the spectral density function near the rotating-frame precession rate, $\omega_H = \gamma H_1$, and provides a direct measure of the low-frequency motion of the resonant group. T_{CH} is related to the carbon–proton dipolar line-width

contribution in an undecoupled conventional ^{13}C-NMR spectrum by

$$T_{CH}^{-1} = C_{CH}\left[\frac{M_2^{CH}}{(M_2^{HH})^{1/2}}\right] \tag{8.33}$$

where C_{CH} is a geometry-dependent term, M_2^{CH} is the (C,H) second moment, and M_2^{HH} is the (H,H) second moment. In general, more motion of a particular resonant group results in smaller residual dipolar interactions and a longer T_{CH}.

The cross-polarization transfer of magnetization is inversely proportional to the sixth power of the C–H internuclear distance. Provided that the carbons in a polymer repeat unit are subjected to the same motions, carbons with directly bonded protons are expected to cross-polarize more rapidly than carbons without direct interactions because the shorter interaction distance results in a larger local dipolar field. Rapid molecular motion attenuates the cross-polarization mechanism. For protonated carbons in rigid solids, most of the signal buildup occurs over about the first 100 μs. For nonprotonated carbons, most of the signal appears in the first few milliseconds.

The rate of signal decay depends on $^{H}T_{1\rho}$ and can differ among carbon types, although $^{H}T_{1\sigma}$ is generally the same for all carbon groups with highly coupled protons. If $^{H}T_{1\sigma}$ is very short, the cross-polarization process is endangered because of the rapid decay process. By varying the contact time prior to observation of the spectrum, T_{CH} and $^{H}T_{1\sigma}$ may be determined for the protons coupled with each resolved carbon resonance.

The preceding analysis assumes that the rf fields H_{1H} and H_{1C} are much larger than their respective line widths. Also, the relaxation parameters are assumed to have the following order: $^{C}T_1 > ^{H}T_1 > ^{H}T_{1\rho} > T_{CH}$. When these conditions are not met, cross-polarization may be ineffective.

Factors influencing cross-polarization

Cross-polarization is more effective for rigid systems than for mobile structures. When extensive motion occurs, the C–H dipolar interactions are reduced, and this reduction causes a lower cross-polarization rate. In some systems, mobile components can exhibit sufficient motional anisotropy to permit cross-polarization because the anisotropy can impart a residual static component to the overall motion [69]. This appears to be the case for elastomeric systems.

Performing cross-polarization experiments on mobile samples is sometimes difficult. If the $^{H}T_{1\rho}$ is in the range of hundreds of microseconds, the ^{1}H rotating-frame magnetization relaxes before appreciable ^{13}C magnetization can be cross-polarized. Polyethylene oxide (PEO) is an example of a polymer that exhibits this effect. The $^{H}T_{1\rho}$ is 100 μs for PEO, and it is approximately 1 ms for polyethylene (PE). Cooling the PEO sample changes the $^{H}T_{1\rho}$ and T_{CH} sufficiently to allow effective cross-polarization.

In PE, the CP enhancement varies with the phase of the polymer. For the crystalline regions, the CP enhancement is 3.5 ± 0.2, and in the disordered regions, the

enhancement factor ranges from 2.4 to 3.0 [70]. The smaller enhancement in the disordered regions arises because molecular motion shortens ${}^{H}T_{1\sigma}$ and lengthens T_{CH}.

The magnitude of T_{CH}^{-1} is related to the strength of the static dipolar interactions between the carbons and protons. T_{CH} should be less than 0.13 ms for a rigid methylene group [71]. In general, TCH values decrease in the following order: nonprotonated carbons > methyl (rotating) carbons > methylene carbons > protonated aromatic-aliphatic methine carbons > methyl (static) carbons.

MAS has only a small influence on the cross-polarization process for rigid polymer systems. In principle, magic-angle spinning reduces the C–H dipolar decoupling, but in order for this averaging process to be efficient, the local ^{1}H–^{13}C coupling must remain static for at least half of a revolution, or $(2\omega_r)^{-1}$, where ω_r is the spinning frequency. When the rotor speed is 2 kHz, the rotor period rate is 500 μs $(1/\omega_r)$. For a speed of 5 kHz, the period is 200 μs. Essentially all of the T_{CH} values of rigid polymers are shorter than these typical rotor periods. Consequently, MAS has little effect on the CP process for glassy polymers. Because the T_{CH} is approximately 100 μs for protonated aromatic carbons in glassy polymers, the cross-polarization is virtually completed by the time the spinner has rotated very far. For the unprotonated aromatic and quaternary carbons, relaxation times increase by about 50% when the speed is increased from 1 to 3 kHz.

MAS does have an effect on the cross-polarization efficiency for mobile systems like elastomers [72]. For a static sample, the transfer rate is a function of ω_C and has a maximum polarization-transfer rate at the Hartman–Hahn match and a slower polarization transfer with increasing mismatch. However, when the sample is spun with MAS, there is a very slow transfer of polarization at the Hartman–Hahn match, where the transfer is expected to be most rapid. A series of maxima in the transfer rate occurs when ω_{1C} and ω_{1H} are mismatched by a multiple of the spinning frequency. Thus, mismatching the ω_{1C} and ω_{1H} produces high signals at multiples of the MAS frequency. A series of maxima in T_{CH} are observed as a result of an amplitude-modulated pattern due to C–H heteronuclear coupling [73].

Cross-polarization as a tool for resonance assignments

Cross-polarization can be used as a tool for the assignment of resonance lines. As the contact time is varied, the spectra change dramatically. The signals observed at the smallest contact times (0.01 ms) are assigned to the carbons that have the largest dipolar ^{1}H–^{13}C interactions. The strong dipolar interactions experienced by these carbons imply that their motions are hindered. The broad line shapes that are observed usually support this conclusion. Evidently, the molecular motions of these carbons cannot average the chemical-shift anisotropies effectively, and the resulting lines are broad. Sharper signals emerge when the contact time is in the 0.25–1-ms range. These signals are assigned to carbons that experience greater motional averaging of their ^{1}H–^{13}C dipolar interactions and their ^{13}C chemical-shift anisotropies.

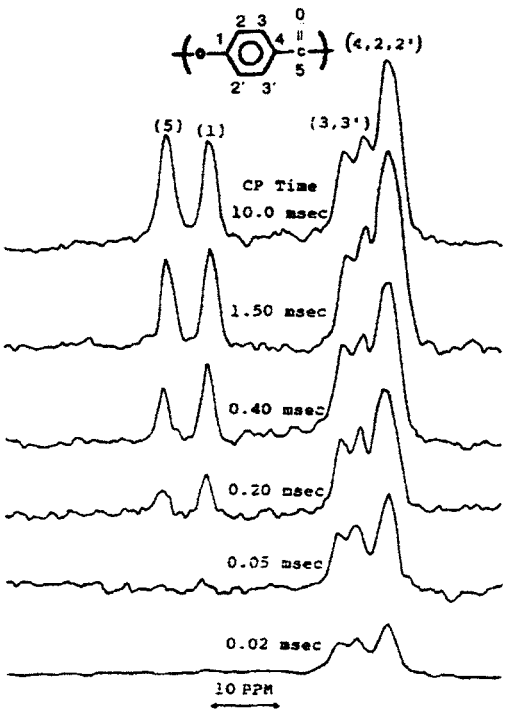

Fig. 8.22. Magic-angle CP ^{13}C-NMR spectra of a *p*-oxybenzoyl polymer as a function of time. The numbered peaks correspond to the numbered carbons in the structure. (Reproduced from Ref. [73]. © 1979 American Chemical Society.)

For example, the carbonyl signals have line widths of 30 ppm compared to the 150-ppm line width observed for a rigid lattice. The sharpest signals are obtained from long contact times because of the efficient relaxation of the motionally hindered carbons.

For example, spectra of poly(*p*-oxybenzoyl) as a function of contact time are shown in Fig. 8.22.

For the very short contact times, only the resonances assigned to *ortho* ring carbons ($C_{2,2'}$ and $C_{3,3'}$) are present. This result reflects the larger static dipolar interaction for the proton-bearing carbons. At long contact times, the line between $C_{2,2'}$ and $C_{3,3'}$ begins to grow at about the same rate as the line associated with C_4. The line assigned to the carboxyl carbon polarizes at the slowest rate.

The interrupted-dephasing CP experiment

An experiment that is useful for assigning nonprotonated carbon resonances in the NMR spectrum is the interrupted-decoupling CP experiment [74,75]. In this experiment, the decoupling of the protons is interrupted (by turning off the proton rf field) for a predetermined time. During the interrupted-decoupling period, ^{13}C

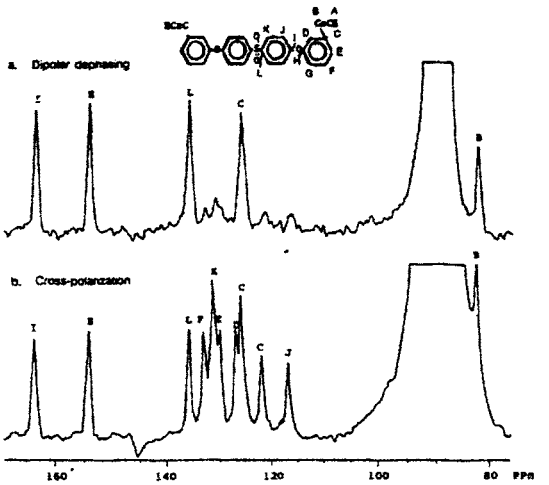

Fig. 8.23. An example of the interrupted-decoupling experiment for suppression of the protonated carbon resonances is shown. The labeled peaks correspond to the labeled carbons in the structure. (Reproduced from Ref. [76]. © 1984 C. Shields.)

magnetizations due to protonated immobile carbons are efficiently dephased by static ^{13}C dipolar coupling. Switching off the carbon field, restoring the proton field, and acquiring the data terminates this dephasing. The quaternary carbons with no bonded protons dephase very slowly and survive the decoupling period. This effect allows a discrimination of the quaternary carbons from the carbons with bonded protons. Unfortunately, motions that are effective in averaging dipolar couplings to reduced values can also cause signals of highly mobile protonated carbons to persist in the interrupted-decoupling experiments. The most common example is the methyl group, which rotates very rapidly even in rigid solids, and the methyl resonance can survive the interrupted-dephasing process.

An example of the use of the interrupted-decoupling experiment for suppression of the protonated carbon resonances [76] is shown in Fig. 8.23.

For the diacetylene polymer, the carbons labeled B, C, H, and I survive the long interrupt cycle and are therefore quaternary carbons [76].

Quantitative aspects of cross-polarization spectra

Under proper experimental conditions, the integrated area of a particular resonance in a ^{13}C-NMR spectrum are related to the fraction of the various carbon types in the polymer structure. One of the problems in a CP ^{13}C spectrum is the possible distortion of the peak areas because of differential cross-polarization times for the various carbons.

In fact, not all of the carbons may be observed in the CP experiment because of

two different problems. Carbons in hydrogen-deficient domains will have minimal dipolar couplings to remote protons and hence will not cross-polarize efficiently. For complex samples like coals, aromatic carbons are likely to have this problem, and the aliphatic carbons will not. Second, a fraction of the carbons in the sample may be near free-radical sites, which either broaden the resonances beyond detectability or greatly reduce the $^{H}T_{1\rho}$ in the vicinity of the radical.

For CP experiments, a spin-counting procedure should be devised to quantify the fractions of detectable carbons in the sample under observation. Basically, the procedure involves measuring a ^{13}C-CP-MAS spectrum of a known quantity of the sample that has been coground with a weighed quantity of a suitable quantitation standard, such as glycine. From the weight fraction of carbon and the integrated peak areas, the fraction of detectable carbons can be calculated.

By comparing known masses of polypropylene (PP) with a calibration standard of hexamethylbenzene, approximately 80% of the carbons in PP were observed [77]. The basis for this loss of detectability of the carbons in PP is the relative values of T_{CH} and $^{H}T_{1\rho}$. When $^{H}T_{1\rho}$ is very short, equilibrium between the two spin systems cannot be obtained before the protons decay.

True relative intensities in the cross-polarization experiment are obtained only when the following three criteria are satisfied [78]:

(1) The cross-polarization times are short compared to the shortest proton rotating-frame relaxation time, $^{H}T_{1\rho}$, for the carbons (if there is extensive motion in the mid-kiloHertz range, then $^{H}T_{1\rho}$ becomes approximately 10^{-4} s and does not meet this criterion).
(2) The proton rf field is much larger than the local proton–proton dipolar fields (rf signals in the 50–60-kHz range create a variation of only a few percent in polyethylene).
(3) Cross-polarization time constants, T_{CH}, are short enough to allow the ^{13}C nuclei to equilibrate with the protons during cross-polarization (if there is extensive motion, the CP process can become very inefficient in the mobile region compared to the more rigid portions) [78].

The recommended procedure is to run a series of different delay times using only DD and MAS to check if the cross-polarization is distorting the CP-MAS spectrum. The best method to obtain quantitative areas is to vary the cross-polarization contact time and then to construct a graph of the magnetizations and extrapolate the linear portion to zero contact time [79], as shown in Fig. 8.24.

Quantitative applications of cross-polarization

Quantitative measurements on solid polymers have been made [80] by using MAS-DD-CP. A cross-polarization technique has been devised not only to determine the number of defects (end-group and branch defects) in PE but also to determine the distribution of the defects between the crystalline and noncrystalline phases. By

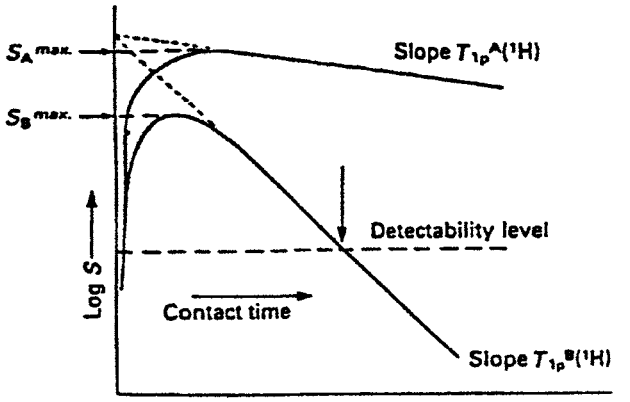

Fig. 8.24. The extrapolation method for obtaining quantitative intensities is to vary the cross-polarization contact time and to construct a graph of the magnetizations and extrapolate the linear portion to zero contact time. (Reproduced with permission from Ref. [79]. © 1985 The Royal Society of Chemistry.)

using a large number of transients to average the signal, carbon fractions on the order of 2×10^{-4} can be detected, and resonance areas accurate to $\pm 10^{-4}$ can be detected if flat base lines are present.

The partitioning of the defects in the two phases was accomplished by generating pure crystalline and amorphous spectra of PE [80]. Three different CP sequences were used. In one sequence, the normal CP experiment was used in which all the carbons had comparable intensities. In the second sequence, a preparation pulse that favored the crystalline phase was used. In the third sequence, the preparation pulse favored the amorphous phase. In this manner, spectra representing different mixtures of the two phases were obtained, and by taking the appropriate linear combination of these three spectra, the 'pure' spectra of the two components were determined. The resulting pure crystal and pure noncrystal spectra generated from linear combinations of the spectra of the samples are shown in Fig. 8.25.

The distribution of the defects was then determined with curve fitting of the pure spectra to the spectra of the samples.

Use of cross-polarization for separation based on mobility

If a ^{13}C resonance line (without dipolar broadening) is not substantially broadened, then cross-polarization discriminates against liquid-like lines. In fact, cross-polarization can be used to distinguish mobile components from rigid components. This ability is illustrated by the study of styrene–butadiene copolymers. For a cross-polarization contact time of 10 ms, only resonances assigned to the butadiene carbons appear, whereas at a contact time of 1.5 ms, both styrene and butadiene signals are observable [79].

This sensitivity of the cross-polarization experiment to more rigid components has been used in the separation of the network and nonnetwork structures in the

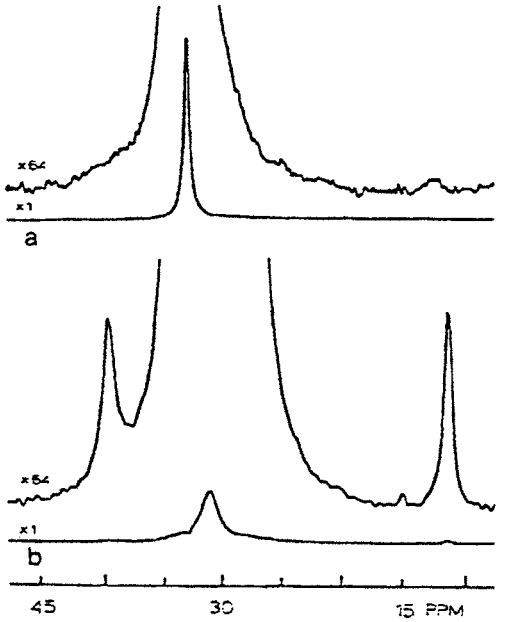

Fig. 8.25. The pure crystal (a) and pure noncrystal (b) spectra of PE generated from linear combinations of the spectra obtained by using different pulse sequences. (Reproduced from Ref. [80]. © 1987 American Chemical Society.)

peroxide crosslinking of polybutadiene [81]. In Fig. 8.26, the gated high-powered decoupled (GHPD) ^{13}C spectrum with MAS but without cross-polarization is shown for polybutadiene networks with increasing amounts of peroxide.

The initial polybutadiene lines decrease significantly as the peroxide level increases. On the other hand, Fig. 8.26 also shows the cross-polarization spectrum, and in this case, the mobile samples have little intensity and the highly cured samples have high intensity, a result that reflects the rigidity of the cured networks.

The cross-polarization experiment for the study of polymer blends

Intermolecular interactions can be probed by using cross-polarization. In the cross-polarization experiment, only carbons that are dipolar-coupled to protons give rise to ^{13}C resonances, so deuterated carbons will not give rise to an NMR signal unless they are in close contact with protons on adjacent molecules. The appearance of deuterated-carbon resonances in a cross-polarized system indicates that the deuterated carbons have neighboring hydrogens only a few angstroms away. The resonances of the deuterated carbons may appear slightly shifted from the resonances of their protonated counterparts as a result of a small deuterium-isotope effect. If the chemical-shift differences are not sufficient, then the deuterated-carbon resonances can be distinguished from the protonated carbons by the use of interrupted decoupling

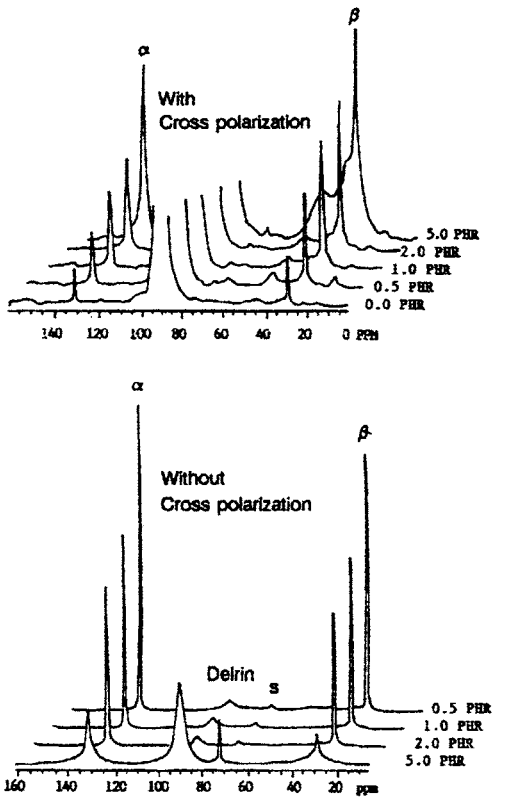

Fig. 8.26. The separation of the network and nonnetwork structures in the peroxide crosslinking of polybutadiene. (Reproduced from Ref. [81]. © 1984 American Chemical Society.)

delay. The protonated-carbon resonances are suppressed by the interrupted decoupling experiment, but the deuterated carbon resonances are only slightly affected. The cross-polarization experiment can be used to probe blends and mixtures and to study spatial order for mixtures of protonated and deuterated polymer blends [82]. Similarly, the degree of mixing of a plasticizer can be studied with this deuterium approach [83].

Contributions to line broadening in solids

Resonance line broadening arises from both homogeneous and inhomogeneous processes. Homogeneous processes result from a *single* structural source and are derived from relaxation effects. Among the homogenous processes are the natural line width that is usually associated with dipolar relaxation and residual static C−H dipolar broadening from incomplete motional narrowing. Processes that produce a distribution of resonance frequencies are *inhomogeneous*. Inhomogeneous processes

arise from *multiple* structural sources producing different chemical shifts, each with small intrinsic widths or spin packets. Among the inhomogeneous processes are inhomogeneity in the static field, a variation in bulk magnetic susceptibility within the sample, a distribution of isotropic chemical shifts, and a residual CSA resulting from incomplete motional narrowing.

Experimentally, homogeneous and inhomogeneous processes can be differentiated in several ways. Higher MAS rotation rates are required to effectively narrow homogeneous processes, and inhomogeneous processes can be narrowed with slower rotation rates [84]. A spin-echo experiment can be used to distinguish between these two mechanisms [85]. The inhomogeneous processes can be refocused by 180° rf pulses, but the homogeneous processes cannot. Any decrease in the echo corresponds to a homogeneous broadening mechanism.

The most obvious source of line broadening is lack of homogeneity of the applied magnetic field. However, instrumental improvements have reduced this effect to a few milliGauss out of 10^4 G. For solids, the homogeneity of the field can be measured by using adamantane, and nonuniformities in the magnetic field result in line broading of only 2 Hz [22]. For studies as a function of temperature, efforts should be made to readjust the homogeneity of the magnetic field because of changes in the sample geometry with changes in temperature as well as other factors. For studies of polymer melts, a broadening contribution of 50–60 Hz from this source has been reported [86].

In solids, the anisotropy of the bulk magnetic susceptibility for a configuration of irregularly shaped particles can be a factor in the broadening of the resonance lines. Under MAS, the shape-demagnetization factors are axially averaged so that the sample appears as if it were a spheroid with a symmetry axis along the spinning axis [87]. Additionally, macroscopic or microscopic inhomogeneities within the sample can cause differences in the bulk magnetic susceptibility. The *macroscopic inhomogeneities* can arise from fissures, bubbles, and other mechanical or structural irregularities in the sample and can be minimized by careful sample preparation. The *microscopic inhomogeneities* can arise from different phases, interfaces, and other structural variations. For example, the bulk susceptibility of a crystalline *n*-alkane is different (approximately 2% smaller) from that of the corresponding liquid [22].

The induced magnetic polarization from a heterogeneous sample can produce a nonuniform screening field, which leads to line broading. However, the susceptibility fields are small for organic materials, and the bulk–volume susceptibility is typically on the order of 1 ppm. The bulk magnetic susceptibility is inherently anisotropic for crystalline solids and cannot be removed by MAS. However, the magnitude of the effect is small (~0.7 ppm).

The T_1 processes effectively limit the lifetime of the Zeeman states, and this broadening effect amounts to $(h/2\pi)T_1$. Because the T_1s for carbons are long (10–1000 s), this effect is negligible for solids.

The broadening introduced by residual dipolar coupling can be estimated from the magnitude of the local magnetic field, H_{loc}. This local field is

$$H_{loc} = \frac{\mu}{r^3} \tag{8.34}$$

By using $r = 2$ Å and $m = 10^{-23}$ erg/G, H_{loc} is approximately 1 G [88]. The homogeneous contribution to the line width, which is primarily attributable to motional modulation of the C–H coupling, is $(\pi {}^{C}T_{1\rho})^{-1}$.

Two types of motion can influence the dipolar coupling and broaden the line widths. In one case, the nuclei undergo random isotropic motion at a rate such that all angles are not averaged within the time interval T_2. Alternatively, the motions may be quite rapid, but the accessible angular motion is severely restricted. The effect of molecular motion on the line widths behaves the same as chemical exchange, which will be discussed in the next section.

Line shapes: chemical-exchange effects

If a nucleus exchanges between two sites B $\leftrightarrow$ B′, with resonance frequencies ω_B and $\omega_{B'}$ and lifetimes τ_B and $\tau_{B'}$ (corresponding to exchange rates of $\tau_B^{-1}$and $\tau_{B'}^{-1}$, the effects of chemical exchange on the line shape may be summarized under three different conditions:

(1) *Slow exchange*, where $[\omega_B - \omega_{B'}] \gg \tau_B^{-1}\tau_{B'}^{-1}$. The resonances at ω_B and $\omega_{B'}$ merely acquire additional widths given by $(\pi\tau_B^{-1})$ and $(\pi\tau_{B'}^{-1})$ (in units of hertz), respectively.

(2) *Fast exchange*, where $[\omega_B - \omega_{B'}] \ll \tau_B^{-1}\tau_{B'}^{-1}$. The two resonances merge into a single resonance with a frequency given by the average of these quantities in the absence of exchange weighted by the fractional concentration of the two species. In the absence of exchange, the averaging of the line widths requires $[\omega_B - \omega_{B'}]^2\tau_B$ and $[\omega_B - \omega_{B'}]^2\tau_{B'}$ to be negligible compared to the linewidths of the B and B′ resonances, respectively.

(3) *Intermediate exchange*, where $[\omega_B - \omega_{B'}] = \tau_B^{-1}$ and $\tau_{B'}^{-1}$. Both frequency shifts and line-width changes occur, to yield a complex line shape.

All of these spectral features can be described quantitatively by means of a simple theory based on the Bloch equations. Computer simulations of the effects of a two-site exchange with no multiplicity from spin–spin effects are shown in Fig. 8.27.

The grand experiment (MAS-DD-CP)

By combining the three previously described experiments into one grand experiment, high-resolution ^{13}C-NMR spectra of solids can be obtained [5]. The

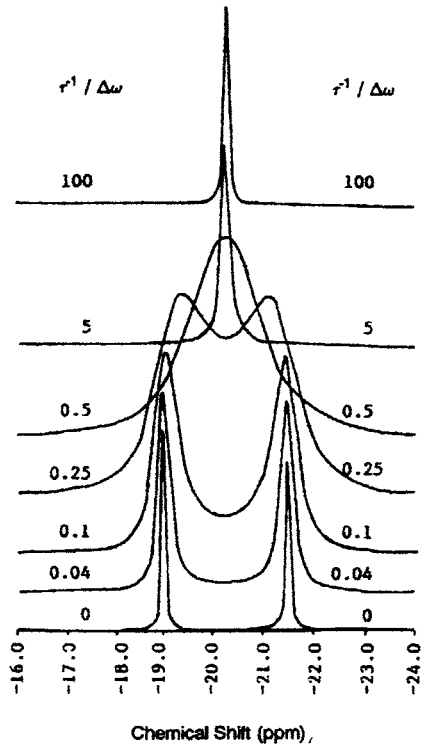

Fig. 8.27. Computer simulation of the effects of a two-site exchange with no multiplicity from spin–spin effects. The exchange rate is expressed as a fraction of the chemical shift (in units of radians per second) at 81 MHz. The concentrations of the two species are taken to be equal. (Reproduced with permission from Ref. [88]. © 1984 Academic Press.)

benefits are demonstrated by comparing the ^{13}C solid-state NMR spectra of a sample of poly(methyl methacrylate) (PMMA) obtained under different conditions (Fig. 8.28).

Spectrum a of the stationary PMMA sample was obtained with scalar decoupling but without CP and shows no observable resonances. When the stationary sample is examined by using DD and CP (spectrum b), broad resonances are observed, and these resonances reflect the effects of chemical-shift anisotropy. With the addition of MAS to the DD experiment and elimination of CP, the lines are narrowed considerably, but the signal-to-noise ratio is poor (spectrum c). Finally, with the grand experiment (MAS-DD-CP), the spectrum is resolved into the specific carbons of the PMMA molecule with good signal-to-noise ratio (spectrum d).

Such are the benefits of the grand experiment. Of course, what applies to PMMA can be used for other samples as well with proper manipulation of the various experimental factors. With modern spectrometers, the grand experiment can easily be accomplished in a routine manner after a preliminary determination of the relevant parameters.

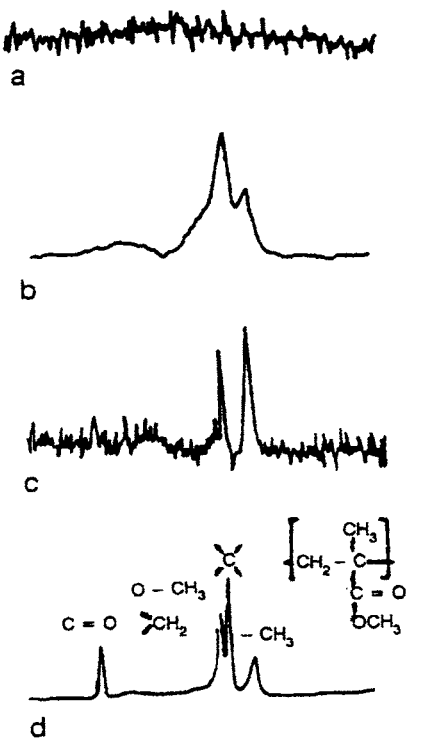

Fig. 8.28. The ^{13}C solid-state NMR spectra of a sample of PMMA obtained under different conditions. (Reproduced from Ref. [82]. © 1981 American Chemical Society.)

Applications of the grand experiment to polymers will be discussed in Chapter 9.

References

[1] Garroway, A.N., VanderHart, D.L., Earl, W.L., Philos. Trans. R. Soc. London, A: 299 (1981), 609.
[2] Mehring, M., High Resolution NMR Spectroscopy in Solids. Springer-Verlag, New York, NY, 1983.
[3] Fyfe, C.A., Solid State NMR for Chemists. C.F.C. Press, Guelph, 1984.
[4] Spiess, H.W., Annu. Rev. Mater. Sci. 21 (1991) 131.
[5] Schaefer, J., Stejskal, E.O., J. Am. Chem. Soc. 98 (1976) 1031.
[6] Axelson, D.E., Solid State Nuclear Magnetic Resonance of Fossil Fuels: An Experimental Approach. Multiscience, 1983.
[7] Havens, J.R., Koenig, J.L., Appl. Spectrosc. 37(3) (1983) 226–249.
[8] Komoroski, R.A. (Ed.), High Resolution NMR of Synthetic Polymers in Bulk. VCH Publishers, Deerfield Beach, FA, 1986.
[9] Mathias, L. (Ed.), Solid State NMR of Polymers. Plenum Publishers, New York, NY, 1989.
[10] Yannoni, C.S., Acc. Chem. Res. 15 (1982) 203.
[11] Gerstein, B.C., Dybowski, C.R., Transient Techniques in NMR of solids. An Introduction to Theory and Practice. Academic Press, Orlando, FL, 1985.
[12] Pake, G.E., J. Chem. Phys. 16 (1948) 327.
[13] Schmidt-Rohr, K., Spiess, H.W., Multidimensional Solid-State NMR and Polymers. Academic Press,

Orlando, FL, 1994.
[14] Andrew, E.R., Eades, R.G., Discuss. Faraday Soc. 34 (1962) 38.
[15] Freeman, R., Hill, H.D.W., Kaptein, R., J. Magn. Reson. 7 (1972) 327.
[16] Lyerla, J.R., Meth. Exp. Phys. Part A: 16 (1980) 241.
[17] Yannoni, C.Y., Acc. Chem. Res. 15 (1982) 201.
[18] Abraham, A., The Principles of Magnetic Resonance. Oxford Press, New York, NY, 1961, p. 571.
[19] Waugh, J.S., Huber, L.M., Haeberlen, U. Phys. Rev. Lett. 20 (1968) 180.
[20] Rhim, W.K., Elleman, D., Vaughan, R., J. Chem. Phys. 58 (1973) 8.
[21] Burum, D., Rhim, W.K., J. Magn. Reson. 34 (1979) 241.
[22] VanderHart, D.L., Earl, W.L., Garroway, A.N., J. Magn. Reson. 44 (1981) 361.
[23] Rothwell, W.P., Waugh, J.S., J. Chem. Phys. 74 (1981) 2721.
[24] Fleming, W.W., Lyerla, J.R., Yannoni, C.S., in: C.D. Craver (Ed.), Polymer Characterization: Spectroscopic, Chromatographic and Physical Instrumental Methods. Advances in Chemistry Series 203, American Chemical Society, Washington, DC, 1983, Chapter 26, p. 457.
[25] Fleming, W.W., Fyfe, C.A., Lyerla, J.R., Vanni, H., Yannoni C.S., Macromolecules 13 (1980) 460.
[26] Veeman, W.S., Prog. NMR Spectrosc. 16 (1984) 193.
[27] Vega, A.J., English, A.D., Macromolecules 13 (1980) 1635.
[28] Duncan, T.M., J. Phys. Chem. Ref. Data 16 (1987) 125.
[29] Haeberlen, U., in: J.S. Waugh (Ed.), Advances in Magnetic Resonance, Supplement 1. Academic Press, New York, NY, 1976, Chapter 3.
[30] Spiess, H., in: P. Diehl, E. Fluck, and R. Kosfeld (Eds.), NMR Basic Principles and Progress. Springer Verlag, New York, NY, 1978, Vol. 15.
[31] Hempel, G., Schneider, H., Pure Appl. Chem. 54 (1982) 635.
[32] Henrichs, P.M., Macromolecules 20 (1987) 2099.
[33] Veeman, W.S., Philos. Trans. R. Soc. London, A: 299 (1981) 629.
[34] Alderman, D.W., Solum, M.S., Grant, D.M., J. Chem. Phys. 84 (1986) 3717.
[35] Stejskal, E.O., Schaefer, J., McKay, R.A., J. Magn. Reson. 25 (1977) 569.
[36] Maricq, M., Waugh, J.S., Chem. Phys. Lett. 47 (1977) 327.
[37] Waugh, J.S., Maricq, M., Cantor, R., J. Magn. Reson. 29 (1978) 183.
[38] Murphy, P.D., Taki, T., Gerstein, B.C., Henrichs, P.N., Masa, D.J., J. Magn. Reson. 49 (1982) 99.
[39] Yarim-Agrev, Y., Tutunjian, P.N., Waugh, J.S., J. Magn. Reson. 47 (1982) 51.
[40] Bax, A., J. Magn. Reson. 51 (1983) 400.
[41] Herzfeld, J., Berger, A.E., J. Chem. Phys. 73 (1980) 6021.
[42] Jelinski, L.W., Macromolecules 14 (1981) 1341.
[43] Jelinski, L.W., Dumais, J.J., Engel, A.K., Macromolecules 16 (1983) 403.
[44] Aue, P., Ruben, D.J., Griffith, R.G., J. Magn. Reson. 43 (1981) 472.
[45] Bax, A., Szeverenyl, N.M., Maciel, G.E., J. Magn. Reson. 52 (1983) 147.
[46] Bax, A., Szeverenyl, N.M., Maciel, G.E., J. Magn. Reson. 51 (1983) 400.
[47] Harris, R.K., Packer, K.J., Thayer, A.M., J. Magn. Reson. 62 (1985) 284.
[48] Naki, T., Ashida, J., Terao, T.J., Chem. Phys. 88 (1989) 6049.
[49] Urbine, J., Waugh, J.S., Proc. Natl. Acad. Sci. USA 71 (1974) 5062.
[50] VanderHart, D.L., J. Chem. Phys. 64 (1976) 830.
[51] Andrew, E.R., Progress in NMR Spectroscopy, Vol. 18. Pergamon Press, New York, NY, 1971.
[52] Spiess, H.W., NMR 15 (1978).
[53] Gall, C.M., Cross, T.A., DiVerdi, J.A., Opello, S.J. Proc. Nat. Acad. Sci. USA 79 (1982) 101.
[54] Inglefield, P.T., Amici, R.M., O'Gara, J.F., Hung, C., Jones, A.A., Macromolecules 16 (1983) 1552.
[55] O'Gara, J.F., Jones, A.A., Hung, C., Inglefield, P.T., Macromolecules 18 (1985) 1117.
[56] Wemmer, D.E., Pines, A., Whitehurst, D.D., Philos. Trans. R. Soc. London, A: 300 (1981) 15.
[57] Sethi, N.K., Pugmire, R.J., Facelli, J.C., Grant, D.M., Anal. Chem. 60 (1988) 1574.
[58] Brandolini, A.J., Dubowski, C., J. Polym. Sci., Polym. Lett. Ed. 21 (1983) 423.
[59] Henrichs, P.M., Macromolecules 20 (1987) 2099.
[60] Andrew, E.R., Bradbury, A., Eades, R.G., Nature (London) 182 (1959) 1659.
[61] Lowe, I.J., Phys. Rev. Lett. 2 (1959) 285.
[62] Yannoni, C.S., in: M. Shen (Ed.), Contemporary Topics in Polymer Science, Vol. 3. Plenum Press, New

York, NY, 1983, p. 155.
[63] Herzfeld, J., Roufosse, A., Haberkorn, R.A., Griffin, R.G., Gilmcher, M.J., Philos., Trans. R. Soc. London, B: 289 (1980) 459.
[64] Gerstein, B.C., Anal. Chem. 55 (1983) 899A.
[65] Earl, W.L., VanderHart, D.L., J. Magn. Reson. 48 (1982) 35.
[66] Pines, A., Gibby, M.G., Waugh, J.S., J. Chem. Phys. 59 (1973) 569.
[67] Miknis, F.P., Bartuska, V.J., Maciel, G.E., Am. Lab., 11(11) (1979) 20.
[68] Hartmann, S.R., Hahn, E.L., Phys. Rev. A: 137 (1952) 2042.
[69] Sullivan, M.J., Maciel, G.E., Anal. Chem. 54 (1982) 1615.
[70] VanderHart, D.L., Khoury, F., Polymer 25 (1984) 1589.
[71] Alemany, L.B., Grant, D.M., Pugmire, R.J., Alger, T.D., Zilm, K.W., J. Am., Chem. Soc. 105 (1983) 2133.
[72] Alemany, L.B., Grant, D.M., Pugmire, R.J., Alger, T.D., Zilm, K.W., J. Am., Chem. Soc. 105 (1983) 2133.
[73] Fyfe, C., Lyerla, J.R., Volkson, W., Yannoni, C.S., Macromolecules 12 (1979) 757.
[74] Opella, S.J., Frey, M.H., J. Am. Chem. Soc. 101 (1979) 1854.
[75] Opella, S.J., Frey, M.H., Cross, T.A., J. Am. Chem. Soc. 101 (1979) 5866.
[76] Shields, C., Masters Thesis, Case Western Reserve University, 1984.
[77] Cudby, M.E.A., Harris, R.K., Metcalfe, K., Packer, K.J., Smith, P.W.R., Polymer 26 (1985) 169.
[78] VanderHart, D.L., Khoury, F., Polymer 25 (1984) 1589.
[79] Harris, R.K., Analyst 110 (1985) 649.
[80] Perez, E., VanderHart, D.L., Crist Jr., B., Howard, P.R., Macromolecules 20 (1987) 78.
[81] Patterson, D.J., Koenig, J.L., in: S.S. Labana and R.A. Dickie (Eds.), Characterization of Highly Cross-Linked Polymers. ACS Symposium Series 243, American Chemical Society, Washington, DC, 1984.
[82] Schaefer, J., Sefcik, M.D., Stejskal, E.O., McKay, R.A., Macromolecules 14 (1981) 188.
[83] Hewitt, J.M., Henrichs, P.M., Scozzafava, M., Scaringe, R.P., Linder, M., Sorriero, L.J., Macromolecules 17 (1984) 2566.
[84] Andrew, E.R., Philos. Trans. R. Soc. London, A: 299 (1981) 505.
[85] Slichter, P., Principles of Magnetic Resonance. Harper and Row, New York, NY, 1980.
[86] Dechter, J.J., Komoroski, R.A., Axelson, D.E., Mandelkern, L., J. Polym. Sci., Part B: Polym. Phys. 19 (1981) 631.
[87] Garroway, A.N., J. Magn. Reson. 49 (1982) 168.
[88] Nagewara Rao, B.D., in: D.G. Gorenstein (Ed.), Phosphorus-31 NMR: Principles and Applications. Academic Press, New York, NY, 1984, p. 63.

Chapter 9

Applications of high-resolution solid-state NMR spectroscopy to polymers

> *The difficulty encountered in using NMR for solids isn't the result of a dearth of chemical information as compared with solution spectra. If anything, the NMR spectrum of the typical solid contains more information on the structure and environment of the molecule than does the spectrum of the same material in solution.* — Cecil Dybowski

Although high-resolution NMR spectroscopy of the solid state has been available for only approximately 10 years, the number of applications has grown rapidly [1]. Solid-state NMR spectroscopy has been used for two general classes of samples:

(1) samples that are insoluble, such as crosslinked or intractable systems,
(2) samples for which solid-state NMR spectroscopy provides information about the nature of the solid state, such as the conformation, crystallographic forms, and the morphological character of the solid.

Interpretation of the spectra from solid-state NMR spectroscopy is more complicated than the interpretation of solution NMR spectra [2]. In solution NMR spectroscopy, the nature of the chemically inequivalent nuclei that give rise to resolved resonances must be determined. In the solid state, however, not only must structural assignments of the chemically inequivalent carbons be made, but also whether the chemically inequivalent nuclei are magnetically inequivalent as a result of their solid-state environments [3].

Theoretically, solid-state NMR spectra are expected to be more complicated and to have more resonance lines than solution NMR spectra, but because the lower inherent resolution of the solid spectra limits the number of resolvable lines, the spectra of solids are instead often simpler. This effect is shown in Fig. 9.1 for poly(vinyl chloride) (PVC), in which solution and solid-state ^{13}C-NMR spectra are compared for the same sample [4].

These spectra suggest that the information content of a solid-state spectrum is considerably less. In terms of number of resonances this is correct. However, the solid state spectra are rich in information.

In amorphous or glassy polymers, a considerable range of conformational states is accessible to the polymer chains. Theoretically, these conformational sequences

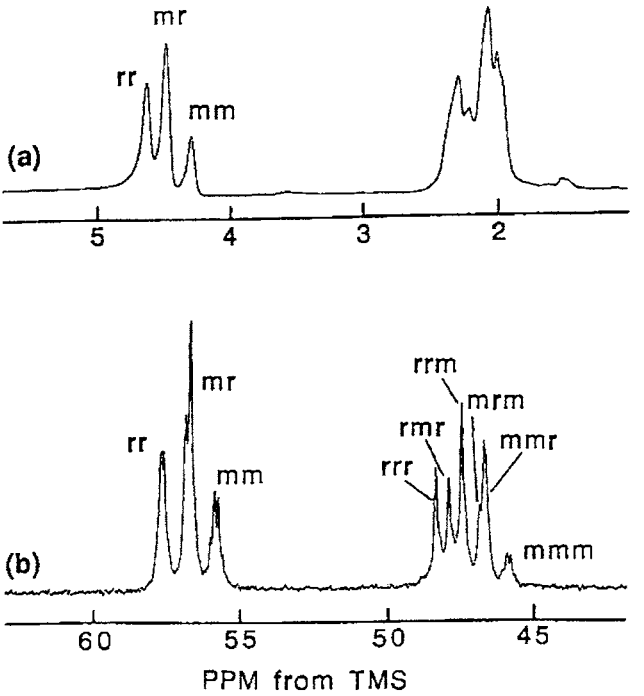

Fig. 9.1. The high resolution carbon and proton NMR spectra of poly(vinyl chloride). The (a) 500 MHz, and (b) 125 MHz carbon spectra of a 10-wt% poly(vinyl chloride) of molecular weight 83,000 in -d_6 solution at 65°C. (Reproduced with permission from Ref. [4]. © 1986 American Chemical Society.)

have different chemical shifts, but broad resonances often occur because the spectral dispersion is not sufficient to resolve the expected lines. Therefore, considerable inhomogeneous line broadening occurs in the solid-state NMR spectra of glassy and amorphous polymers because of configurational, conformational, and sequential effects.

Chemical shifts in the solid state

By using the grand experiment, well-resolved ^{13}C-NMR spectra for polymers in the solid state can be observed [5]. One of the first questions that must be resolved concerns the magnitude of the measured isotropic chemical shifts of solids compared to that of solutions. It has been concluded that:

> *The same influences which determine the dependence of carbon-13 shifts on chain microstructure in the solution NMR spectra of macromolecules appear to be operative also in the solid state.* — L.A. Belfiore et al. [6]

To a first approximation, there should be very little difference between the chemical shifts of the same chemical species of carbons found in the liquid or solid states. The exceptions are substances exhibiting either rigid conformational isomeric species or substances in which intermolecular effects in the solid state arise from differences in molecular packing.

Changes in molecular packing in the solid state can lead to differences in the chemical shifts, although this effect appears to be small. For example, the ^{13}C chemical shifts of methylene carbons with the trans zigzag structure in the orthorhombic, triclinic, and monoclinic forms are 33, 34, and 35 ppm, respectively [7]. It has been suggested that molecular-packing interactions beyond 1 nm do not influence the isotropic chemical shifts in amorphous systems [8].

Grant and Cheney developed a steric-hindrance model that predicts the effect on the chemical shifts of the additional crowding of the C−H bonds in the solid state [9]. In this model, a C−H bond is compressed or expanded by mutual repulsion of the bonded hydrogens and nearby nonbonded hydrogens. The chemical-shift differences depend on the hydrogen–hydrogen distance, r (nm), the angle θ between the C−H bond, and the inter-hydrogen separation vector. Thus,

$$\Delta^{13}C = -1680 \cos\theta \exp(26.71r) \tag{9.1}$$

The solid-state spectrum of diglycidyl ether of bisphenol-A (DGEBA) has been compared with the liquid-state spectrum [9], and the chemical shifts were examined using the steric-hindrance model. This model has also given consistent results in the analysis of chemical shifts of the α and β conformers of *trans*-1,4-polyisoprene in the solid state [10]. The steric-hindrance model predicts shifts that are the same order of magnitude as those observed.

Thus, the chemical shifts observed in solution can be used, as a first approximation, to ascertain the chemical nature of the carbons. However, caution must be exercised because conformational and intermolecular effects can play a role in solids.

Chemical shift studies of vulcanization of rubbers

Elastomeric systems are one of the most important classes of materials in industry because of their specific dynamic properties. Elastomers are typically crosslinked to a greater or less degree in order to improve their properties. The crosslinking process termed vulcanization prevents permanent deformation under load and ensures elastic recovery on removal of the load. The introduction of crosslinking, however, limits the ability to characterize those systems because of the insolubility of the resulting network. Additionally, the extremely low concentration of the chemically modified structures induced by the vulcanization challenge many of the traditional analytical techniques. Many approaches including physical tests and chemical analysis have

been attempted in an effort to relate the chemical microstructure to the physical properties of both raw and cured elastomers.

Solid state ^{13}C-NMR spectroscopy is a powerful method to directly observe the chemical species and types of molecular connections existing in vulcanized rubbers. The information obtainable from high-resolution NMR spectroscopy include main chain microstructures, comonomer composition and sequence, terminal structures, branching, abnormal structures (cyclic and isomerized structures), bonding direction, and the crosslink structure in the sample. In the modern solid-state NMR spectroscopy, high-resolution spectra with sharp resonance lines are obtainable in solid bulk samples by applying specific line narrowing techniques. Under magic-angle spinning (MAS) conditions, high quality spectra can be recorded for the lightly crosslinked elastomers above the glass transition temperature. Recently, solid-state ^{13}C NMR has been widely applied for the characterization of vulcanized rubber systems [11]. The chemistry of sulfur vulcanization of natural rubber was studied by using standard ^{13}C FT-NMR without MAS [12]. Prior to the actual NMR observation of the natural rubber vulcanizates, model compounds were examined to determine where the chemical shifts of the crosslink sites occur, and how different crosslink structures may be resolved. Based on the chemical shifts of the model compounds having different levels of sulfurization, it is found that the chemical shift of the α-carbon in a disulfide is about 7 ppm down field compared to the corresponding monosulfide. Hence, one could expect to resolve monosulfidic and disulfidic crosslinks attached to the polymer chain. On the other hand, there is usually little

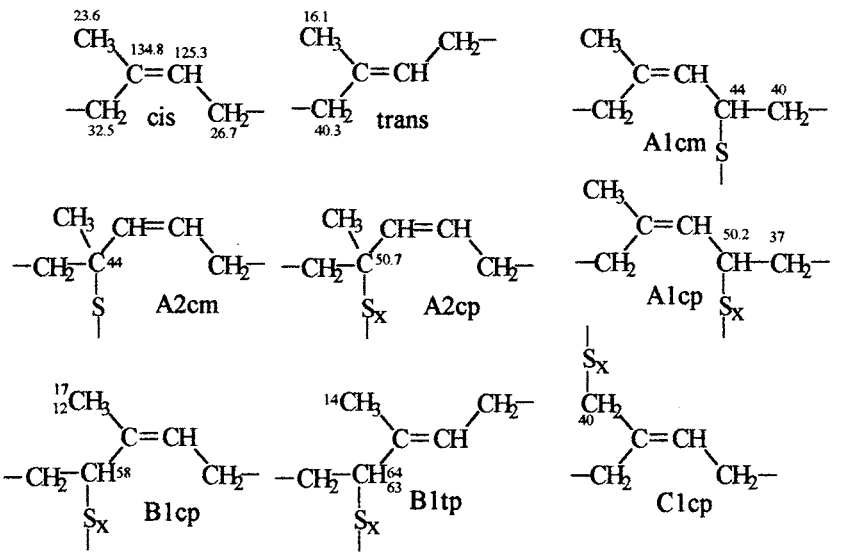

Fig. 9.2. Diagrams of the more likely chemical structures resulting from sulfur vulcanization of natural rubber. The nomenclature used for the substitution of the sulfur is also indicated. The chemical shifts, which were calculated for each of the designated carbons, are also shown.

difference between the α-carbon chemical shift in a trisulfide and the corresponding disulfide.

Fig. 9.2 shows some of the more likely structures occurring in the vulcanization of the natural rubber. The approximate chemical shifts for carbons in these structures have been calculated by using ^{13}C chemical shift substituent effects. The initial substituent effect values used are taken from Wehrli and Wirthlin [13] but were slightly modified based on model compound studies. The values are: monosulfidic, $\alpha = +18$ ppm, $\beta = +6$ ppm, $\gamma = -4$ ppm; di- and polysulfide, $\alpha = +25$ ppm, $\beta = +6$ ppm, $\gamma = -4$ ppm.

Chemical-shift studies of polymer conformation

> *The NMR spectrum of a solid is much like a complex piece of beautiful music. Its texture is so rich that it's impossible to analyze except in a cursory way. Modern solid-state NMR spectroscopy provides the same control of information that a careful analysis of an individual piece provides in appreciation of music, the ability to separate and examine the elements and to present them coherently and conveniently. In this manner, a greater understanding of the total structure is obtained, be it a symphony or a spectrum.*
>
> — Cecil Dybowski [14]

Solid-state NMR experiments using chemical shifts can lead to a determination of the conformational states in the solid [15]. The restricted motion in the solid state creates unique chemical environments for nominally equivalent carbons. The chemical-shift differences generated by these environments in the solid state are seen as additional line splittings when compared to the observations in solution. This effect was first observed with poly(phenylene oxide). The protonated aromatic carbon resonance is a doublet in the solid state, whereas in solution it is a singlet [16]. The doublet in the solid state arises because the two protonated carbons of the ring are magnetically inequivalent in the solid state due to the nonlinearity of the C–O–C bond. However, these two carbons are magnetically equivalent in solution, where free rotation occurs.

NMR evidence exists for more than one conformation of the monomer of DGEBA based on the number of resonance lines observed in the solid state [17]. For the monomer, although there are only meta and ortho carbons next to the oxygen carbon in the two phenylene rings, the spectrum shows four and five (possibly six) lines, respectively. At low temperatures, the resonances from the carbons ortho and meta to the oxygen are partly resolved doublets. At higher temperatures, these lines become a singlet. This result is consistent with molecular motion involving a 180° flip-flop of the phenylene ring at higher temperatures.

The γ-gauche effect

The effect of the conformation on the chemical shift is mainly due to the rotation about the next neighbor bond. Conformationally related chemical-shift variations in polymers are generally reflected through two effects: the *γ-gauche* effect and the *vicinal-gauche* effect [18]. In a model with three conformations for each bond, there are two magnetically distinguishable γ positions, the trans (or anti) position and the gauche position (Chart 9.I). Replacement of a trans by a gauche position in the polymer conformation results in an upfield chemical shift. The magnitude of the shift depends on the type and number of carbons involved and the relative orientations of the substituents [19].

The C−C backbone in organic polymers usually adopts the three staggered rotational states of trans (t), gauche$^+$ (g^+), and gauche$^-$ (g^-), ($\phi = 0°, \pm 120°$) as illustrated in Chart 9.I. A rotational barrier of 2 kcal/mol exists between these staggered states for polyethylene. In the gauche conformation, the observed and γ carbons are in close proximity, and they are distant in the trans arrangement. This spatial difference produces a shielding effect for the gauche isomer relative to the trans conformation. This effect is termed the *γ-gauche* effect and has a value of approximately −5 ppm but can exhibit angular dependence [19].

For the *vicinal-gauche* effect, the conformation of the α bonds affects the chemical shift if the α and β carbons exchange positions. The *vicinal-gauche* effect results in an upfield shift of about 6 ppm compared with the chemical shift of all-trans carbons of cyclic paraffins.

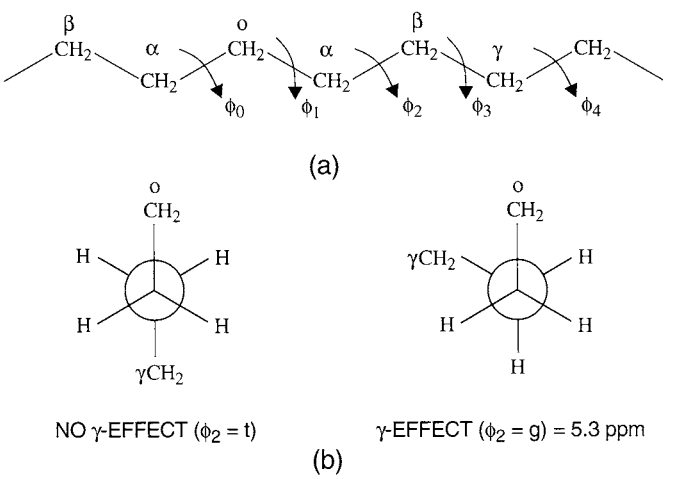

Chart 9.I. (a) The C−C backbone in organic polymers usually adopts the three staggered rotational states of trans (t), gauche$^+$ (g^+), and gauche$^-$ (g^-), ($\phi = 0°, \pm 120°$). (b) In the gauche$^\pm$ conformation, the observed and γ carbons are close; they are distant in the trans (t) arrangement.

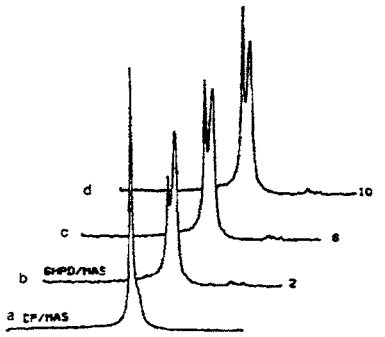

Fig. 9.3. The high-resolution solid-state NMR spectra at 37.7 MHz of PE. The ^{13}C CP-MAS-DD spectrum (a) and the GHPD-MAS spectra (b–d) of the PE sample with recycle times of (b) 2 s, (c) 6 s, and (d) 10 s. (Reproduced with permission from Ref. [21]. © 1987 Society for Applied Spectroscopy.)

Polyethylene

The ^{13}C-NMR spectrum of solid polyethylene (PE) has a sharp peak separated from a weak shoulder by 2.36 ppm (±0.1 ppm) [20]. By comparing the CP-MAS spectra with the gated high-powered decoupled (GHPD) spectra with different delay times, the upfield peak at 30.7 ppm can be assigned to the amorphous region, and the downfield peak at 32.9 ppm can be assigned to the crystalline region (Fig. 9.3) [21]. The differences in the chemical shifts are associated with conformational differences between the all-trans crystalline region and the equilibrium populations of trans and gauche conformations in the amorphous regions. The chemical shift of the methylene carbons in the disordered region can be approximated by the following equation:

$$\sigma = \sigma_0 - 2\gamma f_g \tag{9.2}$$

where σ_0 is the chemical shift of the all-trans methylene chain and is taken as 32.9 ppm; γ is the γ-gauche effect, which is -5.3 ppm; and f_g is the equilibrium fraction of gauche bonds. The calculated value of f_g is 0.25, which corresponds to the known liquid-like distribution of gauche and trans bonds. For bulk-crystallized high-density polyethylene, the noncrystalline region is further separated into the crystalline-amorphous interfacial region and amorphous components by using differences in the T_{2C}s without ^1H dipolar coupling [22,23].

Studies of cyclic paraffins in the solid state have also been made [24,25]. For cyclic paraffins, the conformations are the same in solution and in the solid state up to $C_{32}H_{64}$, and the observed chemical shifts are the same [26].

CP-MAS ^{13}C-NMR studies of folding in solution-grown crystals of PE have been reported. If the fold carbons are in a sharp-folded structure with little molecular motion, they should resonate 5–10 ppm upfield from the all-trans carbon resonance. However, the observed shift for single crystals of PE is only 2.3 ppm, a

result suggesting that "the fold carbons are not in a sharp-folded structure but are in a mobile state with slightly less gauche character than truly amorphous or molten PE" [24].

Assuming that cycloalkanes are suitable model compounds for adjacent reentry tight folds in polyethylenes, solid-state ^{13}C-NMR spectroscopy yields information about the conformation in the fold. Generally, the ggtgg fold conformation along the *b* axis is well-established for the monoclinic modification. With increasing ring size, the formation of lamellar-type crystals, in which pairs of adjacent stems are connected by tight folds, is essential for the arrangement of the molecules within a crystal lattice. The NMR spectra are consistent with two parallel all-trans arranged stems connected by tight ggtgg folds [25].

Molecular packing in the various crystalline forms can produce additional chemical shifts. In *n*-paraffins, differences of 1 ppm are observed between the triclinic and orthorhombic crystal forms [27].

Chemical-shift determination of helical conformation

Differences in bond angles of the various helical conformations also can produce variable chemical shifts in the solid state. Consequently, measured chemical shifts can be used to diagnose the helical conformations of polymers (Table 9.1).

Polypropylene

Isotactic polypropylene (iPP) exhibits a stable crystalline α form consisting of chains in the 3_1 helical conformation $(tgtgtg)_n$ packed in a monoclinic unit cell. Left- and right-handed helices face each other in the α form. The metastable β-form crystals contain hexagonally packed 3_1 helical chains arranged in groups of the same helical handedness (left or right). There is also a smectic, or partially ordered, form

Table 9.1
The observed ^{13}C chemical shifts (ppm from external TMS) of the principal features of the NMR spectra of various solid forms of iPP and sPP

	CH_2	CH	CH_3
Isotactic PP			
α-Crystalline	45.2, 44.2	26.8	22.6, 22.1
Smectic (quenched)	44.2	26.8	22.1
β-Hexagonal	45.0	27.1	22.9
Syndiotactic PP			
Amorphous $T_g > 360$ K	48.1	29.1	21.4
Crystalline	40.2, 49.0	27.4	21.9, 22.1
Stretched	50.2	28.9	20.8

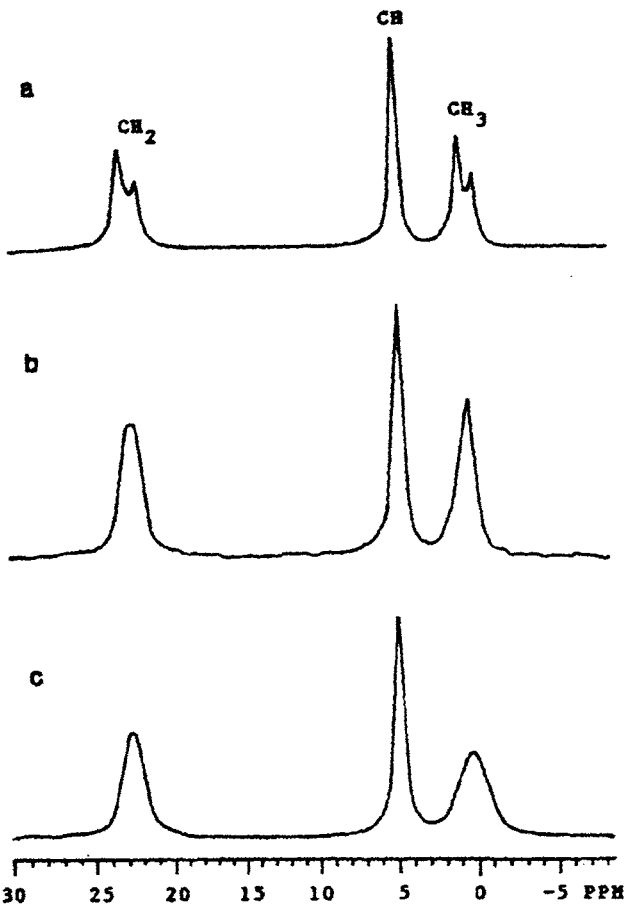

Fig. 9.4. The CP-MAS ^{13}C spectra of isotactic polypropylene in the α form (a), the β form (b), and the smectic form (c). (Reproduced with permission from Ref. [30]. © 1987 Butterworth-Heinemann, Ltd.)

consisting of hexagonally packed 3_1 helical chains with disorder occurring in the intermolecular packing of the chains.

The CP-MAS ^{13}C-NMR spectra of the different forms of iPP are shown in Fig. 9.4 (Tabel 9.1) [28–30]. Both the methylene and methyl carbon resonances in the α form are split by approximately 1 ppm, but the methine resonance shows only a shoulder.

When the spectra of the annealed and quenched polypropylenes are compared, the ratio of the methylene and methyl resonance intensities is 2 : 1, with the more intense peak being the high-frequency resonance in each case. These chemical-shift differences are interpreted in terms of the unit cell having paired left- and right-handed 3_1 helices that generate distinguishable sites A and B for the methyl, methine, and methylene carbons in a 2 : 1 ratio through interchain interactions (Fig. 9.5). Thus two interhelical distances give rise to the observed splitting. The A sites apparently correspond to a separation of 5.28 Å between helical axes, and the helices of the B sites are 6.14 Å apart.

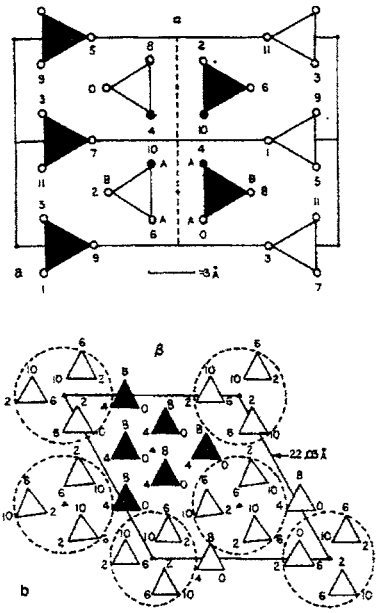

Fig. 9.5. Crystal structures of the α form (a) and the β form (b) of iPP. Full (RH) and open (LH) triangles indicate 3_1 helical iPP chains of different handedness. The labels A and B designate the inequivalent sites. Numerals at the triangle vertices indicate heights of methyl groups above a plane perpendicular to the c axis in twelfths of c. The circle at the triangle vertices in (a) corresponds to methyl carbons, and the cross-hatched and stippled pairs of circles correspond to the enmeshed A-site methyls. (Reproduced with permission from Ref. [30]. © 1987 Butterworth-Heinemann, Ltd.)

The CP-MAS ^{13}C-NMR spectrum of the β form of iPP exhibits only a single resonance for each carbon. The chemical shifts nearly correspond to those of the B sites in the α form. The packing of iPP helices in the β form is 6.36 Å and is thus closer to the more distant of the two interhelical packings (B); this closeness results in the near coincidence of the resonances. For the quenched smectic iPP, the chemical shifts correspond to those of the β form, and hence the smectic packing of the helices closely resembles the β form. It was suggested that the smectic form consists of 3_1 helices of opposite handedness but without the interlocking of the methyl groups of the A sites of the α form [30]. Thus, the local packing arrangement in the smectic form of iPP can be characterized by inter-helical distances comparable to the α-form B sites. This model of the smectic phase allows for a transformation to the α form through rotations and translations about and along the 3_1 helix axis rather than an unwinding and rewinding of the 3_1 portions of helical chains.

The CP-MAS ^{13}C-NMR spectrum of syndiotactic polypropylene (sPP) is compared with the spectrum of iPP in Fig. 9.6 [31]. The solid state NMR spectra are substantially different in spite of the common chemical structure because of the differences in the conformations in the solid state. The sPP has a 2_1 helix with a (gg)(tt)(gg)(tt) structure. This structure involves *external* (outside the helix) and *in-*

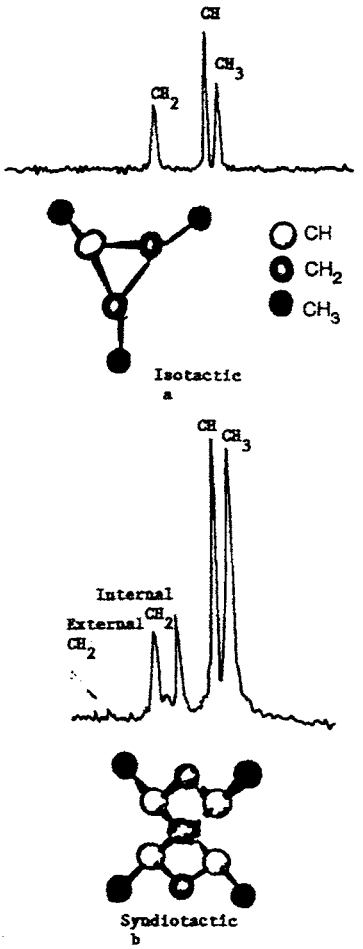

Fig. 9.6. The solid state ^{13}C spectra and helical conformations of (a) iPP and (b) sPP. (Reproduced with permission from Ref. [31]. © 1981 American Chemical Society.)

ternal (inside the helix) methylene units that have substantially different resonances [31]. In sPP the methylene carbon resonance is split 1 : 1 at 8.7 ppm. Consideration of the shielding effects of γ substituents suggests a shift difference of approximately 8 ppm between the external and internal methylene carbons. Therefore, the conformation sequences must contain two gauche contributions. Since two successive gauche conformations of opposite sign are prevented for steric reasons, the only possible succession of bonds are pairs of g conformations with the same sign. Since an s(2/1)2 helix is required from X-ray evidence the following sequences can occur $(ttg^+g^+)_n$ or $(ttg^-g^-)_n$ where the sign depends on the chirality. This suggests a general $(ttgg)_n$ conformation [32] shown in Fig. 9.7. Information about the chain packing of the chains can be obtained from the NMR results based on the 1 : 1 splitting of the CH_3

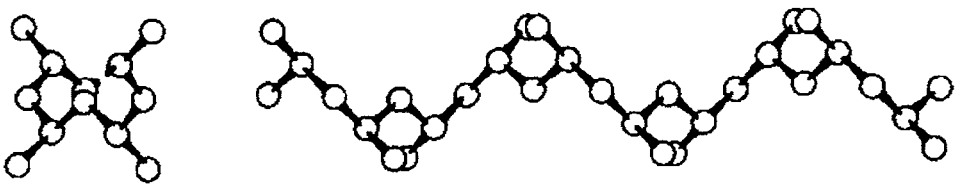

Fig. 9.7. Chain conformation of sPP in the crystalline state. (Reproduced with permission from Ref. [32]. © 1993 American Chemical Society.)

resonances. The methyl splitting arises from the present of two different methyls arising from the symmetry of the crystal cells and the chirality of the chains. The statistical replacement of chains of opposite chirality within a regular disposition of the chains is suggested [32] as shown in Figs. 9.8 and 9.9.

Stretched sPP [33] has also been studied and the spectra are shown in Fig. 9.10. The spectra suggest an increase in the tttt sequences at the expense of the tggt sequences.

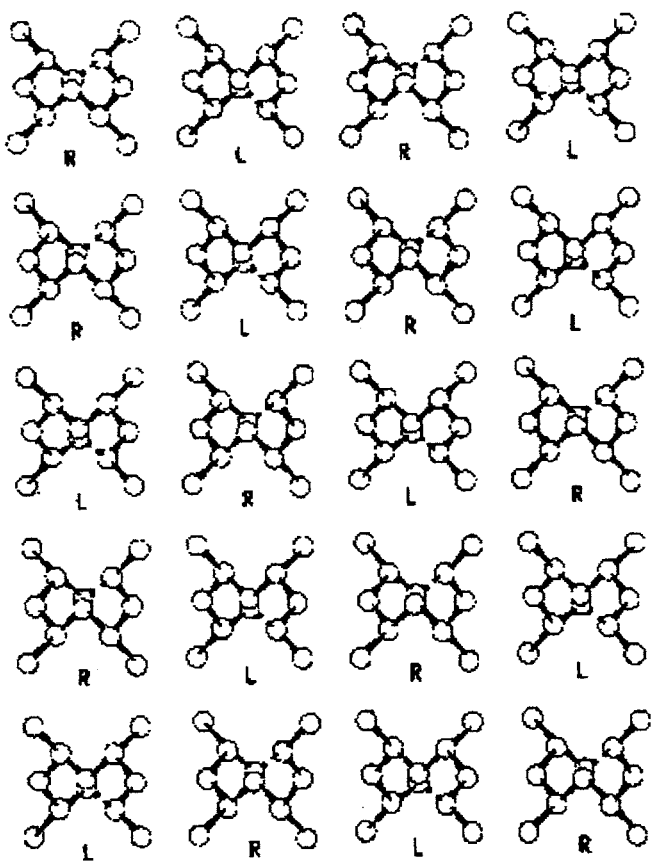

Fig. 9.8. Crystal packing of sPP in a highly crystalline sPP showing a statistical disorder of the chain chirality in one dimension. (Reproduced with permission from Ref. [32]. © 1993 American Chemical Society.)

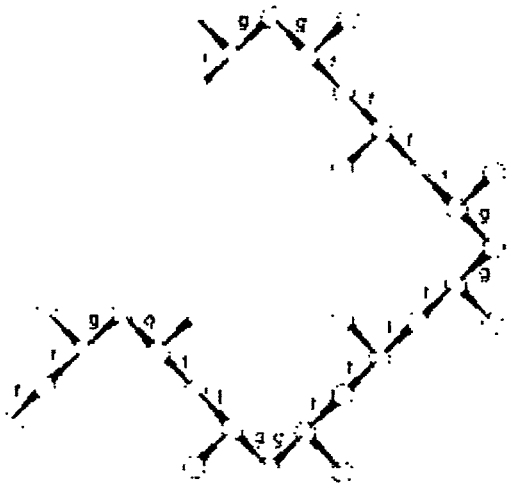

Fig. 9.9. Chain segment of sPP showing the high content of trans conformation in the amorphous phase. (Reproduced with permission from Ref. [32]. © 1993 American Chemical Society.)

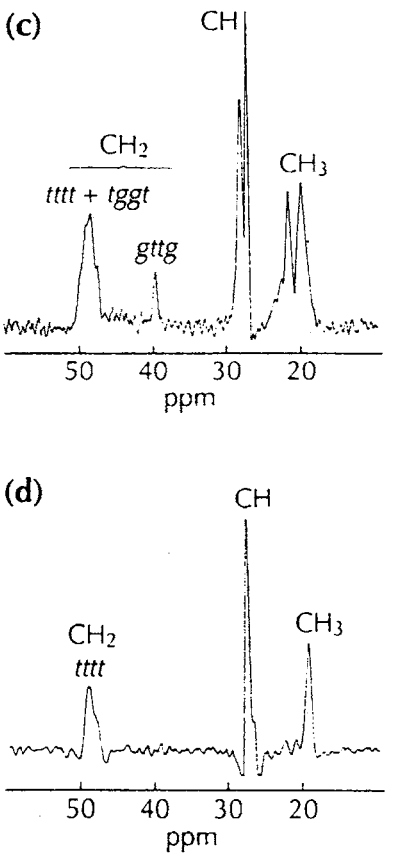

Fig. 9.10. The spectrum of stretched iPP sample. (Reproduced with permission from Ref. [33]. © 1993.)

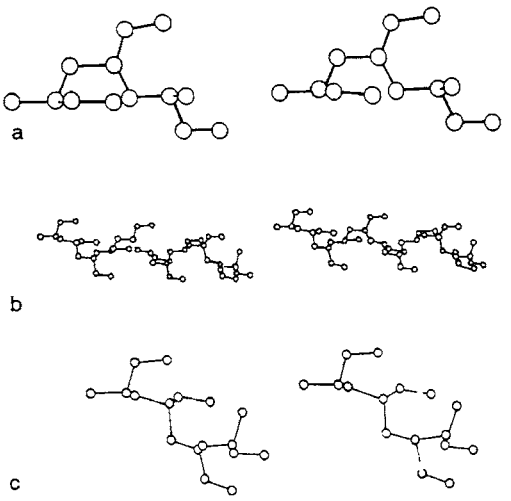

Fig. 9.11. Stereoscopic drawing of three crystalline polymorphs of isotactic poly(1-butene): (a) form I, 31 helix; (b) form II, II3 helix; and (c) form III, 41 helix. (Reproduced with permission from Ref. [34]. © 1984 American Chemical Society.)

Poly(1-butene)

Poly(1-butene) exists in three different helical conformations in the solid state [34] (Fig. 9.11). The CP-MAS spectra of the three crystalline polymorphs and the amorphous polymer of poly(1-butene) (Fig. 9.12) have been reported, and the spectra were interpreted by using a γ-gauche shielding parameter that is dependent on the dihedral angle. The γ-gauche shielding parameter is reduced to half its standard value when the angle is increased to $82 \pm 1°$.

This angular dependence of the interaction parameter can be extended by using the rotational isomeric state approximation to calculate the conformer populations. This approach was used to interpret the solid-state spectrum of poly(3-methyl-1-pentene), which in the amorphous state can have either a four-fold right-handed helix or a nearly equi-energetic four-fold left-handed helix. Three of the six chemical shifts of a right-handed unit differ from the corresponding resonances of a left-handed unit, and these stereochemical differences are observed [35].

Poly(oxymethylene)

Poly(oxymethylene) (POM) exists in two crystallographic forms: a trigonal form with a 95 helical (all-gauche) conformation and an orthorhombic form with a 21 helical conformation. The chemical shifts for the orthorhombic form are displaced upfield by about 2 ppm compared with the trigonal form [36]. The ^{13}C-NMR spectrum of trigonal POM shows a sharp peak at 88.3 ppm, and the noncrystalline peak is displaced downfield to 89.6 ppm [37]. The crystalline and amorphous peaks can

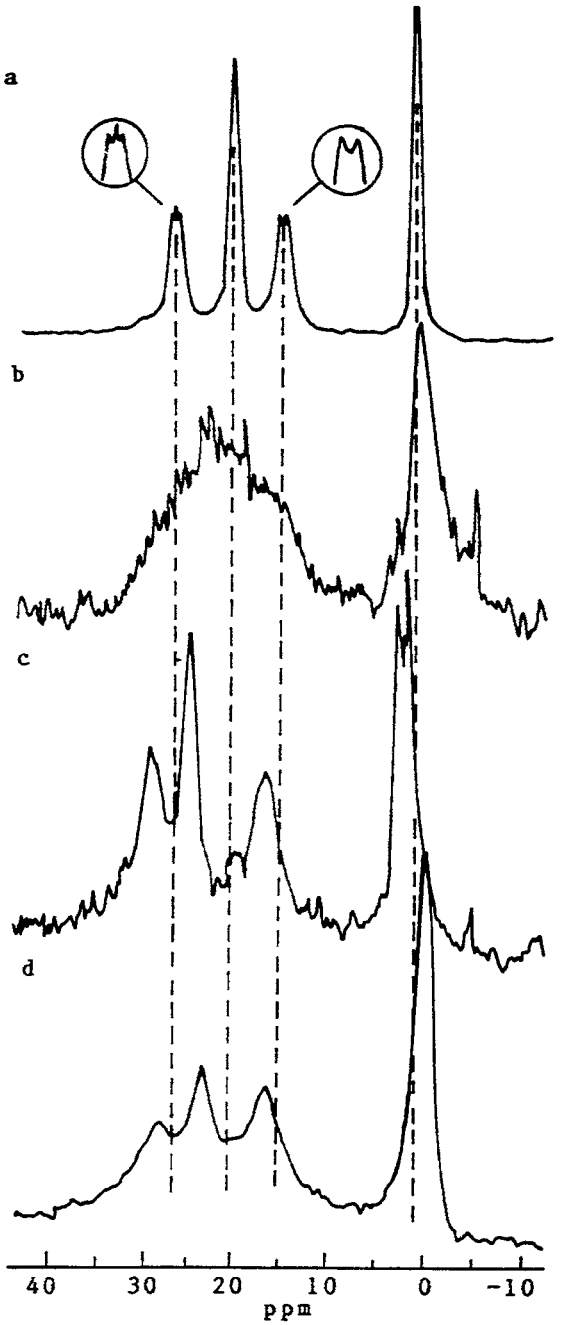

Fig. 9.12. High-resolution solid-state ^{13}C-NMR spectra at 50.3 MHz of poly(1-butene): (a) form I at 20°C, (b) form II at −60°C, (c) form III at −10°C, and (d) the amorphous form at 43°C. The vertical dashed lines represent the peak positions of form I. (Reproduced with permission from Ref. [34]. © 1984 American Chemical Society.)

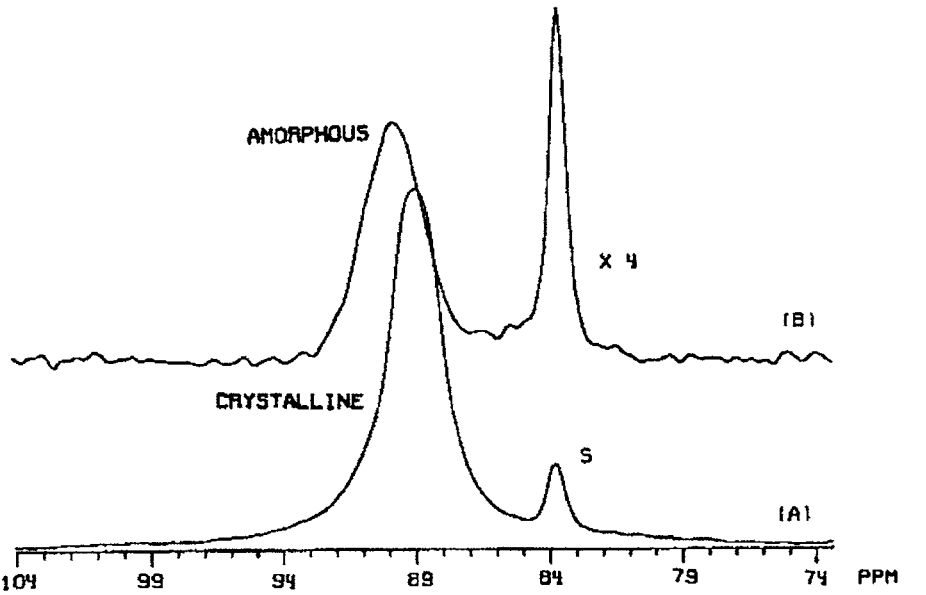

Fig. 9.13. Separation of the amorphous and crystalline phases of POM by using a modified CP-MAS experiment. The amorphous spectrum has been enlarged by a factor of 4. (Reproduced with permission from Ref. [37]. © 1983.)

be separated by taking advantage of the differences in mobility. This is accomplished by performing the NMR experiments with different delay times, which allow the magnetization of the crystalline peak decay to allow observation of the amorphous resonance (Fig. 9.13).

Poly(ethylene terephthalate)

The dipolar decoupling (DD)-CP-MAS ^{13}C-NMR spectra of a glassy poly(ethylene terephthalate) (PET), a PET sample annealed for 76 h at 200°C, and a solution-crystallized PET sample are compared in Fig. 9.14 [38]. The spectra show substantial differences that reflect the differences in the conformations and molecular packing of the chains. An increase in the crystallinity narrows the lines by limiting the number of conformational sequences to long sequences rather than to a series of short, disordered ones.

Poly(butylene terephthalate)

Poly(butylene terephthalate) (PBT) is an unusual material because uniaxial extension is accompanied by a reversible crystal–crystal transition. The α (relaxed) to β (strained) transition occurs at strains as low as 5%, and the transition is complete at 15% strain. When the tension is released, the polymer reverts rapidly back to the α

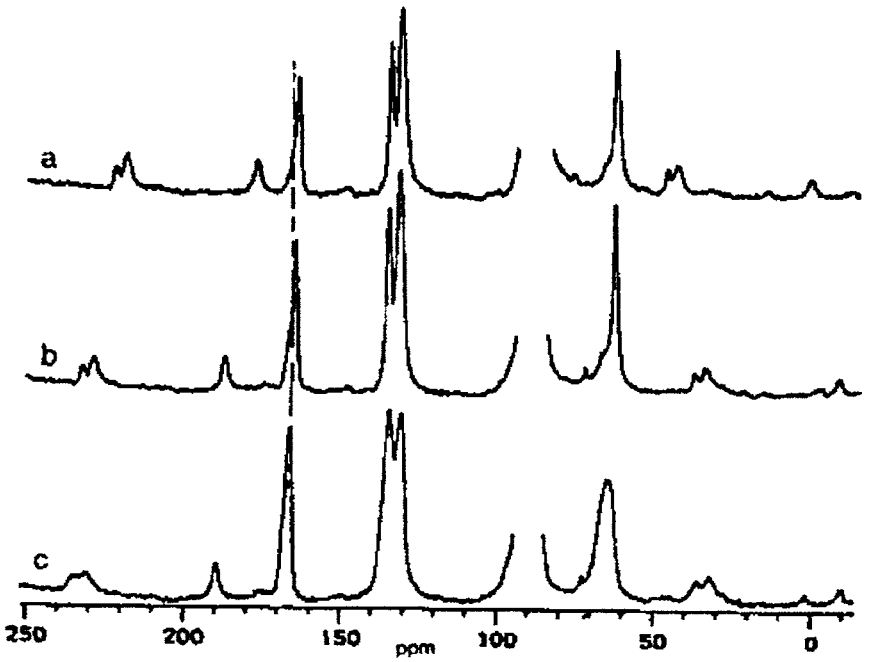

Fig. 9.14. DD-MAS-CP ^{13}C-NMR spectra of solution-crystallized (a), annealed 76 h at 200°C (b), and glassy-state (c) PET. (Reproduced with permission from Ref. [38]. © 1980 American Chemical Society.)

phase with little hysteresis. Static measurements have shown that the major difference between the phases is in the conformation of the tetramethylene segment. The α phase is A–T–A (where A = non-trans, non-gauche, and T = trans), and the β phase is the extended T–T–T configuration (see Chart 9.II).

The spectrum of the β phase is shown in Fig. 9.15 [39]. There are five peaks: the carbonyl (C=O) peak at 116.1 ppm, the nonprotonated aromatic peak at 135.2 ppm, the protonated aromatic peak at 131.5 ppm, the exterior methylenes (OCH_2) at 66.3 ppm, and the internal methylene peak at 25.8 ppm. The chemical shift of the internal methylene carbon resonance is substantially different between the two phases; for the undrawn fiber it appears at 27.8 ppm, and for the drawn fiber it appears at 25.8 ppm. This shift of the CH_2 carbon resonance confirms past data that indicated that the main difference between the two phases involves the conformation of the tetramethylene segment. The shift is due to the spatial effects of the oxygen atom relative to the interior methylene carbons in the crumpled form, which shield the CH_2 carbon to a greater extent.

The aforementioned results are in conflict with other literature data, in which no shifts in the internal methylene resonances were reported for the phase transition in PBT [40]. On this basis, it was concluded that no differences exist in the conformation of the methylene carbons between the two phases. The change in length of the repeat unit (10%) during the phase transformation from the α to the β phase is, on

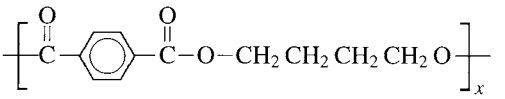

POLY(BUTYLENE TEREPHTHALATE)

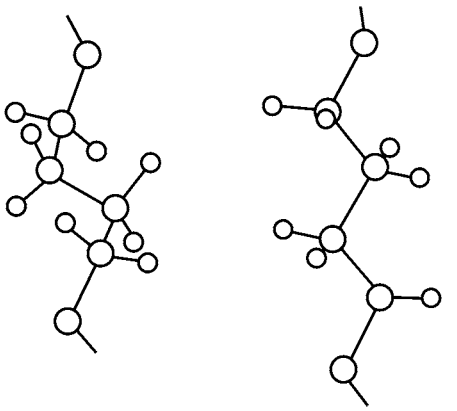

(ALPHA)
RELAXED

(BETA)
STRAINED

Chart 9.II. The repeat unit of PBT and the conformations of the α and β phases.

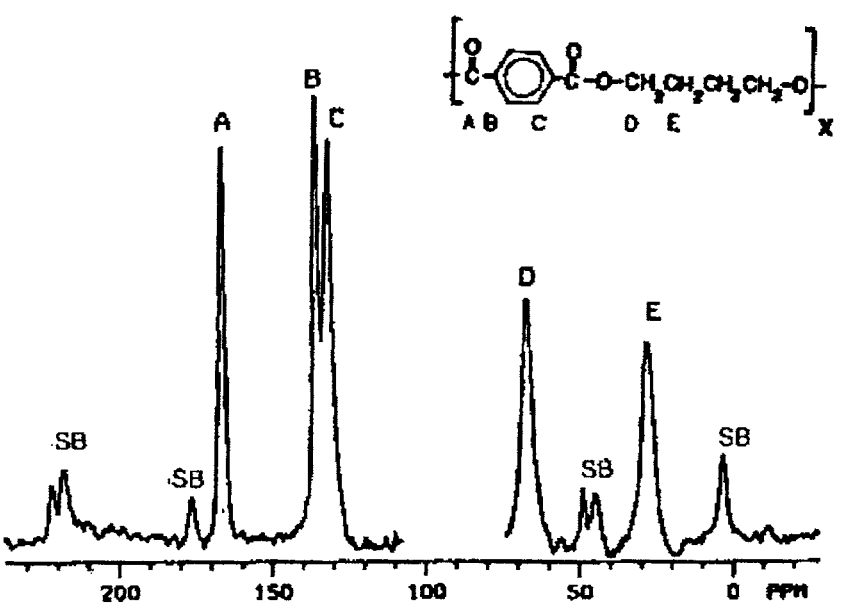

Fig. 9.15. DD-MAS-CP spectrum of the stretched (β) form of PBT fibers (>50% crystallinity). The letters labeling the peaks correspond to the labeled carbons in the structure, and the peaks labeled SB are spinning side bands. (Reproduced with permission from Ref. [39]. © 1987 American Chemical Society.)

this basis, associated with changes in the conformation of the terephthaloyl residue but not of the glycol residue.

Polyesters

Polyesters are an important class of industrial polymers. The polyester of 4-hydrobenzoic acid (PHBA) has been studied by solid state NMR. PHBA at room temperature exists in two different orthorhombic crystal modifications designated modification I and II. The high symmetry and regularity of the chain structure gives rise to a high degree of crystallinity and reduced solubility in all common solvents. Above 330°C these modifications reversibly transform to a pseudo-hexagonal structure (III). The solid state ^{13}C-NMR spectrum at 75.14 MHz of PHBA whiskers [41] in modification I is shown in Fig. 9.16. A comparison is shown in Table 9.2 of the chemical shifts of the ^{13}C resonances of PHBA in modification I and the tetramer in solution in ppm downfield from TMS.

In solution, carbons 3 and 3′ as well as 2 and 2′ are equivalent as indicated by their resonances. This equivalence reflects the fact that the phenylene ring can rotate freely about the 1,4 axis in solution. In the solid state they are inequivalent, reflecting the restricted motion of the aromatic rings leading to only small amplitude motions about

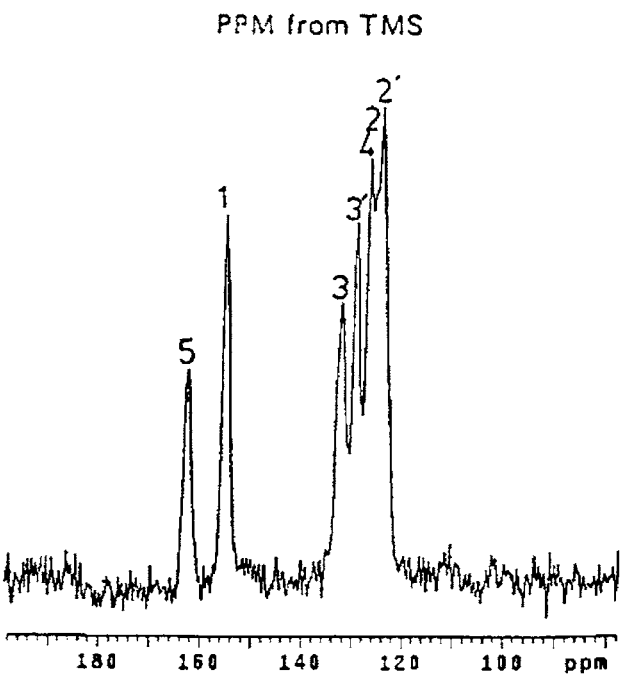

Fig. 9.16. The solid state ^{13}C-NMR spectra at 75.14 MHz of PHBA whiskers in modification I. (Reproduced with permission from Ref. [41]. © 1996 American Chemical Society.)

Table 9.2
The chemical shifts of the ^{13}C resonances of PHBA in modifications I, II and III; the tetramer in solution

Carbon	Tetramer in solution [a]	PBHA [a]		
		modification I	modification II	modification III
5	162.9	162.77	161.90	162.82
1	154.7	155.45	154.32	154.59
3	131.0	132.48	132.02	133.27
3′	131.0	129.43	128.42	129.92
4	126.0	126.91	125.41	126.37
2	121.0	125.76	124.27	122.85
2′	121.8	124.66	123.34	122.85

[a] in ppm downfield from TMS.

an axis which is not axially symmetric. Consequently, the single lines of the meta and ortho carbons are doublets in the solid state. The chemical shift splitting suggests that the molecules in PHBA modification I have a conformation in which the ester linkage and the phenylene ring plane form a torsional angle which deviates slightly from 90°. Such a conformation for modification I is in agreement with X-ray scattering results.

In comparing the spectra of the solid state modifications of PHBA, one observes that the chemical shift splitting of the 3 and 3′ carbons of modification I is smaller than of PHBA in modification II. This data suggests that the conformation deviation of the torsional angle between the ester plane and the phenylene ring plane is smaller in modification I than in modification II. Likewise the chemical shift splitting for the 3 and 3′ for modification III is intermediate between modifications I and II reflecting an intermediate torsional angle.

Polypeptides

The differences in ^{13}C chemical shifts of amino acid residues in polypeptides are as large as 2–7 ppm, depending on the particular conformations, such as the right-handed α helix, the left-handed α helix, the ω helix, and the β sheet forms. Surprisingly, the ^{13}C chemical shifts are not affected by the neighboring units in solution unless the neighbor is proline. Thus, ^{13}C chemical shifts of the individual amino acid residues can be used to probe the local conformations of the residues both in solution and in the solid state.

For polypeptides in the solid state, the resonances of the backbone carbon of the β sheet are shifted upfield by 5.4–7.1 ppm compared to the α helix (Fig. 9.17) [42]. The chemical shift of the random coil in solution is between the shifts of the α-helix and β-sheet forms. This result is consistent with the concept that the chemical shift observed for the random coil arises from an averaging of the ^{13}C shifts of at least two energetically favored conformations due to rapid chain isomerization.

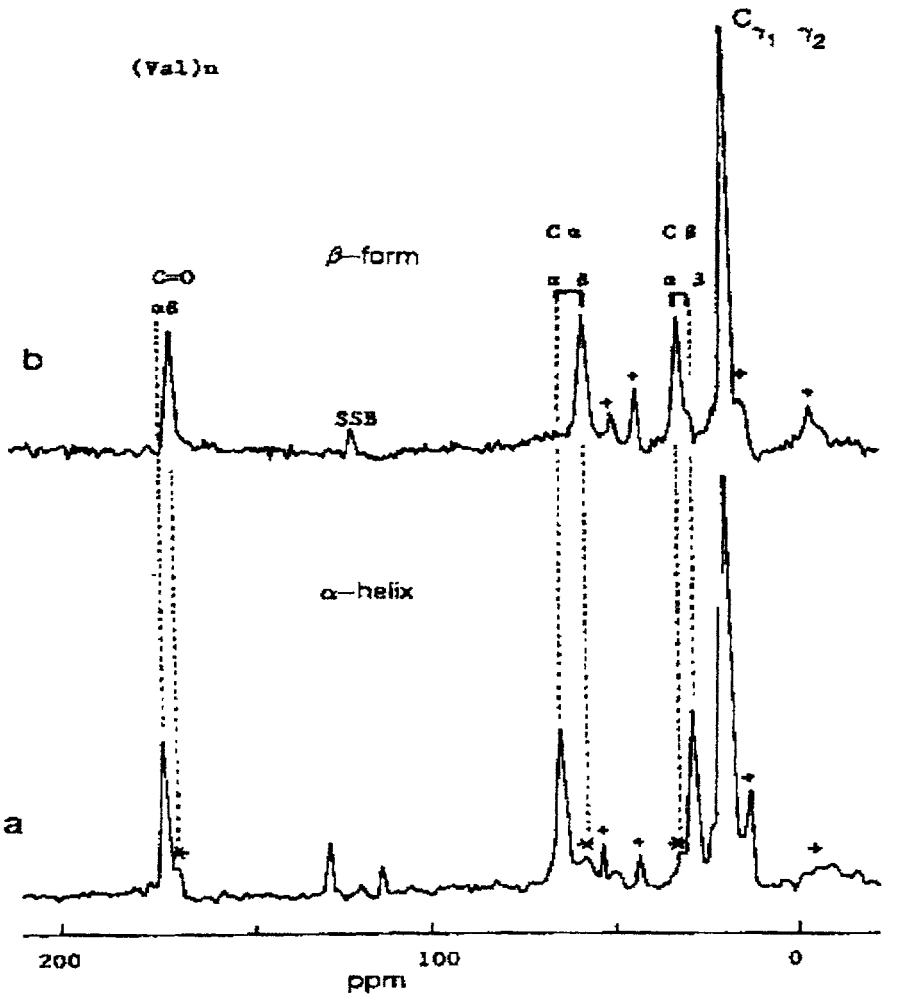

Fig. 9.17. CP-MAS ^{13}C-NMR spectra of solid $(Val)_n$. Spectrum a is of the α form, and spectrum b is of the β form. Peak labels are as follows: C_α, backbone carbons in valine; C_β, side chain carbons in valine; $C_{\gamma 1 \gamma 2}$, carbons in side chain of valine. (Reproduced with permission from Ref. [42]. © 1981.)

Analysis of crosslinked systems by solid-state NMR spectroscopy

Thermosetting systems

Since the discovery of cured phenolic formaldehyde resins and vulcanized rubbers, interest has grown in such areas as the mechanisms of network formation, the chemical structures of crosslinked systems, and the dynamics of networks. Although the vast majority of polymers used industrially are crosslinked to a greater or lesser degree, the ability to characterize these systems is highly limited. Traditional tech-

niques such as high-resolution NMR spectroscopy cannot be used because of limited solubility, although efforts have been made to swell the networks and examine the NMR spectra under high-resolution solution conditions. The spectra obtained by this solvent-swelling method usually have broad resonance lines, but these spectra can still provide valuable information.

The problem of limited solubility is overcome by the use of the grand NMR experiment to obtain well-resolved spectra of solid samples. However, the resolution achieved is still less than that for solution spectra, and the finer details (such as information on tacticity) are lost.

A second problem that makes analysis of crosslinked systems difficult is the low level of crosslinking required to produce substantial effects on the physical and mechanical properties. For rubbers, the level of crosslinking involves less than 1% of the carbons. This low level makes detection difficult because very small amounts of structure are being analyzed. Fortunately with solid-state NMR spectroscopy, the combination of available enhancement techniques and the use of a bulk sample (rather than a dilute solution) improve the sensitivity substantially.

Because of the importance of epoxy resins, it is not surprising that they received early attention from researchers using the solid-state NMR technique [43,44]. A number of other crosslinked systems have been investigated, including acetylene-terminated polyimide resins [45,46], poly(*p*-phenylene) [47], 2-propenenitrile polymer with 1,3-butadiene and ethenylbenzene (ABS) resins [48], furfuryl alcohol resins [49], phenolic resins [50], acrylic resins [51,52], melamine–formaldehyde resins [53], polynuclear hydroxymethyl phenol (resol)–formaldehyde resins [54], and plasma-polymerized materials [55].

Because of the large number and the broad range of chemical systems studied, these individual systems will not be discussed here. The references listed in the preceding paragraph provide further study as well as a review that deals specifically with NMR spectroscopy of crosslinked systems [56]. Instead, we will examine one class of systems in considerable detail in order to demonstrate the methods used for crosslinked systems.

Elastomeric materials

Elastomers are one of the most widely used industrial polymers. Historically, vulcanized natural rubbers have been used since their discovery in the 19th century. The elastic property of natural rubber, i.e. elongation up to several hundred percent with recovery of its initial state upon removal of the external stress is the characteristic property of this class of polymers. Rubbers are the only materials capable of reversible extension to strains of 6–700%. No other materials exhibit an increase in modulus with increase in temperature.

A rubber is generally defined as a material which can be stretched to at least twice its original length and which will retract rapidly and forcibly to substantially its origi-

nal dimensions on release of the force. An elastomer is a rubber-like material from the standpoint of modulus but which has limited extensibility and incomplete retraction.

The resistance to deformation in conventional elastomers is largely entropic. The number of conformations accessible to a chain diminishes when its end points are separated. When entropy drops, the free energy rises and an external applied stress is required to impose such a deformation.

Rubbers are particularly suitable for solid-state NMR studies because of their extensive reorientational motion above their glass transition. Consequently, relatively weak dipolar couplings occur in elastomers compared to solid glassy polymers. Thus, the ^{13}C resonance lines are intrinsically narrow, and high-resolution spectra of this group of polymers can be obtained by applying relatively low spinning speeds and proton-power decoupling. The effects of applying the different techniques used in high-resolution solid-state NMR spectroscopy (such as magic-angle spinning, multiple-pulse, and high-power decoupling) on the spectra of an elastomer produce narrow resonances above that induced by the molecular motion. The resulting spectra are thus of high quality and contain substantial information concerning the network structure.

One can take advantage of the large chemical shift dispersion of ^{13}C to resolve nuclei in different chemical environments in elastomers. Measurements of the relaxation rates at each resolvable carbon are also possible because the low abundance of ^{13}C precludes averaging of relaxation rates by spin diffusion. In this manner structural information can be obtained and the solid state NMR spectra give quantitative indications of the type and amount of the chemical crosslinked structures. It has been possible to relate the reinforcement mechanism of carbon black to the relative amount of chemical versus physical crosslinks (entanglements) using NMR and equilibrium swelling measurements.

Vulcanization

Useful rubber articles are made by vulcanization. Unvulcanized rubbers are generally not very strong, do not maintain their shape after a large deformation, and can be very sticky (about the same consistency as chewing gum). In order to produce a rubber having the proper elastomeric physical properties, the polymer chains must be very flexible and chemically crosslinked. Vulcanization can be defined as a chemical crosslinking process that generates a rubber material with useful properties.

In the rubber industry a sulfur-based crosslinking system is generally used. Since the vulcanization rate with sulfur alone is slow, chemical accelerators and activators are necessary. This vulcanization process may occur via different reaction mechanisms, depending on the chemicals/fillers used.

Vulcanization mechanism

The exact mechanism under which accelerated sulfur vulcanization occurs is a function of the class of accelerators/activators. However, a generally accepted sequence of reactions is as follows [57,58]:

- An interaction of the curatives occurs to form the active sulfurating agent, $Ac-S_x-Ac$ by a reaction of accelerator (Ac) and activator with sulfur:

  $$Ac + S_8 \rightarrow Ac-S_x-Ac \text{ [}\textit{active sulfurating agent}\text{]}$$

- The polymer chains interact with the sulfurating agent to form polysulfidic pendant groups terminated by accelerator groups;

  $$Ac-S_x-Ac + RH \rightarrow R-S_x-Ac \text{ [}\textit{pendent sulfurating agent}\text{]}$$

  where RH is the rubber chain.
- Polysulfidic crosslinks are formed;

  $$R-S_x-Ac \rightarrow R-S_x-R \text{ [}\textit{crosslinks}\text{]}$$

- Network maturing and competing side reactions also occur which do not lead to effective crosslinks. Thermal decomposition leads to the following reactions:

  $$R-S_x-Ac \rightarrow \text{cyclic sulfides} + \text{dienes} + ZnS \text{ [}\textit{degradation}\text{]}$$
  $$R-S_x-Ac \rightarrow R-S-Ac + S8 \text{ [}\textit{desulfuration}\text{]}$$
  $$R-S_y-R \rightarrow R-S-R \text{ [}\textit{monosulfidic crosslinks}\text{]}$$
  $$R-S_{x+y}-R + Ac-S_z-Ac \rightarrow R-S_x-R + Ac-S_{y+z}-Ac \text{ [}\textit{sulfur exchange}\text{]}$$

During the curing and network maturing periods, there are at least three competing reactions: crosslinking, desulfuration, and degradation reactions. The network structures formed depend not only on temperature but accelerator type and its concentration. The ratio of poly-, di-, and monosuldic crosslinks strongly depends on the ratio of sulfur to accelerator in the formulation. Typically benzothiazole or sulfenamide accelerators are used. Zinc oxide is the activator and a fatty acid such as steric acid is the coactivator.

Role of carbon black

Carbon black is a universal reinforcing filler and light stabilizer used in rubber compounds. Carbon black imparts strength and toughness to a tire as well as it improves the rubber's resistance to tearing, abrasion, flex fatigue and also increases traction and durability. A tire would last less than 5000 miles without the addition of carbon black.

Carbon black, produced largely from oil, consists of irregular, branched aggregates of firmly fused nodular subunits. The dispersed carbon black agglomerates form a network themselves in the polymeric media. With increasing filler content, the network chains become shorter and the number of entanglements between two crosslinks decreases [59]. Single molecules are likely to adsorb on several carbon black surface sites, so the bound rubber is essentially immobile. Reactive groups including acid groups, phenolic groups, quinonic groups and lactone groups have all been identified on the carbon black surface and influence adsorption.

Carbon black not only improves the 'strength' of the rubber but it also influences the curing characteristics. Carbon black decreases the vulcanization induction time and decreases the cure rate as the amount of surface acid groups on the carbon black increases. The mechanism appears to be one of a competitive reaction between the rubber and the filler for the zinc oxide activator. Channel carbon blacks exhibit high amounts of surface groups (due to about 3.5% oxygen content) as opposed to furnace carbon blacks which have a very small amount of these surface groups. Carbon black (regardless of the type) acts as a catalyst for the initiation of vulcanization. The initiating effect of carbon black increases with loading. Recently, there has been a trend to replace carbon black with silica to improve tire rolling resistance and tire mileage rating and to decrease auto fuel consumption.

The vast range of properties that can be produced with cured natural rubber (NR) is due to the structural variations of the crosslinked network that can occur during the curing process. The use of sulfur to cure NR is inefficient (requiring 45–55 sulfur atoms per crosslink) and tends to produce a large portion of cyclic and polysulfidic structures. To overcome this problem, accelerator cure recipes that produce a higher ratio of mono- and disulfidic crosslink structures were developed.

Although these systems make more efficient use of sulfur, they suffer maturing reactions. The modulus and the crosslink density go through their maximums but then decrease with additional cure times (due to the loss of network structure by nonoxidative thermal aging). This process is known as *reversion* and can occur in addition to the maturing reactions. Reversion occurs when the desulfurization reactions are faster than the crosslinking reactions. Rubber researchers have divided these sulfur maturing reactions into two categories (see Scheme 9.I).

The first category is the *desulfurization* of polysulfides to di- and monosulfidic crosslinks. This pathway is affected by the Zn–accelerator complex (found in accelerated sulfur vulcanization). The routes in the other category are characterized as *thermal decomposition*, in which the crosslinks and the sulfuration species decompose into conjugated species, cyclic sulfides, shorter sulfur crosslinks, and main-chain modifications.

Unaccelerated sulfur vulcanization

The first use of high resolution solid-state ^{13}C-NMR to study sulfur-crosslinked carbon structure was by Zaper and Koenig [62]. An increase in linewidths and decrease in the resolution are observed with increase in cure time. A dominant new resonance is observed at 58 ppm which is assigned to the polysulfide or vicinal crosslink. Other new resonances appear at 47 and 129 ppm which are assigned to monosulfide and trans-NR species, respectively. Broad resonances are observed in the 18~21 ppm and 30~33 ppm regions which are attributed to the products of chain scission and cyclic structures, respectively.

Samples containing zinc oxide, steric acid, natural rubber and sulfur were vulcanized at 140–150°C varying the percentage sulfur at 10, 20, and 30% by weight. In

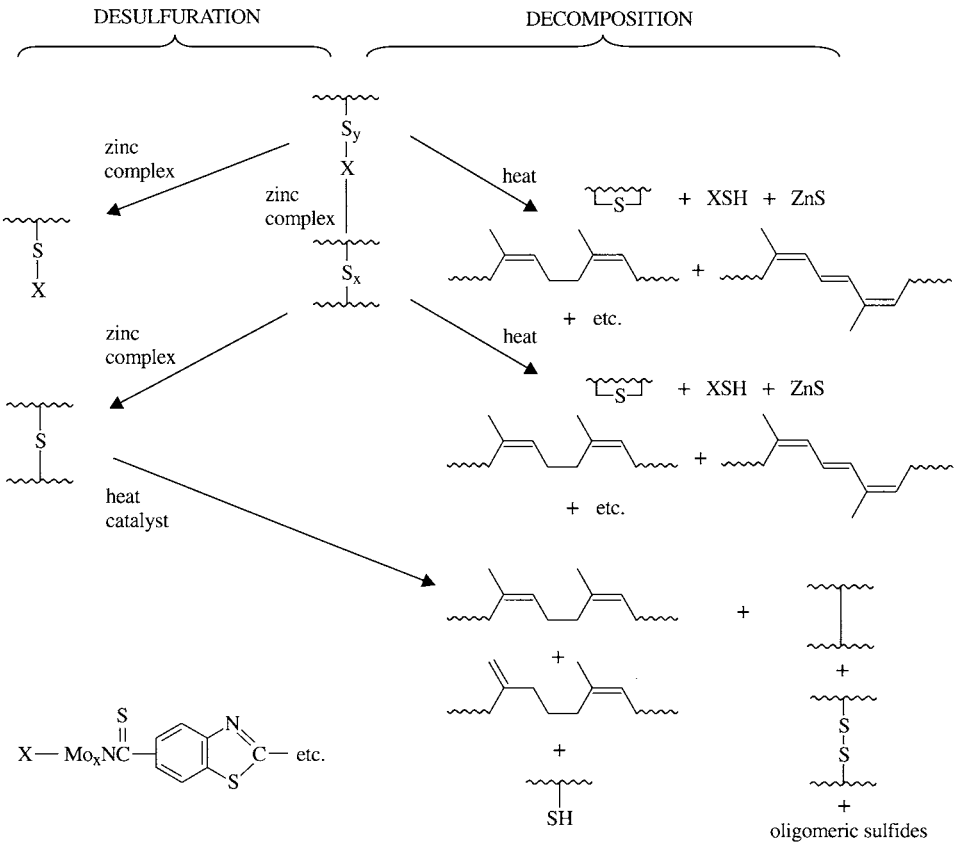

Scheme 9.I.

^{13}C-NMR spectra with increasing cure time at each sulfur concentration, new peaks began to appear as a result of the sulfurization of the chains. After 10 minutes of cure, peaks at 57.5, 50.2, 44.6, 40.1, 30.0, 18.0, 16.1, and 14.0 ppm were observed. At longer cure states peaks at 58, 64, 73, and 81 ppm were found which are probably the result of oxidation. The peaks at 16.1 and 14.0 ppm are possibly due to the chain-end methyl groups occurring by chain scission.

In a further study [63], inversion recovery spin-relaxation time measurements and computer fitting of overlapping spectra regions were used to identify additional peaks in vulcanized natural rubber cured with 1, 3, and 5% sulfur for different time intervals. Those overlapping crosslinked carbons with different T_1 times showed different peak intensities which could be determined by computer fitting of the peaks. Two new peaks at 37.8 ppm and 25.5 were identified.

Initial studies were made on sulfur vulcanization of *cis*-polybutadiene [64]. The NMR of the vulcanized rubber showed peaks representing crosslinked structures. With increasing cure at 10% sulfur, new peaks at 50, 38, and 33 ppm emerged

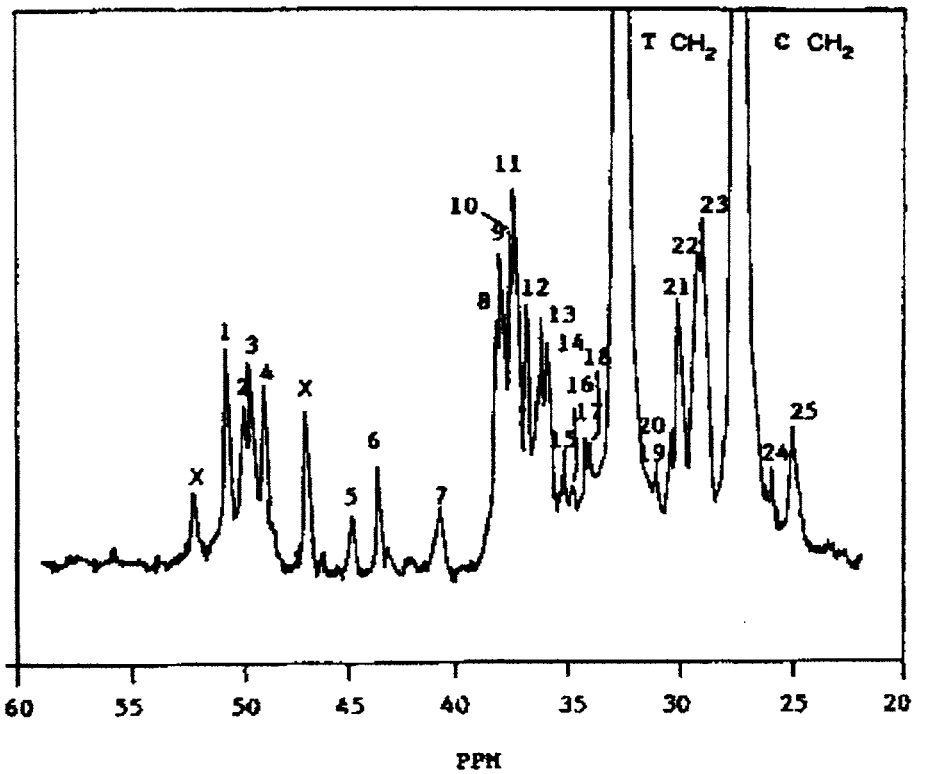

Fig. 9.18. The aliphatic region of the ^{13}C GHPD-MAS at 75.5 MHz of *cis*-polybutadiene cured with 10 phr sulfur at 150°C for 30 min. (Reproduced with permission from Ref. [65]. © 1989 American Chemical Society.)

with an additional peak at 29 ppm appearing in the 20% sulfur vulcanization.

Clough and Koenig also examined sulfur vulcanized polybutadiene using a higher field NMR at 75.5 MHz [65]. As shown in Fig. 9.18, after 30 minutes of cure, a total of 25 new peaks emerged in addition to the normal 1,2- and 1,4-cis and trans isomers present in uncured polybutadiene in a range of 51–25 ppm. A DEPT (Distortionless Enhancement by Polarization Transfer) experiment (Fig. 9.19) showed that the peaks in the range from 40–52 ppm were methine carbons while at the lower range below 40 ppm the peaks represented methylene carbons. The DEPT results confirm the proposed assignments. Peaks 1–4 at 48–52 ppm are methine carbons, and peak 6 at 43.7 ppm is due to a methine carbon in the 1,2 structure. Peak 7 at 40.9 ppm was identified as a methine carbon by using DEPT, and this peak is assigned to carbons bonded to sulfur in monosulfidic crosslinks. Peaks 19–25 are most likely methylene carbons in monosulfidic cyclic structures. The different resonances correspond to isomeric forms of crosslinked and cyclic butadiene structures.

The results of the chemical-shift calculations for the structures in Chart 9.III are shown in Table 9.3 [65].

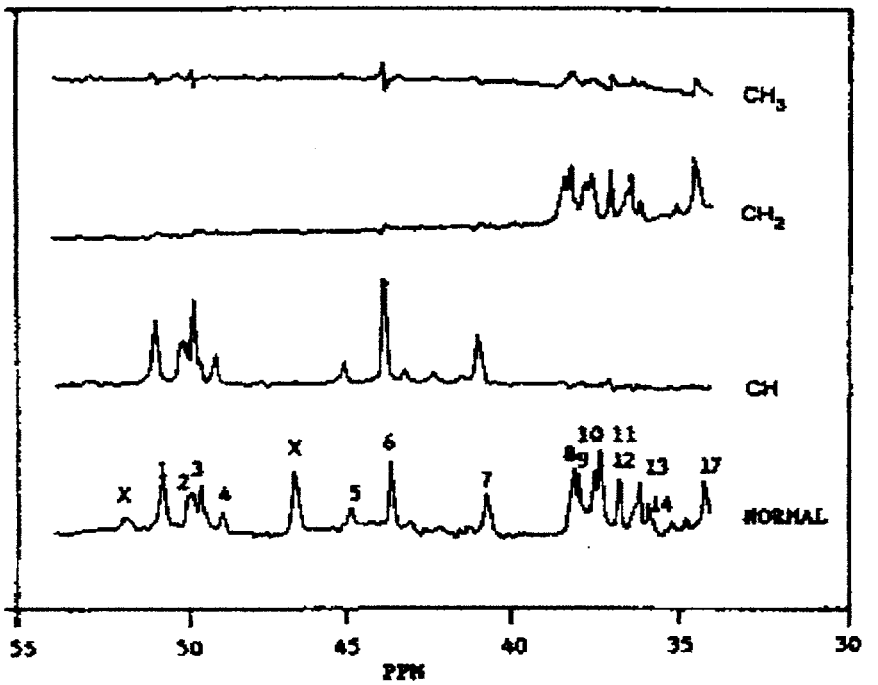

Fig. 9.19. The DEPT ^{13}C-NMR subspectra at 75.5 MHz of a high *cis*-1,4-polybutadiene vulcanizate cured with 10 phr of sulfur for 15 min at 150°C. (Reproduced with permission from Ref. [65]. © 1989 American Chemical Society.)

These calculations indicate that the peaks at 48–52 ppm represent carbons bonded to sulfur (α to sulfur) in polysulfidic crosslinks and tertiary carbons in monosulfidic cyclic structures. The resonances at 34–40 ppm are due to methylene carbons β to sulfur in monosulfidic and polysulfidic crosslinks and methylene carbons in the monosulfidic cyclics. The chemical-shift calculations suggest that the 48–52-ppm region contains all methine carbon resonances and that the resonances in the 34–40-ppm region are all methylene carbons.

Accelerated sulfur vulcanization

The accelerated sulfur vulcanization of *cis*-polyisoprene and natural rubber [66] has also been studied. Three different accelerators were used: tetramethylthiruam disulfide (TMTD), *N*-oxydiethylene-2-benzothiazole sulfenamide (MOR), and *N*-cyclohexyl-benzothiazole-2-sulfenamide (CBS). The NMR peaks that appeared with the 3 different accelerators were found to give similar peaks as in unaccelerated sulfur cured samples. The differences in network structure were reflected in differences in the relative peak intensities between the sulfur and accelerated sulfur cures as well as differences between the 3 accelerator cured samples. Varying the accelerator–sulfur ratio also produced changes in peak intensities. Examination of vulcanizations with and

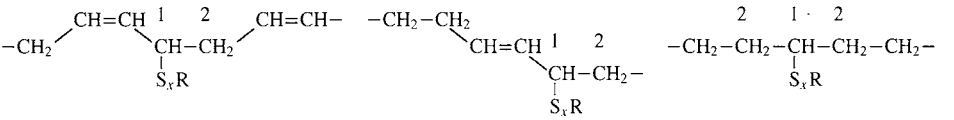

Structure I (cis) Structure II (trans) Structure III

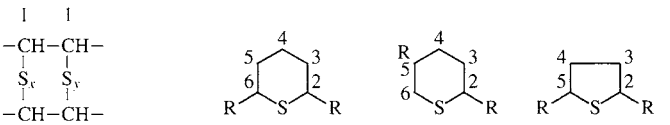

Structure IV (vicinal) Structure V Structure VI Structure VII

Chart 9.III.

Table 9.3
Calculated chemical shifts of potential structures for sulfur-vulcanized polybutadiene

Structure	Carbon	Monosulfidic crosslinks	Di- and polysulfidic crosslinks
I	1	27.6 + 16.1 = 43.7	27.6 + 23.9 = 51.5
I	2	27.6 + 6.9 = 34.5	27.6 + 6.6 = 34.2
II	1	32.9 + 16.1 = 49.0	32.9 + 23.9 = 56.8
II	2	32.9 + 6.9 = 39.8	32.9 + 6.6 = 39.5
III	1	31.7 + 16.1 = 47.8	31.7 + 23.9 = 55.6
III	2	31.7 + 6.9 = 38.6	31.7 + 6.6 = 38.3
IV	1	27.6 + 16.1 + 6.9 = 50.6	27.6 + 23.9 + 6.6 = 58.1
		cis-cyclic	trans-cyclic
V	2,6	38.3 + 8 = 46.3	33.4 + 8 = 41.4
	3,5	36.0	34.8
	4	27.1	20.8
VI	2	35.4 + 8 = 43.4	37.1 + 8 = 45.1
	3	32.2	37.4
	4	30.6	35.5
	5	29.6 + 8 = 37.6	32.9 + 8 = 40.9
	6	33.4	36.6
VII	2,5	44.4 + 8 = 52.4	44.3 + 8 = 52.3
	3,4	37.9	39.5

without the activator, ZnO, yielded spectra where the peaks at 57 and 44 representing monosulfide linkages were absent.

Krejsa and Koenig studied the behavior of the sulfur crosslinked carbons using *N-t*-butyl-2-benzothiazole (TBBS) with conventional, semi-efficient, and efficient formulations [67]. ^{13}C NMR was used to follow the nature of the crosslinked carbon structures with increasing cure time. At low cure states, polysulfide crosslinked peaks at 38 and 51 ppm appeared. As these resonances decreased in intensity, new resonances appeared at 44, 57, 64, 17, 14, and 12 ppm. The majority of the later peaks are

mono-sulfide crosslinks while the 64 peak is a trans poly-linkage. Similar behavior was shown between the three formulations.

Effect of carbon black filler on vulcanization chemistry

More recently, the TBBS accelerator was used in a system containing natural rubber and HAF-HS grade carbon black (N347) [68] and compared with synthetic polyisoprene.

As the carbon black content increases, the NMR resonance lines became broader due to molecular immobilization of the rubber chains by the carbon black. In addition there is a decrease of the S/N ratio of the spectra due to the decrease in the amount of rubber displaced by the carbon black. Broadening also occurred with increase in cure time as a result of the decrease in molecular mobility due to crosslinking, but this line broadening was less significant than the broadening due to the presence of the carbon black.

The new resonances which appeared with vulcanization were qualitatively the same as observed for the unfilled formulation systems, i.e., new resonances at 50.7, 50.2, and 37 ppm were detected at lower cure times. At longer cure times these three resonances disappeared and new resonances were detected at 58, 64, and 45 ppm along with new peaks at 17 and 12 ppm and the growing of the intensity of the peak at 14 ppm. As the amount of carbon black content increased, the latter features were observed at an earlier stage of cure.

At low cure times (Fig. 9.20), doublet peaks at 50.7 and 50.2 ppm were detected along with the peak at 37 ppm, and these peaks disappeared at longer cure times.

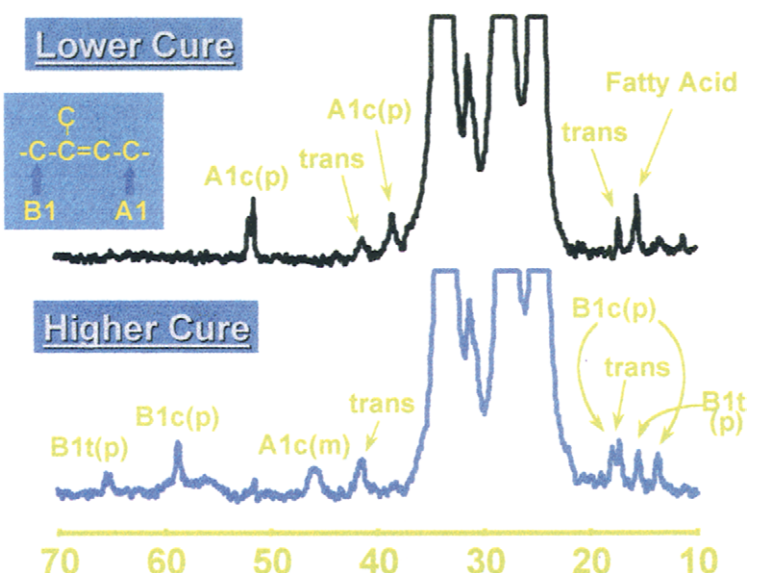

Fig. 9.20. The high resolution solid state NMR spectra of carbon-black-filled natural rubber at two degrees of cure. (Reproduced with permission from Ref. [68]. © 1995 American Chemical Society.)

The intensities of these two peaks were comparable for every detected pair. In the previous studies, the peaks at 50.7, 50.2, and 37 ppm were assigned to a quaternary carbon of A1c polysulfide, a methine carbon of A1c polysulfide, and a β methylene carbon of A1c polysulfide, respectively.

While at longer cure times, resonances at 58, 64, 45, 17, and 12 ppm were detected along with increasing intensity of the 14 ppm peak. The peaks at 58, 64, 17 and 12, and 14 ppm are assigned to B1t monosulfide (α methine), B1t polysulfide (α methine), B1c polysulfide (β methylene), and B1t polysulfide (β methylene), respectively.

Accordingly, there are observed two phenomena involving the effect of carbon black. One is the reduction in sulfur rank for the A1c sulfide structure, and the other, is the formation of the A1 type product at an earlier cure stage and an increase in the B1 products at a later stage.

The first effect was interpreted to be due to an entropy change. The disulfide crosslinks have less mobility than the monosulfide crosslinks due to the rigid nature of $-S-S-$ linkage. Similarly, the mobilities of the polysulfidic crosslinks are probably lower than that of the monosulfidic crosslinks. Therefore the polysulfidic crosslink would occupy more space in the network structure than the monosulfidic crosslink. Considering this fact, the change in sulfur rank from polysulfide to monosulfide would occur along with the increase in entropy when the curing process is extended. Since the system becomes more rigid by the incorporation of the carbon black, the reduction in sulfur rank to monosulfide would eventually be accelerated.

During the vulcanization process (Scheme 9.II), polysulfidic A1c and B1t are formed by the reaction (1) and (2), and (3) and (4), respectively. Considering the fact that A1c polysulfide reduces its sulfur rank to monosulfide and reaction (3) and (4) is the predominant process in the later stage of cure, the system may favor reaction (3) and (4) rather than (1) and (2) in the whole reaction scheme. BtSH is formed

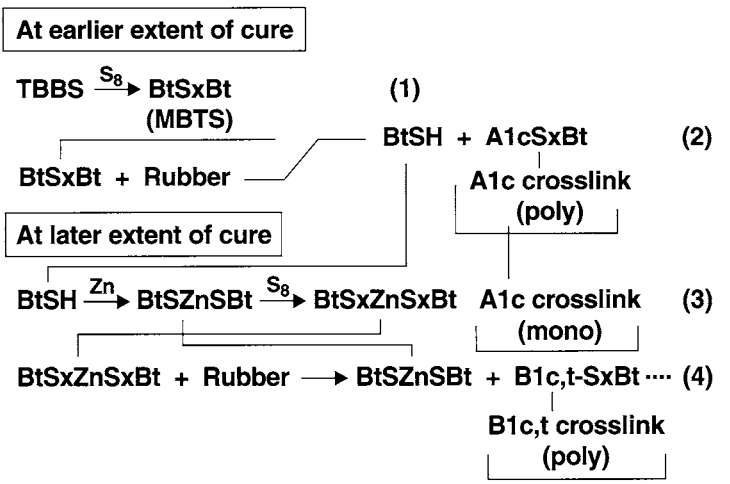

Scheme 9.II.

from the reaction producing polysulfidic A1c at the earlier stage of cure, which is the reactant for reaction (4) producing the B1 structure. As previously mentioned, the sulfur and accelerator to rubber ratio may be higher for the system with high carbon black content. As a result, reactions (1) and (2) would occur more rapidly and, consequently, produce enough BtSH for the initiation of reactions (3) and (4), which means that the B1t polysulfides initiate at the earlier stage of cure for the sample with higher filler content. Since reactions (3) and (4) would occur until the elemental sulfur is consumed, the total amount of B1 structure would be larger for the sample with higher carbon black content.

The network chain density measured by equilibrium swelling includes both the chemical and physical crosslinks while the ^{13}C-NMR measurements determine only the chemical crosslinks. The observed differences in network chain density between the results of the two measurements ($\nu_{SWELL} - \nu_{NMR}$) reflect differences in the physical crosslinks induced by entanglements involving polymer–polymer interactions and polymer–carbon black interactions. The magnitude of the differences between the two methods of measuring the network chain density increases with the volume fraction of the carbon black for the same stage of cure. The differences in network density values reach a maximum at around the 90% cure stage for the filled formulations. These results coincide to a similar observation from tensile tests where the maximum filler reinforcement effect occurs at an optimum (90%) stage of cure. Consequently, the comparisons of the network densities determined by the swelling and ^{13}C-NMR measurements give a measure of the effectiveness of the filler reinforcement at the molecular level.

Effect of silica filler on vulcanization chemistry

Solid state ^{13}C-NMR spectroscopy was used to identify and characterize the effects that silica has on the network structures that form during the vulcanization of zinc activated, sulfur-cured *cis*-1,4 polyisoprene [69]. It was determined that the cis-trans isomerism and chain scission were enhanced when silica was added as a filler. The monosulfidic linkages, especially the A1cis and the B1trans type monosulfide linkages, had an increased concentration in the silica-filled systems. Also, the polysulfidic linkages, namely the A1-cis-and B1-trans-type linkages, decreased in concentration. Finally, it was also determined that the intermolecular crosslinks decreased in the presence of silica, while the intramolecular structures, including pendant side groups and cyclic sulfides, increased in the presence of silica, resulting in a lower overall crosslink density when silica is used as a filler.

When silica is used as a filler, the cure ingredients are adsorbed, causing the initial overall lower cure rate mentioned above. Several ways exist to counteract this effect by inhibiting the silica absorption by adding a silane coupling agent, or polyethylene glycol. Both additives have been shown in the literature to improve the vulcanizate properties. Therefore, solid state ^{13}C-NMR spectroscopy was used to identify and characterize the effects on the network formation when additives, such as a coupling

agent and polyethylene glycol, were added along with silica filler. It was determined that cis-trans isomerization was inhibited by the inclusion of both the coupling agent and the polyethylene glycol. However, there was only a slight influence on the chain scission of the main chain carbons. The presence of coupling agent or polyethylene glycol both caused an increase in the concentration of the polysulfidic structures, especially the A1-cis- and B1-trans-type linkages, as well as a decrease in the monosulfidic structures, namely the A1-cis- and B1-trans-type structures. Therefore, the intermolecular crosslinks, mainly the polysulfidic structures, increased with the use of the additives, while the intramolecular structures, which are mainly monosulfidic in nature, decreased. Therefore, the network chain density of the silica-filled rubber system increased when additives were included in the formulation.

Thermal oxidation of network structures

Elastomeric materials undergo both thermal and oxidation degradation over time. Main chain scission and loss of sulfur crosslinks can occur with either factor or by both factors by a thermo-oxidative mechanism. The chemical changes that occur in thermal and oxidative degradation of sulfur cured natural rubber were investigated using ^{13}C-NMR analysis [70]. The crosslinked carbons formed during TBBS accelerated vulcanization appear in the NMR spectra as peaks representing the various structures formed. Samples of vulcanized rubber were heated at 100°C and 150°C under both air (oxidative) and nitrogen (inert) environments to assess both temperature and oxidative effects. Changes were observed by measuring peak areas under the crosslinked carbon resonance peaks. A- and B-type monosulfide linkages were found to decompose much faster by oxidative factors at both 100°C and 150°C than under nitrogen at either temperature. The polysulfide linkages, however, showed the opposite result of thermal degradation predominating over oxidative factors. Cis-trans isomerization of the main chain carbons was observed at the higher temperature while absent at 100°C.

Epoxide systems

Epoxy resins have been studied extensively with high-resolution solid-state ^{13}C-NMR spectroscopy. The epoxy spectra are shown in Fig. 9.21 of four phases of DGEBA: the resin cured with 5% piperidine, an amorphous resin, a polycrystalline resin, and the starting resin in the liquid state [71].

In the spectrum of the polymerized epoxy resin, the opening of the epoxide ring results in the shift of the two epoxide resonances downfield. The aromatic peaks in the spectra of all phases are identical. Because the crystalline environment has high regularity, the resonance lines are narrow. The amorphous phase has a distribution of local environments and exhibits broad lines; these factors limit the detection of structural detail. The polymerized epoxy freezes in the random distribution of orientations, an effect that further decreases the resolution.

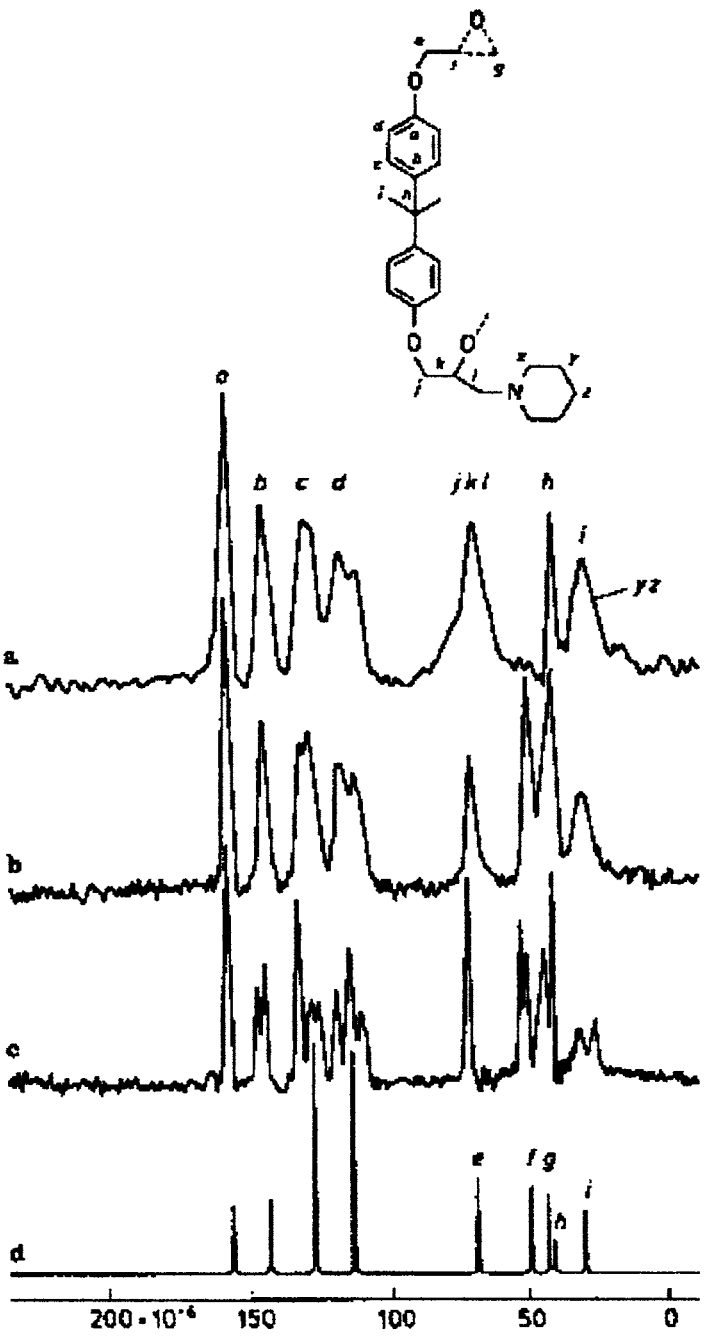

Fig. 9.21. ^{13}C spectra of the epoxy resin DGEBA in four different phases: (a) polymerized with 5% (by mass) piperidine, 247 K; (b) amorphous resin, 230 K; (c) polycrystalline resin, 230 K; and (d) in CCl_4, with the solvent peak deleted. (Reproduced with permission from Ref. [71]. © 1981 American Chemical Society.)

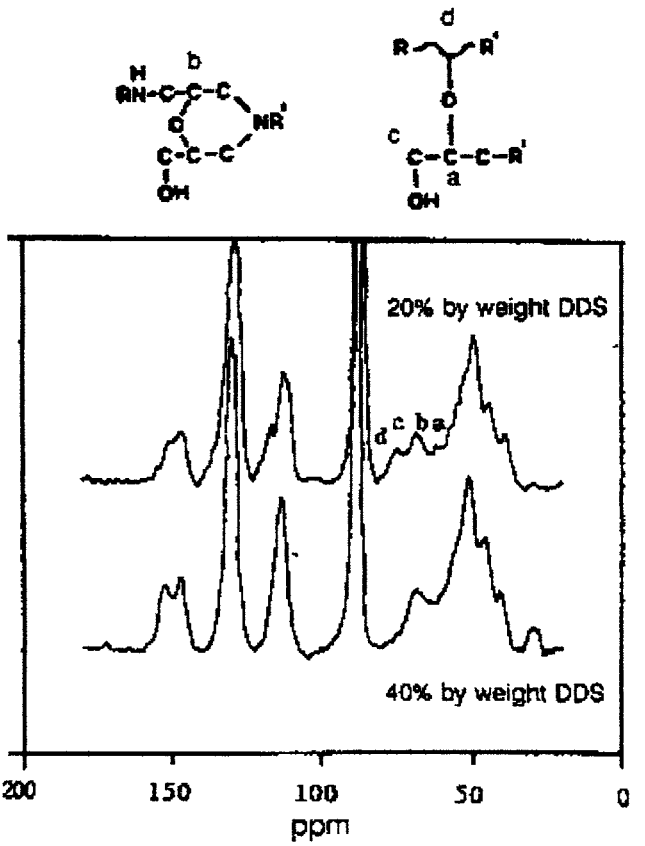

Fig. 9.22. The DD-MAS-CP ^{13}C-NMR spectra at 37.7 MHz of two concentrations of DDS-TGDDM. (Reproduced with permission from Ref. [71]. © 1981 American Chemical Society.)

The butanediol diglycidyl ether (BDGE) cured with phthalic anhydride has also been studied with high-resolution solid-state ^{13}C-NMR spectroscopy [71]. In this system, the hydroxyl group attacks the carbonyl group of the anhydride, and this attack forces the opening of the anhydride ring to produce a carboxylic acid. Similarly, the hydroxyl group of the acid opens the epoxy ring to form a diester linkage and an alcohol. The ^{13}C-NMR spectra confirm such a mechanism, but the resolution in the glassy state is not sufficient to isolate specific resonances that can be assigned.

The tetrafunctional epoxy tetraglycidyl(diaminodiphenyl)methane (TGDDM) and the tetrafunctional amine diaminodiphenyl sulfone (DDS) have also been examined with solid-state ^{13}C-NMR spectroscopy (Fig. 9.22).

The chemical structures resulting from the polymerization of TGDDM with DDS are complex; multiple reactions take place during cure. In the CP-MAS ^{13}C spectrum at 38 MHz, resonances due to carbons attached to hydroxy groups, intramolecular ether linkages, and intermolecular linkages are discernible. The peaks resulting from the four different carbons involved with oxygen appear between 80 and 60 ppm in all

of the spectra. The carbon attached to the hydroxyl group formed by the epoxy-amine reaction (peak c) appears at 70 ppm. The peak for the two carbons involved in the intramolecular ether groups appears at 68 ppm. Both carbons in the CHOCH structure have the same environment. Therefore, only one peak is seen. The carbons involved in the intermolecular ether linkage contribute two peaks. The extent of reaction for TGDDM and the number of total epoxy junctions can be determined from the NMR experiment.

Solid state NMR studies of polymer blends

Molecular interactions between components of polymer blends

Solid state NMR has been widely used to ascertain the miscibility in multicomponent polymer blends [72,73]. Traditionally, the miscibility of polymers is characterized by differential scanning calorimetry: a single glass transition with a composition-dependent temperature, T_g, defines a miscible blend [74,75].

With NMR, one can identify by a determination of the perturbation of the isotropic chemical shifts, the nature of the interactions between the components of the blend and determine whether the specific interactions are due to hydrogen bonding, molecular complexes or charge–transfer interactions. For example, a hydrogen bonding interaction is the basis for the miscibility of blends of poly(methyl methacrylate) (PMMA)–novolac [76] as reflected in a broadening and down field shift of the carbonyl carbon resonance in PMMA with a corresponding upfield shift of the hydroxyl-substituted carbon on the novolac. Complex formation is responsible for the miscibility of nylon 6–Zn salts of sulfonated polystyrene blends as indicated by the change in line shape of the amide nitrogen on nylon 6 rather than the carbonyl oxygen [77].

Evidence for the existence of a template complex formation in blends of poly(methacrylic acid) (PMAA) and poly(*N*-vinylimidazole) (PVIm) was generated using a triple $^{1}H/^{13}C/^{14}N$ resonance experiment [78]. For this triple resonance experiment, the loss of ^{13}C-echo intensity depends on the distances between carbon and nitrogen, because the dipolar coupling between a carbon and a nitrogen spin is proportional to the inverse third power of the separation distance. A substantial loss of the ^{13}C-echo intensity (30%) at 183.3 ppm assigned to the PMAA carbonyl group and a loss (~50%) in the 136.9-ppm mode assigned to the imidazole ring of PVIm where the carbons are adjacent to the ring nitrogen. This loss in spin-echo intensity suggests a specific interaction between the carbonyl group of PMAA and the imidazole ring of PIVm reflecting the formation of the polymer template complex in the blend.

NMR also allows the characterization of molecular homogeneity in blends on a scale from the molecular level to a few hundred angstroms. In principle, phase information can be obtained on three different size scales. The size at the molecular level is studied using changes in the chemical shifts. If a blend shows two different

$^{H}T_1$s and two different $^{H}T_{1\rho}$ times, the single domain sizes are larger than about 500 Å. If there is just one $^{H}T_{1\rho}$ but two $^{H}T_1$s, the domain sizes are between 50 and 500 Å. Only one $^{H}T_{1\rho}$ and one $^{H}T_1$ represent domain sizes smaller than about 50 Å [78]. The limitation of the NMR method for determining miscibility occurs when the proton relaxation times of the pure components show no significant differences.

Spin diffusion is not associated with the diffusion (movement) of the nuclei but rather with the flow of polarization, initially in a nonequilibrium state, towards an internal spin equilibrium through local polarization exchange events. Spin diffusion can be used to characterize the heterogeneity of blends [79]. Spin diffusion experiments typically consist of: an evolution stage which generates an initial polarization gradient between the components of the blend; followed by a mixing stage, during which time spin diffusion takes place and, finally, a detection stage for observing the resulting ^{1}H magnetization. For blends, the spin gradient can be generated based on mobility differences or on ^{1}H chemical shift differences.

Because the spin diffusion rate strongly depends on the distance between nuclei, spin diffusion is confined to neighboring molecules. So if spin diffusion occurs between two species, they must be mixed intimately on the molecular level. Useful semiquantitative information about domain size can be obtained from the equation:

$$\langle r^2 \rangle = 6D_s\tau$$

where $\langle r^2 \rangle$ is the mean square diffusive path length, D_s is the spin-diffusion constant and τ is the time for a fundamental step in the random walk. The spin diffusion is governed by the dipolar–dipolar interaction and for a dense rigid proton system, D_s is of the order of $4–7 \times 10^{-16}$ m^2 s^{-1} in the laboratory frame and half this magnitude in the rotating frame. Since $^{H}T_1$ is typically of the order of 7×10^{-1} s and $^{H}T_{1\rho}$ of the order of 10^{-2} s, the maximum diffusive path lengths range from 50 nm to about 2 nm, respectively. So a single relaxation time will be observed if the two polymers in the blend are from two independent domains where the domain size is smaller than $\langle r^2 \rangle$, and two relaxation times when the domains are larger than $\langle r^2 \rangle$.

NMR of liquid crystal-polymer interactions

Polymer-dispersed liquid crystals (PDLCs) are important to liquid-crystal technology. Nematic LC microdroplets are dispersed in a polymer matrix. These films are used similarly to liquid crystal displays such as displays, switchable windows, and light shutters. PDLC devices operate on the principle of electrical modulation of the LC refractive index to match or mismatch the refractive index of an optically transparent, isotropic solid. PDLC films are made between conductive, transparent substrates, and can be switched from being opaque to being transparent with the application of an electric field. Solid state NMR methods have been used to study (PCLCs) and to identify the LC/polymer interface [80,81]. Using NMR one can iden-

tify the concentration of liquid crystal, the droplet configuration, the polymer used for the matrix material and the concentration of crosslinker. The interface in PDLCs from E7/poly(*n*-butyl methacrylate) and E7/poly(isobutyl methacrylate) is identified as a result of the large differences in the molecular dynamics of the two phases. E7 is a commercial eutectic liquid crystal mixture consisting mostly of molecules related to 4-pentyl-4′-cyanobiphenyl. The E7 is liquid-like and cannot be observed with magic-angle spinning and cross-polarization whereas the polymer matrix is more rigid and can be observed by these methods. The NMR signals from the E7 liquid-crystal mixture can be observed in the PDLCs with poly(isobutyl methacrylate) using cross-polarization. The E7 in the PDLCs is in one of three possible states; bulk E7 inside the droplets, E7 dissolved in the matrix, and E7 in the interfacial layer. It is most probable that the NMR signals under cross-polarization arise from E7 at the interface [81].

NMR spectroscopy of surface species

Polymer composites are high-performance materials with a large range of applications. The reinforcements are typically glass fibers that are often treated with organosilane coupling agents to promote adhesion between the glass fibers and the polymer matrix. The macroscopic properties of composites depend on the nature of the glass fiber, the coupling agent–polymer interface, and the polymer matrix. These structures must be optimized in order to determine the potential of the system. Therefore, the investigation of the nature of these components on the molecular level is useful and necessary for the optimization of performance properties.

Upon the deposition of a hydrolyzed coupling agent onto a silica surface, a chemical reaction takes place, and this reaction leads to the formation of a covalent bond between the two components. Silica surface hydroxyls react with the hydrolyzed alkoxy groups of the organosilane coupling agents in a condensation reaction. In surface studies of this kind, the CP-MAS NMR experiment has the advantage of avoiding interference effects from glass, which is a problem that arises in other surface methods [82]. Changes in the molecular structure of the material caused by sample preparation are avoided because the bulk material serves as the sample without modification.

The CP-MAS ^{13}C-NMR spectra of surface-modified silicas and the corresponding 3-aminopropyltriethoxysilane (γ-APS) spectrum are shown in Fig. 9.23 [83]. When the coupling agent is bound to silica, the peaks corresponding to the carbons of the propyl chains are shifted upfield approximately 0.4–2.0 ppm as compared to the same resonances in the bulk polymer. Those carbons in close proximity to the binding sites (especially the α-methylene carbon) tend to show a larger upfield shift. This close proximity leads to steric hindrance of the organosilane, which causes the chemical shift. The spectrum of condensed γ-APS shows an additional prominent peak arising at 166.0 ppm (as observed in Fig. 9.23) that corresponds to the carbon resonance of

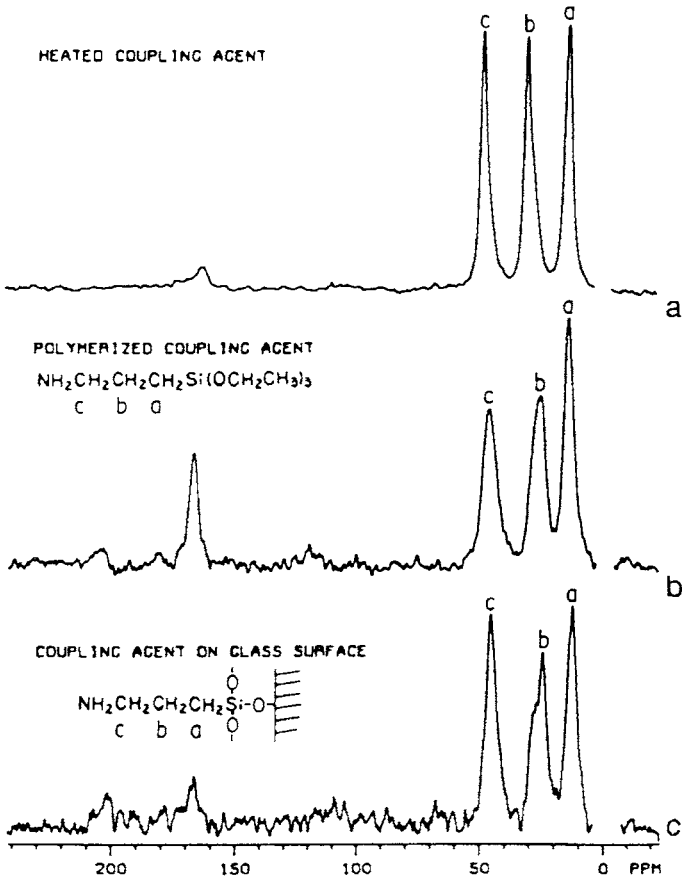

Fig. 9.23. The CP-MAS ^{13}C-NMR spectra at 37.7 MHz of surface-modified silicas and the corresponding γ-APS. Spectrum a is of the polymerized coupling agent subjected to heat treatment, spectrum b is of the polymerized coupling agent, and spectrum c is of the coupling agent on a silica surface. (Reproduced with permission from Ref. [83]. © 1989 American Chemical Society.)

a carbonyl group. If this peak is attributed to a carbonyl group, then the carbonyl is most probably part of the amine–bicarbonate salt formed by a reaction of the free amine groups with carbon dioxide in the air. This reaction can occur with both bulk γ-APS and with γ-APS on the silica surface. The amine–bicarbonate salt is thermally unstable, and with heat treatment at 100°C, the salt decomposes, and the carbon dioxide is removed from the silica surface. Removal of the carbon dioxide from the bulk polymer requires more intensive heat treatment. When the condensed amine functional coupling agent is subjected to a heat treatment of 200°C for 12 h in a vacuum oven, the carbonyl-carbon resonance is greatly reduced in intensity as a result of the evolution of carbon dioxide (Fig. 9.23a).

The problem with using CP-MAS ^{13}C-NMR spectroscopy in the study of interfaces is that the structure of the silane molecule cannot be directly observed, nor can

the mechanism by which the silane molecule is bonded to the glass be determined. An obvious approach is to use ^{29}Si-NMR spectroscopy because this method is superior to ^{13}C-NMR spectroscopy for the study of silanes because it is sensitive to the siloxane network structures. ^{29}Si CP-MAS has been used to study silane coupling agents and

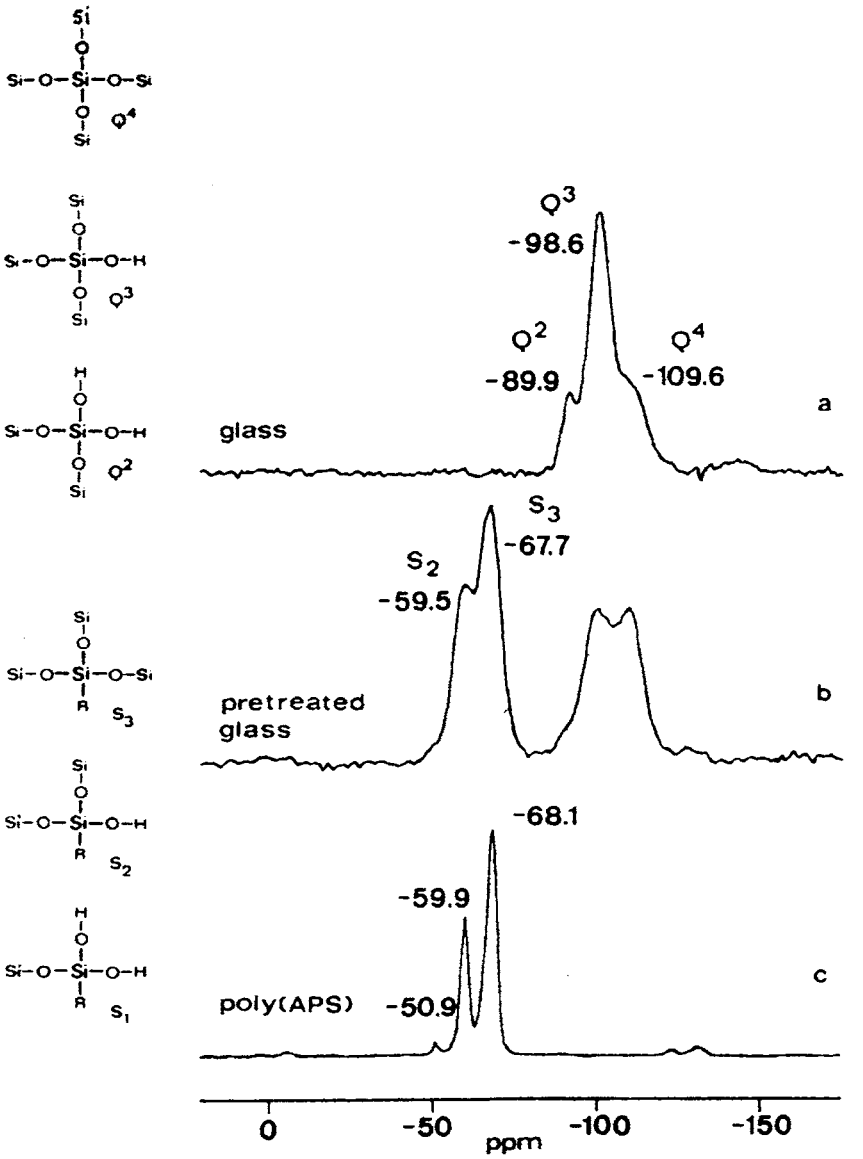

Fig. 9.24. The CP-MAS ^{29}Si-NMR spectra at 59.6 MHz of pure glass microspheres (a), glass microspheres pretreated with 8.4% γ-APS (b), and poly(γ-APS) (c). (Reproduced with permission from Ref. [83]. © 1989 American Chemical Society.)

their surface reactions. In one ^{29}Si-NMR study, polyamide-6 (PA6) was used as the matrix, γ-APS was used as the coupling agent, and glass microspheres were used as the filler material [83]. With CP for ^{29}Si, only nuclei that are near protons will be observed, and therefore silicon nuclei in the bulk glass will not be detected. The solid-state CP-MAS ^{29}Si-NMR spectrum of pure glass microspheres is shown in Fig. 9.24.

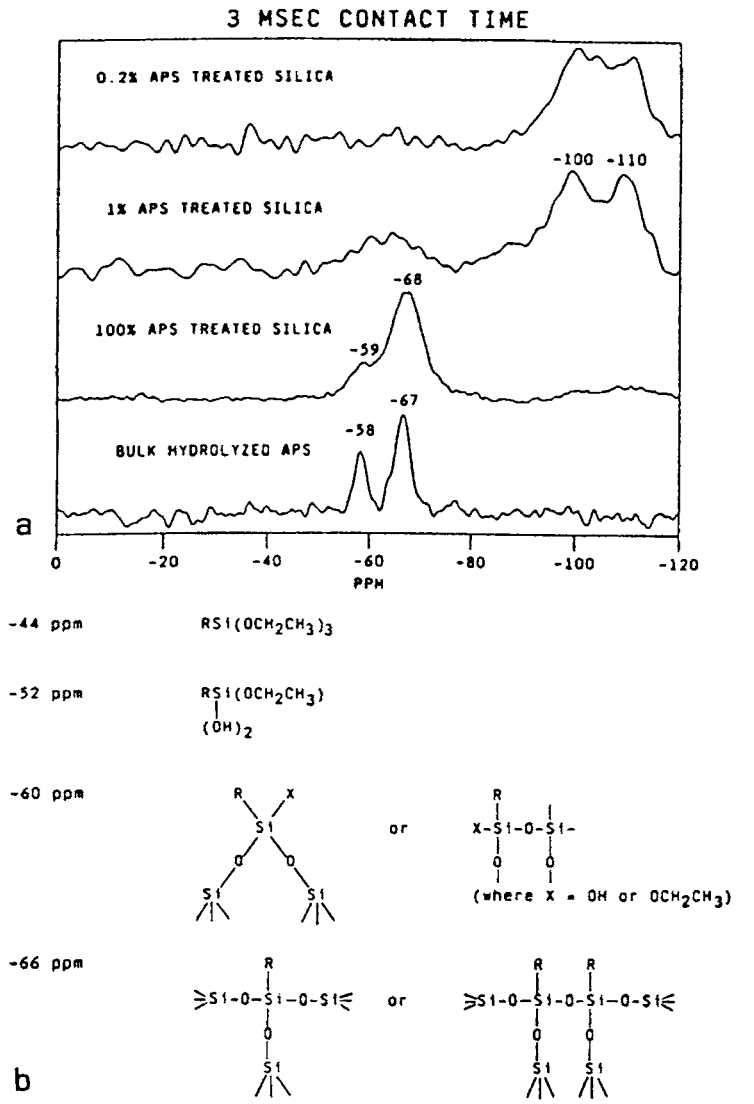

Fig. 9.25. (a) The CP-MAS ^{29}Si-NMR spectra at 59.6 MHz of bulk-hydrolyzed APS, silica-treated with 100% APS, silica-treated with a 1% solution of APS, and silica-treated with a 0.2% solution of APS. (b) Structures assigned to the CP-MAS ^{29}Si-NMR chemical shifts of the γ-APS. (Reproduced with permission from Ref. [83]. © 1990.)

One intense central line at −98.6 ppm (Q^3) has two side peaks at −89 ppm (Q^2) and at −109.6 ppm (Q^4). After treatment with γ-APS, a line denoted S_3 is observed at −67.7 ppm and is assigned to ^{29}Si bonded to three other Si atoms (either on the surface or in a poly(γ-APS) polymer via oxygen bridges) with a fourth bond to the aminopropyl substituent. The −59.5-ppm peak, denoted S_2, is due to Si bonded to two other Si atoms via oxygens, and to one hydroxyl group and an aminopropyl group. The high intensity of the S_3 peak indicates that the polysiloxane is highly crosslinked.

^{29}Si-NMR spectra of bulk hydrolyzed γ-APS and silica treated with different amounts of γ-APS are shown in Fig. 9.25a [84]. The resonances are assigned as shown in Fig. 9.25b. In addition, the resonances at −100 and −110 ppm are due to $(=Si-O)_3Si-OH$ and $(=Si-O)_4Si-OH$ moieties of the silica surface. No peak is observed at −45 ppm, which is the ^{29}Si chemical shift of liquid APS. For the bulk hydrolyzed γ-APS, the line widths are narrow, and the resonance at −58 ppm appears. For the 100% APS-treated silica, the resonances are much broader, and the band at −59 ppm appears as a shoulder. The results indicate that CP-MAS ^{29}Si-NMR spectroscopy of the solid state is a very powerful tool for studies of silane coupling agents.

Summary and conclusions

The utility of solid state NMR in the study of polymer systems is increasing at a rapid rate. This is largely because of the unique information that is available from the NMR measurements including information relative the chemical structure, the molecular conformation and packing in the solid state. The type of molecular motions can also be determined as well as the rates of the motions.

References

[1] Stejskal, E.O., Memory, J.O., High Resolution NMR in the Solid State: Fundamentals of CP/MAS. Oxford University Press, New York, NY, 1994.
[2] Schmidt-Rohr, K., Spiess, H.W., Multidimensional Solid-state NMR and Polymers. Academic Press, Orlando, FL, 1994.
[3] McBrierty, V.J., Packer K.J., Nuclear Magnetic Resonance in Solid Polymers. Cambridge University Press, Cambridge, 1993.
[4] Jelinski, J.W., Chem. Tech. (1986) 312.
[5] Axelson, D.E., Carbon-13 Solid State NMR of Semicrystalline Polymers. VCH, Deerfield Beach, FL, 1986.
[6] Belfiore, L.A., Schilling, F.C., Tonelli, A.E., Lovinger, A.J., Bovey, F.A., Macromolecules 17 (1984) 2561.
[7] Earl, W.L., VanderHart, D.L., Macromolecules 12 (1979) 762.
[8] Tonelli, A.E., Macromolecules 12 (1979) 255.
[9] Grant, D.M., Cheney, B.V., J. Am. Chem. Soc. 89 (1967) 5315.

[10] Schaefer, J., Stejskal, E., Buchdahl, A., Macromolecules 10 (1977) 384.
[11] Mori, M., Koenig, J.L., High-Resolution NMR Studies of Vulcanized Elastomers, Annu. Rep. NMR Spectrosc. 34 (1997) 1.
[12] Komoroski, R.A., Schockcor, J.P., Gregg, E.C., Savoca, J.L., Rubber Chem. Technol. 59 (1986) 328.
[13] Wehrli, F.W., Wirthlin, T., Interpretation of Carbon-13 NMR Spectra. Heyden, London, 1978.
[14] Dybowski, C., Chem. Tech. 15 (1986) 186.
[15] Mathias, L.J. (Ed.), Solid State NMR of Polymers. Plenum, New York, NY, 1991.
[16] Schaefer, J., Stejskal, E., Buchdahl, A., Macromolecules 10 (1977) 384.
[17] Garroway, A.N., Ritchey, W.M., Moniz, W.B., Macromolecules 15 (1982) 1051.
[18] Toneli, A., NMR Spectroscopy and Poymer Microstructure: The Conformational Connection. VCH, New York, NY, 1989.
[19] Tonelli, A.E., Macromolecules 12 (1979) 255.
[20] Earl, W.L., VanderHart, D.L., Macromolecules 12 (1979) 762.
[21] Cholli, A.L., Ritchey, W.M., Koenig, J.L., Appl. Spectrosc. 41 (1987) 1418.
[22] Kitamaru, R., Horii, F., Murayama, K., Macromolecules 19 (1986) 636.
[23] Kitamaru, R., Horii, F., Zhu, Q., Bassett, D.C., Olley, R.H., Polymer 35 (1994) 1171.
[24] Ando, I., Yamanobe, T., Sorita, T., Komoto, T., Sato, H., Deguchi, K., Imanari, M., Macromolecules 17 (1984) 1955.
[25] Drotloff, H., Emeis, D., Waldron, R.F., Moller, M., Polymer 28 (1987) 1200.
[26] Yamanobe, T., Sorita, T., Ando, I., Makromol. Chem. 186 (1985) 2071.
[27] Yamanobe, T., Sorita, T., Komoto, T., Ando, I., Sato, H., J. Mol. Struct. 131 (1985) 267.
[28] Bunn, A., Cudby, M.E.A., Harris, R.K., Packer, K.J., Say, B.J., Polymer 23 (1982) 694.
[29] Aujla, R.S., Harris, R.K., Packer, K.J., Parameswaran, M., Say, B., J. Polym. Bull. 8 (1982) 253.
[30] Gomez, M.A., Tanaka, H., Tonelli, A.E., Polymer 28 (1987) 2227.
[31] Bunn, A., Cudby, M.E.A., Harris, R.K., Packer, K.J., Say, B.J., J. Chem. Soc., Chem. Commun. 15 (1981).
[32] Sozzarni, P., Simonutti, R., Galimberti, M., Macromolecules, 26 (1993) 5782.
[33] Segre, A.L., Capitani, D., TRIP 1 (1993) 289.
[34] Belfiore, L.A., Schilling, F.C., Tonelli, A.E., Lovinger, A.J., Bovey, F.A., Macromolecules 17 (1984) 2561.
[35] Ferro, D.R., Ragazzi, M., Macromolecules 17 (1984) 485.
[36] Kurosu, H., Komoto, T., Ando, I., J. Mol. Struct. 176 (1988) 279.
[37] Cholli, A.L., Ritchey, W.M., Koenig, J.L., Spectrosc. Lett. 16(1) (1983) 21.
[38] Earl, W.L., VanderHart, D.L., J. Magn. Resonance 48 (1980) 35.
[39] Perry, B.C., Koenig, J.L., Lando, J.B., Macromolecules 20 (1987) 422.
[40] Gomez, M.A., Cozine, M.H., Tonelli, A.E., Macromolecules 21 (1988) 388.
[41] Guo, M., Zachmann, H.G., Macromolecules, 29 (1996) 6786.
[42] Taki, T., Yamashita, S., Satoh, M., Shibata, A., Yamashita, T., Tabeta, R., Saito, H., Chem. Lett. Chem. Soc. Jpn. (1981) 1803.
[43] Garroway, A.N., Moniz, W.B., Resing, H.A., Org. Coat. Plast. Chem. 36 (1976) 133.
[44] Garroway, A.N., Moniz, W.B., Resing, H.A., in: W.M. Pasika (Ed.), Carbon-13 NMR in Polymer Science. ACS Symposium Series 103, American Chemical Society, Washington, DC, 1979, p. 67.
[45] Sefcik, M.D., Stejskal, E.O., McKay, R.A., Schaefer, J., Macromolecules 12 (1979) 423.
[46] Patterson, D.W., Shields, C.M., Cholli, A., Koenig, J.L., Polym. Prepr. 25 (1984) 358.
[47] Brown, C.E., Khoury, I., Bezoari, LM.D., Kovacic, P., J. Polym. Sci., Part A: Polym. Chem. 20 (1982) 1697.
[48] Jelinski, L.W., Dumais, J.J., Watnick, P.I., Bass, S.V., Shepherd, L., Polym. Sci., Part A: Polym. Chem. 20 (1982) 3285.
[49] Maciel, G.E., Chuang, I.-S., Myers, G.E., Macromolecules 15 (1982) 121.
[50] Bryson, R.L., Hatfield, G.R., Early, T.A., Palmer, A.R., Maciel, G.E., Macromolecules 16 (1983) 1669.
[51] Haw, J.F., Maciel, G.E., Anal. Chem. 55 (1983) 1262.
[52] Bauer, D.R., Dickie, R.A., Koenig, J.L., J. Polym. Sci., Part B: Polym. Phys. 22 (1984) 2009.
[53] Bauer, D.R., Dickie, R.A., Koenig, J.L., Ind. Eng. Chem. Prod. Res. Dev. 24 (1984) 121.
[54] Maciel, G.E., Chuang, I.-S., Gollob, L., Macromolecules 17 (1984) 1081.

[55] Kaplan, S., Dilks, A., J. Appl. Polym. Sci.: Appl. Polym. Symp. 38 (1984) 105.
[56] Andreis, M., Koenig, J.L., Adv. Polym. Sci. 89 (1989) 71.
[57] Coran, A.Y., Rubber Chem. Technol. 68 (1995) 351.
[58] Kresja, M.R., Koenig, J.L., Rubber Chem. Technol. 66 (1993) 376.
[59] Heinrich, G., Vilgis, T.A., Macromolecules 11 (1993) 09.
[60] Mori, M., Koenig, J.L., Annu. Rep. NMR Spectrosc. 34 (1997) 231.
[61] Komoroski, R.A., Schocker, J.P., Gregg, E.C., Savoca, J.L., Rubber Chem. Technol. 59 (1986) 328.
[62] Zaper, A.M., Koenig, J.L., Rubber Chem. Technol. 60(2) (1987) 252.
[63] Andreis, M., Liu, J., Koenig, J.L., J. Polym. Sci., Polym. Physics 27 (1989) 1389.
[64] Zaper, A.M., Koenig, J.L., Makromol. Chem. 189 (1988) 1239.
[65] Clough, R.S., Koenig, J.L., Rubber Chem. Technol. 62(5) (1989) 908.
[66] Zaper, A.M., Koenig, J.L., Rubber Chem. Technol. 60(2) (1987) 278.
[67] Krejsa, M.R., Koenig, J.L., Rubber Chem. Technol. 67 (1994) 348.
[68] Mori, M., Koenig, J.L., Rubber Chem. Technol. 68(4) (1995) 551.
[69] Hill, C., Koenig, J.L., Polym. Bull. 40 (1998) 275.
[70] Parker, D.D., Koenig, J.L., J. Appl. Polym. Sci. 70 (1998) 1371.
[71] VanderHart, D.L., Earl, W.L., Garroway, A.N., J. Magn. Resonance 44 (1981) 361.
[72] Belfiore, L.A., Lutz, T.J., Cheng, C., Solid State NMR Detection of Molecular Level Mixing Phenomena in Strongly Interacting Polymer Blends and Phase Separated Copolymers. Plenum, New York, NY, 1991.
[73] Guo, M., TRIP 4 (1996) 238.
[74] Colemen, M.M., Painter, P.C., Prog. Polym. Sci. 20 (1995) 1.
[75] Olabisi, O., Robeson, L.M., Shaw, M.T., Polymer–Polymer Miscibility. Academic Press, New York, NY, 1979.
[76] Zang, X., Solomon, D.H., Macromolecules 27 (1994) 4919.
[77] Kwei, T.K., Dai, Y.K., Lu, X., Weiss, R.A., Macromolecules 26 (1993) 6583.
[78] Ruhnau, F.C., Veeman, W.S., Macromolecules 29 (1996) 2916.
[79] Campbell, G.C., VanderHart, D., J. Magn. Resonance 96 (1992) 69.
[80] Buchert, K.L., Koenig, J.L., Wang, S.Q., Appl. Spectrosc. 47 (1993) 933.
[81] Mirau, P.A., Srinivasarao, M., Appl. Spectrosc. 51 (1997) 1639.
[82] Zaper, A.M., Koenig, J.L., Adv. Colloid Interface Sci. 22 (1985) 113.
[83] Weeding, T.L., Veeman, W.S., Jenneskens, L.W., Gaur, H.A., Schuurs, H.E.C., Huysmans, W.G.B., Macromolecules 22 (1989) 706.
[84] Hoh, K.-P., Ishida, H., Koenig, J.L., Polym. Compos. 11 (1990) 121.

Chapter 10

Mass spectrometry of polymers

Introduction

Mass spectrometry (MS) is the study of ions created as a result of ionization/fragmentation as determined electrically in the gas phase (neutral molecules are not observed) [1]. The mass spectrum is a graphical representation of the ion abundance versus the mass-to-charge ratio (m/z where m is the mass and z is the charge) of the ions separated in a mass spectrometer. The most important peak for identification of a molecule is the molecular ion ($M^{+\bullet}$) or quasimolecular ion (e.g. MNa^+) as this peak has the same mass as the molecule. The mass spectrometer actually measures the mass-to-charge ratio of ions; therefore, the molecular ion with a single charge is detected at a m/z value that represents the mass of the molecule.

MS is used to study the formation, separation, detection and interpretation of ions in the gas phase. Due to the low volatility of macromolecules, the use of MS was limited in the past. Pyrolysis of polymers was a necessary step in order to use the available MS ionization techniques. However, useful information could be obtained by direct analysis of polymers [2]. Until the mid 1980s, it was felt that the molecular mass range above 10 kDa especially labile and involatile compounds was not within reach of practical MS. However recent progress in MS has met the demands of higher mass measurements such that MS is now a valuable technique for the identification and characterization of polymeric materials and has been used in a wide number of structural applications [3].

MS is a rapid, highly sensitive technique with high spectroscopic selectivity which yields specific structural information particularly as relates to the role of molecular weight in determination of structure. Spectroscopic methods such as infrared and Raman yield structural averages whereas MS examines the individual oligomers. However, special MS techniques are required for nonvolatile, polar, thermally labile, and higher molecular weight molecules. Direct desorption of ions from polymer surfaces, make it possible to circumvent the necessity of reducing the M_w of the polymer before analyzing them by MS [4].

MS allows the measurement of the mass of the isotopes of molecular ions. An isotope is any of the forms of an element that differ in the number of neutrons in the nucleus. The isotopic envelope for an ion of a known empirical formula is measured

by MS reflects the number of isotopes for a given element as well as the natural abundance of the isotopes for that element. Isotopic patterns can often be used to identify the presence of certain atomic species in a molecule by observing the unique isotopic pattern that they have.

To analyze any material by MS, the sample must first be vaporized and ionized in the instruments vacuum system. It is generally possible to measure the mass of initial charged species (molecular or parent ion) and those obtained by fragmentation (fragments). In MS, the behavior is studied of the mass-to-charge ratios of volatilized and ionized molecules. The mass spectrum of the fragmentation ions is unique to each molecule as the ion mass pattern is different for each molecule resulting in characteristic mass spectra.

The MS technique offers:

- high sensitivity (ppm),
- large dynamic range,
- linearity,
- isotopic resolving power for polymers up to ~4000 Da,
- requires very little sample (<1 nmol),
- very fast (~10 min),
- low or high cost instrumentation,
- sample preparation and/or isolation steps reduced,
- structural details of polymer chains,
- information regarding additives.

For application of MS to synthetic polymers, MS must have:

- efficient detection of ions over a wide mass range,
- mass scale properly calibrated,
- high mass resolution depending on the application.

The resolution of MS is defined as the mass divided by the difference in mass number between two distinguishable neighboring lines of equal height in the mass spectrum. Thus a resolution of one part is 200 adequately distinguishes between mass 200 and 201. MS is a microanalysis technique as very little sample (micrograms) is needed for analysis. The MS technique is best suited for volatile, thermally stable gaseous molecules.

MS requires gas phase ions. The low volatility of macromolecules has served to limit the application of MS to the study of molecules. The use of mass spectrometry for the analysis of synthetic polymers can be divided into degradational characterization of polymers and direct analysis of molecular ions (or quasimolecular ions) of intact polymers.

In direct pyrolysis of polymers, polymer pyrolysis is accomplished in the ion source, adjacent to the ionization region so that the pyrolysis products are immediately ionized once formed, minimizing rearrangements or secondary thermal reactions. Although the M_ws of oligomers detected seldom exceeded 100–2000 Da, structural information sufficient for identification was possible [5,6].

The challenge for application of MS to polymers is to obtain stable, charged macromolecules in the vapor phase. Polymers are too big and fragile to survive the high temperatures required to generate samples in the gas phase by heating for MS analysis. In order to obtain structural information it is necessary to minimize fragmentation during desorption and ionization.

In recent years, the development of 'soft' desorption-ionization methods has allowed the application of mass spectrometry to the characterization of polymers [7]. Using these new direct introduction methods the sample is admitted in the condensed phase and subsequently vaporized, pyrolyzed or bombarded so as to emit useful intact ions.

Correlation of mass spectra with molecular structure

> *It has long been known that the elemental composition of an organic ion can be established if its mass can be measured with sufficient accuracy* [8]. *For low molecular weight compounds, the number of possible compositions is small, or the composition may be unique, if the mass can be measured to within 5 parts-per-million of the theoretical value.* [9]

The mass spectra are plots of the ion intensities vs. mass-to-charge ratio. It is the usual practice to normalize the data by assigning the most intense mass peak (termed base peak) and reporting the other peaks as percentage of the base peak. A molecule may simply lose an electron in which case the mass of the parent M^+ is the mass of the molecule (unless there are attached species do to the nature of the process, i.e. K^+, etc.). For polymers, under conditions of 'soft' ionization, this results in the mass spectra of the oligomers in the sample.

However, under high energy electron bombardment, the polymer molecules are more likely to fragment into ions. The fragment ions, in turn, may break down further. The mass spectrum of a compound contains the masses of the ion fragments and the relative abundance of these ions plus the molecular or quasimolecular ion. Although the fragmentation may appear to random, in fact, the dissociation fragments will generally occur in the same relative abundance for a particular compound. Thus it is generally unique to each molecule and as such aids in the identification. The mass spectrum becomes a 'fingerprint' of the molecule as no two molecules are ionized and fragmented in exactly the same manner on electron bombardment. In fact, to some degree, the fragmentation pattern can be predicted.

MS can also be used to characterize chemical functionality in complex molecules. In the analysis of the mass spectra, some functional group correlations have been observed. For example, for all linear alkanes higher than C_4, a mass peak at 43 is always observed. Masses at 31, 45 and 59 indicate the presence of oxygen as an alcohol or

ether. Mass 19 indicates fluorine, Mass 77 indicates the presence of a benzene ring. The analytical applications of MS to polymers include:

- polymer and additive identification,
- residual volatile chemicals,
- end group determination,
- measurement of average molecular weights and molecular weight distributions,
- polymer structure,
- copolymer microstructure,
- polymer degradation products and mechanisms.

The principal difficulty of analyzing polymers is their lack of volatility!

In the past, for polymer analysis, the polymers were decomposed into volatile fragments and these fragments were analyzed. The technique of pyrolysis of polymers was commonly used. However, new soft ionization methods have been developed and the amount of polymer fragmentation has been reduced greatly and in some cases, no fragmentation occurs.

Assuming there is not excessive fragmentation or detector efficiency is independent of molecular weight (no mass discrimination), MS gives absolute molecular weights and distributions in a single measurement which can be done in less than an hour. Molecular weight determinations can be made in the range of 100 to 400,000 Da. The measurements are absolute and do not require calibration only the calibration of the mass scale as with other techniques such as GPC and viscosity.

MS instrumentation — how to make macromolecules fly!

The MS instruments have four components: a sample input, ion source, a mass analyzer, and an ion detection and recording device with a data system for instrument control, data manipulation, and output. A block diagram of a generic mass spectrometer is shown in Fig. 10.1.

There are a variety of types of MS instrumentation, which utilize a range of types of the different components. In principle, any combination of source and analyzer can be made and many combinations have been reported.

The cost of MS instrumentation varies from ~$50,000 for a simple quadrupole instrument with a limited mass range to well over $1 million for a four sector tandem mass spectrometer.

Ion sources

The classical ion source vaporizes and ionizes the sample. Thermal energy is generally used to vaporize the sample and electron currents are provided which

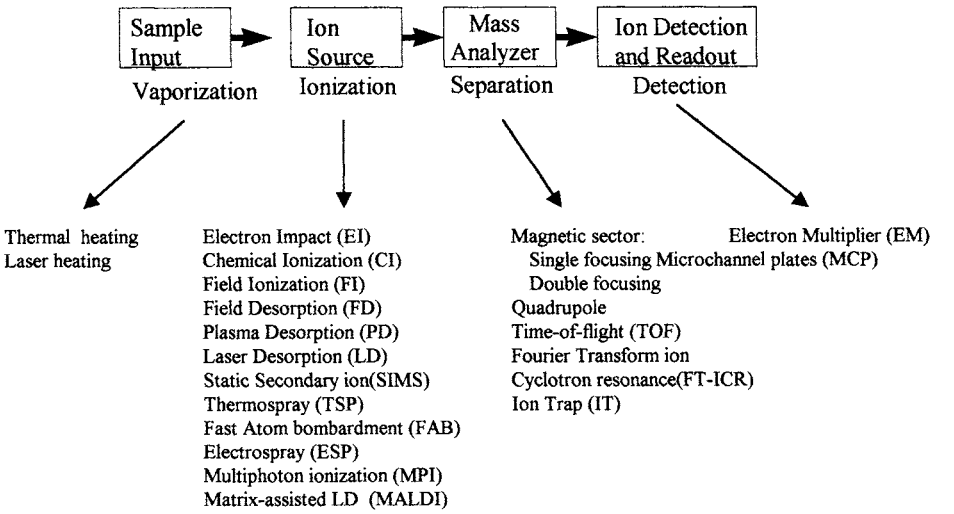

Fig. 10.1. A generic mass spectrometer indicating the four essential components and the role of each component in the mass analysis process is given below the block diagram.

exceed the ionization energy of the molecule. Classically, the sample is vaporized by heating, then ionization and fragmentation occurs in the gas phase. Ion acceleration and ion focusing may also take place in the ion source. Ionization can be induced in a number of ways including electron impact (EI), chemical ionization (CI), field ionization (FI), and multiphoton ionization (MPI).

More recently, ion sources using desorption ionization have been developed where vaporization and ionization occur essentially at the same time. This approach is required for nonvolatile, polar, thermally labile, and higher molecular weight molecules. These methods include bombardment, rapid heating, spray and electron tunneling. Plasma desorption (PD), static secondary ion (SSIMS) and fast atom bombardment (FAB) are the bombardment methods. Laser desorption (LD) and matrix-assisted LD/I (MALDI) methods are used for rapid heating. There are two spray techniques: thermospray (TSP) and electrospray (ESP). The electron tunneling method involves field desorption (FD).

Electron impact

Electron impact (EI) is the classic method for MS and was the dominant technique for many years. In EI the molecules are volatilized with heat and ionized by a beam of electrons from a hot wire filament. EI is the first technique to consider for any sample that can be thermally vaporized in the mass spectrometer. It provides rich structural information because of the distinctive fragmentations and rearrangements that occur that can be used for structural analysis and identification. For EI, an energetic electron beam (typically 70 eV) ionizes a gaseous sample by electron

ejection ($M^{+\bullet}$) or electron attachment ($M^{-\bullet}$). The process for atoms or molecules may be written:

$$M + e^- \Rightarrow M^{+\bullet} + 2e^-$$

The molecular ion $M^{+\bullet}$ formed by EI must be stable on the time scale of a few microseconds in order to be observed in the mass spectrum. If the molecule is prone to dissociate, fragment ions will appear in the mass spectrum and the intensity of the $M^{+\bullet}$ will be reduced.

The EI method is a universal technique, as all molecules will give ions. The EI fragmentation process is fairly well understood and can aid in the structure determination. Some simple rules for the fragmentation processes are used:

(1) the charge preferably resides on heteroatoms (O, N S, Cl)
(2) the initial fragmentation is at the radical site, normally α-cleavage (β-scission in terms of the organic chemists).

EI has high sensitivity and yields a long-lasting stable ion current. Because of the extensive use of EI, standard spectral catalogues are available for comparison and identification purposes.

The limitations of EI are primarily the requirement that the sample be vaporized by heating, thus higher mass and thermally labile compounds may not be amenable to analysis. For polymers, one can simply heat the polymer in the direct probe of the MS for EI. In some cases, oligomers of lower molecular weight will be evaporated and detected. Care must be taken not to heat the sample to a temperature where it thermally decomposes. The problem on the interpretive side for polymers is to determine whether the detected species are a result of vaporization or decomposition. The study of polymers by EI has only had limited success. Some success has been achieved by 'rapid' heating. At higher temperatures, vaporization may be favored over thermal decomposition [10,11].

Chemical ionization

Chemical ionization (CI) was developed in 1968 and is based on the use of reagent gas ions at 'high' pressure which softly ionize a gaseous sample by proton transfer $(M–H)^+$ or $(M–H)^-$ or charge transfer ($M^{-\cdot}$) [12]. CI occurs when an ion (the reagent ion) and a gas phase neutral sample molecule collide and react by transferring a proton. CI has been used to obtain mass spectra with enhanced selectivity for particular classes of molecules which supplement EI ionization data. CI uses a variety of reagent gases including methane, water, ammonia and isobutane and is widely used for polar and semipolar organic molecules.

In CI, the reagent gas at a pressure $\approx$1 Torr is subjected to a closed EI source which is of high electron energy (250–500 eV rather than 70 eV). If methane is the reagent gas, $CH_4^{+\bullet}$ then encounters a neutral gas molecule. Since the methane is at 1 Torr pressure and the sample gas pressure of $\sim 10^{-5}$–10^{-6} Torr, the most

likely encounter is another methane molecule. This encounter produces a reaction that creates CH_5^+ ions and $CH_3^\bullet$ radicals. The primary reactant ion is usually CH_5^+, which protonates any gas-phase sample molecule more basic than methane.

One particularly intriguing aspect of CI for molecular weight determination for polymers is the appearance of the quasimolecular ion (MH^+). CI leads to less fragmentation compared to EI. Proton attachment preferentially occurs on heteroatoms, and the initial fragmentation is at the charge site normally by heterolytic cleavage (inductive effect).

CI is a 'softer' ion source than EI and so produces less fragmentation. CI has been used to examine polymer systems with some success [13].

Static secondary ion mass spectrometry

In secondary ion mass spectrometry (SIMS), the sample is deposited as a thin film on a metal foil and the sample is then bombarded with a primary ion beam (perhaps a Ar^+ pulsed primary ion beam) and secondary ions are sputtered from the surface and analyzed. The SIMS process begins by pulsing a primary ion beam onto the sample surface. This pulse is on the order of one to a few nanoseconds in length and contains from one to several thousand primary ions. The impact of this primary ion beam leads to sputtering of atomic and fragment species and the desorption of molecular ions.

The SIMS technique, as originally developed, was limited to relatively low molecular weights (m/z < 500 Da) due to limitations of the quadrupole mass analyzer. Latter, the development of TOF-SIMS extended the mass range to ~10,000 Da. The problem with SIMS is that organic compounds often yield both intense structurally characteristic secondary ions and abundant nonspecific secondary ions. Quantitative analysis with SIMS is difficult mainly because of ion optical and matrix effects. With inorganic samples, uses of internal standards are required. For organic systems, factors such as sample/matrix evaporation, sputtering, and irreversible chemical reaction need to be determined. SIMS is always a surface technique [14].

With the development of SIMS-TOF it is possible to investigate polymers in the high mass range (up to 10,000 Da) [15].

Fast atom bombardment

Fast atom bombardment (FAB) (developed in 1981) [16] utilizes a stream of fast-moving atoms (rather than ions as in SIMS) (Cs° or Xe° at 6–9 keV energy) which bombards the sample contained in a viscous liquid matrix (e.g. glycerol) on a metal probe. The viscous matrix constantly resupplies fresh sample to the surface so the spectra are intense and long lasting.

FAB allows the study of nonvolatile, polar chemicals of fairly high molecular weight (<5000–10,000 Da). Nonpolar materials do not yield good FAB spectra so one is limited to polar polymers. This FAB method is widely used for biomacro-

molecules (e.g. polypeptides and polysaccharides) [17]. Ionization is usually by proton attachment/extraction [MH+ or M − H] or cation attachment [MNa+, MK+). Most synthetic polymers have no acidic or basic functional groups that can be utilized in ion formation through acid–base equilibria, hence, the limitation for these systems.

Since high molecular weight polymers are inert to FAB, in order to obtain information about the structure a degradation method must be applied to produce low molecular species which are then subjected to FAB. Photolysis, hydrolysis, methanolysis, ammonolysis, pyrolysis and ozonolysis have been employed in the partial degradation of polymers for FAB.

The limited mass range of FAB are that extensive fragmentation occurs especially at lower mass resulting in complex spectra including extraneous signals (cluster ions) due to the matrix and, unfortunately, contamination of the instrument.

Field desorption/field ionization

In field desorption (FD), the sample is deposited on a specially prepared emitter consisting of a tungsten wire on which microneedles of pyrolytic carbon have been grown. Desorption is a process in which a compound is released from a surface and ionized. The sample is deposited from solution by microsyringe or by dipping the probe into a solution of the sample. The sample is then introduced into a special ion source, where a very high electric field (~10–100 MV/cm) causes the sample to be ionized and desorbed. Nonpolar organics yield odd-electron molecular ions ($M^{+\cdot}$ or $M^{-\cdot}$) that are apparently formed by sublimation-field ionization (electron tunneling) at or near the fine microneedle tips on the emitter. FD works rather well for hydrocarbon and other polymer systems of low polarity. The technique makes it possible to ionize molecules with molecular weights up to about 3–5 kDa.

Low concentrations of alkali halides can improve the ionization of polar-desorbing polymers [18].

Field ionization (FI) uses the same ion source as FD. The sample, however, is vaporized by heating from a direct probe (as in EI and CI analysis). The major advantage of FI and FD is that they are truly 'soft' ionization methods. Fragmentation is either absent or very minor.

Electrospray ionization

Electrospray ionization (ESI) is a method of transforming ions that are present in a solution into characteristic ions in the gas phase. In ESI, the sample liquid is introduced into a chamber via a hypodermic needle. An electrical potential difference (usually 2–4 kV) between the needle inlet and the cylindrical surrounding walls promotes ionization of the emerging liquid and disperses it into charged droplets. ESI involves four processes; production of charged droplets, shrinkage of the charged

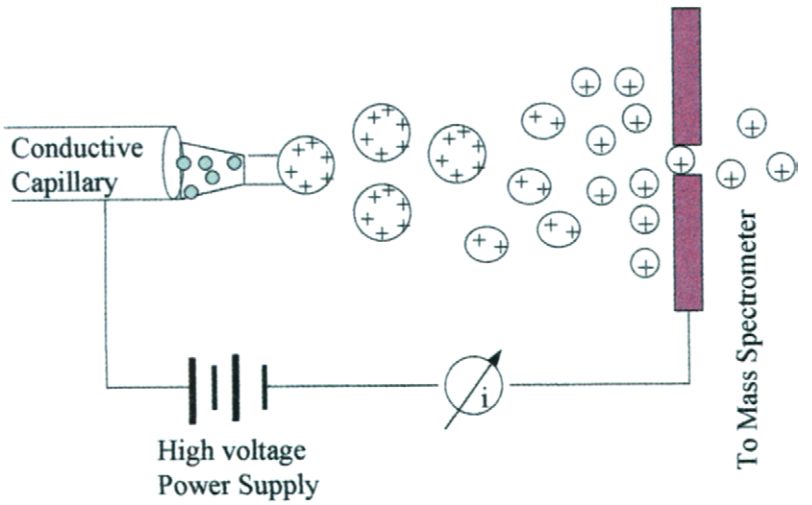

Fig. 10.2. Schematic diagram of the electrospray ion formation process.

droplets by solvent evaporation and drop disintegrations, production of gas-phase ions, and modifications of the gas-phase ions in the atmospheric and ion-sampling regions of the mass spectrometer. Fig. 10.2 shows a schematic of the ESI process.

Solvent evaporation upon heat transfer from the ambient gas leads to shrinking of the droplets and to the accumulation of excess surface charge [19]. At some point, the electric field becomes high enough (up to 10^9 V/cm) to desorb analyte ions.

ESI spectra are relatively simple consisting primarily of molecular ions (M+) ions for the quaternary ammonium salts and $[M + H]^+$ and/or $[M + 2H]^{+2}$. The presence of multicharged ions also can occur especially for higher M_w polar molecules. This problem becomes very real for samples containing mixtures of polymers, copolymers, or differing average molecular weights.

However, multicharged ions are also formed which fold the mass/charge ratio into the sensitive area for the detector. One practical observation has been that the mass spacings between two adjacent ions which differ by a single charge can be used to derive the molecular mass [20]. One of the limitations of ESI is that only polymers that are soluble in an electrospray compatible solvent are amenable to ESI analysis [21]. An additional problem is the interfering presence of overlapping charge distributions.

Laser desorption

In laser desorption ionization (LD), a sample is irradiated with a laser beam [22]. In the case of solid samples, vaporization/ionization occurs via a thermal (rapid heating) process [23]. The laser energy of 10 to 1000 nJ is normally used which yields power densities at the surface of the sample of 2.12×10^7 to 2.12×10^8 W cm^{-2}.

The nanosecond UV lasers can easily produce 10^{10}–10^{11}K/s with a spot diameter approximately 100 microns. Rapid heating desorbs molecules before they have time to decompose. Typically, LD produces primarily singly charged ions. Ionization efficiency and fragmentation is determined by the laser power and wavelength. UV lasers give a better ion yield and a softer fragmentation process. Most organic molecules have ionization potentials in the range 7–10 eV. The energy of 266 nm photons is ~4.66 eV, whereas a 193 nm photon has an associated energy of 6.42 eV. In both cases, absorption of two photons is required in order to achieve ionization. Laser desorption typically gives (MNa^+). This is different than MPI, which gives M^+. Efficient multiphoton ionization requires the target molecule to have significant absorption at the photoionization wavelength.

Matrix-assisted laser desorption ionization (MALDI)

A sample can be subjected to LD in a matrix (termed matrix-assisted) or more commonly as MALDI [24]. MALDI is a 'soft' ionization technique for transferring large molecular ions into a mass-spectrometer without fragmentation. The matrix isolates the sample molecules from each other, absorbs most of the laser energy, and assists in the formation of protonated or metalated ions. Nicotinic acid and other compounds can be used as matrix materials. In principle, the sample to be investigated is mixed in such a ratio that matrix separation of the sample molecules is achieved. Such a ratio ranges from 500 : 1 to 10,000 : 1. After drying, a laser pulse is directed onto the solid matrix to photoexcite the matrix material. This excitation causes the matrix to decompose explosively, resulting in the expulsion and soft ionization of the sample molecules. The matrix strongly absorbs the radiation to enhance the rate of heating.

For MALDI experiments the matrix compound, which produces primarily molecular ions of the molecule with little or no fragmentation, must also:

- strongly absorb the laser radiation,
- have solubility properties similar to those of the sample,
- isolate the molecules from each other,
- co-crystallize with the analyte,
- provide good ionization conditions,
- produce no ionic interference with the sample.

For MALDI experiments, one needs to dissolve the polymer in very dilute (1×10^{-5} m solution of polymer with the matrix (1 to 2×10^{-1} M) generally using the same solvent e.g. methanol, acetone, THF). Typical matrices are Indole, or acrylic acid. One mixes the matrix/polymer solution (varies a lot) and places it on probe (0.5–2 μl) to dry. The MALDI experiment can then be undertaken.

For high molecular weight polymers, much higher ratios of matrix to polymer are recommended [25]. Insoluble polymers are analyzed by mounting a small portion of polymer to a sample disk with double sided adhesive tape.

MALDI is compatible with a time-of-flight (TOF) mass spectrometer in which the ions are released at one point and accelerated by an electric field. The masses of the ions are then determined by measuring the time required for them to traverse a fixed distance in a field-free drift tube [26].

MALDI is used to transform non-absorbing samples into absorbing samples. MALDI works best if the matrix is a strong absorber at the chosen laser wavelength. Nictonic acid, the first useful matrix for polymer molecules, absorbs at the 266 nm laser wavelength. Threshold irradiances for ion formation is $\approx 10^5$–10^6 W cm^{-2}.

MALDI has the advantage that the singly charged ion, either a proton or alkali metal ion adduct, is typically the most intense high-mass ion. Multiple charging is not usually observed, except for high M_w polymers.

MALDI-TOF can be used to make direct determination of very large molecules (10^5–10^6 Da). However, there is a reduced instrumental detection sensitivity for higher-mass ions.

MALDI-TOF may have an inherent upper mass limit due to the availability of suitable matrices and ionization agents and suitable solvents. A matrix may perform well for one class of polymers but have undesirable chemical and photochemically induced reactions with other polymer systems. For some classes of polymers there is a lack of suitable matrices, cationizing agents, and/or solvent systems for sample preparation. Polyethylene is an example of a polymer not readily amenable to MALDI [27].

Photoionization

Photoionization occurs via expulsion of an electron when a molecule absorbs the energy in one or more photons. Resonance-enhanced multiphoton ionization under supersonic jet conditions has great potential as a soft and highly selective ionization method. The resonance-enhanced process proceeds via the absorption of two photons in which the first photon excites the molecule to a resonant intermediate excited state, and the second photon ionizes the molecule. The ability to obtain energy-resolved ionization is a unique feature of resonance-enhanced photoionization.

Mass-resolved excitation spectra are performed by selecting the time interval which corresponds to the molecular ion of interest and monitoring its intensity as a function of excitation wavelength. A molecular ion sometimes undergoes dissociation to produce fragment ions, which is attributed to fast energy relaxation and the succeeding dissociation from an intermediate state.

Fragments are ionized by absorption of a single vacuum ultraviolet photon with an energy just above the ionization threshold. Unlike field ionization which may produce significant amounts of both protonated molecules (MH^+) and radical ions ($M^{\bullet+}$) during ionization, photoionization results only in the formation of radical cations.

Mass analyzer

The mass analyzer separates ions according to the mass/charge (m/z) ratio. The type of mass analyzer used determines the mass resolution ($R = M/\Delta M$) and the dependence of the resolution on mass. Several types of mass analyzers are used in mass spectrometry including:

- classic magnetic sector with single and double focusing,
- quadrupole analyzer,
- time-of-flight (TOF),
- Fourier transform ion cyclotron resonance (FT-ICR),
- ion trap (IT).

Magnetic sector

The magnetic sector instrument was the basis of MS spectrometry for many years. Magnetic sector instrumentation is based on the principle that ionized substances moving through a magnetic field do so in curved paths. Due to momentum characteristics, heavier substances will curve less than lighter ones. Cycling the strength of the field causes the ions of different masses to strike a detector at different times in the cycle. A diagram of the magnetic sector analyzer is shown in Fig. 10.3.

This magnetic analyzer technique uses a direction-focusing device that produces a magnetic field perpendicular to the direction of ion travel. The effect is to bring to a common focus all ions of a given momentum with the same mass-to-charge ratio.

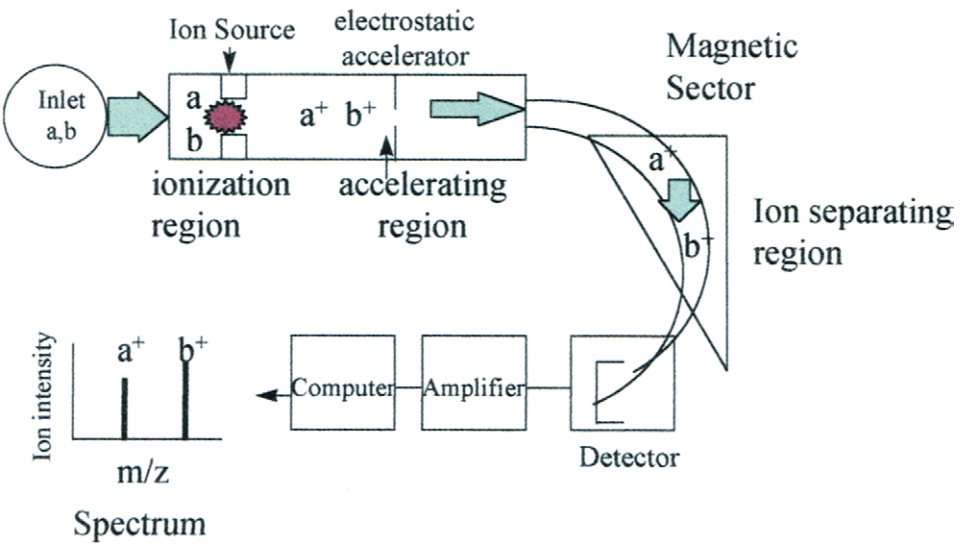

Fig. 10.3. Diagram of a magnetic sector mass analyzer with electron ionization.

The mass to charge ratio for a single focusing magnetic sector is given by:

$$\frac{m}{z} = \frac{er^2B^2}{2V}$$

where m is the ion mass, z is the charge, e is the electron charge, r is the radius of the magnet, B is the magnetic field and V is the accelerating voltage. To obtain a mass spectrum, either the accelerating voltage or the magnetic field strength is varied exponentially.

One can also have double and triple focusing mass spectrometers which significantly enhance the resolution. These instruments are expensive, difficult to operate and maintain, require high voltage operation, and a good vacuum. Magnetic sector systems have high resolution that is independent of the mass.

Quadrupole analyzer

A quadrupole analyzer is a mass filter that creates a quadrupole electric or negative field with a direct current component and a radio-frequency (rf) component in such a manner to allow transmission only of ions having a selected mass-to-charge ratio. Positive ions formed in the ion source are extracted with the quadrupole filter with a 600- or 1000-Da mass range. The system consists of four rods which form the parallel sides of a rectangular tube (Fig. 10.4). The rods have charges of the same type opposing each other. A dc voltage superimposed on a rf field connected to the quadrupole creates an electric field between the poles. Ions of a known mass will pass through this field and are detection. Variation of the field allows different ions to be detected.

Quadrupole ion trap analyzer

A quadrupole ion trap analyzer produces a three-dimensionally rotationally symmetrical quadrupole field capable of storing ions at selected mass-to-charge ratios [28,29]. The system is relatively inexpensive, simple in design with moderate scan rates (>0.2 s/scan). However, it is limited to a low mass range (~2000 Da) and only has unit mass resolution.

Time-of-flight MS

A time-of-flight (TOF) mass analyzer is the simplest type of mass spectrometer. A TOF spectrometer measures the flight time of ions with an equivalent kinetic energy over a fixed distance of usually 1–2 m [30]. A diagram of the basic components of the linear TOF mass spectrometer [31] is shown in Fig. 10.5.

Ions are formed in a short source region (Fig. 10.5) under an electric field E_s which accelerates the ions into the long tubular drift region which has no electric

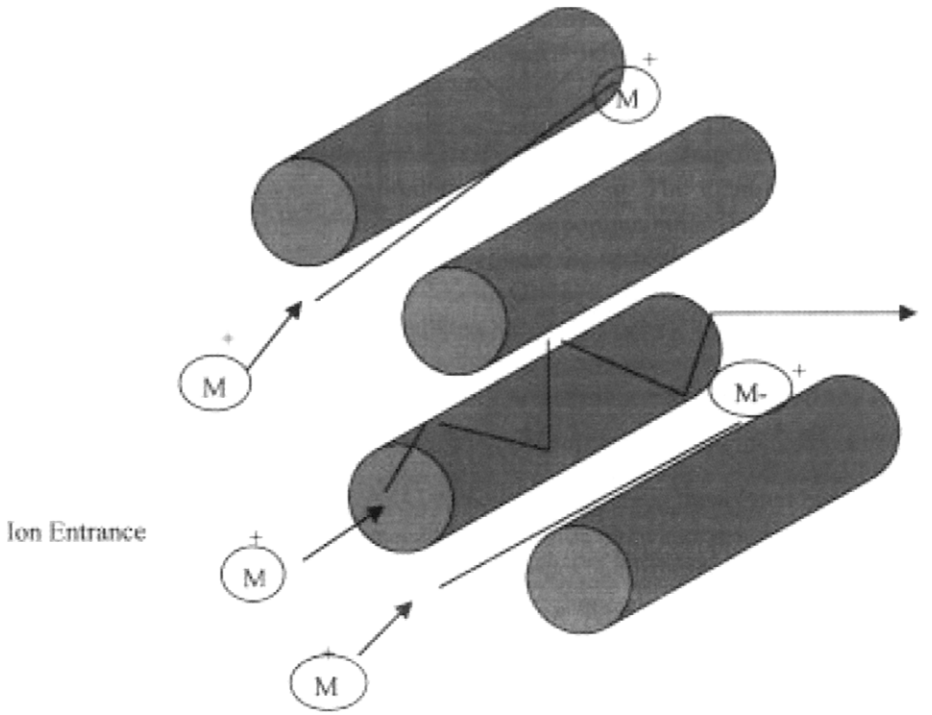

Fig. 10.4. A schematic diagram of quadrupole MS instrumentation.

field. Mass separation in a TOF mass spectrometer is accomplished when a packet of monoenergitic ions is released into the field-free drift region. Ideally, all ions enter the drift region with the same kinetic energy, KE,

$$\mathrm{KE} = zeE_s$$

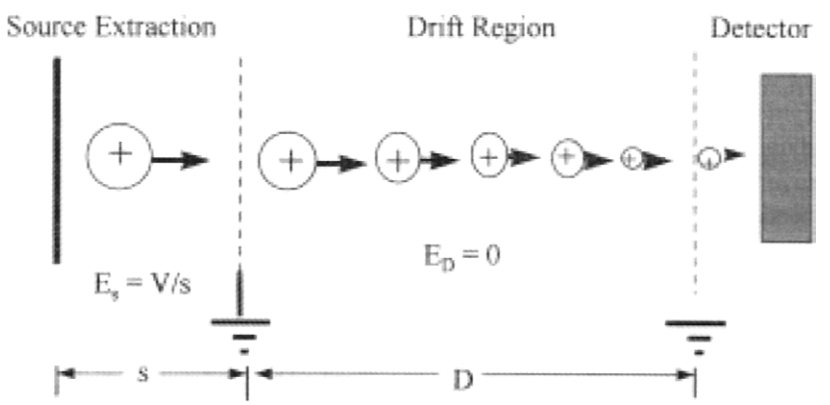

Fig. 10.5. Schematic of the basic components of the linear TOF instrument. (Adapted from Ref. [31, fig. 1].)

where e is the charge on the electron and z is the number of charges. However, they will have different velocities, v,

$$v = \left[\frac{zeE_s}{m}\right]^{1/2}$$

where m is the mass. The flight time (t) is proportional to the square root of the mass of the ion. The flight time required to move through the drift region is given by:

$$t = \left[\frac{m}{zeE_s}\right]^{1/2} D$$

where D is the length of the tube or drift region. At the end of the drift path, the ions will within a time span of some tens to some hundreds of ms (micro), arrive at the detector as mass selected ion packages one after another. The TOF spectrum is initially obtained as a temporal spectrum reporting the number of ions arriving at each time. The time spectrum can be converted directly to mass spectrum using:

$$\frac{m}{z} = 2eE_s\left(\frac{t}{D}\right)^2$$

If the accelerating voltage ($V = E_s$) and drift length are known, one can determine the mass-to-charge ratio (m/z) directly. However, masses are calibrated using an internal calibrant or external standard and the empirical equation

$$\frac{m}{z} = at^2 + b$$

where the constants a and b are determined by measuring the flight times for known masses. The accuracy in mass determination approaches 0.1% (i.e. 10 mass units at 10,000).

The unique advantage of TOF is the measurement of the masses of all the ions produced essentially at the same time with the production of complete spectra from each ion-gating event. This combined with a mass range limited only by the detector's ability to convert the arrival of an ion into a measurable electric signal makes TOF a powerful mass analyzer. Most of the ions injected into a TOF mass analyzer can be detected and this yields sensitivity improvements over scanning analyzers such as magnetic sectors, quadrupoles and ion traps.

Due to the small differences in time (ns to ms) fast detectors are required (typical detectors are 1–4 ns). In a TOF mass spectrometer, the resolution of the mass analysis is directly related to the resolution of the time measurement itself. A complicating effect for TOF is that ions can be generated with non-zero initial kinetic energy which leads to line broadening and loss of resolution. Thus $E + \Delta E = (1/2)(v + \Delta v)^2$ causes this amount of broadening of the peak at each mass. TOF is a simple and reliable method which yields very fast scanning times (<0.1 ms/scan) and can

separate very large masses (~1,000,000 Da). However, due to the broadening effect discussed above the resolution is relatively low and is proportional to 1/M.

One means of correcting for the effects of the initial kinetic energy distribution is to use the reflectron [32]. The use of a reflectron more than doubles the effective path length. The reflectron consists of a series of rings and/or grids with voltages that increase up to a value slightly higher than the voltage of the ion source. The ions are reflected depending on their incoming energies. Ions with larger energies will penetrate the reflectron more deeply and will have longer flight paths. Thus arriving at the detector at about the same time as less energetic ions. The reflectron does not diminish the energy spread of the ions, it corrects for the effects on their arrival at the detector. Because the path length is increased, the mass resolution is improved. Delayed extraction is the other technique that improves resolution.

Fourier transform MS

FT-MS is an ion cyclotron resonance instrument in which trapped ions are excited rapidly and detected simultaneously using Fourier transform techniques [33]. The term FT-ICR is also used. The ICR is a device to determine the mass-to-charge ratio of an ion by measuring its cyclotron frequency. The advantages of FT-MS are accurate mass determination (sub-ppm) with very high resolution (tens of thousands or even millions), high sensitivity (sub-femtomole) and multistage capability [34].

The basic hardware for FT-MS consists of an analyzer cell which is centered in a strong homogeneous magnetic field. When the ions are formed in the analyzer cell, they move in circular orbits. Ion trapping along the z-axis (magnetic field direction) results from applying an electrostatic potential to the two plates on the ends of the cell. The trapped ions are stored in the analyzer cell. The polarity of the voltage applied to the trapping plates determines whether positive or negative ions are retained in the cell. The ion motion is the cyclotron motion whose frequency is directly proportional to the magnetic field and inversely proportional to the mass-to-charge ratio, m/z, of the ions. Ions of different m/z have unique cyclotron frequencies.

FT-MS detection is carried out by monitoring the image current induced by the orbiting ion packet as it cycles between the two receiver plates. In order to detect the cyclotron frequency, an excitation pulse is applied so the ions become packets. As a result of the excitation step, a time-dependent signal is generated on the receiver plates. The image current is converted to a voltage, amplified, digitized and Fourier transformed to yield the frequency spectrum. A mass spectrum is then obtained by converting the frequency to mass. Because the frequency can be measured accurately, the mass of an ion can be determined to one part in 10^9 or better.

Increasing the magnetic field strength will increase both the upper mass range and the mass resolution. A theoretical investigation of the factors concluded that the upper mass limit is m/z 50,000 in a 3-T magnet, m/z 300,000 in a 7-T magnet, and $> m/z$ 1,000,000 in a 14-T magnet [35].

FT-MS ion detection is nondestructive and can be repeated in order to signal average and improve the S/N ratio. For mass resolution in the low to medium range, the FT-MS experiments require a few milliseconds to acquire a complete mass spectrum.

Multiple steps of ion isolation and subsequent dissociation can be linked together to investigate of several 'generations' of fragment ions. This process, referred to as MS^n (where n is the number of MS/MS stages), is easily accomplished with FT-MS.

Electrical detection

The primary detection event for MS is the ion-to-electron conversion in microchannel plates (MCP) or secondary electron multiplier (SEM) detectors. An electron multiplier is used as a detection device to multiply current in an electron beam by incidence of the accelerated electrons upon the surface of the electrode. This collision yields a number of secondary ions greater than the number of incident ions. The background noise of these detectors is extremely small, so the signal to noise ratio is very high making for high sensitivity. Detectors based on MCP technology are more prone to loss of gain with increase in signal strength (saturation) than those based on electron multiplier technology. When saturated, the individual channels in an MCP require a finite time for 'recovery' before the benefits of their maximum gain can be reestablished [36]. Detector issues such as jitter, sampling rates, band width and detector response influence the performance of the MS instrumentation and must be properly controlled.

Data stations

All modern MS instruments have dedicated computer systems for control of the spectrometer, collection of the data, and analysis. The mass plots are normalized to a common gain factor and the electronic baseline is subtracted. From the measurement of the absolute mass of an oligomer or a polymer fragment ion, the most probable elemental composition can be computed by the mass spectrometer data station. The more accurate the mass measurement, the greater are the restrictions on the chemical formulas that can be computed. Generally, this elemental composition information is all that is needed to confirm a suspected molecular structure.

An example of the use of the computational capabilities of the data station to assist in the identification of a chemical substructure in a crosslinked polymers has been reported [37]. A mass spectrum from a melamine-based paint was obtained using a carbon dioxide laser. A peak at m/z 163.075700 was observed. Using a data station, a value of 163.075356 was calculated corresponding to a chemical formula of ^{16}O-2, ^{12}C-10, ^{1}H-11. Choices are limited by specifying that the chemical composition only

contains C, H, and O. This formula is only 2.11 ppm from the measured peak. The computer also calculated that this formula would have 5.5 ($C_{10}H_{11}O_2$ = 5.5 RDB) rings plus double bonds. The structure identified was:

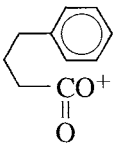

Tandem mass spectrometry (MS/MS)

Tandem mass spectrometry (MS/MS) provides enhanced capabilities for elucidating molecular structures, especially for compounds present in mixtures. Tandem mass spectrometry provides a dimension of supplemental ion analysis which may be more discriminating than increased mass resolution. The technique is particularly useful for analysis of the individual components in mixtures of oligomers.

Pyrolysis-MS of polymers

MS has been used extensively to investigate the fragmentation of polymers. This information is important for understanding polymer thermal stability and the related degradation mechanisms. In MS terminology, a *fragment* refers to a segment cut from a polymer chains. A *cluster* is a group of peaks corresponding to ions from a particular fragment. A *pattern* refers to a repeating sequence of clusters.

Pyrolysis can be induced in at least four ways:

(1) Curie-point pyrolysis which involves rapid inductive heating (10^2–10^4 K/s),
(2) laser irradiation,
(3) slower resistive heating of a sample in a direct insertion probe or furnace pyrolyzer,
(4) heating resistively with a metal filament.

Direct pyrolysis mass spectrometry

Pyrolysis, when coupled with spectrometric techniques is a generally useful approach to the analysis of polymers and other complex nonvolatile organic materials. Direct probe heating is carried out over a suitable temperature range and spectra are obtained using EI, CI (others may be used) and field ionization. For polyolefin polymers, volatile products are typically observed at every carbon number to masses well above 1000 Da using FI-MS. In general, the distributions are similar for the various polyolefin polymers. In general, alkene oligomer ($M_w = x_n$, where x is the mass of the olefin monomer and n is the oligomer number) are dominate at low

masses. Dialkene oligomers tended to be the most prominent pyrolysates at higher masses.

MS of a polymer sample can be obtained by pyrolysis through the use of a direct exposure probe in which the sample is placed on a surface such as a metal plate or wire and is inserted into the ion source of the mass spectrometer and rapidly heated. The pyrolysis products formed are quickly volatilized. The pyrolysis is achieved adjacent to the electron emitter so that the pyrolysis products, once formed are immediately ionized. The flight time of the ions from the ion source to the detector is of the order of microseconds and sample and the degraded species flow into the spectrometer for ionization. Short residence times for the sample in the hot zone allow detection of high masses and some insight into the primary steps in the degradation reaction. There is a kinetic competition between evaporation and decomposition which is temperature dependent. At higher temperatures, vaporization processes are favored over decomposition. Short residence times for the sample in the hot zone allow detection of high masses and some insight into the primary steps in the degradation reaction. But inevitably, for thermal vaporization of polymers, considerable degradation and fragmentation occurs. For direct analysis, the limitation of MS is that these two processes may not be reproducible or well understood mechanistically.

The degradation mechanism suggests that the first step is homolytic main chain cleavage which produces two free radicals. These may be primary, secondary or tertiary radicals, depending on the polymer structure. The chain end radicals then undergo 'back biting' processes in which the radical site is transferred along the chain, with concurrent rearrangement of the hydrogen atoms. When the formation of both secondary and tertiary internal radicals is possible, the tertiary radicals are strongly preferred. These internal radicals then undergo γ-scission and hydrogen abstraction to yield both volatile and nonvolatile products.

The main problem connected with direct pyrolysis technique is the identification of the products in the spectrum produced by the thermal degradation. In fact, in the mass spectrum of a polymer, the molecular ions of the thermal products will appear mixed with the fragment ions formed in the ionizing step.

Pyrolysis-GCMS of polymers

Commonly, gas chromatography combined with mass spectrometry is used to characterize pyrolysates. Pyrolysis gas chromatography/MS is particularly useful as the pyrolysis products are separated prior to the mass determination. A further innovation is to combine TGA with MS which allows the observation of the thermal behavior of components in the sample. In this system, one can identify the gases evolved from a polymer sample as the sample is heated under controlled conditions. The real time data enables assessment of the temperatures at which various components evolve and also readily aids in identification of overlapping weight losses in the thermogravimetric data.

Applications of mass spectrometry to polymers

Identification of polymeric systems

MS is a powerful technique for identifying chemical compounds, and vast catalogs of spectra have been acquired for this purpose. The identification relies on reproducible pyrolysis and fragmentation of the compound [38]. High mass resolution to determine chemical formula can facilitate the identification.

Polymers contain primarily only C, H, O, N. S, Si, P and the halogens. The nominal mass of an element is defined as the mass of the element's most abundant naturally occurring isotope. For all of these elements, the most abundant isotope is the isotope with the lowest mass; therefore, the nominal mass is equal to that of the lowest mass isotope.

The common elements are divided into X, X + 1 and X + 2 elements based on their naturally occurring isotopes. X elements are those elements that have only one naturally occurring isotopes such as H, F, I and P. X + 1 elements are those elements which have only two naturally occurring isotopes, and these are separated by one mass unit such as C and N. X + 2 elements are those elements that have an isotope two mass units higher than the most abundant isotope such as Cl, Br, S, Si. Ions containing the X + 2 elements exhibit a distinguishing pattern of peaks, two m/z units apart. All molecules that contain only atoms of C, H, O, S, Si and P and the halogens will have an even molecular weight.

When MALDI is used, fragmentation is minimized. The MALDI-FT spectrum of polyoxypropylenediamine (a difunctional primary amine polymer used in epoxy systems) is shown in Fig. 10.6.

Identification of polymeric additives

The problem in additive analysis for polymers is the presence of bulk polymer with a low concentration of additives. MS has demonstrated great utility recently in identifying polymer additives that are stable or yield meaningful fragment ions [39]. MS is the method of choice for identifying polymer additives. There is a need for being able to identify additives directly in the polymer matrix. Extraction and separation techniques which are normally used for isolating the additive are slow and laborious processes. There is also the possibility of compromising the integrity of the additive mixture. MS offers rapid generation of the mass spectra of polymer additives directly from their host polymer matrices.

The laser desorption/laser photoionization (L2MS) offers a strategy to analyze the additives in the presence of the bulk polymer [40]. The feature of this approach is the ability to selectively ionize the species of interest — in this case, the additives. For efficient ionization, a molecule must possess a suitable chromophore at the wavelength of the ionizing radiation. Therefore, by careful choice of the UV ionization

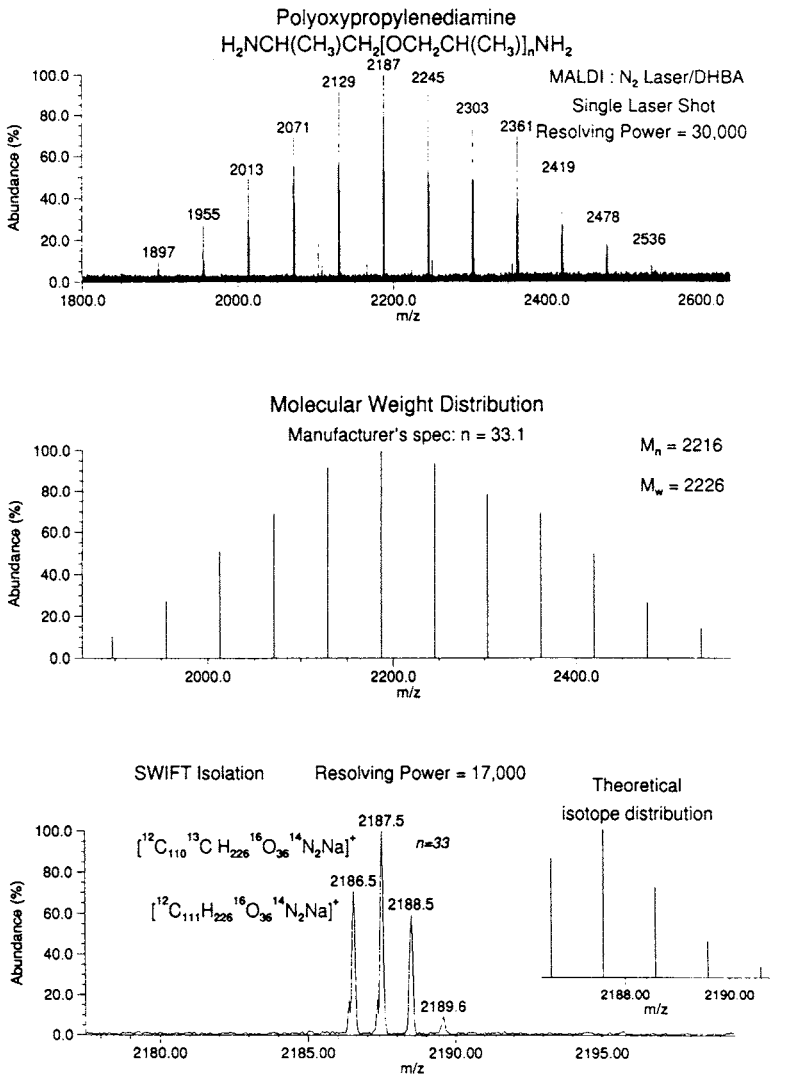

Fig. 10.6. MALDI-FTMS determination of a common industrial polymer, polyoxypropylenediamine (top). The oligomers observed are cationized by sodium attachment and the average molecular mass information is shown in the middle spectrum. The manufacturer's specification of average molecular mass corresponding to 33.1 (mass 2170) repeating units agrees with the mass distribution of 2193. The measured isotopic peak distribution for the $n = 33$ oligomer is compared with the theoretical isotopic distribution in the bottom spectrum. (Source: Ref. [37, fig. 2].)

wavelength, the additives can be selectively detected relative to the polymer itself. The polymer additives such as antioxidants and UV stabilizers have appreciable absorption in the UV region of the spectrum and are selectively ionized in preference to the non-UV absorbing host polymer. No extraction, purification, or preconcentration steps are required for the L2MS experiment.

L2MS has been used to directly analyze additives in a range of polymers [41]. The L2MS method decouples the desorption and the ionization step in order that each step can be optimized. An infrared laser at 10.6 μm is used to irradiate the polymer and cause ablation through a pyrolysis mechanism. During this step, the polymer is thermally decomposed and ejected while the additives remain intact. With a delay time of about 20 μs, the additives are then subjected to a selective ionization with a UV laser at 266 nm through a resonant two-photon ionization step. Finally, the ions are mass separated, and recorded in a time-of-flight mass spectrometer.

This approach was tested by examining the MS of polypropylene containing 0.15 wt% of a commercial antioxidant termed Irganox 1330 (1,3,5,-tris(3,5-di-*tert*-butyl-4-hydroxybenzyl)-2,4,6, trimethylbenzene) and 0.05% of a second antioxidant termed Irgafox 168 (tris(2,4-di-*tert*-butylphenyl)phosphite). The photoinization was developed using UV wavelengths of 193 and 266 nm yield mass spectra which unambiguously indicated the presence of Irganox 1330 and Irgafos 168 in the polypropylene matrix. No signals are observed indicating the presence of the polymer matrix in the mass spectra.

Fig. 10.7 shows the L2MS spectra of a pure antioxidant Santowhite powder (4,4′-butylidene-bis-6-(4-methyl-2-*tert*-butylphenol) and the in situ spectrum of Santowhite powder in a POM injection molded bar. The Santowhite powder was present at only 0.1 wt%. The laser desorption was produced with an CO_2 IR laser with power density of$\sim 6 \times 10^6$ W/cm^{-2} at 10.6 μm and laser photoionization was produced at UV 266 nm with a power density of $\sim 2\, M_w$ cm^{-2}.

Mass spectrometric determination of molecular weight and molecular weight distribution

Classical methods (SEC, vapor pressure osmometry, light scattering) of determining molecular weight of polymers are averaging methods whereas MS may examine the individual oligomers. Classical methods do not normally determine directly the molecular weight distribution (MWD), where (in principle) MS does. If the intensity of the mass peaks in mixtures is proportional to the molar amount of each species, mass spectra of polymers can yield number-average molecular weights. In order to achieve correct mass measurements, the ionization yield of the various oligomer species present must not undergo any discrimination with respect to their mass values, and the detector must show a constant response to ions over a wide range of mass numbers. The problem with MS is that the transformation probability for cationized oligomers can decrease by 1–2 orders of magnitude with increase in mass [42,43]. For PEG this occurs between 100 and 3500 mass units, and for PS between 2000 and 7000 mass units.

As the molecular weight increases, the sensitivity of mass spectrometry is challenged by:

- decreased sensitivity due to loss of detector efficiency,
- decreased sensitivity from the requirement of lower (molar) sample loading.

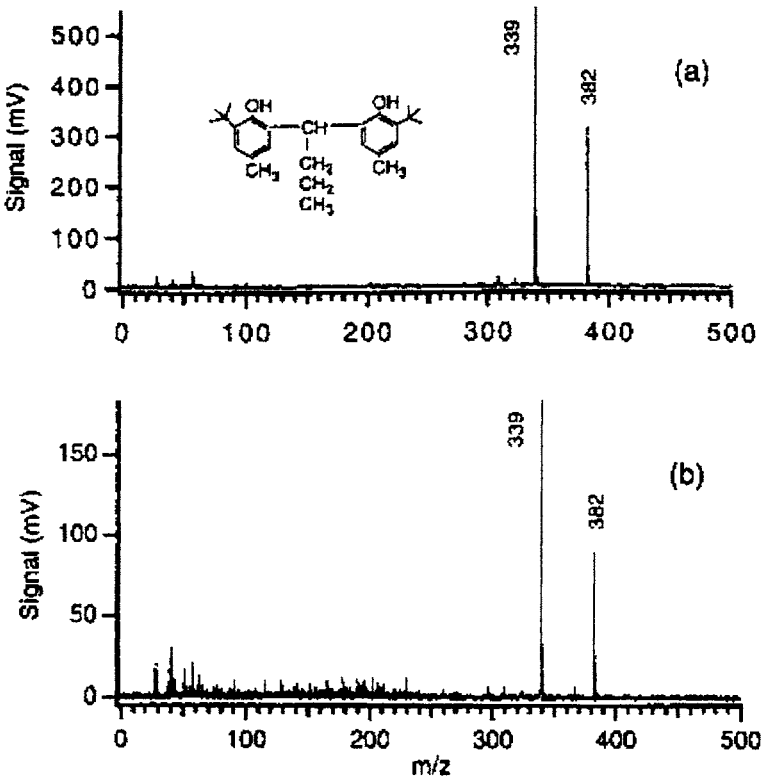

Fig. 10.7. The two-step laser mass spectra of (a) a pure antioxidant Santowhite power and (b) the in situ spectrum of Santowhite power in a POM injection molded bar. The Santowhite powder was present at only 0.1 wt%. (Source: Ref. [41, fig. 4].)

These sensitivity limitations are most difficult to overcome. Another problem in determining the molecular weight of polymers in the high-mass range is mass calibration.

It has been suggested "that the nature of the MALDI sample preparation is the principle impediment to the analysis of high molecular weight polymers, rather than instrumental limitations". The mass limit of the MALDI process is affected by the chemistry/photochemistry of the polymer, the availability of suitable matrices and ionization agents, and suitable solvents. MALDI analysis fails to resolve the high molecular weight regions of the distributions [44].

Concerns have also been expressed about extending the technique to the determination of M_w for polydispersed polymer samples (PD $>$ 1.5). Success has been achieved in overcoming these limitations by fractionation using GPC and MALDI MS for analysis of the collected fractions [45,46]. Using MS as the detector for GPC, it is possible to measure absolute molecular weights.

In summary MALDI only works when $M_w/M_n < 1.5$. Otherwise mass discrimination is too much to accurately give MWD. The best approach for polydisperse materials is to take SEC fractions and use MALDI to calibrate the SEC.

Determination of polymer structure using mass spectroscopy

For relatively low molecular weight polymers, where the instrumental resolution is sufficient to separate oligomer peaks, accurate mass and MS/MS analysis of the individual oligomers can be achieved to provide information about the repeat unit, end groups and other modifications of the polymer [47].

An example is shown in Fig. 10.8 in which the MALDI mass spectrum of the poly(ethylene glycol 3841), molecular weight standard, $HO-P_{87}-OH$.

The distribution of oligomers is clearly resolved. The peaks are equally spaced at 44 mass units apart demonstrating the molecular weight of the repeating oxyethylene unit. There are also a series of smaller peaks at 16 mass units higher than each of the main oligomer peaks due to the corresponding potassiated chains. No evidence of fragmentation is observed in this spectrum. M_w and M_n were calculated to be 3881 and 3841 gms/mole respectively. This gives a dispersity of M_w/M_n of 1.01 and a corresponding number average degree of polymerization of 87. When a comparison

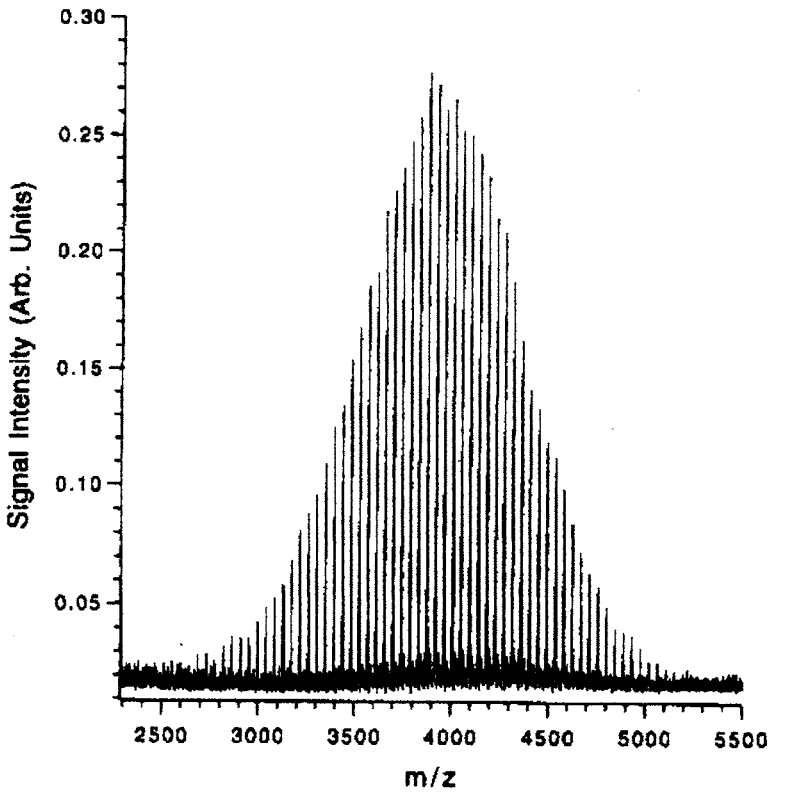

Fig. 10.8. The MALDI mass spectrum of the poly(ethylene glycol 3841), molecular weight standard, $HO-EP_{87}-OH$. (Source: S. Lee, M.A. Winnik, R.M. Whittal and L. Li, Macromolecules 29 (1996) 3060, fig. 7.)

is made with GPC a higher dispersity of 1.05 was noted for the polymer. The matrix used was 2-[(4-hydroxyphenyl)azo]benzoic acid (HABA).

End group determination in polymers using MS

For many polymers, the characterization of the polymer chain ends is important. The identification and determination of the end groups helps clarify the polymerization mechanism. Polymers synthesized by radical polymerization generally have a variety of end groups such as initiator fragments, chain transfer agents, solvent residues and the olefinic and saturated groups formed through disproportionation termination.

Identification of end groups

A study of anionically polymerized PMMA ($M_n \sim 10^6$) and radically polymerized PMMA with BPO (Benzyl Phennylene Oxide) as an initiator using pyrolysis GC and GC-MS. The pyrolysis GC was dominated by peaks up to trimers. The most abundant peak in the MS is the MMA monomer arising from the depolymerization of PMMA. The strongest end group peaks were assigned as cumene and α-methyl styrene suggesting that the anionic initiator was cumyl-K. An additional 5 end groups peaks were assigned on the basis that they were also formed from the moiety of the cumyl end group [48].

Insight into the polymerization of poly(bisphenol-A-carbonate (PC) was obtained from the MALDI-TOF spectrum. The spectrum consisted of two series of peaks corresponding to molecular ions of cyclic oligomers (m/z at $254n + 23$) and open-chain ethyl carbonate terminated compounds (m/z $254n + 141$). The presence of the ethyl-terminated oligomers indicates that the polymerization reaction was stopped by addition of ethanol [49].

Determination of termination mode in radical polymerization

Evaluation of the termination mode in free radical polymerized styrene and methacrylate thermally initiated with 2,2′-azo(isobutyronitrile (AIBN) using MALDI-TOF was made by integrating the peaks in the MS which corresponded with either one or two initiator fragments per polymer chain. Table 10.1 shows a comparison of the experimentally determined mass values for the oligomers 9,10 and 11 for PMMA demonstrating that both disproportionation and coupling are occurring. The mass of the oligomer chains comprises the monomeric MMA units, one or two initiator fragments and a sodium cation originating from the MALDI ionization process.

The ratios of the termination modes (disproportionation to recombination) were determined by summing all of the disproportionation peak areas and dividing by the sum of all of the combination peak areas. This ratio for methyl methacrylate and styrene was 4.37 ± 1.1 and 0.057 ± 0.032, respectively, at 90°C.

Table 10.1
Comparison of experimental vs. theoretical mass for PMMA for different modes of termination

Mode of termination	Origin	Theoretical mass (Da)	Experimental mass (Da)
Disproportionation	Na^+ + 1AIBN + 9MMA	1059.5	1060.2
Combination	Na^+ + 2AIBN + 9MMA	1091.5	1092.5
Disproportionation	Na^+ + 1AIBN + 10MMA	1159.6	1160.1
Combination	Na^+ + 2AIBN + 10MMA	1191.6	1192.6
Disproportionation	Na^+ + 1AIBN + 11MMA	1259.6	1260.2
Combination	Na^+ + 2AIBN + 11MMA	1291.6	1292.6

Characterization of end groups in functionalized polymers

Functionally heterogeneous polymers can be analyzed by MS with respect to the degree of polymerization and the type of functional groups [50].

End group analysis is important for polyester polymers as their condensation with isocyanates to form polyurethane elastomers depends on hydroxyl termination. Using MALDI MS, isotopic abundance spectra of a carboxyl–hydroxyl-terminated intact oligomer chain at 1241.8 was in agreement with the theoretical formula. Similarly, MS spectra for a hydroxyl–hydroxyl-terminated oligomer showed a 1113.8 peak in agreement with the theoretical formula. The presence of the acid termination was confirmed by acid titration which gave a value of 20.2 mg of KOH/g of sample which compared well with the value of 18.2 mg of KOH/g of sample calculated from the MS spectra [51].

Poly(ethylene glycol) derivatives are used for controlled drug delivery or slow release drugs. The full characterization of these compounds is important in studying their function and metabolism and in quality control and regulatory approval. Poly-(ethylene glycol) derivatives have one or two end groups as functional molecules. The dosage determination is partially dependent on the success of the derivatization of the polymer and on the number-average molecular weight. Examples of such molecules are polyoxyethylene bis(ephedrine) and polyoxyethylene bis(acetaminophen). The structures of these molecules are shown below.

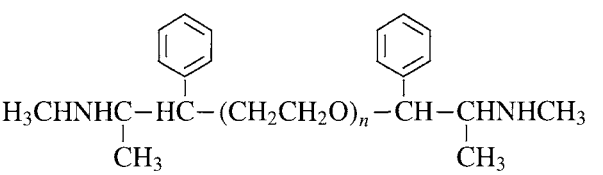

polyoxyethylene bis(ephedrine)

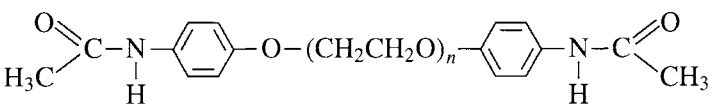

polyoxyethylene bis(acetaminophen)

Table 10.2
Mass measurement of selected oligomer peaks for polyoxyethylene bis(ephedrine) showing experimental and theoretical masses for one and two labeled species

Oligomer of PEO	One label ephedrine	Oligomer of PEO	Two labels ephedrine	Observed
63	2963.59	60	3978.66	3978.66
73	3404.13	70	3419.19	3419.03
83	3844.66	80	3859.72	3859.70
93	4285.20	90	4300.26	4299.99

MALDI MS can determine if the polymer is derivatized on one or both ends and can determine the number average molecular weight simultaneously. The mass difference between a singly labeled polyoxyethylene bis(ephedrine) with n oxyethylene repeat units and a doubly labeled polymer with $n = 3$ oxyethylene units is 15.06 units. This makes it possible to determine whether the oligomers are singly or doubly labeled with ephedrine. The experimental data is shown in Table 10.2.

Clearly, the data shows that the sample has ephedrine linked at both ends of the polymer [52].

Nature of linkages between monomers in polymers

The determination of the type of linkages between monomers in oligosaccharides has been determined by partial degradation and subsequent mass spectroscopic analysis [53]. Discrimination of the 1-4, 1-6, 1-3 and 1-2 linkages in linear oligosaccharides was possible. Negative ion FAB mass spectra showed that the ion fragmentation was found to be diagnostic of the glycoside linkage between adjacent sugar units.

Characterization of copolymers

> *...copolymer mass spectra are extremely rich in information, providing both chain length and composition data. This gives mass spectrometry the potential to become the ideal analytical technique for the study of copolymerizations since it is capable of providing not only the chain length distribution but also the composition distribution at each chain length. Currently, no other analytical technique offers this kind of potential.*
>
> — K.G. Suddaby et al. [55].

For characterization of copolymers, it is desirable to separate the composition from the chain length. From a mass spectrum, it is necessary to deconvolute the spectrum, assigning each peak to a unique molecular species. The mass spectrum, if sufficient mass resolution exists, is representative of all of the reactions that have occurred during the formation of the copolymer. Thus, the mass spectrum is determined by the kinetics of the copolymerization. The mass spectrum allows the determination

of the average composition at each chain length, so each mass spectrum can be considered to contain internal replicates. Thus the data for each chain can be used for an estimation of the reactivity ratios.

Characterization of intact copolymer oligomers

There are two approaches to the analysis of mass spectra of copolymers. First, a direct analysis of the spectra from intact copolymer oligomers and using selective fragmentation techniques with analysis of the structure of the fragments in terms of *n*-ads.

An example of the approach using MS of intact copolymer [54] is shown in Fig. 10.9 for a copolymer of methylmethacrylate/methacrylic acid (MMA/MAA) obtained by ESI-FTMS when electrosprayed with a 0.5% NH_4Cl, tetrahydrofuran–methanol solution.

A distribution of the various sequences of MMA and MAA that make up the $n = 8$ oligomer is measured. The sequences range from MMA_3MAA_5 to MMA_8. MALDI-TOF has been used to characterize the copolymerization of methyl methacrylate (MMA) and *n*-butyl methacrylate (BMA) [55]. The mass spectrum of a 50/50 MMA/BMA obtained using 2,5-dihydroxybenzoic acid doped with sodium acetate as the matrix is shown in Fig. 10.10.

The spectra show a large number of peaks reflecting the large number of identifiable species in the copolymer. Many of the peaks can be assigned with masses corresponding to mass $= x(100.12) + y(142.20) + 22.99$, where x and y correspond to the numbers of MMA and BMA units, respectively. Thus, the copolymer mass spectrum can be deconvoluted into a bivariate distribution of composition and chain length. The result is shown in Fig. 10.11.

An analysis of the MS of three different copolymer compositions was made using the terminal copolymerization model and the kinetic parameters were calculated.

Characterization of copolymers by fragmentation methods

MS analysis of copolymer microstructure utilizes oligomers from partial degradation obtained by random or selective cleavage of the AA, BB or AB bonds by a variety of processes including hydrolysis, methanolysis, aminolysis, photolysis, pyrolysis, or ozonolysis [56]. The oligomers generated in the partial degradation process retain the sequence distribution present in the original copolymer.

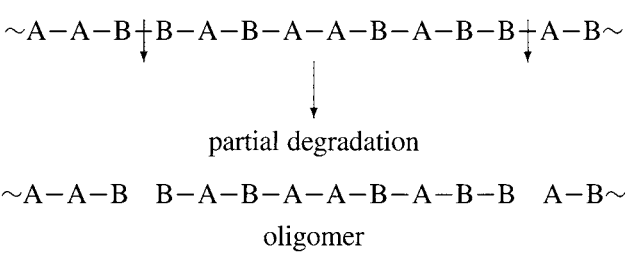

If one assumes that ion fragmentation and detector efficiency are independent of molecular weight, the spectra can be correlated by associating the mass intensities with the number of the various n-ads. The advantage of the MS technique is the detection of longer n-ads then for NMR or IR.

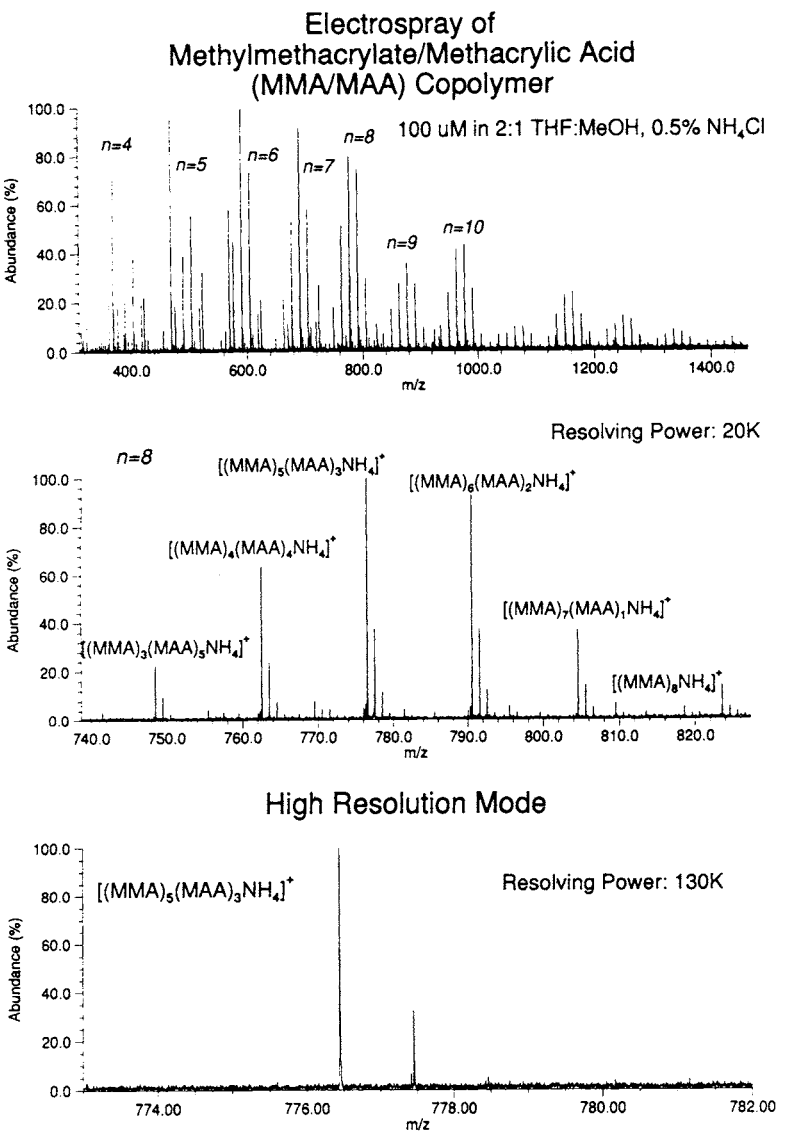

Fig. 10.9. Electrospray ionization FTMS spectrum (top) of a methyl methacrylate/methacrylic acid copolymer. The distribution of methacrylate and methacrylic acid repeating units is illustrated for the $n = 8$ oligomer (middle). The mass spectrum at the bottle illustrates the high resolution that is possible with this technique. (Source: Ref. [37, fig. 4].)

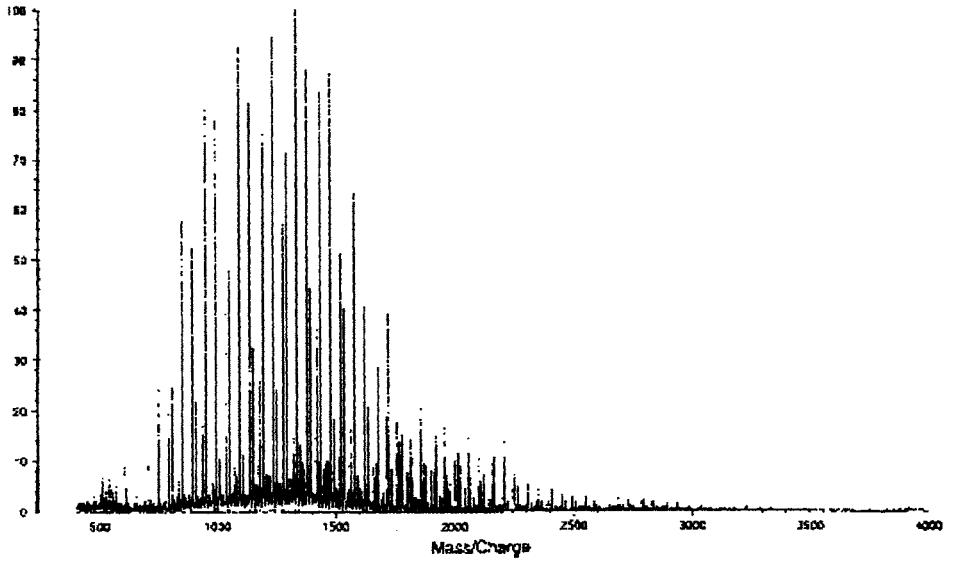

Fig. 10.10. The MALDI-TOF mass spectrum of a 50/50 MMA/BMA copolymerized with AIBN as a thermal initiator. The spectra was obtained using 2,5-dihydroxybenzoic acid doped with sodium acetate as the matrix. (Source: Ref. [55, fig. 3].)

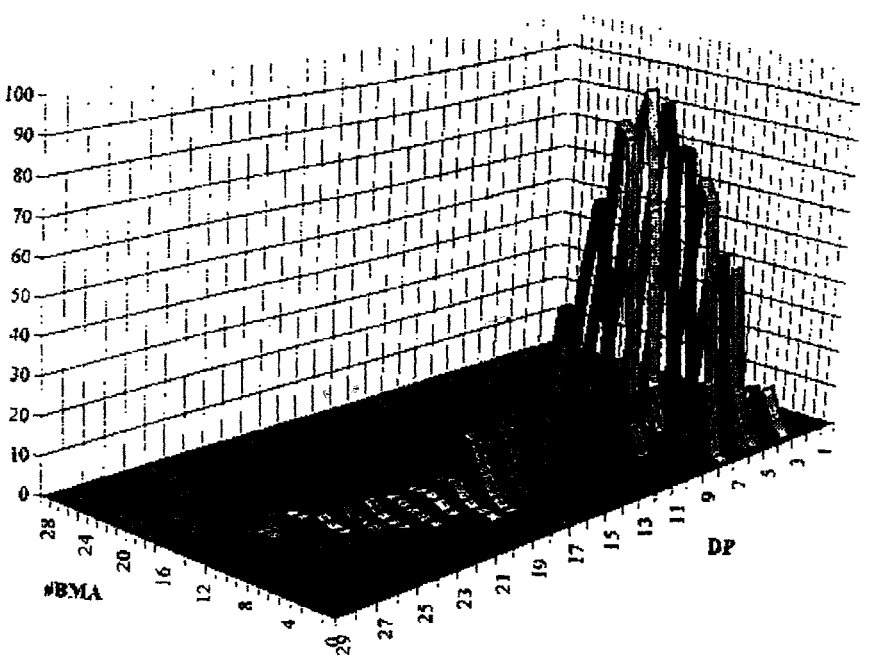

Fig. 10.11. Bivariate distribution in composition and chain length obtained by the deconvolution of MALDI-TOF of the copolymer obtained from a 50/50 mixture of MMA and BMA shown in Fig. 10.10. (Source: Ref. [55, fig. 4].)

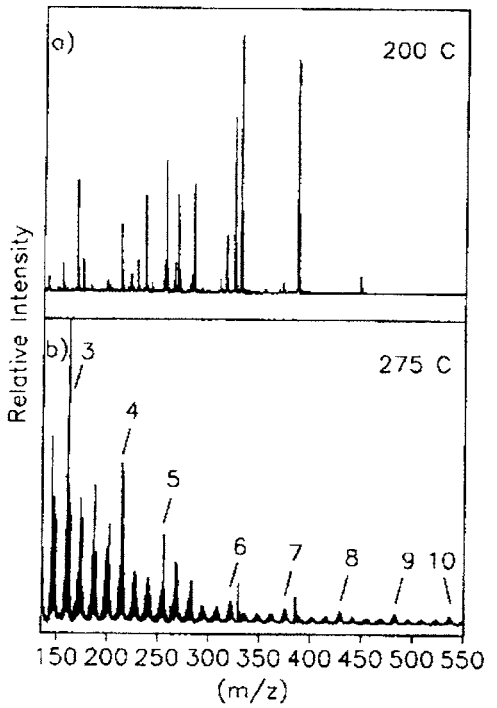

Fig. 10.12. Pyrolysis-photoionization mass spectrum of acrylonitrile–butadiene copolymer: (a) additives at 200°C, and (b) pyrolysis products for the 30–32% acrylonitrile copolymer at 275°C. (Source: Ref. [57, fig. 2].)

Pyrolysis of acrylonitrile-*co*-butadiene copolymers ranging from 19 to 51 wt% acrylonitrile was performed directly in the source region of a TOF mass spectrometer. Initially the samples were heated to 200°C (just below the temperature of polymer degradation) to bake off additives and impurities within the copolymer. The mass spectra of the additives are shown in Fig. 10.12a. When the 30–32% acrylonitrile copolymer was heated to 275°C, the pyrolysis-photoionization mass spectrum obtained is shown in Fig. 10.12b. Preferential cleavage occurs at the β(C−C) bond to either the nitrile bond in an acrylonitrile unit or the C=C in a butadiene unit. This cleavage produces oligomers that are grouped according to the total number of monomers along the backbone. The mass of each oligomer in the group depends on the relative number of acrylonitrile and butadiene units. Oligomer distributions up to the 11-mer are observed [57].

Fig. 10.13 shows the octamer series for four different compositions of the acrylonitrile–butadiene copolymers in the mass range from 19–22% to 51% acrylonitrile.

A plot of the number of acrylonitrile units in each of the measured oligomers is shown in Fig. 10.14 for the four different compositions of the acrylonitrile–butadiene copolymers.

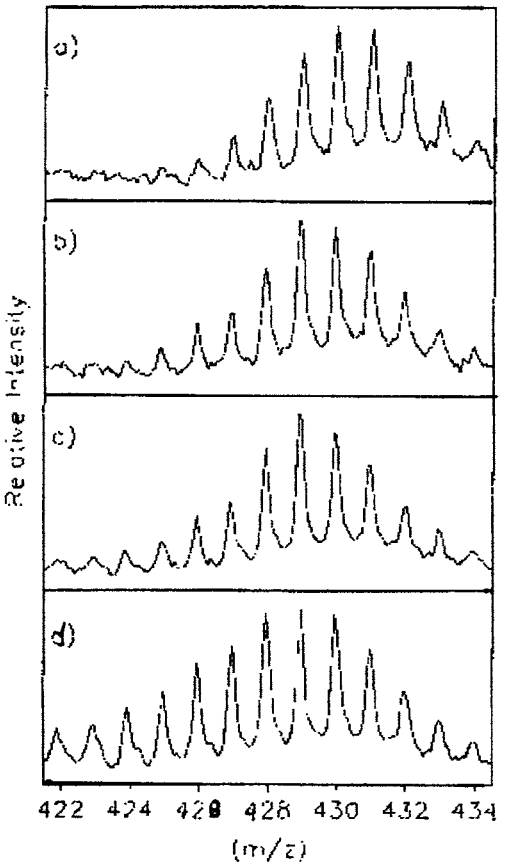

Fig. 10.13. Pyrolysis-photoionization mass spectra expanded in the octamer region for acrylonitrile–butadiene copolymers with compositions of (a) 19–22%, (b) 30–32%, (c) 37–39%, and (d) 51%. (Source: Ref. [57, fig. 3].)

From these results the composition can be calculated and the MS results agree with those reported for the copolymers. Using the knowledge obtained from the oligomers concerning the number of different sequences, it is possible characterize the copolymerization mechanism. The terminal model was found to give the best fit to the data.

Characterization of block copolymers

In principle, a determination of the mass allows for a measurement of the unique composition of block copolymers. It has been possible to determine the molecular weights and molecular weight distributions of both components of a block copolymer of polystyrene-*block*-poly(α-methylstyrene) by using MALDI-TOF [58]. The MALDI/TOF mass spectrum of a block copolymer sample containing 69% styrene and 31% α-methylstyrene is shown in Fig. 10.15.

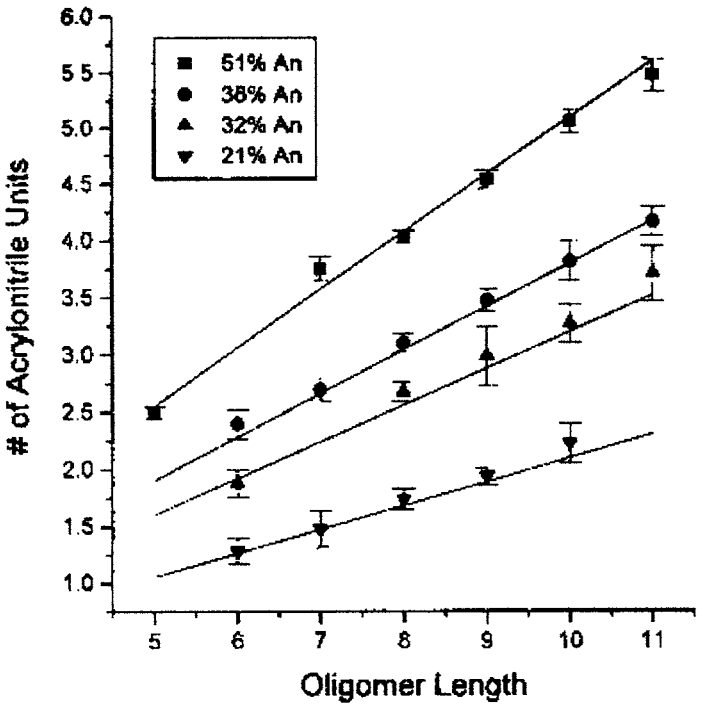

Fig. 10.14. A plot of the number of acrylonitrile units in each oligomer determined from the centroid of each oligomer series. (Source: Ref. [57, fig. 4].)

It is possible to find the number of segments n_A and n_B in a block copolymer by comparing the experimental value of m/z with the calculated molecular weight:

$$\left(\frac{m}{z}\right)_{\text{calc}} = n_A M_A^\circ + n_B M_b^\circ + (\text{additional structural contributions})$$

In the case of the block copolymers of polystyrene-*block*-poly(α-methylstyrene), each molecule contained one butyl group, one hydrogen and a Ag ion acquired during ionization so the

$$\left(\frac{m}{z}\right)_{\text{calc}} = n_A M_A^\circ + n_B M_b^\circ + (M_{\text{butyl}}^\circ + M_{\text{ag}} + M_H)$$

There are two variables in this equation, n_A and n_B so additional information is required to determine the chemical composition. In the MALDI-TOF mass spectrum, the strongest peak was observed at 2970.5 which corresponds to values of $n_A = 7$ and $n_B = 10$ and yields a calculated m/z of 2971.1. Not only did these values give the smallest deviation from the experimental value but agrees with the information that the molar ratio of α-methylstyrene to styrene is less than one. These rules were

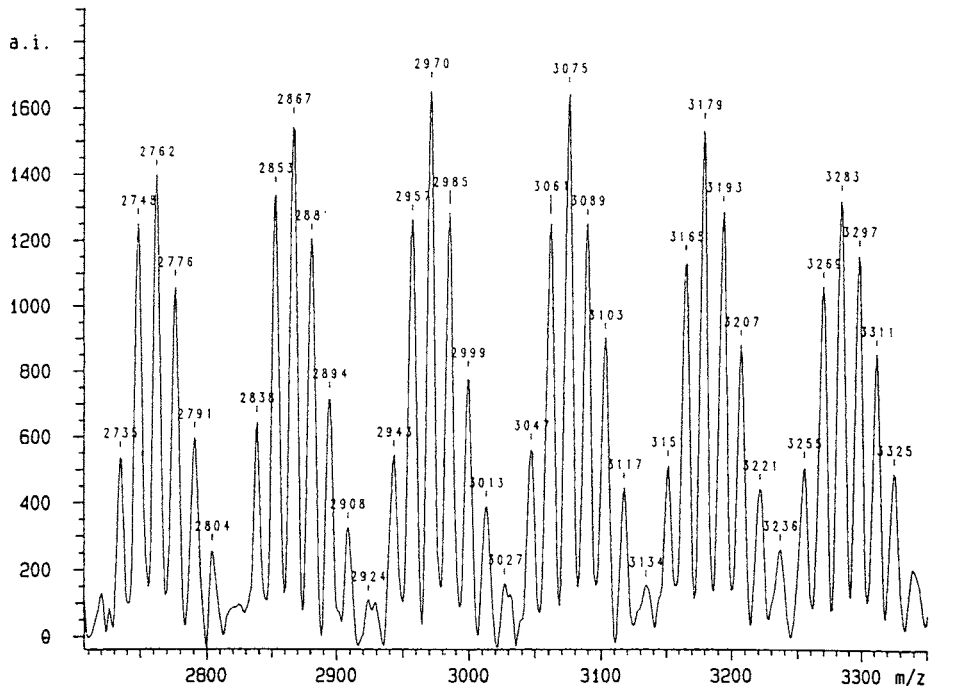

Fig. 10.15. Enlarged detail of the MALDI/TOF mass spectrum of a block copolymer sample containing 69% styrene and 31% α-methylstyrene. (Source: Ref. [58, fig. 1].)

Table 10.3
Assignments of the chemical composition for the strongest MALDI-TOF mass peaks near $m/z = 2970$ for a block copolymer sample containing 69% styrene and 31% α-methylstyrene.

$(m/z)_{exp}$	Block length		$\Delta = (m/z)_{cal} - (m/z)_{exp}$	Integral intensity
	α-methylstyrene	styrene		
2942.9	5	21	1.1	3865
2956.5	6	20	1.6	9442
2970.5	7	19	1.6	11760
2984.7	8	18	1.4	9077
2998.8	9	17	1.3	5285
3012.6	10	16	1.6	2552
3027.0	11	15	1.2	1239

(Source: Ref. [58, table 2].)

applied to the spectra for the series of peaks near 2970 as shown in Table 10.3.

From this table, one can observe that the difference between neighboring peaks within a group is 14 Da. This corresponds to the difference in the molecular weight of α-methylstyrene (118.18) and styrene (104.15). It means that in a group of peaks with increasing mass, the values of the block length of α-methylstyrene are increas-

ing and values of the block length of styrene are decreasing. Based on these mass assignments, it is possible to calculate the experimental distribution of block lengths. The results are shown in Fig. 10.16.

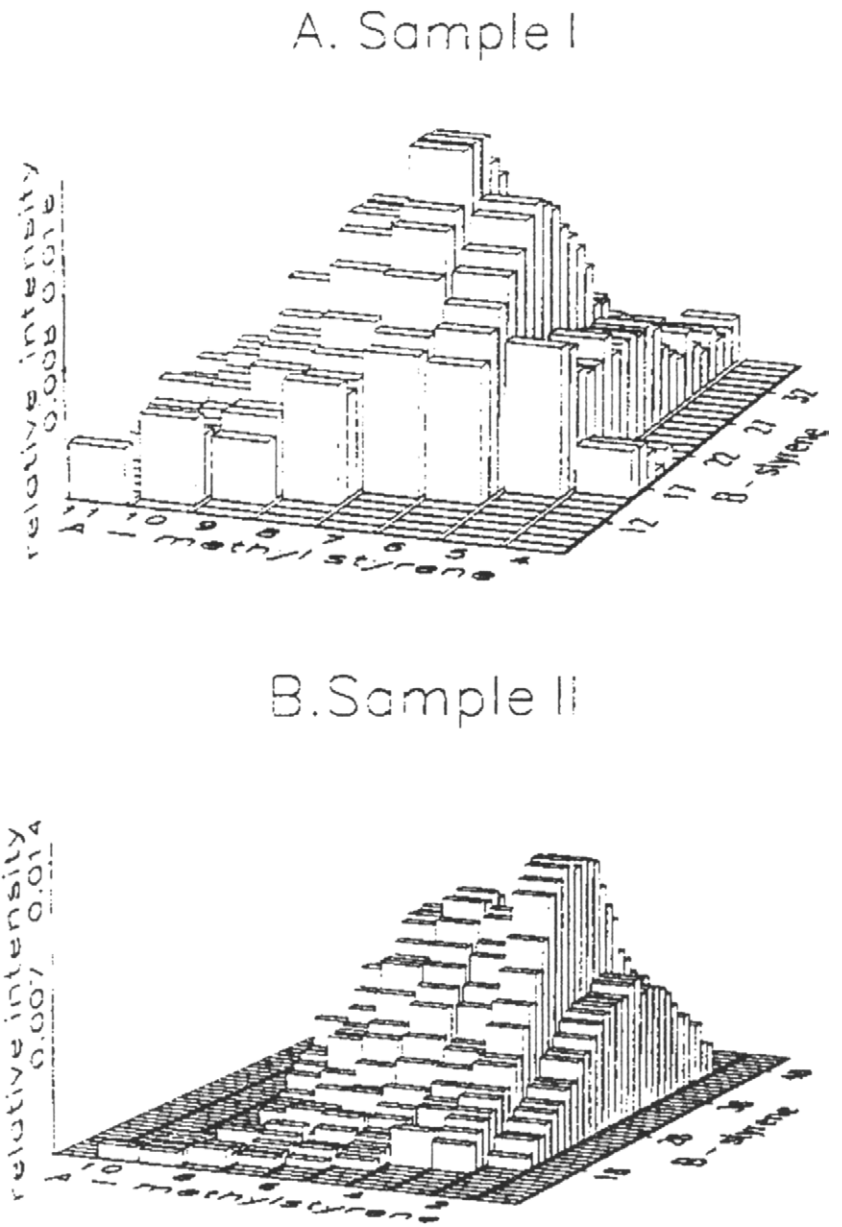

Fig. 10.16. The experimental normalized distribution of units for a block copolymer sample containing 69% styrene and 31% α-methylstyrene. (Source: Ref. [58, fig. 2a].)

Random coupling statistics suggests that for a block copolymer of the (poly A–poly B) type, the distribution of molecular weight of part A is independent of the distribution of molecular weight in part B. The calculated relative intensities reproduce well the shape of the experimental intensities indicating that random coupling statistics apply to the block copolymers of polystyrene-*block*-poly(α-methylstyrene).

Characterization of macrocyclic polymers

Organic macrocycles are difficult to characterize as these large molecules show very small differences in their molar mass and functionality. MALDI-TOF offers the possibility for characterization of these systems if the macrocyclics can be examined without fragmentation or reorganization. Macrocyclic polystyrenes have been synthesized and compared to their linear precursors [59]. A linear precursor of α-diethyl acetal-ω-styrenyl-polystyrene is first prepared. The chain cyclization by end-to-end ring closure was performed by transforming the acetal end group into a iodo ether end group followed by the addition of $SnCl_4$ for promoting the cyclization reaction. Macrocyclic polystyrenes were obtained in the mass range up to 20,000 g/mol. The linear precursor is expected to have the following chemical structure:

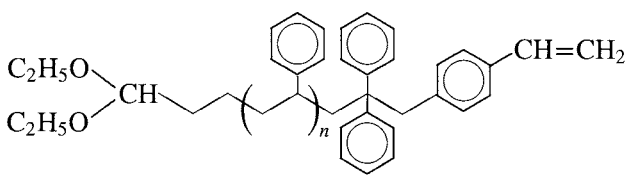

The MALDI-TOF spectrum of a low molar mass linear precursor (M_w = 1860) is shown in Fig. 10.17.

The spectrum in Fig. 10.17 shows a number of peaks having a peak-to-peak mass increment of 104 g/mol which corresponds exactly to the mass of the repeat unit in the linear precursor. Additionally, only one oligomer series is observed. For the

Table 10.4
Calculated and measured mass numbers (m/z) for oligomers of the linear precursor PS (M_w = 1860; $M + Ag^+ = 536 + 104_n$)

Length of oligomer	Calculated mass	Expected mass	Length of oligomer	Calculated mass	Expected mass
6	1160.9	1160	14	1994.1	1993
7	1265.1	1265	15	2098.3	2098
8	1369.2	1369	16	2202.2	2202
9	1473.4	1473	17	2306.6	2307
10	1577.5	1577	18	2410.7	2411
11	1681,7	1682	19	2514.9	2516
12	1785.8	1786	20	2619.0	2619
13	1890.0	1890	21	2723.2	2724

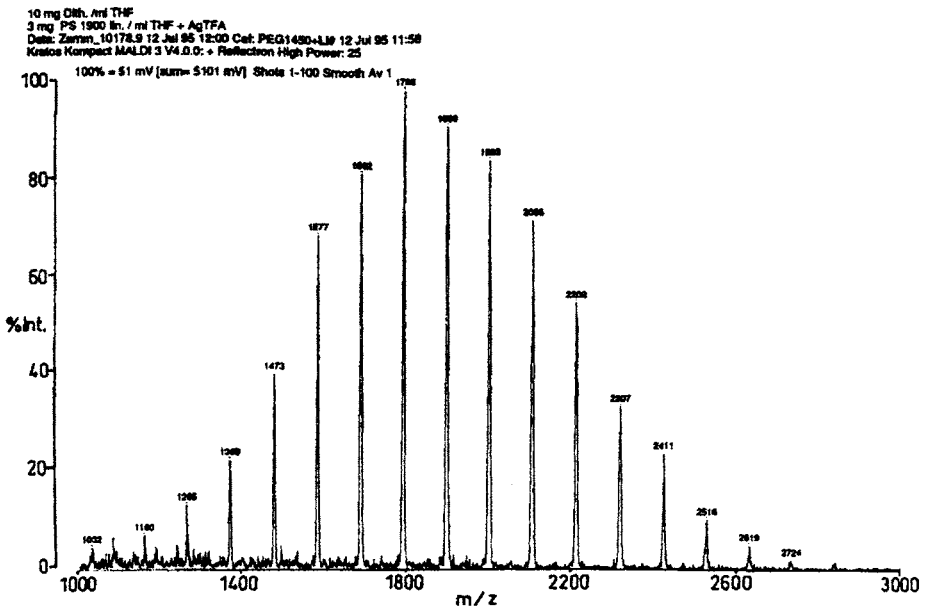

Fig. 10.17. The MALDI-TOF spectrum of a low molar mass linear precursor (M_w = 1860). (Source: Ref. [59, fig. 1].)

proposed chemical structure of the linear precursor the mass numbers are calculated by $M + Ag^+ = 536 + 104n$. The observed peaks are compared with the calculated peaks in Table 10.4.

The mass spectrum corresponds to the proposed chemical structure of the linear precursor. After the linear precursor is subjected to the cyclization reaction, the MALDI-TOF mass spectrum obtained is shown in Fig. 10.18.

Again, an oligomer distribution with peak-to-peak mass increments of 104 Da is obtained (peak series 1). This peak series is accompanied by two minor peak series 2 and 3 with the same mass increment. The expected cyclic structure is shown below:

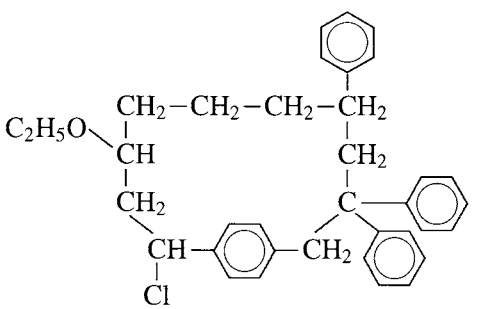

However, *the observed mass numbers do not fit this structure*. Apparently, during the preparation or the UV irradiation, the Cl was extracted and the following structure

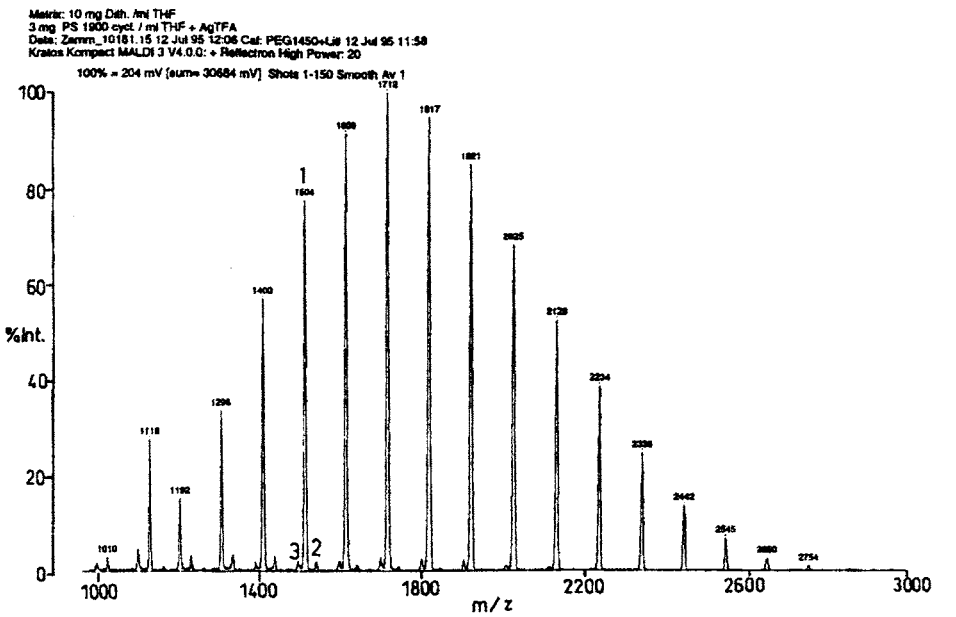

Fig. 10.18. The MALDI-TOF spectrum with a matrix of dithranol of the cyclized polystyrene obtained from the low molar mass linear precursor (M_w = 1860). (Source: Ref. [59, fig. 2].)

was formed:

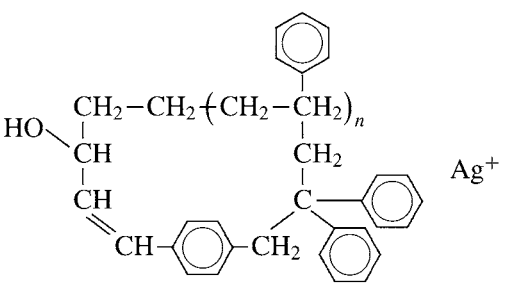

(I)

$$M + Ag^+ = 463 + 104n$$

This structure fits the peak series 1 by $M + Ag^+ = 463 + 104n$ and can be formed via the intermediate formation of a α-formyl-terminated precursor from the α-acetal compound and subsequent cyclization. The differences in the mass values of the cyclized oligomers are 73 g/mol resulting from the transformation of the acetal group in the cyclization reaction. The minor peak series 2 and 3 correspond to slightly rearranged cyclic structures. There is no evidence of residual linear structures in the MALDI spectra.

Expectations for the future

Modern MS, particularly with advent of MALDI, is finally causing polymer chemists to be interested in MS as a structural analysis tool. Historically, most polymer people have used IR and NMR routinely — but have pretty much ignored MS. I expect that in the future MS will join IR and NMR as regular techniques using by polymer chemists. Each technique has unique capabilities, and often a combination of more than one method is needed to solve complex problems in identification and chemical structure determination.

References

[1] Biemann, K., Mass Spectrometry: Organic Chemical Applications. McGraw Hill, New York, NY, 1962.
[2] Schulten, H.-R., Lattimer, R.P., Mass Spectrom. Rev. 3 (1984) 231.
[3] Montaudo, G., TRIP 4 (1996) 81.
[4] Montaudo, G., Rapid Commun. Mass Spectrom. 5 (1991) 95.
[5] Lattimer, R.P., Harris, R.E., Schulten, H.-R., Rubber Chem. Technol. 58 (1985) 3188.
[6] Wampler, T.P. (Ed.), Appl. Pyrolysis Handbook. Marcel Dekker, New York, NY, 1995.
[7] Prokai, L., Field Desorption Mass Spectrometry. Marcel Dekker, New York, NY, 1990.
[8] Beynon, J., in: J.D. Waldron (Ed.), Advances in Mass Spectrometry, Vol. 1. Pergamon Press, New York, NY, 1959.
[9] Tyler, A.N., Clayton, E., Green, B.N., Anal. Chem. 68 (1996) 3561.
[10] Beckewitz, F., Hewsinger, H., Angew. Makromol. Chem. 46 (1975) 143.
[11] Foti, S., Maravigna, P., Montaudo, G.J., J. Polym. Sci., Polym. Chem. Ed. 19 (1981) 1679.
[12] Harrison, A.G., Chemical Ionization Mass Spectrometry, 2nd edition. CRC Press, Boca Raton, FL, 1992.
[13] Shimizu, Y., Munson, B.J., J. Polym. Sci., Polym Chem. Ed. 17 (1979) 1991.
[14] Benninhoven, A., Hagenoff, B., Niehuis, E., Anal. Chem. 65 (1993) 630A.
[15] Dong, X., Proctor, A., Hercules, D.M., Macromolecules 30 (1997) 63.
[16] Barber, M., Bordoli, R.S., Sedgwick, R.D., Tyler, A.N., Nature 293 (1981) 270.
[17] Barber, M., Bordoli, R.S., Elliot, G.J., Sedgwick, R.D., Tyler, A.N., Anal Chem. 54 (1982) 645A.
[18] Gardella, J.A., Graham, S.W., Hercules, D.M., in: E.D. Carver (Ed.), Structural Characterization of Polymeric Materials by Laser Desorption Mass Spectrometry. Advances in Chemistry Series 303, American Chemical Society, Washington DC, 1983, p. 635.
[19] Kebarle, P., Tang, L., Anal. Chem. 65 (1993) 972A.
[20] Mann, M., Meng, C.K., Fenn, J.B., Anal. Chem. 61 (1989) 1702.
[21] Fei, X., Murray, K.K., Anal. Chem. 68 (1996) 3555.
[22] Vertes, A., Gijbels, R., Adams, F. (Eds.), Laser Ionization Mass Analysis. John Wiley and Sons, New York, NY, 1993.
[23] Vaeck, L., Van F., Gijbels, R., Fresenius J. Anal. Chem. 337 (1990) 755.
[24] Creel, H.S., Trends Polym. Sci. 1 (1993) 336.
[25] Schriemer, D.C., Li, L., Anal. Chem. 68 (1996) 2721.
[26] Bahr, U., Deppe, A., Karas, M., Hillenkamp, F., Giessmann, U., Anal. Chem. 64 (1992) 2866.
[27] Schriemer, D.C., Li, L., Anal. Chem. 69 (1997) 4160.
[28] March, R.E., Hughes, R.J., Quadrupole Storage Mass Spectrometry. Wiley, New York, NY, 1989.
[29] Todd, J.F.J., Mass Spectrom. Rev. 19 (1991) 3.
[30] Wiley, W.C., McLaren, I.H., Rev. Sci. Instrum. 26 (1955) 1150.
[31] Cotter, R.J., Anal. Chem. R. J. 64 (1992) 1027A.
[32] Mamyrin, B.A., Karatajev, V.H, Shmikk, D.V., Zagulin, V.A., Soviet Phys. JETP 37 (1973) 513.

[33] Marshall, A.G., Schweikhard, L., Int. J. Mass Spectrom. Ion Proc. 118/119 (1992) 37.
[34] Buchanan, M.V., Hettich, R.L., Anal. Chem. 65 (1993) 245A.
[35] May, M.A., Grosshans, P.B., Marshall, A.G., Int. J. Mass Spectrom. Ion Proc. 120 (1992) 193.
[36] Schriemer, D.S. Li, L., Anal Chem. 69 (1997) 4176.
[37] Campana, J.E., Sheng, L.-S., Shew, S.L., Winger, B.E., Trend Anal. Chem. 13 (1994) 239.
[38] Chapman, J.R., Practical Organic Mass Spectrometry, 2nd edition. Wiley, New York, NY, 1994.
[39] Lattimer, R.P., J. Anal. Appl. Pyrol. 26 (1993) 65.
[40] Wright, S.J., Dale, M.J., Langridge-Smith, P.R.R., Zhan, Q., Zenobi, R., Anal. Chem. 68 (1996) 3585.
[41] Zhan, Q., Zenobi, R., Wright, S.J., Langridge-Smith, P.R.R., Macromolecules 29 (1996) 7865.
[42] McCloskey, J.A. (Ed.), Methods in Enzymology, Vol. 193. Academic Press, San Diego, CA, 1990, p. 61.
[43] Mattern, D.E., Hercules, D., Anal. Chem. 57 (1985) 2041.
[44] Zammit, M.D., Davis, T.P., Haddleton, D.M., Suddaby, K.G., Macromolecules 30 (1997) 1915.
[45] Montaudo, G., Montaudo, M.S., Puglisi, C., Samperi, F., Rapid Commun. Mass Spectrom. 9 (1995) 1158.
[46] Danis, P.O., Sauch, D.A., Huby, F.J., Polym. Prepr. (Am. Chem. Soc., Div. Polym. Chem.) 37 (1996) 311.
[47] Whittal, R.M., Li, L., Lee, S., Winnik, M.A., Macromol. Rapid Commun. 17 (1996) 59.
[48] Ohtani, H., Takehana, Y., Tsuge, S., Macromolecules 30 (1997) 2542.
[49] Vitalini, D., Mineo, P., Scamporrino, E., Macromolecules 30 (1997) 5285.
[50] Braun, D., Ghahary, R., Pasch, H., Polymer 36 (1996) 1999.
[51] Chaudhary, A.K., Critchley, G., Diaf, A., Beckman, E.J., Russell, A.J., Macromolecules 29 (1996) 2213.
[52] Whittal, R.M., Schriemer, D.C., Li, L., Anal Chem. 68 (1997) 2734.
[53] Ballistreri, A., Garozzo, D., Guiffrida, M., Impallonmeni, G., Montaudo, G., Anal. Chem. 62 (1990) 279.
[54] Campana, J.E., Sheng, L.-S., Shew, S.L., Winger, B.E., Trend Anal. Chem. 13 (1994) 239.
[55] Suddaby, K.G., Hunt, K.H., Haddleton, D.M., Macromolecules 29 (1996) 8642.
[56] Montaudo, M.S., Montaudo, G., Makromol. Chem. Macromol. Symp. 65 (1993) 269.
[57] Zoller, D.L., Johnston, M.V., Anal. Chem. 69 (1997) 379.
[58] Wilczek-Vera, G., Danis, P.O., Eisenberg, A., Macromolecules 29 (1996) 4036.
[59] Pasch, H., Deffieus, A., Ghahary, R., Schapacher, M., Rique-Lurbet, L., Macromolecules 30 (1997) 98.

Subject index